UNIVERSITY OF ŽILINA

TRANSCOM PROCEEDINGS 2015

11-th EUROPEAN CONFERENCE OF YOUNG RESEARCHERS AND SCIENTISTS

under the auspices of

Tatiana Čorejová
Rector of the University of Žilina

SECTION 7

CIVIL ENGINEERING

ŽILINA June 22 - 24, 2015
SLOVAK REPUBLIC

Edited by Andrea Porubiaková, Michal Mokryš

ISBN: 978-80-554-1049-4
ISSN of Transcom Proceedings CD-Rom version: 1339-9799
ISSN of Transcom Proceedings online version: 1339-9829
(http://www.transcom-conference.com/transcom-archive)

TRANSCOM 2015
11th European conference of young researchers and scientists

TRANSCOM 2015, the 11th international conference of young European scientists, postgraduate students and their tutors, aims to establish and expand international contacts and co-operation. The main purpose of the conference is to provide young scientists with an encouraging and stimulating environment in which they present results of their research to the scientific community. TRANSCOM has been organised regularly every other year since 1995. Between 160 and 400 young researchers and scientists participate regularly in the event. The conference is organised for postgraduate students and young scientists up to the age of 35 and their tutors. Young workers are expected to present the results they had achieved.

The conference is organised by the University of Žilina. It is the university with about 13 000 graduate and postgraduate students. The university offers Bachelor, Master and PhD programmes in the fields of transport, telecommunications, forensic engineering, management operations, information systems, in mechanical, civil, electrical, special engineering and in social sciences incl. natural sciences.

SECTIONS AND SCIENTIFIC COMMITTEE

1. TRANSPORT AND COMMUNICATIONS TECHNOLOGY.

Scientific committee: Adamko Norbert (SK), Bugaj Martin (SK), Buzna Ľuboš (SK), Drozdziel Paweł (PL), Jánošíková Ľudmila (SK), Madleňák Radovan (SK), Rievaj Vladimír (SK), Teichmann Dušan (CZ)

2. ECONOMICS AND MANAGEMENT.

Scientific committee: Blašková Martina (SK), Hittmár Štefan (SK), Borkowski Stanisław (PL), Gregor Milan (SK), Kucharčíková Alžbeta (SK), Matuszek Józef (PL), Mičieta Branislav (SK), Rostášová Mária (SK), Sroka Włodzimierz (PL), Tomová Anna (SK), Zhivitskaya Helena (BLR)

3. INFORMATION AND COMMUNICATION TECHNOLOGIES.

Scientific committee: Dado Milan (SK), Hudec Róbert (SK), Kharchenko Vyacheslav (UKR), Klimo Martin (SK), Kršák Emil (SK), Matiaško Karol (SK), Pancerz Krzysztof (PL), Spalek Juraj (SK), Švadlenka Libor (CZ), Vaculík Juraj (SK), Vašinek Vladimír (CZ), Vrček Neven (HR)

4. ELECTRIC POWER SYSTEMS. ELECTRICAL AND ELECTRONIC ENGINEERING.

Scientific committee: Altus Juraj (SK), Brandštetter Pavel (CZ), Bury Peter (SK), Cacciato Mario (I), Čápová Klára (SK), Dobrucký Branislav (SK), Chernoyarov Oleg Vyacheslavovich (RU), Janoušek Ladislav (SK), Luft Mirosław (PL), Szychta Elżbieta (PL), Špánik Pavol (SK), Vittek Ján (SK)

5. MATERIAL ENGINEERING. MECHANICAL ENGINEERING TECHNOLOGIES.
Scientific committee: Adamczak Stanisław (PL), Guagliano Mario (I), Konečná Radomila (SK), Kunz Ludvík (CZ), Kuric Ivan (SK), Meško Jozef (SK), Neslušan Miroslav (SK), Takács János (H), Ungureanu Nicolae Stelian (RO)

6. MACHINES AND EQUIPMENT. TRANSPORT MEANS. APPLIED MECHANICS.
Scientific committee: Gerlici Juraj (SK), Chudzikiewicz Andrzej (PL), Malcho Milan (SK), Medvecký Štefan (SK), Zapoměl Jaroslav (CZ), Žmindák Milan (SK)

7. CIVIL ENGINEERING.
Scientific committee: Bujňák Ján (SK), Ižvolt Libor (SK), Segalini Andrea (I)

8. NATURAL SCIENCES (APPLIED MATHEMATICS). SOCIAL SCIENCES.
Scientific committee: Dopita Miroslav (CZ), Dzhalladova Irrada (UKR), Grecmanová Helena (SK), Katuščák Dušan (SK), Marčoková Mariana (SK), Růžičková Miroslava (SK), Šindelářová Jaromíra (CZ)

9. SECURITY ENGINEERING. FORENSIC ENGINEERING.
Scientific committee: Kasanický Gustáv (SK), Kohút Pavol (SK), Navrátil Leoš (CZ), Řehák David (CZ), Sventeková Eva (SK), Šimák Ladislav (SK), Zagorecki Adam (UK), Zamiar Zenon (PL)

ORGANIZING COMMITTEE

CHAIRPERSONS Čelko Ján, Bokůvka Otakar

EXECUTIVE SECRETARY Vráblová Helena

MEMBERS Bašťovanský Ronald, Belan Juraj, Bendík Ján, Brída Peter, Brůna Marek, Bulej Vladimír, Číba Jakub, Čičmancová Silvia, Dulina Ľuboslav, Ďurovec Martin, Florková Zuzana, Gašová Zuzana, Grajcaríková Petra, Grejták Marek, Herda Miloš, Hőger Marek, Hrbček Jozef, Hruboš Marián, Hudák Martin, Koman Gabriel, Kutaj Milan, Kuzmová Mária, Kvet Michal, Magdolen Marián, Malichová Eva, Maňurová Mária, Masárová Gabriela, Metruk Rastislav, Murgašová Veronika, Nosek Radovan, Odrobiňák Jaroslav, Olešnaníková Veronika, Oriešková Veronika, Palkechová Marcela, Porubiaková Andrea, Pšenáková Zuzana, Račko Ján, Rusinková Jana, Rypáková Martina, Semanová Štefánia, Stankovičová Zuzana, Šarafín Peter, Šimková Ivana, Šušlik Ľuboš, Vaško Alan, Vincúrová Gabriela.

SECTION 7 CIVIL ENGINEERING

REVIEWERS:

Brodňan Miroslav
Bujňák Ján
Čelko Ján
Decký Martin
Drusa Marián
Ďurčanská Daniela
Ďurica Pavol
Grinč Michal
Grúňová Zuzana
Hlinka Richard
Hodas Stanislav
Chebeň Vlastimil
Ižvolt Libor
Ižvoltová Jana
Jandačka Dušan
Jandačka Jozef
Juráš Peter
Komačka Jozef
Korenková Renáta
Kortiš Ján
Koteš Peter
Kotula Patrik
Kováč Matúš
Krušinský Peter
Liptáková Tatiana
Leštach Jaroslav
Malcho Milan
Markovičová Lenka
Masarovičová Soňa
Nikolič Ružica
Nguyen Giang
Odrobiňák Jaroslav
Pais Luis José Andrade
Papán Daniel
Ponechal Radoslav
Remek Ľuboš
Remišová Eva
Slabej Martin
Šestáková Janka
Šrámek Juraj
Štaffenová Daniela
Vičan Josef
Vlček Jozef
Zgútová Katarína

Note:

Author/s are responsible for language contents of their papers

CONTENTS

TRANSCOM 2015, 22-24 June 2015
University of Žilina, Žilina, Slovak Republic

An Influence of the Cyclic Load on Shear Capacity of the Reinforced Concrete Beams

[*]Kamil Bacharz
[*]Kielce University of Technology, Faculty of Civil Engineering and Architecture, Department of Materials Strength and Concrete Structures, Al. 100-lecia P.P., 01026 Kielce, Poland,
{kbacharz}@tu.kielce.pl

Abstract. In this paper, an influence of cyclic load on the shear capacity of a reinforced concrete beams is investigated. The study was conducted on 4 statically determinate single-span reinforced concrete beams with the rectangular cross section. Those beams were loaded monotonically and cyclically. The cyclic was a sinusoidal with 100,000 cycles at each stage of load. Cycles were varied by different ranges of loading forces. The results in the form of destructive force were obtained. On the basis of a comparative analysis of those forces from monotonic and cyclic load it can be concluded that in the cyclic load decreases the shear capacity.

Keywords: reinforced concrete, beam, shear, capacity, cyclic load.

1. Introduction

The current trend in the design of striving for ever smaller cross sections of construction elements leads to increase their strain. Hence it is necessary to the development of modern science, both in the field of materials science and methods of dimensioning. Development of modern materials science, provides opportunities for the use of more durable materials. In the case of reinforced concrete elements those are concrete and reinforcing steel. Also important role is played increasingly sophisticated computational methods such as, the very popular and widely used in the computational computer programs, a finite element method, or a neural networks, which are in the phase of research but giving very promising results. These methods include a large number of factors affecting on the work of structure including a load method of the element. As demonstrated in papers [1] and [2] there is not just a matter of the load values are important. Also the way of its realization affects on the work the element. Therefore, method of implementation load should be considered in the analysis of the limit states of reinforced concrete beams, namely, whether the beam is subjected to a monotonically load or a variable either a cyclic load. In [3] is presented an analysis of the impact of the way of the realization of the load to bending capacity of statically indeterminate reinforced concrete beams. It shows a significant effect of the cyclic loading on the bending capacity of a reinforced concrete elements statically indeterminate. In the case of double-span beams tested under cyclic load the actual bending capacity with respect to the theoretical load capacity, estimated by plastic hinges was lower by 20%. Such behavior of the elements wasn't found in the case of statically determinate single-span beams cyclically loaded which failure was caused by the bending moment

Due to above, it was decided to expand the analysis of the effect of cyclic load on the load capacity of the reinforced concrete beams, which failure was caused shear force. The analysis was based on the results of the study of four single-span reinforced concrete beams destroyed by shear, varied by loading program. Beams had a rectangular cross section with dimensions 120x300mm and the length between the axes of supports was 3000 mm. The longitudinal reinforcement ratio was 2% and shear reinforced ratio was 0.13%. The tested elements were loaded by two concentrated forces equally spaced over the length of the beams, in the distance 0.6 m from the axis of the support. The cyclic load was taken as the simultaneous movement of both actuators applied

to the top surface of the beam. On the basis of these results, it was found that the cyclically variable loads cause a significant reduction in load capacity (the destructive force), up to more than 27% compared to the beams loaded monotonically. Taking into account that the issue of shear is constantly modified in the standards provisions as exemplified by the Model Code 2010, which in Poland was published in the form of pre-standards [4]. In this standard the approach to the shear is different in relation to the currently used European standard Eurocode 2 [5]. As a consequence of that the research and analytical work aimed at more accurate approach to the problem of load capacity of support areas of the reinforced concrete beam is fully justified.

2. Description of research

2.1. The research element

Tests were carried out on four single-span reinforced concrete beams with rectangular cross section 0.12x0,30 m, 3.3m total length and 3.0m effective span. Beams were made in the prefabrication plant of designed concrete class C40/50 and steel BS500. In order to determine the actual strength of the concrete and steel, from which have been made, the research element an accompanying studies have been conducted on the previously prepared concrete samples in the form of cubic and cylindrical samples with dimensions respectively 150x150x150mm and 150x300 mm. Moreover, a clippings of the reinforcing bars were collected and tested. The construction of the beams S2 reinforcement is shown in Fig 1.

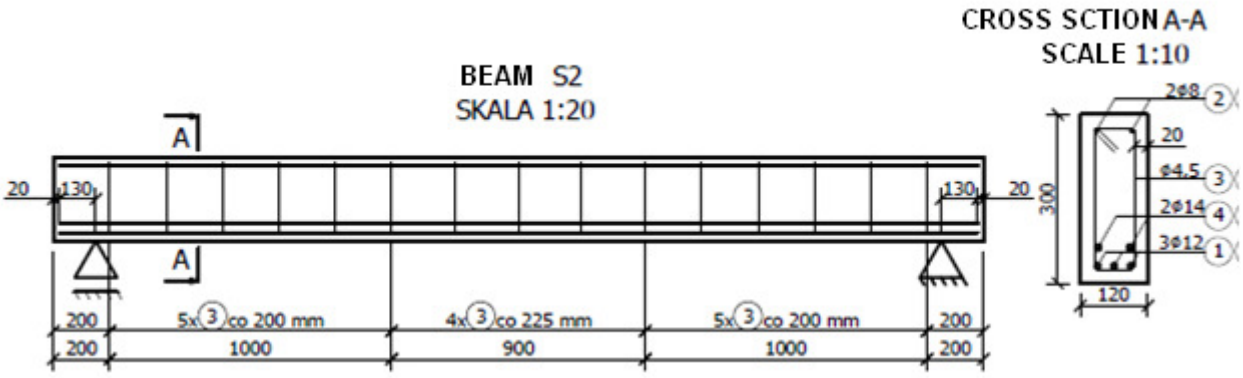

Fig. 1. Construction of single-span reinforced concrete beams type S2

2.2. Test stand

The study was conducted on a test stand presented in Figure 2. It allows to study beams with a maximum length of 20 m, with the possibility of loading by five independent controlled actuators implementing individually programmed loads programs. Measuring apparatus [6] can be "in sync" with each other by common impulse and record the realization of the load programmed by using the controller and actuators as a function of time recorded in seconds. Deformation of the beam can be comparatively measured by using inductive sensors (max. 60 measurement channels) and a 3D optical scanner.

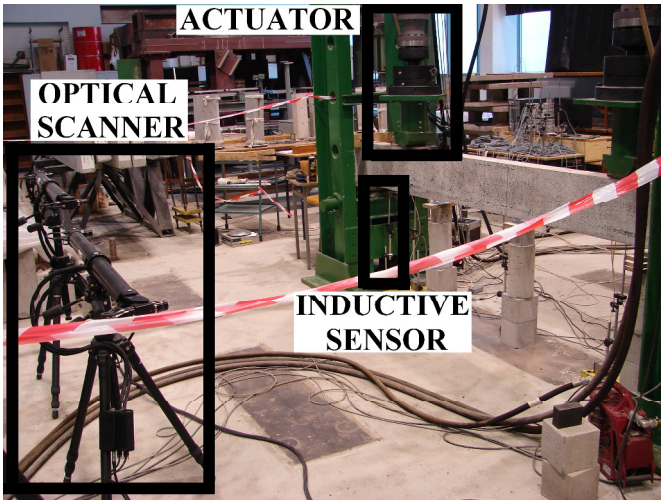

Fig. 2. The test stand

In this study, beams are supported by rotary-sliding bearings and loaded by two actuators according to the diagram shown in Figure 3.

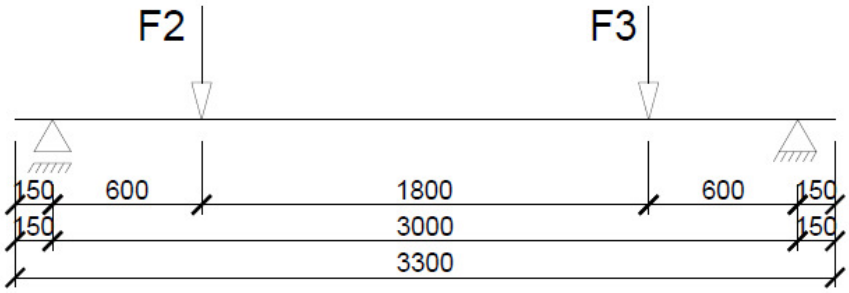

Fig.3. The static schema of single span reinforced concrete beams

2.3. Load program

Studied single-span beams were loaded with two actuators labeled as F3 and F2 marked schematically in Figure 3. In the case of monotonically loaded elements (beams S2M-1 and S2M-2) the load was carried out at a constant speed of force growth of 0.4 kN/min. While the realizing the cyclic loading program, it was adopted with 100 thousand cycles in each of three different loading load range and it's frequency.

There were used follows steps of load:

- Step I - from 5 to 30 kN with a frequency of 0.5 Hz
- Step II - from 5 to 70 kN at a frequency of 0.5 Hz
- Stage III - from 5 to 110 kN at a frequency of 0.25 Hz.

The maximum values of forces in the various phases of loading were respectively 20, 47 and 70% of the actual destructive force obtained from studies of monotonically loaded beams. Schematic process adopted load programs is shown in Figure 4.

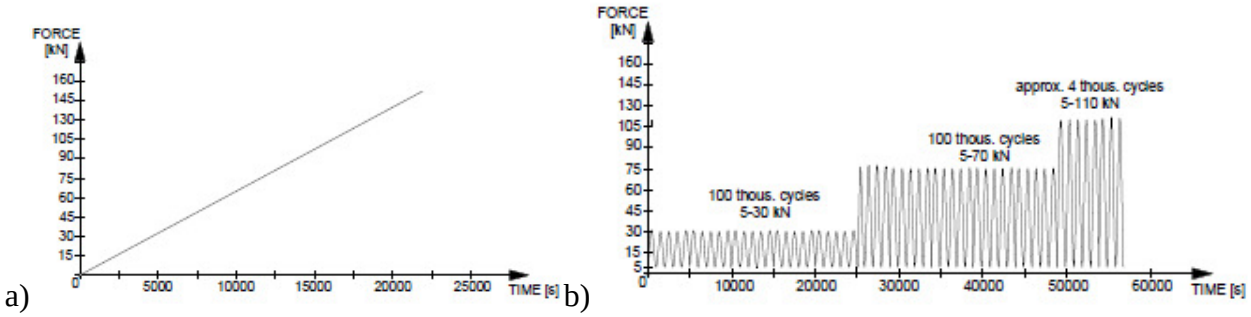

Fig.3. The load sequence for single-span beams a) monotonic, b) cyclic

3. Results

Destructive forces obtained from the study of beams loaded monotonically considered as a load capacity of beams studied and compared with the results obtained on the basis of cyclically loaded beams. It was summarized in Figure 5, where in addition to the capacity of the individual beams plotted lines corresponding to the average values of destructive force form a monotonic and cyclic load. This figure also shows the average theoretical load capacity of the beam bending and shear calculated using experimental data material (concrete and steel).

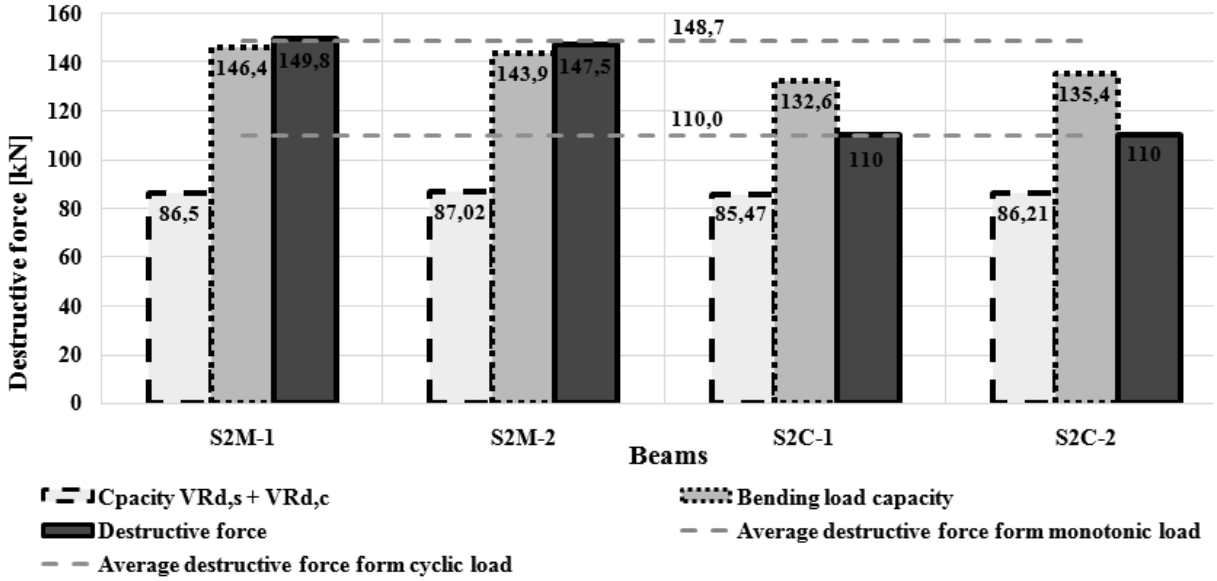

Fig.5. The results of the destructive force of the tested beams

4. Conclusion

On the basis of results shown in Fig. 5 it can be concluded that the carrying capacity of concrete elements subjected to low cyclic load as the fatigue loads is difficult to estimate [1], [7]. Despite the fact that the process of fatigue are considered when the element is subjected to at least 106 load cycles, however, in carried out studies the total number of cycles was up to 3 * 105, so there should not be any typical fatigue effects, but these effects have occurred . The effect of fatigue [8] manifesting itself in:

- loss of bond between steel and concrete,
- capacity reduction of stirrups steel,
- weakening the concrete in the compression zone over the diagonal crack,

appeared in the beam S2C-1 during the third stage of the load after 3825 cycles. As a result, the beam under the cyclic load was damaged and destroyed due to the shear. While failure of beams, which were under monotonically load was related to exceeded of bending capacity, which gave the type of destruction in the literature called as flexo-shear failure.

In both cases, the determined shear capacity based on the current European standard Eurocode 2 was much lower than the capacity resulting from the study. However, only in the case of cyclic loading an effect of typical destruction due to shear with rupture of the stirrups was observed.

The research found that:

- experimental load capacity of respondents beams loaded in a cyclically variable is less than the load capacity of beams loaded monotonically,
- registered decrease of the load capacity of tested beams cyclically loaded was to 27% relative to the loaded monotonically,
- in the case of beams loaded monotonically, observed destruction type was flexo-shear due to the exceeded bending capacity, however, for components under cyclic load destruction has occurred due to shear with rupture the stirrups,
- shear theoretical capacities determined on the basis of standard Eurocode 2 is much lower than the capacity of the experimental tested beams.

Acknowledgement

The work was carried out in the framework of the development Project N R04 0007 10 "Non-invasive monitoring and diagnosis of reinforced concrete structures with particular emphasis on engineering objects"

References

[1] GODYCKI-ĆWIRKO T. Mechanika Betonu, Arkady, Warszawa 1982.

[2] DĄBROWSKI k., KOTWICA J., Wpływ sposobu przyłożenia obciążenia i podparcia na nośność strefy przypodporowej belek żelbetowych, Zeszyt Naukowo-Techniczny Wyższej Szkoły Inżynierskiej w Lublinie, październik 1971 r. , str. 63 -89

[3] GOSZCZYŃSKA B., TRĄMPCZYŃSKI W., BACHARZ M., BACHARZ. K., Nośność belek żelbetowych obciążanych cyklicznie, Budownictwo i Architektura, Vol. 13(3), Politechnika Lubelska, Lublin 2014 r.

[4] Fib Bulletin 66: Model Code 2010, Final draft – Volume 2

[5] PN-EN 1992-1-1 :2008. Eurokod 2: Projektowanie konstrukcji z betonu – Część 1 : Reguły ogólne i reguły dla budynków, PKN, Warszawa 2008r.

[6] GOSZCZYŃSKA B., TRĄMPCZYŃSKI W., BACHARZ K., BACHARZ M., TWORZEWSKA J., TWORZEWSKI P., Doświadczalna analiza odkształceń przestrzennych belek żelbetowych z zastosowaniem skanera optycznego 3D., Inżynieria i Budownictwo 3/2014, 156-159

[7] MANFREDI G., PECCE M., Low cycle fatigue of RC beams in NSC and HSC., Engineering Structures, Vol. 19, No 3, (1997) 217-223.

[8] DYDUCH K., DYDUCH M., Konstrukcje betonowe, żelbetowe i sprężone komentarz naukowy do PN-B-03264:2002 Tom 2 -Rozdział 17: Stan graniczny zmęczenia konstrukcji żelbetowych i sprężonych, Instytut Techniki Budowlanej, Warszawa 2005, str. 179-192.

[9] GOSZCZYŃSKA B., ŚWIT G., TRĄMPCZYŃSKI W., Monitoring of active destructive processes as a diagnostics tool for the structure technical state evaluation, Biulletin of the Polish Academy of sciences, Technical Sciences, Vol. 61, No. 1, 2013

TRANSCOM 2015, 22-24 June 2015
University of Žilina, Žilina, Slovak Republic

Micro cracks of unloaded concrete made based on the limestone aggregate in the early stage of maturing

[*]Magdalena Bacharz
[*]Kielce University of Technology, Faculty of Civil Engineering and Architecture, Department of Strength of Materials and Concrete Structures, al. Tysiąclecia Państwa Polskiego 7, 25-314 Kielce, Poland, {mbacharz}@tu.kielce.pl

Abstract. The paper presents an analysis of destructive processes in the early stage of unloaded concrete maturing, based on the limestone aggregate, using acoustic emission method. The samples after demoulding without care in water (in order to induce the phenomenon of autogenous shrinkage) were placed in a chamber and subjected to cyclic (daily - 57 days) temperature changes in the range from -5°C to + 42°C. Based on the identification of acoustic emission signals, it was confirmed that this method could be an effective tool for studying micro cracking in the initial stage of concrete maturing regardless of the conditions of care.

Keywords: shrinkage, acoustic emission, micro cracking

1. Introduction

Already at an early stage of maturation of concrete during the binding, hardening and drying processes, the internal stresses caused by shrinkage, temperature and moisture gradients are created. When those stresses exceed the strength of concrete, the micro cracks in the cement paste and in the interface between the cement paste and aggregate are formed [1]. These micro cracks may propagate to the surface of the concrete reducing its protective functions. In the later stage of loading, these cracks expose reinforcing bars on the impact of corrosive factors aggression, reducing the durability and utility functions of objects.

Therefore, it is important to study these destructive processes in the early stage of concrete maturing and to search for methods to assess the quality of its preparation regardless of the strength, composition, maturing and care conditions of tested element.

Preliminary studies of the IADP (Identification of Active Destructive Processes) acoustic emission method, used to analyze the destructive processes in unloaded concrete, made of limestone aggregate, subjected to care in water in the early days of hardening, in order to eliminate autogenous shrinkage. [2, 3]. In [2] are described the test results of concrete maturing at room temperature, whereas in [3] the cyclically varying conditions of temperature. It has been found that this method can be used to study the destructive process caused by shrinkage in unloaded concrete. The study indicated the presence of three classes of destructive processes, including Class 3 of signals, which was evidence for cracks detectable on the surface of the concrete. Observations of the specimen confirmed the presence of cracks on its side surfaces.

The aim of this study is to evaluate the possibility of identifying the destructive processes taking place in unloaded concrete (not subjected to the initial care in water) exposed to the effects of autogenous shrinkage, using the acoustic emission method. The verification was performed based on the results obtained for the three samples of concrete, made of limestone aggregate and CEM I 42.5 N MSR/NA cement, C30/37 class of concrete, and immediately after demoulding subjected to cyclic (daily – 57 days) temperature changes within the temperature range from -5^0C to $+42^0$C in a thermal chamber.

2. The IADP acoustic emission method

The method of acoustic emission signals analysis, accompanying the destructive processes (RPD – Recognition of Destructive Processes), was presented and verified in [4, 5, 6] in application to the diagnostics of prestressed concrete structures subjected to external load. In [7, 8] was shown a modification of this method (under the name of IAPD – Identification of Active Destructive Processes) and applied for detection, identification and location of active destructive processes generated by the action of the load in reinforced concrete elements. In papers [2, 3] it was used to analyze the destructive processes in unloaded concrete.

A defect occurring in the concrete sample (Fig. 1) emits elastic waves that are received by the acoustic sensors and converted into electrical signals. The signals are then amplified by a preamplifier and recorded in the form of acoustic emission signals by the processor. Then the signals are grouped, compared to the signal reference database of destructive processes, created earlier in the laboratory and assigned to appropriate Classes of signals [5].

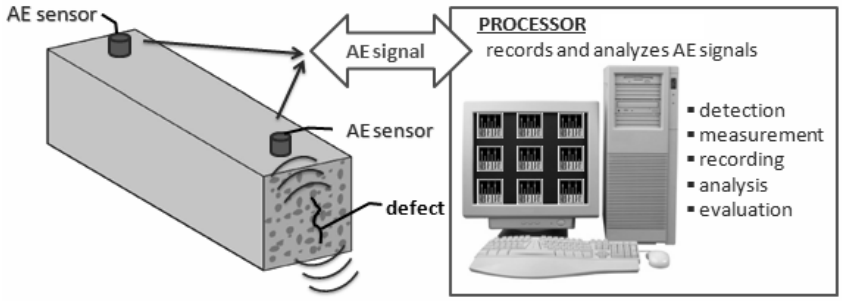

Fig. 1 Setup for IADP test of unloaded concrete

The initial signal reference database was developed based on 12 AE signal parameters, recorded for the samples subjected to uncontrolled temperature and humidity conditions [2]. The initial signal reference database comprises four classes of signals, assigned on the basis of literature to particular destructive processes, that may be the sources of an acoustic wave in the maturing concrete [2, 3]:

Class 1 – Micro cracks in the cement paste
Class 2 – Micro cracks at the paste-aggregate interface
Class 3 – Formation of micro cracks on the concrete surface
Class 4 – Crack growth

3. Research

The tests were performed on three concrete specimens denoted A, B and C, 15x15x60 cm, made of C30/37 concrete and with lime aggregate and no admixtures. After demoulding (point) markers for strain measurements were fixed on the four walls and two AE sensors were mounted on one wall of each of the specimens, 3.5 cm from the upper and lower edge, as in Fig. 2a. The prepared samples were placed in a thermal chamber (Fig. 2b), which was subjected to 12-hour cycles of heating and cooling for a period of 57 days (Fig. 3). During the cycles, the AE signals were measured and occurring classes of signals (the destructive processes) were recorded.

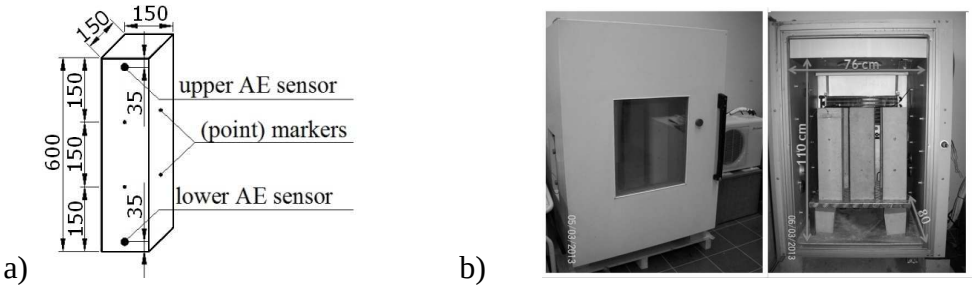

Fig. 2. **a)** AE sensors mounted on the specimen, **b)** Test setup

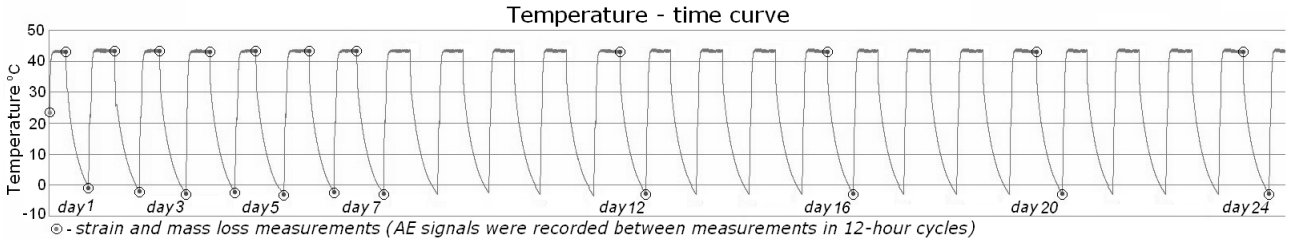

Fig. 3. Temperature versus time for the first 24 days of measurements

Each cycle was followed by a strain measurement performed by using an extensometer with 8-inch gauge length and the specimens were weighed to measure the loss of water. Figure 4 shows the results of measurements, which were made initially every day, then every four days and finally every ten days.

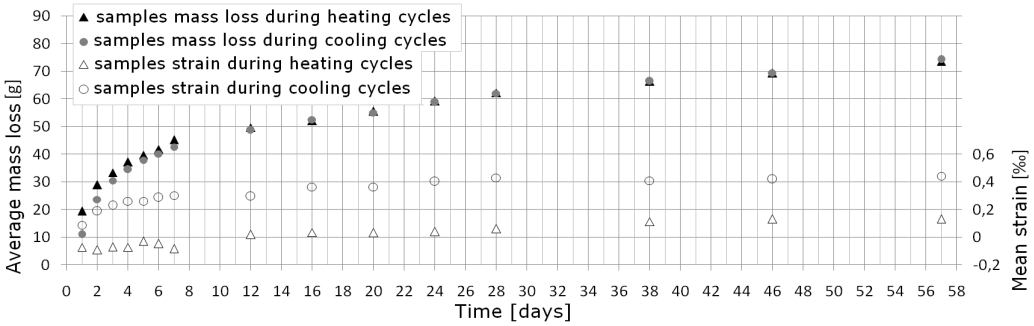

Fig. 4. Diagram of mean strain and average mass loss in function of time measured for samples A, B and C

In the above Figure it can be seen much smaller strain of the sample during the heating cycle than during the cooling, in the temperature range from -5^0C to $+42^0$C. While loss of water in samples was almost the same.

Figure 5 shows exemplary graphs of number of AE signals for each class of destructive processes in function of time, illustrating the results obtained from the sensor (No. 3) on concrete specimen denoted as B.

The two destructive processes were mostly observed during the heating cycle:
Class 1 – Micro cracks in the cement paste
Class 2 – Micro cracks at the paste-aggregate interface, whereas during the cooling cycle three processes were observed:
Class 1 – Micro cracks in the cement paste
Class 2 – Micro cracks at the paste-aggregate interface
Class 3 – Development of cracks on the concrete surface

The Class 3 acoustic signals appeared together with the cracks appearing on the specimen surface. The cracks were measured using a Brinell magnifier and their location was marked (Fig. 6).

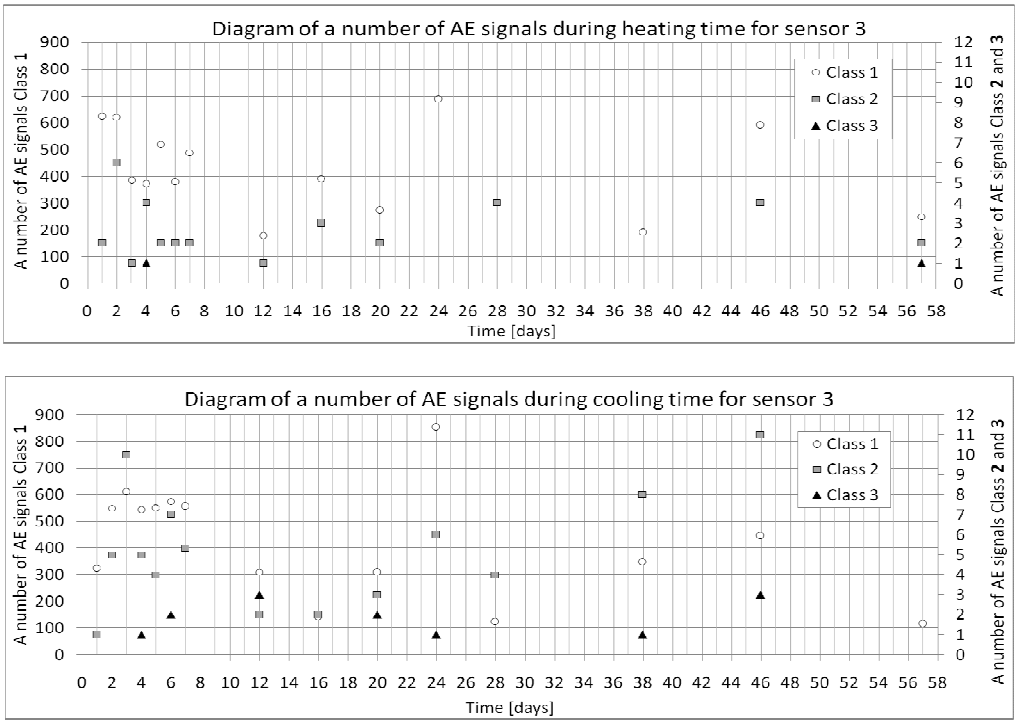

Fig. 5. Diagrams of a number of acoustic emission signals during the heating and cooling cycles

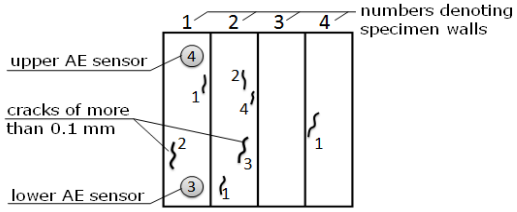

Fig. 6. Cracks on the extended side surface of specimen C.

4. Conclusion

The paper presents the results of an unloaded concrete, made based on the limestone aggregate stored in the variable conditions of temperature cycles without preliminary care in water (including the impact of autogenous shrinkage). The results confirm the correctness of the assignment of three classes of signals (especially the Class 3 signal) destructive processes that accompany maturing of concrete. In a study the Class 3 of acoustic signals was recorded, which was evidence of the appearance of scratches on the surface of the concrete. Observation of the sample confirmed the scratching of the element.

The obtained results confirm the possibility of the using acoustic emission method for testing unloaded concrete regardless of the curing conditions.

The research program of the application of acoustic emission method for testing of destructive processes in unloaded concrete takes into account factors that affect deformation of concrete: the ratio of w/c, strength and grade of concrete, cement class, type of aggregate, admixtures content, the presence of reinforcement, element size, consistency and the period of care.

Acknowledgement

The research was financed from an international project No. POIG 01.01.02-10-106/09-01.

References

[1] GODYCKI-ĆWIRKO T. *Crack morphology in concrete structures (in Polish)*, Scientific study No. 13, Białystok 1992, p.1-149

[2] GOSZCZYŃSKA B., ŚWIT G., TRĄMPCZYŃSKI W., BACHARZ K., GODOWSKA M., KRAMPIKOWSKA A. *Identification of acoustic emission signals in unloaded concrete (in Polish)*. Zeszyty Naukowe Politechniki Rzeszowskiej z. 59 (nr 3/2012/III), Rzeszów 2012, p.189-196.

[3] BACHARZ M. *Acoustic emission for monitoring internal defects in unloaded concrete*, Wiedza i eksperymenty w budownictwie, Wydawnictwo Politechniki Śląskiej, Gliwice 2014, p. 421-428

[4] GOŁASKI L., ŚWIT G., KALICKA M., KANJI O. *Acoustic non destructive techniques as a new method for evaluation of damages in prestressed concrete structures: Failure of concrete structures*, Journal of Acoustic Emission, Vol. 24, 2006, p. 187-195.

[5] ŚWIT G. *Predicting failure processes for bridge – type structures made of prestressed concrete beams using the acoustic emission method (in Polish)*, Politechnika Świętokrzyska, Kielce, 2011, p. 1-177.

[6] GOŁASKI L., GOSZCZYŃSKA B., ŚWIT G., TRĄMPCZYŃSKI W. *System for the global monitoring and evaluation of damage processes developing within concrete structures under service load*, The Baltic Journal of Road and Bridge Engineering, vol. 7, No 4, December 2012, p. 237-245.

[7] GOSZCZYŃSKA B., ŚWIT G., TRĄMPCZYŃSKI W., KRAMPIKOWSKA A., TWORZEWSKA J., TWORZEWSKI P.: *The application of acoustic emission method to analyze the process of reinforced concrete beams scratching*. Zeszyty Naukowe Politechniki Rzeszowskiej z. 59 (nr 3/2012/II), Rzeszów 2012, p.77-84.

[8] GOSZCZYŃSKA B. *Analysis of the process of crack initiation and evolution in concrete with acoustic emission testing*, Archives of Civil and Mechanical Engineering, 14, 2, 2014, p.134-143.

TRANSCOM 2015, 22-24 June 2015
University of Žilina, Žilina, Slovak Republic

Temporary bridges after floods in 2013

[*]Martin Benda
[*]University of Defence, Faculty of Military Technology, Department of Engineer Technology, Kounicova 65, 662 12 Brno, Czech Republic, {martin.benda}@unob.cz

Abstract. The paper deals about operation of Czech Army Engineer Corps in year 2013. There were three units of Czech Army participate in this operation. University of Defence, Military Geodetical and Hydrometeorological Office and 15 Engineer Brigade. The aim of this operation was to construct temporary bridge after flood. During this operation was used REACH-BACK concept between University of Defence and Geodetical and Hydrometeorological Office and between University of Defence and 15 Engineer Brigade. Communication and cooperation between these units was supported by Information portal of engineer corps. The portal works as a support element for REACH-BACK concept.

Keywords: Reach-Back, Engineer, Temporary bridges.

1. Introduction

The Czech Republic territory was hit by floods in June 2013. There were damaged bridges mainly in middle part of part of Czech near the Prague. The engineer experts from University of Defence have essential experience with overcoming the obstacles caused by flood. They designed 20 bridges in the disaster affected areas of the Czech Republic in 2010. The most of them were bridges from MS set but one the longest and the most difficult was bridge from TMS set.

Last year the soldiers from battalions 15 Engineer Brigade erected 4 MS type bridges and soldiers from Bridge Company 151 Engineer Battalion built the bridge TMS. The operation of designing and constructing of temporary bridge TMS took almost 5 weeks (from end of June to start of August).

There were three units of Czech Army participate in this operation - University of Defence (Department of Engineer Technology), Military Geodetical and Hydrometeorological Office, and 15 Engineer Brigade. Every mentioned unit organized particular team or teams that were included in this operation.

REACH-BACK concept was used for the first time as support for so large operation in 2009. Basic principles of the concept demonstrated that it can operate successfully in praxis. That was the reason why the concept REACH-BACK together with Information Portal of Engineer Corps (IPEC) was used for support during this operation again.

It is suitable to introduce the Reach-Back concept at first and explain the main possibility of its usage. It is a new model of cooperation and communication between the units deployed directly in action and main corps supporting them. This concept supposes units used for tasks compliance (for example in foreign mission) and these units do not necessary consist of all components as well as home. The components staying “home” fill tasks for “in theatre” units as their support team [1].

2. Temporary bridging sets MS and TMS

As a suitable temporary bridge for overbridging four gaps was chosen MS bridge set. Only one bridge was replaced by TMS set because of higher carrying capacity requirement. There were damaged bridges of short span mainly. That is why most of them were replaced by temporary bridge MS type. The longest MS type bridge in Nový Knín village had span 24 m, but for launching was used longer construction (27 meter). The requirements of civilian authority for carrying

capacity were the next reason. The most of them needed carrying capacity up to 20 ton. Temporary bridge from TMS set was built up in Chlum u Sedlčan village and was only 15m long.

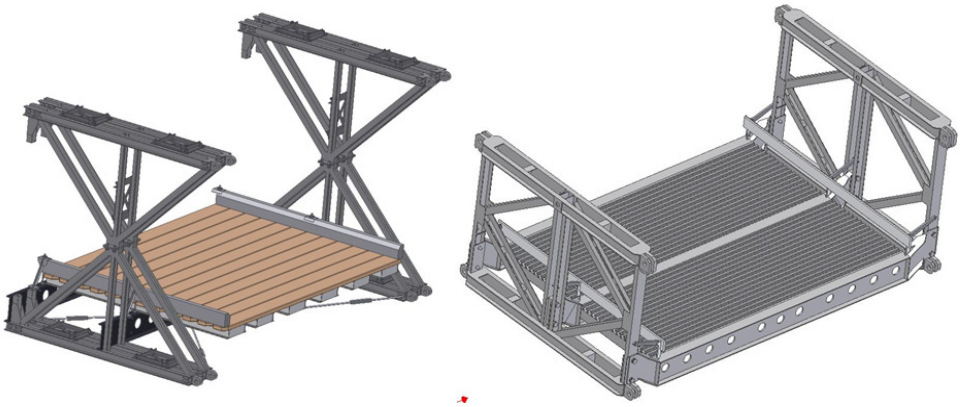

Fig. 1. Model of bay TMS and MS bridge set created by Autodesk Inventor SW.

Bridging set MS ant TMS are standardized portable steel bridges with two primary truss and lower bridge deck. It is used only for one-way traffic lane with maximum carrying capacity 60 ton. It is the most suitable to build one span bridge with length 21 m (carrying capacity 60 t) for MS type and one span bridge with length 36m (carrying capacity 70 t) for TMS type [2], [3]. It is possible to build a bridge with longer span but the carrying capacity must be reduced. When using pier (e.g. PIŽMO), it is possible to build also bridges with more spans. The 3m long bay is the basic assembly element for both sets (Fig. 1). It is possible do assemblage for both sets by the help of plain rollers, rocking rollers, and cantilever. The other alternative is to assemble the bridge on flat ground and put it over the obstacle by a suitable crane. The main advantage of MS type is that it is not necessary to do special modification of banks for placing the bridge and ramp. The ramp is created by folding ramps which belong to the end bridge bay. TMS type need complex ground shaping not only for placing but also for construction. The ramp for TMS must be done by special ramp or abutment wall (Fig. 2).

Both these bridge sets are not equipment of Czech Army. These bridge sets are in storage of Ministry of Transport. The soldiers of Engineer Corps are trained in special courses in Training centre of Ministry of Transport, where they get the experience with this bridge construction and also with other bridge constructions.

3. Reconnaissance and geodetic surveing

The main task for reconnaissance team (reco-team) was the reconnaissance of area where the bridge was planned to be built. This team consists of experts from Military Geodetical and Hydrometeorological Office from Dobruška and one member from Department of Engineer Technology who has experience with TMS and MS sets. This team configuration is possible to use for future similar tasks. Geodesists were responsible for geodetical survey of the construction site of temporary bridge. The reco-team carried out inspection of the construction site and made photo documentation. They found out span of the obstacle and suggested which type of bridge is suitable for particular gap. All information was included in Reconnaissance Report. When the reco-team accomplished the report, they placed it on IPEC.

The geodesists were lead by commander of the reco-team and under his control they made detailed geodetical survey. The data gained from survey were essential part of the Reconnaissance Report and were attached to the report as soon as geodesists prepared them. The data consisted of coordinates of important points and construction site drawing in MicroStation software. The data were used for preparation of every project of temporary bridge.

Fig. 2. Assembling of the bridges.

4. Project of temporary bridge

The project team was put together first of all. The five-member project team was from Department of Engineer Technology at University of Defence. Two members of the team worked with geodetists as members of the reco-team and other two members designed projects. Last member was leader of the team who was responsible for communication with civilian authorities. The project team used experience from regularly practised actions in collaboration with Dobruška Military Geographic and Hydro-Meteorological Office. They improved their skills and cooperation that they gathered in 2009 and 2010 during similar operation [4]. The project team repeatedly proved that the involvement of university Reach-Back laboratory in "life operation" brings good results, making the collaboration with the geodesists from Dobruška and 15th Engineer Brigade personnel smooth and easier.

Project team took data (photos, video and geodetic surveying) and Reconnaissance Report that was on IPEC server and started work on project. They also implement suggestion of reco – team that would be suitable to use TMS bridge for this situation. The project team had to accept the requirements of civilian authorities. They had two particular requirements.

The first one was that the construction of the bridge had to be above 50 years flood water level. That is why the lower chord of the truss was placed approximately 1,2 m above terrain. The second was that construction had to be easily attached to existing road on the both sites of the banks.

The leader of project team specified type of construction, site for construction and span of the bridge. Team created 3D model of bridge construction (Fig. 3). This 3D model was also used for making project documentation. Designing necessary ground shaping in area of construction was other part of project. Microstation situation data were converted into proper CAD format. Then team created into terrain ground shaping and other modification. Then the 3D model of bridge was placed into model of terrain.

Fig. 3. Model of bridge placed in photo.

Sometime it was very suitable placed model of bridge into photo. It made placing bridge construction in real situation more illustrated.

The last part of designing was creating the final project and drawing documentation. The final project with drawing was placed on server IPEC. Then Request to prepare bridge and assembly material from store houses of Ministry of Transport was created. The Request to prepare was sent to responsible person to Ministry of Transport by the help IPEC. They prepared entire material necessary for bridge construction in the nearest store.

5. Construction of bridges

As was mentioned above there were erected four bridges from MS set but only one from TMS set. Since TMS bridge construction is more complicated then MS type, commander of 151 Engineer Battalion was tasked to organize the construction of the bridge. Soldiers from this unit have the best experience with this type of construction and some of their commanders work as instructors in Ministry of Transport´s courses for construction TMS bridge in Kojetín training center. The commander of building unit read up the project and made eventually consultation with the project team with the help of web conference on IPEC.

Date	Location and type of the bridge
25.7.2013	Červený Hrádek MS – 24m
26.7.2013	Chlum u Sedlčan TMS – 15m
10.-11.7.2013	Nový Knín MS -24m
27.7.2013	Velké Číčovice MS – 15m
30.7.2013	Zadní Třebáň MS – 18m

Tab. 1 Time table of construction process

At the first of all it was necessary to prepare building site. The commander of each building unit made meeting with local civilian authority and explain them his requirements (e.g. cut off power line, get down trees or remove fence). The requirements came from project and other commanders drafts (Fig. 4). When whole the building site was prepared the commander sent unit to pick up the material of bridge set from the store house and to transport it into building site.

The commander started building of the bridge after the unit with bridge construction came into building site. The first step was to construct the rocking rollers and plain rollers trays. The rocking rollers were placed on concrete panels. The grillage from the timber was often used. The short ramp and concrete panel were used as foundation for the grillage (Fig. 2). When the plain rollers trays were assembled the launching nose were erected on rollers. When the assemblage of the nose was complete, assemblage the first bay of the bridge followed. Then the next bays of the bridge were

assembled by the same way except the end bay. When the complete construction of the bridge was launched the jack down procedure started. The most of units were equipped with hydraulic jacks with load capacity 50tons. Unfortunately, neither of them was able to work. Jacks were from the storage of Ministry of Transport and we identified that their future using is impossible due to the life span of them. The jacks had to be replaced by the jack from vehicle accessories. These jacks had load capacity only 20 tons but it was sufficient in this case.

Load test by using car crane was the last task and then the commander made inspection of the bridge construction. The whole building process of one bridge (from picking it up from the store house to giving into traffic) took one or two day. There is not included the time that was necessary for ground shaping. The building process of TMS bridge took approximately four days because of the type and span of the bridge.

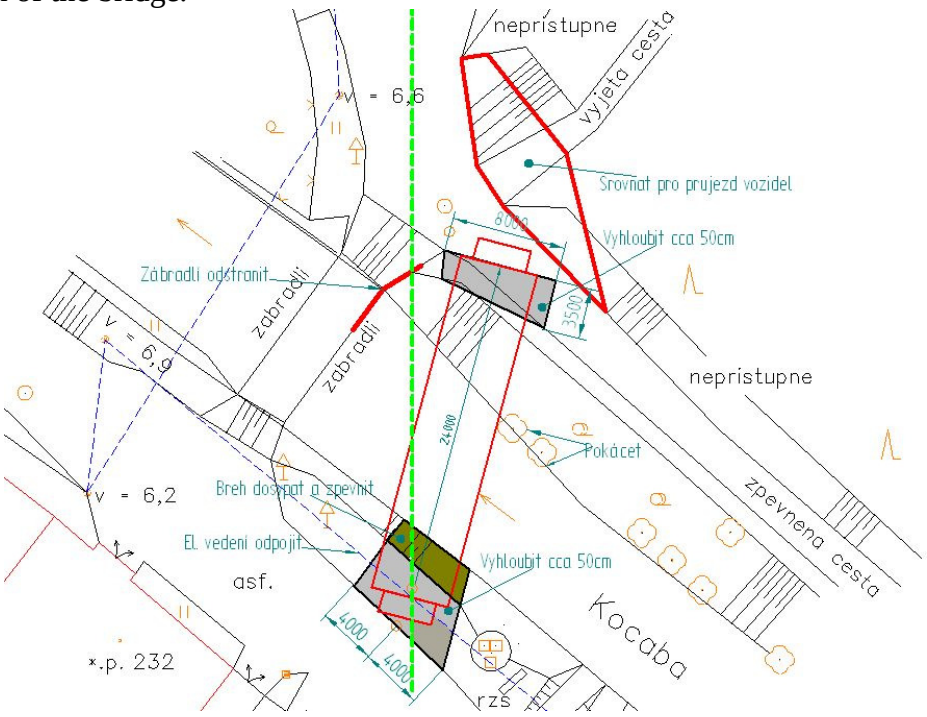

Fig. 4. Requirements for preparing the building site

6. Conclusion

The range of transport infrastructure recovery by using temporary bridge was less extensive than in 2009 and 2010. All units involved in the operation “building temporary bridges” learned from the mistakes committed in last years and have made considerable progress. This progress was reached mainly in the area of MS type construction.

On the other hand, we have found that there are many problems that we have to cope with in the future. Some of them persisted from past. For example problems in communication between units which participate in construction of the bridge and Ministry of Transport. It was caused by the fact, that in our army there still exist units that have very rare access to internet. The problem that persisted from the past is that unist are not equipped by timber that is in many cases very useful. Many soldiers participated in “live” action in 2009 and 2010 and they got valuable experience, in spite of the fact that they did not take part specialized course.

A significant progress was achieved in area of designing temporary constructions due to modern software tools [4]. The communication and data transmission between University of Defence and Military Geodetical and Hydrometeorological Office is on high level quality. It is due to periodical practise between these two units. It will be necessary also to determine the command and control responsibilities and to divide them between civilian and military authorities in the future [5].

References

[1] MAŇAS, Pavel; MAZAL, Jan. The Reach-Back Concept in The Czech Army Corps of Engineers. In International Conference on Military Technologies. Brno : Faculty of Military Technology, University of Defence, 2009. ISBN 978-80-7231-648-9.

[2] MAŇAS, P., SOUŠEK, R. BENDA, M a kol.: Stavba provizorních mostů ze soupravy MS. Brno : Institut Jana Pernera, o.p.s., 2010, 120 s. ISBN 978-80-86530-73-4.

[3] MAŇAS, P., SOUŠEK, R. BENDA, M a kol.: Stavba provizorních mostů ze soupravy TMS. Brno : Institut Jana Pernera, o.p.s., 2010, 120 s. ISBN 978-80-86530-74-1.

[4] SOBOTKA, Jan. Comparison of elevation data of the Czech Republic for designing military constructions**.** Advances in Military Technology**,** 2013, vol. 7, no. 2, p. 57-63. ISSN 1802-2308.

[5] MAŇAS, Pavel; SOUŠEK, R. On Cooperation between Military and Civilian Authorities in the Czech Republic during Crisis Situation in Transport. In International Conference on Engineering and Meta-Engineering icEME 2010. Orlando, Florida, USA : IIIS, International Institute of Informatics and Systemics, 2010, p. 12-14. ISBN 978-1-934272-83-1.

TRANSCOM 2015, 22-24 June 2015
University of Žilina, Žilina, Slovak Republic

Aerodynamic processes in naturally ventilated multi-zone buildings

[*]Karol Biernacki
[*]Kielce University of Technology, Faculty of Environmental Engineering, Geomatics and Power Engineering, Department of Building Physics and Renewable Energy, Al. Tysiąclecia Państwa Polskiego 7, 25-314 Kielce, Poland, {biernackikarol2}@gmail.com

Abstract. The paper presents computations for gravity and wind ventilation in clear span industrial sheds. The amount of ventilation air was computed using the two available methods. For each method, computations were made for three different ratios of heat source areas to the building floor area. Also, the computations were performed for ventilation openings area, for the ventilation resulting from thermal load, the action of wind and from both factors acting concurrently. Computations were performed with the Microsoft Excel software. Comparison of computational methods was made for both the amount of ventilation area and the area of ventilation openings. The computational methods presented in the paper concern the simplest solutions for calculating gravity ventilation in industrial buildings. The literature on the subject, however, does not provide calculations for more complex cases.

Keywords: natural ventilation, gravitational forces, wind action, multi-zone buildings.

1. Introduction

The purpose of the ventilation system is to exchange air in the building. The system effectiveness depends on the delivery of the fresh air, ensuring appropriate air flow between rooms and effective removal of waste air. In ventilation, the technology of forming air flows in the rooms, based on the knowledge of ventilation aerodynamics, plays a crucial role.

For natural ventilation, the inflow of external air occurs through the building leakage (infiltration) and ventilation openings, without using a mechanical system powered by electricity. The processes that occur in natural ventilation and types of this ventilation were described, among others, in [1, 5, 8, 9].

Three types of natural ventilation can be differentiated:

- airing, which results from opening the windows,
- gravitational ventilation, provided by vertically installed ducts or ventilation openings located at different heights,
- transverse (wind) ventilation, characterised by air flow induced by the pressure action on the building envelope.

2. Factors inducing air movement within the building indoor space

The key feature of natural ventilation is that air flow is induced only by pressure difference, the action of the wind and the gravitational force, which are caused by temperature differences inside and outside the building. Both factors vary in time, which makes it difficult to determine the correct size of ventilation openings.

2.1. Natural ventilation induced by the gravitational forces

To determine the pressure difference caused by the gravitational force (3) acting on a given surface, it is necessary to determine, on the basis of the dependences below, pressure outside (1) and inside the building (2) [1, 9, 10].

$$P_{I-I}^{Z} = \frac{F_1}{S} = \frac{m_z \times g}{S} = \frac{V \times \rho_z \times g}{S} == \frac{S \times h \times \rho_z \times g}{S} = h \times \rho_z \times g [Pa] \quad (1)$$

$$P_{I-I}^{W} = \frac{F_2}{S} = \frac{m_w \times g}{S} = \frac{V \times \rho_w \times g}{S} = \frac{S \times h \times \rho_w \times g}{S} = h \times \rho_w \times g [Pa] \quad (2)$$

$$\Delta P = P_{I-I}^{Z} - P_{I-I}^{W} = (h \times \rho_z \times g) - (h \times \rho_w \times g) = h \times (\rho_z - \rho_w) \times g \quad (3)$$

The air flow through the building indoor space is presented in Fig. 1. Major parameters that affect air movement induced by the gravitational force include the following: distance h between the supply and exhaust openings and temperature difference inside and outside the building, thus the difference in the air density ρ.

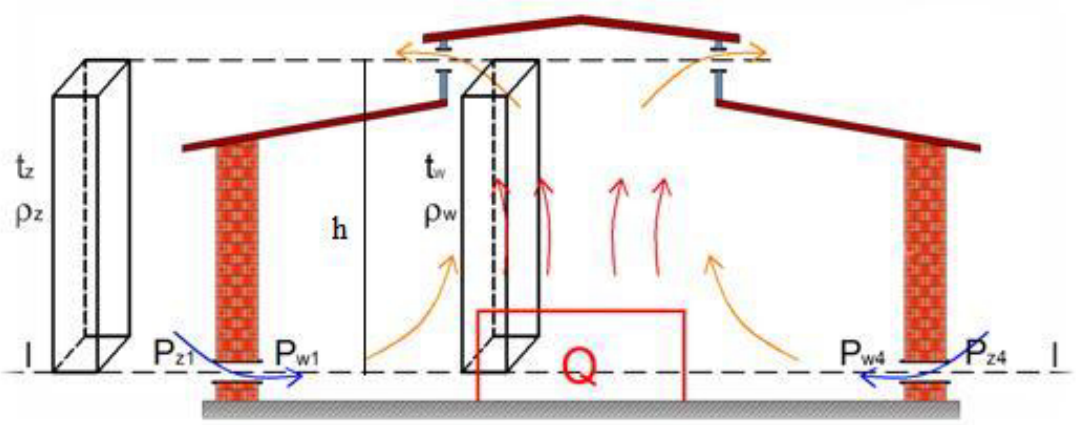

Fig. 1. In-room air flow induced by the gravitational force.

2.2. **Natural ventilation driven by the wind**

The impact of wind on the building envelope produces positive pressure on the exterior closures on the building windward side, whereas on the building leeward side, negative pressure is created. In the action of wind around the building, the wind dynamic pressure p_d increases, whereas the static pressure p_s decreases. That is related to the air potential energy conversion to kinetic energy [9].

To determine the magnitude of positive or negative pressure (6) outside the building, created due to the wind action, it is necessary to know the values of the aerodynamic parameters (4). The value of the aerodynamic parameter expresses the ratio of the static pressure at a given point of the exterior closure to the wind dynamic pressure (5) [2].

$$K = \frac{p_s}{p_d} [-] \quad (4)$$

$$p_d = \frac{v^2}{2} \times \rho_z \quad [Pa] \quad (5)$$

$$p = K \times p_d \quad [Pa] \quad (6)$$

If those values, and the values of negative and positive pressures p_w in the building are known, it is possible to determine pressure difference in individual openings (6). If the pressure inside the building is lower than the pressure outside, (7.1) is employed, otherwise, (7.2) is used.

When pressure difference in ventilation openings, induced the gravitational force and the wind action are known, it is possible to determine the stream of ventilation air. It should be remembered, however, that the balance of air amount must be maintained.

$$\Delta P = p_z - p_w = K \times \frac{v^2}{2} \times \rho_z - p_w \tag{7.1}$$

$$\Delta P = p_w - p_z = p_w - K \times \frac{v^2}{2} \times \rho_z \tag{7.2}$$

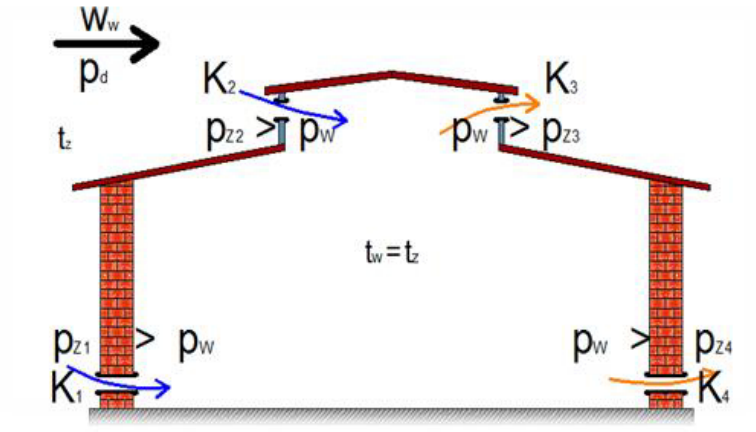

Fig. 2. In-room air movement driven by the wind.

3. Ventilation computations in multi-zone buildings

Many models are available to predict air flow within the building. Those can be categorised as empirical, theoretical, network, zonal or Computational Fluid Dynamics (CFD) ones [3, 4, 6, 7]. The simplified formula for the phenomenon description in empirical or theoretical models makes it possible to calculate the amount of ventilation air relatively quickly, but those calculations yield only inferred values. Those can be applied, similar to empirical models, for estimating air flow in single-zone buildings.

Network, zonal or CFD models allow predicting air flow in multi-zone buildings. However, the literature on the subject is sparse. The reason might be the fact that the application of those techniques to natural ventilation is extremely time-consuming.

Air stream distribution in individual ventilation openings is presented in the physical model (Fig. 3). Fresh air is supplied into the room through the openings 1 and 4. The exhaust air outlets are openings 2 and 3. Opening 5, located between the bays, allows air flow from the first to the second bay.

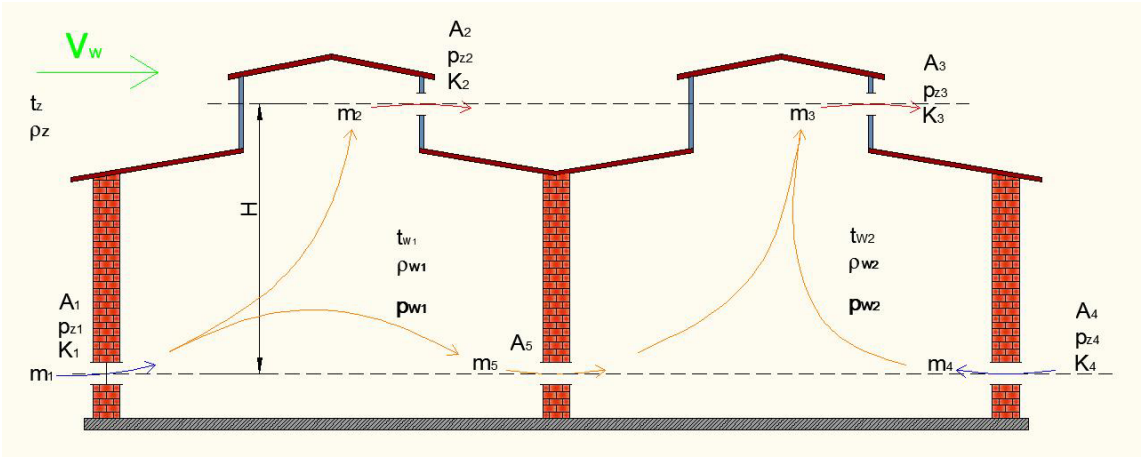

Fig. 3. The physical model showing natural ventilation operation in the two-bay building.

The mathematical model (8) in the form of the system of equations, describing the air movement within two-bay building, is presented below. The model is used to determine the amount of ventilation air flowing through individual openings. Maintaining mass flux balance is taken into account. The model can also be employed to determine positive and negative pressures prevalent in the individual bays of the building.

$$\begin{cases} H \times (\rho_z - \rho_{w1}) \times g + K_1 \times \frac{v_w^2}{2} \times \rho_z - p_{w1} = \frac{1}{\mu^2 \times 2 \times A_1^2 \times \rho_z} \times m_1^2 + \frac{1}{\mu^2 \times 2 \times A_2^2 \times \rho_z} \times m_2^2 + \frac{1}{\mu^2 \times 2 \times A_5^2 \times \rho_z} \times m_5^2 \\ p_{w1} - K_2 \times \frac{v_w^2}{2} \times \rho_z = \frac{1}{\mu^2 \times 2 \times A_2^2 \times \rho_z} \times m_2^2 \\ H \times (\rho_{w1} - \rho_{w2}) \times g + p_{w1} - p_{w2} = \frac{1}{\mu^2 \times 2 \times A_5^2 \times \rho_z} \times m_5^2 + \frac{1}{\mu^2 \times 2 \times A_3^2 \times \rho_z} \times m_3^2 \\ p_{w2} - K_3 \times \frac{v_w^2}{2} \times \rho_z = \frac{1}{\mu^2 \times 2 \times A_3^2 \times \rho_z} \times m_3^2 \\ H \times (\rho_z - \rho_{w2}) \times g + p_{w1} + K_4 \times \frac{v_w^2}{2} \times \rho_z = \frac{1}{\mu^2 \times 2 \times A_4^2 \times \rho_z} \times m_4^2 + \frac{1}{\mu^2 \times 2 \times A_3^2 \times \rho_z} \times m_3^2 \\ m_1 = m_2 + m_5 \\ m_3 = m_4 + m_5 \end{cases} \quad (8)$$

where:

H – height between ventilation openings, [m];
ρ_i – air density, [kg/m^3];
g – gravitational acceleration, [m/s^2];
K_i – aerodynamic coefficient, [-];
v_w – wind velocity, [m/s];
p_{zi} – positive or negative pressure outside the building, [Pa];
p_{wi} - positive or negative pressure inside the building, [Pa];
A_i – cross-sectional area of ventilation openings, [m^2];
m_i – mass flux of the airflow, [kg/s];
μ – local resistance in the ventilation opening, [-];

4. Computational results and their analysis

Mathcad software was used to compute air stream and positive pressures in individual bays of the building. On the basis of the model developed, computations were performed for the exemplary data:

- H =12 [m]; g = 9.81 [m/s^2]; v_w = 1.0 [m/s], 1.5 [m/s], 2.0 [m/s];
- ρ_z = 1.248 [kg/m^3] for an external temperature of 10 [°C]; ρ_z = 1.27 [kg/m^3] for an external temperature of 5 [°C];

- ρ_{w1} = 1.205 [kg/m^3] for the temperature of 20 [°C] in the first bay; ρ_{w2} = 1.185 [kg/m^3] for the temperature of 25 [°C] in the second bay;
- K_1 = 0.6; K_2 = -0.5; K_3 = -0.45; K_4 = -0.4;
- A_1 = 20 [m^2]; A_2 = 15 [m^2]; A_3 = 20 [m^2]; A_4 = 10 [m^2]; A_5 = 30 [m^2].

The computations were made for three different wind velocities and two temperatures of the external air. On the basis of computational results, it is possible to assume that the model developed by the author was correct, because the balance of mass fluxes was maintained (m_1=m_2+m_5 and m_3=m_4+m_5).

v_w	t_z	m_1	m_2	m_3	m_4	m_5	p_{w1}	p_{w2}
m/s	[°C]	[kg/s]	[kg/s]	[kg/s]	[kg/s]	[kg/s]	[Pa]	[Pa]
1	5	56,74	42,66	44,86	30,78	14,08	7,63	4,74
	10	45,80	34,02	38,04	26,26	11,78	4,74	3,33
1,5	5	56,96	42,25	44,38	29,67	14,71	7,08	4,28
	10	46,06	33,53	37,49	24,96	12,53	4,21	2,88
2	5	57,26	41,62	43,67	28,03	15,64	6,29	3,62
	10	46,42	32,77	36,67	23,02	13,65	3,44	2,23

Table 1. Results of computations of the air stream flowing through the building

For the external temperature of 5 [°C], the air exchange rate is much higher than for the external temperature of 10 [°C]. That results from the fact that the values of mass fluxes in individual ventilation openings for the temperature of 5 [°C] (Fig.4) are greater than the values of the same parameter for the temperature of 10 [°C]. It happens so because, for the lower external temperature, the difference in air density inside and outside the building is higher, which enhances air exchange. Figs 4 and 5 indicate that a change in the wind velocity does not significantly affect the amount of ventilation air.

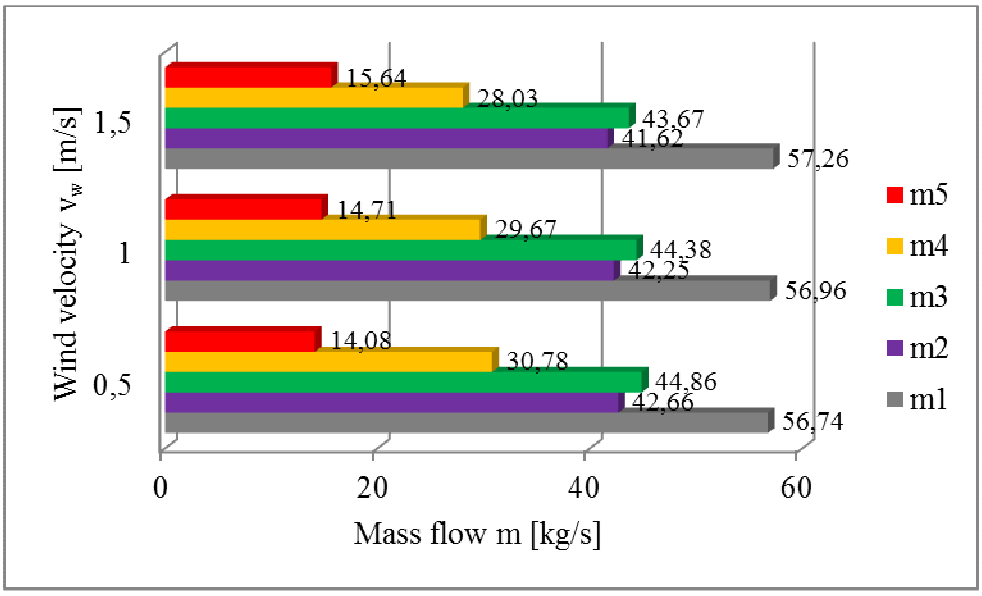

Fig. 4. Values of mass fluxes in the ventilation openings for different wind velocities at the external temp. of 5 [°C].

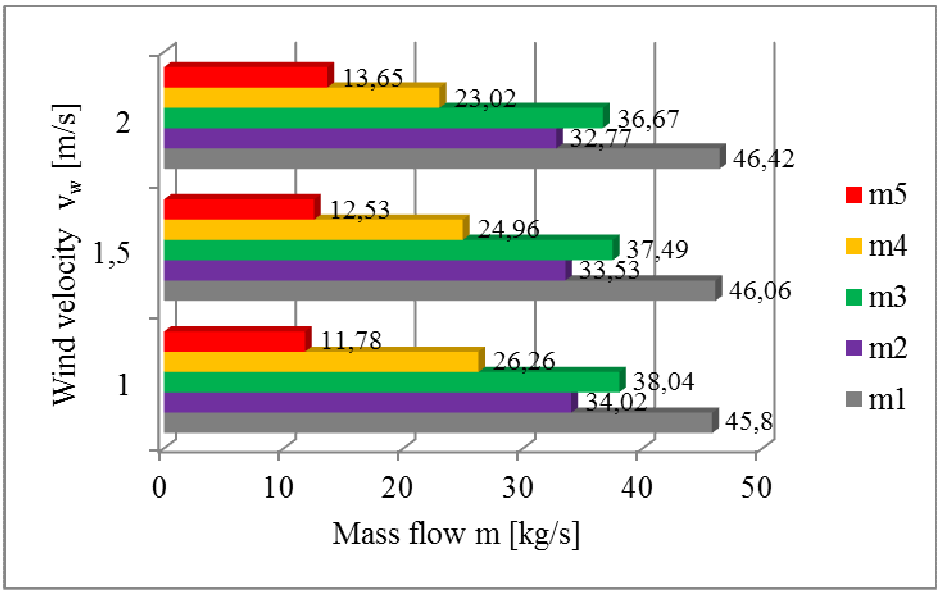

Fig. 5. Values of mass fluxes in the ventilation openings for different wind velocities at the external temp. of 10 [°C].

Positive pressure created in each bay inside the building decreases with an increase in wind velocity and temperature (Fig. 6). The pressure shows higher values for the external temperature of 5 [°C], which is caused by a greater pressure difference inside and outside the building. It can be assumed that with a further increase in wind velocity, negative pressure will be created in the building, which may lead to a change in the operation of ventilation openings, namely instead of supplying the air, they will extract it. As wind velocity and temperature constantly fluctuate, it is difficult to determine the optimal area of ventilation openings. It should also be noted that the value of the pressure inside the building does not significantly affect the amount of ventilation air.

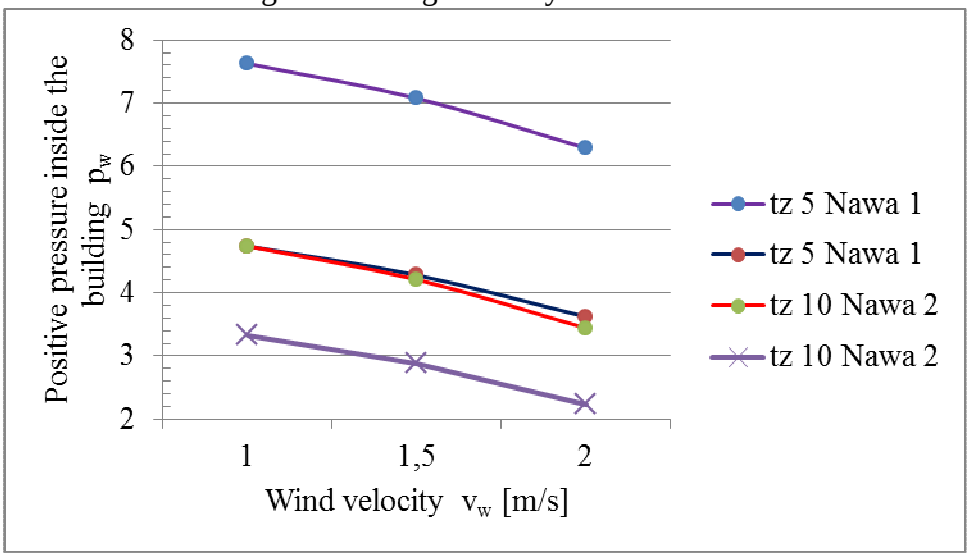

Fig. 6. Values of negative pressure in individual bays of the building for different wind velocities and external temperatures.

5. Conclusions

Architects or design engineers, who are usually not concerned about issues related to aerodynamic processes occurring in the building, reduce the problem to the installation of air-conditioning systems. The activities aimed at lowering the energy demand to protect the natural environment have enhanced interest in natural ventilation.

The reason why an attempt was made to investigate the aerodynamic processes involved in natural ventilation is related to the issues of air distribution in various zones of the building. Performing computations for natural ventilation in multi-zone buildings, e.g. the ones having many bays, is a very complex process, in which multiple assumptions need to be made. The models that would make it possible to compute ventilation aerodynamics in such structures are not available. The amount of air is determined on the basis of heat load. The air distribution and the values of negative and positive pressure in individual bays are assumed. These assumptions are based on estimations depending on various types of building occupancy, which may lead to erroneous results of calculations.

References

[1] Allard F. *Natural ventilation in buildings: a designed handbook*. James & James, 1998.

[2] ASHRAE *Fundamentals Handbook, Ch. 26, Ventilation and infiltration.* American Society of Heating, Refrigeration and Air-Conditioning Engineers, Atlanta, 2001.

[3] Awbi H. B. *Ventilation of buildings*. Chapman & Hall, 1991.

[4] Awbi H. B. *Application of computational fluid dynamics in room ventilation*. Building and Environment, 24, 73-84.

[5] Baturin W. W. *Wentylacja naturalna w zakładach przemysłowych*. Arkady, Warszawa 1974.

[6] Bzowska D. *Dynamika procesów wymiany ciepła i naturalnej wymiany powietrza w budynkach o różnej strukturze materiałowej przegród.* Instytut Podstawowych Problemów Techniki PAN, Warszawa 2007.

[7] Clifford M., Hand J., Clarke R., Riffat S. *Using computational fluid dynamics as a tool for naturally ventilated buildings.* Building and Environment, 32(4), 305-312, 1997.

[8] Kreider J. F. *Handbook of heating, ventilation and air conditioning*. Boca Raton, CRC Press LLC. 2001.

[9] Malicki M. *Wentylacja przemysłowa.* Arkady, Warszawa, 1967.

[10] Piotrowski J. Zb. *Przepływ powietrza przez przegrody i pomieszczenia budynku.* Politechnika Świętokrzyska, Kielce, 2013.

TRANSCOM 2015, 22-24 June 2015
University of Žilina, Žilina, Slovak Republic

The ambient air quality monitoring in Kielce on the example of the nitrogen dioxide.

[*]Paweł Bilski
[*]Kielce University of Technology, Department of Civil Engineering and Architecture, al. Tysiąclecia Państwa Polskiego 7, 25-314 Kielce, Poland, {Pawelbilski1989}@gmail.com

Abstract. This study is an example of the cognitive measures concerning researches of the atmospheric air pollution in the experimental scope. An object of discussed researches is a suitable distinguished part of the earth's atmosphere of the Świętokrzyskie Voivodship located above the city of Kielce. The basic knowledge concerning methodology of measurements were presented in the study as well as the results of own measurement the concentration of the nitrogen dioxide made by T200 Analyzer of the Teledyne Company being on equipment of the Kielce University of Technology. Comparing data from measurements obtained in the Kielce Province Environmental Protection Inspectorate station and in the laboratory of the Kielce University of Technology were also performed.

Keywords: air pollution / nitrogen dioxide / the air quality monitoring / concentrations of gas pollutant

1. Introduction

The State Environmental Monitoring (SEM) was established pursuant to the Act of 27 April 2001 - Environmental Protection Law [5]. The main assumption, being aimed at a protection of the atmospheric air, is a collecting information and data about the levels of substances in the air as well as the results of analyses and evaluations in the scope of fulfilling quality standards. Measurements and examinations being aimed at delivering this information are carried out within the subsystem titled: 'The air pollution monitoring'.

Data obtained via the State Environmental Monitoring is being sent by Province Environmental Protection Inspectorates (PEPI) and Chief Environmental Protection Inspectorate (CEPI) through the EKOINFONET IT System to the National Repository of SEM Data. This system was created for the purpose of storage, editing and disclosing data and researches, and the state of the environment obtained during the tasks execution of the Environmental Monitoring. These databases contains information from units of Environmental Protection Inspectorates throughout the country is being registered. Created databases contain the results of air pollution measurements and specific information concerning the network and test-benches. This data is a foundation for creating the air protecting programs, the short-term plans and the implementation of the air protection strategies. To sum up, collected data are a base for the air quality planning and management in the country.

2. Methodology of the nitrogen dioxide measurements within the research

Measurements of the nitrogen dioxide concentrations in air surrounding the building of the Faculty of Civil Engineering and Architecture of the Kielce University of Technology were performed in spring of 2013. Researches were performed in the period between 25 April and 25 July 2013. Authentic records of measurements results were carried out automatically in the computer system with the frequency of 6 measurements per minute. Measurements of the nitrogen dioxide concentrations were undertaken by the T200 Nitrogen Oxides Analyzer.

The T200 Analyzer is a microprocessor controlled instrument that determines the concentration of nitric oxide (NO), total nitrogen oxides (NO_X) and nitrogen dioxide (NO2) in a

sample gas drawn through the instrument. The instrument is working in the low measuring scope from 0 to 2000 ppb. The instrument measures the amount of chemiluminescence to determine the amount of nitric oxide in the sample gas. A catalytic-reactive converter converts nitrogen dioxide in the sample gas to nitric oxide which, along with the nitric oxide present in the sample is reported as total nitrogen oxides. The nitrogen dioxide is calculated as the difference between total nitrogen oxides and nitric oxide. The instrument measures the amount of nitric oxide present in a gas by detecting the chemiluminescence which occurs when nitrogen oxide is exposed to ozone. This reaction is a two-step process:

In the first step, the molecules of nitric oxide and ozone collide and chemically react to produce one molecule of oxygen and nitrogen dioxide. Some of NO_2 molecules produced during this reaction retain excess energy from the collision and exist in an excited state. The recording of the equation of chemical reaction occurring between the nitric oxide and ozone molecules is presenting the equation no. 1.

$$NO+O_3 \rightarrow NO_2^*+O_2 \quad (1)$$

The second step the excited NO2 molecule quickly returns to its ground state, releasing the excess energy. This release takes the form of a quantum of light. The distribution of wavelengths for these quanta range between 600 and 3000 nm. The constant parameters cause that the relationship between the amount of NO present in the reaction cell and the amount of light emitted from the reaction is linear. The reaction created in the second step is presented by following equation no. 2.

$$NO_2^* \rightarrow NO_2+h\nu_{1200nm} \quad (2)$$

The next step to detect the amount of light created by the reaction in the reaction cell is using a special kind of vacuum tube, called a photo-multiplier tube PMT. The optical filter is placed directly in front of the PMT and pass only transparent to wavelengths of light above 645 nm. Photons enter to the Photo Multiplier Tube and strike a negatively charged photo cathode which cause it to emit electrons. The electrons are accelerated by an applied high voltage and multiplied through a sequence of similar acceleration steps. The acceleration lasts till the useable current signal is generated. The more light present, the more current is produced, what means that the more NO present in the reaction cell, the more current is produced by the PMT. Figure 1 shows the scheme of reaction cell with PMT Tube and Optical Filter.

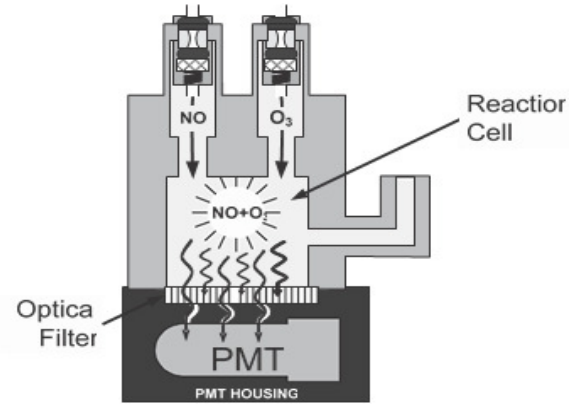

Fig. 1. The scheme of the reaction cell with PMT Tube and Optical Filter. Source: [8]

In order to measure the concentration of NO_2 and NO_x, the instrument periodically switches the sample air stream. Due to that the pump pulls the air through a special converter cartridge filled with molybdenum chips that are heated to a temperature of 315°C. The heated molybdenum reacts with NO_2 in the sample air and produces nitric oxide and a variety of molybdenum molecules. The

reaction created during converted nitrogen dioxide to nitric oxide in the molybdenum converter, with the temperature of 315°C is showed by the equation no. 3.

$$xNO_2 + yMo \rightarrow xNO + M_yO_z \quad (3)$$

By converting the NO_2 in the sample gas into NO, the nitric oxide is routed to the reaction cell where it undergoes the chemiluminescence reaction. Figure 2 presents the scheme of the measurement system of T200 instrument.

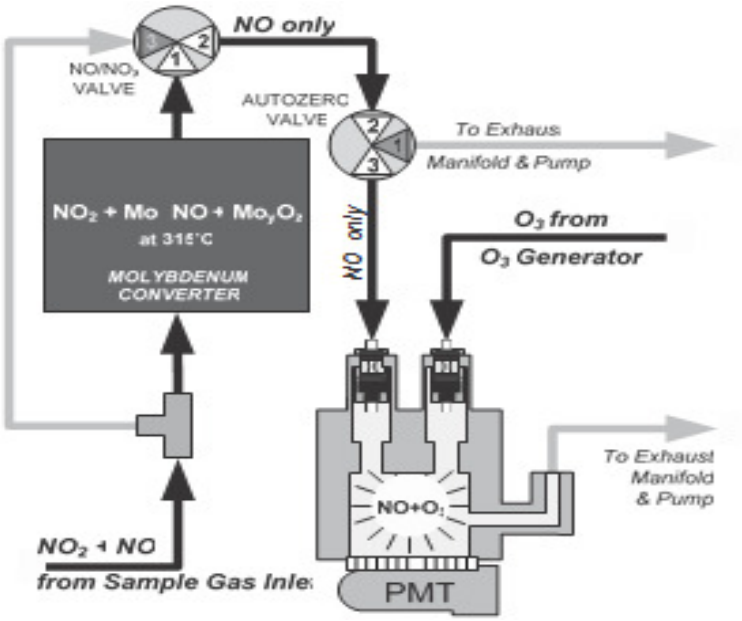

Fig. 2. The scheme of the measurement system of T200 instrument. Source: [8]

3. Results

Presenting results achieved in the laboratory including concentration of air pollution in ppb and in µg/m^3 for the concentration of the nitrogen dioxide was an admission to drawing results. Values of concentration for individual gas pollution in air were counted for current terms i.e. temperature 273 K and the atmospheric pressure 101.3 kPa.

In order to count the concentrations of gas pollutions from ppb following equation was used:

$$\rho = C * \frac{M * P_{PEPI} * 273}{0{,}0224\,m^3 * 1013 * T_{PEPI}} \quad (4)$$

where:
ρ- concentration of pollution [µg/m^3],
C- concentration of pollution in ppb as a fraction,
M- molar mass of pollution [g/mol],
PPEPI- pressure registered on a meteorological station at PEPI in Kielce [hPa],
TPEPI- temperature registered on a meteorological station at PEPI in Kielce [K].

Data was processed to the figure on average of values an hour long of concentrations. In this way 840 data for each examined compound was obtained. Original data were processed to standardized name [µg/m^3]. The results of own measurements of the NO2 concentration named NO2 (KUT) compared with measurements of the Province Environmental Protection Inspectorate in Kielce named NO2 (PEPI) were presented on the figure no. 3.

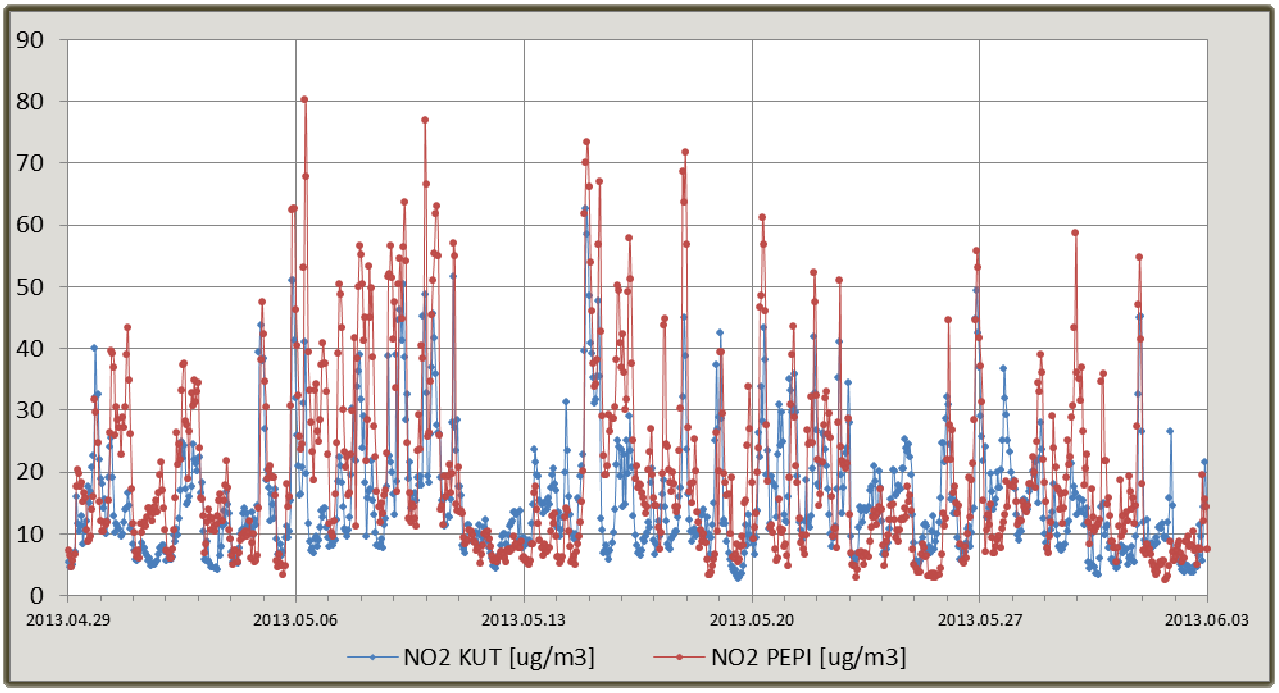

Fig. 3. Concentrations of NO_2 [µg/m3] in own measurements (NO2 KUT) and in measurements of the Province Environmental Protection Inspectorate in Kielce (NO2 PEPI). Source: own research and PEPI data.

4. Discussion

Drawing examinations up was begun with the data representation from the NO2 measurement on the graph. For the combination including 840 data on average of values an hour long of concentrations basic statistical characterizations reporting about central values and data dispersion were counted.

The NO2 average value is 15.31 [µg/m^3]. The smallest measured value is 2.72 [µg/m^3], whereas the highest value is 62.55 [µg/m^3]. The standard variation is a measure of the scattering data, which is 9.75 [µg/m^3]. Data mentioned above can prove about the symmetrical arrangement, similar to the normal arrangement.

At establishing applying the so-called empirical rule [1] for the examined sample, we can conclude that about 68% of the observation results is included in a bracket {average - standard variation; average + standard variation}. For the results from NO2 measurements this range is included between values {5.56; 25.06}. It is possible to conclude farter, that about 16% of data will has values smaller than 5.56 [µg/m^3] and the similar amount of data will get higher values than 25.06 [µg/m^3]. From data presented on the figure no.3 results, that dynamics of the values of changes are great and it is possible to recognize the process of changes as stable.

5. Conclusion

Comparison of the average value of concentrations between own measurements and measurements of the Province Environmental Protection Inspectorate in Kielce showed that, in own measurements obtained results were about 20% lower.

After detailed comparing of all data, the stated relation of the variation is regarding almost all values, because for the majority of data at the same time local extremes are appearing. The source of these differences were mainly differences in the location of measuring places. In the case of

Province Environmental Protection Inspectorate the measuring place is compatible with the standard recommendations.

However, measurements in the laboratory of the Kielce University of Technology were performed by the wall of building, where the finish of the inlet pipe was put in depression area about 20 cm above the level of ground covered with grass and separated by grass from the road that is located about 50 m from the test point. It could influence to differences between NO2 concentrations registered in the Province Environmental Protection Inspectorate in Kielce station and in the laboratory of the Kielce University of Technology.

References

[1] Aczel, A.D. *Statistics in menagement*. Scientific Publishing PWN, Warsaw 2000.

[2] van Andel, T.H. *New look at the old planet, Changeable face of the Earth*, Scientific Publishing PWN, Warsaw 1997.

[3] Zwoździak A., Zwoździak J., Szczurek A. *Meteorology of the atmosphere*. Publishing house of the Wroclaw University of technology, Wroclaw 1998.

[4] *Act of 20 July 1991. about Inspection of the State Environmental Protection* (Dz.U. 1991 nr 77 poz. 335).

[5] *Act of 27 April 2001. Environmental Protection Law* (Dz. U. z 2001 r. Nr. 62, poz. 627).

[6] Department of Monitoring and Information about Environment by Province Environmental Protection Inspectorate, *The State Environmental Monitoring Programme for years 2013-2015*. Warsaw 2012.

[7] *PN-EN 14211: Ambient Air Quality: Standard chemiluminescence method of measurement of the concentration of nitrogen oxide and nitrogen dioxide*.

[8] Teledyne Advanced Pollution Instrumentation, *Manual: Model T200 Nitrogen Oxide Analyzer*, San Diego 2010.

[9] http://smjp.kielce.pios.gov.pl/index.php?page=analiza-pomiarow.

TRANSCOM 2015, 22-24 June 2015
University of Žilina, Žilina, Slovak Republic

Influence of geometry on stress intensity factor of the welded lap joint subjected to tensile load

[*]Jelena M. Djoković, [**]Ružica R. Nikolić, [***]Ján Bujňák
[*] University of Belgrade, Technical Faculty in Bor, Vojske Jugoslavije 12, 19210 Bor, Serbia
{jelenamdjokovic}@gmail.com
[**] University of Kragujevac, Faculty of Engineering, Sestre Janjić 6, 34000 Kragujevac, Serbia *and*
University of Žilina, Research Center, Univerzitna 1, 010 26 Žilina, Slovakia
{ruzicarnikolic}@yahoo.com
[***] University of Žilina, Faculty of Civil Engineering, Univerzitna 1, 010 26 Žilina, Slovakia
{Jan.Bujnak}@fstav.uniza.sk

Abstract: The welded lap joint is analyzed in this paper for determining the influence of the welds geometry on the fracture mechanics parameters. The stress intensity factor (SIF) is calculated analytically by application of the *Mathematica*® symbolic programming routine, based on the concept of linear elastic fracture mechanics, with taking into account existence of the weld and loads through the corresponding correction factors. Results obtained in this paper show that decrease of the lapped plates thickness lead to decrease of the stress intensity factor, while the SIF increases with extension of the lap length.

Keywords: Lap joint, Fillet weld, Stress intensity factor

1. Introduction

Welded joints are widely applied in engineering practice for joining the structural elements of various sizes and geometries and for transferring load from one structural element to another. The welded joint resistance is especially important for integrity of a structure, which is being welded. Numerous factors influence the resistance of the welded joint. Those factors are quality of the weld, cleanness of the surface before the welding, control of the environmental temperature before and after the welding, geometrical discontinuities like the root of the weld and lack of overlap between the parts that are joined by welding. All those factors directly affect the weld's resistance and its vicinity. A fatigue crack can develop in the area immediately adjacent to the weld, or in the weld itself, due to action of those factors. The geometrical discontinuities of the welded joint are causing an increase of the local stress field's intensity. Therefore, the load carrying capacity of the joint is decreased, what then causes reduction of the welded structure safety and reliability.

Design of the welded engineering structures represents a very complex task, due to many reasons like: large number of welds and difficulties in selecting the weakest point in the structure; difficulties in determination of material characteristics, since they are changing in the weld and in the heat affected zone (HAZ); presence of high residual stresses and problems in determination of the exact weld's geometry; problems in definition of the precise model that would idealize geometry of the weld and its vicinity, considering that fatigue fracture is one of the most frequent type of fracture of the welded structures; difficulties in proposing the unique criterion for estimate of the total fatigue life, etc.

Resistance of the welded joints, from the fracture mechanics aspect, was the subject of interest of numerous authors. Atzori et al. [1] have investigating the possibility of unification of various criteria, which were used for analyzing the fatigue strength of welded joints, based on influence of geometry on the local stress field and prediction of the residual working life by application of the linear elastic fracture mechanics. Motarjemi et al. [2] have analyzed influence of geometry of the

main and attachment plates in the T and cruciform welded joints exposed to tension. Lee at al. [3] have considered influence of geometry on the fatigue life of the non-load-carrying cruciform fillet welds. Baik et al. [4] have conducted an analysis of fatigue crack propagation of the welded structures exposed to bending. Chattopadhyay et al. [5] proposed a method, which enables determination of stress concentration and stress distribution in the area of the weld's root, by using the special shell technique of the Finite Element Method. Shen and Choo [6] have determined the stress intensity factor of the welded tubes exposed to tension.

Influence of geometry on the welded lap joint's fracture resistance was studied in this paper through determination of the stress intensity factor by application of the concept of linear elastic fracture mechanics.

2. Determination of the stress intensity factor

The considered problem is shown in Figure 1. Two plates of length *L*, width *B* and thickness *T* are lap welded with other two plates of width *B* and thickness *t*. The length of the lap is *u*. The welded joint is subjected to axial tensile force *F*, laterally. As can be seen from Figure 1, in front of the weld there is a crack of length *a*. The weld's height is *h* and width *w*. The fillet weld is triangular.

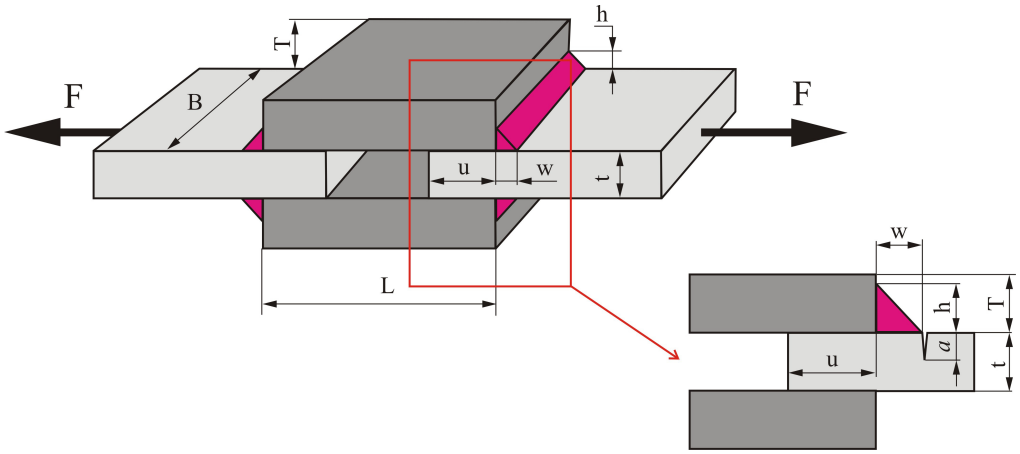

Fig. 1. Welded lap joint – loads and geometry.

Stress intensity factor for the welded joints can generally be calculated according to expression, Hobbacher [8]:

$$K_i = Y_i \cdot C_i \cdot \sigma_0 \sqrt{\pi a} \,. \tag{1}$$

where σ_0 is the referent straining (axial tension, bending or torsion), Y_i is the dimensionless parameter, which depends on the sample's geometry and applied load and *C* is the correction factor, which takes into account the stress concentration due to presence of the weld.

Mode I stress intensity factor, for the problem presented in Figure 1, based on equation (1), can be written as:

$$K_I = Y_F C_F \sigma_F \sqrt{\pi a} \,, \tag{2}$$

where:

$$Y_F = \sqrt{\sec\left(\frac{\pi}{2}\frac{a}{a+w}\right)} \,. \tag{3}$$

$$C_F = \left[1.0210 - 0.3772\left(\frac{h}{t}\right) + 0.1844\left(\frac{h}{t}\right)^2 - 0.0187\left(\frac{w}{t}\right)^2 - 0.1856\left(\frac{u}{t}\right) + \right.$$
$$\left. + 0.1362\left(\frac{u}{t}\right)^2\right]\left(\frac{a}{t}\right)^{-0.4535-0.1121\left(\frac{h}{t}\right)+0.3409\left(\frac{w}{t}\right)-0.0824\left(\frac{w}{t}\right)^2-0.0877\left(\frac{u}{t}\right)-0.0417\left(\frac{u}{t}\right)^2} \cdot \quad (4)$$

3. Results and discussion

In Figure 2 is shown the variation of the Mode I stress intensity factor in terms of the normalized crack length, for the case of the triangular fillet weld, with h/w = 1, for four different thicknesses of the overlapping plates. It is determined according to expression (3) by application of the programming package *Mathematica*®. The Mode I stress intensity factor is normalized by $1[\text{MPa}]\cdot\sqrt{\pi\cdot 0.01[\text{m}]}$. Characteristics of the material used in the analysis were Young's elasticity modulus E = 210 GPa and Poisson's ratio ν = 0.3.

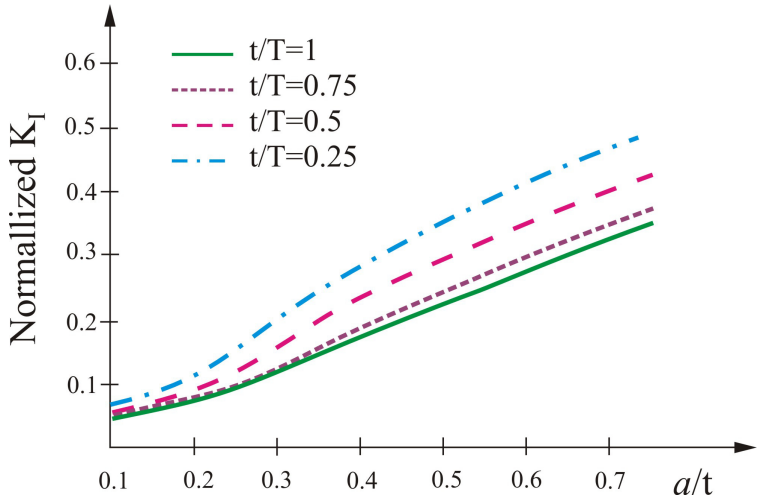

Fig. 2. Normalized Mode I stress intensity factor in terms of the normalized crack length for various thicknesses of the overlapping plates.

From Figure 2 follows that reducing the thickness of the overlapping plate leads to decrease of the stress intensity factor.

In Figure 3 is shown the normalized Mode I stress intensity factor in terms of normalized crack length, for the case of the triangular weld, with h/w = 1, for four different lengths of the overlapping plates. All data are the same as for Figure 2. From Figure 3 follows that stress intensity factor is increasing with increasing of the plates overlap.

4. Conclusion

In this paper is analyzed the welded lap joint exposed to axial tensile load. The objective was to determine the influence of the fillet weld's geometry on the fracture mechanics parameters.

The stress intensity factor was determined analytically with application of the *Mathematica*® programming routine. The presence of the weld was taken into account via the corresponding correction factors.

Results obtained in this paper show that the Mode I stress intensity factor decreases with decrease of the overlap thickness, while it increases with the overlap length increase.

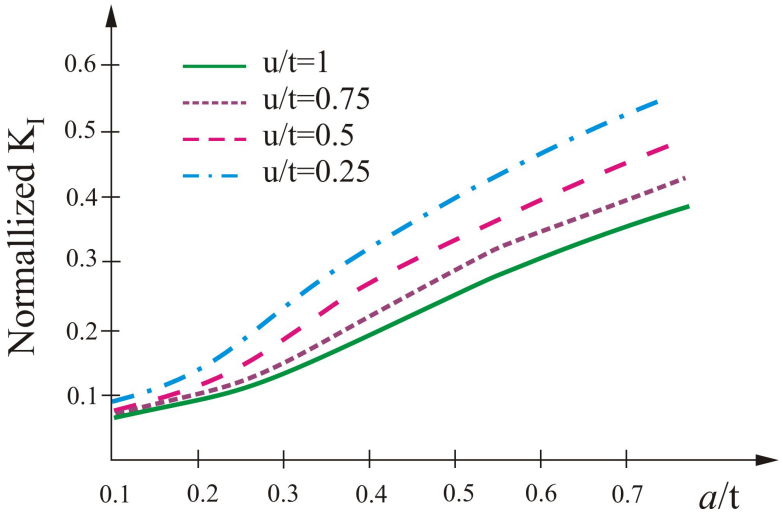

Fig. 3. Normalized Mode I stress intensity factor in terms of the normalized crack length for various lengths of the plates overlap.

Acknowledgement

This research was partially supported by the Ministry of Education, Science and Technological Development of Republic of Serbia through Grants ON174001, ON174004 and TR32036 and by European regional development fund and Slovak state budget by the project "Research Center of the University of Žilina" - ITMS 26220220183**.**

References

[1] ATZORI B., P. LAZZARIN, P., TOVO, R., *From the local stress approach to fracture mechanics: a comprehensive evaluation of the fatigue strength of welded joints,* Fatigue and Fracture of Engineering Materials and Structures, Vol. **22**, 1999, pp. 369-382.

[2] MOTARJEMI A. K., KOKABI, A. H., ZIAIE, A. A., MANTEGHI, S., BURDEKIN, F. M., *Comparison of the stress intensity factor of T and cruciform welded joints with different main and attachment plate thickness,* Engineering Fracture Mechanics, Vol. **65**, 2000, pp. 55-66.

[3] LEE C. H., CHANG, K. H., JANG, G. C., LEE, C. Y., *Effect of weld geometry on the fatigue life of non-load-carrying fillet welded cruciform joints*, Engineering Failure Analysis, Vol. **16**, 2009, pp. 849-855.

[4] BAIK B., YAMADA, K., ISHIKAWA, T., *Fatigue crack propagation analysis for welded joint subjected to bending*, International Journal of Fatigue, Vol. **33**, 2011, pp. 746-758.

[5] CHATTOPADHYAY A., GLINKA, G., EL-ZEIN, M., QIAN, J., FORMAS, R., *Stress analysis and fatigue of welded structures*, Welding in the World, Vol. **55** (7-8), 2011, pp. 2-21.

[6] SHEN W., CHOO, Y. S., *Stress intensity factor for a tubular T-joint with grouted chord*, Engineering Structures, Vol. **35**, 2012, pp. 37-47.

[7] CARPINTERI A., RONCHEI, C., VANTADORI, S., *Stress intensity factors and fatigue growth of surface cracks in notched shells and round bars: two decades of research work,* Fatigue and Fracture of Engineering Materials and Structures, Vol. **36**, 2013, pp. 1164-1177.

[8] HOBBACHER A., *Stress intensity factors of welded joints*, Engineering Fracture Mechanics, Vol. **46**, 1993, pp. 173-182.

TRANSCOM 2015, 22-24 June 2015
University of Žilina, Žilina, Slovak Republic

The content of heavy metals in the leachate from municipal landfill in Promnik

[*]Joanna Długosz
[*]Kielce University of Technology, Faculty of Environmental Engineering, Geomatics and Power Engineering, Department of Environmental Engineering and Protection, Al. Tysiąclecia Państwa Polskiego 7, 25-314 Kielce, Poland, {jdlugosz}@tu.kielce.pl

Abstract. The composition of leachate generated in the landfill site operation varies widely. It depends primarily on the morphology of waste, processes occurring in the landfill layer, storage technologies, the amount of water infiltrating into the landfill, and the age of the site. The most troublesome contaminants in the leachate are heavy metals. This study deals with an analysis of selected heavy metals content in leachate from functioning landfills. Leachate for the analysis were collected from an active landfill for non-hazardous and inert in Promnik (Świętokrzyskie Region). Attempts leachate were collected in accordance with the guidelines contained in the Polish Standard PN-ISO 5667-10-1997 - Water quality - Sampling - Guidance of sampling wastewater. Most of the analyzed concentrations of metals are low in relation to occupational exposure limit values and the values of the mean and median do not exceed standards specified in Polish law (Regulation of the Minister of Environment of 18 November 2014. on the conditions to be met when placing waste in water or ground or on substances particularly harmful to the aquatic environment (Journal of Laws of 2014, item. 1800)).

Keywords: heavy metals, leachate, landfill

1. Introduction

The amount of municipal waste generated in the EU in 2011 according to data of the Central Statistical Office was 253.1mln Mg or 503kg /capita. Waste prevention is a priority in Community law as laid down in the hierarchy of waste management practices. Decisions on waste prevention are adopted at the stage of the design phase of the product, as well as at the stage of its manufacture, use and are associated with the ultimate waste disposal arising from the articles after completing their life cycle. At the moment, the most common method of waste disposal in Poland is its storage. However, this method is the least desirable for environmental reasons. According to the National Waste Management Plan in 2014 [1] at the end of 2009 in Poland, there were 729 municipal waste landfills and only 238 other facilities for the management of municipal waste (eg. composting, sorting, incineration etc.). The total area of controlled landfills in 2010 amounted to approximately 2500ha [2]. Then in the stored waste take place a series of reactions and transformations: physical, chemical and biological. These processes resulting in a number of threats to the environment as a landfill gas emissions, odors and leachate formation [3,4]. Contaminated leachate have the longest emission in the landfill compared to other threats. (Fig. 1). As defined in the so-called Landfill Directive [5] leachate is "any liquid percolating through the deposited waste and emitted from or contained within a landfill."

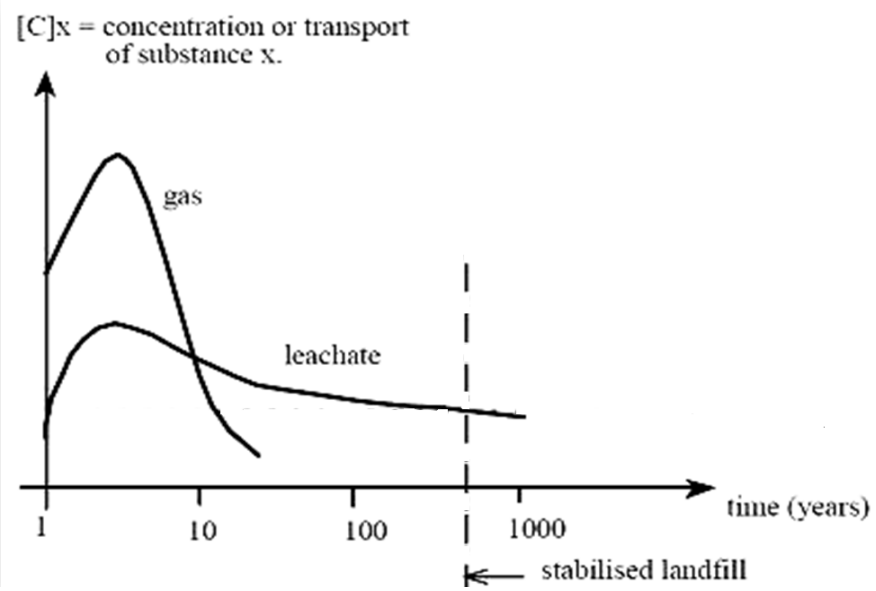

Fig. 1. Emissions from landfill as a function of time [6]

A specific feature of the leachate is varied chemical composition changing over time and depends on the type of deposited waste and a method of storage exploitation [7]. Based on observations during the chemical changes in the basic indicators of leachate from landfills (pH, BOD5, COD, TOC, ammonia nitrogen, Kjeldahl nitrogen, total phosphorus, the total alkalinity, total suspended solids and heavy metals content) there is a possibility to determination a stabilization process of the transitions processes in the waste [8]. It should be emphasized that the mentioned indicators of contaminants in landfill leachate are many times higher than those found in municipal wastewater. According to the literature the amount of heavy metals deposited in the landfill, which enters the effluent, is less than 0.05% [9]. Bioaccumulation and extraction processes promote to migration of heavy metals from landfills to the leachate. Chemical processes such as elution, oxidation and reduction can influence the differentiation of the chemical forms of heavy metals in the leachate many of which can pass directly from the effluent to the soil environment.

2. Research methods

Analyzed leachate come from landfills for non-hazardous and inert located in Promnik (Świętokrzyskie Province). The village is located approximately 15 km from the center of Kielce. The landfill covers an area of about 15ha, and the gross floor area of the new landfill is 10.8ha. It is located outside of urban areas. Landfill has a substrate insulating layer in the form of an impermeable membrane. For each layer of waste with a thickness of 2 m is used an insulating layer having a thickness of 0.15-0.20m in the form of, inter alia, earth, sand, small rubble and ash. At present landfill Promnik has three quarters of landfill for non-hazardous and inert waste:

• Section I - closed and undergoing reclamation; storage area approx. 45 500 m^2; active capacity of 864 000 m^3;

• Sectiont II - closed and undergoing reclamation; storage area approx. approx. 38 000 m^2; active capacity of 590 000 m^3.

• Section III - operated (currently enter here waste from the Kielce city and 15 municipalities); area of approx. 40 400 m^2; capacity of 680 000 m^3.

If the section III is exploited it will be closed and begin the process of remediation. The waste destined for disposal will be directed to the newly designed section IV.

Drainage water is collected from the tanks at checkpoints eg. for section I - S1 checkpoint. Attempts leachate were collected in accordance with the guidelines contained in the Polish Standard

PN-ISO 5667-10-1997 - Water quality - Sampling - Guidance of sampling wastewater. The emoluments of the leachate were made on a quarterly basis. Study the composition of the leachate from the landfill in Promnik were carried out under the monitoring of the landfill by Company Geological Polgeol SA from Warsaw and SGS EKO-Projekt Sp z o.o. Pszczyna. Samples were transported after collection at a temperature range 1°C÷5°C (in accordance with the standards).

Symbol	Unit	Methodology
1	2	3
pH	-	PN-90 C-04540.01
Pb (lead)	mg Pb/dm^3	PN-EN ISO 11885:2009; KJ-I-5.4-174
Cd (cadmium)	mg Cd/dm^3	PN-EN ISO 11885:2009; KJ-I-5.4-174
Cu (copper)	mg Cu/dm^3	PN-EN ISO 11885:2009; KJ-I-5.4-174
Zn (zink)	mg Zn/dm^3	PN-EN ISO 11885:2009; KJ-I-5.4-174
Cr^{+6} (chromium (VI))	mg Cr^{+6} $/dm^3$	PN-77/C-04604.08
Hg (mercury)	mg Hg/dm^3	KJ-I-5.4-35
As (arsenic)	mg As/dm^3	PN-EN ISO 11885:2009; KJ-I-5.4-174

Tab. 1. Methodology perform some indications in the leachate.

3. Results and Discussion

The content of heavy metals in the leachate is highly variable and depends on many factors. Furthermore, according to various authors, the content of metals in the leachate contained in the wide numerical ranges (Table 2). Therefore, the actual data usually do not exceed the given literature data - so it is in the case of these leachate.

Parameter	Range by Christensen T.H. and others [mg/dm^3]	Range by Pleczyński J. and others [mg/dm^3]
As	0.005÷1.6	0÷0.025
Cd	0.0005÷0.14	0.004÷0.375
Ni	0.02÷2.05	0.007÷1.04
Pb	0.008÷1.02	0.034÷2.89
Cr	0.03÷1.6	0÷0.271
Cu	0.004÷1.4	0.004÷0.375
Hg	0.0002÷0.05	0÷0.0045

Tab. 2. The average content of heavy metals in the leachate [10]

The maximum values of contaminants regarding leachate can be found in the Regulation of the Minister of Environment of 18 November 2014. on the conditions to be met when placing waste in water or ground or on substances particularly harmful to the aquatic environment (Journal of Laws of 2014, item. 1800). Individual values of heavy metals from the above-mentioned regulation are shown in Tables 3 and 4 (column 7).

Parameter	Unit	Minimum	Maximum	Mean	Median	Limit value by [11]
1	2	3	4	5	6	7
pH	-	7.54	8.2	7.80	7.735	6.5-9.0
As	mg/dm^3	0.01	0.15	0.0565	0.045	0.1
Hg	mg/dm^3	0.00005	0.00863	0.001191	0.0005	0.06
Cr^{+6}	mg/dm^3	0.005	0.5	0.033	0.01	0.1
Zn	mg/dm^3	0.02	0.76	0.16195	0.115	2.0
Cu	mg/dm^3	0.005	0.27	0.03125	0.0165	0.5
Pb	mg/dm^3	0.005	0.02	0.0098	0.01	0.5
Cd	mg/dm^3	0.001	0.003	0.0014	0.001	0.4

Tab. 3. Content of heavy metals in the leachate from the landfill in Promnik - tank S1 (2007-2012)

Parameter	Unit	Minimum	Maximum	Mean	Median	Limit value by [11]
1	2	3	4	5	6	7
pH	-	7.35	9.1	8.36	8.4	6.5-9.0
As	mg/dm^3	0.01	0.1	0.03625	0.02	0.1
Hg	mg/dm^3	0.00005	0.00348	0.000709	0.00034	0.06
Cr^{+6}	mg/dm^3	0.005	0.23	0.01925	0.01	0.1
Zn	mg/dm^3	0.025	0.5	0.1048	0.085	2.0
Cu	mg/dm^3	0.006	0.199	0.03585	0.0295	0.5
Pb	mg/dm^3	0.005	0.03	0.0121	0.01	0.5
Cd	mg/dm^3	0.001	0.003	0.0014	0.001	0.4

Tab. 4. Content of heavy metals in the leachate from the landfill in Promnik - tank S2 (2007-2012)

In Tables 3 and 4 are presented the results of analysis of leachate from cyclic tests conducted under functioning landfill monitoring. Landfill monitoring obligations prescribed by the Decree of the Minister of the Environment of 30 April 2013 on the landfill of waste [12] and in the case of active landfill leachate testing are collected quarterly. The obtained data were calculated: the minimum, maximum, mean arithmetic and median (in order to reduce the influence of extreme values). By comparing the obtained values with the values defined in [11] it can be seen that the level of heavy metals in the leachate analyzed in most cases is below the permissible limits in force in the Polish law. A low content of heavy metals may be associated with a variety of factors, including the particular case include with a pH level of 8.36 on average (median 8.4) in the section I and 7.8 (7.73) in the section II. It should be noted that the pH increases the solubility metals decreases. In addition, the concentrations of heavy metals have significant influence adsorption and precipitation reactions (by co-anions sulfides, carbonates, hydroxides). A small amount of heavy metals is also related to the type of waste landfilled in Promnik (Table 5).

Composition of the group	Contents [%]	Methodology
1	2	3
Plant food waste	29.1	PN-93/Z-15006 PN-93/Z-15008.02
Paper and cardboard	21.3	
Glass	17.1	
Plastics	16.9	
Metals	5.0	
Animal food waste	4.9	
Fine fraction 0-10mm	4.4	
Textiles	0.6	
Other organic	0.5	
Other inorganic	0.2	
Total	100.0	

Tab. 5. Composition of the group of municipal waste in 2010

Exceedance occurred in the case of two elements: As (section I) and Cr^{+6} (section I and II). The maximum value of arsenic was higher than the limit of 0.05mg / dm^3, however, the mean and median are much lower than the limit value (Table 3). In the case of chromium limit value is exceeded by five (section I) and almost twice (section II). Least with respect to the maximum permissible value of Hg (approx. 0.08%). On the basis of the analyzed results of studies investigated the concentration of metals in the leachate are shown in the following ranks decreasing the content of:

- Section I: Zn>As>Cu>Cr^{+6} = Pb>Cd>Hg
- Section II: Zn>Cu>As> Cr^{+6} = Pb>Cd>Hg

Determining the order of the series taken into account the value of the median as a more representative (more resistant to extreme values in comparison with the arithmetic mean).

4. Conclusion

Landfill leachate are produced, among others, due to eluting different types of chemicals by rainwater from landfill deposits and their quantity and composition depend on many factors. Moreover, in the literature [10] can be found quite wide scope of heavy metals concentrations in the leachate so analyzed leachate from the landfill in Promnik fit in this range very well. In the years 2007-2012 in the leachate from the landfill in Promnik were reported exceedings the maximum content of heavy metals in the case of As (section I) and Cr^{+6} (section I and II). In addition, the concentrations of metals analyzed are low in relation to occupational exposure limit values and the values of the mean and median do not exceed standards specified in Polish law.

References

[1] Krajowy Plan Gospodarki Odpadami 2014, Warszawa 2014

[2] Infrastruktura komunalna w 2010 roku, Główny Urząd Statystyczny, Warszawa 2011

[3] Kulig A., Metody pomiarowo-obliczeniowe w ocenach oddziaływania na środowisko obiektów gospodarki komunalnej, Oficyna Wydawnicza Politechniki Wrocławskiej, Wrocław 2004

[4] Długosz J., Characteristics of the compostion and quantity of leachate from municipal landfills – a review, Archives of Waste Management and Environmental Protection, ISSN1733-4381, vol. 14, issue 4 (2012), p. 19-30

[5] Dyrektywa Rady 1999/31/WE z dnia 26 kwietnia 1999r w sprawie składowania odpadów

[6] Kjeldsen, P., Morton Barlaz, A., Rooker, P., Baun, A., Ledin, A, Christensen, H.Present and Long-Term Composition of MSW Landfill Leachate: A Review. Critical Reviews in Environmental Science and Technology, 2002, 32 (4) 297 - 336

[7] Gawdzik J., Latosińska J., Żygadło M., Application of Fenton for the landfill leachate teratment, Archives of Waste Management and Environmental Protection, 14, 3, 2012, 21-26, 2012

[8] Żygadło M., Strategia gospodarki odpadami komunalnymi, Wydawnictwo PZITS, Poznań 2001

[9] Christensen, T.H., Kjeldsen, P. (1989): Basic biochemical processes in landfills, in: Sanitary Landfilling: Process, Technology and Environmental Impact, (Christensen, T.H.,Cossu, R., Stegmann, R. Eds.), Academic Press, London UK,1989, s. 29 – 49

[10] Klimek A., Wysokiński L., Zawadzka – Kos J., Osęka M., Chrząszcz J., Poradnik metodyczny w zakresie PRTR dla składowisk odpadów komunalnych, Warszawa, 2010

[11] Rozporządzenie Ministra Środowiska z dnia 18 listopada 2014r. w sprawie warunków, jakie należy spełniać przy wprowadzaniu ścieków do wód lub do ziemi oraz w sprawie substancji szczególnie szkodliwych dla środowiska wodnego

[12] Rozporządzenia Ministra Środowiska z dnia 30 kwietnia 2013r w sprawie składowisk odpadów

TRANSCOM 2015, 22-24 June 2015
University of Žilina, Žilina, Slovak Republic

Experimental monitoring of moisture changes in railway track structure

[*]Peter Dobeš, Libor Ižvolt
[*]University of Žilina, Faculty of Civil Engineering, Department of Railway Engineering and Track Management, Univerzitná 8215, 010 26 Žilina, Slovakia, {peter.dobes}@fstav.uniza.sk, {libor.izvolt}@fstav.uniza.sk

Abstract. There is characterised the experimental stand (railway track model in 1:1 scale) in the introduction of the paper, which is used to monitor the temperature and water regime of railway track structure. In the second part of the paper there are characterised the results of monitoring the course of moisture in individual structural parts of railway track model obtained by the TDR method (time domain reflectometry), which are required, among others inputs, for mathematical modelling of temperature regime of the structure of the railway track.

Keywords: railway, subgrade, water regime, moisture, time-domain reflectometer

1. Introduction

The moisture content of materials inbuilt in the structure of the railway track, in particular, in the body of the track substructure, or its subsoil (or embankment, in the case of lines of railway track), has a decisive effect on the resistance of the track substructure and ultimately to the stability and security of the railway track. The amount of water that is contained in the structural layers of the subgrade structure and earthwork depends primarily on the type of rock, its volume weight / permeability, groundwater levels, subsoil capillarity and climatic conditions. The moisture content of the track substructure is not constant, but it varies in the course of the year, depending on the amount of downfall (water, snow), temperature and water regime of the body of the track substructure, and its shape as well (embankment, cutting, cut) [1].

Department of Railway Engineering and Track Management (DRETM) of the Faculty of Civil Engineering of the University of Žilina has been dealing with one of the research activities for several years (since 2002) focused on the issue of the influence of non-traffic load (influence of weather factors — water, frost, snow cover, etc.) on the temperature regime of the railway track – subgrade structure. For this purpose there was built the Experimental stand DRETM I, which served and is still used to monitor the temperature regime of the model of railway track in 1:1 scale, in particular, in the intersection of zero isotherm into the subgrade structure. Soilvision software [2], which is used, among others, for mathematical modelling of the temperature regime of the subgrade structure, requires specific details. For reasons to obtain the data for relevant modelling of the temperature regime of the structure of subgrade structure, there was built the Experimental stand DRETM II (*Fig. 1*), which not only allows to continuously monitor the temperature and water regime of structural layers of railway track of embankment shape 1:1 and its subgrade, but also provides the required data for mathematical modelling.

Monitoring and identifying moisture in individual structural parts of Experimental stand DRETM II, there have been inbuilt moisture tests during its setting up consisting of TDR probes (Time Domain Reflectometers), allowing to monitor moisture of materials inbuilt at any time. Since the moisture TDR probes are designed primarily for the determination of moisture of fine-grained materials (contain calibration curves for fine-grained materials) and structural parts of the Experimental stand DRETM II are made up of coarse-grained material (subsoil, however, is made of fine-grained soils), it was necessary to carry out the initial calibration. Therefore, in the following

parts of the paper the attention will be paid not only to the characteristics of the test method for the determination of the moisture content of materials built in the experimental stand and its subgrade, but there will be also given concrete results of measurements for monitoring the course of moisture in different structural parts of the Experimental stand DRETM II.

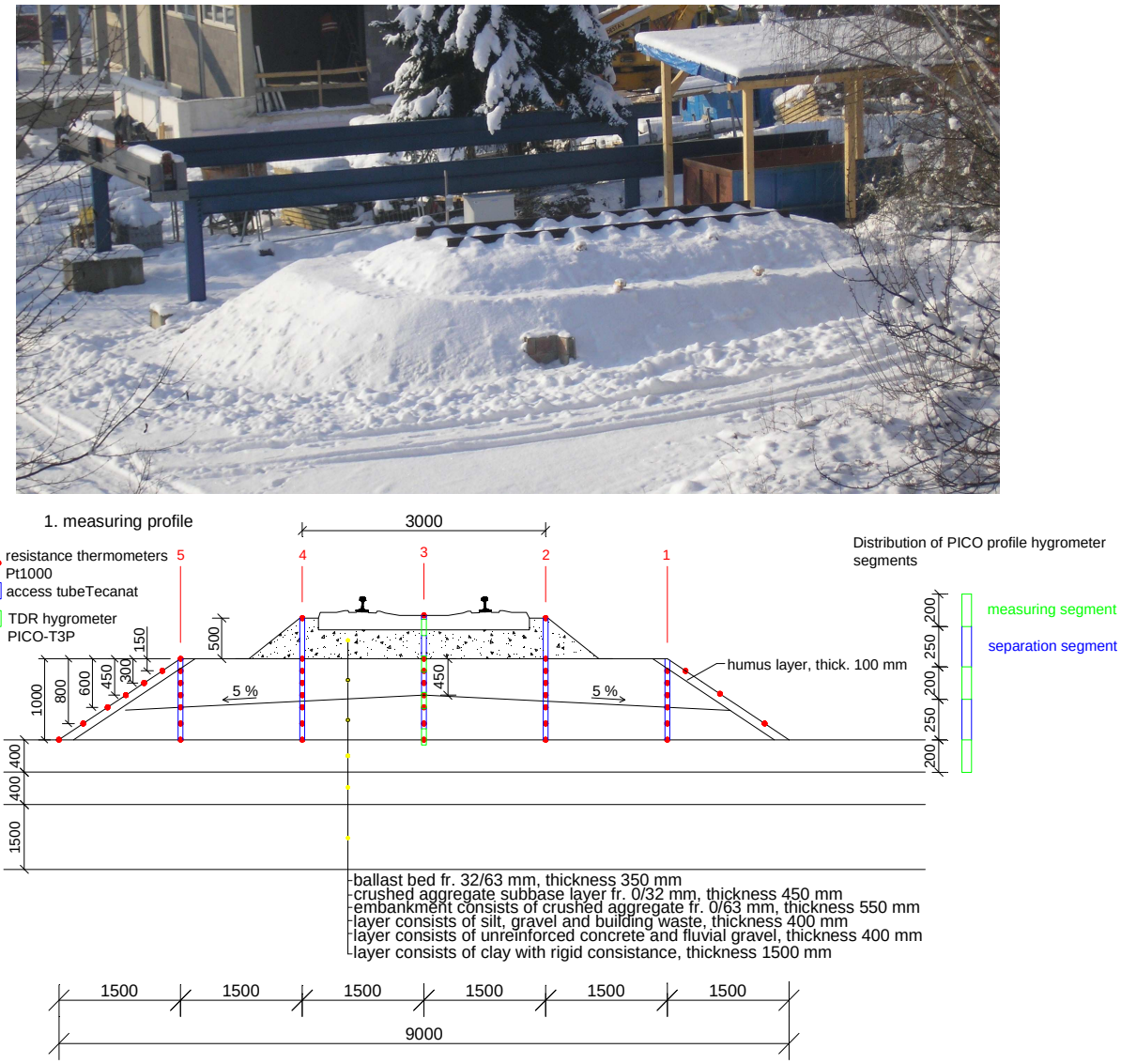

Fig. 1. Experimental stand DRETM II

2. Determination of dielectric constants

Dielectric constant indicates the ability of non-conducting material (the rock, in our case) to transmit electromagnetic waves. Dielectric constant of water is much greater than its value for the solid particles and air, which means that even relatively small changes in the amount of water in soils have a large impact on its value. There are typical values of dielectric constant for all 3 phases of the soil shown in *Tab. 1*.

Component	Water	Air	Solid particles
Dielectric constant	79 – 81	1	2 – 6

Tab. 1. Typical values of dielectric constants for soil

Dielectric constant is determined by reflectometry TDR [3]. The principle of its establishment lies in the fact that the TDR probe spreads electromagnetic waves along the coaxial metal cable, connected to the parallel guide probes acting in the soil as an element guiding the waves. The signal

transmitted is reflected from its end back into the external unit serving to take measurements. The system measures the time between sent and received wave and calculates the speed of its spread. This is just influenced by the dielectric constant of the material surrounding the measuring element guiding electromagnetic waves, which is reflected in its design length. The higher the speed of waves spreading is, the smaller the dielectric constant of soil is and thus the lower representation of phase (quantity) of water in soils, or lower its moisture.

In order to ensure the protection of the TDR probe against mechanical damage, it was necessary to incorporate a protective PVC tube into the profile of measurement. Protective PVC tube had to be built into the material to be measured at least 2 weeks prior to making its own measurement of moisture, while the material mainly around the tube must be sufficiently consolidated, since any air gaps around tube could affect the measurement result (lower values of moisture up to 10 %). Distribution of electromagnetic field of the TDR probe is shown in *Figure 2*.

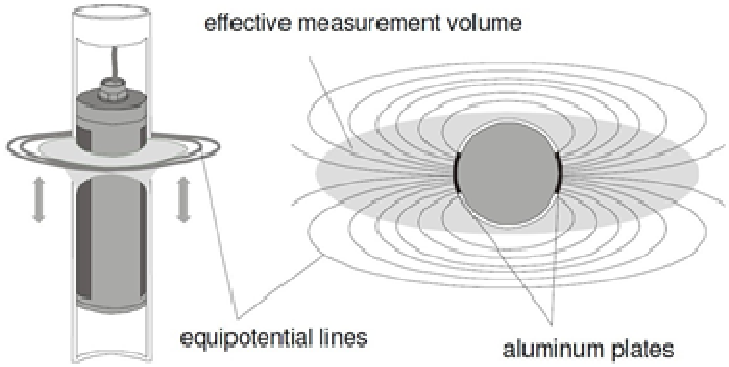

Fig. 2. Distribution of electromagnetic field of probe [4]

2.1. Detection of material moisture of structural layers in Experimental stand DRETM II

As it has already been pointed out in the introduction to the paper, water in structural layers of the railway track has a major impact not only on the deformation, but also thermo-technical features of building materials inbuilt. The amount of water changes with the time, and depending on the amount of rainfall and water movement in the soils in the course of achieving balance in dry season. With regard to the possible establishment of failures in railway subgrade structure it is also important to know what is the representation of water in individual structural layers of subgrade structure just before winter period (water freezing and formation of ice formations) and also in the spring, when the snow cover melts and the subgrade structure defrosts and, consequently, reduction of deformation resistance in the individual components of subgrade structure. Yet it was not possible to obtain the necessary data from the literature on the moisture content of materials inbuilt into the subgrade structure and thus there has not been any information about the fluctuations in the course of the year. Since the moisture data are essential, in addition to other inputs, for mathematical modelling of the temperature regime of subgrade structure, it was necessary to identify them. As can be seen in *Figure 1*, for this purpose there were 5 protective tubes for TDR probes built in Experimental stand DRETM II and the next was additionally built in the foot of embankment in order to identify the course of subgrade moisture in experimental stand. Structural parts of experimental stand consists of a track ballast fr. 31.5/63 mm, the moisture of which cannot be established using the TDR method (impossibility of adequate consolidation and removal of air spaces), while its moisture content, with respect to the fact that it is clean, varies in a minimum, and protective layer of crushed aggregate fr. 0/32 mm and embankment of crushed aggregate fr. 0/63 mm.

Measurement of moisture content has been running on Experimental stand DRETM II since October 2014, and the measurement preceded calibration for the materials built into the structure of railway track model (Experimental stand). Considering the calibration there were determined

coefficients *m*0 a *m*1 (*Tab. 2*), which are used for the calibration curve necessary for determination of the moisture content of the material.

Material	*m0*	*m1*
Crushed aggregate fr. 0/32 mm	-4.2010	0.0263
Crushed aggregate fr. 0/63 mm	-5.3136	0.0317
Clay blended with river gravel	-15.6753	0.04698

Tab. 2. Coefficients calculated necessary to establish the calibration curve of the material

Measurement of moisture content of materials built in experimental stand were carried out, for practical reasons, twice a week (the beginning and end of the work week), since it was not expected that there would occur significant changes in moisture state of these materials in a shorter period of time. In *Fig. 3*, there is shown measurement of the moisture content of materials built in the structural layers of Experimental stand DRETM II.

Fig. 3. Measurement of moisture content of structural layers (left) and subgrade (right) of the Experimental stand DRETM II.

The depth of the TDR probe in measuring profile, where the moisture is determined, was designed so that the centre of the probe was approximately in the middle of each of the structural layer monitored. Considering the material of protective layer of crushed layer fr. 0/32 mm there was thus established depth of the surface of the TDR probe for the measuring range no. 2, 3 and 4 (see *Fig. 1*) in the value of about 650 mm below the surface of the track ballast (approx. 150 mm below the surface of the protective layer) and for the measuring range no. 5 in the value of about 225 mm (without track ballast in overburden). For technical reasons it was not possible to measure in the measuring range no. 1 (a new incorporation of protective tube required). In the embankment, which is built from the crushed aggregate fr. 0/63 mm there was determined depth of the surface of the TDR probe from the surface of track ballast in the value of about 1 225 mm for measuring ranges no. 2, 3 and 4, and about 725 mm for no. 1 and 5 (no track ballast in overburden).

There have been compiled charts of the results of the measurements obtained (*Fig. 4*), including the obvious course of moisture in the structural layers of the railway track model in the autumn period, just before the oncoming winter period and subsequently, during the winter period in 2014/2015.

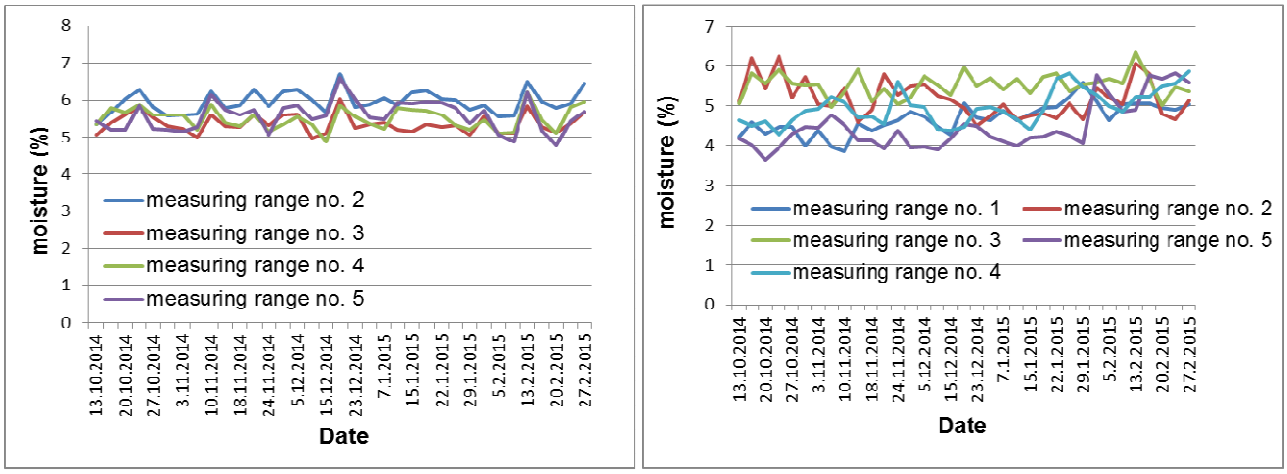

Fig. 4. Course of moisture in structural layers of Experimental stand DRETM II (left - protective layer of the crushed aggregate fr. 0/32 mm, right - embankment of the crushed aggregate fr. 0/63 mm)

Fig. 4 shows that the moisture of protective layer formed by the crushed aggregate fr. 0/32 mm, which is between the track ballast and earthwork material (embankment) was in the range of 5 to 6.5 % and the moisture of the embankment material formed by the crushed aggregate fr. 0/63 mm was in the range of 4 to 6 %.

2.2. Detection of moisture of subgrade material in experimental stand DRETM II

The subgrade of Experimental stand DRETM II is made up of clay with river gravel. Before the actual measurement of the moisture content of the subgrade material, it was also necessary to perform the calibration, and the coefficients needed to establish a calibration curve are shown in *Tab. 2*.

The depth of the TDR probe in measuring profile, where the moisture was determined was designed so that the centre of the probe was approximately 1 000 mm below the level of the original terrain. There has been compiled a chart from the results of the measurements obtained (*Fig. 5*), including the obvious course of soil moisture of subgrade earthwork in the depth in the autumn period, just before the oncoming winter period and subsequently, during the winter period in 2014/2015.

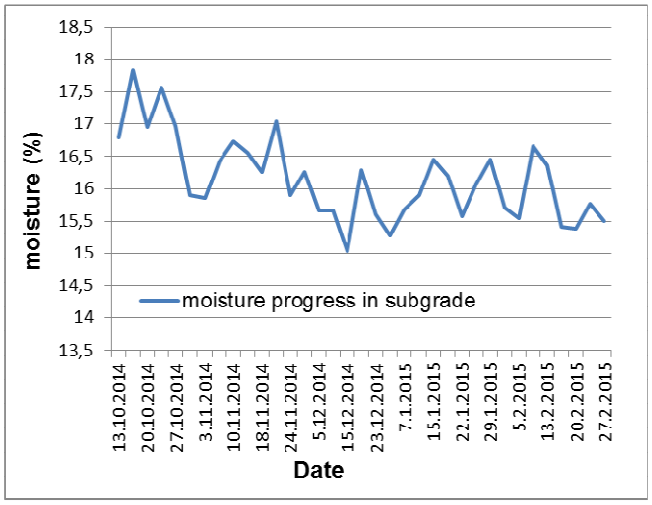

Fig. 5. Moisture in the subgrade of Experimental stand DRETM II.

Fig. 5 shows that the moisture content of the subgrade of Experimental stand DRETM II formed by the clay with river gravel varied from 15 to 17.5 %.

3. Conclusion

By using the TDR probes and method of measurement of dielectric constant, which was the input parameters for the determination of the moisture content, we can achieve high precision of the measured values of the moisture in accordance with the conditions (sufficient consolidation to avoid air gaps, non-exceeding maximum moisture, sufficient engagement of the probe in soil) and providing high-quality calibration. Even coarser grading of the material tested in the calibration of the probe and also during the implementation of actual measurements on the Experimental stand DRETM II did not have an impact on its accuracy, in spite of the fact that moisture probe is designed especially for fine-grained materials. It can be concluded that this is a method that allows determining very easily, without required sampling, moisture content in any place of earthwork and its subgrade and obtaining relevant inputs for the subsequent modelling of the temperature regime of the subgrade structure.

Acknowledgement

The presented results are the results of solving the VEGA grant project 1/0756/12 Experimental monitoring and mathematical modelling of thermal regime of railway subgrade structure.

This paper was created with the support of the project "Supporting of quality education and research in the field of transport as the engine of the economy" (ITMS: 26110230076), supported by the Education Operational Program funded by the ERDF.

References

[1] IŽVOLT, L.: Railway substructure – stress, diagnostics, design and implementation of body construction layers of railway subgrade (Železničný spodok – Namáhanie, diagnostika, navrhovanie a realizácia konštrukčných vrstiev telesa železničného spodku). (Scientific monograph). University of Žilina, 2008, ISBN 978-80-8070-802-3.

[2] FREDLUND, M.: SoilVision – A Knowledge-Based Soils Database (User's Manual), SoilVision Systems Ltd., Canada, 2011

[3] SEBESTA, S., OH, J., LEE, S. I., SANCHEZ, M., TAYLOR, R.: Initial review of rapid moisture measurement for roadway base and subgrade, Texas A&M Transportation Institute College Station, Texas, 2013

[4] Trime Pico-profile manual (http://www.imko.de/en/products/soilmoisture/soil-moisture-sensors/trimepicoipht3)

[5] IŽVOLT, L., HODAS, S.: Software support for temperature regime modelling of railway track construction, Systemy transportowe, IX. konferencja naukowo-techniczna, Katowice, 2013, ISBN 978-83-926923-5-5

TRANSCOM 2015, 22-24 June 2015
University of Žilina, Žilina, Slovak Republic

Influence of reinforcement corrosion on moment resistance of RC bridge girder subjected to bending

[*] K. Dubała, [**]P. Koteš, J. Selejdak
[*] Department of Building Structures and Engineering, Faculty of Civil Engineering, Technical University of Czestochowa, ul. Akademicka 3, 42-200 Czestochowa, Poland, kdubala@bud.pcz.czest.pl, jaceksel@poczta.onet.pl
[**]Department of Structures and Bridges, Civil Engineering Faculty, University of Žilina, Univerzitná 8215/1; 010 26, Žilina; Slovakia, kotes@fstav.uniza.sk

Abstract. The reliability of existing bridge structures is significantly affected by many factors, from which the reinforcement and structural steel corrosion together with effect of traffic action are the most important. Corrosion is the destructive attack of metal by chemical or electrochemical reaction with its environment. The quality and the durability of the concrete structures are affected by lots of degradation processes. Reinforced concrete is considered as a versatile, economical and successful construction material. Usually it is durable and resistant material, performing well throughout its service life. The corrosion of reinforcing steel in concrete due to severe environment is the phenomenon that highly affects the reliability and durability of reinforced concrete structures.

Keywords: corrosion, reinforcement, bridge, existing structure, active stage, passive stage, reliability level, remaining lifetime

1. Introduction

Reinforced concrete is a widely used construction material for bridges, buildings and platforms as well as for underground structures such as tunnels or reinforced concrete pipelines [1]. Generally, reinforced concrete is very durable material capable of withstanding a large range of severe environments including marine, industrial and mountains conditions. Despite the fact that the majority of these structures show good long-term performance and high durability, there are still a large number of failures of concrete structures as results of premature reinforcement corrosion [1].

Bridges are structures mostly affected by corrosion. Owing to either carbonation of the concrete or the ingress of chloride into the concrete, depassivation of the reinforcing steel occurs, leading to rapid steel corrosion with significant loss of cross-section. From a scientific point of view, the depassivation of the reinforcing steel and the subsequent corrosion reactions are very complex due to various interactions of environmental exposure conditions, the different materials involved as well as the design of the structure. With regard to economic aspects at the end of the 20 century, the cost of corrosion damage to reinforced concrete bridges in the United States, Australia, Europe and the Middle East due to the use of deicing salts alone is estimated to be €250 and €800 million/year [2]. In regions with a marine environment and warm climatic conditions, the corrosion process may be significantly accelerated [3].

In order to evaluate existing structures, a theoretical approach was developed using conditional probability. The new information concerning the actual structure condition is used in this mathematical model. This information is not available in the process of the new structure design. Periodic inspections regularly performed within lifetime of the observed structure are main resources of this information. The obtained extra information unknown in the design phase can be used for verification of the correct structure performance and also helps to reduce some uncertainties related to the structure resistance, measurements and load parameters [4, 5].

2. Reinforcement corrosion and moment load-carrying capacity

The reinforcement corrosion influenced the remaining lifetime severely. The corrosion does not only decrease the reinforcement cross-section, but also causes the cracks and dropping out the concrete cover. It means that the flexural stiffness is decreasing [6, 7, 8 and 9].

The reliability margin G(t) [6, 10] is the basic parameter of structural reliability and it is described by formula

$$G(t) = R(t) - E(t). \tag{1}$$

where: R(t) is the generalized function of random variable structural resistance,

E(t) are random variable load effects of the same element.

The resistance R(t) has been changed in time due to many factors. The different types of degradation are the best-known factors changing the resistance in time. The most significant way of degradation of concrete structures is diffusion of CO_2 to the concrete member called as a carbonization, and consecutive corrosion of reinforcement. Moreover in the case of bridges, the penetration of chloride ions Cl- into bridge structure is also caused the corrosion of reinforcement.

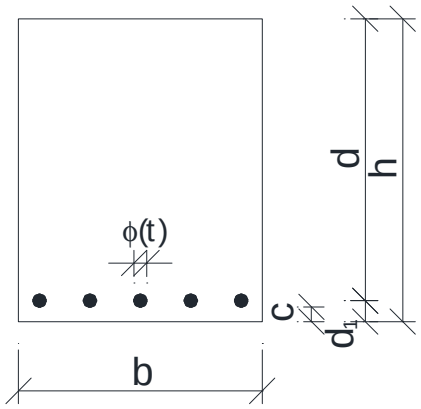

Fig. 1. The rectangular cross-section

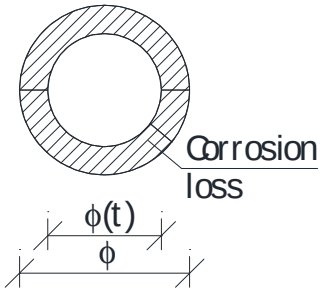

Fig. 2. The uniform corrosion loss of reinforcement cross-section

In the ultimate limit state, the time dependent change of resistance R(t) of reinforced concrete rectangular cross-section (Fig. 1) depends mostly on loss of reinforcement cross-section area. Commonly, there are used two approaches to the calculation of the reinforcement cross-section area loss. In the case of uniform corrosion loss (Fig. 2), the first model according to Andrade [11] was considered. That model of corrosion is one of the most used models. The loss of diameter ϕ(t) for uniform corrosion is described by formula

$$\phi(t) = \phi. \qquad \text{for} \quad t \le t_o \tag{2a}$$

$$\phi(t) = \phi - 0.0232 \cdot (t - t_o) \cdot i_{corr}. \qquad \text{for} \quad t > t_o \tag{2b}$$

where: i_{corr} is the corrosion current density [μA/cm2],
(1 μA/cm2 is equal to 11.6 μm/year of corrosion),
t is the time,
t_o is the time of passive stage.

Next, the second model of corrosion according to Thoft-Christensen [12] (see Fig. 2) was considered. The loss of diameter ϕ(t) is described by formula

$$\phi(t) = \phi. \qquad \text{for} \quad t \le t_o \tag{3a}$$

$$\phi(t) = \phi - (t - t_o) \cdot r_{corr}. \qquad \text{for} \quad t > t_o \tag{3b}$$

where: r_{corr} is the corrosion rate [μm/year].

The resistance R(t) of the reinforced concrete rectangular cross-section subjected to bending is given by formula

$$R(t) = M_{Rd}(t) = F_s(t) \cdot z(t) = A_{s1}(t) \cdot f_y \cdot z(t) =$$
$$= A_{s1}(t) \cdot f_y \cdot \left(\left[h - c - \frac{\phi(t)}{2} \right] - \frac{A_{s1}(t) \cdot f_y}{2 \cdot b \cdot f_c} \right) \quad (4)$$

where: $F_s(t)$ is the time dependent force in tensioned reinforcement due to corrosion [kN],

$z(t)$ is the time dependent lever of internal forces [m],

f_y is the steel yield strength [kN.m^{-2}],

f_c is the compressive strength in concrete [kN.m^{-2}],

h is the height of cross-section [m] (Fig. 1),

b is the width of cross-section [m] (Fig. 1),

c is the concrete cover [m] (Fig. 1),

n is the number of reinforcement in cross-section [-] (Fig. 1),

$A_{s1}(t)$ is the time-dependent reinforcement cross-section due to reinforcement corrosion [m^2],

$$A_{s1}(t) = \frac{n \cdot \pi \cdot \phi^2(t)}{4} = \frac{n \cdot \pi \cdot (\phi - 0.0232 \cdot (t - t_o) \cdot t_{corr})^2}{4}, \text{ or} \quad (5)$$

$$A_{s1}(t) = \frac{n \cdot \pi \cdot \phi^2(t)}{4} = \frac{n \cdot \pi \cdot (\phi - (t - t_o) \cdot r_{corr})^2}{4}, \text{ or} \quad (6)$$

Numerical application calculating time dependent resistance R(t) is mostly realized by simulation of the method Monte-Carlo. It is possible to use other methods for simulation, for example LHS, Important sampling [12] etc. For further using, results of simulations are in a general way approximated by mathematical relations of second polynomial given by formulas [13, 14]

$$m_R(t) = m_R + p_1.t + p_2.t^2, \text{ respect } s_R(t) = s_R + p_3.t + p_4.t^2 \quad (7,8)$$

where m_R and s_R are mean value and standard deviation of the element resistance in accordance with (4),

p_1, p_2, p_3, p_4 are constants.

The constants were achieved from simulations by curve transferring using least square method. The values of constants depend on various parameters, but according this way of their achieving, they do not have physical significance and they must be determined for all cases and parameters.

The corrosion has indispensable influence for all structures, not only for concrete structures, e.g. masonry, steel and composite members. In addition, the corrosion influences not only members subjected to bending, but also subjected to shear, compression and their combination and fatigue [15].

3. Analytical solution

The resistance R(t) of the reinforced concrete rectangular cross-section subjected to bending given by formula (4) taking into account equations (2) and (5) or (3) and (6) depending on reinforcement diameter ϕ(t) is equal to

$$R(t)=M_{Rd}(t)=-\frac{\pi^2\cdot n^2\cdot f_y^2}{32\cdot b\cdot f_c}\cdot\phi^4(t)-\frac{\pi\cdot n\cdot f_y}{8}\cdot\phi^3(t)+\frac{\pi\cdot n\cdot f_y\cdot(h-c)}{4}\cdot\phi^2(t) \quad (9)$$

then simplified

$$R(t\le t_0)=M_{Rd}(0)=A\cdot\phi^4+B\cdot\phi^3+C\cdot\phi^2 \quad \text{for } t\le t_o \quad (10a)$$

$$R(t>t_0)=M_{Rd}(t)=A\cdot\phi^4(t)+B\cdot\phi^3(t)+C\cdot\phi^2(t) \quad \text{for } t>t_o \quad (10b)$$

where A, B, C are parameters constant in time

$$A=-\frac{\pi^2\cdot n^2\cdot f_y^2}{32\cdot b\cdot f_c}\left[kN/m^3\right] \quad (11)$$

$$B=-\frac{\pi\cdot n\cdot f_y}{8}\left[kN/m^2\right] \quad (12)$$

$$C=\frac{\pi\cdot n\cdot f_y\cdot(h-c)}{4}\left[kN/m\right] \quad (13)$$

Moreover, it is possible to derive the resistance R(t) depending just on time, so, it means that other values are considered as constant (not changing in time)

$$\begin{aligned}R(t)=M_{Rd}(t)=&\left[A\cdot 0.0232^4\cdot t_{corr}^4\right]\cdot(t-t_o)^4-\\&-\left[(4\cdot A\cdot\phi+B)\cdot 0.0232^3\cdot i_{corr}^3\right]\cdot(t-t_o)^3+\\&+\left[(6\cdot A\cdot\phi^2+3\cdot B\cdot\phi+C)\cdot 0.0232^2\cdot i_{corr}^2\right]\cdot(t-t_o)^2-\\&-\left[(4\cdot A\cdot\phi^3+3\cdot B\cdot\phi^2+2\cdot C\cdot\phi)\cdot 0.0232^2\cdot i_{corr}\right]\cdot(t-t_o)+\\&+A\cdot\phi^4+B\cdot\phi^3+C\cdot\phi^2\end{aligned} \quad (14)$$

or

$$\begin{aligned}R(t)=M_{Rd}(t)=&\left[A\cdot r_{corr}^4\right]\cdot(t-t_o)^4-\left[(4\cdot A\cdot\phi+B)\cdot r_{corr}^3\right]\cdot(t-t_o)^3+\\&+\left[(6\cdot A\cdot\phi^2+3\cdot B\cdot\phi+C)\cdot r_{corr}^2\right]\cdot(t-t_o)^2-\\&-\left[(4\cdot A\cdot\phi^3+3\cdot B\cdot\phi^2+2\cdot C\cdot\phi)\cdot r_{corr}\right]\cdot(t-t_o)+A\cdot\phi^4+B\cdot\phi^3+C\cdot\phi^2\end{aligned} \quad (15)$$

It is able to write in simplified form

$$\begin{aligned}R(t)=M_{Rd}(t)=&M_{Rd}(0)+k_1\cdot(t-t_o)+k_2\cdot(t-t_o)^2+\\&+k_3\cdot(t-t_o)^3+k_4\cdot(t-t_o)^4\end{aligned} \quad (16)$$

where k_1, k_2, k_3, k_4 are parameters depending on materials' and geometrical' characteristics with their physical significance.

The equation (16) is similar to formulas (7, 8), but the analytical solution indicates that real moment resistance of RC girder subjected to bending moment is changed in time depending on polynomial of fourth degree, not second degree.

4. Parametric study

In the parametric study, the rectangular RC girder subjected to bending was considered. The influence of reinforcement corrosion on moment resistance changing in time was investigated. The material characteristics are shown in Tab. 1. These characteristics were measured on real structure. Due to parametric study, the bar diameter (ϕ16, ϕ20, ϕ28) and the corrosion current density (i_{corr}) were changed. The design lifetime for bridge structures is equal to Td = 100 years. Moreover, there was considered the reinforcement corrosion from t = 0 year in the parametric study. The changing the moment resistance of the rectangular RC bridge girder in time and influence of the corrosion is shown in Fig. 3.

Material characteristics	denotation	value
Strength of concrete in compression	f_c [N.mm^{-2}]	24.60
Yield strength of reinforcement	f_y [N.mm^{-2}]	400.80
Height of cross-section	h [m]	0.798
Width of cross-section	b [m]	0.496
Concrete cover	c [m]	0.024
Number of bars (reinforcement)	n [pcs]	7
Bar diameter	ϕ [m]	16
		20
		28
Corrosion current density	i_{corr} [μA/cm^2]	0.5
		1.0
		3.0
		5.0

Tab. 1. Material characteristics used in the parametric study.

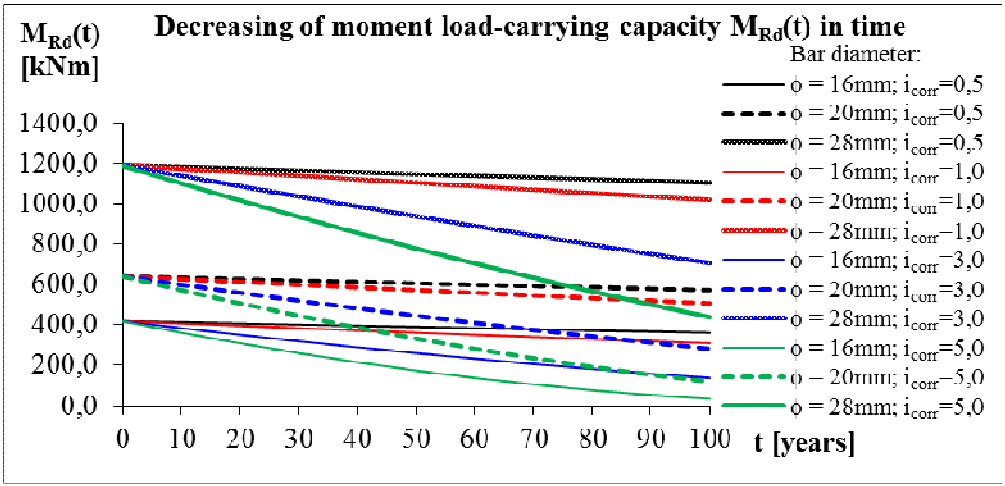

Fig. 3. Time dependent moment resistance of RC bridge girder due to reinforcement corrosion

5. Conclusions

This paper presents the results of research concerning the influence of the reinforcement corrosion on the time dependent moment resistance of the rectangular RC bridge girder. From the

results follows that the reinforcement corrosion has significant influence and may cause the fact that the moment resistance of more reinforced girder (girder with bar diameter ϕ20 or ϕ28) embedded into more aggressive environment (i_{corr} = 5,0 μA/cm2) can decrease more rapidly as the moment resistance of less reinforced girder (girder with bar diameter ϕ16) embedded into less aggressive environment ($i_{corr} \leq$ 1,0 μA/cm2) and be lower after 100 years. From this reason, it is needed to pay attention to durability and reinforcement protection during design of new bridge structures and on views and diagnostics of existing bridge structures.

Moreover, the work benefit is also the fact that k_1, k_2, k_3, k_4 are parameters depending on materials' and geometrical' characteristics and they have their physical significance, so, it is not problem to calculate them for various girders.

Acknowledgement

The research is supported by the Slovak Research and Development Agency under contract No. APVV-0106-11 and by Research Project No. 1/0566/15 of Slovak Grant Agency.

References

[1] BÖHNI, H., *Corrosion in reinforced concrete structures*, Woodhead Publishing Limited, 2005, p. 248.

[2] Transportation Research Board, Special Report 235, *Highway Deicing – comparing salt and calcium magnesium acetate*, Transportation Research Board, National Academy of Science, Washington, DC. 1991.

[3] BROOMFIELD JP., *Corrosion of steel in concrete*, in Winston R (ed.), John Wiley & Sons, Uhlig's Corrosion Handbook, 2nd ed., New York, 2000.

[4] KOTEŠ P., VIČAN J. "Recommended reliability levels for the evaluation of existing bridges according to Eurocodes", Structural Engineering International – SEI, Vol. 23, No. 4, publisher IABSE c/o ETH Zurich, Switzerland, copyright © IABSE, www.iabse.org/application, pp. 411-417.

[5] KOTEŠ P., VIČAN J. *"Reliability levels and partial safety factors according to eurocodes for evaluation of existing bridges"*, IABSE Conference /International association for bridge and structural engineering/, Proceedings of abstracts - volume 99, CD, Rotterdam, The Netherlands, 06.-08.05.2013, editor-publisher: IABSE c/o ETH Hönggerberg, CH-8093 Zürich, Switzerland, printed: The Netherlands, pp. 228-229, CD-8 pages.

[6] KALA Z., OMISHORE A. *"Applications of Advanced Variance-based Methods in Civil Engineering"*, in: Proc. of the Lightweight Structures in civil Engineering, Warsaw (Poland), 2009, pp.68–73.

[7] BILČÍK J., HOLLÝ I. *"Effect of reinforcement corrosion on reliability"*, Journal "Beton TKS", No. 3, 2012, pp. 16-20.

[8] VOŘECHOVSKÁ D., PODROUŽEK J., CHROMÁ M., ROVNANIKOVÁ P., TEPLÝ B. *"Modeling of chloride concentration effect on reinforcement corrosion", Journal "Computer-Aided Civil and Infrastructure Engineering"*, number 24, 2009, pp. 446-458.

[9] WENDNER R., STRAUSS A., GUGGENBERGER T., BERGMEISTER K., TEPLÝ B. *"Ansatz zur Beurteilung von chloridbelasteten Stahlbetonbauwerken mit Bewertung der Restlebensdauer"*, Journal "Beton – und Stahlbetonbau", Heft 12, number 105, 2010, pp. 778-786.

[10] MRÁZIK, A. *Reliability theory of steel structures*, VEDA Bratislava, 1987 (in Slovak)

[11] ANDRADE C., SARRIA J. ALONSO C. *"Corrosion rate field monitoring of post-tensioned tendons in contact with chlorides", Conference "Durability of building materials and components"*, Stockholm, 1996, pp. 959-967.

[12] KALA Z. *"Approximation and Advanced Numerical Simulation Methods"*, II. Conference "Reliability of Structures", Ostrava, 2001, pp. 97-100.

[13] ENRIGHT, M.P. – FRANGOPOL, D.M.: *Service-life prediction of deteriorating concrete bridges*. Journal of Structural Engineering, March 1998, p. 309-316

[14] KOTEŠ P. VIČAN J. SLAVÍK J. "*Influence of Reinforcement Corrosion on Reliability of Existing Concrete Structures*". Communications- Scientific Letters of the University of Žilina, No. 4, EDIS, 2001, pp. 41-49.

[15] KREJSA, M. "*Probabilistic reliability assessment of steel structures exposed to fatigue* ". Safety, Reliability and Risk Analysis: Beyond the Horizon - Proceedings of the European Safety and Reliability Conference, ESREL 2013, Amsterdam; Netherlands, pp. 2671-2679.

TRANSCOM 2015, 22-24 June 2015
University of Žilina, Žilina, Slovak Republic

Usage of 3-D based methods for the detection of aggregate microtexture

[*]Zuzana Florková
[*]University of Žilina, Faculty of Civil Engineering, Department of Highway Engineering, Univerzitna 8215/1, 01026 Žilina, Slovakia, {zuzana.florkova}@fstav.uniza.sk

Abstract. Some of the available advanced three-dimensional based methods for measurement of microtexture have been described. These methods are generally divided into three categories, namely image analysis based methods, laser based methods and photogrammetry methods. Moreover, a particle of aggregate can be captured using a stereomicroscope and using the appropriate software to obtain a 3-D image of investigated aggregate. Software also includes an interactive measurement tool that allows to obtain a profile of aggregate particle. The stereomicroscope method is also presented in the paper. The usage of the microscope for the detection of aggregates microtexture allows to eliminate some of the disadvantages of described methods and provides additional opportunities for microtexture evaluation.

Keywords: Microtexture, Aggregate, 3-D based methods, Microscope method

1. Introduction

Microtexture is defined as configuration of particular peaks on the surface of aggregates particles. Microtexture is very considerable parameter in term of skid resistance and mainly influence friction at low speeds on dry pavement surface [1]. Microtexture is also necessary to assure high friction value between a tire and pavement [2]. Microtexture is characterized by wavelengths and amplitudes in the range between 1μm – 0,5 mm [3].

In [4], the microtexture is defined as the angularity of the aggregate particle, which represents geometric attribute of the aggregate to have sharp edges (Fig.1). The more shaped surface of the aggregate, firmer and also sharper material of surface means that better and more lasting friction is expected.

It is clear, that the possibilities of measuring microtexture and the knowledge of the roughness of aggregate particles are particularly important for road traffic safety.

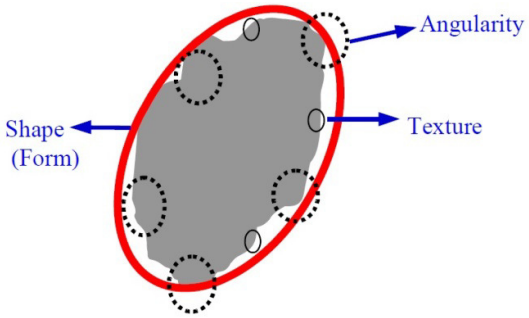

Fig. 1. Geometry of aggregate [5].

Variety of methods has been developed for detection of microtexture. These methods can be generally divided into manual measurements, detection of microtexture based on comparison and digital image analysis methods. The manual methods and the methods on basis of comparison are easy to realize, but are considered as a subjective and time consuming. The current development of

technique provides enhancement of microtexture detection methods by the methods obtaining outputs in form of three-dimensional image of investigated particle.

2. Methods based on an image analysis

Determination of microtexture using digital image analysis methods (DIAM methods) generally consists of image acquisition, the image processing (image editing) and subsequent evaluation of the image by various methods. The image analysis means conversion of image on data. Because the digital image is used, all transformations and calculations are implemented in pixels. In most cases, the evaluation is carried out by various mathematical algorithms in different computing programs. Many of used algorithms are complicated and very difficult to programming. Therefore, this method requires considerable computer knowledge and longer processing time.

A wide range of complex systems based on digital image analysis which allow obtaining a 3-D view of the particle and then evaluate of aggregate microtexture have been developed. These systems generally consist of mechanisms for obtaining high-quality images of aggregates and evaluation software. These systems include, for example, the system UIAIA (University of Illinois Aggregate Image Analyser – Fig.2). The UIAIA uses three cameras to capture projections of a particle from three orthogonal directions. The UIAIA features a moving conveyor belt that carries the individual aggregate particle into the view of a sensor, which detects the particle and immediately triggers the cameras. The use of three images for each particle allows creating the 3-D view of each particle. This system uses for microtexture evaluation the outline slope angularity index. The outline slope angularity index measures the angularity of a particle as change in the slope of the particle polygon outline (Fig.2).

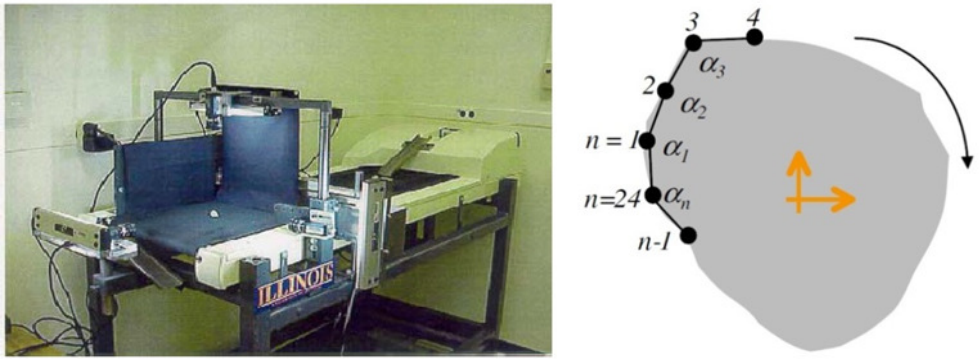

Fig. 2. Left: UIAIA system [5]. Right: Placed the polygon outline of particle [6].

The other complex systems in addition to the UIAIA are Camiser, Wip Shape system and AIMS system (Aggregate Imaging System). Each of these systems uses its own algorithm for microtexture evaluation. These systems are described in detail in [5].

The main disadvantage of these systems is that the available parameters for angularity characteristics of aggregate particles by these methods are based on analysis of 2-D images. Despite of this disadvantage complex systems provide outputs in the form of 3-D view of the particle, the appropriate evaluations software's of these systems allow microtexture evaluation of individual particles only by 2-D parameters. Then, the resultant value is assessed as the average value of the parameters obtained from the evaluation of 2-D images of many projected sides of an aggregate particle.

In general, disadvantage of 2-D parameters based on digital image analysis is that, these parameters allow capture only the larger peaks on the surface of aggregates particles. As the result of this, only the upper part of microtexture range is included into the evaluation. Used microtexture parameters are described in the [6].

3. 3D laser scanning device

This laser-based method is intended for simple three-dimensional (3-D) reconstruction of aggregate particles. The 3-D laser scanning device in Fig. 3 uses advanced non-contact laser sensors to scan an object in three dimensions. Aggregate particles are scanned on rotating plate using a laser beam, which travels vertically up the rotating object to generate three dimensional digital scan file. Data processing software is an integral part of the 3-D laser device [7].

This method has the same disadvantage as in the case of the above presented methods of digital image analysis. The entire evaluation is carrying out automatically, but by the 2D parameters. The capture of the entire field of microtexture values is also problematic, because of the laser device software, which scans objects with a 0.1 mm scanning resolution.

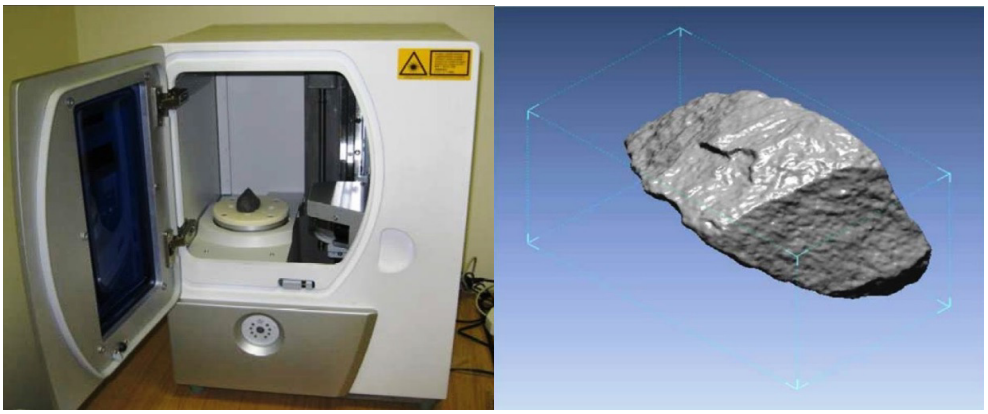

Fig.3. Left: 3D laser scan device. Right: Obtained 3D image of aggregate particle [8].

4. Photogrammetry method

The photogrammetry method is another method for the detection of microtexture, which allows obtaining the outputs in the 3-D form (Fig.4). Photogrammetry is a set of methods for obtaining the coordinates of object from analogue or digital photography. The principle of this method is in obtaining photographs, getting the coordinates of the surface using the appropriate software and the further transformation of the coordinates in the 3-D model.

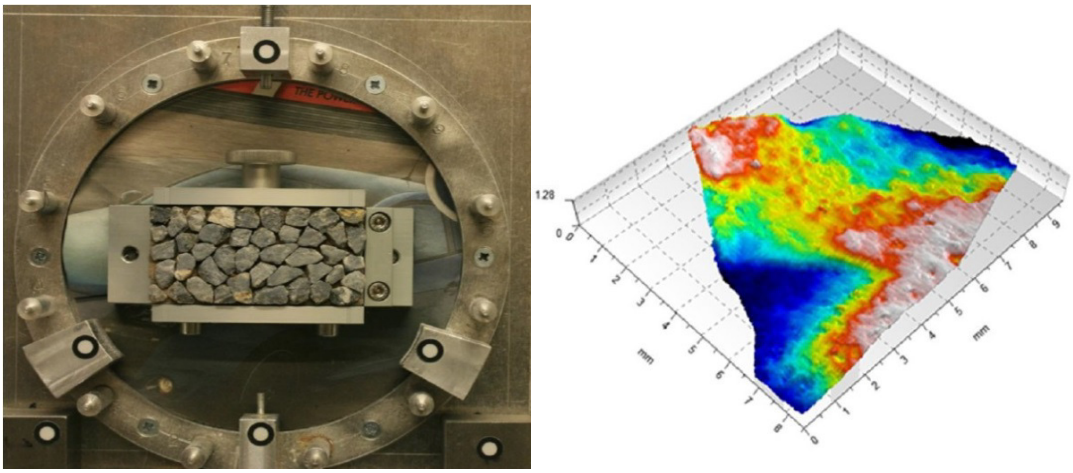

Fig.4. The photogrammetry method used for obtaining of the 3D aggregate image [9].

This method uses software Mountain Map for microtexture evaluation. The advantage of this software is that it enables to include into evaluation the entire particle surface by volume

characteristics. One of the possibilities is to use the material ratio curve so-called the Abbott-Firestone curve.

Using the Abbott curve, a graphical analyse can be performed in order to retrieve volume parameters characterizing the roughness of aggregate particle. According to Fig. 5, the curve distributes the surface texture into four volume parameters: Vmp (peak material volume), Vmc (core material volume), Vvc (core void volume) and Vvv (valley of the void volume) [9]. Then, the resultant characteristic of microtexture represents the volume parameter Vmp (peak material volume). The downside is that this method requires considerable computer knowledge and longer processing time.

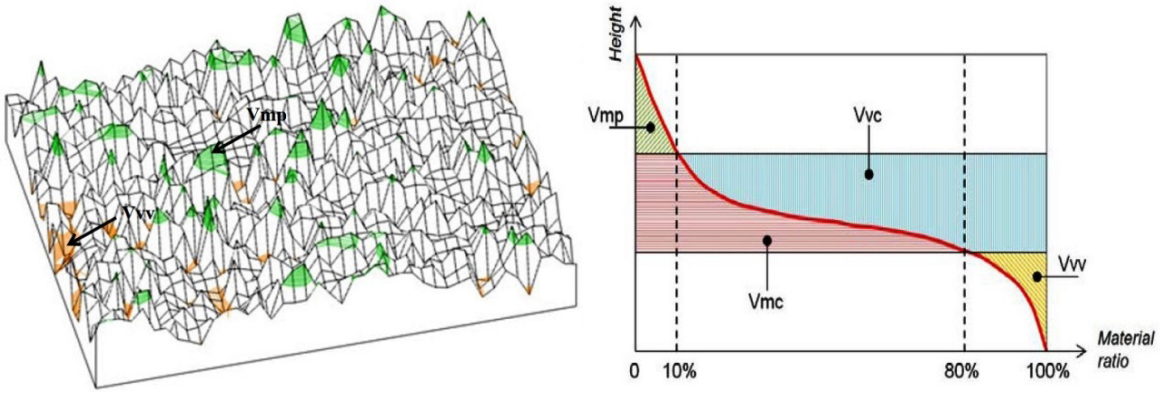

Fig.5. Principle of Abbott-Firestone [10].

5. Usage of microscope method for the detection of microtexture

It is possible to scan a particle of aggregate by a microscope (e.g. NIKON AZ 100). On the basis of the software Nis Elements D it is possible to achieve a 3-D view of investigated aggregate. This view can be exported into the wrml (Virtual Reality Modelling Language) format. It makes possible to image the aggregate in 3-D also apart from the software Nis Elements D in the work background of different programs (e.g. in the working background of Matlab program – Fig.6). The appropriate software also includes an interactive measurement toll EDF profile. Usage of this one allows obtaining the coordinates of singular profiles of aggregate. The acquired profile of aggregate is then expressed by x (y) and z coordinates. This data file can be also exported to various formats.

The principle of 3-D view acquirement by microscope rests in scanning of aggregate particle by cameras at different height levels. Aggregate particle is scanned on the microscope stage, which is vertically moved in micro steps by rotary knob. Then, the software creates the resultant 3-D image from the images obtained by scanning. The accuracy of the obtained output depends on the before selected range of scanning, of the number of steps and the required zoom level.

The main advantage of this method is the possibility to image aggregate particle in 3-D apart from the software Nis Elements D in the work background of different programs. Then, a program can be used for following evaluation. The program allows microtexture evaluation by 3-D parameters and eventually deals with creation of new parameters, which provide new possibilities of microtexture evaluation using the surface areas and volumes.

An aggregate particle can be capture by microscope in different zoom levels. It provides the capturing of the entire field of microtexture values and it gives more accuracy and better representativeness of results (compared to other detections methods of microtexture).

In all, the process of measuring by microscope is not time-consuming and it is quite simple.

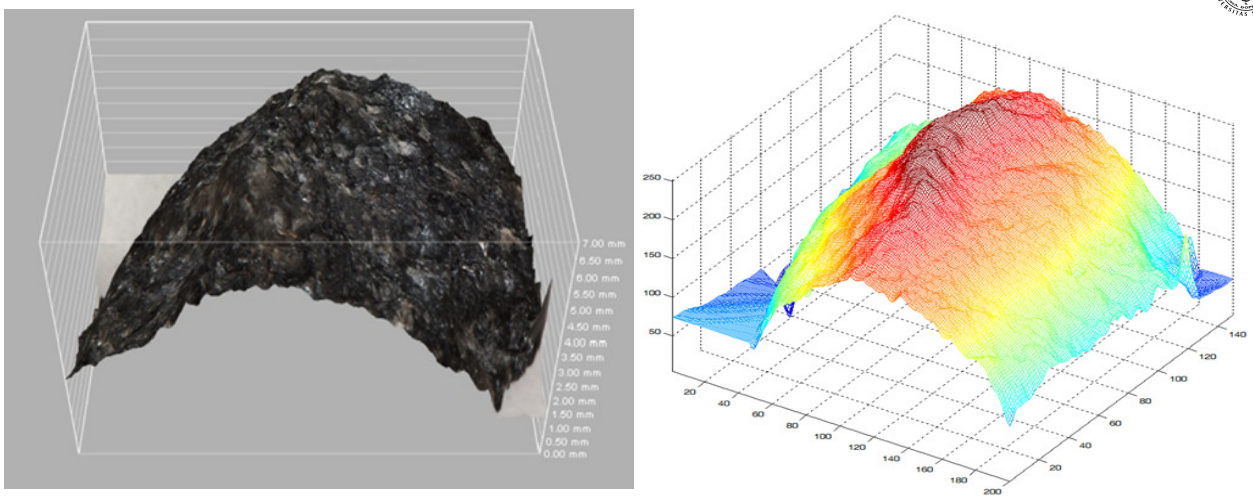

Fig.6. Three-dimensional view of aggregate. Left: Aggregate particle obtained by microscope. Right: Image of aggregate in the working space of Matlab program.

6. Conclusion

The possibility that microtexture information can be obtained from three-dimensional data by the 3-D image methods involves the series of advantages in monitoring the aggregate microtexture. By these outputs, it is possible to detect aggregate microtexture in more realistic way. In particular, it allows determination of microtexture characteristics with high accuracy and reliability of the results when compared to other used microtexture detections methods.

Despite of these advantages, these methods have still some limitations. The main limitation of these systems is the systems provide outputs in the form of a 3-D view of the particle and the appropriate evaluations software's of these systems allow microtexture evaluation of individual particles only by 2-D parameters.

Generally, approach on quantification of aggregates microtexture based on the microscope methods is not advanced as compared to other 3-D based methods. The usage of the microscope method for the detection of aggregates microtexture allows eliminating some of the disadvantages of described methods and mainly the limitation in the form of resultant 2-D image analysis. Using these outputs in the tree-dimensional form obtained by microscope method gives possibility to include into the evaluation the entire surface of the investigation particle of the aggregate and also deals with microtexture evaluation based on volume characteristics.

The previous considerations can be used as a start point for further studies of aggregate microtexture by the microscope method. Working with a 3-D surface, it is possible to go one step further and move to evolution of new parameters, with the main aim to find the most suitable parameter as the best characterization of microtexture. Possible further applications of these indicators can be very useful for more complex evaluation of pavement microtexture.

Acknowledgement

The paper is an output of the project VEGA 1/0804/12 Influence of material composition of asphalt on characteristics of pavement surface texture, noise emission and air pollution supported by funds of Scientific Grant Agency of the Ministry of Education, science, research and sport of the Slovak Republic.

References

[1] HIBBS, B., LARSON, R.: *Tire Pavement Noise and Safety Performance: PCC Surface texture Technical Working Group*. Report No. FHWA-SA-96-068. Federal Highway administration. Washington, D.C. Máj 1996. Available on: https://www.google.sk/search?client=opera&q=Tire+Pavement+Noise+and+Safety+Performance:+PCC+Surface+texture+Technical+Working+Group&sourceid=opera&ie=UTF-8&oe=UTF-8&gws_rd=cr&ei=T_y8U5XdEcOP7Ab3kIGYCQ

[2] KOVÁČ, M. a kol.: *Diagnostika parametrov prevádzkovej spôsobilosti vozoviek*. Žilina: EDIS vydavateľstvo Žilinskej Univerzity v Žiline, 2012. 265 s. ISBN 978-80-554-0568-1.

[3] STN EN ISO 13473-5. *Charakterizovanie textúry vozovky s použitím profilov povrchu. Časť 5: Stanovenie megatextúry* (ISO 13473-5:2009)

[4] KIM, Y., SOUZA, L.: *Effects of Aggregate Angularity on Mix Design Characteristics and Pavement Performance*. December 2009. Available on: http://neltap.unl.edu/Documents/NDOR/Aggregate_Angularity_on%20Mix_Design.pdf

[5] MASAD, E. et al.: *Appendixes to NCHRP Report 555: Test Methods for Characterizing Aggregate Shape, Texture, and Angularity*. Máj 2005. Available on: http://onlinepubs.trb.org/onlinepubs/nchrp/nchrp_w80.pdf

[6] TAFESSE, S. et al.: *A new image analysis technique to quantify particle angularity*. Available on: http://kth.diva-portal.org/smash/get/d iva2:499535/FULLTEXT01

[7] KOMBA, J.: *Analytical and laser scanning techniques to determine shape properties of aggregates used in pavements*. June 2013. Available on: https://www.google.sk/search?client=opera&q=Analytical+and+laser+scanninf+technuques+to+dtermine+shape+properties+of+aggregates+used+in+pavements&sourceid=opera&ie=UTF-8&oe=UTF-8&gws_rd=cr&ei=xW4SVY7lDcXyUvvYg_gL

[8] ANOCHIE-BOATENG, J. et al.: *Evaluation of 3D laser device for characterizing shape and surface properties of aggregates used in pavements*. Available on: https://www.google.sk/search?client=opera&q=+Evaluation+of+3D+laser+device+for+characterizing+shape+and+surface+properties+of+aggregates+used+in+pavements&sourceid=opera&ie=UTF-8&oe=UTF-8&gws_rd=cr&ei=_3ASVaTFNsbfUdWcgsgF#q=3d+laser+scanning+device+aggregate

[9] MCQUAID, G. et al.: *Use of Close Range Photogrammetry to Assess the Micro-texture of Asphalt Surfacing Aggregate*. International Journal of Pavements Conference, São Paulo, Brazil 2013.

[10] BITELLI, G. et al.: *Laser Scanning on Road Pavements: A New Approach for Characterizing Surface Texture*. Sensors. July 2012. ISSN 1424-8220.

TRANSCOM 2015, 22-24 June 2015
University of Žilina, Žilina, Slovak Republic

Production of non-exhaust particulate matter from abrasion of pavement´s surface and adverse health impacts

[*]Daša Fullová
[*]University of Žilina, Faculty of Civil Engineering, Department of Highway Engineering, Univerzitná 8215/1, 010 26 Žilina, Slovakia, {dasa.fullova}@fstav.uniza.sk

Abstract: The article presents current issues related to environmental pollution by non-exhaust particulate matter and their impact on the human body. It briefly indicates the negative impacts of them. The abrasion is presented as a main source of the airborne particulate matter from road traffic. It deals with the emitting of particulate matter into the atmosphere during the abrasion of different types of pavement surfaces. The abrasion of several samples of asphalt mixtures is performed in wheel tracking machine. The article describes the selected methodology and used machine technology. It presents an example of the results of measurements on three trial samples of asphalt mixtures and measurements of abrasion of pavement surface in road simulator abroad.

Keywords: Particulate matter, human health, abrasion, wheel tracking machine.

1. Introduction

Air pollution is a global problem therefore the governments around the world participate in the air quality in their countries. Monitoring of air pollution involves finding and understanding the sources of pollution, monitoring of contaminants, air quality modelling, performing laboratory experiments, the using satellite pictures to quantify the levels of the air quality and permanent checking. In every aspect of air pollution around the world the research activities are constantly realized for reducing pollution and negative impact on human health [4, 6, 9].

2. Impact of road traffic on creation of particulate matter

2.1. Road traffic and environment

Road traffic is known as one of the major sources of air pollution [4]. The issue of emissions from road traffic is multiplied by the fact that the numbers of vehicles and the numbers of kilometers are growing each year, and with them the emissions [1]. In recent years the road traffic has contributed to the creation of particulate matter in the greatest extent among all types of traffic, the increased attention should be given to heavy vehicles.

Road traffic produces approximately 30-35% NO_X, 20-25 % SO_X, 25-30 % CO, 15 % of volatile organic compounds, 15-20% of $PM_{2.5}$, 10-15% of PM_{10} [2].

Due to the traffic there are producing as coarse particles, as well fine and ultrafine particles. Fine and ultrafine particles are mainly formed by the incineration processes in an engine. A significant source of pollution is the road dust. Coarse particles situated in the atmosphere near by frequented roads are mainly due to abrading of pavement surfaces, wearing tyres, brakes and repeated swirling of particles (resuspension). In the winter and spring seasons contribute to air pollution particles from chemical and inert spreading materials used for winter maintenance and falling off dirt from cars [6; 9].

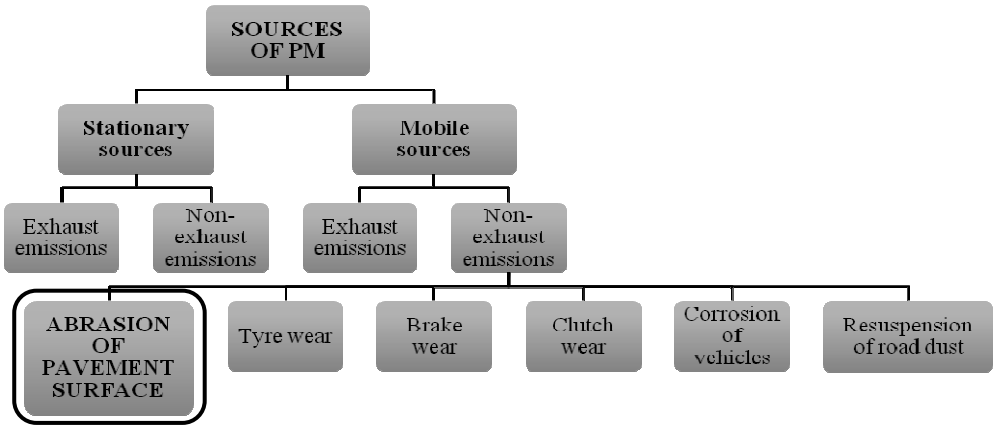

Fig. 1. The sources of particulate matter from road traffic [5].

2.2. Characteristics of pollutants

Airborne particulate matter covers a wide particle size range, from diameters of a few nanometres (nm) to around 100 micrometers (μm). For the purposes of monitoring and regulation, there are two commonly used particle metrics – PM_{10} a $PM_{2.5}$ [9]. It is now necessary to pay close attention to the suspended particles with a diameter smaller than 10μm. Particles of this fraction are divided into two groups on the basis of a different size, the mechanism of formation, compositions and behaviour in the atmosphere [6]. The size of particles has been directly linked to their potential for causing health problems. Small particles of concern include ,,inhalable coarse particles,, with a diameter of 2.5 to 10μm and ,,fine particles,, smaller than 2.5μm in diameter [6; 9].

Fine particles $PM_{2.5}$ originate from the chemical reaction, nucleation, condensation of the gaseous emissions generated on the surface of the particles, or coagulation of the finest particles. The main source of these particles is combustion of fuels, wood, coal, chemical production, transformation of NO_X and SO_2 in the atmosphere (nucleation) and transformation of organic matter.

Coarse particles $PM_{2.5}$ - PM_{10} come into existence by mechanical abrasion (crushing, abrasion of surface) and swirling road dust. Their main sources are especially industrial dusts, building activities, transport, quarrying, soil management and road dust. This fraction also includes various biotic particles such as bacteria, pollen, plant particles. Very important source of these particles are also combustion processes of coal, oil and diesel emissions also fuel particles and carbon black [6; 9].

2.3. Impacts of particulate matter on human health

The health risks associated with the occurrence of particulate matter are undeniable. It depends mainly on the size of particles and the content of hazardous or carcinogenic substances contained in the particulate matter.

More than two million deaths are estimated to occur globally each year as a direct consequence of air pollution through damage to the lungs and the respiratory system. Numerous scientific studies have explained particle exposure as the source of various health problems including premature death in people with lung or heart disease, irregular heartbeat, nonfatal heart attacks, aggravated asthma, decreased lung function, and increased respiratory symptoms such as irritation of the airways, coughing or difficulty breathing [6; 9]. Penetration of the particles into the lungs depends on the size. It is true that the smaller particles we breathe, the deeper penetrate into the lungs.

Limit values for $PM_{2.5}$ and PM_{10} are determined in the Decree of Ministry of Agriculture, Environment and Regional Development no. 360/2010 on air quality. $PM_{2.5}$ limit has been set at 25 mg/m^3, to be fulfilled by 2015. By 2020, to be fulfilled limit 20 mg/m^3. For PM_{10} limit values are given for short-term (24 h) and long-term (annual) exposure, while for $PM_{2.5}$ is given by annual

exposure. Limits of short-term exceeding the set values for PM_{10} is not possible more than 35times per year, with an average daily concentration exceeding 50 mg/m^3 [12].

The following figure (Fig.2) shows the human respiratory system and the possible imposition of different particle size distribution.

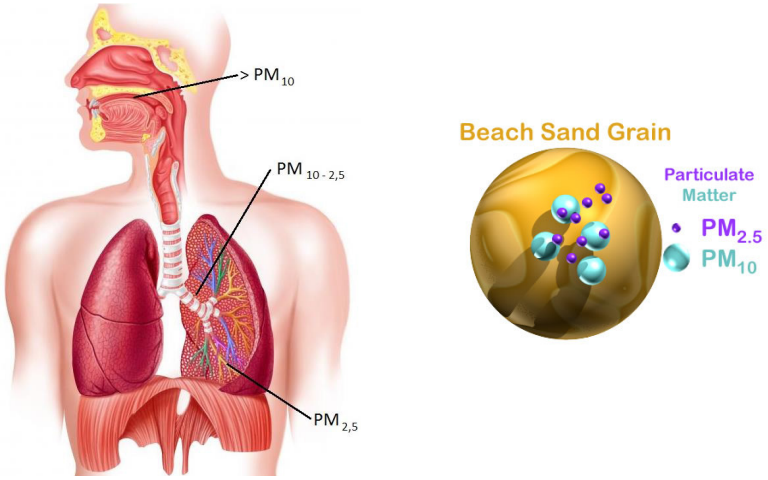

Fig. 2. Human respiratory system [7] and size comparison of $PM_{2.5}$ and PM_{10} against the average diameter of a fine beach sand [6].

3. Abrasion of pavement surface as a source of particulate matter

Based on the information from several foreign and Slovak scientific articles and studies about creation of particulate matter from road traffic, we decided to deal with abrasion of pavement surface as a source of particulate matter.

The main task is to assess the impact of particulate matter from pavement, depending on the composition of the asphalt mixture. Our work is to compare different types of asphalt mixtures in terms of release of particulate matter in the air during the abrasion of the samples of asphalt mixture in wheel tracking machine. The final result would be a comparison of the different types of asphalt mixtures and an assessment of the suitability of their use in terms of air pollution and negative impact on our health.

Each of the tested samples is specific in its composition - the type of asphalt, the amount of asphalt, type of aggregate, different lines of granularity of aggregate in mixtures. In connection with the material are formed samples with different structure of surface, which can ultimately affect abrasion of the samples.

3.1. Description of the chosen methodology

Laboratory measurements will be performed in the laboratory at the Department of highway engineering. For laboratory measurements will be used samples of asphalt mixtures (asphalt concrete AC, asphalt concrete for very thin langers BBTM, stone mastic asphalt SMA, porous asphalt PA). The samples will be rutted in wheel tracking machine DYNA-TRACK which is used to assess the resistance to rutting of asphaltic materials under conditions, which simulate the effect of traffic.

The wheel tracking apparatus consists of a loaded wheel, which bears on a sample held on a moving table. The wheel tracker is fitted with a temperature controlled cabinet with a temperature range from environment to 65°C ± 1.0°C. The wheel is fitted with a solid rubber tyre of outside diameter 200 mm. The wheel load under standard conditions is 700 ± 10 N. The table reciprocates with simple harmonic motion through a distance of 230 ± 5 mm with a frequency of 53 passes (± 1%) per minute. The sample may be either a 200 mm diameter core or a 300 x 400 mm slab of asphaltic mixture from 25mm to 100 mm thick [13].

Air circulation and thus the loose particles in wheel tracking machine provide fans which create favourable conditions for the circulation of PM in facilities APS and SMPS and Leckel LVS 3.1. The measured values will be analyzed on the basis of:

- the number of emitted particles
  - in the range of 0,0122 – 0,5725 μm (SMPS)
  - in the range of 0,523 – 19,810 μm (APS)
- the mass of emitted particles
- the concentration of particles retained on the filters
- the chemical analysis of the filters

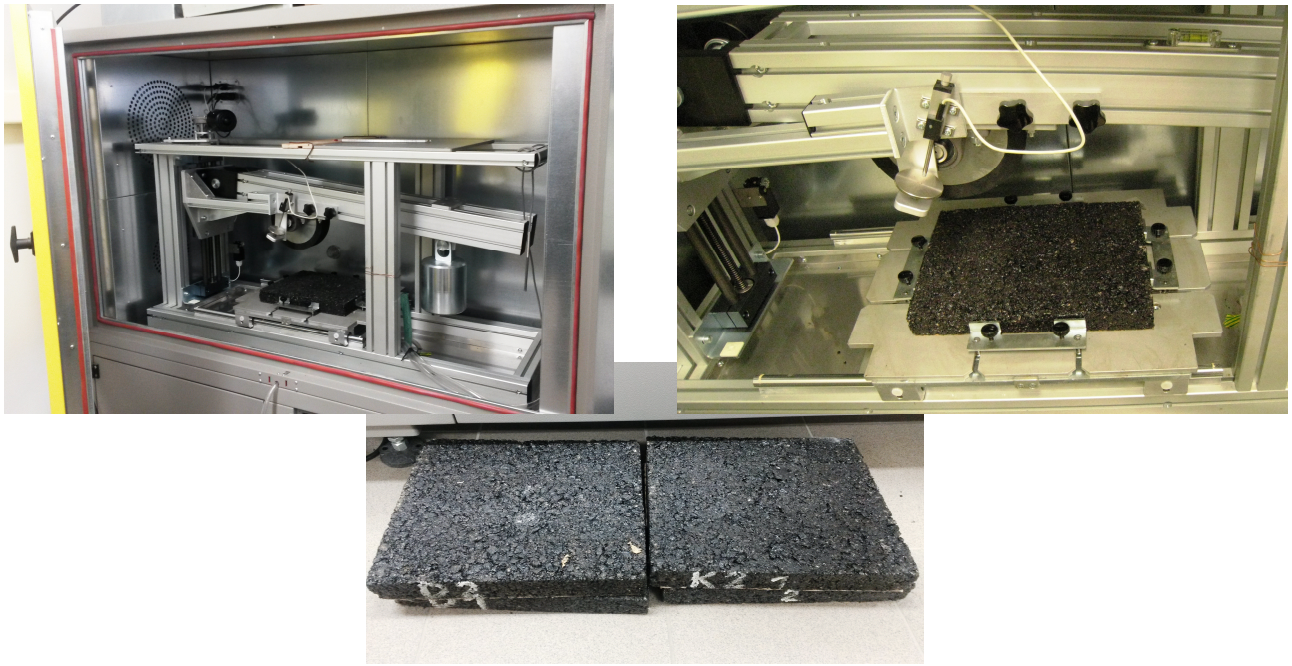

Fig. 3. The wheel tracking machine DYNA-TRACK and rutting of tested sample of asphalt mixture [author].

3.2. Used machine technology

For individual measurements will be needed the following equipment [3]:

- SMPS (Scanning Mobility Particle Sizer)
- APS (Aerodynamic Mobility Particle Sizer)
- Wheel tracking machine – DYNA-TRACK
- Leckel – LVS 3.1 (Low Volume Sampler)
- Computer, software for the evaluation of the number of emitted particles
- XRF analyser (X-ray fluorescence spectroscopy) – SPEKTRO iQ II

3.3. An example of results of laboratory measurements

The following graphs show the results of test measurements performed at our department. Four test samples of asphalt mixtures were used:

- sample no.1: AC 11 O PmB 45/80 – 75; I
- sample no.2: AC 11 O PmB 45/80 – 75; I
- sample no.3: SMA 11 PmB 45/80 – 75; I
- sample no.4: AC 11 O PmB 45/80 – 75; I

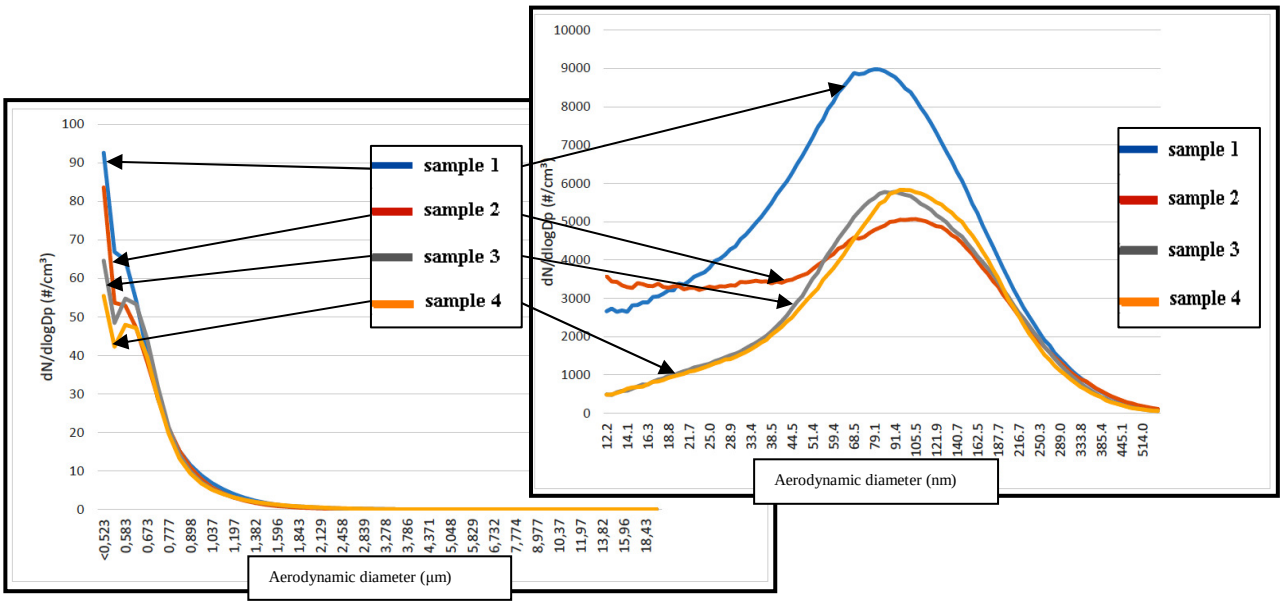

Fig. 4. The comparison of the test samples in terms of concentration of PM with SMPS and APS [10].

3.4. Measurements of abrasion of pavement surfaces abroad

Swedes have dealt with the issue of the creation of PM from abrasion of pavement surface, especially VTI – The Swedish National Road and Transport Research Institute. It is an independent, internationally known research institute in the transport sector [11].

Particle sampling in the VTI road simulator hall makes it possible to sample wear particles with very low contamination from surrounding sources and no influence from tail-pipe emissions. The road simulator consists of four wheels that run along a circular track with a diameter of 5.3 m. A separate DC motor is driving each wheel and the speed can be varied up to 70 km/h. The tyres used during the road simulator tests were summer tyre and winter tyre. Before each test the simulator hall is thoroughly cleaned using high pressure water. The hall is then left to dry up and before each measurement a filter equipped fan rinses the air from particles to minimize contribution from other sources than the tested pavement and tyres. Since temperature is an important factor influencing pavement and tyre wear, the same start temperatures were used for the each tyre type. The pavements used for the tests were both asphalt concrete pavements with maximum stone size 11 mm. The main difference between the pavements was the stone material. One of the pavements (ACO 11 S, asphalt 50/70) had a relatively wear resistant diorite, while the other pavement (AC 11 surf, B70/100) had a softer limestone [8].

Subsequent use of instrumentation for generating, Dimensioning and the measuring of particulate matter were collected and analyzed samples. During the test showed that the PM is influenced by the type of pavement surface, speed, and type of tyres.

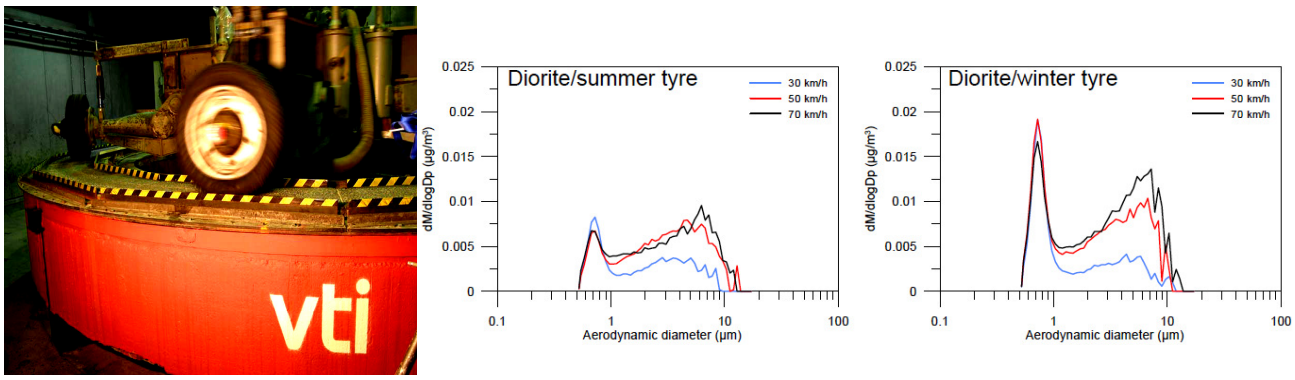

Fig. 5. The VTI road simulator and examples of measured results with APS [8].

4. Conclusion

The article presents problems of creating particulate matter from abrasion of pavement surface, which adversely affect our health. On the basis of knowledge and information from various sources, we can say that the chosen methodology is possible to use and can be further developed.

Our task for the future is the implementation processing and evaluation of as many measurements. It is necessary to make a number of tests and the results will be necessary to evaluate by relevant statistical methods.

The final assessment should serve to compare the tested samples of asphalt mixtures and determine which asphalt mixture is suitable for use in intra-urban and regions where it is necessary to reduce road dust.

Acknowledgement

The paper is a result of the research supported by the research project VEGA 1/0804/12 *Influence of material composition of asphalt on characteristics of pavement surface texture, noise emission and air pollution.*

References

[1] ĎURČANSKÁ, D.: *Hodnotenie znečisťovania ovzdušia v meste tuhými časticami.* Medzinárodný seminar ,,NOVÉ TRENDY V TECHNIKE OCHRANY OVZDUŠIA 2009“, 16. jún 2009. Zvolen. ISBN 978-80-228-2003-5

[2] EEA 2012. Available at: <http://www.eea.europa.eu/>

[3] FULLOVÁ, D.: *Obrus povrchu vozovky ako zdroj tuhých častíc (Abrasion of pavement surface as a source of particulate matter).* In: Juniorstav 2015 [elektronický zdroj]. 17. odborná konference doktorského studia (17^{th} International Conference of PhD students). Vysoké učení technické v Brně, Fakulta stavební, 29.1.2015. Brno. ISBN 978-80-214-5091-2.

[4] HARRISON, R.M., DEACON, A.R., JONES, M.R., APPLEBY, R.S.: *Sources and processes affecting concentrations of PM_{10} and $PM_{2.5}$ particulate matter in Birmingham.* Atmospheric Environment 31, 4103-4117, 1997.

[5] JANDAČKA, D.: *Vplyv cestnej dopravy na výskyt tuhých častíc*. Dizertačná práca. Žilinská univerzita v Žiline, 2013.

[6] KIM, K., KABIR, E., & KABIR, S.: *A review on the human health impact of airborne particulate matter*. In Environment International, 74, 136-143, 2015.

[7] Respiratory system of human body. Available at: <http://www.wisegeek.org/what-is-a-normal-respiratory-rate.htm>

[8] Sustainable Pavements for European New Member States. *Guidelines for the environmental assessment of various pavement types including recommendations to road authorities in NMS.* EUROPEAN COMMISSION DG RESEARCH. SIXTH FRAMEWORK PROGRAMME. 29 May 2009.

[9] THORPE, A. & HARRISON, R. M.: 2008. *Sources and properties of non-exhaust particulate matter from road traffic: A review*. In Science of the Total Environment, 400(1-3), 270-282.

[10] VÁCLAVÍK, P.: *Laboratórne testy obrusu povrchu vozovky ako zdroja tuhých častíc.* Diplomová práca. Žilinská univerzita v Žiline, 2014.

[11] VTI – The Swedish National Road and Transport Research Institute. Available at: <http://www.vti.se/en/>

[12] Vyhláška Ministerstva pôdohospodárstva, životného prostredia a regionálneho rozvoja Slovenskej republiky o kvalite ovzdušia č. 360/2010 Z. z.

[13] Wheel tracking machine DYNA-TRACK. Cernusco, Italy : Controls S.R.L., 2000.

TRANSCOM 2015, 22-24 June 2015
University of Žilina, Žilina, Slovak Republic

Long-term monitoring of thermal properties sandwich envelope

*Vladimír Gašpierik, *Pavol Ďurica
*University of Žilina, Faculty of Civil Engineering, Department of Building Construction and Urban Planning, Univerzitna 2, 01026 Žilina, Slovakia, {vladimir.gaspierik}@svf.uniza.sk

Abstract. The subject is following the latest findings concerning the issues of theory, design and execution of building envelope energy-efficient buildings. The contribution is devoted to experimental evaluation of the test wall with unconventional layer order built in the laboratory pavilion type of the Department of Building Engineering and Urban Planning. The measurements were carried out after 4 years from construct the wall.

Keywords: Thermal properties, sandwich construction, building envelope, experimental evalution.

1. Introduction

All experimental measurements based on exterior wall built in an air conditioned room pavilion type laboratory Department of Building Construction and Urban Planning. Exterior wall was exposed to the effects of four years of real change from the exterior of the outer and stationary indoor climate controlled at an internal temperature of 20 ° C and relative humidity of the internal air about 50%. These were maintained climate unit. Since the exterior side of the wall was exposed to a real test, randomly changing weather, climate indoor environment was stable, but during the day fluctuating around the setpoint the response to external influences. After 4 years, the wall had to be analyzed to the depth. Consequently, it was necessary to take samples of insulation in the fields no. 1,3,4,5 and measure the moisture content of wood support structure envelope. The second field was not measured because of the ongoing test measurements using fiber optic cables.

2. Description

2.1. Description of wall

Dimensions of monitored experimental walls are 3670 x 2670 mm and wall comprises five fields (Fig. 1.,2.). They differ in material composition and colorful surface. First, second, fourth and fifth fields are diffusion sealed construction and third field is a diffusion open construction (Fig. 1.). The composition of wall from the interior to the exterior is as follows: OSB board, vapor barrier (except the third field), filling insulation, exterior insulation MDF board Hofatex, thin coating plaster (Fig. 1.). Color is used in yellow reflectance of solar radiation is 61%, white (fields no. 2,3,4) reflectance of sunlight is 100% and gray (field no. 5) reflectance of sunlight is 34% (Fig. 2.). All fields samples of lightweight external wall exposed to same conditions of interior and the exterior side.

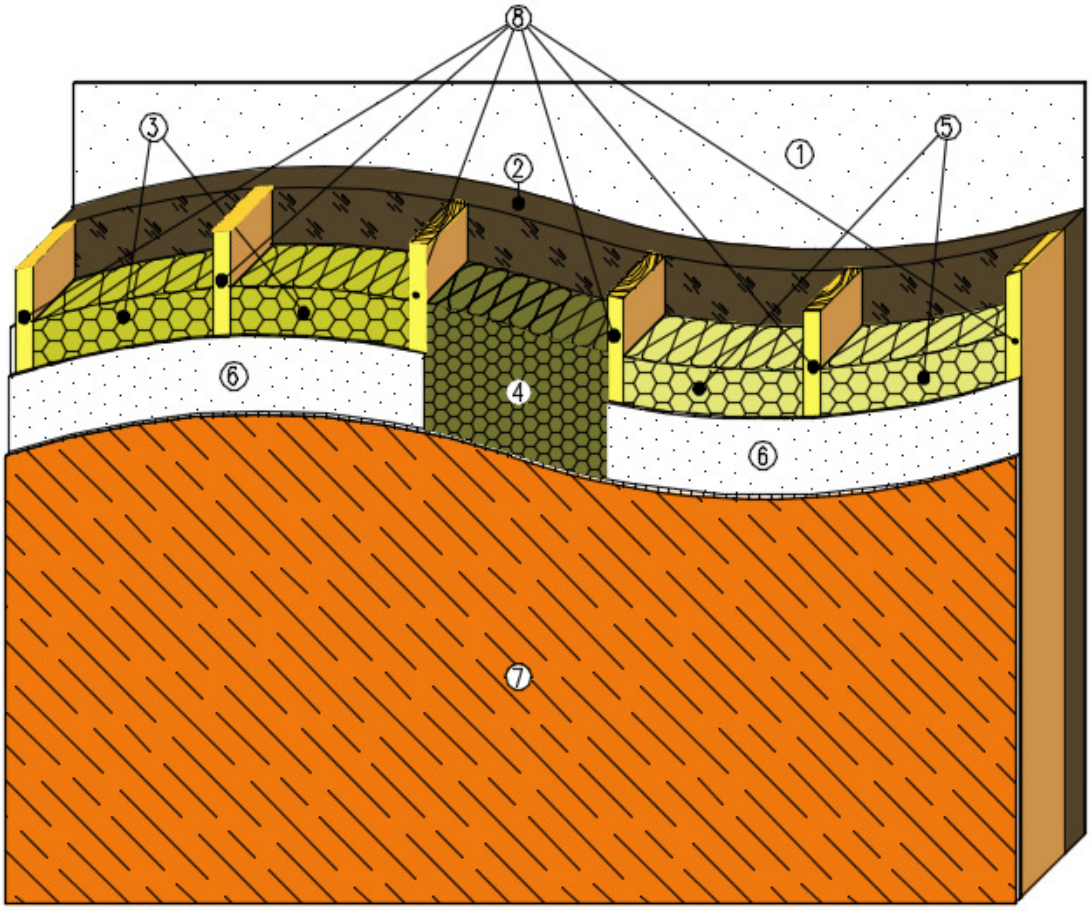

Fig. 1. Types of test walls: 1 - external plaster - 4 mm; 2 - MDF board – 100 mm; 3 - glass wool - 220 mm; 4 - hemp insulation - 220 mm; 5 - mineral wool - 220 mm; 6 - vapor barrier; 7 - OSB boards - 12 mm; 8 - wooden column - 60x220 mm

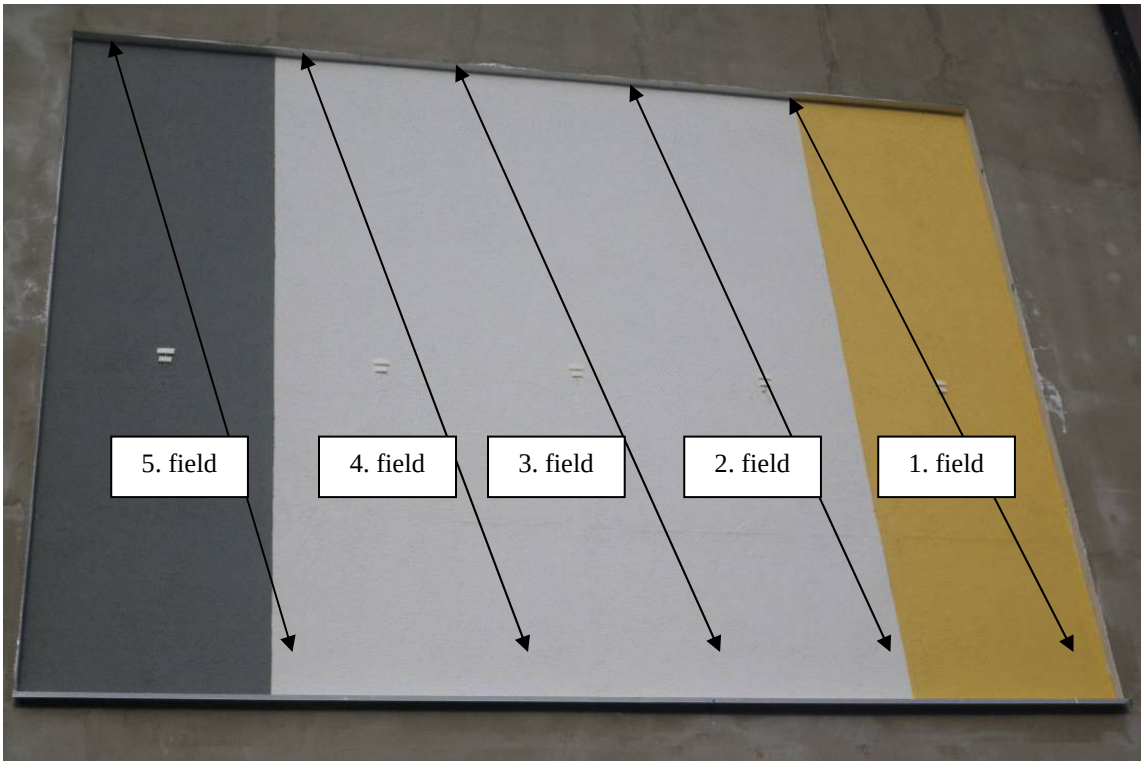

Fig. 2. Wiew of the test walls from exterior side

2.2. Description of experimental measurements

Marginal conditions:

Date:	29. September 2014
Relative air humidity in the interior:	50%
Relative air humidity in the exterior:	76,7%
Indoor temperature:	20°C
Outdoor temperature:	11,9°C

Applying devices:

1. Heating and drying oven Kendro - Heraeus
2. Moisture meter Greisinger GMH 3850, accuracy 0,01%
3. Electronic weighing-machine Radwag PS 6000/C/2, accuracy 0,01 g

To determine humidity in insulating materials, used in particular elements, we applied gravimetric method (mass moisture method). The method is based on weighting wet and dry substances. The places where we took off samples are shown in Fig. 3.. Every time we used to take three samples from each layer of insulation and from facade MDF border. The first sample was from the bottom third, the second one from the middle and third one from the top.

After taking samples we put them to the hermetic and vapor proof package, and brought to the lab. The samples was preciously weighed before placed into the dying oven. Drying temperature for insulating materials is 105 °C. After 24 hours of drying we weighed samples, and then we repeated a cycle drying and weighting in the 6 hours intervals. After reached constantly weight samples, was completed cycle and recorded values. The difference in weight was equal to amount of evaporated water. The weight this water was compared with the weight of dry samples per formula. Mass moisture is defined as follow:

$$w = \frac{m_w - m_d}{m_d} \times 100\ [\%] \qquad (1)$$

m_w - weight of wet specimen
m_d - weight of dry specimen

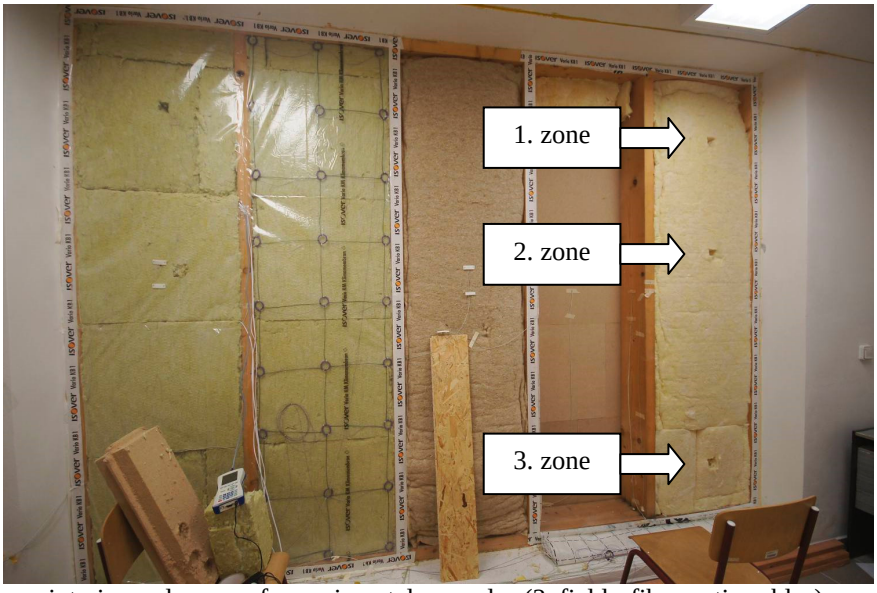

Fig. 3. Test walls from interior and zones of experimentals samples (2. field - fiber optic cables)

3. Evaluation

The evaluations of measurements in first insulation layer are the following graphs (Fig. 4.). The graph clearly shows that the moisture in the field no. 1 (glass wool) and fields no. 4, 5(mineral wool) is less than 5%. In the field no. 3 moisture in hemp insulation reaches values greater than 10%.

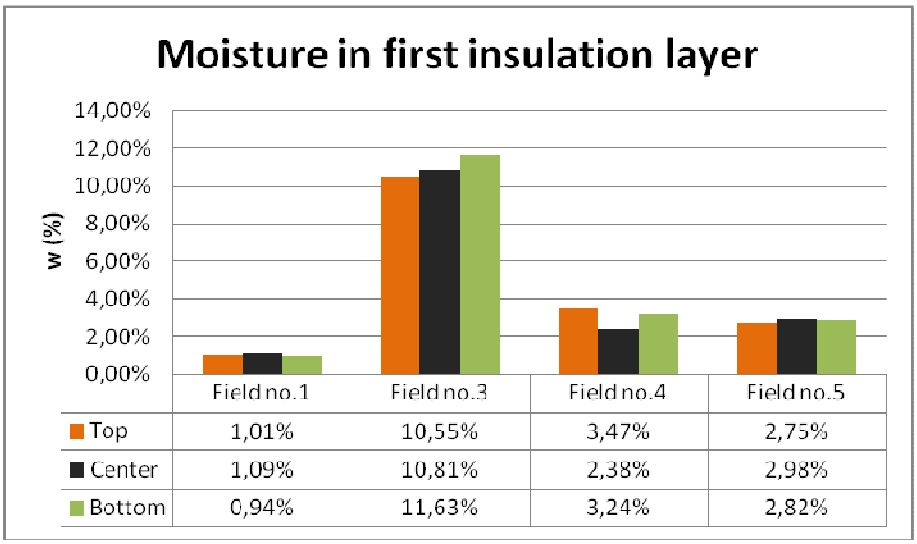

	Field no.1	Field no.3	Field no.4	Field no.5
Top	1,01%	10,55%	3,47%	2,75%
Center	1,09%	10,81%	2,38%	2,98%
Bottom	0,94%	11,63%	3,24%	2,82%

Fig. 4. Graph of moisture in first insulation layer

In the second insulation layer are similar to the results in the first layer(Fig. 5.). The graph clearly shows that the moisture in the field no. 1 (glass wool) and fields no. 4, 5 (mineral wool) is less than 5%. In the field no. 3 moisture in hemp insulation reaches values greater than 10%.

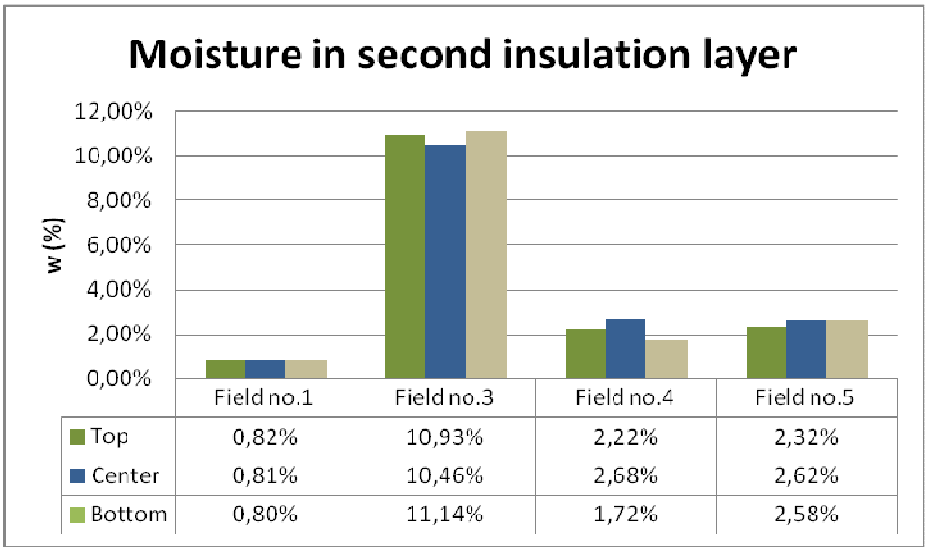

	Field no.1	Field no.3	Field no.4	Field no.5
Top	0,82%	10,93%	2,22%	2,32%
Center	0,81%	10,46%	2,68%	2,62%
Bottom	0,80%	11,14%	1,72%	2,58%

Fig. 5. Graph of moisture in second insulation layer

The moisture in the MDF boards shows next graph. To determine moisture MDF insulating boards we applied humidity meter Greisinger GHM 3850. The device was set up to auto correction moisture depending on the temperature 20°C. Totally, 12 measurements in 4 zones were taken, in the same way. The first sample was from the bottom third, the second one from the middle and third one from the top.

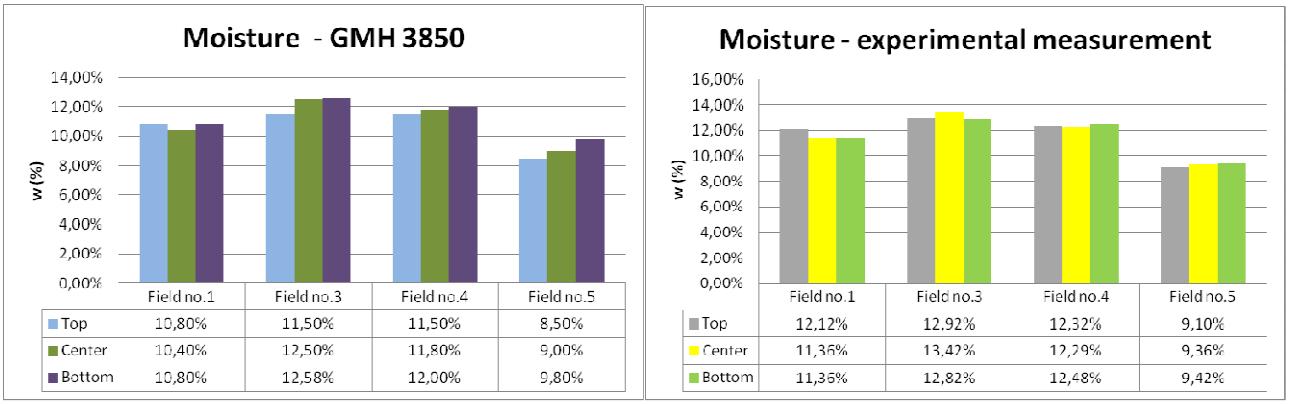

Fig. 6. Graphs of moisture in the MDF boards

Wooden column - head						
	Field no.1	Field no.2	Field no.3	Field no.4	Field no.5	
Top	**12,60%**	**13,00%**	**11,60%**	**11,20%**	**10,80%**	**11,60%**
Center	**12,30%**	**11,30%**	**12,50%**	**11,70%**	**11,80%**	**11,20%**
Bottom	**12,80%**	**12,10%**	**12,50%**	**11,70%**	**12,40%**	**11,80%**
Wooden column - inside						
	Field no.1	Field no.2	Field no.3	Field no.4	Field no.5	
Top	**13,80%**	**14,00%**	**14,10%**	**12,60%**	**12,60%**	**12,70%**
Center	**14,30%**	**14,00%**	**15,00%**	**12,80%**	**13,20%**	**13,60%**
Bottom	**14,70%**	**13,70%**	**15,20%**	**14,70%**	**14,00%**	**14,50%**

Tab. 1. The table of moisture in wooden construction

Area of Insulation	Field no. 1			Field no. 3			Field no. 4			Field no. 5		
	min λ	**max λ**	**Δλ**	**min λ**	**max λ**	**Δλ**	**min λ**	**max λ**	**Δλ**	**min λ**	**max λ**	**Δλ**
	[W/(m.K)]			[W/(m.K)]			[W/(m.K)]			[W/(m.K)]		
infill insulation	**0,0387**	**0,0399**	**0,0012**	**0,0621**	**0,0637**	**0,0016**	**0,0377**	**0,0402**	**0,0025**	**0,0384**	**0,0396**	**0,0012**
external insulation	**0,1044**	**0,1115**	**0,0071**	**0,102**	**0,1076**	**0,0056**	**0,1057**	**0,121**	**0,0153**	**0,0994**	**0,1291**	**0,0297**

Tab. 2. The table of thermal conductivity measured in the laboratory

4. Conclusion

On the basis of the measurements of light sandwich wall construction based on wood, exposed to long-term effects of outdoor climate conditions and constant internal environment we can say the following conclusions: The measured values of moisture in the fields 1, 4, 5 have no significant impact on the thermal conductivity of glass wool and mineral wool. The moisture of glass wool was measured max 1,09 % and the thermal conductivity was measured max 0,0399 W/(m.K). The moisture of mineral wool was measured max 3,47% and the thermal conductivity 0,0402 W/(m.K). These fields were constructed as diffusion sealed structures. But moisture in the field 3 has a big impact on the thermal conductivity of hemp insulation, because the producer define the thermal conductivity of hemp insulation 0,04 W/(m.K). The moisture of hemp insulation was measured max 11,63 % and the thermal conductivity 0,0637 W/(m.K). That field was constructed as diffusion open construction. The facade has an impact on moisture in MDF board but no on the individual layers of insulation between the wooden poles. The moisture in the MDF boards under the gray plaster was on average 27% lower than under the white plaster. Also moisture under the yellow plaster was lower but only an average of 9%.

The measured values of moisture in all fields MDF boards were approximately the same. On the moisture of MDF boards does not affect the design. But moisture has a big impact on the thermal conductivity of MDF boards, because the producer define the thermal conductivity of MDF boards 0,049 W/(m.K) (Tab. 2.). The real moisture of MDF boards were measured max 13,42 % and the thermal conductivity 0,129 W/(m.K) (Tab. 2.). Differences measurement results on MDF by GMH 3850 (resistance method) and gravimetric method were in the range from 2% to 11% for gravimetric method, however, the differences are insignificant, because the GMH 3850 was showed variations in measurements.

The measured values of moisture in the wooden construction were less than 15,2 %. Moisture content less than 15,2% does not affect on the characteristics of wooden structures. Lower values were measured on the faces of the columns of the interior side than on the side edges, measured at the center of the width of columns.

The measurements will be repeated in April 2015 after the cold period of the year and the results will be compared with each other.

Acknowledgement

The contribution is part of the solution grant research project VEGA no. 1/0729/13 "Theoretical, experimental and numerical analysis of the constructional design of proposal on energy saving and environmental convenient building envelope constructions".

References

[1] ANDERSON, B. R. The measurement of U-values on site. (online), homepage: http:// web.ornl.gov/sci/buildings/2012/1985%20B3%20papers/001.pdf, (date of access: 2013-11-4).

[2] ĎURICA P., ŠTÚŇOVÁ M. The Course of temperature in construction of lightweight external wall instationary conditions of the internal environment and the actual of outdoor climate. Transcom 2013, 10-th European conference of young researchers and scientists, Žilina: 2013, p.319-324. ISBN 9788055406961

[3] CHMÚRNY I. Thermal protection of buildings. Bratislava : Jaga Group. 2003. 230 p. ISBN 8088905273.

[4] STN 73 0540:2012 Thermal properties of building structures and buildings. Thermal protection of buildings. Part 2: The functional requirements. Bratislava, Slovak Standards Institute, 2012 32 s.

[5] STN 73 0540:2012 Thermal properties of building structures and buildings. Thermal protection of buildings. Part 3: Characteristics of the environment and building products, Bratislava, Slovak Standards Institute 2012. 68 s.

[6] STN EN ISO 12570/A1Hygrothermal performance of building materials and products. Determination of moisture content by drying at elevated temperature (ISO 12570:2000). Bratislava, Slovak Standards Institute, 2013.

[7] ŠTÚŇOVÁ M. Teoretické, technické a technologické aspekty navrhovania a zhotovovania ľahkých obvodových stien. Thesis. FCE ZUZ, Žilina. 2014. 156 p.

TRANSCOM 2015, 22-24 June 2015
University of Žilina, Žilina, Slovak Republic

Assessing the corrosion impact on bearing capacity of steel girder bridges in Poland

*Anna Chwastek, *Małgorzata Ulewicz, **Josef Vičan
*Czestochowa University of Technology, Faculty of Civil Engineering, Department of Building Engineering and Building Physics, ul. Akademicka 3, 42-200 Czestochowa, Poland, {achwastek}@bud.pcz.czest.pl
**University of Žilina, Faculty of Civil Engineering, Department of Structures and Bridges, Univerzitna 8215/1, 010 26 Žilina, Slovakia

Abstract. The paper presents a methodology to determine the ultimate limit state and the use of a steel road bridge construction. The process of estimating the impact of corrosion on the elements subjected to bending and support cross-sections of girders was discussed. Methods of measuring the thickness loss of structure components caused by corrosion are characterized. Reduction coefficients which are necessary to estimate the effect of corrosion in a steel bridge structure were presented as they make the cross-sectional design subject to change its geometric and strength characteristics. The method to define corrosion parameters of girders and cross-sections of support was presented. The algorithm for calculating the percentage of bearing capacity loss in a corroded bridge structure was introduced.

Keywords: steel bridges, bearing capacity loss of a structure, corrosion phenomenon.

1. Introduction

National road network in Poland includes more than 19,000 kilometers of public roads and 6,900 bridges with its total length of 365,000 meters and an area of over 5.1 million square meters. According to General Directorate for National Roads and Motorways (Generalna Dyrekcja Dróg Krajowych i Autostrad) road steel bridges account for 13.60 percent of all road bridges in Poland [1]. Most of them are structures built according to outdated technology, which makes them especially susceptible to corrosion. Inadequate maintenance, repair and improper operation of a given structure often lead to corrosion. Corrosion damage adversely affects the load - bearing capacity of steel bridges which causes its long-term renovations or a closedown.

2. Load-bearing capacity of a steel road bridge structure

Bearing capacity of steel bridge structures is checked by means of the ultimate limit states (ULS) and the serviceability limit states (SLS) in accordance with PN-EN 1993-2:2010 standard [2] on the assumption that the condition they operate in is elastic. Checking the ultimate limit state involves determination of the cross-sectional design resistance, stability of the element shape and the degree of fatigue. Serviceability limit state calculations verify whether the deformation and vibration of a bridge structure adversely affect its operation. Load capacity can be decreased due to the destructible effects of corrosion on bearing elements. The occurrence of corrosion introduces the reduction of the effective cross-sectional areas of structural elements, which may result in failures within the structure elements. The bigger corrosive loss of steel cross-sectional area of the element means the greater impact on the bearing capacity of the structural element. The loss is expressed as the percentage ratio of the total cross-sectional area of the element.

Estimation the impact of corrosion on steel bridges is based on a preliminary study in suit of a structure or its components. The degree of corrosion damage of steel elements, and geometric and strength characteristics of corroded sections are identified. The method of approximate evaluation

of the degree of corrosion refers primarily to the steel beam girder bridges. This method is the most popular one in Poland as 97 percent of steel bridges are girder bridges with plate or truss beams. Bridges on the Polish territory are mostly fabricated as the composite structures and steel supports are rare which is why corrosion of the steel substructures is not considered in the paper [2 - 4].

3. Corrosion phenomena in cross-section subjected to bending

Taken into account the bending, the reliability of steel bridge members can be verified in accordance with PN-EN 1993-2:2010 standard [2] in the case of ultimate limit states by the checking the cross-sectional resistance, lateral-torsional buckling (LTB) and local stability, while the serviceability limit states require to check deflection or vibration. A reduction within the cross-sectional area of a steel member, thereby reducing the load-carrying capacity, is caused by the corrosive loss of steel, which is calculated by measuring the thickness loss of the cross-section in the lower and upper flanges of the girders and in their webs. Measurement of the corrosion loss in bridge members and decks in the form of a steel orthotropic plate is taken considering the width of the deck subpanel defined in accordance with PN-EN 1993-2:2010 standard [2]. When the load-carrying capacity reduction of corroded structure is being calculated the corrosion phenomena should be taken into account as it is often developed in the orthotropic plate longitudinal and transversal stiffeners. The reduction measurement is taken when a reduction factor - u_7 is applied.

Estimating the loss resulting from the unfavourable influence of corrosion on the thickness of the cross-sections subjected to bending moments consists in measuring the area identified as the calibration distance (Fig. 1), where there is the maximum stress according to the structural analyse. The test must be carried out in all the girders within the calibration distance. Three measurement points are selected within the most corrosion - affected areas. These should be cleaned 25 mm along the whole length of the member. Measuring points can be randomly chosen for each girder and the choice depends on the degree of corrosion in the profiles. Cleaning process should result in metallic colour of the element with no sign of rust. The measurement points should be within 50 mm from each other to obtain reliable results. The arithmetic mean should be assumed as the representative value of the measurements for each test point. The readings should be recorded separately for the components of the steel girder i.e. the lower flange, the upper flange and the web. The lowest mean value of a bridge girder measuring point forms the result [2 - 6].

a) Simply supported beam

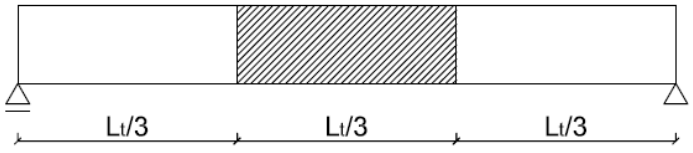

b) Continuous beam

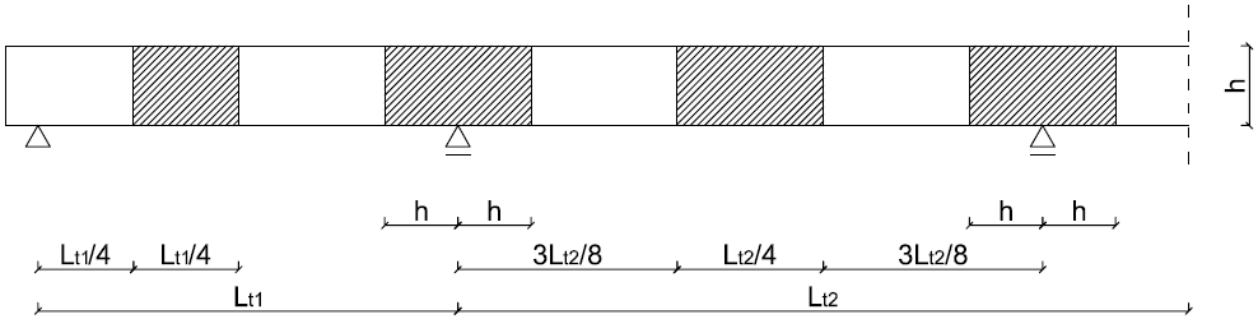

Fig. 1. The calibration distance of a structure due to a structure's static scheme [3]

When changing the girder cross-section the calibration distance should be taken as the length of 40 - times the nominal thickness of the segment prior to the change of thickness from its previous position.

The corrosive parameter of girders is directly proportional to the ratio of flexural resistance of the corroded cross-section and inversely proportional to the flexural resistance of the nominal cross-section. The corrosion value of the *i*-th bridge girder is calculated relatively to the upper and lower fibers of the cross-section with the formulas [3]:

$$w_{iu} = \frac{W_{iu\_cor}}{W_{iu\ nom}} \tag{1}$$

$$w_{il} = \frac{W_{il\_cor}}{W_{il\ nom}} \tag{2}$$

where:

w_{iu}, w_{il} – is the corrosive girder parameter *i*,

W_{iu_cor}, W_{il_cor} – is the flexural resistance indicator (elastic section modulus) of a corroded girder *i* to the upper and lower fibre, [m^3],

W_{iu_nom}, W_{il_nom} – is the flexural resistance indicator (elastic section modulus) of a corrosion-free girder *i* to the upper and lower fibre, [m^3].

Flexural resistance indicator of a corrosion-free girder is the geometric quotient of the second moment of area about the neutral axis by the distance from the extreme fibre of cross-section to the axis – elastic section modulus. The second moment of area about the axis overlapping with the neutral axis of the nominal cross-section is determined by measuring the geometry of the corrosion-free girder. Corrosion phenomenon changes the cross-sectional geometry which is why the second moment of area and indicators of the corroded cross-sectional resistance should be calculated taking into account another position of the neutral axis of a steel profile. For further calculations the minimum value of each corrosive parameters w_{id}, w_{ig} should be applied.

Load-carrying capacity of a structure which was damaged by corrosion is also determined by measuring the web thickness loss of the girder´s cross-section at the point of support to check its local stability loss. The cross-sectional thickness loss of transverse stiffeners located in the place of support is also to be determined. Examination of cross-sectional thickness loss consists in measuring the supporting web over the entire width of the support girder on the bearing, or determining the width of 15 times the nominal thickness of the web on each side of the centre point of support, as well as transverse stiffeners over the entire width of them.

As in the case of cross-section subjected to bending, the test area should be cleaned and the thickness of the cross-sectional parts in the most corroded areas should be measured. For the computation, the arithmetic mean of all the readings for the web and individual stiffeners should be employed. The cross-sectional area of corroded stiffeners and web for each girder [2 - 6] is determined on the basis of results. Corrosion parameter of the girder support cross-section *i* is described by the formula [3]:

$$a_i = \frac{A_{i\_cor}}{A_{i\_nom}} \tag{3}$$

where:

a_i – is the corrosive parameter of the cross-section in the support *i*,

A_{i_cor} – is the area of the corroded cross-section in the support *i*, [m^2],

A_{i_nom} – is the area of the not corroded cross-section in the support *i*, [m^2].

4. Characteristics of reduction factors used to assess the effects of corrosion on the steel bridge structures

Load-carrying capacity of a structure depends on the degree of corrosion of each girder and their interaction when service load is being transferred. There are numerous factors which impact the interaction of bridge girders: their number and spacing in the bridge cross-section, type of deck, and method of interaction with the main girders as well as bracing type, number and state of transverse girders. Table 1 shows the reduction coefficients developed by Road and Bridge Research Institute (Instytut Badawczy Dróg i Mostów). [3, 5].

Coefficient of main girder number– decreasing			
Number of main girders		Symbol	Coefficient value
2		u_1	0.95
3 – 5			0.98
1 or more than 5			1.00
Coefficient of main girder spacing – increasing			
Spacing of main girders, [m]		Symbol	Coefficient value
over 4.00		u_2	1.00
1.75 – 4.00			1.10
below 1.75			1.20
Coefficient of deck type			
Deck type		Symbol	Coefficient value
interactive	steel	u_3	0.98
	concrete		1.00
not interactive			0.95
Coefficient of transversal bracing type – decreasing			
bracing type		Symbol	Coefficient value
solid-section		u_4	1.00
truss			0.98
none			0.90
Coefficient of transversal bracing concentration along the structure length excluding support bracing - decreasing			
Number of transverse bracing		Symbol	Coefficient value
1 or none		u_5	0.90
from L/2 to L/5			0.95
every L/5 or every 4.00 m and more often			1.00
Coefficient of corrosion degree in transversal bracing			
Corrosion type		Symbol	Coefficient value
Corrosion of the cross-sectional area is over 10% compared to nominal transversal bracing cross-section		u_6	0.97
Corrosion of the cross-sectional area is from 0% to 10% and less to nominal transversal bracing cross-section			0.98
No corrosion of transversal bracing			1.00

Tab. 1. Reduction coefficient - u_i [3].

The reduction coefficients allow to determine the decrease of the structural load capacity resulting from corrosion phenomenon.

5. Analytical perspective of load capacity in a corroded bridge construction

Analysis of parameters of corrosive cross-sections subjected to bending, cross-sections in the support of *i*-th bridge girders as well as the reduction factors leads to analytical percentage of decrease of load capacity of a steel road bridge structure which can be presented by the formula [3]:

$$S_M = \left[1 - \frac{\min\left(\sum_{i=1}^{k} w_{id},\ \sum_{i=1}^{k} w_{ig}\right)}{k} \cdot \prod_{j=1}^{n} u_j\right] \cdot 100\% \qquad (4)$$

where:

S_M – is the flexural load capacity decrease due to corrosion, [%],

w_{id}, w_{ig} – is the corrosion parameters of the girder $i = 1,\ldots, k$, $w_i \in \langle 0;1 \rangle$,

u_j – is the reduction factors $j = 1,\ldots, n$, $u_j \in \langle 0{,}9;1{,}2 \rangle$,

k – is the number of girders.

The ultimate loss of the structural load capacity due to corrosion also depends on the load decrease being associated with the support's reaction, which is determined from the formula [3]:

$$S_p = \left[1 - a_i \cdot \prod_{j=1}^{n} u_j\right] \cdot 100\% \qquad (5)$$

where:

S_p – is the shear load capacity decrease due to corrosion, [%],

a_i – is the corrosion parameter of the most corroded girder i, $a_j \in \langle 0;1 \rangle$,

u_j – is the reduction factors $j = 1,\ldots, n$, $u_j \in \langle 0{,}9;\ 1{,}2 \rangle$.

The formulas (4) and (5) allow determining the total load capacity decrease resulting from destructive phenomenon of corrosion in bridges with plate girders, which is described with the formula [3]:

$$S_U = max\{S_M, S_p\} \qquad (6)$$

where:

S_U – is the structural load capacity decrease due to corrosion phenomenon, [%].

6. Conclusion

Analytical method to estimate the impact of corrosion on steel load-carrying capacity of road bridges was developed by the Road and Bridge Research Institute. It is the most common method for determining the percentage of load-carrying capacity decrease in bridge structures, taking into account cross-sections of steel girders subjected to bending moments and shear forces in the support. The geometric characteristics of steel bridges components and the reduction coefficients which we obtain make reliable value of load capacity decrease, which can be directly applied to the nominal values of load-carrying capacity which were determined in accordance with PN-EN 1993-2: 2010 standard [2]. Twelve percent of cross-sectional thickness loss of steel bridge members results in a significant load-carrying capacity loss, and requires another testing calculation to be taken and what is more the whole structure or its components need to be measured again, taking into account their geometrical changes. The result of calculation will imply strengthening or reconstruction of a bridge structure. When safety cannot be provided, the bridge decommission is recommended.

References

[1] GENERAL DIRECTORATE OF NATIONAL ROADS AND MOTORWAYS. *Dane statystyczne o drogowych obiektach inżynierskich*, Warsaw, 2015.

[2] PN-EN 1993-2: *Eurocode 3: Design of steel structures - Part 2: Steel bridges.* PKN Warsaw 2010.

[3] CZEREPAK A., CZUDEK H., PRYGA A., WYSOKOWSKI A. *Metoda szacowania wpływu korozji na nośność konstrukcji stalowych mostów drogowych.* Published by Road and Bridge Research Institute, Żmigród, 2003.

[4] MADAJ A., WOŁOWICKI W. *Budowa i utrzymanie mostów*. Published by Komunikacji i Łączności, Warsaw, 2013.

[5] WYSOKOWSKI A. *Limitation of corrosion effect on the reduction of load capacity of steel bridges by thermal spraying*, IP, 1/2007, 39 – 47.

[6] VIČAN J., ODROBIŇÁK J. *Steel structures*, Published by University of Žilina, Žilina 2008.

[7] ŁUBIŃSKI M., FILIPOWICZ A., ŻÓŁTOWSKI W. *Konstrukcje metalowe Podstawy projektowania.* Vol. I, Published by Arkady, Warsaw, 2007.

[8] WYSOKOWSKI A. *Trwałość mostów stalowych w funkcji zjawisk zmęczeniowych i korozyjnych.* Published by Road and Bridge Research Institute, Warsaw, 2001.

[9] BARANIAK A., NOWOWIEJSKI K. How to design a steel structure with proper corrosion protection. IP, 1/2007, 15 – 21.

[10] KAYSER J.R, NOWAK A.S. *Reliability of corroded steel girder bridges*, J. Struct. Safety, 6/1989, 53 – 63.

[11] KAYSER, J., NOWAK A.S. *Capacity Loss Due to Corrosion in Steel-Girder Bridges*. J. Struct. Eng., 115(6)/1989, 1525 – 1537.

[12] CZARNECKI, A. A., NOWAK, A. S. *Reliability Assessment for Evaluation of Steel Girder Brides.* P I Civil Eng. – Civ. En., 160/2007, 9 – 15.

[13] CZARNECKI A.A, NOWAK A.S. *Time-variant reliability profiles for steel girder bridges*. J. Struct. Safety, 30/2008, 49 – 64.

[14] NAKAI T., MATSUSHITA H., VAMAMOTO N. *Effect of pitting corrosion on the ultimate strength of steel plates subjected to in-plane compression and bending*. J. Mar. Sci. Tech., 11/2006, 52 – 64.

TRANSCOM 2015, 22-24 June 2015
University of Žilina, Žilina, Slovak Republic

The influence of particular parameters on the temperature distribution in the impletion of regenerative heat exchanger for cooling process

[*]Diana Chylińska, **Jerzy Zbigniew Piotrowski
* Kielce University of Technology, Faculty of Environmental, Geomatic and Energy Engineering, Department of Building Physics and Renewable Energy, al. Tysiąclecia Państwa Polskiego 7, 25-314 Kielce, Polska, {dianachylinska}@gmail.com
** Kielce University of Technology, Faculty of Environmental, Geomatic and Energy Engineering, Department of Building Physics and Renewable Energy, al. Tysiąclecia Państwa Polskiego 7, 25-314 Kielce, Polska, {piotrowski}@tu.kielce.pl

Abstract. The article describes the process of unsteady heat transfer that occurs between the impletion of regenerative heat exchanger and the surrounding air. A mathematical model of this phenomenon and its exemplary solution using the method of elementary balances were presented. Numerical calculations using Mathcad were applied. As a result, the set temperature field is formed in the heat exchanger wall. The temperature changes, for cooling process, in the various nodes of the model in the subsequent time intervals, with incorporation of two variants of the air-flow rate and two variants of dimensions (length of the filling) were presented. With it, you can better understand the processes of heat exchange occurring in the device, which has an impact on the determination of optimum operating conditions of the heat exchanger.

Keywords: regenerative heat exchanger, heat transfer, non-stationary state, the method of elementary balances

1. Introduction

Continuous growth of electricity prices, both renewable and conventional fuels leads to rationalize heat and power facilities in the construction industry (commercial as well as residential). The integration of a heat recovery system with a mechanical ventilation system has gained a lot of attention due to the energy saving potential. Rich assortment of energy recovery devices producers and public awareness of the need for energy saving, make energy recovery ventilation systems starts to be a standard. A popular option for energy recovery in the mechanical ventilation systems with heat recovery became rotary regenerative heat exchangers [1].

In the early stages of the regenerators' development, the lack of algorithms to calculate them limited progress in the field of regenerative heat exchangers. There was an availability only of analytical solution of simplified problem, or graphic solutions based on complicated techniques. Therefore, the study of wide range of applications, the influence of design parameters and operating conditions were complicated. Several analytical models of heat exchange processes occurring in rotating heat exchangers, has been proposed in the literature [2].

This paper presents the computational model that allows the analysis of the temperature distribution in completing the regenerative heat exchanger for the mural. The model assumes one-dimensional temperature field. As an initial condition assumed uniform temperature fill (all nodes), and adopted the boundary condition of the third kind. The influence of the geometrical dimensions (length of the filling), and air velocity on the temperature distribution in the fill were analysed.

2. A mathematical model of heat transfer in the impletion of regenerative heat exchanger (cooling process)

Non-stationary one-dimensional heat conduction in the layer of filling in the regenerative heat exchanger was considered. As a filling thickness was adopted δ. Due to the fact that next to the both sides of the element, air flow with identical parameters, analysis of temperature distribution was made in the mid-filling element δ / 2. The heating process of filling was considered. Heat transfer model was developed using one of the numerical methods for solving heat conduction problems, namely the method of elementary balances. The test area was divided into geometric elements, for which the energy balance sheet based on the following assumptions was prepared:

- the average air temperature $Tpow_{sr}$,
- a one-dimensional temperature field: T=f(x,τ),
- precondition: temperature of the plate: T(τ=0)=40°C,
- boundary condition of the third type: $\lambda\left(\frac{dt}{dx}\right)_{x=0} = \alpha[Tpow_{sr} - T(0,\tau)]$,
- constant plate parameters (c_{pm}, ρ_m, λ) and air (c_p, ρ, α) are known,
- there are no internal heat sources,
- each element is represented by a node that is located in the center of gravity of the element,
- each element has temperature equals node's temperature,
- whole heat capacity of the element is focused in the node,
- nodes lying on the surface of the body are regarded as without capacity.

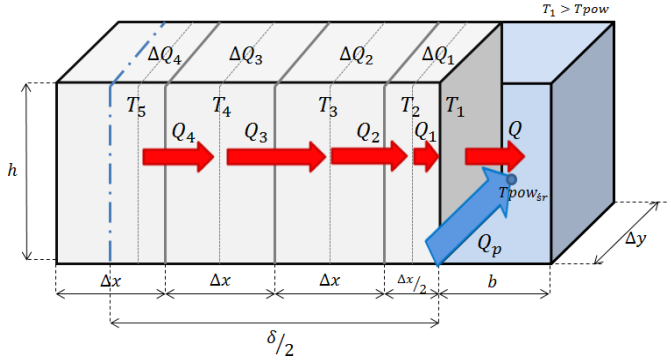

Fig. 1 The division of the test area on the geometric elements (physical model of cooling process)

In the non-stationary conditions, assuming isobaric heat flow, the heat inflow to the relevant node or nodes from the adjacent or surface of the body will increase in enthalpy. Energy balance equation in the nodes in each intervals of can be written as follows:

$$\begin{cases} Q_p = Q \\ Q = Q_1 \\ Q_1 = \Delta Q_1 + Q_2 \\ Q_2 = \Delta Q_2 + Q_3 \\ Q_3 = \Delta Q_3 + Q_4 \\ Q_4 = \Delta Q_4 \end{cases} \quad (1)$$

The result is:

$$\begin{cases} c_p \cdot G \cdot (Tpow_k - Tpow_p) = \alpha \cdot F \cdot \left(T_{1.i+1} - \dfrac{Tpow_p + Tpow_k}{2} \right) \\ \alpha \cdot F \cdot \left(T_{1.i+1} - \dfrac{Tpow_p + Tpow_k}{2} \right) = (T_{2.i+1} - T_{1.i+1}) \cdot F \cdot \dfrac{\lambda}{\dfrac{\Delta x}{4}} \\ (T_{2.i+1} - T_{1.i+1}) \cdot F \cdot \dfrac{\lambda}{\dfrac{\Delta x}{4}} = c_{pm} \cdot \dfrac{m}{2} \cdot \dfrac{T_{2.i} - T_{2.i+1}}{\Delta \tau} + (T_{3.i+1} - T_{2.i+1}) \cdot F \cdot \dfrac{\lambda}{\dfrac{3\Delta x}{4}} \\ (T_{3.i+1} - T_{2.i+1}) \cdot F \cdot \dfrac{\lambda}{\dfrac{3\Delta x}{4}} = c_{pm} \cdot m \cdot \dfrac{T_{3.i} - T_{3.i+1}}{\Delta \tau} + (T_{4.i+1} - T_{3.i+1}) \cdot F \cdot \dfrac{\lambda}{\Delta x} \\ (T_{4.i+1} - T_{3.i+1}) \cdot F \cdot \dfrac{\lambda}{\Delta x} = c_{pm} \cdot m \cdot \dfrac{T_{4.i} - T_{4.i+1}}{\Delta \tau} + (T_{5.i+1} - T_{4.i+1}) \cdot F \cdot \dfrac{\lambda}{\dfrac{3\Delta x}{4}} \\ (T_{5.i+1} - T_{4.i+1}) \cdot F \cdot \dfrac{\lambda}{\dfrac{3\Delta x}{4}} = c_{pm} \cdot \dfrac{m}{2} \cdot \dfrac{T_{5.i} - T_{5.i+1}}{\Delta \tau} \end{cases} \quad (2)$$

Where:

α – thermal diffusion coefficient, W/m^2K

c_p – heat capacity of air, J/kgK

G – mass flow, kg/s

$Tpow_p$ – initial air temperature, $^\circ C$

$Tpow_k$ – final air temperature, $^\circ C$

F – surface, m^2

λ – thermal conductivity coefficient, W/mK

$T_{.i}$ – node temperature, $^\circ C$

Δx - distance, m

c_{pm} – specific heat capacity of plate, J/kgK

m – mass, kg

$\Delta \tau$ - time, s

3. The influence of air velocity on the temperature distribution in the impletion of regenerative heat exchanger – the example of calculation

The numerical calculations by means of Mathcad were presented. The following data were used: initial air temperature $Tpow_p = 20^o C$, thermal diffusion coefficient $\alpha = 40W/m^2K$, specific heat capacity of air $c_p = 1005J/kgK$, air density $\rho_p = 1{,}205kg/m^3$, thermal conductivity coefficient (alluminium) $\lambda = 200W/mK$ [3], specific heat capacity of plate $c_{pm} = 870J/kgK$, density of plate material $\rho_m = 2700kg/m^3$, $\Delta x = 0{,}002m$, $\Delta y = 0{,}2m$, h=0,5m, b=0,02m,

$\Delta\tau = \frac{\Delta y}{\upsilon}$. At the initial time a constant temperature in all nodes in the analyzed area was assumed T(τ=0)=const=40°C.The following air velocities were considered: $\upsilon_1 = 2m/s, \upsilon_2 = 1m/s$. The figure below shows fragmentary results of made simulation.

The Figure 2 illustrates the temperature changes, for cooling process, in the various nodes of the model in the subsequent time intervals, with incorporation of two variants of the air flow rate.

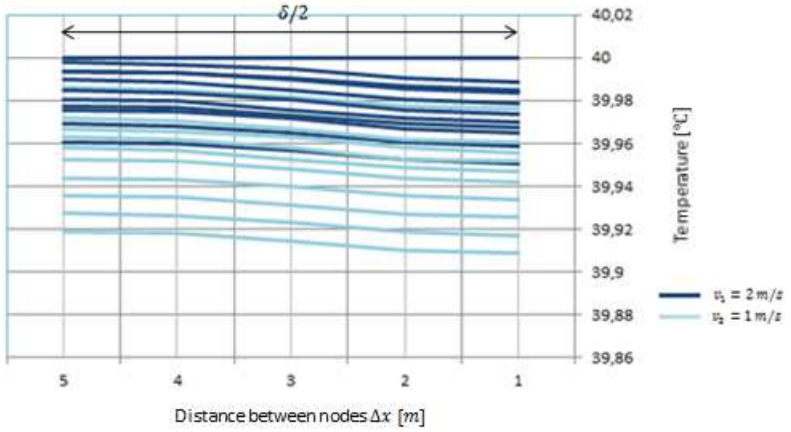

Fig. 2 The temperature distribution, for cooling process, in the various nodes of the model in the subsequent time intervals (with incorporation of two variants of the air flow rate)

4. The influence of the geometrical dimensions on the temperature distribution in the impletion of regenerative heat exchanger – the example of calculation

For the same data as in section 3 computational simulation was performed taking into account the length of the impletion $\Delta y = 0{,}1m$ and $\Delta y = 0{,}2m$.

The figure below shows fragmentary results of made simulation. The Figure 3 illustrates the temperature changes, for cooling process, in the various nodes of the model in the subsequent time intervals, with incorporation of two variants of the length of the impletion.

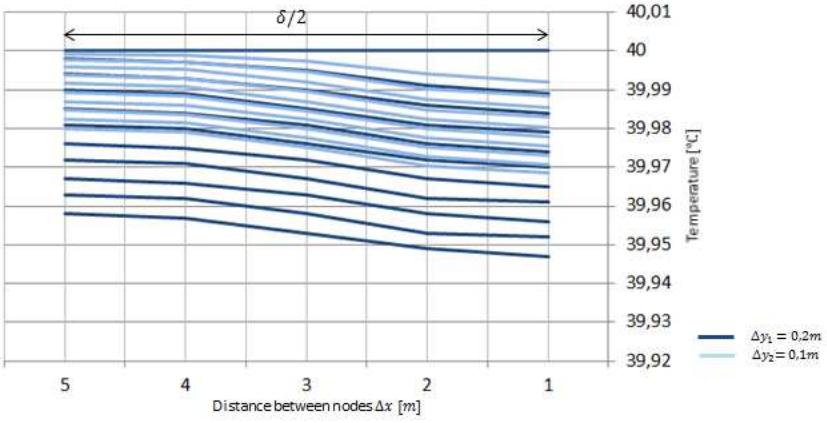

Fig. 3 The temperature distribution, for cooling process, in the various nodes of the model in the subsequent time intervals (with incorporation of two variants of the length of the impletion

5. Conclusion

Adopted mathematical model and the sample solution allow to make a simplified calculation of the temperature distribution in completing the regenerative heat exchanger. It also allows to estimate

the final temperature of the air at a given initial temperature of the air. With it you can better understand the processes of heat exchange occurring in the device, which has an impact on the determination of optimum operating conditions of the heat exchanger. Through various computational simulations it shows how a significant impact on the work of the regenerator have the individual parameters: geometric dimensions and airflow.

References

[1] SCHONTALE J., MULLER J., SKRZYNIOWSKA D., SIKORSKA-BĄCZEK R.: *Instalacje i urządzenia do uzdatniania powietrza dla celów wentylacji i klimatyzacji*, Politechnika Krakowska, Kraków 2010.

[2] [2] ZHUANG W., RODERICK V.N. MELNIK, FINN BORUP: *Model-based analysis and simulation of regenerative heat wheel*, Energy and Buildings 38 (2006)

[3] http://pl.wikipedia.org/wiki/Przewodno%C5%9B%C4%87_cieplna

TRANSCOM 2015, 22-24 June 2015
University of Žilina, Žilina, Slovak Republic

Modeling of the composite steel and concrete truss beams

[*]Róbert Idunk, [*]Ján Bujňák,
[*]University of Žilina, Faculty of Civil Engineering, Department of Structures and bridges, Univerzitná 8215/1, 01026 Žilina, Slovakia, {robert.idunk, jan.bujnak}@fstav.uniza.sk

Abstract. Composite steel and concrete structures in the civil engineer are used for long time. In the past behavior of structures could be described either by theoretical knowledge, or experiments. Experiments are always expensive matter. Today, various problems can be modeled using available computer technology and software. The article describes the creation of preliminary FE model of composite steel and concrete truss with full shear connection. It offers procedures and comparisons to solve the similar problem.

Keywords: beam element, top chord, truss, stress, model.

1. Introduction

Nowadays, the most commonly used material for load-carrying structures in civil engineering and building construction are steel and concrete. Both materials have advantages and disadvantages. Their disadvantages are eliminated by combining into the one structural element. The idea of the combination of steel and concrete is good but practical design has considerable problems.

Composite structures are structures which are associated with at least two structural members of two different materials. Composite steel and concrete beams are most commonly used elements in civil engineering. These beams can be either a solid beam or a truss. Design of composite steel and concrete beams is a relatively well managed and currently is supported by the European standards [1], [2]. However, the design of composite steel and concrete trusses has not general recommendations, respectively European standards do not offer a specific design procedure.

This article deals with the creation of the finite element model of composite steel and concrete truss. This FE analysis provides a view on behavior of the beam under loading, thus, on its deformation and state of stress. Data obtained from the FE analysis is very useful before testing specimens of beams, for example it can be used for monitoring system arrangement.

It is necessary to point out that the present article analyzes only the composite truss with full shear connection.

2. The geometry of composite steel and concrete truss

The geometry of composite steel and concrete truss is shown in Fig. 1 and is given by a specimen. Same beam with the same geometry was the subject of research [5].

The theoretical length of the beam is 3.75 m and real length is about 0.4 meters greater.

Steel truss rods are made of steel grade S355. The top chord is formed by half of rolled profile IPE160 and bottom chord is made by profile 2xUPE120. Diagonals members are SHS70x70x6.3 and SHS40x40x3.

The concrete slab is 800 mm wide and 100 mm thick. Class of concrete C25/30 is used.

Full shear interaction is achieved by the perforated shear connector.

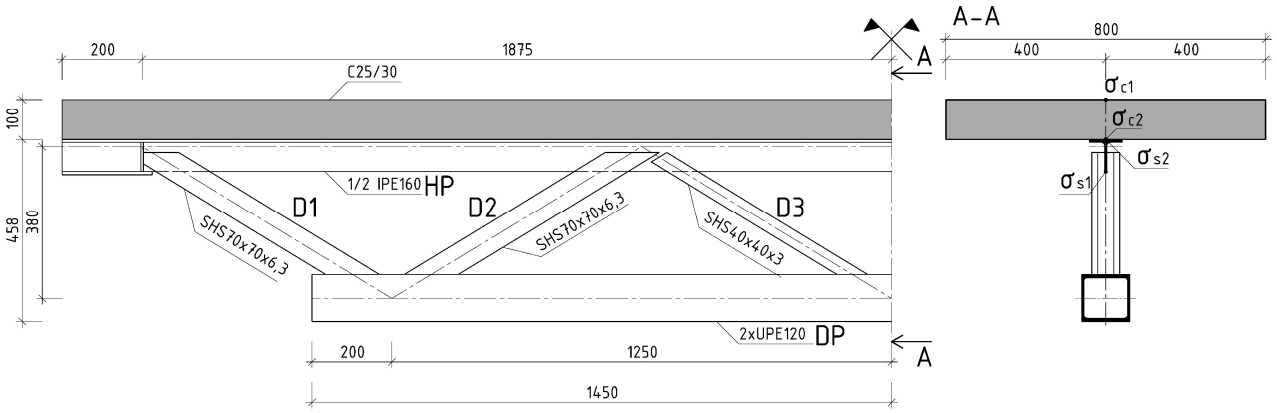

Fig. 1. The geometry of composite steel and concrete truss.

3. Creation of FE model

FE model was created by software ADINA [6], allowing for a static and dynamic incremental nonlinear analysis.

In the first step it would be necessary to choose elements for structural modelling. The relevant elements should adequately describe the real behavior so that the modeling process would not be too complicated.

Two alternative models were produced, illustrated in Fig. 2 and 3. The first one referred as "A" is considering the continuous top chord. The other calculation procedure "B", the top chord takes as cut in the areas between the joints.

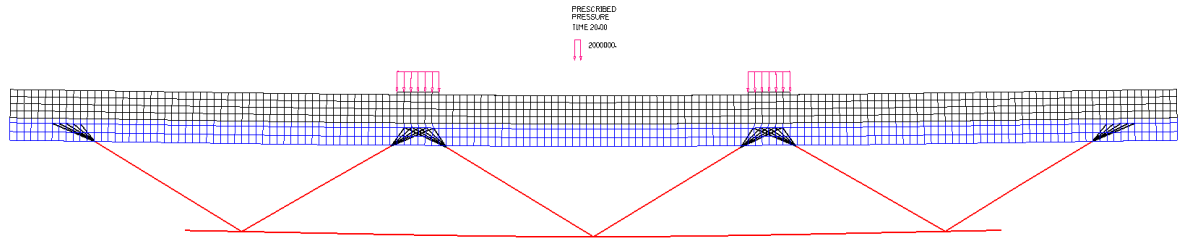

Fig. 2. FE model of alternative "A".

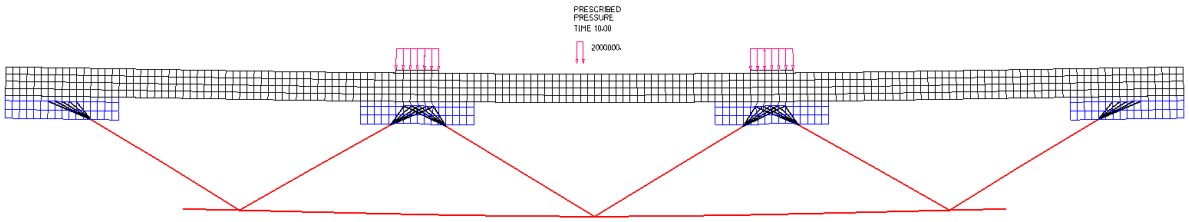

Fig. 3. FE model of alternative "B".

Bottom chord and diagonals are modeled using beam elements and the top chord using shell elements. For the concrete slab, 3D solid elements are used.

For regular mesh with subdivisions of 0.025 m, 4-node elements (for shell elements) and 8-node elements (for 3D solid) were applied. Completed mesh is shown in Fig. 4 and 5.

The beam loading consisted of uniformly distributed load of intensity p=2 N/mm^2 in areas between intermediate nodes (see Fig. 4 and 5).

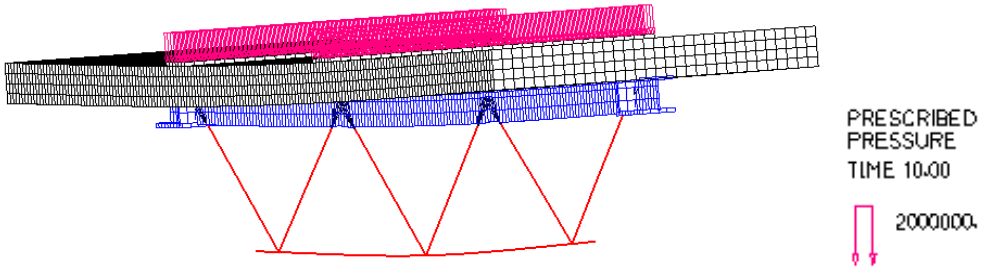

Fig. 4. FE model alternative "A" – 3D view.

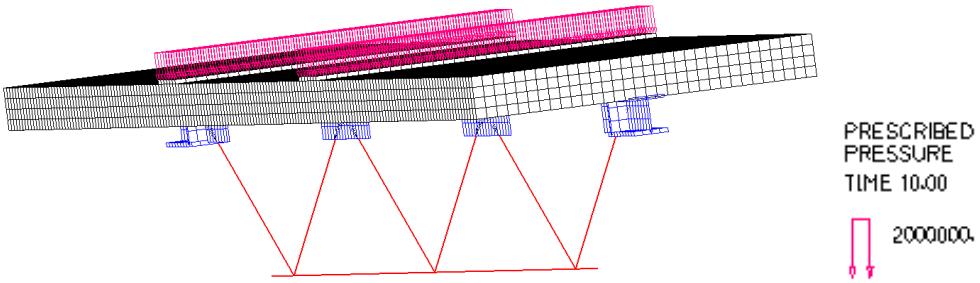

Fig. 5. FE model alternative "B" – 3D view.

Member struts connection to the chords presents the next difficulty. Model in which the diagonal is connected to the top chord through one point (see Fig. 6) is only applicable if the steel and concrete will be considered as elastic materials. However, this analysis does not reflect an actual performance of the structure at ultimate limit state. In this behavior phase, it should be necessary to take into account that the plasticity of steel and non-linearity of the concrete slab. In this way local stresses in the joint, resulting from only a nodal connection of diagonals as beam elements to the top chord simulated by shell elements, can be eliminated.

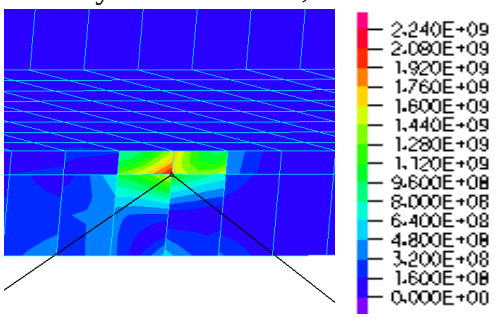

Fig. 6. Connection of diagonals with top chord through one node mesh. Also effective stress at the area of joint is shown.

This challenging type of connection can be improved by splitting of the diagonal beam members into five nodes of top chord shell mesh and linking them rigidly by truss element, as illustrated
in Fig. 7.

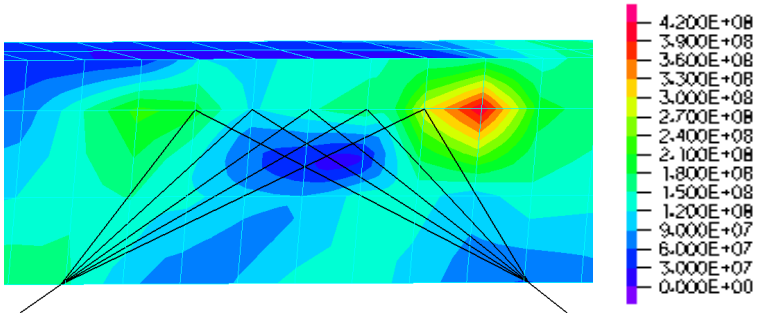

Fig. 7. Connection of diagonals with top chord through rigid bond. Also effective stress at the area of joint is shown.

Also, a full shear connection at the interface of the steel flange and the concrete slab can be modeled by two ways. The first system consists of attaching the nodes of both mesh. This procedure can be applied only if the nodes of both meshes are compatible. The second approach should be used when nodes are not well-matched. This method is based on tied contact. Details of the modeling of the contacts are described in [7].

For steel, bilinear relation between stresses and strains was used without hardening. With characteristics according to [3], particularly the following characteristics were considered E=210 GPa, μ=0.3, f_y=355 MPa. According to standards [4], the concrete was taken as linearly working, with the properties E=31 GPa, μ=0.2, f_{ck}=25 MPa.

4. Comparison of models

Resulting normal stresses in the mid-span of the beam have been compared as main truss performance indicators. For typical structural elements, these values are in Tab. 1. It can be concluded that the presence of the top chord has no great influence on the stress in the other elements. A difference between stresses in the beam with continuous top chord (alternative "A") and this one practically without top chord, as it was cut out (alternative "B") is less than 10%.

Designation of elements	Alternative "A"			Alternative "B"			
	N [kN]	A [m^2]	σ [MPa]	N [kN]	A [m^2]	σ [MPa]	Difference [%]
DP	586.87	0.003086	**190.18**	590.53	0.003086	**191.36**	**1.61**
D1	357.36	0.00156	**229.08**	360.68	0.00156	**231.21**	**1.09**
D2	-328.19	0.00156	**-210.38**	-329.25	0.00156	**-211.06**	**3.11**
D3	-10.37	0.000434	**-23.89**	-11.36	0.000434	**-26.18**	**8.71**

Tab. 1. Stresses in the beam elements – Alternative "A" and "B".

Also the slab performance (3D solid element) and the top chord behavior (shell element) have been considered. An overview of the stresses in these structural parts is given in Tab. 2. Only one value σ_{c1} in the top slab fibers might be relevant. Stresses in the bottom fibers of the slab cannot be properly compared, due to significant stress produced by the absence of the top chord between joints.

Normal stress	Alternative "A"	Alternative "B"	Difference [%]
σ_{c1} [MPa]	**-26.44**	**-29.03**	**8.92**
σ_{c2} [MPa]	**-0.28**	**15.57**	------
σ_{s2} [MPa]	**-58.57**	------	------
σ_{s1} [MPa]	**264.28**	------	------

Tab. 2. Stresses in the shell element and 3D solid element – Alternative "A" and "B".

Note: Strut and stresses location are given in Fig. 1.

5. Conclusion

The influence of different parameters of the steel-concrete composite truss on its behaviour was investigated by elastic and plastic analysis. The improvement of this promising model is in progress on the basis of discreet model using solid elements and local damage evolution of concrete. The aim is to take better into account of the local phenomena such as the plastic deformation between the connectors and the top chord on all the length of the chord including the panel points. The experimental program of bending test of composite truss beam would go on to test the finite model and investigate real behavior of the composite truss with connection only above the nodes.

Acknowledgement

The paper presents results of works supported by the Scientific Grant Agency of the Slovak Republic under the project No. 1/0583/14.

References

[1] EN 1994-1-1: Eurocode 4: *Design of composite steel and concrete structures. Part 1-1: General rules and rules for buildings*. CEN, Brussels 2004.

[2] EN 1994-2: Eurocode 4: *Design of composite steel and concrete structures. Part 2: General rules and rules for bridges*. CEN, Brussels 2005.

[3] EN 1993-1-1: Eurocode 3: *Design of steel structures. Part 1-1: General rules and rules for buildings*. CEN, Brussels 2005

[4] EN 1992-1-1: Eurocode 2: *Design of steel structures. Part 1-1: General rules and rules for buildings*. CEN, Brussels 2004

[5] BUJNAK, J. DURATNA, P., BOUCHAIR, A. *Theoretical and experimental research on composite truss beams.* Eurosteel 2014: 7th European Conference on Steel and Composite Structures, Napoli, Italy. ECCS Brussels 2014.

[6] ADINA, System for linear and nonlinear finite element analysis of solids and structures, heat transfer, CFD and electromagnetics, http://www.adina.com/

[7] ADINA, Theory and Modeling Guide, Volume I, December 2012, http://www.adina.com/

TRANSCOM 2015, 22-24 June 2015
University of Žilina, Žilina, Slovak Republic

Influence of sand-lime materials modification on their porosity

[*]Iga Jasińska, [*]Ryszard Dachowski
[*]Kielce University of Technology, Faculty of Civil Engineering and Architecture, al. Tysiąclecia PP 7, 25-314 Kielce, Poland {tobrd, igajas}@tu.kielce.pl

Abstract. The main objective of the study is to create ecological lime-sand product having a reduced bulk density as compared to traditional elements which compressive strength (in the meaning of construction and technology) is greater than 5.0 MPa. The test procedure consisted of experiments to determine the basic properties of the modified sand-lime products (the study of compressive strength and determination of bulk density) and of changes in the distribution of pores over traditional silicate materials.

Keywords: sand-lime product, porosity, silicate bricks, bulk density, foamed glass granulate

1. Introduction

Development of science and industry in the field of contemporary building materials technology is widely developed. In the manufacturers offers there are materials with a wide range of properties and applications. Their characteristics are dictated by the requirements of both consumers and architects. To improve the properties of building materials many scientists and technologists work on who thanks to the use of all kinds of additives, fillers, additives modify the physical and mechanical properties of traditional products mainly cement pastes, mortars and concretes. Less common is the modification of the mixture in the range of sand-lime materials which in Poland there are very good conditions for raw materials [1] and their commonness increases each year. Lime-sand products known as silicates they are building materials which the basic components are the natural materials (lime 5-8% and 90-92% quartz sand) mixed with water to the wet consistency. Formed and thickened in the press the substance is subjected to autoclaving high temperature conditions (203°C) and with the pressure (1.6 MPa) steam-induced [1,2]. These products are primarily characterized by high compressive strength which for traditional products exceeds 20 MPa.

Modification which is widely known for sand-lime substances is the one with the basalt usage which the compressive strength of the newly derived products increased significantly reaching close to 50 MPa. In addition, these products are characterized by reduced water absorption compared to traditional products [3].

In order to meet environmental requirements and increased amount of waste in the form of commonly used in the industry recycled polymers there are many efforts made to find the aims for their usage. One of them is to use their regrind as fillers in the lime-sand substances. The research was conducted on three types of regrind: high impact polystyrene (HIPS), a mixture (a mix of polypropylene and polyethylene) (PP + PE). The test results showed that the presence of these fillers in the sand-lime substance affects the change in the properties of the products. The addition of a mixture of HIPS and PP + PE helped to reduce the amount of absorbed water and at the same time contributed to a significant increase in the strength of the newly derived products [4]. Different impact on the physical and mechanical properties obtained from tests performed on elements obtained from the of sand-lime substance with the additives (copolymer of acrylonitrile-butadiene-styrene ABS) ABS and (low density polyethylene) LDPE. These fillers have contributed to reduction of the absorbed water but also resulted in a reduction in the compressive strength of sand-lime brick elements [4,5].

2. Purpose of the study

The main objective of the study is to create ecological lime-sand product having a reduced bulk density as compared to traditional elements which compressive strength (taking into account the construction and technology) is greater than 5.0 MPa. The accompanied feature will be an increase of porosity in relation to the traditional product.

The porosity of the material is of great importance for the properties of building materials. It determines the characteristics, ie .: compressive strength, frost resistance, insulating properties, thermal properties and soundproof. The porosity of the building material comprises seeding the range from 0% (glass, bitumen, metals) to 95% (mineral wool, polyurethane foam) [6]. Among the many products available on the market, which may serve reduced bulk density of mentioned above products the particular attention is paid to the foamed glass molded in the form of pellets about the size of 0.5-1.0 mm. This supplement is a product of ground cullet subjected to foaming and formed into fine pellets and sintered. Therefore, it is a recycled mineral product. It also creates an ultra light product with a density of 110-600 kg/m^3. It is characterized by, among others, high resistance to compression, non-flammability and chemical resistance [7]. All these advantages have led to the usage of this product as a silicate filler product in order to reduce the density of the products obtained.

The usage of foamed glass granules for sand-lime products offers many benefits to both producers and consumers, e.g .:

- savings of raw materials, ie. sand and lime,
- use in the production of recycled products,
- reducing the transport cost of goods from the manufacturer to the construction site,
- reduce the workload on the masonry work.

3. Examination methodology

The test procedure consisted of experiments to determine the changes in the distribution of pores in the lime-sand elements. The tests were performed on samples of conventional and modified by the foamed glass granulate. The initial product was the traditional sand-lime mixture. The content of filler in the elements was prepared with 5, 10, 15 and 20% of total weight. Thus prepared substance was formed in rectangular bars with the dimensions of 40×40×160 mm and then subjected to the compaction with subsequent 8-hour autoclaving in silicate production plant in Ludynia.

For the obtained products bulk density was determined. They were also subjected to compressive strength tests using a press Tecnotest KC 300 [8,9] as well as the porosity of the materials was tested using a mercury porosimetry method on samples of dimensions 8×8×10 mm. The mercury porosimetry method is based on a mercury penetration under pressure into the pores of the tested material allowing for the measurement of the macropores size (diameter greater than 0.05 microns) and mesopores (diameter 0.05 - 0.002 microns) [10,11]. With this method it is possible to determine the total open pores volume and determining the pores volume of a given diameter [12].

The sample was placed in the penetrometer with capillary edges. Prior to the proper test, the vapor pressure in the pores was carefully evacuated and then penetrometer was completely filled with mercury. The test consisted of continuous appropriate increase in pressure in the chamber, whereby the mercury can penetrate into smaller and smaller pores of the sample. The quantity of mercury "pressed" into the pores indicated the porosity of the sample [13].

4. Results of research

Tests and calculations of selected physical parameters are made on each of the six samples of the identical qualitative composition. Subsequent studies were performed on separate samples of silicate.

The compressive strength of a conventional product is 20.5 MPa. At about 7% - at that additive participation the strength has decreased twice. However, due to the adopted, the preferred compressive strength in the application in the construction industry should be greater than 5 MPa, noteworthy products containing additive of no more than 13%. The change in compressive strength as a function of the foamed glass granulate is shown in Fig. 1a.

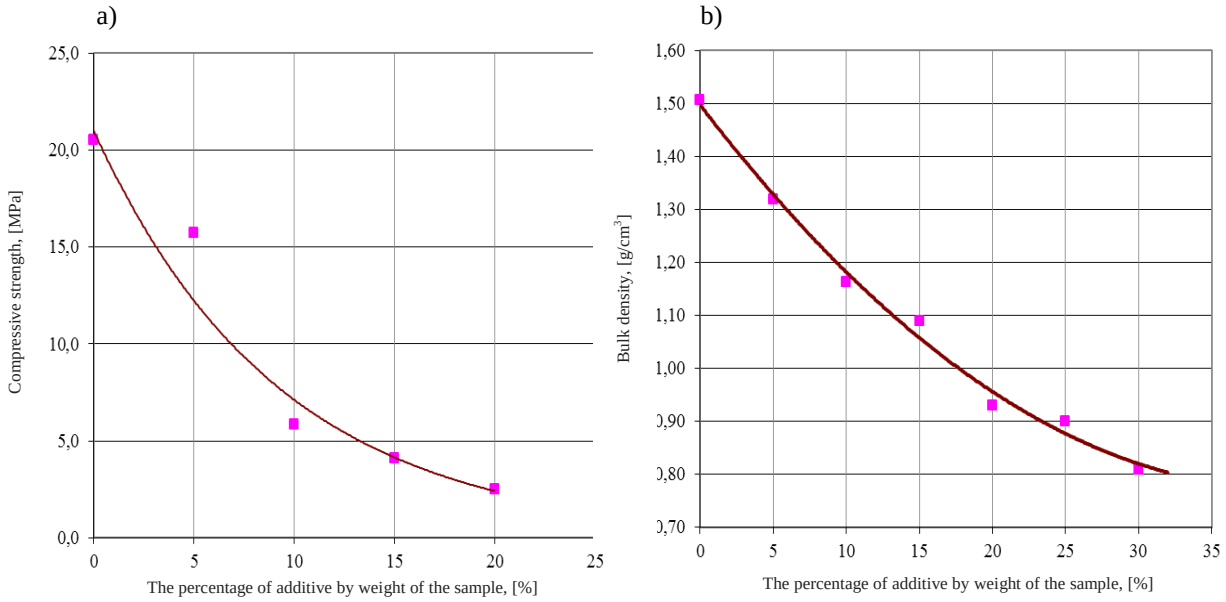

Fig. 1. Effect of additive: a) the compressive strength of calcium silicate products, b) the bulk density

Partial modification of a mixture of lime and sand with additive used effects the mass reductively the produced element which is confirmed by bulk density values obtained. Even with a small proportion of granules (5%) of silicate mass of the product the element reduced about 0.2 g/cm3 its density in relation to the baseline (Fig. 1b).

Changing the mass volume of the modified product is dictated by the change of its porosity as compared to a conventional product. A study done by mercury porosimetry showed that traditional products has gained 13.89% porosity, while the modified products with 10% of foamed glass granulate contents increased the porosity to 32.57%. The increase in porosity results in a comparable increase in surface area of the pore space. Graph of the pore size of their total volume is shown in Fig. 2.

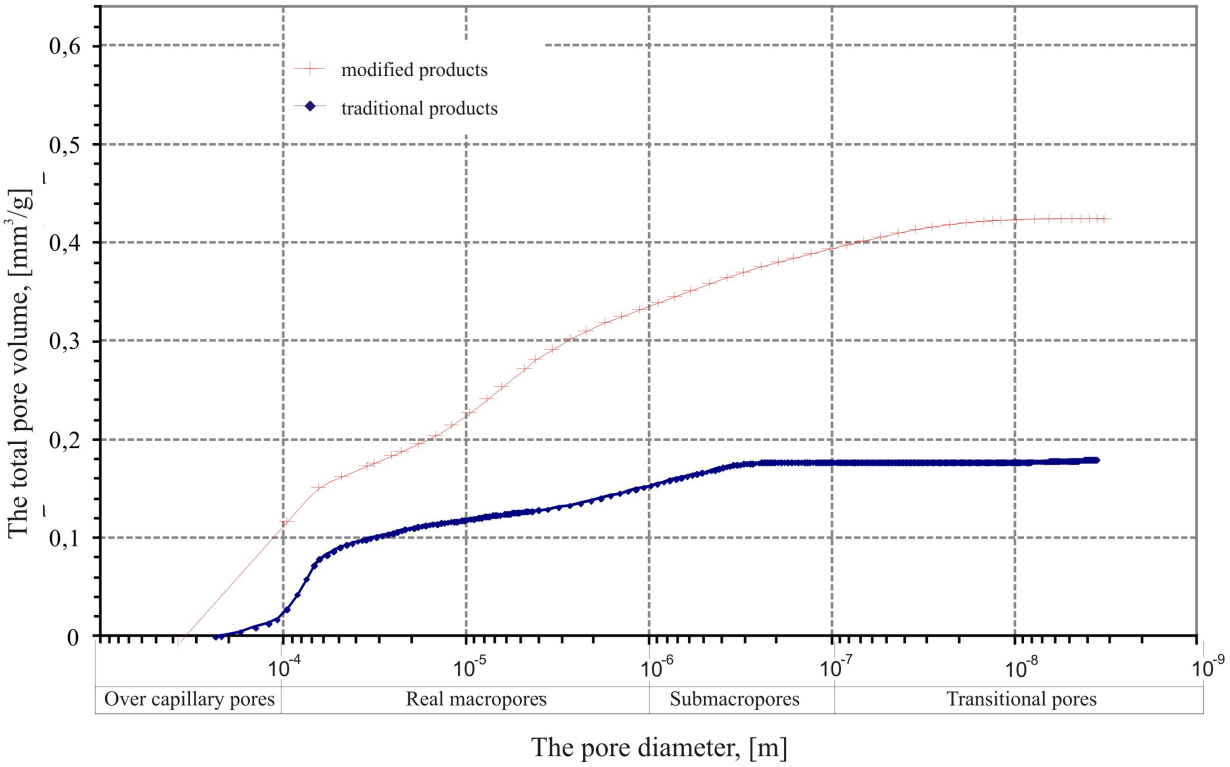

Fig. 2. The pore volume distribution of the silicate products

From this graph it can be seen that the conventional products there are pores with a diameter which ranges of $3.6 \cdot 10^{-9} \div 2.36 \text{ -}10^{-4}$ m and the diameter distribution of modified product changes and is in the range of $3.0 \cdot 10^{-9} \div 3.55 \cdot 10^{-4}$ m.

In order to compare the distribution of pores in the test samples to analyze the following groups (Table 1):

Pore classes	Diameter, [m]	Symbol
Transitional pores	$< 10^{-7}$	T
Submacropores	$10^{-7} – 10^{-6}$	S
Real macropores	$10^{-6} – 10^{-4}$	R
Over capillary pores	$> 10^{-4}$	O

Tab.1. Border diameters of selected pore groups

Using the cumulative pore volume (Fig. 3) and a column chart group (Fig. 4) the presence of pores with diameters characteristic for each of the identified classes. However, there are some changes in the proportions in which they occur. While in traditional products more than 70% of the volume there are pores with a diameter range of 10^{-6} - 10^{-4} m, then in the modified products containing foamed glass granulate its volume decreases (50%) for the growth of the pores and over capillary pores transition.

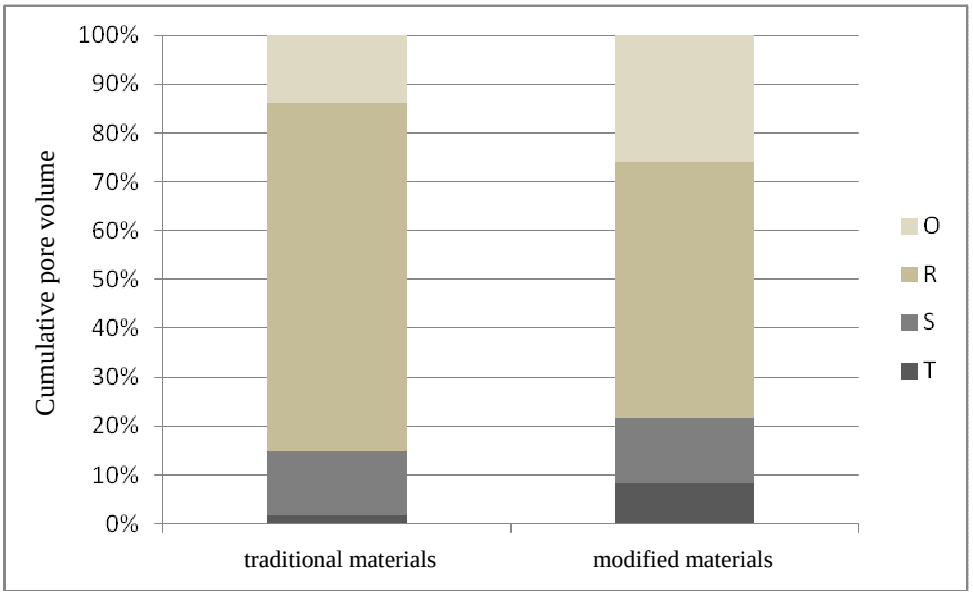

Fig. 3. Cumulative pore volume components in conventional and modified materials

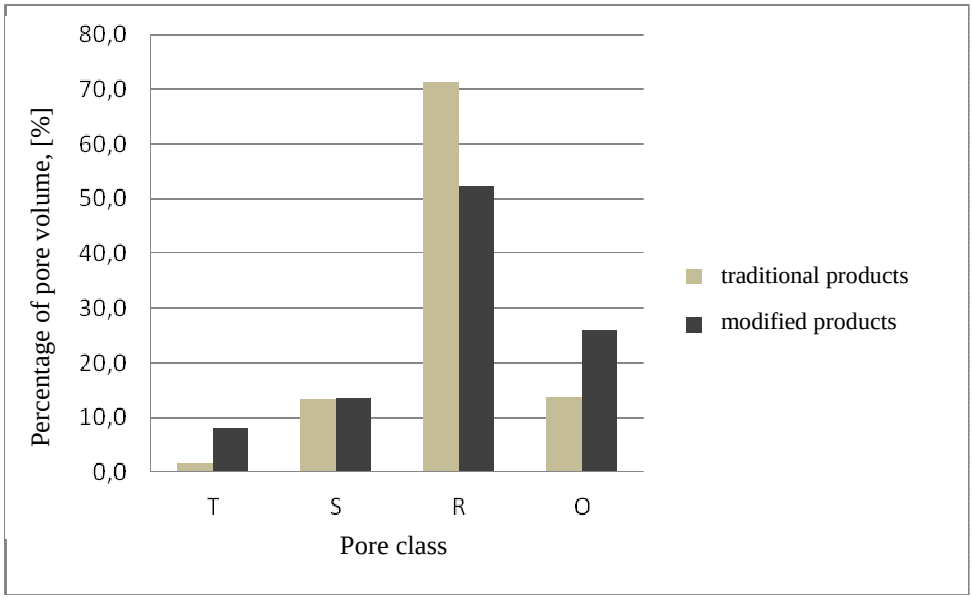

Fig. 4. Percentage of pore volume in the particular class of modified and conventional products

5. Conclusion

The study gave the base to the formulation of the following conclusions:

1. Due to the design and technological considerations the relevant products modified with silicate foam glass granulate are those which presence of filler used in the mass does not exceed 13%.

2. The lime-sand additive granulate foam glass caused a change in its structure.

3. The bulk density of the newly formed product is less than the bulk density of the traditional product and it is approx. 1.10 g/cm3.

4. The lime-sand product of a 10% of filler consistency has a porosity of 2.34 times greater than the traditional products silicate.

5. The mercury porosimetry studies have shown that the traditional silicate products are characterized by uneven distribution of particle size. The appropriate macropores have the largest

content (over 70%) . The diameters of the pores in the conventional product are in the range 3.6· 10-9 ÷2.36· 10-4 m.

6. In the modified silicate product particle size distribution is less diversified. It also noted the presence of pores with a diameter up to 3.55· 10-4 m. The lower limit has not changed significantly.

7. In the modified products containing foam glass granulate appropriate macropore volume decreases (is a little over 50%) in favour of increasing the amount of transitional pores and over capillary ones.

8. Further studies will be conducted to improve the compressive strength of modified silicate products while reducing their density analyzed by the usage of techno-economic nanoadditives.

References

[1] WOLFKE, S., *Technologia wyrobów wapienno-piaskowych, wyd ARKDY*

[2] SKALMOWSKI, W. *Technologia materiałów budowlanych*, tom II, wyd. ARKADY.

[3] Dachowski R., Stępień A., *The impact of various additiveson the microsrtucture of silicate products*, Procedia Engineering Vol. 21, 2011, 1173-1178.

[4] NOWEK M., *The impact of recycled polymers on the features of modified sand-lime produckts*, Technical Transactions, Civil Engineering, Vol. 1-B/2014, p.47-54.

[5] JASIŃSKA I., Nowek M., *Wpływ modyfikacji wyrobów silikatowych dodatkiem w postaci LDPE na ich podstawowe właściwości użytkowe*, Konferencja Młodzi dla Techniki, Wybrane problemy naukowo-badawcze budownictwa i inżynierii środowiska, Płock 2013, p.153-158.

[6] JASICZAK J., Praca zbiorowa pod kierunkiem prof. dr. hab. inż. Bogusława Stefańczyka, *Budownictwo Ogólne, Tom I Materiały i Wyroby Budowlane*, Arkady, Warszawa 2005.

[7] RAŹNY J., *PORAVER – nowe spojrzenie na szkło*, Izolacje, 1 (2011), p. 54–56.

[8] PN-EN772-13/2001, *Metody badań elementów murowych. Część 13.*

[9] PN-EN 772-1:2011 *Metody badan elementów murowych. Część 1.*

[10] Instrukcja do ćwiczeń laboratoryjnych, *Badanie tekstury porowatej metodą porozymetrii rtęciowej*, Politechnika Wrocławska.

[11] HOBLER H., *Badania fizykochemicznych właściwości skał*, PWN, 1977.

[12] FALACIŃSKI P.: *Przepuszczalność hydrauliczna zawiesin twardniejących z dodatkiem popiołów fluidalnych*, Rozprawa doktorska, Warszawa 2006.

[13] PN-EN 771-2 *Wymagania dotyczące elementów murowych. Część 2.*

TRANSCOM 2015, 22-24 June 2015
University of Žilina, Žilina, Slovak Republic

Expansion and changes in the microstructure of air-entrained cement mortars subjected to sodium sulphate attack

*Monika Jaworska
*Kielce University of Technology, Faculty of Civil Engineering and Architecture, al. Tysiąclecia Państwa Polskiego 7, 25-314 Kielce, Poland,{monikajaworska}@o2.pl

Abstract. The paper shows the results from the tests for the expansion in the Na_2SO_4 solution, strength, water absorption of cement mortars and changes in the cement paste microstructure, illustrated in diffractograms and photographs taken with a scanning electron microscope. The air-entrained cement mortars containing 11.5% tricalcium aluminate (C_3A) expanded faster and experienced the breakdown earlier than the non-air-entrained mortars made of the same cement. In the corrosion resistance test conducted on Portland cement containing 5.2% C_3A, the air-entrained samples failed faster than the non-air-entrained samples, regardless of the C_3A phase content of Portland cement. In all the mortars, gypsum and ettringite were the reaction products. The highest amount of ettringite occurred in the air voids.

Keywords: Air-entrained mortars, non-air-entrained mortars, expansion, sulphate attack, ettringit.

1. Introduction

In the view of many researchers, the sulphate attack due to environmental conditions carries the highest risk for the durability of the concrete structure. Sulphate attack is potentially one of the most damaging degradation mechanisms combining expansion with dissolution. The processes of dissolution of the cement paste components cause the loss of bond/cohesion in its microstructure, leading to accelerated deterioration. Expansion results in cracking and damage to concrete due to the formation of low solubility compounds, which by precipitating from the liquid phase cause crystallization pressure [1, 2]. Because of air-entrainment, spherical air voids are formed in the cement paste. These air voids, which will never be filled with cement hydration products, with dimensions typically from 10 to 300 μm and derived from the deliberate air-entrainment, counteract two concrete deterioration mechanisms during freezing – create space for increased volume of freezing water and prevent disruptive osmotic pressure. Osmotic pressure results from the locally occurring increase in the solution concentration due to ice formation in the pores [3].

2. Experimental

2.1. Purpose and scope of the study

The study aimed to determine the influence of air-entrainment on the sulphate resistance of mortars. The testing program involved evaluating the strength, water absorption and linear strain of the samples subjected to the effect of 5% sodium sulphate. Other tests included SEM microstructure analysis and phase mapping by X-ray diffraction.

2.2. Methods

The linear strain of the hardened cement mortar samples was determined with a Graf-Kaufman apparatus. The tests were carried out on 20×20×160 mm and 25x25x250 mm bars stored in a 5% solution of Na_2SO_4. The samples were immersed in the solution after 28 days in the supersaturated solution of calcium hydroxide. The measurements were performed every four weeks. The test procedure complies with PN-B-19707 [4]. In addition, compressive strength of mortar samples

40x40x160 mm was studied at 28 days of curing in water and 168 days of storing in the sodium sulphate solution. Water absorption of the mortars was determined on three samples, which, after 28 days of curing in water, were dried at 105˚C for three days. The SEM microstructure analysis and phase mapping by X-ray diffraction were conducted. The air content in fresh mortars was studied by the pressure method in the 1 dm^3 (1000 mm^3) capacity apparatus.

2.3. Materials

The samples were made from Portland cement CEM I 42,5 R with various chemical and phase compositions. The chemical and phase compositions are summarized in Tables 1 and 2. The w/c ratio was 0.6 and it was constant. The proportions of cement, send and water were 1:3:0.6, respectively. Half of the samples were air-entrained with a 2.5 g of air entraining admixture. The percentage content of air in the fresh mortars was 10 % ±1%.

Cement	SiO_2	Al_2O_3	Fe_2O_3	CaO	$CaO_{(free)}$	MgO	SO_3	Cl^-	Na_2O_{eq}
A CEM I	19,5	6,0	3,1	62,1	1,75	1,7	2,6	0,03	0,8
B CEM I	21,31	5,01	3,36	65,06	1,53	1,95	0,74	0,03	0,79

Tab. 1. Chemical composition of Portland clinker of the cements [%].

Cement	C_3S	C_2S	C_3A	C_4AF
A CEM I	54,0	17,0	11,5	10,1
B CEM I	71,0	9,19	5,12	11,45

Tab. 2. The phase composition of Portland clinker of the cements [%].

3. Test results and discussion.

Figure 1 shows the results of the water absorption by weight measurements. The graph illustrates the mean values of four samples with a scatter. The absorption results indicate the difference between the absorption of air-entrained and non-air-entrained mortars. The results range from 9.9% for non-air-entrained mortar A CEM I to 11.3 % for air-entrained mortar B CEM I.

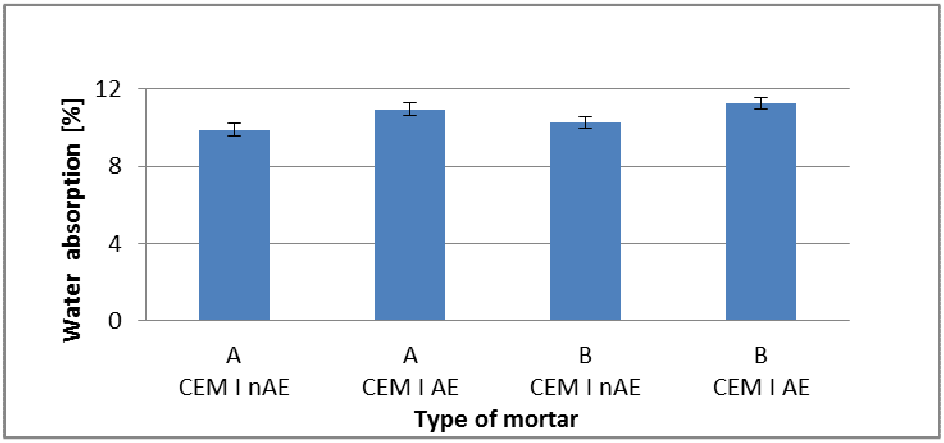

Fig. 1. Water absorption of non-air-entrained and air-entrained mortars.

The results from the tests indicate that the highest water absorption by weight equals to 11.3% and it was recorded for the air-entrained mortar made from cement B CEM I. Analysis of the results shows that water absorption is higher in the air-entrained mortars. The test results indicate that air entraining reduced the strength of mortars by 16 % to 22%. The strength results for the mortars at 28 and 168 days are summarized in Fig. 2.

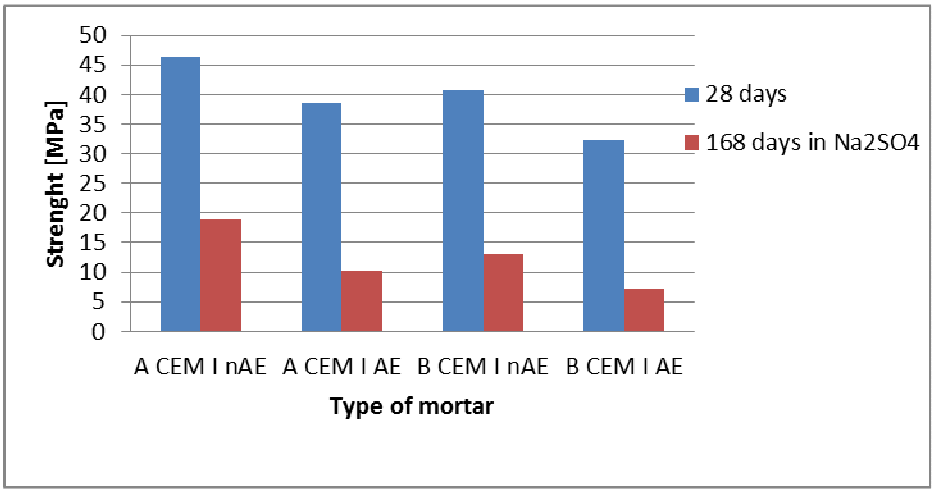

Fig. 2. The strength of non-air-entrained and air-entrained mortars.

Figure 3 shows expansion of 20x20x160 mm samples immersed in the solution of sodium sulphate. All the samples of the air-entrained mortar from A CEM I (11.5% C_3A in the clinker) were destroyed as early as after 56 days, at expansion of 6.9‰. The non-air-entrained samples collapsed after 84 days, when the strain reached more than 7 ‰.

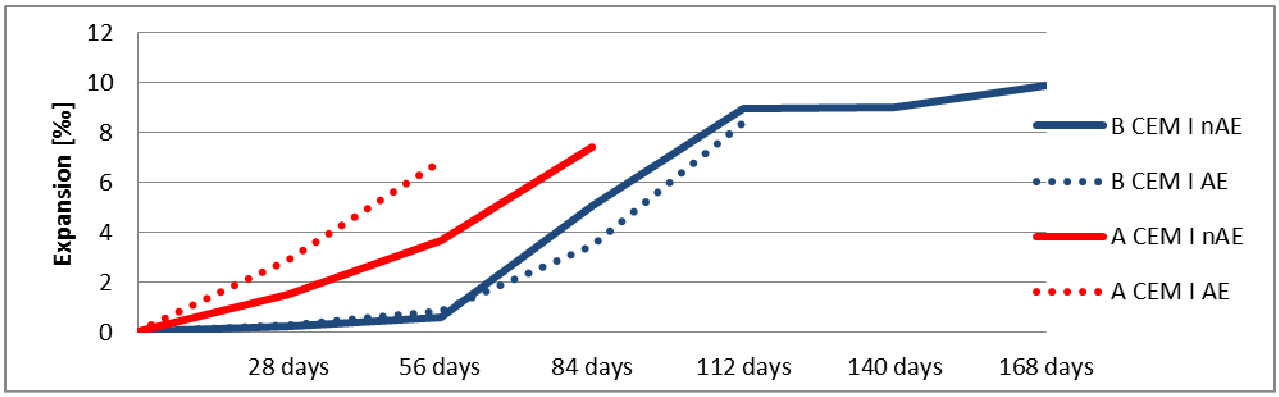

Fig. 3. The expansion of the samples immersed in the solution of 5% Na_2SO_4

For the air-entrained mortars, based on cement B CEM I (with 5,3% C_3A in the clinker), the strain of 8.4‰ was recorded after 112 days. The samples made from non-air-entrained mortar were damaged after 168 days, with an expansion of 9.9 ‰.

The samples from the cement with a higher content of C_3A showed the least resistance to the action of sodium sulphate. Analysis of the results indicates that, regardless of the amount of C_3A, the samples with air-entrained admixture were destroyed first.

In order to confirm the findings, expansion tests were conducted on 25x25x250 mm samples (Fig. 4). Because of the size of the samples, the destruction time was extended, but as in the case of the smaller, the air-entrained mortars were destroyed faster than the non-air-entrained mortars.

The samples (Figs. 3. and 4.) of mortars made from A CEM I with a higher content of C_3A showed expansion and total damage far earlier than the mortars from B CEM I with the lower C_3A content. The results confirm that sulphate resistance of air-entrained mortars is related to the C_3A content in the clinker cement.

The XRD analysis (Figs. 5. and 6.) indicates that ettringite and gypsum are the basic products of the reaction with sodium sulphate. The presence of quartz and portlandite was also recorded.

The SEM studies confirmed the results from the X-ray diffraction analysis and indicated that ettringite and gypsum were the main reaction products (Fig. 7.). It is clear that ettringite was the predominant product of sulphate attack, with its characteristic morphology. The non-air-entrained

mortar contained ettringite crystals loosely arranged in the capillary pores, as well as embedded in the C-S-H phase.

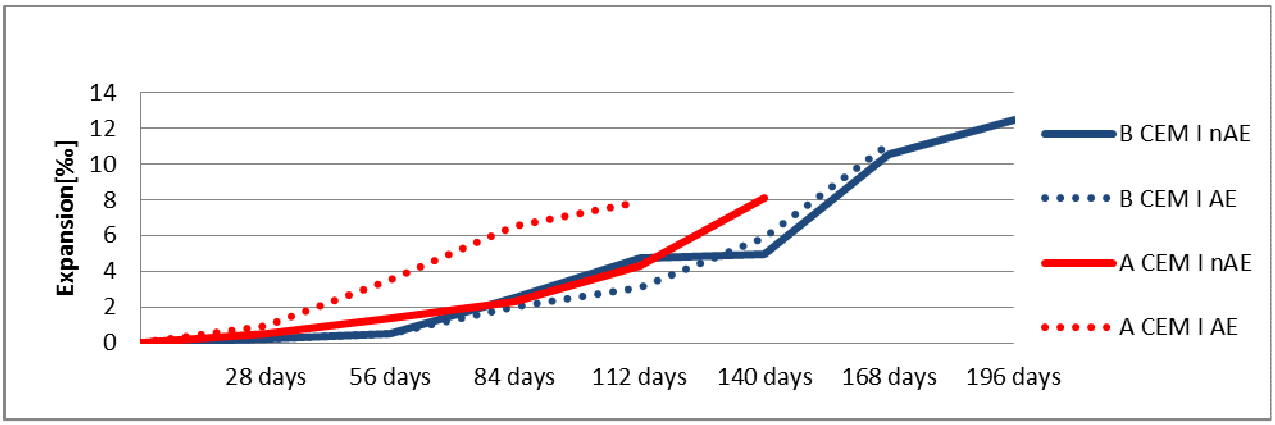

Fig. 4. The expansion of the samples immersed in the solution of 5% Na_2SO_4

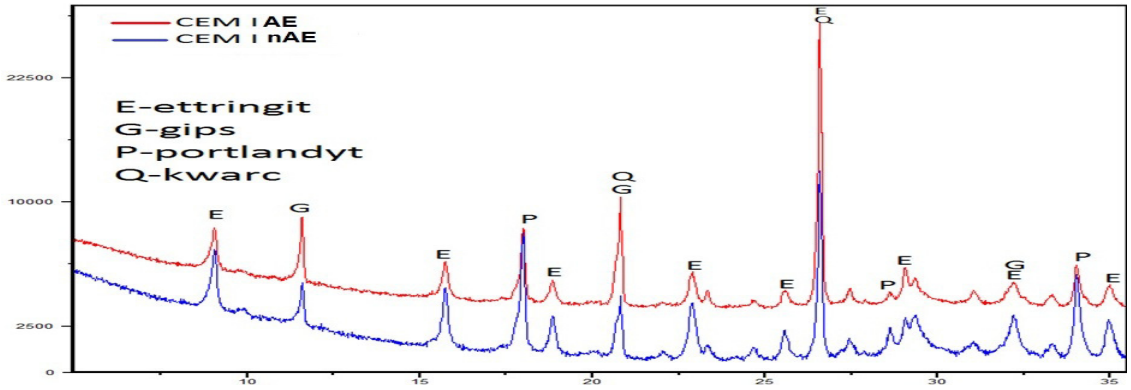

Fig. 5. XRD analysis of cement mortars A CEM I immersed in the solution of 5% Na_2SO_4 for 168 days.

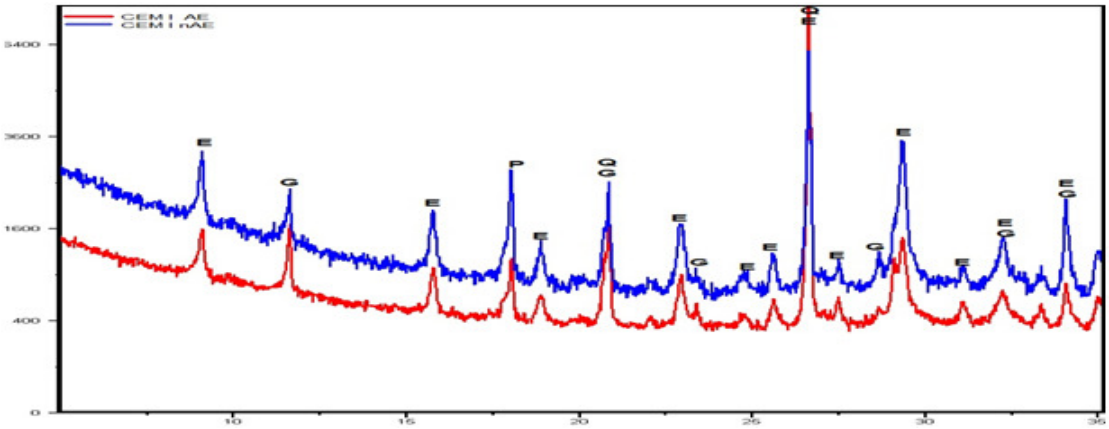

Fig. 6. XRD analysis of cement mortars B CEM I immersed in the solution of 5% Na_2SO_4 for 168 days.

4. Conclusion

As the results demonstrate:

- The air-entrained mortars from both cement types experienced expansion and breakdown faster than the non-air-entrained mortars. A higher amount of ettringite occurred in the air-entrained mortars, detected in air voids and in the microstructure of the paste away from the pores. It is

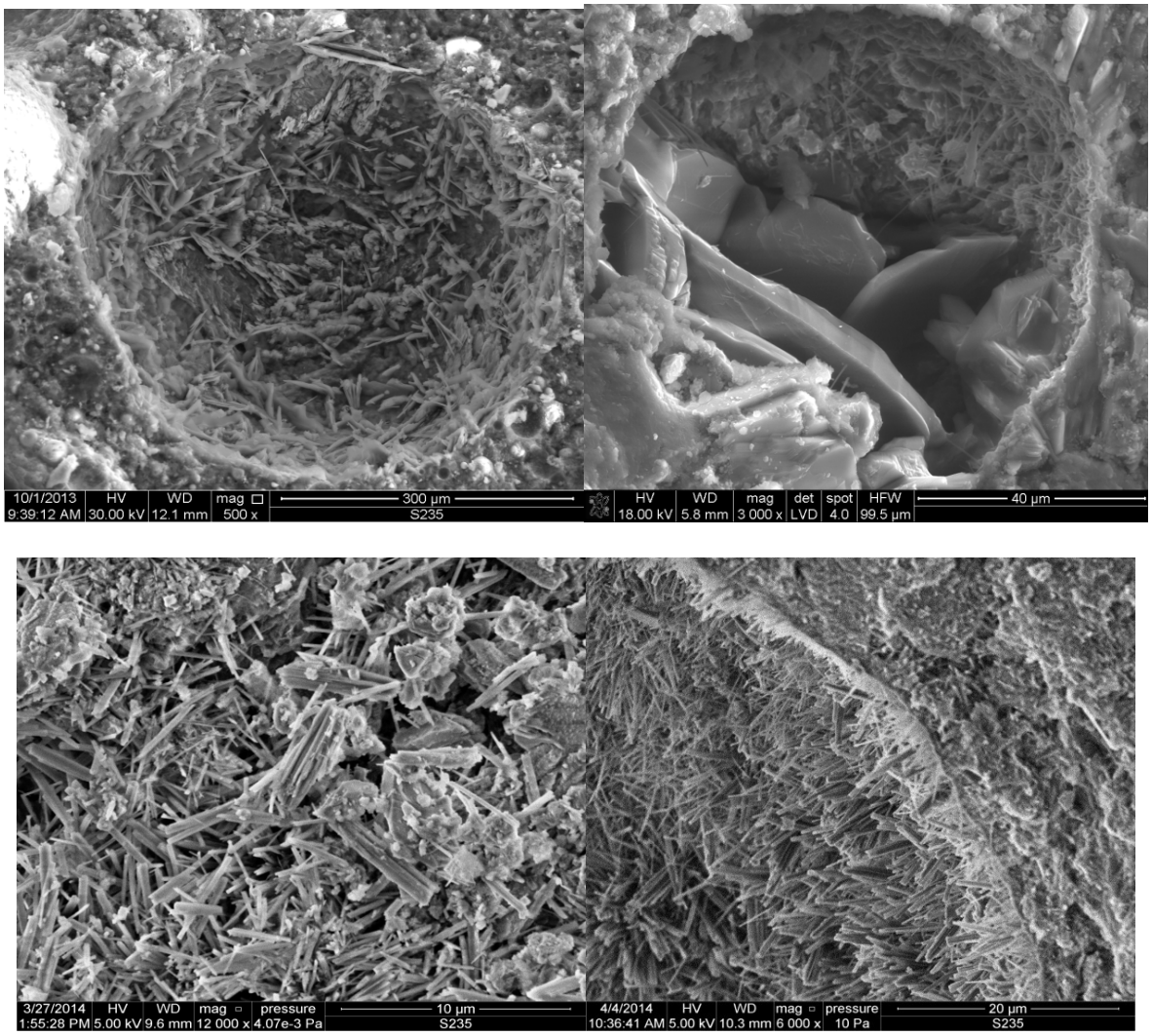

Fig. 7. Microstructure of mortars immersed in a solution of 5% Na2SO4 - mortar of air-entrained and non-air-entrained Portland cement.

- suggested that the ettringite crystals might migrate from the compact microstructure into the pores.
- Air-entrainment had a significant effect on the Portland cement mortars resistance to sulphates.
- The main cause of the damage to the cement composites was related with the ettringite and gypsum formation.

The mortars made from the cement with a higher content of C_3A phase had considerably lower resistance to sulphates.

References:

[1] KUROWSKI, W. *Chemia cementu i betonu*, Polski Cement, Kraków 2010.
[2] PIASTA, W. *Korozja siarczanowa betonu pod obciążeniem długotrwałym*, Politechnika Świętokrzyska, Kielce 2000.
[3] NEVILLE, A. M. *Właściwości betonu*, Polski Cement, Kraków 2012.
[4] PN-B-19707 Cement - Cement specjalny - Skład, wymagania i kryteria zgodności.

TRANSCOM 2015, 22-24 June 2015
University of Žilina, Žilina, Slovak Republic

The influence of type and quality of thermal insulation of external walls on energy performance of wooden buildings

[*]Jakub Jura, [*]Małgorzata Ulewicz, [**]Pavol Ďurica
[*]Czestochowa University of Technology, Faculty of Civil Engineering, Akademicka 3, 42-200 Częstochowa, Poland, {Jakub.Jura,}jura@bud.pcz.czest.pl
[**]University of Žilina, Faculty of Civil Engineering, Univerzitna 8215/1, SK-010 26 Žilina, Slovak Republic

Abstract. The article characterizes buildings with log walls and buildings with timber framing. It analyzes the possibility and a method of application of thermal insulation with regard to the type of an external wall structure. The possibilities of improving energy performance of external walls with regard to the type and quality of the used insulating materials are characterized. The analyses allow to define the influence of a chosen thermal insulation variant on the thermal performance of a building and allow to choose an optimal type of thermal insulation.

Keywords: timber buildings, frame buildings, thermal insulation.

1. Introduction

Currently, due to the necessity to save energy and protect the environment, buildings with high energy performance are popular. New buildings have to meet restrictive requirements concerning energy consumption. Moreover, there are constantly more energy-saving passive buildings created using different technologies. It becomes popular in the countries of Central Europe to build timber buildings, which were earlier considered as maladjusted for inclement climate. Thanks to modern materials and thermal insulation technologies, it is possible to construct timber buildings of very high energy performance. Another advantage is their high thermal efficiency and the fact that timber used for construction is a renewable material. Additionally, one can use recycled materials, e.g. cellulose, which can also have the coefficient λ within 0.039 – 0.042 W/(m·K) and whose another advantage is wall sound-proofing function. It is also possible to use other materials, including fully natural coir mats [1, 2]. Wood can be used in several structure types of timber building external walls. It can be walls made of logs and walls of various timber framing designs.

2. Thermal insulation of timber buildings

2.1. Log houses

Log houses of a conventional technology are constructed by putting one log on another or by settling logs with use of notch joints. High requirements placed on external envelopes, mainly concerning the rates of heat transfer, to some extent make it impossible to construct such buildings. It is so because, in order to meet the required coefficient U < 0.25 W/(m2·K) for the walls, the log should be 50 cm thick, and in order to meet the requirements of the year 2021 (U < 0.2 W/(m2·K)), even 62 cm thick. Due to so large thickness of timber, constructing such buildings would be very expensive [3, 4].

In order to maintain representative look of such buildings, it is possible to use thermal insulation allowing to reduce the log thickness. Log structure can be complemented with insulating layer placed between light wooden frame (Fig. 1), which makes it possible to use 20 cm thick logs for construction. For insulation, one can use materials such as polystyrene foam or mineral wool,

whose coefficient λ is 0.040 – 0.030 W/(m·K), or polyurethane foam, whose λ is even 0.020 [W/(m·K)], which also allows to fill up every slit between components. Additionally, on the internal side, one can use wooden finishing fully masking the structure of such a solution. Such a structure of walls allows to construct envelopes of high energy standard and consequently makes it easy to build an energy-saving or even passive object [5,6].

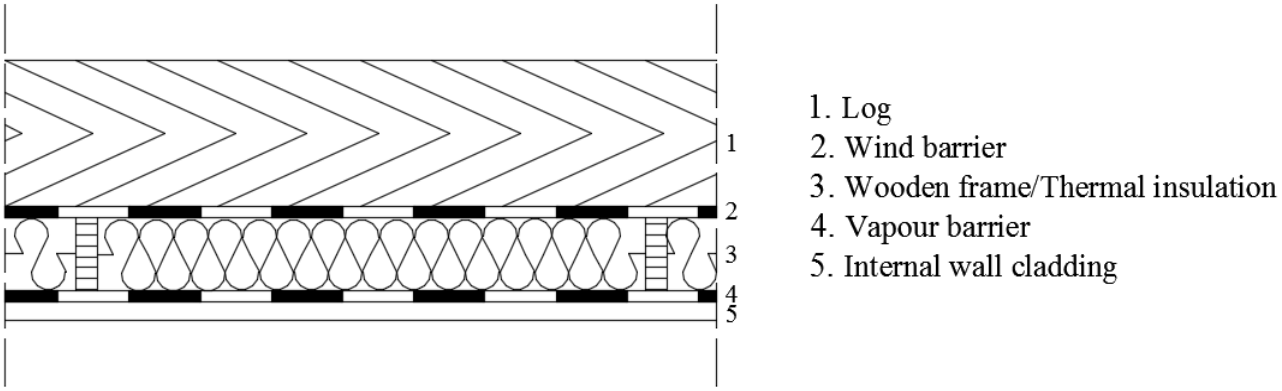

Fig. 1. Insulating technology for walls of log houses.

Materials used in the envelope	**External envelope thickness required to achieve the coefficient U, cm**	
	U < 0.25 W/(m^2·K)	**U < 0.20 W/(m^2·K)**
Solid wood logs λ = 0.13 W/(m·K)	50	62
Logs 20cm + coir λ = 0.045 W/(m·K)	10	14
Logs 20cm + cellulose λ = 0.040 W/(m·K)	9	12
Logs 20cm + thermal insulation λ = 0.030 W/(m·K)	8	10
Logs 20cm + polyurethane foam λ = 0.020 W/(m·K)	5	6

Tab. 1. The use of various types of thermal insulation in order to improve the performance of a log wall.

The table 1. presents calculated (with use of program ArCADia Termo) thickness of materials in external walls allowing to achieve required thermal conductivity coefficient. As visible in the analysis, the type and quality of the used insulation elements have a great influence on the achieved thermal performance of the wall. In order to achieve an envelope meeting current requirements, depending on the type of material and its coefficient λ, it is necessary to make a thermal insulation 5 – 10 cm thick. However, in order to achieve the coefficient U that would be in compliance with the requirements for the year 2021, the thickness of the thermal insulation in an envelope constructed in such a way should be from 6 to 14 cm [7].

2.2. Frame houses

It is constantly more common in Poland to build timber framing houses. Wooden posts make a frame filled up with thermal insulation (Fig. 2). Additionally, the frame is stiffened with use of, e.g. OSB boards and supplemented with necessary insulation. On the inside, such a structure can be finished with plasterboard or decorative materials, on the outside - with use of any material, e.g. polystyrene foam, wool, cellulose, coir mats or polyurethane foam [8].

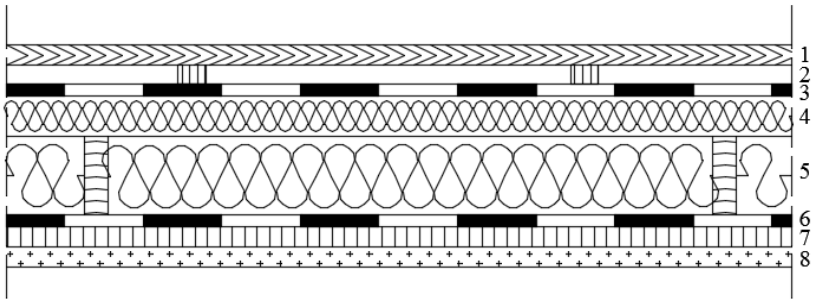

Fig. 2. Technology of walls of timber frame house.

Materials used in the envelope	External envelope thickness required to achieve the coefficient U, cm	
	U < 0.25 W/(m^2·K)	**U < 0.20 W/(m^2·K)**
Frame structure + coir λ = 0.045 W/(m·K)	16	20
Frame stucture + cellulose λ = 0.040 W/(m·K)	15	18
Frame structure + thermal insulation λ = 0.030 W/(m·K)	11	14
Frame structure + polyurethane foam λ = 0.020 W/(m·K)	7	9

Tab. 2. The use of different types of thermal insulation in order to improve the parameters of frame building walls.

The calculations carried out by the computer program show that the thickness of the thermal insulation materials of different λ values, in order to achieve envelopes having the required thermal conductivity coefficient, is 7 – 16 cm. However, for the buildings newly constructed from 2021, the thermal insulation should be thickened up to 9 – 20 cm. Because of the fact that in the presented types of buildings it is possible to use most of the types of thermal insulation materials, one should pay attention mainly to their thermal conductivity coefficient λ. Additionally, it is worth to carry out a short analysis of the material quality and its price - the possibility to achieve intended effect with regard to the incurred cost and time in which the investment would pay off. The use of technologically advanced materials of an adequate thickness will allow to achieve envelopes of required thermal conductivity coefficients.

3. Conclusion

Computer program calculations allowed to analyze the influence of the used thermal insulation material and its performance on the possibility to improve the quality of the external envelopes of timber buildings. A frame building can be considered optimal because of the short time of its construction, possibility to use any type of thermal insulation and little demand for wood in comparison with, e.g. log building. Polyurethane foam can be considered the best insulating material due to its lowest coefficient λ of 0.020 W/(m·K), easy application and ability to fill up all the spaces between materials. Of the materials proposed for the calculations, the coir mats seem to be the worst because of high coefficient λ, however, they are fully natural.

References

[1] ASSOCIATION OF WOODEN HOUSES - www.domydrewniane.org

[2] AUDENAERT A., DE CLEYN S.H., VANKERCKHOVE B., *Economic analysis of passive houses and low-energy houses compared with standard houses*, Energy Policy, 36, 2008, 47–55.

[3] *Dz. U. 2013 poz. 926 – Rozporządzenie Ministra Transportu, Budownictwa i Gospodarki Morskiej z dnia 5 lipca 2013 r. zmieniające rozporządzenie w sprawie warunków technicznych, jakim powinny odpowiadać budynki i ich usytuowanie*.

[4] MAJOR I., RÓŻYCKA J., *Współczesne domy drewniane – budynki o zoptymalizowanym potencjale energetycznym,* Budownictwo o zoptymalizowanym potencjale energetycznym, 1, 2014, 63-70.

[5] JURA J., *Wpływ budynków zeroenergetycznych i plusenergetycznych na emisyjność,* Budownictwo o zoptymalizowanym potencjale energetycznym, 1, 2014, 33-40.

[6] LIS A., *Dostosowanie izolacyjności termicznej przegród do nowych warunków technicznych,* Budownictwo o zoptymalizowanym potencjale energetycznym, 1, 2014, 55-62.

[7] ŠTÚŇOVÁ M., ĎURICA P., *The course of temperatures in construction of lightweight external wall in stationary conditions of the internal environment and the actual conditions of outdoor climate,* Conference XXII Russian – Slovak – Polish, Seminar, Žilina 2013.

[8] POLISH PASSIVE HOUSE AND RENEWABLE ENERGY INSTITUTE – www.pibp.pl

TRANSCOM 2015, 22-24 June 2015
University of Žilina, Žilina, Slovak Republic

The regulation of groundwater heat pumps systems with vertical ground heat exchangers during their lifetime

*Anna Jurek, *Paweł Purgał
[*] Kielce University of Technology, Faculty of Environmental Engineering , Geomatics and Power Engineering, Department of Structure Physics and Renewable Energy, {anna.jurek85}@o2.pl
[**] Kielce University of Technology, Faculty of Environmental Engineering , Geomatics and Power Engineering, Department of Structure Physics and Renewable Energy, {ppurgal}@tu.kielce.pll

Abstract. The article presents a proposal of regulation the performance of ground heat exchangers during their lifetime. There are presented the results of the theoretical analysis of the impact of applied regulations to the work of the ground heat pump based on a computational model describing nonstationary processes of heat transfer in vertical ground heat exchangers. In the result it was designated the temperature field which was formed in the ground surrounding the probes in case of the application of regulation and its absence, as well as its effect on the amount of heat taken from the ground and the efficiency of the ground heat pump itself.

Keywords: vertical ground heat exchangers, groundwater heat pump, efficiency, regulation, heat transfer processes.

1. Introduction

Currently, there are more and more information about the incorrect operation of the heat pump installation. According to the general belief the most important part of system is the heat pump and all attention is focused on it . However, in practice, it appears that the most important element of the installation, having essential for its proper operation, is the ground heat exchanger. And it is the most common cause expensive or unreliable operating systems with ground heat pump.

There are many reasons too small capacity vertical ground heat exchangers. At the design stage it may be bad assigned length of the heat exchanger or the mutual distance between them or thermal efficiency of land, for example unsupported by geological analysis of the soil medium. There are also errors at the stage of execution, such as a leak or malfunction filling of the boreholes.

An important factor affecting the heat transfer conditions in the surroundings of probes is the mutual distance between them. Over the years, the recommendations on this issue have changed.

Source	The minimum distance between the vertical ground heat exchanger a_p
PORTPC (2013) [1]	• a_p =6m (the depth of the vertical ground heat exchanger: hw<70m), • a_p =8 m (the depth of the vertical ground heat exchanger: 70 m≤hw<100 m) • a_p >0,08 h_w (the depth of the vertical ground heat exchanger :>100 m)
Marian Rubik (2011) [2]	• a_p =5m, when the depth of the probes is 40-50 m • a_p =6m, when the depth of the probes is 50-100 m
Wojciech Zalewski (2001) [3]	a_p =5m

Tab. 1 The minimum distance between the geothermal probes [1], [2], [3]

2. The proposal for capacity regulation of vertical ground heat exchangers during their lifetime

The problems during the operation of the installation of geothermal probes prompt to looking for their solutions. The performance of geothermal probes can be adjusted during their lifetime by disconnecting or connecting individual loop of the ground collectors in the distributor of the saline depending on the demand for heat in the building during the year. Assuming that the heat demand of the building changes during the year, it can believe that the needed the length of geothermal probes also will be changing.

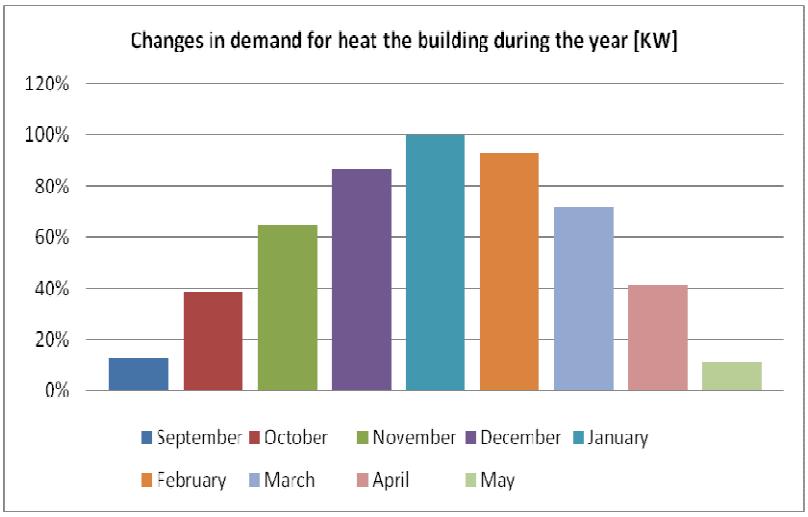

Fig. 1. Percentage of the heat demand of the building during the year (chart developed for Polish conditions based on WP-OPT program Calculation and optimization of the heating system heat pump)

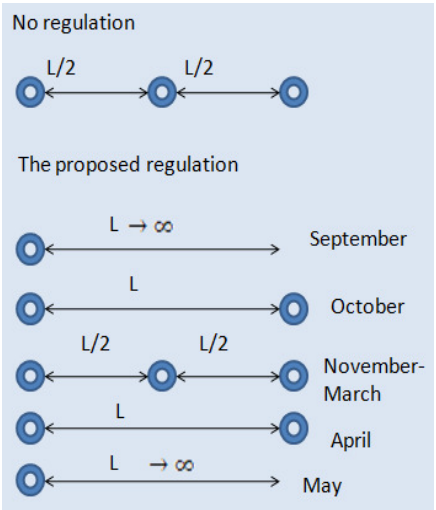

Fig. 2. The proposed capacity control of group of geothermal probes connected by a common collector

In the absence of regulation for the whole season there are three probes. While in case of application of regulation in September operates only one probe, the others are cut off on the valves in the distributor.
In October, it works two boundary probes. Between November and March are active all three probes. In April the central collector is cutted off and in May heat from a ground takes only on probe.

3. Mathematical model

The purpose verify the correctness of the observations, there was prepared mathematical model describing the heat transfer processes occurring in the vertical ground heat exchanger. The heat flow in vertical ground heat exchanger is represented by a cylindrical model which was established in order to simplify one-dimensional heat flow (only in the direction r). Between the ground heat exchanger wall, filling borehole and the surrounding soil is the conduction of heat, while the possible movement of deep water or groundwater is omitted.

Case under consideration was limited to what is happening on the surface of the wall borehole assuming the boundary condition of the third kind, it means convective heat transfer between the wall of the probe and the fluid that fills it.

It was assumed transient, one-dimensional heat conduction through the layer of soil, solid density values, specific heat and thermal conductivity of the soil and the material from which is made the wall of probe and the symmetry of the whole system with respect to the axis located in the core of the liquid that filling heat exchanger.

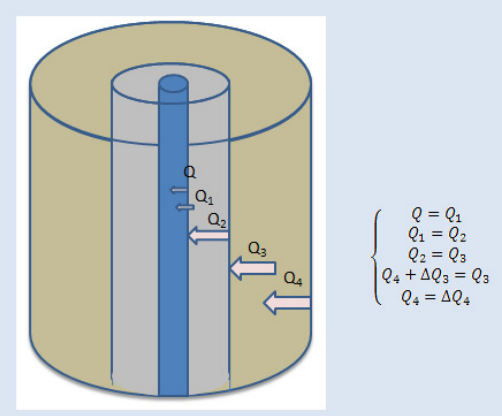

Fig. 3. The physical model of heat exchange processes in a vertical ground heat echanger, where: Q – Convection [W], Q_1 – Conduction in the pipe wall [W], Q_2 – Conduction in the grouth [W], Q_3 – Conduction in the ground [W].

$$\begin{cases} \alpha_g \cdot \left(T_1 - T_f\right) = \lambda_r \cdot \left.\dfrac{\partial T(r)}{\partial r}\right|_{r=r_1} \\ q_1\big|_{r=\frac{d_w}{2}} = q_2\big|_{r=\frac{d_z}{2}} \\ T_1\big|_{r=\frac{d_w}{2}} = T_2\big|_{r=\frac{d_z}{2}} \\ \lambda_r \cdot \left.\dfrac{\partial T(r)}{\partial r}\right|_{r=\frac{d_z}{2}} = \lambda_{wyp} \cdot \left.\dfrac{\partial T(r)}{\partial r}\right|_{r=\frac{d_{wyp}}{2}} \\ q_2\big|_{r=\frac{d_z}{2}} = q_3\big|_{r=\frac{d_{wyp}}{2}} \\ T_2\big|_{r=\frac{d_z}{2}} = T_3\big|_{r=\frac{d_{wyp}}{2}} \\ cp_{gr} \cdot \rho_{gr} \cdot \dfrac{\partial T_2(r)}{\partial \tau} = \lambda_{gr} \cdot \left.\left(\dfrac{\partial^2 T_2(r)}{\partial r^2} + \dfrac{1}{r} \cdot \dfrac{\partial T_2(r)}{\partial r}\right)\right|_{r_2 > r > r_k} \\ q_k\big|_{r=r_k} = 0 \end{cases} \quad (1)$$

Where:
T_f –temperature of the transfer medium, [°C]
r – radius [m]
α - heat transfer coefficient for the glycol, [W/(m^{2}K)]
λ – thermal conductivity, [W/(mK)]
c_p- heat capacity, [J/(kgK)]
ρ – density , [kg/m3]
q- heat flux density, [W/m2]
d-diameter [m]

- the indexes :
  - w- internal
  - z- external
  - wyp- grout
  - r- pipe
  - gr- ground

Solution of equations of heat transfer model [1] was obtained using the method of elementary balances.

4. The example of calculation

It was assumed, for example, that the heat demand for the building is 8kW. With commonly used methods of dimensioning of ground heat exchangers, the length of probes was determined. It amounted to 246 m, and therefore it was planned three probes a depth of 82 m each spaced 5m. In the course of theoretical calculations were analyzed how proposed regulation affects on the temperature distribution in the ground surroundings the probes.

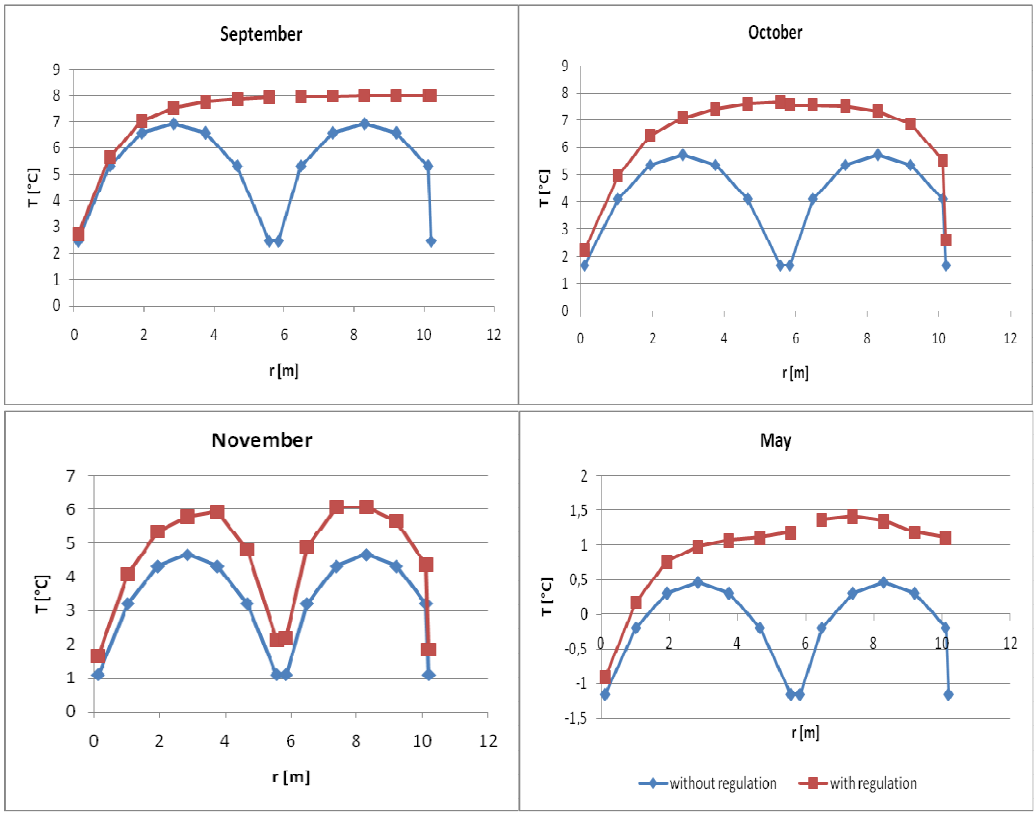

Fig. 3. The impact of the proposed regulation on the temperature distribution in the ground near the vertical ground heat exchangers

It was determined how much heat can be obtained from the ground in each of these cases.

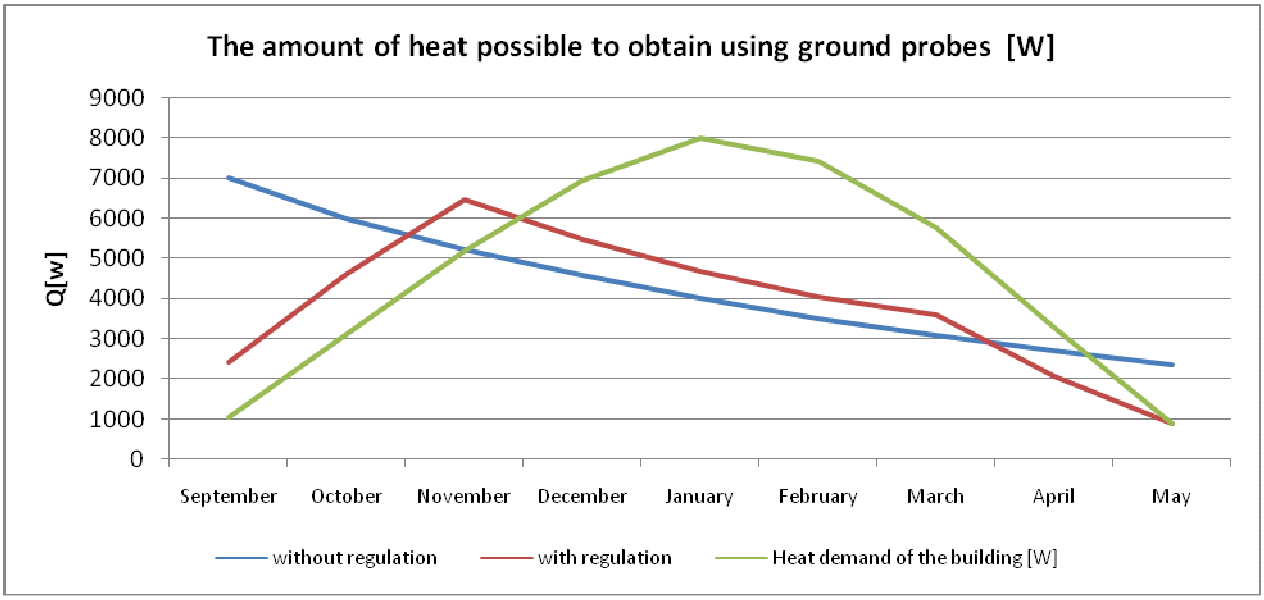

Fig. 4. The impact of the proposed regulations on the amount of heat possible to obtain from the ground.

And also how the proposed solution will affect on the efficiency of the heat pump itself.

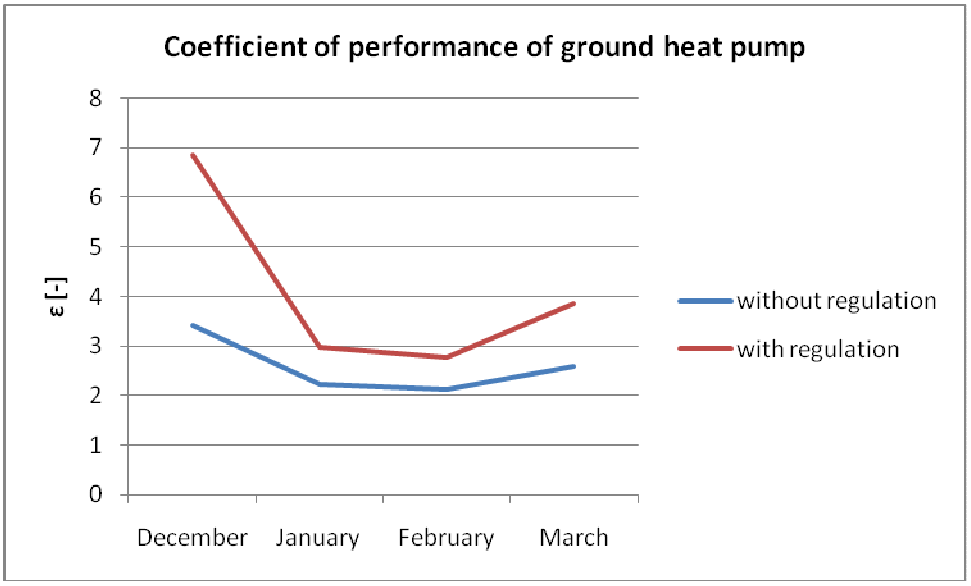

Fig. 5. The impact of proposed regulations on the coefficient of performance of ground heat pump.

5. Conclusion

The proposed method of regulating performance of vertical ground heat exchangers during their lifetime reduces temperature drop soil surrounding the probes which in turn results in an increase in the amount of heat absorbed from the soil as well as the reduction of the phenomenon of frozen soil in the vicinity of the probe. In addition, an increase in the coefficient of performance of ground heat pump means a decrease electrical power required to drive the compressor which results in reduction in operating costs of the device.

References

[1] POLSKA ORGANIZACJA ROZWOJU TECHNOLOGII POMP CIEPŁA. *Wytyczne* projektowania, wykonania i odbioru instalacji z pompami ciepła. Część 1: Dolne źródła ciepła. PORT PC, Kraków 2013.

[2] RUBIK M.: *Pompy* ciepła w systemach geotermii niskotemperaturowej, Monografia, MULTICO Oficyna Wydawnicza, 2011

[3] W. ZALEWSKI. *Pompy* ciepła sprężarkowe, sorpcyjne i termoelektryczne, IPPU MASTA Gdańsk, 2001

[4] PIOTROWSKI J. Zb., JUREK A.: *The Analysis* of the temperature of the field around a single vertical ground heat exchanger. TRANSCOM 2013, University of Žilina.

TRANSCOM 2015, 22-24 June 2015
University of Žilina, Žilina, Slovak Republic

Stiffness effect influence on arching in piled embankment

[*]Ladislav Kais, [*]Roman Bulko, [*]Marián Drusa
[*]University of Žilina, Faculty of Civil Engineering, Department of Geotechnics, Univerzitná 8215/1, 010 26 Žilina, Slovakia, {ladislav.kais, roman.bulko, marian drusa}@fstav.uniza.sk

Abstract. Nowadays design of piled embankment is realized according to BS 8006 or German recommendation EBGEO, but we do not have EU Standard or national code. Therefore, investigation in this field is demanded and thanks to CUR 226 analytical solutions are complete. Development of this methods can be supported by 2D or 3D numerical modelling.

Keywords: Piled embankment, physical model, arching, soft subsoil, reinforcement, geogrids

1. Introduction

Construction of civil structures often reaches to the places with soft or highly compressible subsoil. This type of subsoil is characterized by unpredictable consolidation settlement in time and influences the selection of type of structure foundations. Designers are constantly facing the challenges for finding new solutions of practical applications.

One of advanced foundation methods is piled embankment supported by group of piles with or without partial subsoil support. The first use of piled embankment consisting of piles with great heads and without reinforced geosynthetics was constructed in early 60's in Finland. Shortly after, the success in Finland was followed by A876 road construction in Great Britain in 1973 [1, 2] reinforced in basal layer. The reinforcement was done by high tensile strength polyester geogrids.

Application of piled embankment structure guarantees low settlement, possibly shortens time of construction, and allows the work during wintertime. The scheme of the aforementioned structures is shown on Fig. 1.

The embankment foundation with piles and basal reinforcement is not the only type of construction solutions. Others common methods include: dynamic consolidations, consolidation preloading of subsoil before construction, basal reinforcement, [3], consolidation drains, parallel or longitudinally oriented, stone columns, deep soil mixing, jet grouting, massive replacement of very soft or organic soils, using of lightweight materials of embankment structures (EPS) [4].

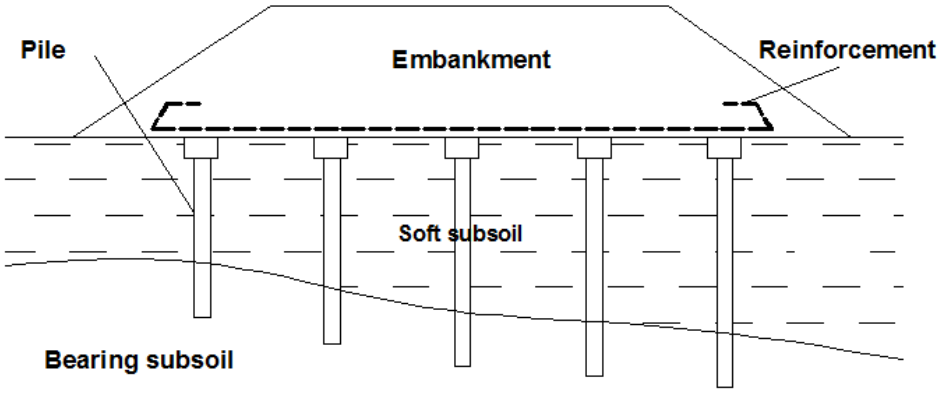

Fig. 1. Piled embankment structure.

2. Distribution of load

The mechanism of distribution of load in the embankment is different depending on the part being investigated. It needs to be distinguished between the distribution of the load at embankment slopes part and distribution inside the embankment.

Load distribution inside the embankment is based solely on the arch effect contrary to the slope of the embankment there is slumping due to crowding of the side slope. In this article, however, we will deal exclusively load distribution inside the embankment.

For explanation. Arched effect or in English literature "arching" defined the McNulty in 1965 [5] as the "ability of a material to transfer load from one place to another in response to a relative decrease between these points. Shear stresses while the system is the mechanism by which this load is transmitted"

For better examination antagonistic force in this type of construction it is necessary to divide the total load into three parts, as shown in Fig. 2:

- **Part of the A load** – is the load (from the traffic and embankment itself) above the arch which is transported directly to the piles or through the arch effect.
- **Part of the B load** – is the remaining load under the arch, which is not transported to the piles directly through the arch effect and which creating vertical load on the geosynthetic reinforcement. Piles then carried out not just the part of the A load, but also the part of the B load into the deeper bearable layer.
- **Part of the C load** – is the remaining load carried by the subsoil, acting opposite to the reaction of the subsoil. This part of the load C is taken into account in the EBGEO.

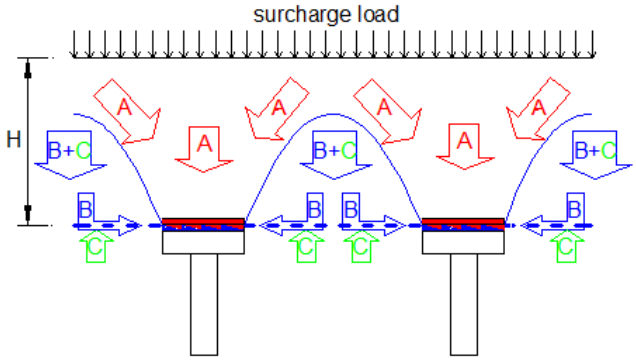

Fig. 1. Model of arching for full arch creation.

3. Calculation steps

Most of analytical design models used for the design of piled embankment with basal reinforcement layer divide calculation into two steps, Fig. 3:

- **The first step** is to investigate the influence of arch effect in the embankment (arching behavior in the fill). This step is called as a step of forming arches, which divides the total vertical load in two parts - part A and remaining load of part B+C.
- **The second calculation step** describes the deformation of the geosynthetic reinforcement. In this step remaining load B+C acting to the reinforcement strip between adjacent piles and determines its deformation and consequently a tensile stress.

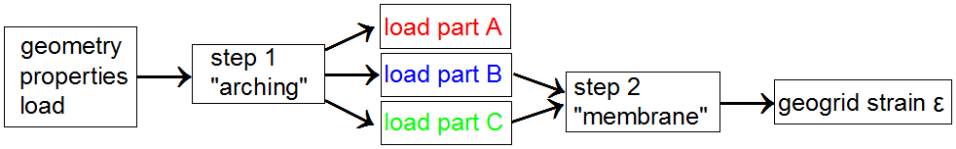

Fig. 3. Principle of calculation of piled embankment.

4. Proposal of geosynthetic reinforcement

There are several guidelines available to design the geosynthetic reinforcement in a piled embankment. The oldest standard is The British Standard BS8006, which was first time published in 1995. The last version was published in 2010. In the same year was published next important guideline – German recommendations EBGEO.

It is necessary noticed that both of them has different methods, how to calculate tensile force in the geosynthetic. For optimal use of geosynthetic reinforcement is necessary to determine vertical load acting on reinforcement (first step) and determine tensile force indicated in reinforcement between adjacent piles (second step). Arching mechanisms allows to determine part of load acting directly on the pile caps and the part of load acting on geosynthetic reinforcement between piles. Tensile force in geogrids depends on two parameters – maximal strain and stiffness of geogrid. Stiffness of geogrid can be determined from design charts, which describe relationships between tensile force and strain in geogrid. Design charts can be obtained from tensile test in laboratory or can be provided by the manufacturer as a certified design graphs.

The strip without subsoil support could be expressed as a cable equation Fig. 4, in the case of subsoil support is differential equation complicated:

$$\frac{\mathrm{d}^2 w}{dx^2} = -\frac{q(x)}{H_T} + \frac{k_s \cdot w(x)}{H_T} \qquad (1)$$

Where:

w - vertical deflection of the cable, [m]
x - horizontal distance, [m]
H_T - constant horizontal component of the tensile force in the cable, [kN.m^{-1}]
$q(x)$ - loading on the cable, [kN.m^{-2}]
k_s - modulus of subgrade reaction, [kN.m^{-3}]

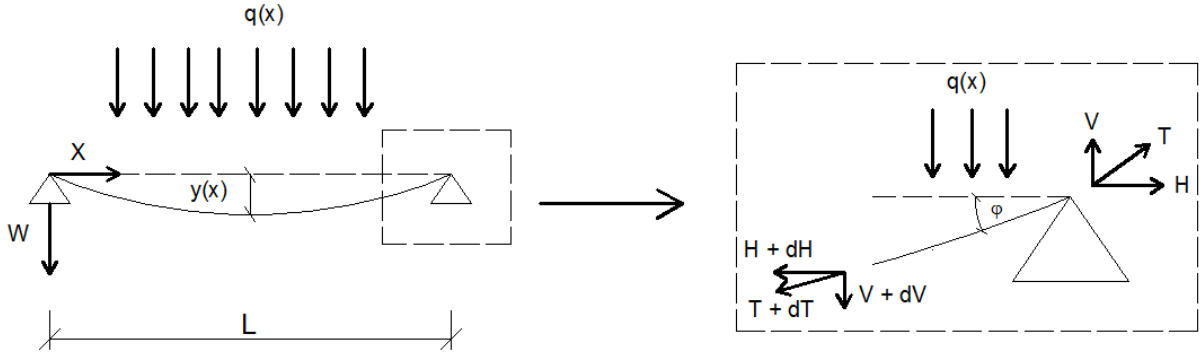

Fig. 4. Theory of the cable equation.

4.1. British Standard BS8006

Tensile force in the geosynthetic reinforcement T_{rp} by British Standard [6]:

$$T_{rp} = \frac{W_T (s-a)}{2a} \sqrt{1+\frac{1}{6\varepsilon}} \tag{2}$$

Where W_T is vertical load carried by geosynthetic reinforcement between adjacent piles, ε is average strain in the geosynthetic reinforcement, a is cross section diameter of pile cap and s is centre-to-centre distance of the piles.

To determine the maximum load W_T carried by geogrids between adjacent piles in the case of modified model by John is necessary to determine the embankment height H, from which depending whether it is the creation of a full arching (for H > 1.4 (s-a)) or partial arching (for H from interval $0.7(s-a) \leq H \leq 1.4\ (s-a)$).

4.2. German method EBGEO

Tensile force in the geosynthetic reinforcement T_V by German recommendation [7]:

$$T_V = \varepsilon \cdot J \tag{3}$$

Where T_v is tensile force in the geosynthetic reinforcement caused by the vertical load, ε is average strain in the geosynthetic reinforcement and J is stiffness of geosynthetic reinforcement (J=E.A).

5. Numerical modelling

Numerical analysis of the scaled physical model of structure, built on the Faculty of Civil Engineering, Department of Geotechnics, (FCE KGt) was carried out by Plaxis 3D Foundation software model.

The scale physical model is formed by 16 supported piles of 300 mm height and diameter of 114 mm. Steel piles are fixed to the concrete slab layer in order to simulate end-bearing piles behaviour. Caps of the piles are made from steel with diameter of 200 mm. Soft subsoil is simulated by synthetic foam (mollitan) with low bearing capacity. Two perpendicular uniaxial geogrids (GGR), type Enkagrid 40, are placed on the pile heads. Crushed stone fraction 0/16mm was selected for the backfill. Static load on the backfill surface is provided by four hydraulic jacks with pressure 100 kPa. The numerical analysis was carried out in seven calculation steps. At each step was simulated an increase of the embankment height by 10 cm, represented one load cycle 100 kPa. The configuration of the scaled model is shown on Fig. 5. Backfill material was modelled as Hardening Soil (HS) model and subsoil as linear elastic model.

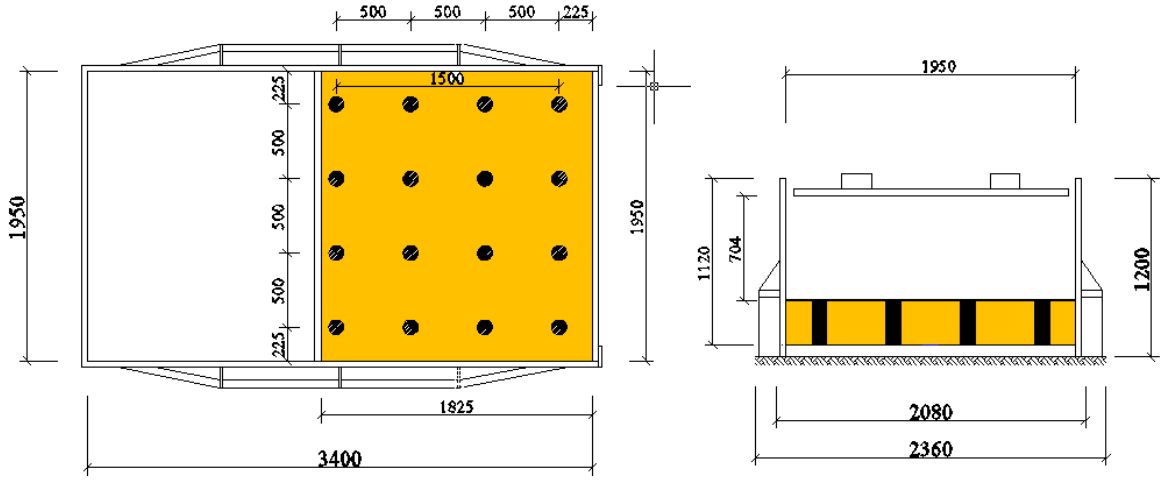

Fig. 5. Model stand of FCE KGt 2015.

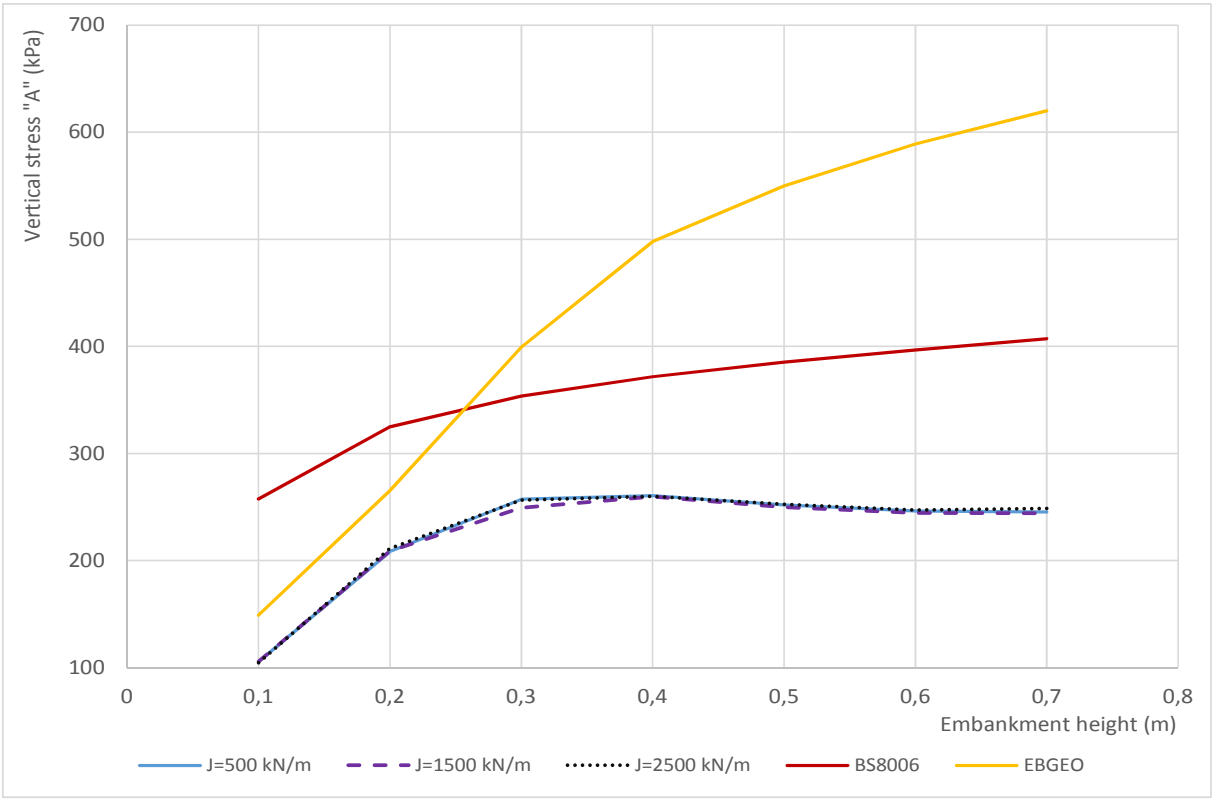

Fig. 6. Vertical stress “A” above pile cap and geogrid.

6. Conclusion

The conclusions of numerical modeling is obvious that the stiffness of geogrid does not have a major impact on the formation of the arch in piled embankment. However, this fact is not very consistent with the fundamental principle of geosynthetics reinforced structures. It is supposed that the lower stiffness of geogrid causes the greater vertical deformations at place between adjacent piles; consequently, there is even more evident activating of shear forces at the embankment at zones between the piles, which results in more massive load transfer into the piles. However, this assumption in our case was not observed, Fig. 6.

It should be noted that geogrid stiffness is not taken into account when calculating the stress according to the British Standard BS8006 nor German regulation EBGEO.

It will be necessary to carry out independent research in this area on scaled physical models of FCE, in order to confirm or refute these findings. By the results of numerical modeling is possible to observe another interesting fact, the creation of a "full arch" i.e. the moment when the stress on the head of pile starts to culminate. This occurs when the embankment reaches a height H > 1.(s - a), which represents in practice very shallow embankment.

References

[1] Reid, W. M. & Buchanan, N.W., 1984. *Bridge approach piling, Piling and Ground treatment*, Thomas Telford Ltd, London.

[2] Prelovsky B, Naughton, P. J., Scotto M., Kempton GT. *The Development of Piled Embankments Techniques Over 25 Years*,

[3] Drusa, M, Lamich, D. et.al. *Design Limits of Reinforced Soil Structures in Difficult Geological Conditions*, In SGEM 2013 Proceedings, DOI:10.5593/SGEM2013/BA1.V2/S02.010

[4] Decky, M., Drusa, M., Pepucha, L., Zgutova, K.: *Earth Structures of Transport Constructions*. Harlow: Essex: Pearson, pp.180, 2013, ISBN 978-1-78399-925-5.

[5] McNulty, J. W. (1965). *An Experimental study of arching in sand*." Technical Report No. I- 674, U.S. Army Engineer Waterways Experiment Station, Corps of Engineers, Vicksburg, Mississippi, 170.

[6] BS8006-1, revision 2010. *Code of Practice for Strengthened/reinforced Soils and Other Fills*. British Standards Institution.

[7] EBGEO, revision 2010. Recommendations for Design and Analysis of Earth Structures using Geosynthetic Reinforcements. Deutsche Gesellschaft für Geotechnik e.V.

TRANSCOM 2015, 22-24 June 2015
University of Žilina, Žilina, Slovak Republic

The effect of additives on the properties of modified autoclaved aerated concrete

[*]Sylwia Kapała , [*]Ryszard Dachowski,
[*]Kielce University of Technology, Faculty of Civil Engineering and Architecture, Department of Building Engineering Technologies and Organization, al. Tysiąclecia Państwa Polskiego 7, 25-314 Kielce, Poland,
{skapala, tobrd}@tu.kielce.pl

Abstract. The objective of this article is to discuss the investigation results concerning primary physical properties, such as bulk density, compressive strength and water absorption, of autoclaved aerated concrete modified with selected additives and admixtures. The modification of autoclaved aerated concrete is aimed at improving the above-mentioned properties.

Keywords: autoclaved aerated concrete**,** dry-state density, compressive strength, water absorption

1. Introduction

Autoclaved Aerated Concrete AAC is a lightweight aerated concrete that, depending on the production process, is obtained from the mix of binder (cement and/or quicklime), aggregate (quartz sand and/or fly ashes), water and expanding agent (aluminum powder or paste) and possible additives enhancing rheological properties of the mix with the application of autoclaving [8].

Autoclaved aerated concrete possesses both a good thermal insulating capacity as well as a relatively good strength. AAC is regarded as a reasonable trade-off between the lightness and strength of products. Although the material has unquestionable advantages, it is, just like all the other materials, not a perfect one. Its weaknesses include high absorbability and low compressive strength (1.5 - 7 MPa) [6] in comparison to e.g. silicates (15-25MPa) [1, 7].

The laboratory tests were designed to determine the effect that the modifications introduced into the composition of autoclaved aerated concrete have on its physical and mechanical properties.

2. Modifications of autoclaved aerated concrete composition

Modifying the composition of autoclave aerated concrete, in order to improve its performance parameters, involved the addition of high impact polystyrene (HIPS) in the form of regranulate and the admixture (D) containing Cl^- ions and NA_2O alkalis. The type and amount of the applied additives in successive trials is presented in Table 1. HIPS is a lightweight high impact material with high rigidity and resistance to cracking. HIPS is a polystyrene containing rubber that is bonded physically or chemically, which changes physical-mechanical properties of a material, depending on the content. HIPS polystyrene is used e.g. in the food industry for packaging, in the refrigeration industry for making refrigerator casing, and in advertising for producing illuminated panels and stands [2, 3]. The admixture applied in the tests increases the resistance against the penetration of water into the structure of concrete. It reacts with calcium hydroxide (the product of cement hydration) to form hydrophobic compounds, which block the pores preventing capillary phenomena.

The above-mentioned fillers have been selected based on their properties. The criterion influencing the samples' composition was an increase in the bulk density, which is associated with an increase in the compressive strength and in the resistance against water absorption.

	Filler content in the sample	
Sample No	HIPS [%]	Admixture (D)
1	-	-
2	10	1
3	30	1
4	50	1

Tab. 1. Mass percentage of the additive and admixture in particular samples.

The sample number 1 is a control sample containing ingredients necessary to produce autoclave-aerated concrete. It was prepared for comparative reasons to determine the effect of additives on the performance parameters of the modified AAC.

The samples marked with numbers 2, 3 and 4 are those in which the mix used to make autoclaved aerated concrete was replaced with 10, 30 and 50% of HIPS regranulate, respectively, and the D admixture was added in the amount of 1% of the cement into each sample.

3. Methods and results

Test samples used in the test were made based on the mixture produced in the aerated concrete production plant. The process of producing the samples was performed in the laboratory in the same plant. Each of the four tests required the use of three cubic samples measuring 100 x 100 x 100 mm. The results are presented as the arithmetic mean of the obtained data.

The investigation focused on such properties of AAC as the dry-state density, compressive strength and water absorption.

3.1. Dry-state density

The dry-state density is the ratio of the aerated concrete weight to its volume (including pores) after drying it to constant weight. The dry-state density results are shown in Figure l.

The manufacturer declares the density of the product made from the mix used in the samples production to be 600 kg/m^3.

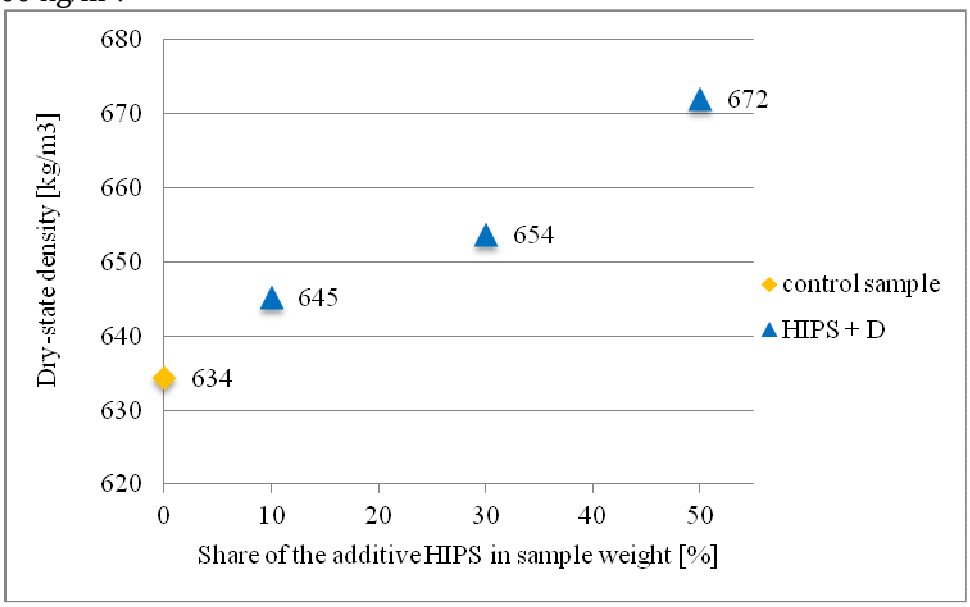

Fig. 1. Dry-state density of the modified AAC.

The real density of the autoclave-aerated concrete is always slightly higher than that declared by the manufacturer. The higher density is caused by technological moisture, present in the products after the autoclaving process [8]. Therefore, the mean value of the control samples is

higher than the one declared by the manufacturer with regard to the mix that provided the basis for the samples preparation.

Based on Figure 1, one may notice that the AAC composition modification caused the increase in density in comparison to the control samples. It may be observed that the density increases with the percentage increase of the HIPS regranulate content in samples.

3.2. Compressive strength

The compressive strength of each sample was determined according to EN 771-4 [4] by subjecting them to a test in the press. Before the examination, the samples were subjected to seasoning to the air-dry state. The results are presented in Figure 2.

With the density declared by the manufacturer, the minimum compressive strength class of the product made from the mix for the sample production is 3 MPa.

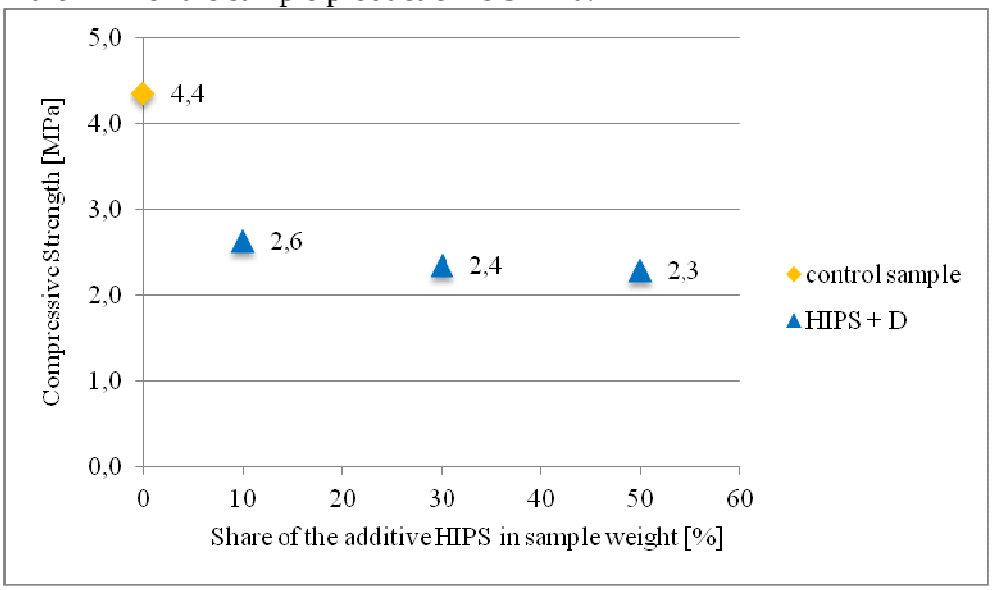

Fig. 2. Compressive strength of the modified AAC.

Figure 2 shows that the modification of the autoclave aerated concrete composition resulted in the decrease in the compressive strength. None of the modified samples achieved the minimum compressive strength class for the density of 600-650 kg/m^3, specified as 3 MPa.

3.3. Water absorption

Water absorption was specified in accordance with the PN-EN 772-11 [5]. Tests were performed after 10, 30 and 90 minutes. The results are presented in Figure 3.

The results of the tests performed on autoclave-aerated concrete revealed the following absorption values:

after 10 minutes 47-204 g/(m^2 · s^{05}),
after 30 minutes 41-179 g/(m^2 · s^{05}),
after 90 minutes 37-162 g/(m^2 · s^{05}).

It was proved that the differences in the absorption values depend on material properties and are characteristic of the products manufactured in a particular plant [8].

Figure 3 shows that the samples in which the autoclave aerated concrete composition had been modified manifested much higher water absorption coefficient than the control samples in all the three tests. In the first test, the value of water absorption coefficient of these samples was higher than the value of the control sample by app. 115 to 160 g/(m^2 · s^{05}). In the successive tests the coefficient value decreased in relation to the control samples and in the last test it was higher by the value of app. 65 to 80 g/(m^2 · s^{05}).

Moreover, the water absorption coefficient for all the samples with the modified AAC composition does not fall within the ranges of water absorption coefficient that were specified on the basis of the previous tests.

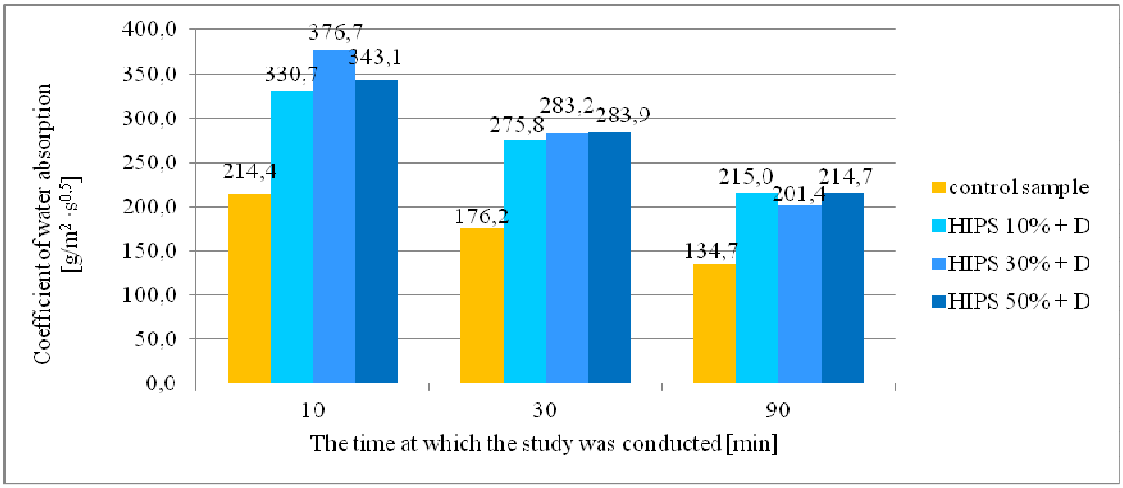

Fig. 3. Water absorption of the modified autoclave aerated concrete.

4. Conclusion

The above-discussed investigation permits the evaluation of the effect that additives have on the properties of the autoclave-aerated concrete concerning: dry-state density, compressive strength and water absorption. The investigation analysis allows the conclusion that the additive in the form of high impact polystyrene regranulate combined with the admixture containing Cl- ions and alkalis NA_2O has the negative effect on the performance parameters of the autoclaved aerated concrete.

This may be due to the high temperature in the process of curing or/and autovization. However, it is difficult to determine whether the deterioration of the performance of autoclave aerated concrete affect either both fillers or one of them.

References

[1] DACHOWSKI R., STĘPIEŃ A. *Research on sand-lime products regarding their physical and mechanical features.* Structure and Environment 1/2010, Kielce University of Technology, pp. 5-8.

[2] NOWEK M., *The impact of recycled polymers on the features of modified sand-lime products.* Technical Transactions. Civil Engineering 1-B/2014

[3] PIELICHOWSKI J., PUSZYŃSKI A., *Chemia polimerów*, Wydawnictwo Naukowo-Techniczne TEZA, Kraków 2004

[4] PN-EN 771-4: 2012 Wymagania dotyczące elementów murowych -- Część 4: Elementy murowe z autoklawizowanego betonu komórkowego

[5] PN-EN 772-11:2011 Metody badań elementów murowych - Część 11: Określenie absorpcji wody elementów murowych z betonu kruszywowego, kamienia sztucznego i kamienia naturalnego spowodowanej podciąganiem kapilarnym oraz początkowej absorpcji wody elementów murowych ceramicznych

[6] www.hplush.pl [27.03.2015 r.]

[7] www.grupasilikaty.pl [27.03.2015 r.]

[8] ZAPOTOCZNA - SYTEK G., BALKOVIC S., *Autoklawizowany beton komórkowy. Technologia, właściwości, zastosowanie*, Wydawnictwo Naukowe PWN, Warszawa 2013.

TRANSCOM 2015, 22-24 June 2015
University of Žilina, Žilina, Slovak Republic

Seismic analysis of the tower construction of Kielce Trade Fairs

[*] Joanna Kłosowska, [**] Paulina Obara
[*] Kielce University of Technology, Faculty of Civil and Environmental Engineering, Aleja Tysiąclecia Państwa Polskiego 7, 25-314 Kielce, Poland {jklosowska}@tu.kielce.pl
[**] Kielce University of Technology, Faculty of Civil and Environmental Engineering, Aleja Tysiąclecia Państwa Polskiego 7, 25-314 Kielce, Poland {paula}@tu.kielce.pl

Abstract. The seismic analyze of the tower construction of Kielce Trade Fairs is presented in this paper. The calculation of the static, dynamic and seismic were made using Autodesk Robot Structural Analysis Professional 2011. The seismic analyze was made according to the Eurocode 8 - *Design of structures for earthquake resistance*. This paper explains how the seismic loads should be included. Displacements and reduced forces occurring in successive floors of the tower of Kielce Trade Fairs were compared based on the results of calculations, taking into account the seismic influence and without this effect. The last part of the paper contains the conclusion drawn on the basis of analyzes and results.

Keywords: Dynamic analysis, seismic analysis, tower construction of Kielce Trade Fairs, Eurocode 8.

1. Introduction

Many types of dynamic loads can affect for buildings. Particularly dangerous are seismic and paraseismic loads. Seismic waves, also named as elastic, are defined as waves propagating in the Earth, which can be caused by earthquakes – seismic, or by human activity – paraseismic vibrations. A common feature of these kinds of dynamic effects is that the load of buildings results from the inertial forces, which arise during a kinematic motion of a foundation [2].

2. The impact of seismic loads on buildings

A mass of structure is not included during static analysis, but it is important in dynamic approach, because during dynamic analysis, the inertia forces are taking into account. These forces are proportional to the mass and affect on the direction of translational movements [4].

An intensity of potential earthquake is not known, during a designing. In such a situation, can use the seismic accelerogram and design a structure, on the assumption that the next shock will not be more destructive than the standard. This is a deterministic approach. Deterministic methods for calculating the influence of seismic loads, can be divided into two classes: static and dynamic methods.

Another method to seismic analyze is the stochastic approach. In this case reliability of structures and the conditional probability of failure-free operation of construction are investigated, provided that an earthquake occurs with certain strength. This approach is not considering in this paper [5].

2.1. Static methods for the seismic analysis

The seismic loads are variable in time. Using static methods for the seismic assessment, dynamic loads are replaced by appropriate static loads and calculations can be made in the field of static. Among the static methods can be replaced primarily Omori's and Korczyński's methods which take into account dynamic characteristics of buildings [4,5].

2.2. Dynamic methods for the seismic analysis

Designing major engineering structures is carried out using dynamic methods. In this case the time-varying seismic load is taking into account. At an early stage of the design must select a seismogram and a dynamic model of a building.

The basis for determining a seismogram is statistics of earthquakes occurring in the past and analysis of the geological structure of the territory. The dynamic model of a building should represent accurately as possible the actual structure. The most important dynamic characteristics are the frequency of vibration, the vibration form, damping properties and elastic forces [6,7].

3. Standards connected with an exceptional load

Designing the structure, taking into account seismic effects, is based on:

- PN-EN 1991-1-7 [9],
- Eurocode 8 – *Design of structures for earthquake resistance* [8].

Eurocode [8] describes the seismic risk in the area, through the reference seismic load, which is specified for a certain probability of an earthquake. For this purpose, the reference acceleration is determined, which may be exceeded with a probability PNCR in 50 years. Eurocode recommends to take PNCR = 10%, which corresponds to the reference return period TNCR=475 years.

An annex to the described standards includes division of the country into zones of seismic, which corresponds to the specified seismic risk. Design ground acceleration is determined from the following formula:

$$a_g = a_{gR} \cdot \gamma_1 \tag{1}$$

where:

a_{gR} – the reference design ground acceleration (corresponding to the reference return period),

γ_1 – the importance factor of the structure.

The importance factor is determined for different types of buildings, according to the different periods of return. Ranges from 0.8 – for agricultural buildings, by 1.2 – for schools, up to 1.4 – for hospitals, power plants, etc. For typical buildings and apartment buildings has a value of 1.0 .

According to [8] for the analysis of buildings that meet the specific requirements of regularity, it is assumed only the first, basic form of vibration and specifies the total horizontal force at the base of the object, called base shear:

$$F_b = S(T_0) \cdot G \tag{2}$$

where:

T_0 – the period of the fundamental mode of vibration for the direction under consideration,

G – the total effective weight of the structure, equal to the weight of the deck plus the weight of the top half of the piers,

$S(T_0)$ – the spectral acceleration of the design spectrum.

The force F_b is separated into individual elements in the form of the forces F_i in accordance with the following formula:

$$F_i = (F_b - F_t)\frac{\omega_i \Sigma G_i}{\Sigma \omega_j G_j} \tag{3}$$

where:

ω_i and ω_j – movements of masses in the basic form of vibrations,

G_i and G_j – weights of i-th and j-th masses,

F_t – a horizontal concentrated force applied at the top of the building, which is calculated according to the formulas:

$$F_t = 0{,}07 \cdot T_0 \cdot F_b \leq 0{,}25 \cdot F_b \text{ if } T_0 > 0{,}7s \quad (4)$$

or

$$F_t = 0 \text{ if } T_0 \leq 0{,}7s \quad (5)$$

4. The analysis of the tower construction of Kielce Trade Fairs

4.1. General characteristics of the tower

The height of the tower is 40 m plus an additional decorative element ("harp") with a height of 20 m. The total height of the object is about 60 m. Utility rooms are at the height 33.5 m. Intermediate platforms are located below. Communications are staircase and elevator. The core of the main tower (40 m height) was performed as reinforced concrete monolithic fixed in the foundation. Platforms and ceilings are a steel grate. "Harp" was made as a steel structure. The dimensions of the shaft in the plan are: 6 x 8.3 m. At the height + 33.5 m, the tower measures in plan 20 x 16m.

The digital model of the tower was built in the Robot Structural Analysis 2011. The calculations include permanent load like the dead weight and variable loads like snow and wind. 10 fundamental combinations were performed due to the ultimate limit state, 6 characteristic combinations due to the serviceability limit state, 114 fundamental seismic combinations due to the ultimate limit state and 82 characteristic seismic combinations due to the serviceability limit state. The linear static, modal and seismic analysis was carried out.

4.2. Linear static analysis

The maximum displacements of the floors structures were determined for the combination taking into account the serviceability limit state (the table 1 contains the maximum displacements of the floors). The reduced forces were determined for the combination taking into account the ultimate limit state (Tab. 2).

Floor	Max U_X (cm)	Max U_Y (cm)	Min U_X (cm)	Min U_Y (cm)
1	-2	-1.1	-2.3	-1.4
2	-1.8	-0.9	-2.1	-1.3
3	-1.6	-0.8	-1.9	-1.2
4	-1.3	-0.7	-1.7	-1
5	-1.1	-0.5	-1.5	-0.9
6	-0.9	-0.4	-1.3	-0.7
7	-0.7	-0.3	-1.1	-0.6
8	-0.5	-0.1	-0.9	-0.5
9	-0.2	0	-0.7	-0.3
10	-0.1	0.1	-0.6	-0.2
11	0.2	0.5	-0.3	-0.1
12	2	0.5	-0.2	-1.4

Tab. 1. Maximum displacements of the floors.

Floor	F_X (kN)	F_Y (kN)	M_Z (kNm)
1	1.08	8.95	-11.71
2	32.5	-28.76	-65.65
3	82.26	-126.65	-22
4	127.58	-179.81	-42.39
5	180.97	-227.42	-87.67
6	228.23	-328.21	78.58
7	272.26	-395.39	-62.9
8	310.23	-405.14	-133.65
9	212.05	-1076.31	5135.63
10	9282.12	12782.62	-24438.4
11	11767.85	12391.83	-17622.9
12	-173.17	-250.99	-70.47

Tab. 2. Maximum reduced forces .

4.3. Modal analysis

Before making seismic analysis, modal analysis should be carried out. The analysis was performed for the following parameters:

the method – subspace iteration,
the number of mode shapes – 10,
the number of iterations – 40,
tolerance – 0.0001,
Struma verification,
mass matrix –focused with rotations,
attenuation – 0.03.

Modal analysis leads to the determination of circular frequency of vibration, periods of vibrations, natural frequency and a matrix which consists of the eigenvectors corresponding to the respective frequency of vibrations.

4.4. Seismic analysis

The seismic analysis was performed according to the standard Eurocode 8, assuming a linear-elastic response spectrum for the proposed acceleration of the ground ranging a_g = 1 [m/s^2].

Assumed the following values that characterize the spectrum of responses:

- S=2.5 – soil factor,
- T_b=0.15,
- T_c=0.6 – corner period of elastic spectrum,
- T_d=3 - corner period of elastic spectrum,
- B=1 – width of the deck.

Loads were converted into dynamic masses. Assumed that 20% of variable loads have a mass character (ratio 0.2), in other cases, the load factor was adopted 1.0. Defined parameters of modal analysis changed its type for seismic analysis. The percentage of participation of the masses was set at 90% [1].

The contribution coefficients for the form of vibrations, the spectral acceleration of the design spectrum for every periods of vibrations and finally displacements of each node of the structure were calculated [6,7,8]. For analyzed structure extreme values of displacements of floors have been determined for the combination due to serviceability limit state, taking into account the seismic force (tab. 3).

Reduced forces were determined for seismic loads in the direction of *X*, *Y*, *Z*, for each floor (tab. 4).

Floor	U_X (cm)	U_Y (cm)
1	-2	-1.2
2	-1.8	-1.1
3	-1.6	-0.9
4	-1.4	-0.8
5	-1.2	-0.6
6	-1	-0.5
7	-0.8	-0.4
8	-0.6	-0.2
9	-0.4	-0,1
10	-0.2	0
11	0.1	0.2
12	0.4	0.3

Tab. 3. Maximum displacements of floors.

Floor	F_X (kN)	F_Y (kN)	M_Z (kNm)
1	1.2	9.15	-12.87
2	32.91	-28.66	-63.8
3	83	-126.89	-24.98
4	128.31	-180.24	-41.39
5	181.65	-227.48	-88.22
6	227.97	-329.7	90.69
7	275.29	-398.67	57.96
8	309.14	-402.51	-149.27
9	252.01	-1254.87	5915.3
10	8572.5	15761.61	-39260.72
11	10767.84	15943.97	-33530.58
12	-81.01	-136.53	301.03

Tab. 4. Maximum reduced forces .

5. Conclusion

This paper attempts to analyze the impact of seismic loads on the structure, for example the tower Kielce Trade Fairs. Based on the analysis, concluded that reduced forces, which are results of seismic analysis, are much greater than those obtained in static analysis. Differences in values are particularly noticeable in the case of M_Z moments occurring at the highest levels of the tower. This would suggest a need to check the capacity of the tower and perhaps increase the dimensions of the load-bearing components.

The displacements of the floors of the tower are virtually identical if were taken into account the seismic effects and if the dynamic interaction was omitted. Probably this is a result of the high stiffness of the structure. The Tower Kielce Trade Fairs does not require structural changes if it would were located in areas at risk of earthquakes.

References

[1] Autodesk Robot Structural Analysis -help.

[2] BIEGUS A. *Projektowanie konstrukcji budowlanych według Eurokodów. Część 2- oddziaływania na konstrukcje*. Builder, 2010.

[3] BŁASZCZYŃSKI T., WDOWICKA E., WDOWICKI J. *Analiza wpływów sejsmicznych na żelbetowy budynek ścianowy według normy ISO/DIS – 3010*. X Sympozjum *Wpływy sejsmiczne i parasejsmiczne* Kraków, 27-28, listopad 2003r.

[4] CHMIELEWSKI T. ZĘBATY Z. *Podstawy dynamiki budowli.* Wydawnictwo ARKADY, Warszawa, 1998.

[5] CHMIELEWSKI T., ZĘBATY Z. *Problem niezawodności budowli w warunkach ryzyka sejsmicznego* Praca przeglądowa, Mechanika teoretyczna i stosowana 3-4, 29, 1991.

[6] DULIŃSKA J., *Odpowiedź dynamiczna budowli wielopodporowych na nierównomierne wymuszenie parasejsmiczne pochodzenia górniczego*, Monografia 338, Wydawnictwo Politechniki Krakowskiej, Kraków, 2006

[7] DULIŃSKA J., ZIĘBA A. *Metody oceny wpływu wstrząsów górniczych na wybrane budowle wielkogabarytowe*. Czasopismo techniczne, Zeszyt 11; Wydawnictwo Politechniki Krakowskiej, Kraków, 2010.

[8] Eurocode 8: *Design of structures for earthquake resistance*.

[9] PN-EN 1991-1-7- *Oddziaływania wyjątkowe*.

[10] THE INSTITUTION OF STRUCTURAL ENGINEERS, *Manual for the seismic design of steel and concrete buildings to Eurcode 8*, The Institution of Structural Engineers, 2010.

[11]ZĘBATY Z. *Zastosowanie normy sejsmicznej Eurokod 8 w projektowaniu budowli narażonych na działanie wstrząsów górniczych*. Czasopismo techniczne, Wydawnictwo Politechniki Krakowskiej 3-B/2010.

TRANSCOM 2015, 22-24 June 2015
University of Žilina, Žilina, Slovak Republic

Experimental Determination of Thermal Conductivity of Selected Kinds of Soil

[*]Marta Kolankowska, [**]Tomasz Kozlowski, [*]Agata Ludynia, [*]Łukasz J. Orman
[*]Kielce University of Technology, Faculty of Civil Engineering and Architecture, Al. 1000-lecia P.P.7., 25-314 Kielce, Poland, {markola19@wp.pl
[**]Kielce University of Technology, Faculty of Environmental, Geomatic and Energy Engineering, Al. 1000-lecia P.P.7., 25-314 Kielce, Poland, tomkoz@tu.kielce.pl, agataludynia@tlen.pl,orman@tu.kielce.pl

Abstract. The paper discusses the issue of thermal conductivity measurements of soil. The problem is especially vital for the proper design of ground heat exchangers whose aim is to extract heat or cool from the ground for various building applications. Determination of thermal conductivity of selected soil types has been done with a heat flow meter working on the principle of different temperatures between two measuring plates. Other crucial soil parameters have also been given in the paper.

Keywords: soil, thermal conductivity.

1. Introduction

Thermal conductivity is a crucial parameter when energy performance of buildings is considered. Walls and other building elements are required to have low values of conductivity (and, consequently, small overall U-values) to ensure minimal heat losses. However, more and more attention is now paid to the integration of renewable energy systems into buildings. The application of ground source heat pumps or ground heat exchangers for ventilation purposes are the examples of it. In both cases heat is transferred in the soil and the heat flux is dependent on thermal conductivity. The knowledge of this parameter is crucial when the required length of bore holes is considered. Moreover, the ground can act as energy storage facility due to its significant mass when there is a surplus of energy. For example heat from solar panels during the summer can be transferred and stored within the ground. Here, precise thermal properties of soil together with their possible non-uniformity within the whole system need to be determined.

The work by [1] discussed the effects of such soil parameters as bulk density, moisture and salt contents as well as organic matter of the sieved and repacked soil specimen. It has been reported that thermal conductivity rose with rising soil density as well as moisture concentration. The obtained values of conductivity were given as 0.29 to 0.76 W/(mK) for loam and 0.36 – 0.69 W/(mK) for clay loam. Higher contents of organic matter led to lower thermal conductivity values. In [2] thermal conductivity of sandy loam as well as clay loam soils was measured. It was concluded that it varied with soil texture, bulk density and water content values. The rise of bulk density led to higher thermal conductivity (at a certain moisture content), while the rise of moisture content resulted in elevated thermal conductivity for a certain bulk density. It was also stated that clay loam was generally characterised by smaller thermal conductivity value than sandy loam. The paper by Ekwue et al. [3] analyses the effect the incorporation of peat into soil has on thermal conductivity. Different moisture contents were used and bulk densities also varied. The main finding was that conductivity decreased with increased peat content. Tang et al. [4] considered thermal conductivity of compacted bentonite. The impact of the content of water, dry density and saturation on conductivity was analysed. What is more, the authors proposed a correlation for determination of this value using the presented experimental analyses. The measurements given in [5] prove that the values of thermal conductivity were elevated with rising soil density. This finding supports the observations made in [1]. The relation between thermal conductivity and moisture of

soil for different moss and organic horizon kinds was the focus of the paper by O'Donnell et al. [6]. The work indicated the existence of a strong positive and linear relation between thawed thermal conductivity values and volumetric water content. The paper by Folaranmi [7] is focused on the influence of additives (ash and sawdust) on thermal conductivity of clay. The smallest value of 0.06 W/(mK) was recorded with the addition of the maximal amount sawdust, while for average clay it was 0.25 W/(mK) with no content of moisture. The concentration of ash and sawdust varied from 1 to 30%. Although the majority of works are experimental investigations, some are more theoretical. Singh et al. [8] analysed a possibility of the application of artificial neural networks for determination of effective thermal conductivity of moist porous systems.

2. Material and method

2.1. Sample specification

Two types of soil have been chosen for the current experiment: clay and clayey silt. Tab. 1 presents the basic physical properties and the determination method used to obtain the following parameters.

PROPERTIES	CLAY	CLAYEY SILT	TESTING METHOD
bulk density of soil [ρ], g/cm^3	2.04	2.03	ring method
water content w_n, %	22.39	17.83	dry method
plastic limit [PL], %	19.78	15.27	thread-rolling method
liquid limit [LL], %	64.21	35.82	Casagrande method
liquidity index [LI], -	0.06	0.12	calculated
degree of plasticity, %	44.41	20.55	calculated
colloidal activity [A], -	1,23	0,89	calculated

Tab. 1. Basic properties of the tested soils.

The samples of soil have also been analysed by using the scanning microscopy method in order to determine the surface structure. Fig. 1a and 1b present the SEM (Scanning Electron Microscope) images of clay and clayey silt, respectively.

a) b)

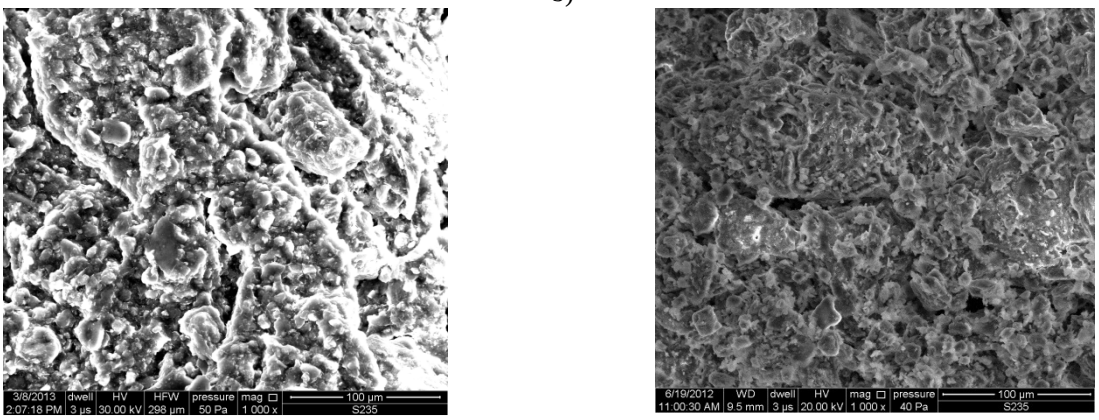

Fig. 1. SEM images of clay (a) and clayey silt (b) – magnification 1000x.

2.2. Thermal conductivity testing method

Determination of thermal conductivity has been done with a heat flow meter. It works on the principle of the temperature difference between two parallel plates (heater and cooler) and the resulting heat flow. The plates are located in the insulated chamber, while between them a sample is situated. The value of conductivity is obtained when the heat flux becomes steady. It is calculated by the software taking into account the temperature difference, sample height and the heat flux

conducted through the soil specimen and measured with the sensors. Fig. 2a and 2b present graphs of temperature changes of the heater and cooler when clay was being tested, while Fig. 3 – changes of the heat flux value (j).

a) b)

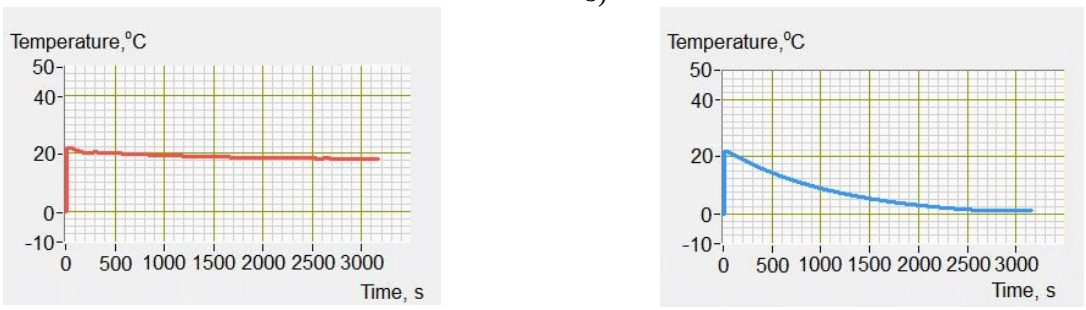

Fig. 2. Temperature changes of the heater (a) and the cooler (b) for the clay sample.

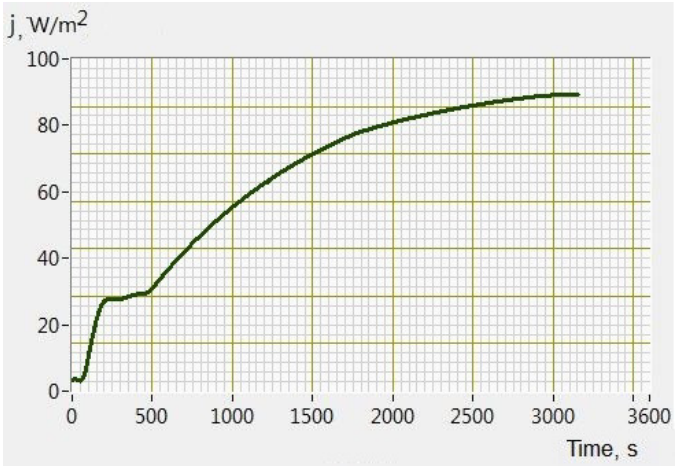

Fig. 3. The heat flux changes with time – the clay sample.

3. Results and discussion

In the course of the research, the following results of the value of thermal conductivity were obtained and have been presented in Tab.2 and Fig. 4 together with data on water content from Tab.1. The results are lower than the values in [9], which might be attributed to sample characteristics.

	CLAY	CLAYEY SILT
Thermal conductivity, W/(mK)	0.735	0.788

Tab. 2. Thermal conductivity of the soil samples.

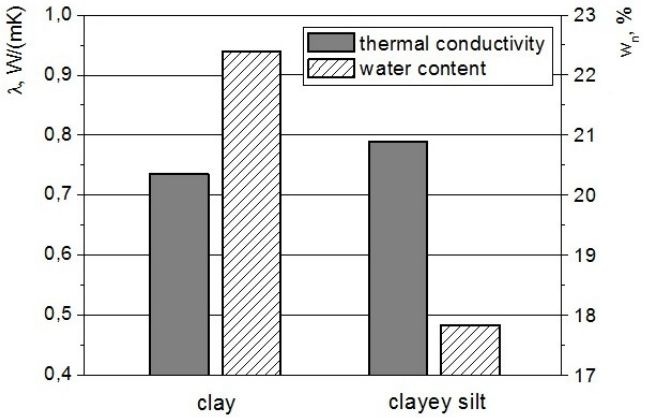

Fig. 4. Thermal conductivity and water content results.

The presented experimental data indicates a possible influence of water content on the value of thermal conductivity for the analysed samples of almost the same bulk density of over 2 g/cm^3. If the density (and, consequently, porosity) was different, this parameter would have a significant impact on the results as mentioned in a number of literature reports. The conductivity of water equals 0.569 W/(mK) at 0^{o}C [10]. As a consequence, for a two – phase system of soil and water, the higher water content would result in lower thermal conductivity of clay in relation to clayey silt as given in Tab. 2 and Fig. 4.

4. Conclusion

Apart from other soil parameters [11, 12], determination of thermal conductivity is crucial in many engineering applications. In the analysed case of the soil samples, it has been observed that water content might have an impact on this parameter. However, other factors could play a role as well, which should be a subject of further studies in view of obtaining more knowledge to enable a possible modelling of thermal conductivity based on physical parameters of the soil.

The practical applications of the issue of experimental investigations and modelling of thermal conductivity of soil are very large. The knowledge of this value is especially vital for the proper design of ground heat exchangers for renewable energy systems such as heat pumps, but also for heat accumulation in the ground as concluded from [13].

References

[1] ABU-HAMDEH, N.H., REEDER, R.C. *Soil Thermal Conductivity Effects of Density, Moisture, Salt Concentration, and Organic Matter*. Soil Science Society of America Journal, Vol. 64 No. 4, pp. 1285–1290, 2000.

[2] ABU-HAMDEH, N.H. *Measurement of the thermal conductivity of sandy loam and clay loam soils using single and dual probes*, J. agric. Engng Res., 80, 2, pp. 209–216, 2001

[3] EWKUE, E.I., STONE, R.J., BHAGWAT, D. *Thermal conductivity of some compacted trinidadian soils as affected by peat content*, Biosystems Engineering, 94 (3), 461–469, 2006.

[4] TANG, A.-M., CUI Y.-J., LE, T.-T. *A study on the thermal conductivity of compacted bentonites*. Applied Clay Science, Vol. 41, 3–4, pp. 181–189, 2008.

[5] ABUEL-NAGAA, H.M., BERGADO, D.T., BOUAZZA, A., PENDER, M.J. *Thermal conductivity of soft Bangkok clay from laboratory and field measurements*, Engineering Geology, Vol. 105, 3–4, pp. 211–219, 2009.

[6] O'DONNELL, J.A., ROMANOVSKY V.E., HARDEN J.W., MCGUIRE, A.D. *The effect of moisture content on the thermal conductivity of moss and organic soil horizons from black spruce ecosystems in interior Alaska*, Soil Science, Vol. 174, 12, pp. 646–651, 2009.

[7] FOLARANMI, J. *Effect of additives on the thermal conductivity of clay*, Leonardo Journal of Sciences, 14, pp. 74 - 77, 2009.

[8] SINGH, R., BHOOPAL, R.S., KUMAR S. *Prediction of effective thermal conductivity of moist porous materials using artificial neural network approach*, Building and Environment, Vol. 46, 12, pp. 2603–2608, 2011.

[9] ISO 10456: *Building materials and products - Hygrothermal properties - Tabulated design values and procedures for determining declared and design thermal values*.

[10] ÇENGEL, Y.A. *Heat transfer, a practical approach*, The McGraw-Hill Companies, 2003

[11] ŻYGADŁO, M., GAWDZIK, J. *Modeling the transport of petroleum products by soil filter method*, Polish Journal of Environmental Studies, 19(4), pp. 841-847, 2010

[12]LATOSIŃSKA, J., ŻYGADŁO, M. *The application of sewage sludge as an expanding agent in the production of lightweight expanded clay aggregate mass*, Environmental Technology 32(13), pp. 1471-1478, 2011

[13]KAPJOR, A., DANIEL, L., FARBAK, M., GOTTWALD, M. *The accumulation and heat transfer in soils*, Structure and Environment, vol. 6 (4), pp. 43 – 46, 2014.

TRANSCOM 2015, 22-24 June 2015
University of Žilina, Žilina, Slovak Republic

Displacement Analysis of Steel-Shell-and-Soil Structure in the Construction Phase.

*Łukasz Kosno
*Kielce University of Technology, Faculty of Civil Engineering and Architecture, Department of Strength of Materials and Concrete Structures, al. Tysiąclecia Państwa Polskiego 7, 25-314 Kielce, Poland, lkosno@tu.kielce.pl

Abstract. The paper below aims to present the results of studies of the flexible SuperCor SC-57S structure. The structure comprised of corrugated steel shell and soil backfill was built by Polish manufacturer "ViaCon Polska Sp. z o.o." in order to examine its behaviour in the construction phase. The values of displacement that occur in the structure were determined through geodetic surveys. The data were collected after the construction of each layer and at 7, 25, 53, 84, 132, 211 and 403 days from the completion date. The conclusions based on the measured values may be helpful in understanding the behaviour of flexible steel shell and soil structures.

Keywords: steel shell and soil structure, corrugated steel plate, flexible structures, the SuperCor structures

1. Introduction

The paper below presents the results from the tests carried out on the SuperCor SC-57S structure by the Polish manufacturer ViaCon Polska Sp. z o.o. The study aimed to determine the behaviour of the steel and soil flexible structure. The displacement was determined through geodetic surveys. The conclusions based on the results from this research may be helpful in understanding the behaviour of steel shell and soil structures in the phase of construction.

2. Description of the structure

The investigated structure was the SuperCor SC-57S. It is a flexible corrugated steel structure that consists of 7mm thick plates made of S315MC steel. Its design span is lt=17.59 m and the curvature radii reaches 3.43 m and 13.74 m. The corrugation profile has a depth of 140mm and pitch of 381mm. The steel plates are bolted with M20 compression bolts. The nuts are tightened up to the required torque of minimum 360 Nm, in compliance with the plate manufacturer's instruction. The SuperCor structure is fixed to a concrete footing. The soil backfill comprises of 25 layers, each being 30 cm in thickness. The soil density index amounts from I_D=0.95 in the direct vicinity of the steel structure to I_D=0.98 in the remaining part of the backfill. The proper execution of this component is very important. The backfill interacts with the steel structure and carries significant part of the load. The positive arching effect is particularly important here. [2] [3]

Fig. 1. The SuperCor SC-57S structure in the construction phase

3. Conducting the research

The displacements were determined through geodetic surveys during the construction process. Basic dimensions and the location of geodetic measurement points are shown in Fig. 2. The surveys were performed after the construction of each layer and at 7, 25, 53, 84, 132, 211 and 403 days from the date of completion. The zero reading (the first survey) was performed after assembling the steel structure. For this reason, the deflections due to the dead load were not accounted for.

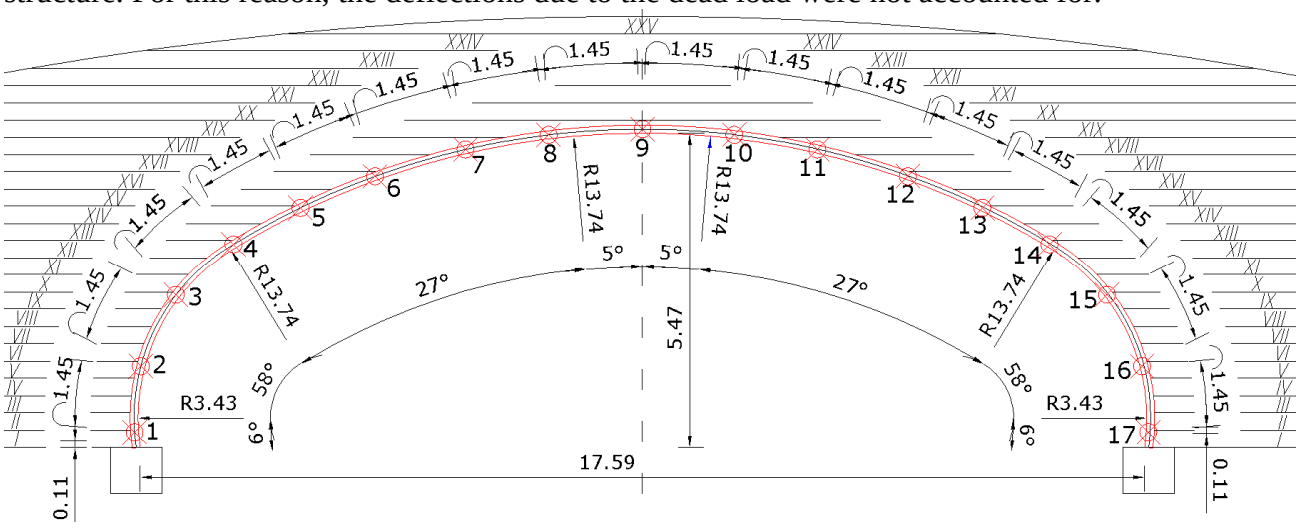

Fig. 2. Basic dimensions of the structure, details of backfill layers and location of geodetic measurement points.

4. Results

In this kind of structures the steel shell shares the load with the backfill. In the construction phase the pressure of the soil on the steel cause the deformation of the structure. The structure arches upwards - it buckles in the upper part and its horizontal size decreases - its width narrows. The deformation decreases after laying consecutive layers of backfill [1]. The diagram below shows the results of geodetic surveys: the vertical displacements in the crown and 'U' value - the narrowing at points 1 and 17. It displays that the buckling and the narrowing reduced after placing layers from XIX to XXV. The measurements conducted at 7, 25, 53, 84, 132, 211 and 403 days of the completion date showed that the soil-steel structure underwent further deformation. The vertical displacements in the crown reached 43 mm. The geodetic measurement points 1 and 17 moved nearly 20 mm away. Both points moved to the left; the point situated at the left corner: 22mm, at the right corner: 3mm.

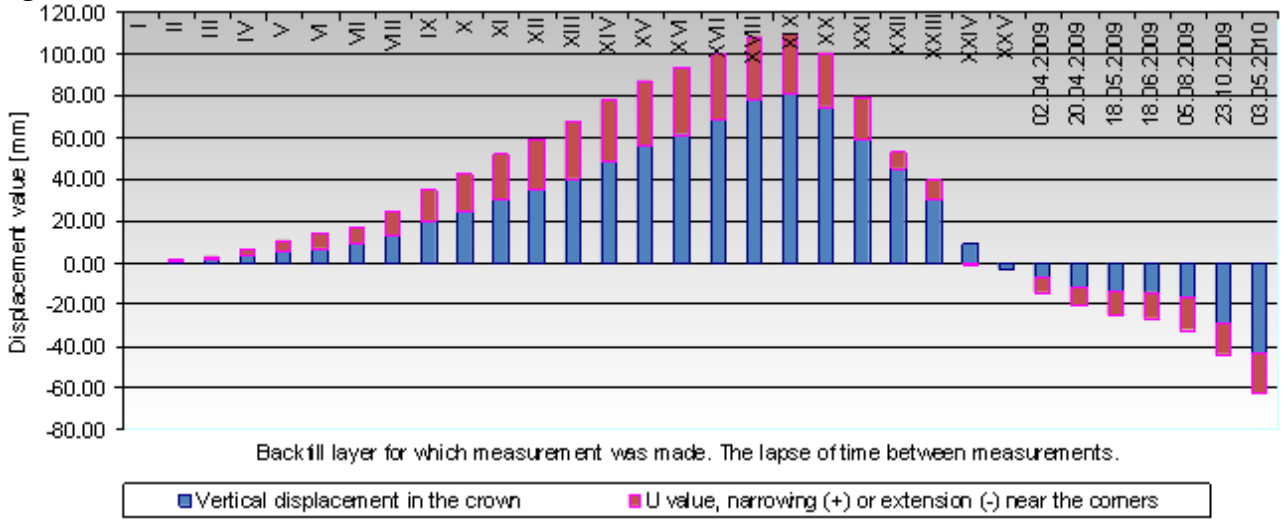

Fig. 3. Displacements in the investigated structure

The measuring points marked as 7, 8, 9, 10 and 11 should be considered in the analysis of the deflections that appear near the crown of the structure. Point 9, which is situated at the crown, is where the largest displacements are expected. Smaller deflections should be recorded at points 8 and 10. The smallest displacements should occur at points 7 and 11. Figure 4 presents the results of the geodetic survey of the displacement obtained after placing layer XXV and at 7, 25, 53, 84, 132, 211 and 403 days from the date of completion. After the placement of layer XXV, vertical displacement at particular points were as follows:

7: -5.09mm;
8: 6.82mm;
9: -3.67mm;
10: -39.75mm;
11: -54.29mm.

Results of the geodetic survey show that the structure did not deflect in the manner anticipated. The survey conducted after 403 days from placing layer XXV showed the following displacement for particular points:

7: -17.23mm;
8: -24.35mm;
9: -43.06mm;
10: -71.48mm;
11: -70.17mm.

At 403 days from the completion date the measured deflection values increased. The largest recorded deflection moved from point 11 to point 10, which is located closer to the crown.

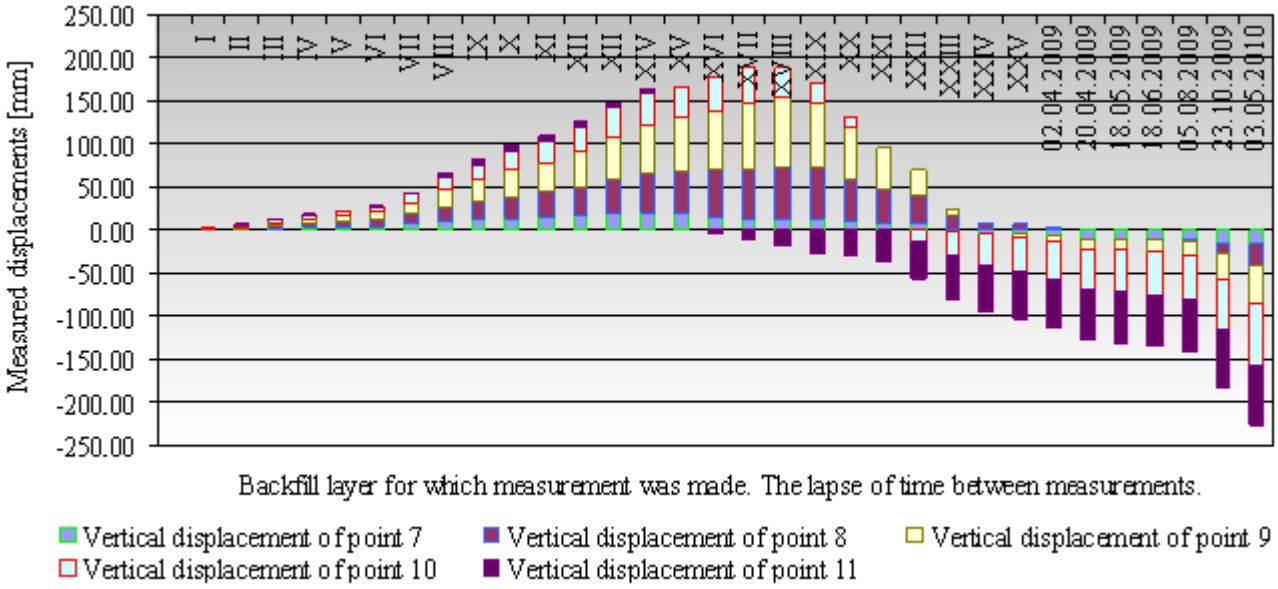

Fig. 4. Geodetic survey results: displacements of points 7-11.

The geodetic survey shows that vertical displacements were caused by not only deflections but also a settlement of the foundations. This is confirmed by displacements of points 1 and 17, which increase with time. Points marked 1 and 17 are located at a small distance from the supports (approximately 10cm).

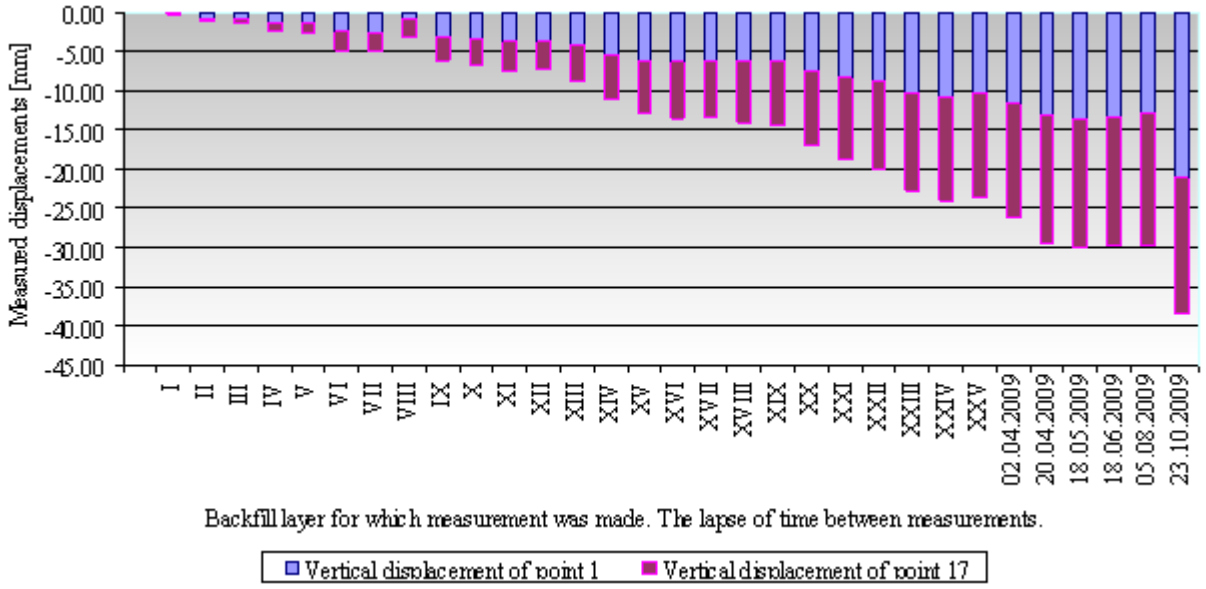

Fig. 5. Geodetic survey results: displacement of points 1 and 17.

5. Conclusions

Based on the studies of SuperCor SC-57S structure, the following conclusions can be drawn. The largest deformation occurs in the phase of construction. It is rising with the backfill height until the crown level is reached. Subsequently, the deformation is decreasing with backfilling continued above the crown. The structure is stressed, thus the upward deflection of the steel shell during the construction of backfill is a positive phenomenon [2]. The tests have confirmed that the most hazardous phase of the work of soil-steel structures is the construction process. Another regularity relates to the change of shape of the structure. It is confirmed by the displacements measured at points 7-11. After placing layer XXV, the displacement at point 7 reached -5.09mm, whereas at point 8, the upward deflection of 6.82mm occurred. Deflections measured at point 9 were -3.67mm and -39.75mm at point 10. The largest deflections recorded at point 11 reached -54.29mm. The structure did not deflect in the manner anticipated. This may be evidence for the improper construction procedure. The survey conducted after 403 days from placing layer XXV revealed that measured deflection values increased. The recorded deflection reached the value of -17.23mm at point 7, -24.35 at point 8 and -43.06mm at point 9. The largest displacement, -71.48mm, moved from point 11 to point 10 located closer to the centre of the crown. It indicates that the shape of the structure changed to one closer to the anticipated shape.

Acknowledgement

Data concerning the studied structure were provided by courtesy of The Management Board of „ViaCon Polska Sp. z o.o.” company.

References

[1] MACHELSKI, CZ. *Deformation of steel shell and soil bridge structures during the backfilling process.* Geoinżynieria drogi mosty tunele, 2010.

[2] MACHELSKI, CZ. *Modelling of steel shell and soil bridge structures*. Dolnośląskie Wydawnictwo Edukacyjne, Wrocław 2008.

[3] JANUSZ, L. MADAJ, A. *Corrugated steel shell engineering objects. Design and execution.* Wydawnictwa Komunikacji i Łączności, Warszawa, 2007.

All references have been originally published in Polish.

TRANSCOM 2015, 22-24 June 2015
University of Žilina, Žilina, Slovak Republic

Measurement and comparison of coefficient of friction on selected road sections

[*]Peter Kotek,
[*]University of Žilina, Faculty of Civil Engineering, Department of Highway Engineering, Univerzitná 2, 01026 Žilina, Slovakia, peter.kotek@fstav.uniza.sk

Abstract. The article deals with the measurement of longitudinal coefficient of friction on the selected road sections. The measurements of the coefficient were done by two devices, the Skidometer BV11 owned by the Slovak Road Association and the TWO (Traction Watcher One) which is the property of Centre of Excellence, University of Žilina. The measurements were performed on selected road sections with different asphalt surface in order to examine the widest possible representation of asphalt mixtures used in Slovakia.

Keywords: Roughness, Pavement surface, Macrotexture, Microtexture, Measuring Equipment.

1. Introduction

There are many methods and equipments to measure roughness which give many different characteristics too. These various characteristics describe an actual value of roughness of the pavement surface. One of the equipment which provide information about roughness is continually working equipment for measuring longitudinal coefficient of friction. These equipment can be divided according to a measuring braking wheel into equipment with blocked wheel and equipment with constant sliding value less than *100 %*. Because of simplicity of the measurement many countries have developed their own equipment and therefore there are many different coefficients of friction. Naturally, results of the equipment on the same surface can be different. They are influenced especially by speed of measuring equipment and also by a type of the wheel, by its load, tire profile and tire pressure rating. Other factors affecting the results of the measurement are depth of water film, pavement surface temperature and calibration setting of the equipment. The greatest effect on the coefficient of the friction has texture of the pavement surface.

2. Texture of the surface

The texture expresses morphological structure of the prominences of material creating pavement surface. It is created by all the material firmly attached to the pavement surface. It forms basic element of interaction of a tire and pavement. All categories of texture, from micro-, macro- and megatexture, affect a contact surface of the tire with a pavement surface. Most frequently the texture is described by surface profile defined by coordinates [1]. It is a combination of prominences described by a wave length, which makes horizontal projection of prominences, and an amplitude showing vertical projection of irregularities within the scope.

The roughness of the pavement surface is often expressed by a non-dimensional coefficient of the skidding friction, which is defined as a relation of a tangential friction force F_T and a normal force F_W between a rubber tire tread and pavement surface [2]. The forces affecting rotating wheel are shown at figure 1.

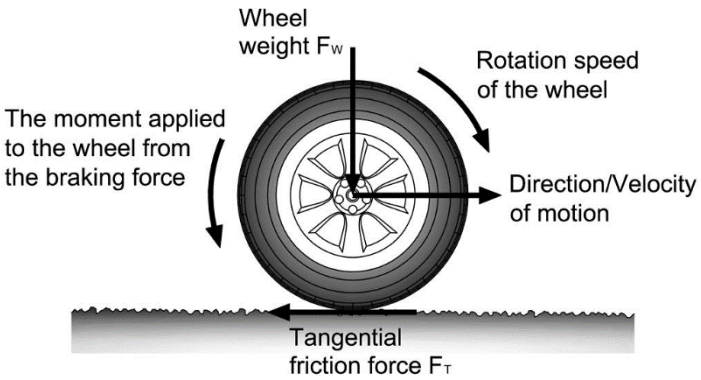

Fig. 1. Scheme of forces acting on rotating wheel.

The coefficient of the friction is most influenced by the pavement texture described by its microtexture and macrotexture. The pavement surface texture together with difference between macrotexture and mixrotecture id showed at figure 2.

Microtexture reflects tiny prominences on aggregate grains and describes how the grains are smooth or rough and therefore the friction between tyre and pavement surface rises. It is characterised by wavelength range from *0,001* to *0,2 mm* and amplitude range from *0,0* to *0,2 mm* [3]. Due to the range there is created impression of rough surface but microtexture is usually too soft to recognize it visually. Microtexture of aggregate surface issues elementary friction level and is important on dry surface by low speed up to *40 km/h*. Another important meaning lies in an interruption of continual water film and creation direct contact of tyre with pavement surface [3]. Values of microtexture are partially influenced by the ability of aggregates to keep sharp edges and so maintain rough surface which should resist to smoothing caused by truck traffic at longest. Microtexture is partly depended on composition of an asphalt mixture as mineralogical structure of aggregates, max grain size, percentage of small aggregates, and content and type of asphalt binding.

Macrotexture of pavement surface is responsible for basic drain ability of pavement. It represents irregularities on pavement surface and describes a way in which single aggregate grains are ordered. It is characterised by wavelength range from *0,25* to *10 mm* and amplitude range from *0,2* to *10 mm* [3]. It is important for fast water diversion from surface of wet pavement because the water acts as lubricant and it shows in the friction between tyre and pavement. Macrotexture plays serious role by middle and higher speeds of vehicle (over *40 km/h*). A good macrotexture can be get by suitable proposal of aggregates-mortar rate. It can be also achieved with proper combination of methods of final surface modification.

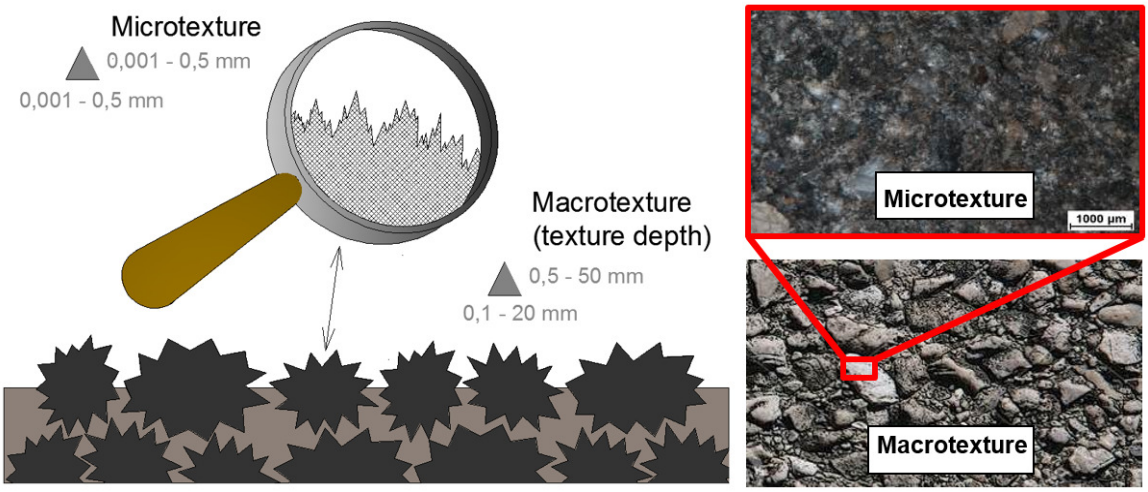

Fig. 2. Texture of pavement surface and differences between macrotexture and microtexture [4].

3. Equipment for measuring coefficient of the friction

3.1. Skiddometer BV11

Skiddometer BV11 is an equipment of Swedish producer (Airport Equipment Company AEC) in ownership of Slovak Road Administration showed at figure 3. Measurements on Slovak road net are performed with the equipment from *1998*. The measuring equipment is composed of an independent two-wheel trailer of the weight *360 kg* equipped by third independent measuring wheel. Thanks to a low constructional height of the equipment the centre of gravity is situated close to the pavement surface and therefore the measurements till *160 km/h* can be done. The equipment is usually pulled by a delivery car with opened bed (MERCEDES-BENZ Sprinter) which is set for transfer of a water tank and equipment itself. Skiddometer records a coefficient of the friction by record machine MI-90. The coefficient of the friction is described by measuring unit *Mu*. During measurement is a measuring wheel of the skiddometer braked and a size of skid ratio is *17%*. The constant value *17%* reflects the best braking effects of cars equipped by antiblock braking system (ABS) [5].

Fig. 3. Skiddometer BV11 together with towing vehicle.

The equipment gains a value of the coefficient of the friction through a tire with tread Trellerborg T 49 4.00-8 with tire pressure *140 kPa* and load of measuring wheel *1 kN*. The water film of *1 mm* is applied by a water pump and dosing machine for water closely in front of the measuring wheel. The trailer is equipped by sensors of longitudinal and vertical force, indicator of lengths and thermometer. The equipment can get local coefficient of the friction every two meters and also average for all the distance.

3.2. TWO – Traction Watcher One

TWO is a measuring equipment (figure 4) developed by a Norwegian company which is commonly used in northern countries for measurements on roads and airports with possible use on icy surfaces. The equipment is mounted directly on a vehicle by a mounting console. The console itself is put on a load machine and then gripped to vehicle body. The equipment is composed of a pair of wheels, referential and measuring wheel, together connected by a chain gear. The wheels are risen up during transportation, there is no need to stop while starting measurement because the wheels are lowered to the pavement surface. The measuring wheel is braked during measurement by a constant slide *17,8%*. The result of the equipment is directly a coefficient of the friction which can be get by speeds from *2* to *100 km/h* with load of measuring wheel *60 kg*. The measurements can be done on dry and wet surfaces too. By wet weather it is possible to put a water film of variable size from *0,1* to *1 mm* in front the second wheel through water pump [6].

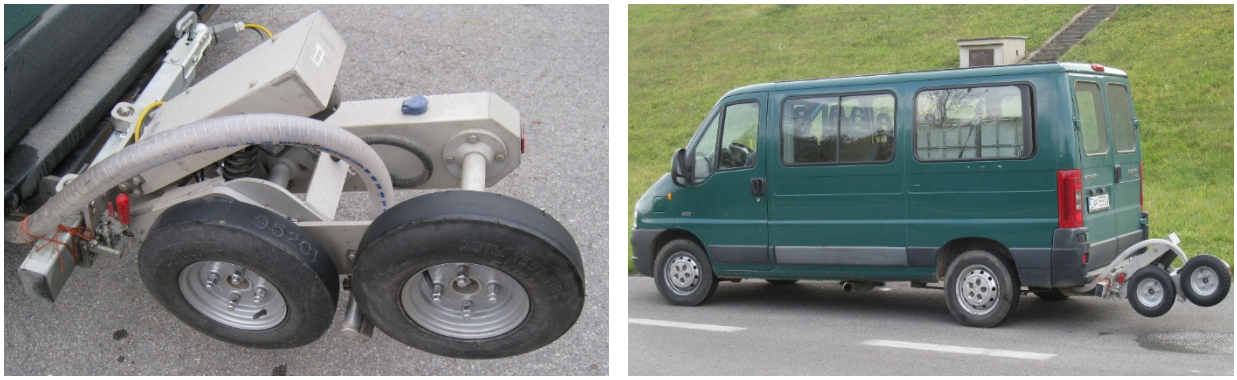

Fig. 4. TWO equipment.

Whole process of recording and measuring is managed by software delivered with TWO installed on laptop in car. The great advantage of the equipment is real-time monitoring of measured values and after finishing of the measurement it enables immediate report of values of coefficient of the friction on the whole section. Values of the coefficient of the friction can be recorded with step *0,5 m* depending on the software. The equipment is equipped with another sensors which register pavement surface temperature, air temperature, air humidity and also location by GPS. During measurement software environment enables a detection of optimal, warning and emergency values by graphic and sound signal depending on their setting.

4. Results analysis

Measurements by both equipment were made on ten different roads, to the greatest possible capture of used asphalt surfaces. These surfaces were different by composition of the asphalt mixture (type of binder and aggregates, grading curve), age and intensity of traffic. The values of the macrotexture expressed by parameter *MTD* (Mean Texture Dept), which is an evaluation output of volumetric method (STN EN 13036-1), ranged from *0,43* to *1,31 mm*. To capture the state of microtexture on the aggregate surface the British Pendulum Tester was used. The values of microtexture of aggregates were obtained by the tester because of the energy loss of the rubber foot after driving over a specified length of the road surface (STN EN 13036-4). Values of microtexture described by dimensionless parameter *PTV* and they ranged from *37* to *65* units on the individual sections.

The measurement of the coefficient of friction was made by three types of tires as described at figure 5: the tire with tread of Trelleborg T49 and smooth tire of ASTM E-1551. The measurement by Skiddometer BV11 was proceeded with tread design of Trelleborg T 49 4.00-8. All measurements were done by the speed of *60 km/h* due to safety.

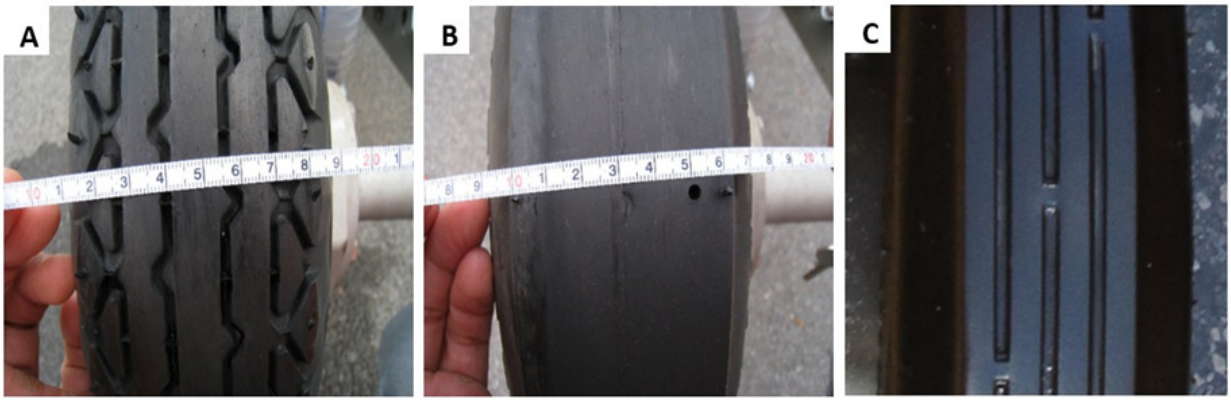

Fig. 5. Use of the tire A) Trelleborg T49, B) ASTM TESTER TIRE E-1551, C) Trelleborg T 49 4.00-8.

We can say that a very high level of correlation rate is between measurements results thanks to the reached value of the coefficient of correlation *(r)* between equipment Skiddometer BV11 and TWO for tire with tread design *r=0,901* and *r=0,906* for smooth tire (fig. 6).

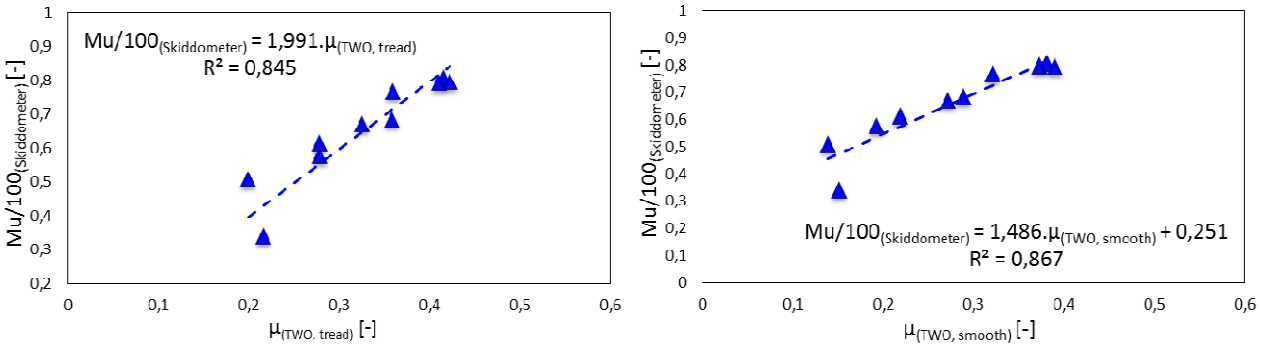

Fig. 6. Comparison of Skiddometer and TWO equipment with tread (left) / smooth (rigth) design.

Relations between the equipment used on Slovak roads for many years and the TWO equipment can be determined because of the reached results. The reached coefficient of determination speaks about credibility these relations between the equipment Skiddometer BV11 and TWO for a tire with tread design $R^2=0,812$ and for smooth tire $R^2=0,756$. Its value says about a scale how variability of first variable determines variability of second variable. In the future it is possible count Mu values and specify if the surface is suitable or not according to skid resistance measured by Skiddometer BV11. In Slovakia the technical rule TP 14/2006 is used for evaluation of skid resistance by Skiddometer BV11.

Two types of tires (tread or smooth) were used by measurement with TWO and therefore it is possible to do mutual comparison of measured values of the coefficient of friction. From the measured values it is clear that the values measured by smooth tire are lower than the values by tire with tread design. The differences moved in scale from *6* to *27* percent depending on the pavement surface when compare with tread tire. In average the values measured by smooth tire were smaller for *17* percent.

The differences between measured values of the coefficient of friction by smooth tire to tire with tread design are caused by insufficient of pushing out water from contact area of tire with pavement. Measurement of the coefficient of friction with smooth tire is more insensitive to the values of aggregates microtexture and is more influenced by drainage features of pavement surface macrotexture.

By comparing measured values of the coefficient of friction with tread and smooth tire it is possible to determine transfer relation for the coefficient of friction between these two types of tire (fig. 7).

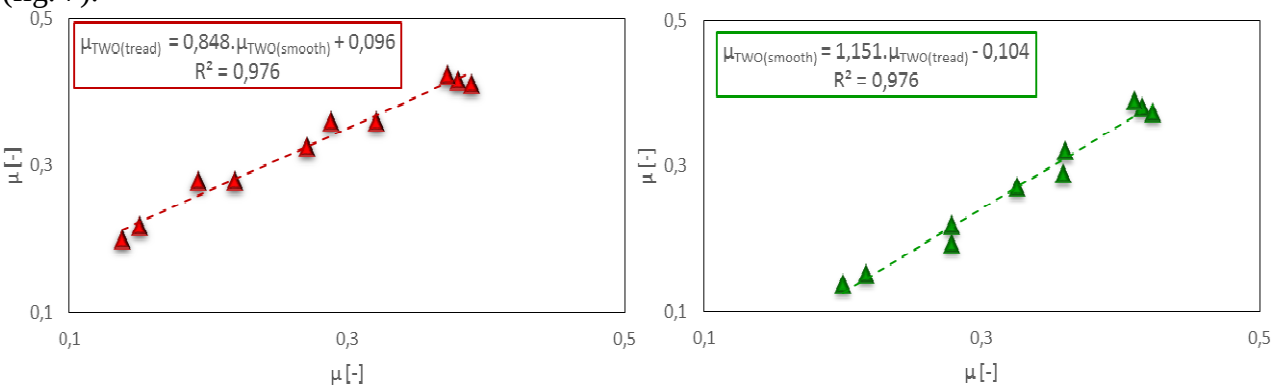

Fig. 7. Comparison between tread and smooth tire by TWO equipment.

The reached coefficient of determination between tread and smooth tire with value of $R^2=0,976$ speaks about importance of the transmissive relation and also a fact that the measurements itself were done on ten different asphalt surfaces.

5. Conclusion

The article spoke about the comparison of the coefficient of friction obtained by two measurement equipment, Skiddometer BV11 used on Slovak roads and TWO equipment. The results by TWO were on average about 47 percent lower than by Skiddometer BV11 depending on the character of the surface. It can be caused by different measurement and evaluation method between the equipments but also by calibration settings itself. The TWO equipment used settings from producer and the Skiddometer BV11 used settings from road databank. Very good correlation follows from the results.

The TWO equipment has many improvements to Skiddometer BV11 as measurement of pavement surface temperature, editable width of water film, possibility to change load of the measured wheel. Great advantage is immediate monitoring of measured values and their fast report or export to excel format for following processing. Last but not least, can be Values of the coefficient of the friction already recorded with step *0,5* m depending on the software

Acknowledgement

The paper is a result of the research supported by the research project VEGA 1/0804/12 Influence of material composition of asphalt on characteristics of pavement surface texture, noise emission and air pollution

The paper is a result of the research supported by the research project VEGA 1/0557/14 The influence of selected characteristics on asphalt pavement serviceability

References

[1] Čelko J. a kol.: The surface properties of pavements, in Slovak: Povrchové vlastnosti vozoviek (Prevádzková spôsobilosť vozoviek), EDIS Žilina, 2000. ISBN 80-7100-774-9

[2] Kováč M. a kol.: Diagnostics of serviceability parameters of pavements, in Slovak: Diagnostika parametrov prevádzkovej spôsobilosti vozoviek, EDIS Žilina 2012. ISBN 978-80-554-0568-1

[3] STN EN ISO 13473-5, , Characterization of pavement texture by use of surface profiles. Part 5: Determination of megatexture, in Slovak Charakterizovanie textúry vozovky s použitím profilov povrchu. Časť 5: Stanovenie megatextúry (ISO 13474-5:2009)

[4] Kováč M, Kotek P.: The usability of different Skid resistance characteristics in Road Assessment. Civil and Environmental Engineering. Volume 10, Issue 2, Pages 80–87, ISSN (Online) 1336-5835, DOI: 10.2478/cee-2014-0015, December 2014.

[5] TP14/2006, Measurement and evaluation of skid resistance using the device SKIDDOMETER BV11 and PROFILOGRAPH GE, in Slovak: Meranie a hodnotenie drsnosti vozoviek pomocou zariadení SKIDDOMETER BV11 a PROFILOGRAPH

[6] Operating manual: TWO friction meter (Traction Watcher One). Olsense Technology AS, VAT reg. No.: 991 206 604

TRANSCOM 2015, 22-24 June 2015
University of Žilina, Žilina, Slovak Republic

Porosity Structure and Frost Resistance of Concretes Air-Entrained by Polymer Microspheres

[*]Wioletta Kozak
[*] Kielce University of Technology, Faculty of Civil Engineering and Architecture, Department of Technology and Engineering, Institute of Technology and Precast Concrete, Al. Tysiąclecia Państwa Polskiego 7, 25-314 Kielce, Poland, wioletta88kozak@gmail.com

Abstract. Obtaining concrete with a specific air-pore structure parameters under laboratory conditions is not usually a problem. However, difficulties begin in industrial conditions, because there are significant problems with the stabilization of the pore system in time. For this purpose the polymer microspheres were used. They allow closing in concrete time-stable air voids of defined dimensions that have not combined with each other. The aim of this study was to determine the composition of air-entrained concrete with predetermined air-pore structure parameters of air-entrained concretes and their frost resistance.

Keywords: air-entrainment, frost resistance, polymer microspheres.

1. Introduction

A basic method that protects concrete from the harmful effects of water, frost and de-icing salt is proper air-entrainment of concrete mixture. According to requirements laid down in PN-EN 206-1 standard [1] at least 4% of air should be introduced to the concrete mix. Unfortunately, not only the volume of air-entrained, but also the parameters of the pore structure, such as: the spacing factor, the content of micropores and the specific surface of air void system, decide about obtaining frost resistance [2]. To ensure freeze-thaw resistance, it is essential to provide a time–stable system of small air bubbles A_{300}, which are located close enough to one another L, at the lowest possible total air content A. Polish standards do not specify these parameters. Approach to the problem in the Danish, German and Austrian standards gives Glinicki [3]. The first document in Poland, which specifies the requirements for these parameters is "Technical requirements for concrete pavements" [4]. According to this document the frost-resistant concrete has a spacing factor L smaller than 200 μm and the content of micropores greater than 1.5%. Obtaining concrete with such a specific air-pore structure parameters under laboratory conditions is not usually a problem. However, difficulties begin in industrial conditions, because there are significant problems with the stabilization of the pore system in time, what is affected by many factors (such as: admixtures and additives, consistency and temperature of the concrete mix, transport and mixing time and type of the concrete mix placing and compaction). Taking into account a large number of factors that affect the quality of air-entrainment, it may happen that air-entraining agents will not generate the required air-pore structure. The pores may connect with each other and may have irregular shapes, which is shown in the figure 1. The result is that distance between adjacent air voids increases. The consequence of this is the increase in the distance, which the freezing water will have to travel from any point of the cement paste to the nearest edge of the air void, measured along the cement paste (spacing factor L), with no apparent change in the total air content A [5]. Similar conclusions were reached by Pleau et al [6], whose results show a weak correlation between the total air content A and spacing factor L. This means that satisfactory air content does not guarantee the proper spacing factor L, which is the main parameter to evaluate the quality of air-entrainment. Therefore, the air-void structure in air-entrained concrete cannot be assessed on the basis of simple measurements of the air content in the concrete mix, but the quality control of air-entrainment, which consists of microscopic evaluation of that structure in the hardened concrete, is required.

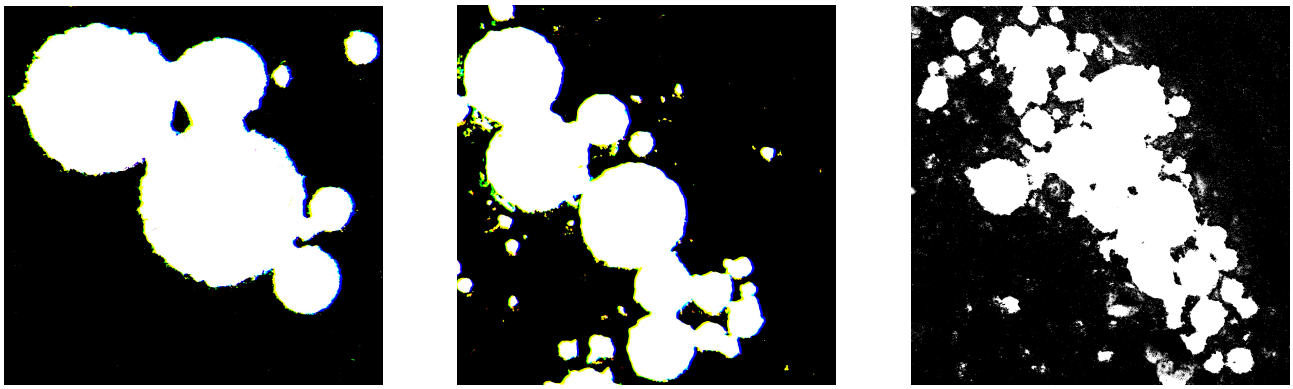

Fig. 1. View of complex pore arrangements in air-entrained concretes.

Research in development of design and diagnosis of air-entrained concretes with a given porosity structure are carried out in the Department of Concrete Technology at Kielce University of Technology. In the following part of the paper the results of the study (designed to determine the composition of air-entrained concrete with predetermined porosity parameters and frost resistance) will be presented.

2. Research description and the analyze of results

The aim of this study was to determine the composition of air-entrained concrete with predetermined air-pore structure parameters of air-entrained concretes and their frost resistance. To make the analyzed concretes the following materials were used: white cement, basalt aggregate, natural sand, water, plasticizer and polymer microspheres D40. The microspheres allow closing in the concrete time-stable air voids of defined dimensions that have not combined with each other, eliminating some of the problems mentioned in the previous section [5]. It was decided to use white cement to increase the contrast between the cement paste and the air pores, because during the microscopic measurement the small pores are difficult to observe and white cement, through appropriate grout coloring, allows better separation of them from the background. The output concrete composition was developed, which then was modified by different doses of microspheres. The exact composition of the tested concrete is presented in Table 1. Concrete mixes were made in a blender with forced mixing. Concrete volume was about 14 dm^3. Portion of the water was added to the dry ingredients, and the remaining amount of water was mixed with microspheres and added to the other components. In order to obtain consistency S3 plasticizer was also added. The mixing time was about 3 minutes.

Concrete	Cement [kg/m^3]	Water [kg/m^3]	Aggregate [kg/m^3]	Plasticizer [kg/m^3]	MSF D40 [kg/m^3]	Density [kg/m^3]
B1	376.1	169.3	2082.0	392.9	-	2627.4
B2	372.2	167.5	2060.5	585.7	0.148	2600.2
B3	367.4	165.3	2033.8	578.6	0.334	2566.6
B4	365.8	164.6	2025.0	585.7	0.594	2555.4

Tab. 1. Compositions of concretes air-entrained by polymer microspheres.

After mixing the measurements of density and consistency were made. The determination of total air content with the pressure method, in case of the use of microspheres, is impossible. Next

samples were formed for further study to determine the air-pore structure parameters and frost resistance. From the sample two plates, which were subjected to grinding and polishing, were cut out. On thus prepared surfaces the pore structure parameters were determined in accordance with PN- EN 480-11 [2] and the obtained results are shown in Table 2.

Concrete	A [%]	A_{300} [%]	L [mm]
B1	1,27	0,21	1,117
B2	2,40	0,33	0,452
B3	1,02	0,42	0,207
B4	1,52	0,63	0,167

Tab. 2. Air-pore structure parameters for the studied concretes.

For the analysis a set consisting of computer with software, optical microscope Nikon SMZ 800, measuring table Prior with the Sony camera was used. Investigations were conducted at the Optical Microscopy Laboratory of the Construction Technology and Organization Department at the Kielce University of Technology. Frost resistance tests were performed on the 8 x 8 x 35 cm beams, frozen in water on a 12-hour cycle. Figure 2 presents the results of deformation changes and figure 3 the results of mass change for the air-entrained concretes.

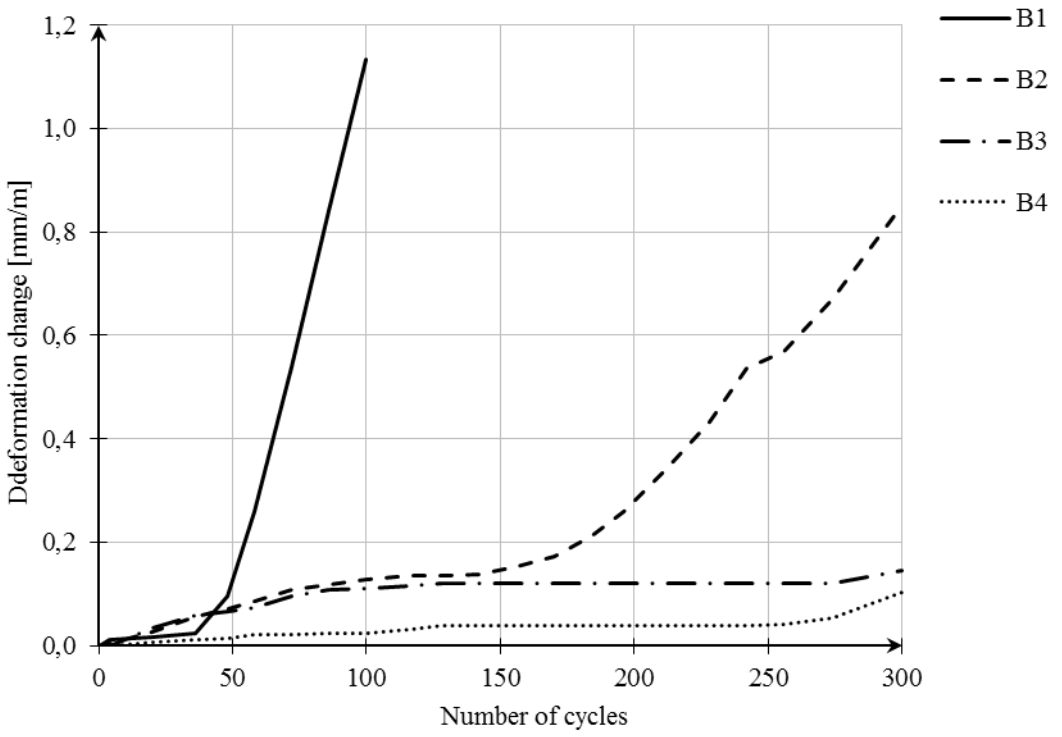

Fig.2. Elongation of samples with D40 microspheres.

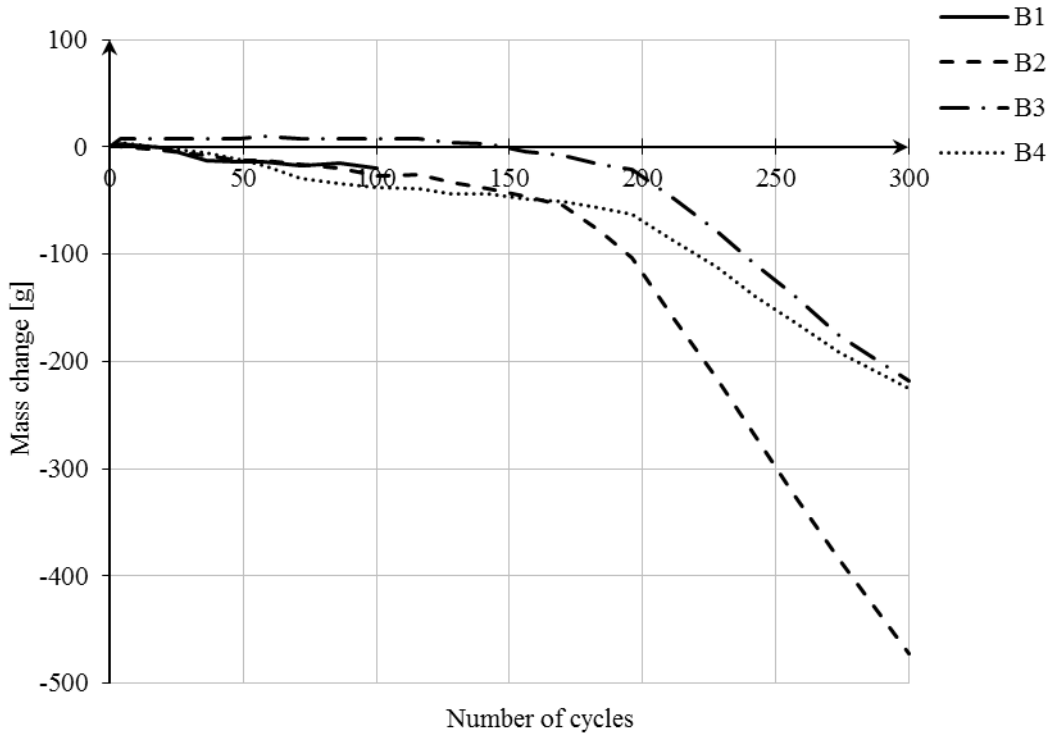

Fig.3. Mass change of samples with D40 microspheres.

After 300 cycles of freezing it turned out that concretes B1 (A = 1.27 %, A_{300} = 0.21 %, L= 1.117 mm) and B2 (A = 2.4 %, A_{300} = 0.33 %, L= 0.452 mm) are not frost resistant – increments of deformation were greater than 0.2 mm/m (respectively 1.133 mm/m and 0.851 mm/m). While with very good resistance to frost stood out concretes B3 (A = 1.02 %, A_{300} = 0.42 %, L= 0.207 mm) and B4 (A = 1.52 %, A_{300} = 0.63 %, L= 0.167 mm), where the increments of deformation were respectively 0.145 mm/m and 0.104 mm/m. All series of concretes recorded significant decreases in mass (Figure 3), which indicates a lack of resistance to surface flaking. Based on microscopic examination it was proved that concrete with a total air content A and the content of the micropores A_{300} a lot smaller than the recommended values may also be frost resistant. It all depends on the pore structure and their uniform distribution in space grout.

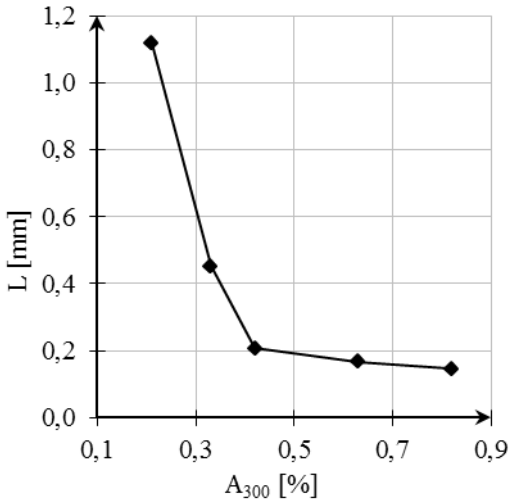

Fig. 4. The relationship between the spacing of the bubbles and the content of micropores.

Designing the composition of concrete with a given porosity structure the primary task is to determine the value of L, A_{300} and A. Assessed the studies performed, it was found that to achieve

L = 0.200 mm, the content of micropores A_{300} = 0.43%, as shown in Figure 4. To obtain the A_{300} = 0.43% a dose of microspheres of about 0.335 kg/m^3 is necessary (Figure 5).

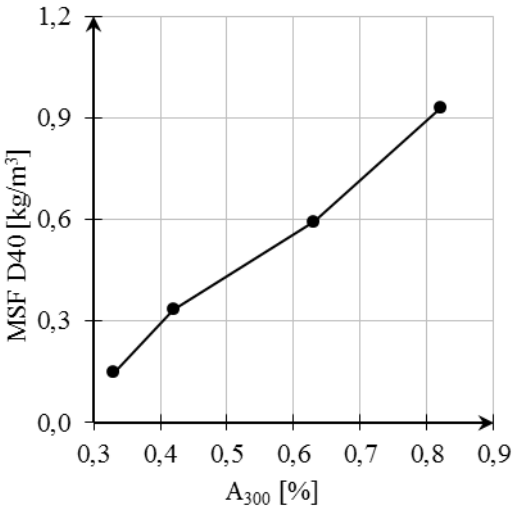

Fig. 5. The relationship between the content of micropores and the amount of microspheres D40.

3. Conclusions

The aim of this study was to determine the composition of concrete air-entrained with polymer microspheres D40 with predetermined parameters of the pore structure and its frost resistance. It is widely recognized that the frost-resistant concrete has a spacing factor L smaller than 200 μm and the content of micropores greater than 1.5%. Performed analysis shows that even with a content of micropores A_{300} = 0.43%, which corresponds to the dose of the microspheres of about 0.335 kg/m^3 properly air-entrained concrete can be achieved with L ≈ 0.200 mm, which linear deformations are smaller than 0.2 mm/m. It is therefore apparent that the proper air-entrainment, and thus the frost resistance of concrete, depends not on the total amount of air introduced into the concrete, but on the smallest pore structure and their uniform distribution in space of cement paste. Using polymer microspheres as an air-entraining agent we have better, but not total, control of the air pore system in concrete, because they allow closing in concrete time-stable air voids of defined dimensions that do not combine with each other. Work on this way of protecting concrete from the harmful effects of water is being continued.

References

[1] PN-EN 206-1:2003-1. *Wymagania, właściwości, produkcja i zgodność*.

[2] PN-EN 480-11:1998 *Domieszki do betonu, zaprawy i zaczynu. Metody badań. Oznaczenie charakterystyki porów powietrznych w stwardniałym betonie.*

[3] GLINICKI M.: *Europejskie wymagania na beton napowietrzony w klasie środowiska XF*, Drogownictwo, nr 3, 2005, s.86-88.

[4] *Wymagania techniczne dla betonowych nawierzchni drogowych*, Etap III, IBDiM, Warszawa, 2010.

[5] WAWRZEŃCZYK J., MOLENDOWSKA A., *Use of microspheres as an alternative method of concrete air-entrainment*, Budownictwo-Technologie-Architektura, No. 4/2011, pp. 51-55.

[6] PLEAU R., PIGEON M., LAURENCOT J.L., *Some findings on the usefulness of image analysis for determining the characteristic of the air-void system on hardened concrete*, Cement and Concrete Composites, V. 23, 2001, pp. 237-246.

TRANSCOM 2015, 22-24 June 2015
University of Žilina, Žilina, Slovak Republic

Decision methods used in Pavement management system

[*]Matúš Kozel, [**]Ján Mikolaj
[*]University of Žilina, Faculty of Civil Engineering, Department of Construction Management, Univerzitná 8215/1, 01026 Žilina Slovakia, matus.kozel@fstav.uniza.sk
[**] University of Žilina, Faculty of Civil Engineering, Department of Construction Management, Univerzitná 8215/1, 01026 Žilina Slovakia, jan.mikolaj@fstav.uniza.sk

Abstract. The article summarizes the progress of decision method used in pavement management system on network level and examines theoretical problems surrounding the prioritization process in condition of Slovak Republic. Here is also described prioritization methods with classification of difficulty of decision model formalization and data need.

Keywords: Decisions methods, Optimization, Network level, Pavement Management System, Economical effectiveness.

1. Introduction

Road infrastructure, as one of the main parts of the transport system, is always loaded by traffic. It causes constant process of pavement performance deterioration. This process is increased by the influence of transport. Therefore, one of the main objectives is to maintain existing communication in working order, using the specified funds. This objective can be achieved, in particular the application of an appropriate repair and maintenance strategy, using the decision-making methods.

Pavement management system (PMS) implemented a procedure that includes the diagnosis of individual parameters, determination of requirements for repair and maintenance, resource optimization and prioritization of individual sections, given for the time of the intervention to achieve the highest possible efficiency.

Decision-making methods used in the PMS gradually evolved from simpler subjective decision-making processes to optimization based on cost effectiveness. They are used primarily to establish the order of urgency, repair and maintenance of the sections, which make the decision-making process one of the most important operations in PMS.

2. Decision methods

These methods used in PMS cover the whole spectrum of methods and evaluation procedures, from simple lists of roads, arranged according to the judgment of the competent person, to complex optimization models. The main objective is to achieve optimum, thus get the most benefit with the use of scarce resources.

As load of communications increases, the need to increase the efficiency of the budget allocation is still growing. This causes that the development of decision-making methods is increasing of their complexity. The very process of development decision-making methods is shown in Table 1.

Shortly, according to development are decision methods divided into:

- Index methods
    - composite index rating method
    - method of economic evaluation

- Optimization Methods
- Programming Techniques of Artificial Intelligence

S.N.	Classification	Advantages / Disadvantages
1	Simple, judgment based subjective ranking overall condition index of decreasing first cost	Simple, quick, with bias and inconsistency, may be far from optimal solution
2	Ranking of parameters, such as serviceability or distress, can be weighted by traffic	Simple and easy to use, may be far from optimum, particularly if traffic weighting not used
3	Ranking based on condition analysis and traffic, with economic analysis	Reasonably simple; may be closer to optimum
4	Annual optimization by mathematical programming model for year-by-year basis over analysis period	Less simple; may be close to optimum; effect of timing not considered
5	Approximate optimization using heuristics including benefit-cost ratio and marginal cost effectiveness	Reasonably simple; suitable for microcomputer environment; close to optimal results
6	Comprehensive optimization by mathematical programming model taking into account the effects of maintenance, rehabilitation and reconstruction timing	Most complex and computationally demanding; can give optimal program (maximization of benefits)

Tab. 1. Different categories of decision-making processes [1].

2.1. Composite index rating method

Evaluation based on index priority, calculated from parameters such as road conditions, driving quality, traffic parameters, economic analysis, accidents, possible shortcomings geometric lines, age of road, roughness and so on.

- It should not be based only on the current state. To streamline the use of forward-looking and communication status. The time interval between diagnosis and the very possibility of adjustment makes more complex organization of resources possible.
- There are known different methods of determining the composite index for road maintenance. The rules include unique methods to the theory of utility, Delphi method, theory of fog sets.

By Sharaf [2] states the calculation of the index classification as "(1),":

$$IP = \frac{Ap}{Fd * Fp}. \qquad (1)$$

IP - Index of priority
Ap- Extent of damage
FD- Transport factor
FP- Deterioration factor

Transport factor is based on the AADT (annual average daily traffic). Deterioration factor is defined according to the fault type and the extent of damage and is defined on a flat number of occurrences of faults in the monitored period [2].

2.2. Economic-based methods

These methods are based on the efficient use of resources and limited budget. The evaluation is based on certain priorities. According to the priority is divided into the following:

- priority of least life cycle cost,
- priority of worst condition,
- priority of traffic,
- priority of the highest ratio –proceeds / costs, NPV,IRR

(NPV- net present value, IRR- internal rate of return).

Using methods based on economic analysis will offer two basic variants of the yield-cost procedures. The first is that for cost are meant only agency costs and the second option is to calculate the road user costs. (fig.1)

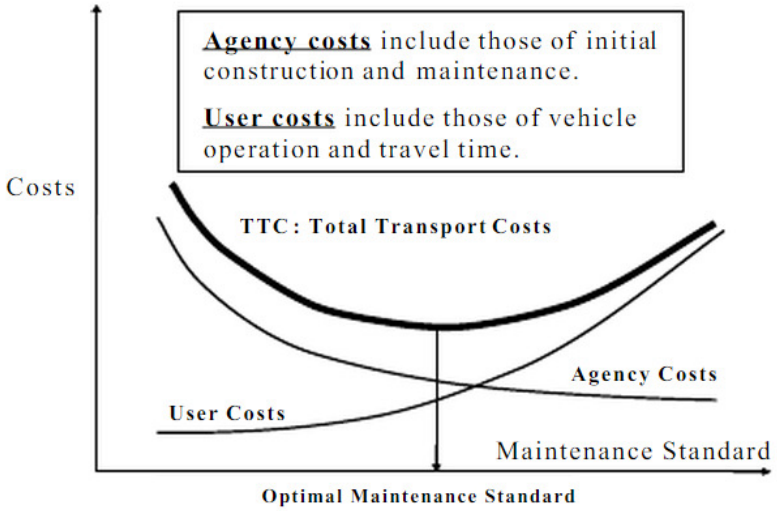

Fig.1 Trade-off between agency costs and user costs.

However, both cases are based on economic assessment of individual treatments, repair or maintenance. In the options are always present an alternative to "do nothing" (not to carry out repairs to the reconstruction) and several options like "do something" (perform repair / maintenance by assessing the current state).

Economic based decision method is also used in Slovak PMS. It is based on priority of the highest ratio –proceeds / costs, expressed in NPV and IRR. One of the constrains is that the road classified in the worst condition must be repaired before other one in good condition but higher IRR or NPV.

2.3. Optimization methods

Optimization is constructed with deterioration functions (degradation curves of each variable parameter). The goal of optimization is to choose the best maintenance strategy for each parameter to achieve the lowest level of spending funds in proportion to the extended lifetime parameter to the next renewal.

In mathematical terms, in this case, optimization considers programming technique that is used to compensate the limited resources to maximize the return.

In the context of optimization, we distinguish two types of mathematical programming and it is direct optimization and heuristic optimization

Direct optimization in itself includes programmable mathematical methods to try and find the optimal conditions for appropriate solutions.

Use the following optimization techniques:

- Linear programmed
- Nonlinear Programming
- Integral programming

- Variables (dynamic) programming

We use in preference heuristic optimization to direct optimization in cases where the extensive mathematical model or use computer data processing is not necessary. Heuristic optimizations are less demanding, faster and easier. They offer optimal conditions and approaches in determining the acceptable accuracy for practical output. One of the known heuristic techniques is Incremental Benefit Cost Technique [3].

2.4. Artificial Intelligence Techniques

Artificial intelligence techniques include expert systems, artificial neural networks, fuzzy logic, genetic algorithms, and hybrid systems. These techniques are particularly appropriate for pavement management because the information may be uncertain and incomplete. The data may involve combinations of objective measurements, subjective rating, and expert inputs, such as those data used to create maintenance, rehabilitation and reconstruction decision criteria and policy tables. They either represent alternative approaches to existing systems or collaborate to make the overall system more efficient. Artificial neural networks and fuzzy systems have been used for needs analysis as alternatives to the traditional priority ranking tools, such as decision trees [4].

3. Conclusion

One of The main aims of this paper was to inform about the pavement maintenance methods used in pavement management system on network level and examines theoretical problems surrounding the prioritization process in condition of Slovak Republic. We can consider that it is still important to incorporate more advanced mathematical techniques to pavement management system.

Acknowledgement

This article was created with the support of the OP Research and development for the project "Centre for Research in Transport" (ITMS 26220220135) co-financed from the European Regional Development Fund.

"We support research activities in Slovakia / project financed by EU funds".

References

[1] Haas, R.C.G., Hudson, W.R. and Zaniewski, J., “Modern Pavement Management”, Krieger Publications, Malabar, Florida, 1994.

[2] Sharaf, E., “Ranking Versus Simple Optimization in Setting Pavement Maintenance Priorities: A Case Study from Egypt”, Transportation Research Record 1397, Transportation Research Board, Washington, D.C., 1993.

[3] MOROSIUK, G. a kol. *HDM – 4 HIGHWAY DEVELOPMENT & MANAGMENT: Applications Guide* La Defénse Cedex, France, The Road Association (PIARC) on behalf of them ISOHDM sponsors, 2006, ISBN 2-84060-058-7

[4] Shah U. Y. a kol., 2nd Internacional Conference on Emerging Trends in Enginering & Technology, A Critical Review of Prioritization Models for Pavment Maintenance Management Decisions, Teerthanker Mahaveer University, Collage of Engineering, 2013

TRANSCOM 2015, 22-24 June 2015
University of Žilina, Žilina, Slovak Republic

Temperature dependence of the specific heat of dry homoionic forms of bentonites from Wyoming (SWy-2) and Texas (Stx-1b)

[*]Tomasz Kozlowski, [*]Anna Rusin
[*]Kielce University of Technology, Faculty of Environmental Engineering,
Geomatics and Power Engineering, Department of Geotechnical and Water Engineering,
al. Tysiąclecia Państwa Polskiego 7, 25-314, Kielce, Poland, {tomkoz, arusin}@tu.kielce.pl

Abstract. The specific heat of Ca^{2+}-, Na^{+}- and K^{+}-forms of bentonites from Wyoming (SWy-2) and Texas (Stx-1b) has been determined in the range between −150°C and 100°C by use of Quasi Isothermal Modulated Differential Scanning Calorimetry. According to expectations, a strong temperature dependency is observed. A proposed simple power function model can predict specific heat of montmorillonites with the standard error of the estimate SEE equal to 0.038 $Jg^{-1}K^{-1}$.

Keywords: specific heat, bentonite, homoionic, temperature dependence, QI-MDSC.

1. Introduction

Knowledge of soil thermal properties is very important for a variety of engineering and scientific applications, such as predicting frost depth, the numerical simulation of the heat and mass transfer phenomena, modelling the heat exchange at the ground surface or the geothermal gradients. Moreover, the determination of the specific heat of a dry soil material is crucial for the investigation of the phase change phenomena in soil-water systems by calorimetry, including the unfrozen water content. The heat capacity of a material, being a thermodynamically well-defined quantity, is also the basis for determination of other thermodynamic quantities such as the enthalpy and entropy changes.

Despite this, there is very little data on the temperature dependence of the specific heat of dry soil material of various types and origin. As a rule, the available data are given for a “soil” in general and some results of the specific heat measurements suggest that the effect of the type of soil is not statistically significant. Also, the effect of the temperature is described as “moderate” and the values oscillate between 0.78 $Jg^{-1}K^{-1}$ at 20°C and about 0.66 $Jg^{-1}K^{-1}$ at −40°C [2].

Yet, the change of the specific heat of different clays and clay minerals with the temperature was measured by a number of researchers. For example, Wolfe and Thieme [8] measured the specific heat of a dry, not identified clay at several temperatures down to −180°C, obtaining a nonlinear decrease from 0.92 $Jg^{-1}K^{-1}$ at 30°C to 0.34 $Jg^{-1}K^{-1}$ at −180°C. Kay and Goit [3] found the specific heat varying linearly with temperature from -73°C to 27 °C. They obtained 0.75 $Jg^{-1}K^{-1}$ at −15°C and 0.88 $Jg^{-1}K^{-1}$ at +10°C. Robie and Hemingway [6] found the temperature dependency nonlinear and the values of the specific heat relatively high (for example: 0.96 $Jg^{-1}K^{-1}$ at 30°C and 0.38 $Jg^{-1}K^{-1}$ at −150°C). The explanation could be the samples were not dried properly and some forms of the adsorbed water may not be removed, so the values of the specific heat could have included the adsorbed water component. Kozlowski [5] reported the temperature dependence of four homoionic forms of bentonite from Chmielnik between −70°C and +30°C. The results were obtained by Modulated Differential Scanning Calorimetry at a relatively high scanning rate, in strongly unsteady conditions.

Quasi Isothermal Modulated Differential Scanning Calorimetry (QI-MDSC) may be a more suitable method for specific heat measurements because of the lack of smearing of results due to the continuous change of temperature during the experiment.

2. Experimental

In the Differential Scanning Calorimetry method (DSC), the temperature of a specimen changes linearly in time, while in the Modulated Differential Scanning Calorimetry method (MDSC), on the linear plot of temperature the sinusoidal one is overlapped. It provides measurement of the sample's heat capacity simultaneously with the total heat capacity. Yet, there is a measuring error related to the continuous change of temperature, which makes the system permanently thermally unstable. To measure the heat capacity avoiding this problem, the Quasi Isothermal Modulated Differential Scanning Calorimetry method (QI-MDSC) was used. In this method, temperature does not change linearly, but oscillates between two values. At low amplitudes of modulation (normally between 0.01 and 0.5 K), the temperature is almost constant.

The TA DSC Q2000 differential scanning calorimeter with a liquid nitrogen cooling system (LNCS) was used in the experiment. The LNCS reaches a temperature range of -180 to 550°C.

After weighing an aluminium pan, a bentonite sample was put inside and the pan was closed. A pinhole was punched in the lid of the pan and the specimen was placed in the calorimetric cell. The temperature was set at a constant value of 110°C and the specimen was dried for 8 hours. During the drying process and the following experiment, the calorimetric cell was purged with dry helium at a flow rate of 25 ml/min. Next, after the equilibration at 100°C, the specific heat determination was done at every 10°C down to −150°C. The temperature modulation was ±0.26°C/min around each measured temperature for 10 minutes. After the experiment, the specimen was heated up to 20°C and the mass of the dry bentonite was determined. Three samples of each homoionic form were examined.

The specific heat calibration was done on the basis of sapphire examination in a mode identical to that described above. Sapphire correction factors were determined by comparing values of sapphire specific heat obtained from the experiment with ones from references. The measured values of the bentonites specific heat were multiplied by temperature related sapphire correction factors.

3. Materials

Homoionic (Ca^{2+}, Na^{+} and K^{+}) forms of bentonite from Texas (Stx-1b) and Wyoming (SWy-2) were used in the research. The forms were fabricated by the repeated saturation of the fraction less than 0.063 mm with an appropriate chloride and the subsequent purifying from chlorine anion by diffusion, until the disappearance of the characteristic reaction with $AgNO_3$. The soil pastes were then air-dried at room temperature.

4. Results and analysis

In order to examine the nature of the size-temperature effect on the specific heat of the homoionic clays, a model in the following form was fitted to the experimental data for all the six homoionic forms:

$$c_p = a(T + 273.15)^{cF^d} \quad (1)$$

where F is the content of the fraction < 2 μm, %, and T is the temperature, °C.

The estimates of the coefficients are as follows: a = 0.59959, b = -1.13976, c = 0.25100, d = 0.31378, and the correlation coefficient R = 0.98595742.

An obvious feature of (1) is that the specific heat approaches zero value at the temperature of absolute zero (−273.15 C°), which satisfies the requirement being a consequence of the application of the third law of thermodynamics to any crystalline material. In view of the presented results, it appears that if precise data on the temperature dependency of the specific heat of bentonite are needed, an empirical relationship should be established in every case. Alternatively, using (1) seems

a reasonable solution as it was obtained by the analysis of 486 data points related to six different homoionic forms of two different natural montmorillonites.

However, in most applications it is possible to accept an error of estimation of the order of, say, 0.1 $Jg^{-1}K^{-1}$ and then some more general formulas can be used.

Winter and Saari [7] proposed the following empirical formula for the temperature dependence of the specific heat of minerals:

$$c_p = a(T + 273.15)^{0.5} + b(T + 273.15) + c(T + 273.15)^{1.5} \quad (2)$$

where T is temperature, ^oC.

By combining data on igneous rocks, quartz, magnesium silicate, calcium feldspar and silica glass, the following values for the constant coefficients were obtained [7]: a = −0.034, b = 0.008, c = −0.0002. According to the authors, the formula is valid "for temperatures in the range of a few tens of degrees Kelvin to 400^{o}C", i.e. approximately between −220^{o}C and +130^{o}C.

A still more unconstrained approach was demonstrated by Kay and Goit [3] who proposed to use a simple linear formula

$$c_p = m(T + 273.15) \quad (3)$$

where the proportionality constant *m* can be predicted on the base of data point related to any temperature.

The application of these two models to the present data yields different results. Equation (2) exhibited very well fitting (R = 0.991), but the estimate of the coefficient *a* appeared statistically insignificant. In turn, according to expectations, the fitting of (3) was poor, independently of the temperature at which the value *m* was determined. It seems that in the case of bentonites the fully statistically significant at $p < 0.001$ fitting may be provided by a simple power equation in the following form:

$$c_p = a(T + 273.15)^b \quad (4)$$

The values of the constant coefficients have been determined by use of the nonlinear estimation method for all the results without the distinction of the kind of the main exchangeable cation. The estimates of the coefficients are as follows: a = 0.012187, b = 0.736304, and the correlation coefficient R = 0.97322328. The fitting of the model is shown in Fig. 1. The standard error of the estimate SEE (i.e. the sum of squares error) for this model is equal to 0.038 $Jg^{-1}K^{-1}$ and the maximum residual equals −0.091 $Jg^{-1}K^{-1}$.

The results in Fig. 1 represent the decrease in the specific heat with temperature to near zero values at temperatures close to zero degrees Kelvin (0.067, 0.041 and 0.014 $Jg^{-1}K^{-1}$ at 10 K, 5 K, and 1 K, respectively). For solids, such a behaviour is predicted both by the Debye and the Einstein models. Numerous attempts to apply the Debye model for minerals led to conclusion that only few minerals can be put in category "Debye-like minerals" (e.g. MgO, Al_2O_3, MgSiO3 perovskite, and olivine, according to Anderson, 1998). For this group, the specific heat can be calculated from data on acoustic sound velocities, ignoring the optic properties [1]. As pointed by Kiefer [4], "the Debye model does not account for the measured calorimetric properties of minerals because it does not allow for anisotropy of elastic parameters, dispersion of lattice waves at Brillouin zone boundaries, and low and high frequency modes arising from optic vibrations". In the temperature region considered in the present experiments, i.e. far above a few degrees Kelvin, the measured values of the specific heats of a mineral as complex as montmorillonite show strong deviations from Debyelike calorimetric behaviour.

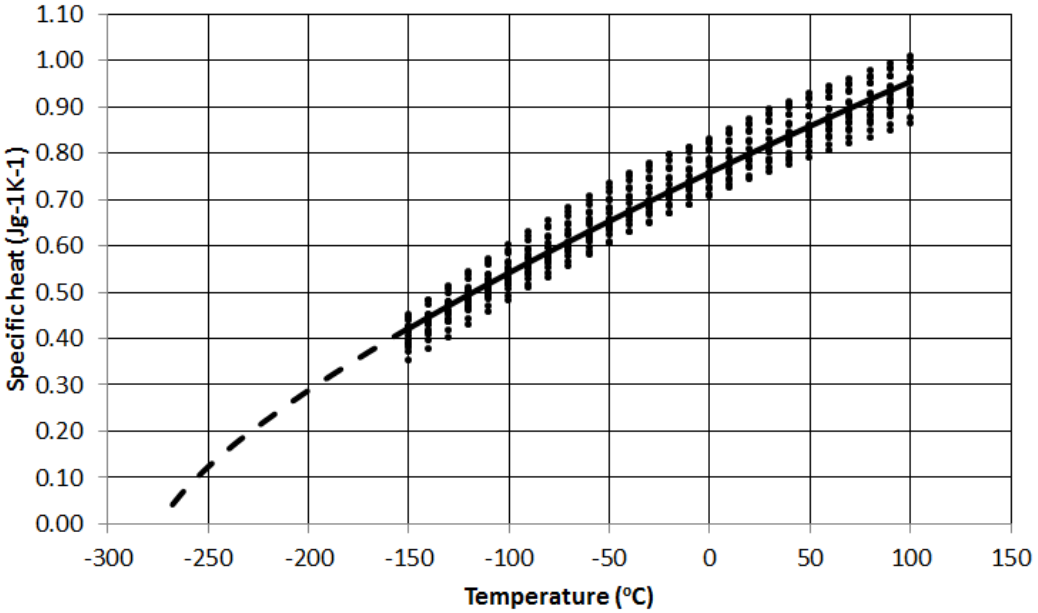

Fig. 1. Fitting of the power function model given by Eq. (4) to experimental data.

5. Conclusions

1. The results obtained for the three homoionic forms (Ca^{2+}, Na^{+}, K^{+}) of the two source clays (SWy-2 and Stx-1b) indicate a strong temperature dependency of the specific heat and significant effects of initial clay and the kind of main exchangeable cation.

2. In view of the presented results, it appears that if a precise data on temperature dependency of the specific heat of a clay material are needed, an empirical relationship should be established in every case. However, the standard error of the estimate SEE for the proposed power function model is equal to 0.038 $Jg^{-1}K^{-1}$, which should be acceptable in most applications.

Acknowledgement

This work was supported by the Polish Ministry of Science under grant N N525 349538.

References

[1] ANDERSON, O.L. *Thermoelastic properties of $MgSiO_3$ perovskite using Debye approach.* American Mineralogist, 83, 23-35,1998.

[2] FRIVIK, P.E. *State-of-the-art report. Ground freezing: thermal properties, modeling of processes and thermal design*. Selected Papers of the 2nd Int. Symp. On Ground Freezing. Elsevier, Amsterdam, 115– 135, 1982.

[3] KAY, B.D., GOIT, J.B. *Temperature-dependent specific heats of dry soil materials. Canadian Geotechnical Journal* 12(2), 209-212, 1975.

[4] KIEFFER, S.W. *Thermodynamics and lattice vibrations of minerals: 1. Mineral heat capacities and their relationships to simple lattice vibrational models.* Reviews of Geophysics and Space 17(1), 1-19, 1979.

[5] KOZLOWSKI, T. *Modulated Differential Scanning Calorimetry (MDSC) studies on low-temperature freezing of water adsorbed on clays, apparent specific heat of soil water and specific heat of dry soil.* Cold Regions Science and Technology 78, 89–96, 2012.

[6] ROBIE, R.A., HEMINGWAY, B.S. *Heat capacities of kaolinite from 7 to 380 K and of DMSO-intercalated kaolinite from 20 to 310 K. The entropy of kaolinite Al2Si2O5(-OH)4.* Clays and Clay Minerals 39, 362–368, 1991.

[7] WINTER, D.F., SAARI, J.M. *A particulate thermophysical model of the lunar soil.* Astrophysical Journal 156, 1135-1151, 1969.

[8] WOLFE, L.M., THIEME J.O. *Physical and thermal properties of frozen soil and ice.* Society of Petroleum Engineers Journal, March, 67-72, 1964.

TRANSCOM 2015, 22-24 June 2015
University of Žilina, Žilina, Slovak Republic

Verification of the location of damage on the bottom of the storage tank Petroleum products with extra composite bottom by using Acoustic Emission (AE) method and visual internal inspection

[*]Aleksandra Krampikowska
[*]Kielce University of Technology, Faculty of Civil Engineering and Architecture, Department of Strength Materials and Concrete Structures, Al. Tysiąclecia P.P. 3, 25-314 Kielce, Poland, akramp@tu.kielce.pl

Abstract. The paper presents the results of the verification of the method of acoustic emission to assess the extent of damage and the location of high-risk sites for the safe operation of the low-pressure tanks with a double steel-composite bottom. The check was made by comparing the results of the sites indicated by using the AE method with the pits made during the visual internal inspection. Construction of the bottom of the tank and the stored product prevents inspection and assessment of the extent of damage during operation. Therefore, using the method of AE makes it possible to the exact location of places with high intensity of acoustic emission signals without the need to shut down the operation of the tank. Based on measurements of AE signals can make a preliminary assessment of the extent of damage accordance with the guidelines proposed by VAN DE LOO, P.J. and KRONEMEIJER, D.A. [1] and with the criteria of the AE method resulting from years of research carried out under the direction of Prof. ŚWIT, G. [2-6], in which I took part. These criteria are based on the analysis of the sum of the acoustic emission signals recorded during an hour of measurement [1] and selected EA parameters such as: amplitude, energy, duration [2-5]. Analysis of selected descriptors allows to assign the bottom of the tank, which was tested, into one of five categories tank failure: A - E [1, 2]. This study allows for the safe operation of the storage base as well as gives the possibility to create a schedule and a work estimate for the work of the individual tanks.

Keywords: Low-pressure tanks with double shell, acoustic emission, location of the damage, diagnostics, internal access eye

1. Introduction

Storage tanks for petroleum products due to the stored products are a serious threat to the environment, especially at a time of uncontrolled failure. Therefore, it becomes important to develop effective diagnostics methods of the technical condition of tanks, particularly techniques that allows to predict the possible formation and development of the dangerous active destructive processes that affect on the safety of the tank. Currently, the traditional way to assess the technical condition of the storage tank is perform internal access eye involving the emptying of the stored product tank, clean the bottom head by sand blasting and indication of areas where additional research such as ultrasonic testing of sheet thickness and quality of welds will be performed. The emptying causes a significant threat to the environment, but the biggest is the utilization of pollution arising from the sediments and from the process of sand blasting bottom head of the tank. This study, especially when we are talking about large tanks above 2000 m^3 is associated with high uncertainty caused by randomness selected sites for further research. Even make an additional bottom head of the tank with the tests performed in that way can not guarantee the reliability of the tank due to the high probability of avoiding dangerous places, which consequently can lead to a variety of destructive processes. Especially dangerous is the corrosion of the bottom head of the tank, because the lack of access to both the surface makes it difficult to inspect and assess the extent of damage in the case of the double bottom head. Service life prediction of the bottom head of the tank and its vulnerability to various damages is difficult because of the variety of factors that have a significant influence on the destructive processes. Therefore, it is important to search diagnostic

methods enabling diagnosis the sheet of tanks in service conditions allowing on the location of dangerous places, the intensity of the possible destructive processes, but also to recognize them.

Technique that meets all requirements is the method of acoustic emission. This technique is based on measurements of acoustic emissions generated by active (developing) destructive processes. These are mainly the signals generated by chemical reactions, development of corrosion processes, cracking corrosion products, percolating stored product, work thinned sheets and welds, or the formation and development of cracks. Acoustic emission signals do not appear in case of stable damage corrosion, it means when it is not increased, and the corrosion products do not change its structure.

The aim of this study was to detect sites of increased acoustic activity of the steel sheets and the composite shell of the tank bottom due to the change of the stored medium from the fuel oil (mazout) to light oil, which is associated with a different chemical constitution. It has a significant influence on the rate of corrosion processes.

2. Tests

The subject of study was a cylindrical tank, with a vertical axis and with a fixed roof. The nominal capacity of the tank is V = 10 000 m^3, and its main dimensions are as follows:

- the inside diameter of the shell – d_i = 31 520 mm
- the outside diameter of the shell – d_o = 32 370 mm
- the height of the shell – h_s = 13 650 mm

The shell of the tank is covered with thermal insulation glass wool gr. 12 cm, shielded from the outside with thin galvanized sheets. The shell of the tank consists of nine sheet rings with designed thicknesses from the bottom: 16, 14, 13, 12, 10, 9, 8, 6, 6 mm (Fig. 1).

Fig. 1. The view of the tank which was tested.

The flat bottom head of the tank according to the design has a 10 mm thickness in a circumferential ring and 7 mm at the middle. Inside the tank was made the inner shell of a composite fiber glass and polyester resin with a warning system for leaks "TANKSYSTEM". The tank was built on a concrete foundation with the height of h = 100 cm. Between the bottom of the tank and the foundation was made a sand-mazout sub-crust. On the shell of the tank was placed eight acoustic emission sensors at a height of 0.70 m from the bottom of the tank in order to locate emission active places. Sensors arrangement was shown in Figure 2. The sensors were marked in numbers from 1 to 8, and arranged equidistantly along the circumference of the tank.

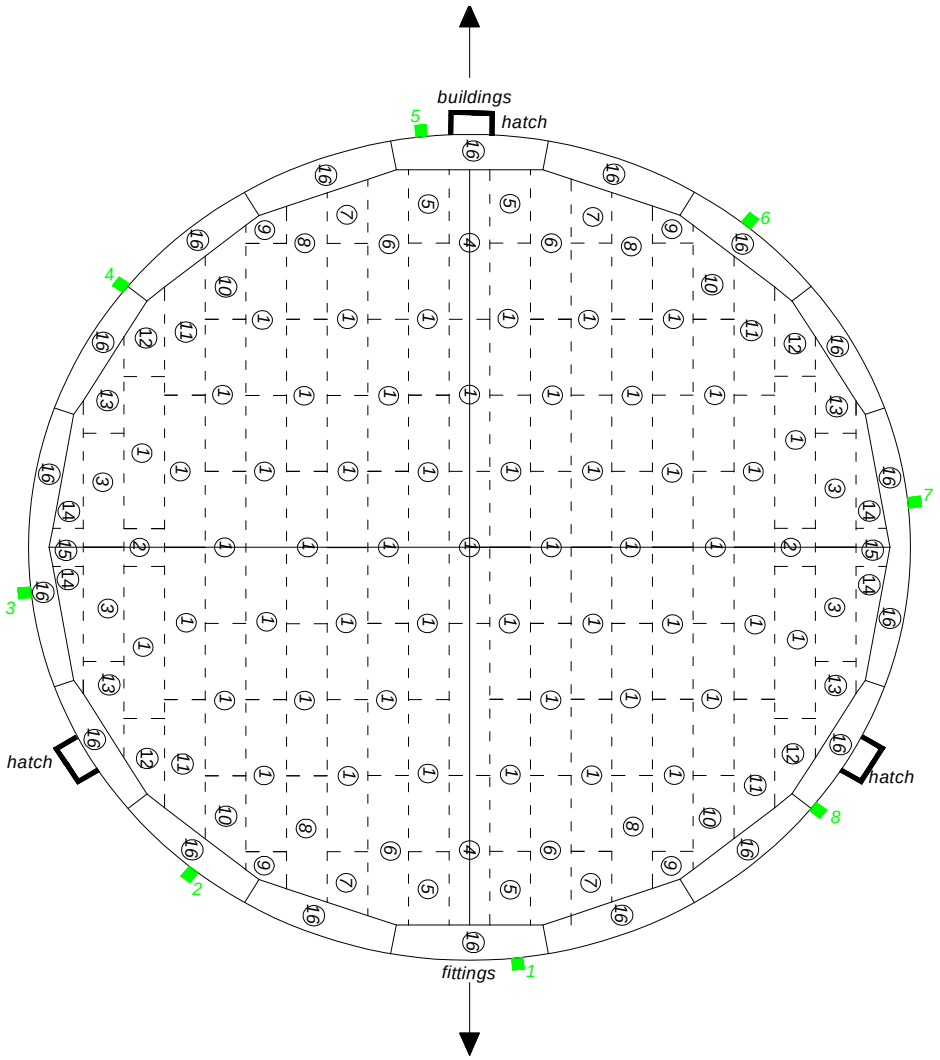

Fig. 2. View of the locations of sensors during the location of places with high intensity of AE signals at the bottom of the tank.

To the test were used the resonance acoustic emission sensors with the frequency of 55 kHz and the 24-channel measuring system μSamos [6] presented in Figure 3.

Fig. 3. The AE measuring set: 24 channels processor μSAMOS and resonace sensor with the frequency of 55 kHz [3-5].

Before the actual measurement was performed calibration of the sensors involving the registration of the reference signal generated at a certain distance from the AE sensor. As a reference signal was used HSU-Nilsen pattern [2-6], an acoustic signal accompanying breaking of

pencil graphite on the surface of the test object. In this way the correctness of operation of the measurement system was verified.

2.1. Results

To the evaluation of the damage was used a modified criterion described in [2]. It is based on the concurrent comparison four parameters: the events of acoustic emission, amplitude, energy and duration of AE signals. During the hour-long measurement were recorded the basic parameters of the acoustic emission signals. The analysis was based on the sum of events. Other parameters such as duration of the signal, the amplitude of the signal and the signal energy in the assessment performs a secondary role. According to the criteria depending on the number of the recorded signals the tank is classified into one of five categories of damage A to E. The classification of the tank to appropriate category allows for a preliminary assessment of the degree of corrosion.

According to the developed classification of the tanks and experience gained on the basis of studies were assumed four degrees of corrosion of the tank bottom (Table 1). These criteria allow an approximate assessment of the technical condition of the bottom of the tank and to determine the schedule for the subsequent inspection or repair [2].

Tank class	Average AE events [1]	Amplitude [dB]	Energia AE [µsv/count]	Duration [µs]
A – Lack of or small corrosion centre, next investigation after 5 years	**<400**	**40-60**	**<10**	**<5000**
B - Lack of or small corrosion centre, next investigation after 5 years.	**<1500**	**40-60**	**<50**	**<50 000**
C - small number of corrosion centre within a substantial bottom surface. If possibile, partial replace of the bottom. Next investigation after 3 years.	**<3000**	**40-80**	**<200**	**<100 000**
D - significant corrosion of the bottom. Partial or total removal of the bottom sheets. Necessary major repair after 1 year. If partial repair then full localisation of corrosion sources using AE is necessary.	**<5000**	**40-70**	**<500**	**<150 000**
E - corroded bottom with significant changings of the bottom sheets structures. The tank is designed to a complete overhaul.	**>5000**	**40-50**	**>500**	**>150 000**

Tab. 1. Classification of tanks depending on selected AE parameters [2].

As shown in the cumulative graphs in Figure 4 within 60 minutes sensor number 1 recorded 421 events. The sensor 4 at the same time recorded 2 579 events. The average value of the number of events recorded by the sensors was 1 500 signals. According to the criterion described in [2] the tank can be assigned to class B.

For a more complete assessment the bottom of the tank the three other parameters were analyzed which selected results are shown in Figure 5.

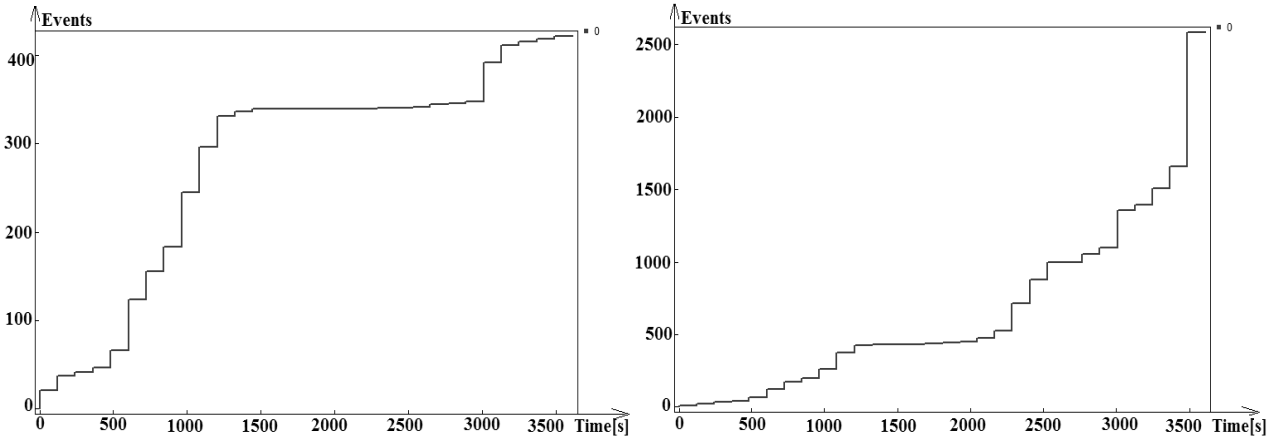

Fig. 4. Sum of acoustic events registered at the same time by sensors 1 and 4 as a function of time.

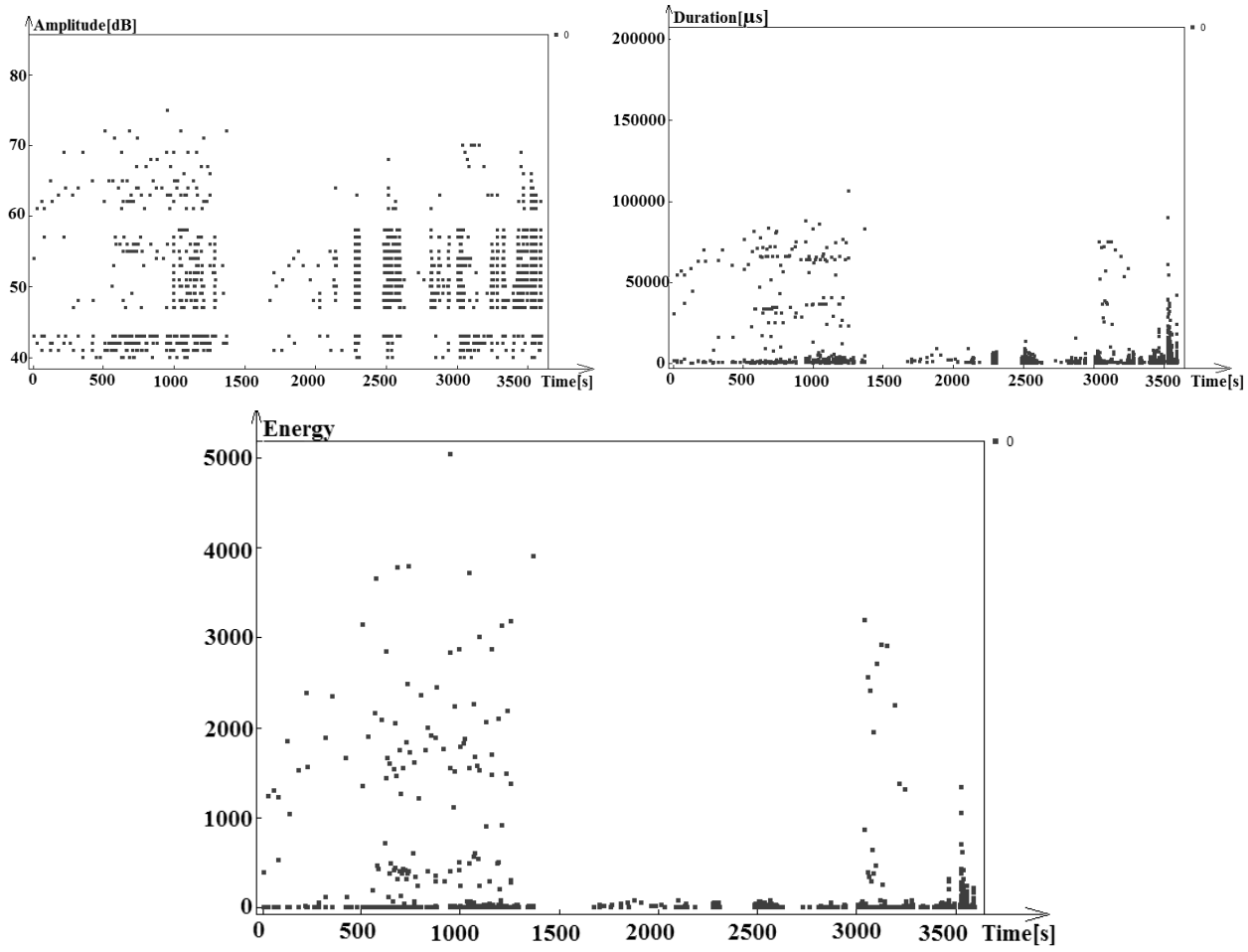

Fig. 5. Scatter plot of the amplitude, duration, and the energy of AE signal recorded by the sensor 4 as function of time.

The recorded values of the parameters by sensor 4 suggest that in the tank at that moment do not run the destructive processes related to the phenomenon of the tank bottom corrosion. In the present case, were recorded signals with an amplitude of up to 80 dB of low energy and long duration. Signals with an amplitude of over 65 dB and the long duration suggest deformation between the connection the bottom sheet ring and the bottom of the tank.

For a complete analysis was made location where there is a thinning of the sheet thickness of the bottom and the ripple under the influence of fluid in the tank. Location of places of intense acoustic emission activity was presented in Figure 6.

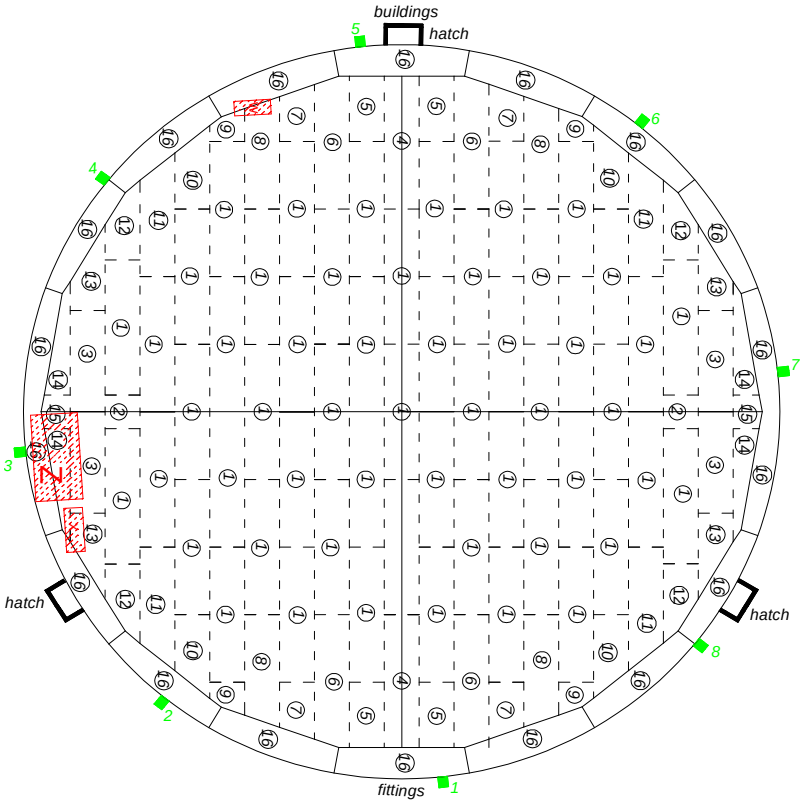

Fig. 6. Location of places with high acoustic emission activity suggesting areas of reduced thickness of the bottom sheets or discontinuities of the weld.

The selected sites were located using acoustic emission method and then were prepared three areas of tests designated with letters [Z; X; W]. Preparation for the test consisted of the removal of the so-called "second bottom", which is covered with the bottom of the tank and cleaned mechanically 100% of the sheets and welds in the areas of research. As a result of magnetic-powder fluorescent method were detected one type of crack with the length of 10mm at the weld in the area ["X"] as shown in Figure 7.

Fig.7. Visible detected crack with the length of 10mm on the line of the fusion butt joint at the weld in the area ['X'].

As a results of the visual inspection in the 100% of the indicated areas of sheets and welds were found:

- visible left small fragments of the structural elements welded to the sheets,
- the bottom head of the tank is made of sheet metal plates joined "lap", but in one site has been identified a butt joint between the connecting metal plates,
- typical height of face of the fillet welds varies from 4.5 to 6.2 [mm].

The most common discrepancy include: non-uniform of the face of weld, incompletely filled groove, improper start of welding, small underuct presented in Figure 8, 9 and 10.

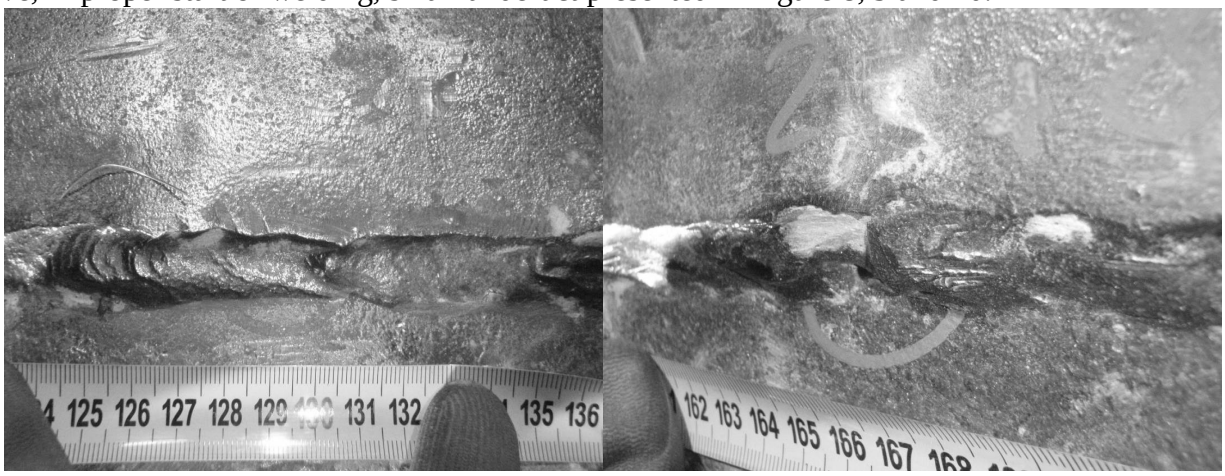

Fig.8. Visible on the weld incompletely filled groove, skewing sheets of 8.5 [mm], the height of the face of the weld 4.5 [mm].

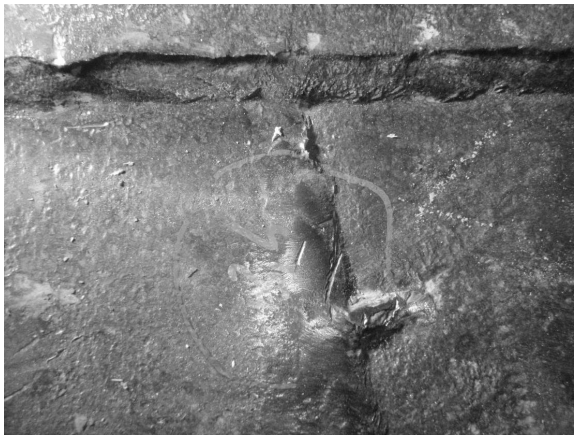

Fig. 9. Indication 3 - wrong shape of the weld and skewing of the sheets 3.4 mm.

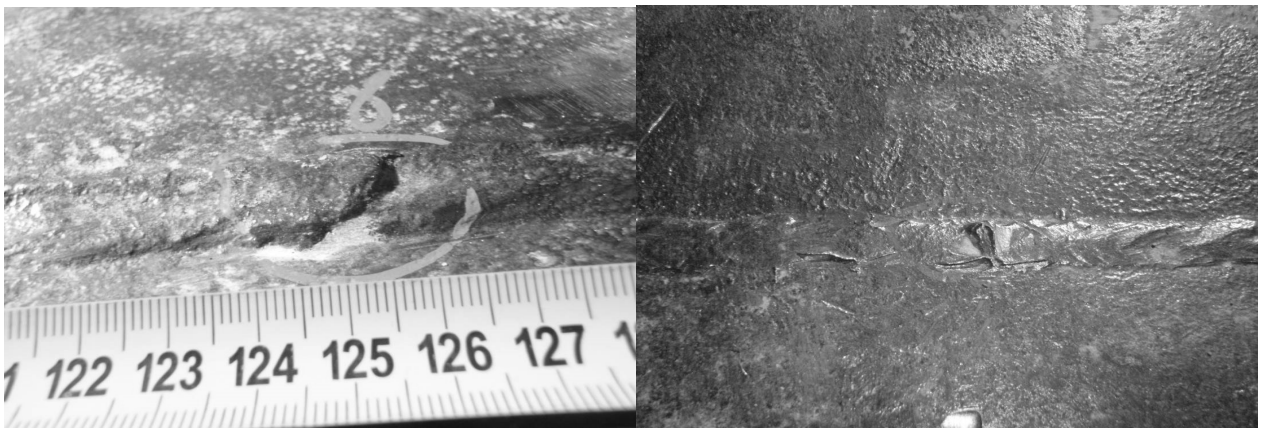

Fig. 10. Improper start of the weld, the lack of fulfillment of the face of the weld and mechanical damage of the weld

3. Conclusion

The presented method of acoustic emission measurement proved to be very effective technique for the assessment of the technical condition of the bottom head of the storage tank for petroleum products. This method allows the location of the potential damage without the need to shut down the operation of the tank and without emptying of the stored product tank which protects the environment from possible contamination. The speed of the tests and the results of visual inspection

lead to the conclusion that the acoustic emission method is one of the most effective, low-cost and environmentally safe. The most important advantage is the ability to assess the extent of damage in the difficult to access areas without to shut down the operation of the tank and without emptying of the hazardous stored products.
The research indicated that:

- The tank is a Class **B** - average number of acoustic signals <1500
- Small corrosion centres and leaking valves
- Special attention is recommended during changing the storage products (possible increase of corrosion processes)
- Imperfections in the performance of the welds
- Location of the cracks weld
- Tank qualified for the next review for 6 years by AE method

References

[1] VAN DE LOO, P.J., KRONEMEIJER, D.A. *Screening of tank bottom corrosion with a single point AE detector: AE- simple*. Journal of Acoustic Emission, No 18, (2000), pp:174-180

[2] ŚWIT, G., TRĄMPCZYŃSKI, W. *Preliminary classification method of damage, of the tanks for petroleum products bottoms caused by corrosion, with use of acoustic emission*. Proceedings of conference scientific-technical "Steel Structures", Kielce – Suchedniów, 2-4 July 2014, pp: 155-158, Poland

[3] GOSZCZYŃSKA, B., ŚWIT, G., TRĄMPCZYŃSKI, W. *Monitoring of active destructive processes as a diagnostic tool for the structure technical state evaluation.* Bulletin of the Polish Academy of Sciences: Technical Sciences 61 (1), pp: 97-109

[4] GOSZCZYŃSKA, B., ŚWIT, G., TRĄMPCZYŃSKI, W. *Assessment of the technical state of large size steel structures under cyclic load with the acoustic emission method IADP*. Journal of Theoretical and Applied Mechanics 52 (2), pp: 289-299

[5] GOSZCZYŃSKA, B., ŚWIT, G., TRĄMPCZYŃSKI, W., KRAMPIKOWSKA, A. *Application of the acoustic emission (AE) method to bridge testing and diagnostics comparison of procedures*. IEEE Xplore - IEEE Proceedings, Bejiging, 2012, pp: 1-10, China

[6] ŚWIT, G. *Diagnostics of prestressed concrete structures by means of acoustic emission*. IEEE Xplore - IEEE Proceedings: ICRMS Reliability, Maintainability and Safety, Chengdu, 2009, pp: 958-962,China

TRANSCOM 2015, 22-24 June 2015
University of Žilina, Žilina, Slovak Republic

Analysis and comparison of thermal effects on prestressed concrete box girder bridge

*Lukáš Krkoška, **Martin Moravčík.
*University of Zilina, Faculty of Civil Engineering, Department of Structures and Bridges, Univerzitna 2, 01026 Žilina, Slovakia, lukas.krkoska@fstav.uniza.sk
** University of Zilina, Faculty of Civil Engineering, Department of Structures and Bridges, Univerzitna 2, 01026 Žilina, Slovakia, martin.moravcik@fstav.uniza.sk

Abstract. Thermal load, especially vertical temperature gradient, is an important factor that should be considered during the bridge design procedure. In the world, several research works focusing on temperature gradient were made, mostly in USA and China, but only a few analyzed real measured temperature gradient at European bridges. In this paper, short overview of temperature loading of bridge structures is described. Then, the temperature measurement of prestressed concrete box girder bridge built by balanced cantilever method is analyzed and obtained vertical temperature gradient is compared with temperature gradients for the concrete box girder cross section recommended in five different bridge design specifications. Last, the thermal stress due these vertical thermal gradients are compared here.

Keywords: prestressed concrete, box girder bridge, thermal effects, thermal loads, temperature gradient, temperature measurement.

1. Introduction

During the service lifetime, designed to 100 years or even more, bridges are exposed to daily, seasonal and yearly temperature variations induced by climatic conditions, as solar radiation, ambient air temperature, humidity and wind speed, as shown in Fig. 1. Temperature variations are secondary affected by orientation of structure, material of structure, deck surface finishing layer, structure dimensions and cross-section geometry. These effects may cause nonlinear thermal load that influences the performance of bridges.

In practice, the variations of temperature affects bridges significantly. Uniform temperature changes cause large total length changes, expansion or contraction. These changes of length influence internal forces, structural dynamic characteristics and the continuous expansion and contraction may damage critical members of the bridge, such as expansion joint, bearing and anchor head. If these deformations are restricted, temperature variations result in thermal stresses, what may leads to unexpected tensile cracks and consequent possible reinforcement corrosion. Vertical and horizontal temperature difference result in additional bending moments in vertical plane and horizontal plane, respectively. This facts are detail described at article [1].

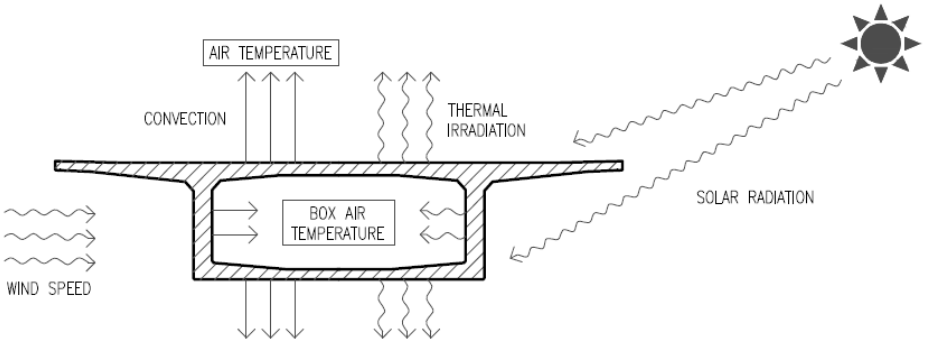

Fig. 1. ***Environment effects on bridge temperature changes [1].***

2. Description of the bridge

In this paper, it is analyzed the prestressed concrete box girder highway bridge structure SO205, highway part from Zilina to Liptovsky Mikulas. This bridge structure is designed as two parallel single 5 spans bridges and the span lengths are 75+120+75+53+37m, built by combination of the balanced cantilever method and casting at bearing scaffold. The deck of the bridge consists of a continuous box girder seated on simple bearings on the piers and abutments. The height of the single cell box cross section of the deck decreases from 6.5 m (pier) to 2.85 m (mid-span), as shown in Fig. 2. The width of the deck slab with symmetrical overhangs is 13.65 m.

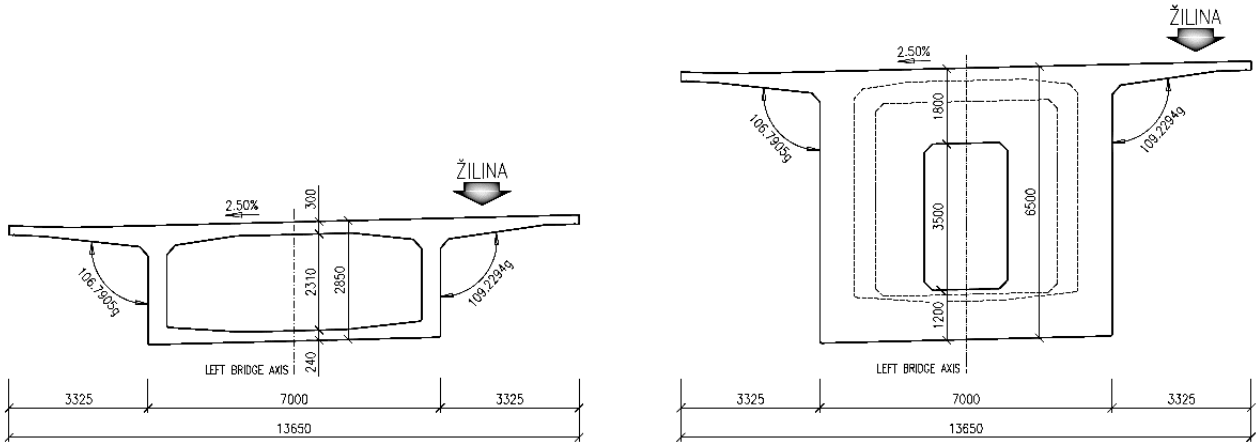

Fig. 2. ***Cross sections of single cell prestressed box girder at mid-span (left) and pier (right).***

3. Bridge monitoring system arrangement

During the construction of the bridge, for the research described in [2], total 24 vibrating wire strain gauges were arranged at three characteristic cross sections of main 120 m span (balanced cantilever), L1 (6 measuring points) and L2 (9 measuring points) are first segment of cantilever and UL (9 measuring points) is the key segment, as shown in Fig. 3. Vibrating wire strain gauges are able to measure strain (as the function of measured value) and temperature. The ambient air temperature, relative humidity and humidity of concrete were measured too. [2]

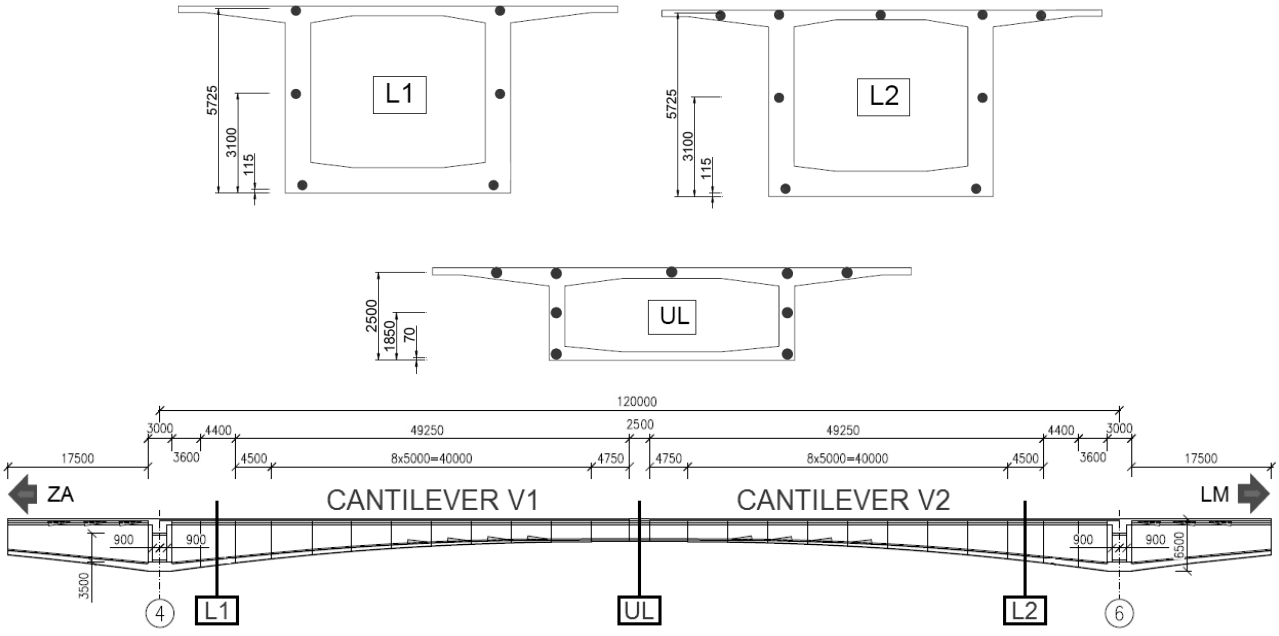

Fig. 3. ***Bridge monitoring system arrangement.***

4. Thermal effects on structures

Thermal load is an important factor that should be considered during the whole lifetime of the bridge. The temperature distribution within an individual structural element may be split into the following four essential constituent components, as illustrated in Fig. 4:

a) a uniform temperature component (effective bridge temperature), ΔT_u,
b) a linearly varying temperature difference component about the z-z axis, ΔT_{MZ},
c) a linearly varying temperature difference component about the y-y axis, ΔT_{MZ},
d) a non-linear temperature difference component, ΔT_E. It results in a system of self-equilibrated stresses which produce no net load effect on the element.

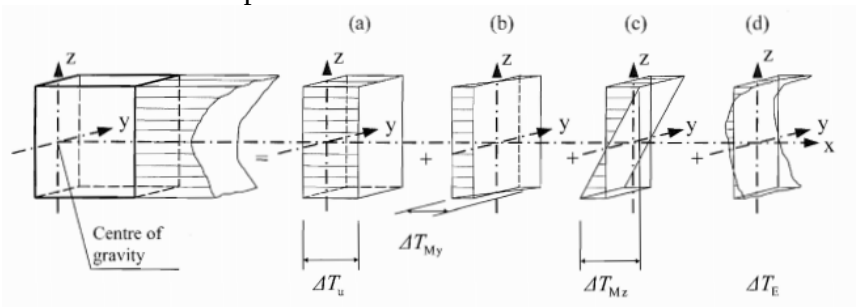

Fig. 4. ***Diagrammatic representation of constituent components of a temperature profile [3].***

Effective bridge temperature depends on the maximum and minimum temperature that bridge reaches over prescribed period and result in the expanding or contracting of bridge components in the longitudinal direction. The movement of the structures associated with effective bridge temperature can be determined by linear elastic method for statically determinate structures. For statically indeterminate structures, as this deformations are restricted, temperature variations result in thermal stresses. Vertical temperature difference (temperature gradient), refers to the differences in temperature between the top surface and other levels through the depth of the superstructure, results in the bending moments in vertical plane. Positive temperature gradient occurs when conditions are such that solar radiation and other effects cause a gain in heat through the top surface of the superstructure. Conversely, reverse temperature gradient occurs when conditions are such that is lost from the top surface of the bridge deck as a result of radiation and other effect. Horizontal temperature difference, refers the differences in temperature between two positions on the same level in the cross section, results in the bending moments in horizontal plane. [3] The effective bridge temperature and vertical temperature difference are included in almost all bridge specifications.

5. Measurement results

Fig. 4 shows temperatures measured from the date of casting L1 segment up to today, 794 days period. High temperatures of concrete in first 10 days are caused due to hydration process of concrete, this effect is not studied in this paper. Day 9.8. 2013 (248^{th} day of structure life) was selected as the day of the highest positive vertical temperature gradient in the girder and it is also a day of highest ambient temperature. Day 11.12.2014 (737^{th} day of structure life) was selected as the day of the highest negative vertical temperature gradient.

Fig. 5 shows the vertical temperature gradients, obtained by subtracting a minimum temperature from the vertical temperatures along the depth of the cross section and comparison of these obtained gradients with temperature gradient for the same concrete box girder cross section recommended in several bridge specifications, namely Slovak eurocode STN EN 1991-1-5 [3], Czechoslovak standard for bridge loading ČSN 73 6203 [4], British standard for bridge loading BS 5400-2 [5], German standard for bridge loading DIN 1072 [6] and United States Highway Bridge Design Code ASSHTO 2012 [7].

Fig. 5 represents measured temperatures during the lifetime of the bridge. For better transparency of diagram, the values of two gauges in the same level are averaged in one value.

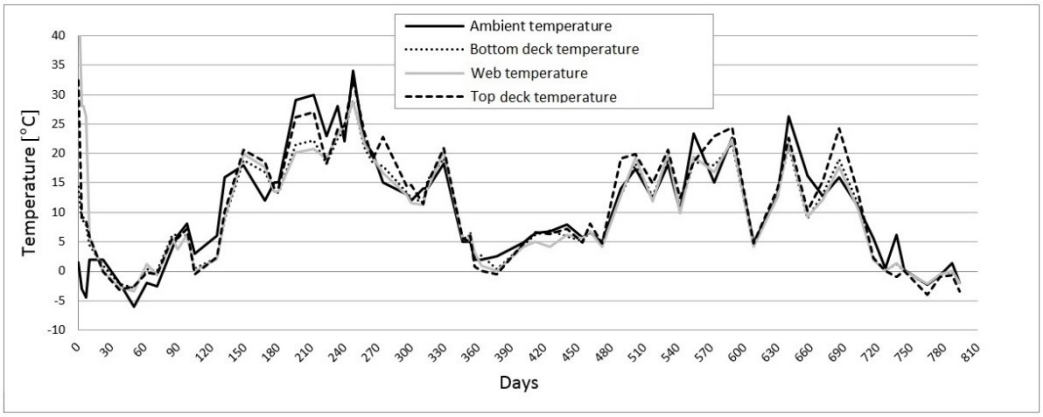

Fig. 5. ***Measured temperatures of L1 cross section and ambient air temperature [2].***

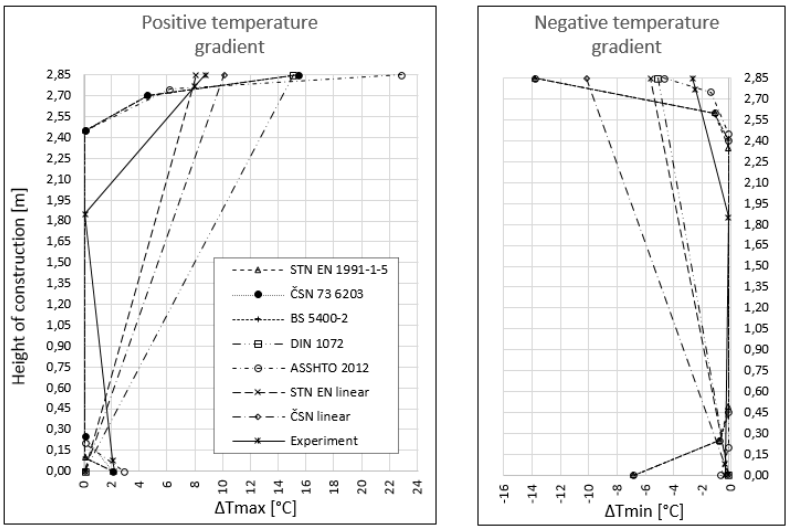

Fig. 6. ***Comparison of obtained temperature gradient with different bridge specifications models.***

Fig. 7 shows comparison of normal stress distribution along the longitudinal axis for top/bottom fibres of box girder cross section of analyzed bridge due to positive vertical gradients illustrated in Fig. 5. As we can see, nonlinear temperature gradient models, according to mentioned bridge specifications, produce significantly higher compressive stress in top fibres, than linear temperature gradient models. On the other side, tensile stress in bottom fibres due to nonlinear vertical temperature gradients do not exceeds tensile strength of concrete, while linear temperature gradients produce significant tensile stress in bottom fibres. The effects of temperature gradient obtained from experiment are similar to those due to linear temperature gradient models. The values of normal stress at the middle of main 120 m span are shown in Tab. 1.

Temperature gradient model		Top fibres stress [N.mm^{-2}]	Bottom fibres stress [N.mm^{-2}]
STN EN 1991-1-5	nonlinear	-4.72	1.23
ČSN 73 6203	nonlinear	-4.66	1.24
BS 5400-2	nonlinear	-4.72	1.23
ASSHTO 2012	nonlinear	-7.13	1.26
DIN 1072	linear	-3.33	5.71
STN EN 1991-1-5	linear	-1.78	3.05
ČSN 73 6203	linear	-2.22	3.81
Obtained from measurement		-2.04	2.00

Tab. 1. ***Normal stress at the middle of main span.***

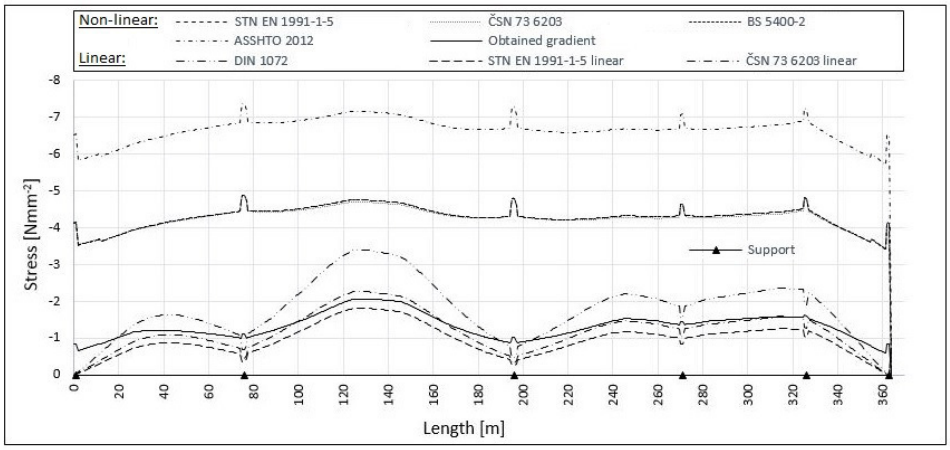

a) top surface

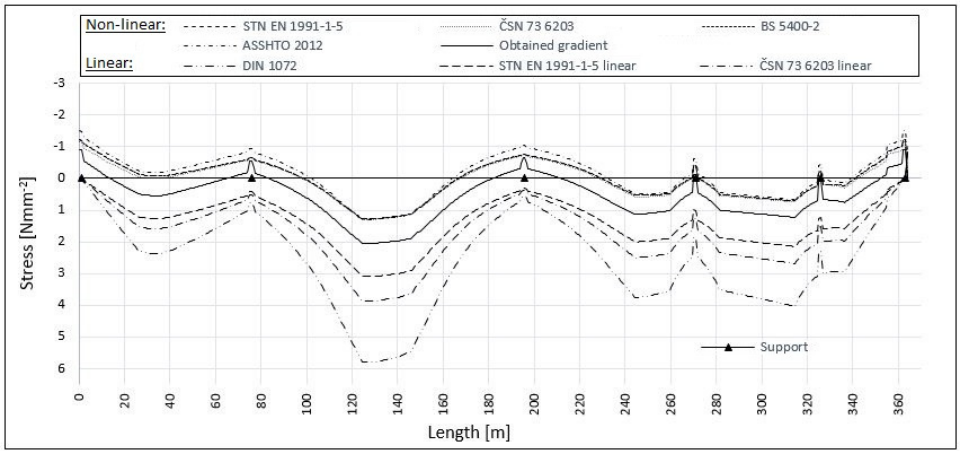

b) bottom surface

Fig. 7. ***Normal stress at top surface due to positive temperature gradients in fig. 5.***

6. Conclusion

Analysis shows, that thermal effects, especially due to vertical temperature gradient, impact significantly on the stress condition of the bridge. Investigated vertical temperature gradients, according to several codes produce significant tensile stress in bottom fibres that in some cases exceeds tensile strength of concrete. From analysis of one bridge, without investigating other types of structures we cannot say, that given results are generally valid, or it is valid only for this type of structure. Therefore is necessary to perform measurements and analysis of temperature gradient on more structures of various types. Measurement, what was made here is not fully sufficient for accurate description and analysis of temperature gradient behavior, therefore it is necessary to perform continuous temperatures measurement, at least in periods with predicted maximum and minimum air temperatures.

Acknowledgement

This article was made by financial support of grant agency VEGA 1/0336/15, grant agency APVV-0763-12, APVV-0106-11 and project “Research center of University of Zilina”, ITMS 26220220183.

References

[1] GUANG-DONG ZHOU, TING-HUA YI. *Thermal Load in Large-Scale Bridges: A State-of-the-Art Review.* International Journal of Distributed Sensor Networks, vol. 2014.

[2] MORAVCIK, M., DOLINAJOVA, K. *Časový Vývoj Pomerných Pretvorení Betónu na Letmo Betónovanom Dialničnom Moste.* Betonárske dni, vol. 2014.

[3] STN EN 1991-1-5: *Actions on Structures. Part 1-5: General Actions - Thermalactions.*

[4] ČSN 73 6203: *Actions on Bridges.*

[5] BS 5400-2: *Steel, Concrete and Composite Bridges. Part 2: Specification for Loads.*

[6] DIN 1072: *Road and Food Bridges: Design Loads.*

[7] ASSHTO 2012: *LRFD Bridge Design Specification*.

TRANSCOM 2015, 22-24 June 2015
University of Žilina, Žilina, Slovak Republic

Transition curves for sewer pipelines inspection and rehabilitation planning

[*]Joanna Król, [*]Andrzej Kuliczkowski
[*]Kielce University of Technology, Faculty of Environmental, Geomatic and Energy Engineering, Department of Piped Utility Systems, Al. Tysiąclecia Państwa Polskiego 7, 25-314 Kielce, Poland, joanna.krol@op.pl, akuli@wp.pl

Abstract. The paper focuses on the issue of sewer pipelines deterioration. Theory of sewer pipes ageing was discussed by using ageing curves (such as "bathtub curve"). It was presented examples of application transition curves - one of these is prediction necessary action in an Operations and Maintenance program.

Keywords: deterioration, ageing of sewer pipelines, ageing curves, transition curves, "bathtub curve", inspection and rehabilitation planning.

1. Introduction

The ageing of material is common phenomenon, which occurs in all life fields of modern human, especially in technical aspects, including these related to underground infrastructure. The concept of ageing is meant the whole of the physical and chemical changes in the structure of the material, which affect the change in its properties during processing, storage and use [19].

The ageing is one of the factors which affects lifetime of pipelines. This lifetime (also called durability) is highly diverse, according to the quality of performance and using materials, the condition of sewer operation etc. Hence, there is a need for prediction of pipelines durability [12]. However, this durability is quite difficult to determine. Properly done pipelines could theoretically survive for hundreds of years. In the literature we can even find cases of pipelines, for example Cloaca Maxima, operating for over 2,000 years [11], or first vitrified clay pipes, which have been preserved in old cities of North America. However, the probability of failure increases dramatically after the occurrence of any damage. And the question is, when should we react? In some polish cities it is still used strategy of fire department, which is based on rehabilitation of pipelines only if any failure arises. This approach generates much higher costs, as confirmed by studies conducted for the City of Edmonton [3]. Based on this research, it was found, that emergency repairs of sewer are, on average, three times more expensive, in comparison to planned repairs

There is no doubt that the planning of inspection and rehabilitation issue, regarding sewer pipelines, which is the subject of this paper, is extremely important. That was proved, for example in [8], [9], [20].

2. Ageing curves

One way to describe sewer networks (or water networks) are the ageing curves, also called the transition curves. They enable researchers to estimate the transition between perfect condition (failure-free) and failure condition of pipe. The starting point is the probability distribution curve of sewer damage, a chance variable is *t* - time of damage.

The "bathtub curve" (Fig. 1) has been applied since the fifties of the last century. This curve presents the course of failure rate function in three characteristic periods:

I. *Infant mortality* - this stage is also called early failure or debugging stage. The failure rate is high but decreases gradually with time. During this period, failures occur because

engineering did not test products or systems, or manufacturing made some defective products. Therefore, the failure rate at the beginning of infant mortality stage is high and then it decreases with time after early failures are removed.

II. *Useful life (normal life)* - the damage, which occurs, is accidental. This period is usually given the most consideration during design stage and is the most significant period for reliability prediction and evaluation activities.

III. *Wear-out period (ageing period)*- this is the final stage where the failure rate increases as the products begin to wear out, because of age or lack of proper maintenance [13], [18].

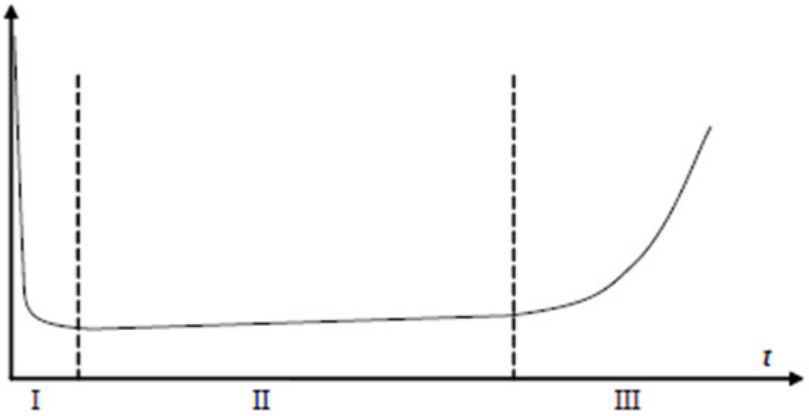

Fig. 1. The failure probability density function - „bathtub curve" [7].

λ(t) means failure rate and it is defined as the probability of a component failing in one small unit of time.

Currently, the model which determines the course of the risk function is the "Hump-shaped curve". The course of failure rate function, in II and III stages, is the same like in case of "bathtub curve". Variant course can occur in infant mortality period (Fig. 2). The rise of failure rate in this stage (I) is the result of structures errors or technological and material errors. This period is related to new pipes or segments after rehabilitation - this sort of errors occur quite often in both of this situation. In the second case, a major cause of damage is incorrect selection of rehabilitation technology, therefore technological errors. This is the result of insufficient knowledge of the designers, regarding new rehabilitation technologies. Failure rate begins to decrease with time (similarly as in the case of "bathtub curve") and finally reaches an almost constant value. The stage, in which failure rate is constant, lasts quite long and is called normal life (II).

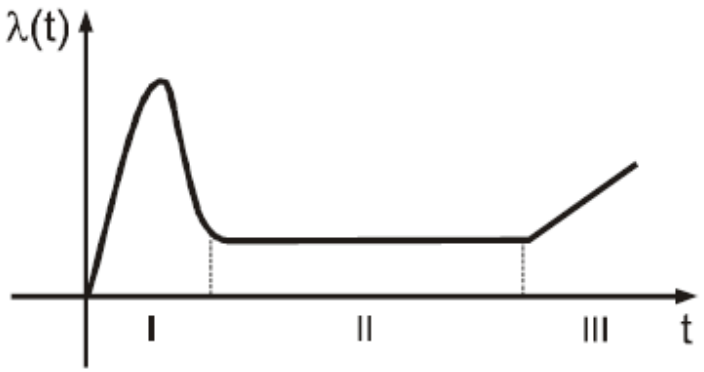

Fig. 2. The failure probability density function - „hump-shaped curve" [13].

After failure-free period, the failure rate rises again, what is mainly the result of sewer pipelines ageing [14].

3. Transition curves between condition states of sewer pipelines

Transition curves between condition states relate to the II and III stages, which were shown in figures 1 and 2. These curves can be used for various analysis, inter alia for prediction necessary actions, regarding Maintenance and Operations.

Figure 3 shows the course of the transition curves between condition states. These curves were developed based on research which was executed for a part of sewer pipelines in Dresden [2] - it was incorporated only these pipelines which work in similar conditions. The number of curves depends on the way of results presentation. In these case, it was established 5 class of the condition state - from PK1, which means the worst state of pipelines, to PK5, which means "perfect" state. The analysis of these curves allows us to establish the average age, when the condition state of 50% of pipelines is getting worse (horizontal line). In addition, it is possible to predict probable condition state of these segments, which were not inspected (regarding these group of pipelines, which characterize of common characteristics, such as the year of building, material, work conditions).

In [21] authors presented example of pipelines inspection planning and establishing time, when rehabilitation of sewer segment should be executed. This analysis was based on the results of research for sewer network in Dresden [2]. It was assumed that transition curves between particular states mean also necessity of rehabilitation actions - rehabilitation of pipelines after achieving PK1 state.

During first inspection, it was found, that segment which was analyzed is in PK4 state (the age of pipe that was inspected - 31 years). Location under line representing 50%, which marks average state of pipelines at this age, is the evidence, that this state is better than expected. By the course of curves, PROG 31 is adopted, which assume the next inspection at the age of 41 and 64, and rehabilitation for 84-year-old pipes. By the program, inspection of this segment was realised after 10 years. It was found, that the condition of it is worse than estimated (PK3 instead of PK3.5). This is a clear signal to the modification of the program - the newly formed one (PROG41) assumes inspection at the age of 52 and rehabilitation for 71-year-old pipes. After next inspection (52-year-old sewer segment) it was found better condition than estimated (still PK3 instead of PK2.5), what allowed to the next modification of inspection program (in this case modification is beneficial) and extending of estimated lifetime of pipelines - PROG 52 [14], [21].

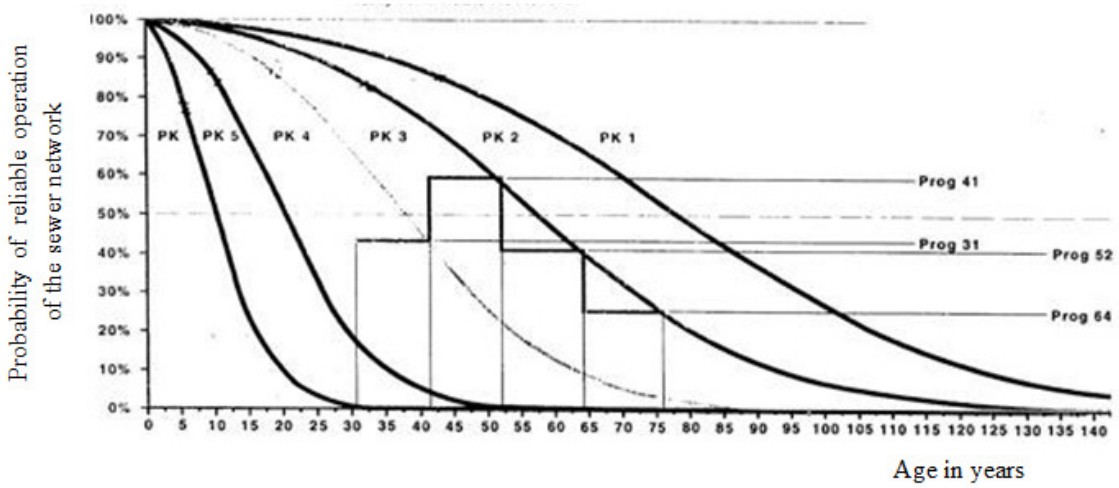

Fig. 3. Pipelines inspection planning, based on current condition [15], [21].

An interesting solution in the above method is, that the frequency of inspection depends on expected condition state - it was assumed, that inspection will be execute, when the state of pipelines is getting worse, instead of after definite time. This makes, that the costs of sewer network

maintenance can be reduced, because this solution prevents unnecessary inspection of these pipelines which are in good condition state (good condition state means, that any actions, regarding rehabilitation, are not necessary). This issue was also mentioned in [6], where application of selective inspection, for general condition state evaluation, was described. This method also allows to unnecessary cost reduction, and this means the rational management of sewer system. The authors of this publication propose selective inspection strategy, which is based on the inspection only picked, characteristic segments. This select group of pipes provides the basis for estimating general condition state of the whole sewer network. The issue of selective inspection was also mentioned in [1]. The European standard DIN EN 752-5 [4] equates the selective inspection with traditional inspection, in which of the entire sewer system is inspected. Whereas the cost of the first one is approximately 60% lower than the second one. The German Ministry of Education and Research (in German *Bundesministeriums für Bildung und Forschung*) run the project, including the analysis of selective inspection, within which Technical University of Aachen did statistic research for 35,000 sewer segments [16]. The main aim was to demonstrate the reliability and the ability to use of selective inspection [17]. Despite the economic aspect and published studies, the big German cities still have not decided to introduce selective inspection of sewer networks. The main reason for this decision is the danger of making a mistake in the first stage of the inspection - the probability sample [22].

4. Summary

The described example of sewer system inspection and rehabilitation planning, in spite of obvious advantages, such as adaptation executed actions to the real state of pipelines, has a one serious problem, which touches all of the methods based on long-term research, namely, a lack of proper data. In practice, the data can have substantial limitations and deviate from a perfect dataset. For this reason, the verification of method, using real world data, is quite difficult to execution. In report from CARE-W, a past EU research project on sewer rehabilitation, we can find an entry: *"[...] even large utilities have very little overview of their physical assets, and in many cases the installation year, the pipe material, and even the location of pipes is unknown [...]. In other cases, data is present, but in a format which makes it very difficult to use for analyses [...]. Data may also be inaccurate or have lacunae."* This is the major weakness of all methods, based on a sufficiently large sample of inspected pipes. In [23] author found, comparing various deterioration models, that a neural network is the most suitable model for predicting the condition changes of individual pipes, but it also needs the large amount of data for training and calibration.

The solution which allows to eliminate difficulties, regarding availability of long-term research results, is ABCDE method [10], which is recommended by Technical University of Kielce. This method allows to the class division of sewer pipelines, due to the rehabilitation priority, based on actual condition state and work conditions of sewer pipelines.

References

[1] Baur, R und Hörold, S. *Modelling sewer deterioration for selective inspection planning - case study Dresden* (http://www.sewer-software.com/pdfs/Dresden.en.pdf 20.03.2015).

[2] Baur, R und Hörold, S. *Verbesserte Inspektionsplanung durch Alterungsprognose von Abwasserkanaltype,* Korrespondenz Abwasser, 2001 (48), Nr 1, 24 - 40.

[3] Chua, K. A., Kwan, Ng. H. *Funding evaluation of trenchless rehabilitation needs for sewer infrastructure management,* 21st No-Dig International Conference and Exhibition, Las Vegas, Nevada, USA, 2003.

[4] DIN EN 752-5 *Entwässerungssysteme außerhalb von Gebäuden, Teil 5: Sanierung,* 1997.

[5] Hafskjold, L.S. and Vanrenterghem-Raven, A. *Experiences from the application of care-w, computer aided rehabilitation of water networks.* In: Proceedings Combined International Conference of Computing and Control for the Water Industry, CCWI2007 and Sustainable Urban Water Management, SUWM2007, 3-5 September 2007, De Montfort University, Leicester, UK.

[6] Hertwig, E., Krug, R. *Selektive Inspektionsstrategie und statistisch/prognostische Sanierungsmodelle*, Korrespondenz Abwasser, 1999 (46), Nr 11.

[7] Kowalski, K., Młyńczyk, M. *Problematyka gotowości systemów uzbrojenia we wczesnej fazie eksploatacji / The issue of readiness of weapon systems at an early stage of service life*, MOTROL, 2009, nr 11c, s. 105 - 112.

[8] Król, J. *Studium starzenia się przewodów kanalizacyjnych. Praca magisterska / The study of sewer pipelines deterioration, Master's thesis*, Politechnika Świętokrzyska, Kielce, 2014.

[9] Kuliczkowska, E. *Kryteria planowania bezwykopowej odnowy nieprzełazowych przewodów kanalizacyjnych / The planning criteria for trenchless rehabilitation of non-man-accessible sewers*, Monografia M3, Wydawnictwo Politechniki Świętokrzyskiej, Kielce, 2008.

[10] Kuliczkowska, E. *Metoda ABCDE zarządzania stanem technicznym przewodów kanalizacyjnych / The ABCDE method of the sewer technical condition management*, Nowoczesne Budownictwo Inżynieryjne, 2014, nr 2, s. 39 - 41.

[11] Kuliczkowski, A. P*rojektowanie konstrukcji przewodów kanalizacyjnych / The design of the construction of sewer pipes*, Skrypt nr 356, Wydawnictwo Politechniki Świętkrzyskiej, Kielce, 2000.

[12] Kuliczkowski, A. *Trwałość rozwiązań stosowanych w budowie i odnowie przewodów kanalizacyjnych / Durability of solutions used in the construction and rehabilitation of sewer pipes*, Instal, 2014, nr 3, s. 54 - 56.

[13] Macha, E. *Niezawodność maszyn / The reliability of machines*, Wydawnictwo Politechniki Opolskiej, Opole, 2001.

[14] Madryas, C., Przybyła, B., Wysocki, L. Badania i ocena stanu technicznego przewodów kanalizacyjnych / *Survey and condition assessment of sewer pipes*, Dolnośląskie Wydawnictwo Edukacyjne, Wrocław, 2010.

[15] Ministerium fur Umwelt und Verkehr, Baden Wurttemberg, Leitfaden für kostenminimierende Instandhaltung von Kanalnetzen, Stuttgart, Dezember 2000.

[16] Müller, K., Dohmann, M. *Entwicklung eines allgemein anwendbaren Verfahrens zur selektiven Erstinspektion von Kanalisationen und Anschlussleitungen, Abschlussbericht Teil C: Handlungsanleitung*, Institut für Siedlungs wasserwirtschaft der RWTH Aachen(ISA), 2002.

[17] Müller, K. *Strategien zur Zustandserfassung von Kanalisationen*, Dissertation, Fakultät für Bauingenieurwesen der Rheinisch-Westfällischen Technischen Hochschule Aachen, Aachen, 2005.

[18] O'Connor, P., Kleyner, A. *Practical reliability engineering, 4th edition*. Chichester: Wiley, 2002.

[19] PN-88/C-89103/14. *Terminologia tworzyw sztucznych. Starzenie*. / *Plastics terminology. The process of ageing.*

[20] Praca zbiorowa pod redakcją A. Kuliczkowskiego *Technologie bezwykopowe w Inżynierii Środowiska* / *Trenchless Technology in Environmental Engineering.* Wydawnictwo Seidel-Przywecki Sp. z o.o., Warszawa, 2010.

[21] Przybyła, B., Szot, A. *Elementy analizy ryzyka w długoterminowych strategiach rehabilitacji technicznej sieci wodociągowo-kanalizacyjnych / The elements of risk analysis in long-term strategies for technical rehabilitation of water and sewage networks*, Inżynieria Bezwykopowa, 2006, nr 2, s. 42-49.

[22] Raganowicz, A., Dziopak, J. Statystyczno-stochastyczny model prognozowania stanu technicznego sieci kanalizacyjnych / *Statistical and stochastic models to predict of sewage networks technical condition*, Zeszyty Naukowe Politechniki Rzeszowskiej, Nr 283, 2012, s. 155 - 172.

[23] Tran, H.D. *Investigation of deterioration models for stormwater pipe systems*, Ph.D. thesis. Victoria University, Melburne, VIC, Australia, 2007.

TRANSCOM 2015, 22-24 June 2015
University of Žilina, Žilina, Slovak Republic

Sewage sludge ash as component of cement

[*]Monika Łukawska
[*]Kielce University of Technology, Faculty of Civil Engineering and Architecture
Department of Building Engineering Technologies and Organization Aleja Tysiąclecia Państwa Polskiego 7
25-314 Kielce monikalukawska@interia.pl

Abstract. This paper presents a brief overview of siliceous fly ash, calcium fly ash and ash from the disposal of sewage sludge as a potential component of cement. According to the literature data lime, fly ash and silica can be used as type II additive for cement and concrete.
Presented in this paper studies the impact of ash relate to deposits on the properties of fresh mortar, as well as the possibility of using this type of ash as an additive for cement mortars. It is noted that the addition of the ashes in the ash respective proportions of 10% and 20% causes a delay in the start and end of hardening of the binder. The loss of fluidity and plasticity virgin mixture is prolonged compared to the fresh mortar mix with Portland cement. In addition, it was observed that the addition of an appropriate proportion such as 10% and 20% causes slow growth compressive strength.

Keywords: sewage sludge, sewage sludge ash, fly ash, lime, fly ash, silica

1. Introduction

Fly ashes are known and are mainly used as a component of cement and concrete. Their use is evident in a number of technological solutions in construction. Usability them allows you to limit the use of cement to produce concrete thus avoiding unnecessary amount of cement thanks to the double advantage in terms of economic and environmental. Fly ash is pozzolanic materials having properties. Only lime fly ash has pozzolanic properties in addition to the hydraulic properties due to the relatively high content of lime. The ashes produced during the combustion of coal in a furnace grate and cyclone at a temperature of from 1000 ºC to 1700º C.

They are collected by means of electrostatic precipitators in particulate form [1]. Ash grains are not full / are characterized by uniform and are filled inside the carbon dioxide or nitrogen. According to DIN EN 197-1: 2012 [2] requirements for the silica ash in the content of reactive calcium oxide CaO is less than 10.0% by weight of free calcium oxide content of less than 1.0% by weight is permissible content of free calcium oxide to 2.5% by weight, provided that the stability of the volume does not exceed 10 mm, the content of reactive silica is not less than 25.0% by weight, while the calcium content of the ash reactive calcium oxide CaO not less than 10.0% by weight for a content of reactive calcium oxide 10.0-15.0% by weight of SiO_2 reactive silica content of not less than 25.0%, volume stability must not exceed 10 mm.

Fly ashes are referred to as type II additive for concrete in accordance with DIN EN 450-1: 2009 [3]. This rule states that an important quality parameter is the activity indicator which is a percentage of the compressive strength of trabecular carried out in appropriate proportions by weight of cement comparative fly ash and compressive strength for trabecular made of mortar standardized. According to the standard activity rate after 28 days of ripening should not be less than 75% of the strength mortar, and after 90 days of ripening should reach at least 85% of the compressive strength of cement made comparator. Cement used for comparative studies must meet the requirements specified in the PN-EN 197-1.

2. Characteristics of fly ash

2.1. Siliceous Fly ashes

Fly ash is a fine-grained silica, powder material, the grains are spherical shape. In the presence of water it reacts with calcium hydroxide to give the product as a hydrated calcium silicates and aluminates. On the pozzolanic properties has a significant impact construction glassy phase and size distribution of fly ash. The main constituents of the ash are silica SiO_2 and alumina Al_2O_3, also in a smaller amount of iron oxide Fe_2O_3 [4].

This is obtained by mechanical or electrostatic precipitation of ash from the flue gases from the combustion of fine coal in power boilers at high temperatures. The addition of silica ash cement compared with Portland cement CEM I brings many advantages such as: delayed onset of bonding grout, proper workability of concrete, high resistance to corrosion, very good strength [5]. Siliceous fly ashes are readily available and used as an additive to mix concrete, precast concrete additive, concrete additive vibropressed, the raw material for the production of Portland cement and fly ash pozzolanic cements, adhesives raw material for the production of cement with fly ash use in building various geotechnical and hydro, and also as a raw material for the production of cellular concrete.

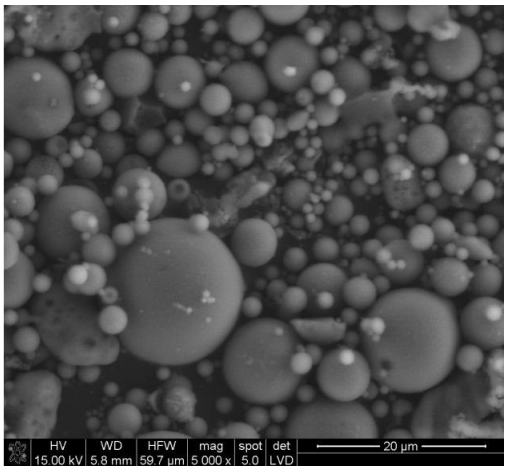

Fig.1. SEM photograph of fly ash silica: Source Institute of Ceramics and Building Materials.

Diversity siliceous ash grains given their form is strictly dependent on the conditions in which coal was burned. The density of the ash is in the range 2.1-2.4 g/cm^3, mainly determines the chemical composition and particle size of the ashes, which affects the water demand of fly ash [5], [6].

2.2. Lime fly ash

Lime fly ash is a fine dust granular of spherical grains. Is obtained by burning coal. A different chemical composition and mineral siliceous fly ash. It is characterized by the activity of hydraulic and / or pozzolanic consists essentially of reactive calcium oxide CaO, reactive silicon dioxide SiO_2 and alumina Al_2O_3 [4]. The usefulness of the limestone ashes for cement production determines particularly high, exceeding 25% by weight of reactive silica content and reactive calcium oxide above 10% [7] characteristic of calcareous fly ash is a large variation in the chemical composition, especially when the content of SiO_2, CaO, SO_3. This ash has a further variation of the chemical composition [8], [9].

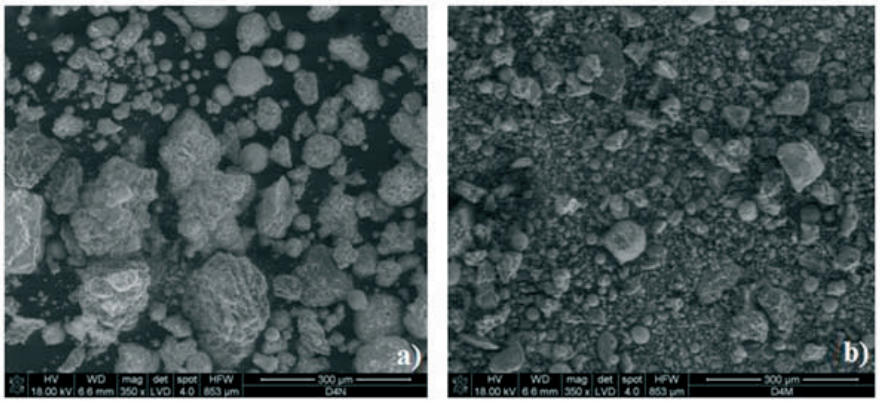

Fig.2 The morphology of the grains of the lime fly ash a) in the natural state, b) the ground [7].

Lime fly ash is used in the cement industry in the production of small concrete elements in the production of dry mortars and road construction industry as strengthening indigenous land and construction of road embankments [10].

2.3. Ash from the disposal of sewage sludge

Sewage sludge is the by-products of municipal wastewater treatment plants. Sediment composition is different and variable, depends on the type of wastewater, as well as how are they treated. Disposal of sewage sludge is associated with the drying and combustion. As a result of the combustion of sewage sludge get a product in the form of ash, which can be used as a mineral additive construction of concrete or cement [11]. However, it must meet all the criteria of the standard EN 450-1 + A1 2009 "Fly ash for concrete. Definitions specifications and conformity criteria" [12]. This standard allows the use of for example ash originating from co-firing of coal dust from plant materials, wood, animal waste, sludge from municipal wastewater. The optimum content of fly ash originating from burned materials should not exceed 10%. An important condition for the use of ash from the incineration of sewage sludge as a replacement component part of Portland cement clinker in cement is the chemical composition and the pozzolanic activity. According to the literature [13] the ash derived from the treatment of sewage sludge can be used as an ingredient in cement. Research confirms that it is possible to add 20% ash for cement used in the concrete. Based on chemical analysis revealed that the ash from the sludge is characterized by a high content of phosphate, which may be a factor in its use, since the release of phosphate ions grout may, however, be delayed harden and create restricting the use of ashes.

3. The own research

3.1. The materials and experimental methods

The aim of the research was ash derived from the combustion of sewage sludge. Thermal Station Sewage Sludge Disposal is located in sewage treatment plant, where sediments are transported, and dehydrated are thermally converted. Object burns 88.8 Mg / d per hour to 740 kg of dry sludge about 80% hydration. Sewage sludge are introduced into the furnace through a hydraulically driven pump.

The exhaust gas leaving the heat exchangers are subjected to purification processes. The first stage of purification technology takes place in a cyclone, and the resulting ashes are stored in special containers. The next purification step involves removal of HCl, HF, SOx, furans, and heavy metals by dispensing sodium bicarbonate and activated carbon. By virtue of purifying the resulting salts are captured on the filter bags and collected as dust.

For the embodiment portland cement CEM I 42.5 slurries was used, and natural aggregates in a ratio of 1: 0.5: 3. Mortar used in the study was a component of 20% by weight of cement

replaced by ash from the disposal of sewage sludge and control mortar contains only with portland cement. The samples were stored in water at 18 +/- 2 until assayed. Ash pozzolanic activity carried out in accordance with DIN EN 450-1 + A1. Pozzolanic activity was expressed in percentage as a ratio of compressive strength trabeculae dimensions 40x40x60 mm mortar made with 80% cement and 20% of comparative material the strength of the trabecular ash made of the same material without the addition of ash. The beginning and the end of the hardening of the binder cement and ash were tested using Vicat apparatus for slurries of 10% and 20% of ash content as compared to cement.

Mortar	Requirements by PN EN 206-1:2003	Ash from sewage sludge	Cem. I 42,5
2dni	-	31,4 MPa	39,4 MPa
28 dni	75%	43,3 MPa	51,3 MPa

Tab.1 The table shows the results of compressive strength.

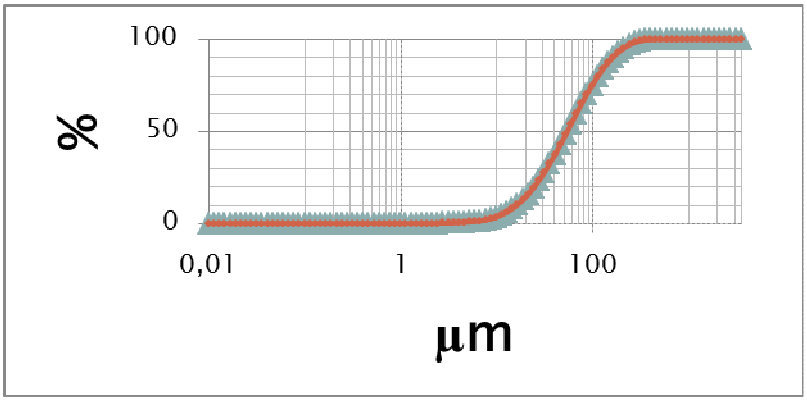

Fig.3 Grain size distribution curve for ash.

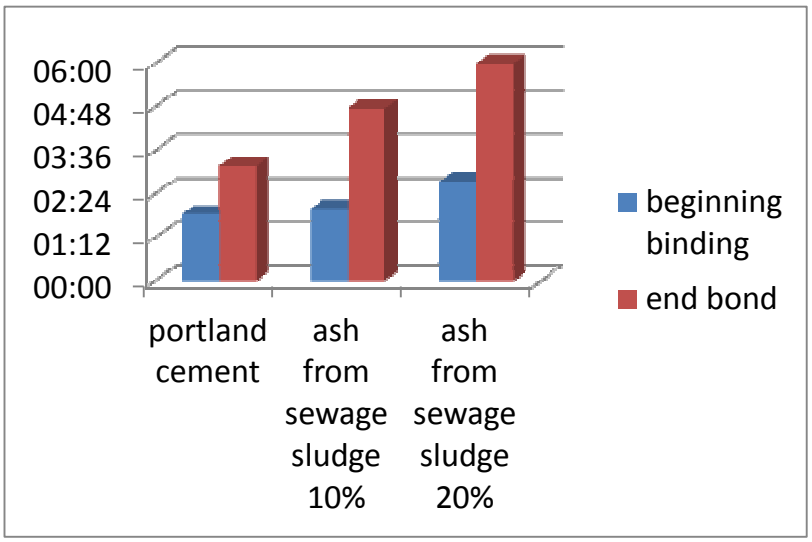

Fig.4 The beginning and the end of the adhesive bonding time.

3.2. The discussion of the results

The compressive strength of mortar is mainly dependent on the ash content in relation to the cement and the ripening period. Attempts to contain the ashes were characterized by slower development of strength. The survey was preceded by setting time fitting the appropriate amount of water to achieve normalization grout consistency. The presence of mineral additives causes a delay in the setting time, which increases with increasing ash in the grout. Another factor delaying the setting time is the fact that the current are larger amount of phosphate in relation to the other hydraulic materials. The ashes are with a small amount of phosphorus that can delay the setting and hardening.

Grain size distribution curve shows the particle size of the ash from the thermal treatment of sewage sludge. Read that in the sample is 78% of the particles with diameters in size from 0 to 100 fractions of microns.

1. Summary

1. The ashes from the combustion of sewage sludge increase / extend the setting time of the binder due to the presence in the composition of phosphorus compounds.
2. Ashes from the disposal of sewage sludge increase the curing time and delay the increase of strength of mortars because they contain significant amounts of phosphorus.
3. The use of fly ash from the combustion of sewage sludge to reduce the time delay loss of ductility and stiffness of the mortar.
4. The ash from the combustion of sewage sludge has sufficient pozzolanic activity that allows for the use of the ash as an additive for mortars replacing up to 20% of cement.

References

[1] zsawicz.wsh-kielce.edu.pl

[2] PN-EN 197-1:2012 Cement – Część 1:Skład, wymagania i kryteria zgodności dotyczące cementów powszechnego użytku

[3] PN-EN 450-1:2009 *Popiół lotny do betonu- część 1, Definicje, specyfikacje i kryteria zgodności* Budownictwo i Inżynieria Środowiska 2 (2011) ISSN 2081-3279

[4] GIERGICZNY Z. *Popiół lotny w składzie cementu i betonu.* Wydawnictwo Politechniki Śląskiej Gliwice 2013

[5] ZAPOTOCZNA -SYTEK G. ŁASKAWIEC, GĘBAROWSKI K., MAŁOLEPSZY P., SZYMCZAK J., *Popioły lotne nowej generacji do produkcji autoklawizowanego betonu komórkowego*, Warszawa 2013

[6] NEWILLE A.M *Właściwości Betonu* Wydawnictwo Polski Cement Kraków 2000

[7] GOŁASZEWSKI J., DREWNIOK M. *Wpływ popiołu wapiennego lotnego na efekty działania domieszek napowietrzających.*

[8] SYNOWIEC K. *Właściwości cementów popiołowo- żużlowych o nienormowym składzie, zawierających popiół lotny wapienny*, Budownictwo i Architektura 12(3) (2013) 215-222

[9] GIERGICZNY Z. *Rola popiołów lotnych wapniowych i krzemionkowych w kształtowaniu właściwości współczesnych spoiw budowlanych i tworzyw cementowych.* Wydawnictwo PK, Kraków 2006

[10] BARAN T., DRÓŻDŻ W., PICHNIARCZYK P. *Zastosowanie popiołów lotnych wapiennych do produkcji cementu i betonu, Instytut Ceramiki i Materiałów Budowlanych, Odział Szkła i Materiałów Budowlanych, CWB-1/2012,*

[11] KOSIOR -KAZBERUK M ,KARWOWSKA J. *Wybrane problemy zagospodarowania popiołów pochodzących ze spalania osadów ściekowych w technologii materiałów cementowych,* Inżynieria Ekologiczna Nr 25,2011

[12] PN-EN 450-1+A1 2009 *„Popiół lotny do betonu, Definicje wymagania i kryteria zgodności"*

[13] KOSIOR -KAZBERUK M. *Nowe dodatki mineralne do betonu.* Budownictwo i Inżynieria Środowiska 2/2011 ISSN 2081-3279

TRANSCOM 2015, 22-24 June 2015
University of Žilina, Žilina, Slovak Republic

Practical Assessment of Hot Mix Asphalt Concrete with RAP and Waste Sand

[*]Krzysztof Maciejewski, [*]Anna Chomicz-Kowalska
[*]Kielce University of Technology, Faculty of Civil Engineering and Architecture, Department of Transportation Engineering, Al. Tysiąclecia Państwa Polskiego 7, 25-314 Kielce, Poland, {kmaciejewski, akowalska}@tu.kielce.pl

Abstract. In this paper authors attempted to assess the impact of introducing simultaneously two waste materials (byproduct broken sand from aggregate production facility and granulated reclaimed asphalt pavement) to hot mix asphalt concrete. First, the basic properties of the waste materials were established allowing their further use in hot mix asphalt. Then, the designed control and experimental mineral-bitumen mixtures were tested for air void content, resistance to moisture and frost damage, wheel tracking and indirect tensile stiffness modulus. Additionally, fatigue life calculations of pavements containing control and experimental mixes were carried out based on the test results. The test results and the estimation of pavement fatigue life showed a promising possibility for utilization of the described waste materials in hot mix asphalt.

Keywords: asphalt concrete, RAP, fatigue calculation, ITSR, ITSM.

1. Introduction

Nowadays, road construction industry attempts to utilize increasing amounts of waste materials in the construction process for economic and environmental reasons [1-5]. These alternative materials, which originate mainly from road disassembly, extraction industries, energy production industry and steelmaking, have to comply with strict standards to fulfill certain technical requirements [6]. A specific set of waste, recyclable materials is acquired from dismantling buildings, engineering objects and mentioned disassembly of road structures. Good examples of such waste materials that can be used in road construction are the reclaimed asphalt and mineral materials obtained as a byproduct in aggregate production processes. Specifically, the use of reclaimed asphalt (RAP) in construction of new roads is often a subject of apprehension due to its possible negative effects on the final properties of the mineral-bitumen mix, which is reflected in the writings of Polish technical requirements WT-2 2008, 2010, and 2014 [7-9]. However, the introduction of those alternative materials brings an opportunity for reducing construction costs, for limiting the use of new materials and for preserving natural environment.

The aim of the presented investigations was to show that some waste materials can be successfully utilized in production of hot mix asphalt (HMA) layers without any visible negative effects as shown in relation to the technical requirements for bituminous mixes WT-2 2010 [8]. The produced experimental HMA mixes utilized simultaneously two types of waste materials: broken sand (A) and granulated reclaimed asphalt pavement material (B).

2. Properties of the waste materials

The used material A was a byproduct broken sand obtained from aggregate rinsing in a limestone aggregate production facility. The following properties of this material were investigated in the preliminary tests: grading (EN 933-1:2012), density (EN 1097-6:2013), fines content (EN 933-1:2012) and quality of fines (EN 933-9:2013). Additionally, the visual inspection of the material did not show any signs of organic parts or clay particles that could disqualify it for use in

asphalt mixes. The fines quality test returned a very good value of MB_F = 2.1 and a moderate fines content of 6.8% found. The acquired material was classified as a 0/2 mm broken sand with grain density of ρ = 2,650 Mg/m^3, fulfilling the requirements for aggregates used in asphalt concrete for roads trafficked by up to 7.4×10^6 equivalent standard loads (100 kN ESALs), as stated by technical requirements for aggregates WT-1 2010 [10].

The material B, reclaimed asphalt pavement (RAP) was obtained by milling worn out bituminous pavement layers, thus its composition was very similar to original mineral-bitumen mix. The aggregates and bitumen are tightly bound in RAP material, making it difficult to utilize in industry other than road construction. Having this in mind, it is popular to incorporate RAP in new road construction and rehabilitation works, in turn decreasing the use of new aggregates and bitumen [11]. RAP material after screening can be used for production of mineral-bitumen mixes if the final product fulfills the given requirements [8].

The studied reclaimed bituminous material was acquired by milling wearing course and was categorized as 16 RA 0/8 graded RAP fulfilling the requirements of EN 13108-8:2008 standard and WT-2 2010. The determined average soluble binder content was 5.2% in accordance with EN 12697-1:2012 standard.

3. Design of mineral-bitumen mixes

The research comprised a design of control mixes (based on solely new materials) and experimental mixes (with RAP and the material A sand) for binding (AC 16W) and base (AC 22P) courses trafficked by up to 7.4×10^6 equivalent single axle loads.

The mineral-bitumen mixes utilized aggregates abundant in the region of Świętokrzyskie Voivodeship: limestone and quartzite (Tab. 1).

<table>
<tr><td rowspan="2">Mineral-bitumen mix</td><td colspan="3">Control Mixes</td><td colspan="3">Experimental mixes</td><td rowspan="2">Comment</td></tr>
<tr><td>Share in mineral mix</td><td>Rock type</td><td>Fraction</td><td>Share in mineral mix</td><td>Rock type</td><td>Fraction</td></tr>
<tr><td rowspan="5">binding course AC 16W</td><td rowspan="2">57%</td><td rowspan="2">Limestone</td><td rowspan="2">added filler; 2/8, 8/16, 16/22.4,</td><td rowspan="2">47%</td><td rowspan="2">Limestone</td><td>added filler;</td><td rowspan="5">mat. A – substitution for quarzite 0/2 - 20% (leaving 13%);
mat. B - substitution for limestone 2/8 - 7%
and filler - 3%;</td></tr>
<tr><td>2/8, 8/16</td></tr>
<tr><td rowspan="3">43%</td><td rowspan="3">Quarzite</td><td rowspan="3">0/2, 16/22.4</td><td>23%</td><td>Quarzite</td><td>0/2; 16/22.4</td></tr>
<tr><td>20%</td><td colspan="2">material A</td></tr>
<tr><td>10%</td><td colspan="2">material B</td></tr>
<tr><td rowspan="3">base course AC 22P</td><td rowspan="3">100%</td><td rowspan="3">Limestone</td><td rowspan="3">added filler; 0/2, 2/8, 8/16, 16/22.4</td><td>70%</td><td>Limestone</td><td>added filler, 0/2, 2/8, 8/16, 16/22.4</td><td rowspan="3">mat. A – substitution for limestone - 0/2;
mat. B - substitution for limestone 2/8 - 7%
and filler - 3%;</td></tr>
<tr><td>20%</td><td colspan="2">material A</td></tr>
<tr><td>10%</td><td colspan="2">material B</td></tr>
</table>

Tab. 1. Framework composition of control and experimental mineral mixes.

The design of experimental and control mixes was conducted so that their properties could be compared and the effects of the introduced recycled materials could be assessed. Additionally, the bitumen for the binding course mixes comprising quartzite aggregates was supplemented with the addition of adhesion promoter in amounts of 0.3% relative to the bitumen mass. Tab. 1 presents the mineral composition of analyzed mixes with comments regarding aggregate swapping due to the introduction of the recycled materials.

Material A (broken sand) was added in amounts of 20% and the RAP material was added without preheating in amounts of 10% relative to the mineral mix mass in accordance to the writings of WT-2 2010. The introduction of RAP enabled to reduce dosing of 0/8 mm aggregate

grades and filler. Additionally, the amount of bitumen in the experimental mixes was substracted by the amount of bitumen in the added RAP to keep the total amount of bitumen in experimental and control mixes even (Tab. 2).

Mineral-bitumen mix	AC 16W (binder course)		AC 22P (base course)	
Control/ Experimental	Co	Ex	Co	Ex
New bitumen added [%]	4.6	4.1	4.0	3.5

Tab. 2. Added bitumen contents in the control and experimental asphalt concrete mixes.

4. Test results

The scope of conducted laboratory tests investigated the basic properties of designed control and experimental mineral-bitumen mixes to assess the influence of the added recycled materials. The mixes were tested for air void content (V_m, EN 12697-8:2005), indirect tensile stiffness modulus at 13ºC (ITSM, EN 12697-26:2012, appendix C), resistance to water and frost damage (ITSR, WT-2 2010 and EN 12697-12:2008), and resistance to permanent deformation (WTS_{AIR}, wheel tracking test at 60ºC, method B, EN 12697-22:2008). Tab. 3 presents the results of conducted tests.

Mineral-bitumen mix	AC 16W (binder course)		AC 22P (base course)	
Control/ Experimental	Co	Ex	Co	Ex
V_m [%]	5.8	5.4	5.4	5.2
ITSM [MPa]	8641	8674	8482	9222
ITSR [%]	82.4	85.5	79.6	78.2
WTS_{AIR} [mm/10^3 cycles]	0.14	0.12	0.35	0.21
Requirements	V_a: 4-7 [%]		V_a: 4-7 [%]	
	$ITSR_{80}$ $WTS_{AIR0.3}$		$ITSR_{70}$ $WTS_{AIR1.0}$	

Tab. 3. Test results of the control and experimental asphalt concrete mixes.

All of the designed mixes fulfilled the requirements stated by the technical requirements WT-2 2010. What is more, the use of recycled materials did not impair the measured properties of the mixes. The experimental mixes attained lower air void contents compared to the control group resulting in a better compaction. The experimental binder course mix AC 16W obtained an increased ITSR score, proving a better resistance to moisture and frost damage. This result was probably caused by the decreased amount of quarzite aggregates (most of the 0/2 quarzite fraction was swapped for the material A limestone broken sand), which show weaker adhesion to bitumen than limestone [12]. A small drop in the ITSR property was observed in the other mix (AC 22 P base course), probably being a result of the introduction of RAP material.

Also the mechanical properties were improved in the experimental mixes. In the binder course mix (AC 16W), the measured indirect tensile stiffness modulus was insignificantly affected by the alternative materials, and the wheel tracking slope (WTS_{AIR}) parameter was slightly decreased, probably due to the presence of aged binder [13]. This behavior was probably caused by swapping more resistant quartzite sand by the material A and by the simultaneous introduction of RAP that compensated for the weaker mineral mix. The experimental base course mix (AC 22P), on the other hand, showed significant improvement in both ITSM and rutting performance.

5. Pavement fatigue life calculation

A pavement fatigue life calculation through the mechanical-empirical design method was performed to show the practical effects of simultaneous introduction of RAP material and broken sand material A to the mineral-bitumen mixes for binder and base course. The calculations were conducted using the principles of multilayer elastic theory.

The polish design practice utilizes the Asphalt Institute fatigue models [14] for predicting cracking (1-3) and for predicting permanent deformation distress (4):

$$N_{asf} = 18.4 \cdot C \cdot (6.167 \cdot 10^{-5} \cdot \varepsilon_r^{-3.291} \cdot |E^*|^{-0.854}) \quad (1)$$

$$C = 10^{M} \quad (2)$$

$$M = 4.84 \cdot (V_b / (V_b + V_a) - 0.69) \quad (3)$$

$$\varepsilon_p = k(1/N_p)^m \quad (4)$$

where: N_{asf} – number of repetitions to fatigue cracking, ε_r – tensile strain at the critical location, $|E^*|$ - complex modulus of the bituminous layer, V_b – volumetric bitumen content (%), V_a – air voids (%), ε_p – compressive strain at the top of subgrade, k=1.05 $\cdot 10^{-2}$, m = 0.223 (coefficients in accordance to Chevron), N_p – number of repetitions to critical structural deformation (12.5 mm).

The pavement design for the calculation was adopted from the polish catalogue of standard pavement designs [15] with a typical asphalt concrete wearing course and the investigated binding and base courses, which properties were shown in Tab. 3. The calculations assumed an equivalent temperature of +13ºC, 100 kN axle load and a wheel-to-surface contact pressure of 850 kPa. The results of fatigue life calculations are presented in Tab. 4.

The use of described waste materials resulted in an improvement of the predicted fatigue life of the analyzed pavement designs. The fatigue cracking was postponed by a magnitude of 1.2×10^6 equivalent single axle loads and a similar case was observed regarding the permanent deformation criterion. Such a positive feedback was caused mainly by the increased stiffness modulus of the experimental binder course mix, but the decreased air void content had also contributed to this outcome.

Design traffic (2.5 to 7.4) × 10^6 ESALs 100 kN		Control mixes		Experimental mixes	
		Layer thickness [cm]	Stiffness modulus [MPa]	Layer thickness [cm]	Stiffness modulus [MPa]
Wearing course	AC 11 S	4	9300	4	9300
Binding course	AC16 W	8	8600	8	8600
Base course	AC 22 P	14	8400	14	9200
Subgrade		-	100	-	100
$\|\varepsilon_r\|$		$9.19 \cdot 10^{-5}$		$8.71 \cdot 10^{-5}$	
ε_p		$-3.10 \cdot 10^{-4}$		$-2.99 \cdot 10^{-4}$	
N_{asf} [ESALs 100 kN]		6 896 464		8 052 700	
N_p [ESALs 100 kN]		7 247 921		8 573 962	

Tab. 4. Results of the pavement fatigue life calculation with the control and experimental asphalt concrete mixes.

6. Conclusions

The research concerned the overall performance of hot mix asphalt concrete mixes designed for binding and base courses, comprising two types of waste materials: byproduct broken sand obtained at limestone aggregate production facility and granulated reclaimed asphalt pavement material

obtained by milling of a worn out wearing course. Control mixes containing only new materials and experimental mixes with waste materials were designed, produced and tested.

The obtained results shown that the simultaneous introduction of both waste materials had no measurable negative influence on the assessed properties of the mineral-bitumen mixes: air voids, resistance to moisture and frost damage, indirect tensile stiffness modulus and wheel tracking slope. What is more, the mechanical properties of the mixes (ITSM and WTS_{AIR}) were improved.

A pavement fatigue life calculation utilizing the mechanical-empirical design method was used to predict the durability of pavements constructed using control and experimental mixes. The slight decrease in air void content and increase in ITSM values resulted in improved fatigue life of the design increasing it capacity by 1.2×10^6 ESALs.

The overall amount of substituted new mineral materials in the experimetal mixes equaled 30%, and through the use of RAP material B, the amount of new bitumen was decreased by 0.5%.

References

[1] IWAŃSKI, M., CHOMICZ-KOWALSKA, A. *Laboratory Study on mechanical Parameters of Foamed Bitumen Mixtures in the Cold Recycling Technology*. Procedia Engineering 57, 433-442 (2013), DOI:10.1016/j.proeng.2013.04.056.

[2] IWAŃSKI, M., CHOMICZ-KOWALSKA, A. Application of recycled aggregates to the road base mixtures with foamed bitumen in the cold recycling technology. 9th ICEE, 22-23 May 2014, Vilnius, Lithuania, DOI:10.3846/enviro.2014.155.

[3] IWAŃSKI, M., CHOMICZ-KOWALSKA, A. Evaluation of the effect of using foamed bitumen and bitumen emulsion in cold recycling technology. 3rd ICTI, Pisa, Italy, 96-76p, 2014.

[4] IWAŃSKI, M., CHOMICZ-KOWALSKA, A. *Laboratory Study on mechanical Parameters of Foamed Bitumen Mixtures in the Cold Recycling Technology*. Procedia Engineering 57, 433-442 (2013), DOI:10.1016/j.proeng.2013.04.056.

[5] IWAŃSKI, M., CHOMICZ-KOWALSKA, A. Experimental study of water and frost resistance of foamed bitumen mixes in the cold recycling technology. Proc. Euroasphalt & Eurobitume Congress 5, 13-15 June 2012 (P5EE-357).

[6] IBDiM. Ocena i badania wybranych odpadów przemysłowych do wykorzystania w konstrukcjach drogowych. Opracowanie pod kierunkiem Dariusza Sybilskiego. Warszawa 2004.

[7] GDDKiA. Wymagania Techniczne: Nawierzchnie asfaltowe na drogach krajowych. WT-2 2008. Mieszanki mineralno-asfaltowe. Warszawa 2008.

[8] GDDKiA. Wymagania Techniczne: Nawierzchnie asfaltowe na drogach krajowych. WT-2 2010. Mieszanki mineralno-asfaltowe. Warszawa 2010.

[9] Wymagania Techniczne: Nawierzchnie asfaltowe na drogach krajowych. WT-2 2014. Mieszanki mineralno-asfaltowe. Warszawa 2014.

[10] GDDKiA. Wymagania Techniczne: Kruszywa do mieszanek mineralno-asfaltowych i powierzchniowych utrwaleń na drogach krajowych. WT-1 2010. Warszawa 2010.

[11] MNISZEK W. SADZIK A., Wtórne wykorzystanie destruktu asfaltowego do budowy dróg. Zeszyty Naukowe Wyższej Szkoły Zarządzania Ochroną Pracy w Katowicach 2012, nr 1(8)/2012.

[12] REMIŠOVÁ, E. Theory and measurements of bitumen binders adhesion to aggregate. Komunikacie, Volume 6, Issue 1, 2004, Pages 58-63.

[13] KOMACKA, J., REMIŠOVÁ, E. et al. Influence of reclaimed asphalt with polymer modified bitumen on properties of different asphalts for a wearing course. Sustainability, eco-efficiency and conservation in transportation infrastructure asset management. Pages: 179-185 Published: 2014.

[14] JUDYCKI, J. *Porównanie kryteriów zmęczeniowych do projektowania podatnych i półsztywnych nawierzchni drogowych. Cz. I*. Drogownictwo 1/1999, Cz. II, Drogownictwo 2/1999, SITK, Warszawa 1999.

[15] GDDKiA. Katalog typowych konstrukcji nawierzchni podatnych i półsztywnych. Opracowanie pod kierunkiem Józefa Judyckiego, Katedra Inżynierii Drogowej Politechniki Gdańskiej. Warszawa 2014.

TRANSCOM 2015, 22-24 June 2015
University of Žilina, Žilina, Slovak Republic

Calculation of air temperature in a ventilated roof void

*Grzegorz Majewski
Kielce University of Technology Faculty of Environmental Engineering, Geomatics and Power Engineering, Department of Building Physics and Renewable Energy, Al. Tysiąclecia Państwa Polskiego 7, 25-314 Kielce, Poland, majewskigrzegorz@wp.pl

Abstract. This paper presents examples of calculating air temperature in a flat room ventilated void providing continuous air flow. The calculations are based on the heat balance equation for any cross section of the gap and for winter conditions. In Case 1, the temperature was calculated for a flat roof without a snow cover. In Case 2, the calculations were made for a flat roof with a 5 cm thick snow cover. In Case 3, the air temperature was calculated for a flat roof under a 10 cm trick snow cover. The determined values included air temperatures at any cross section of the ventilation gap and the amount of heat permeating through this partition.

Keywords: ventilated roof void, air temperature, air flow, heat permeation through the partition.

1. Introduction

Flat roofs are structures that act as both roofs and ceilings. Typical flat roof construction includes a structural deck, thermal insulation, a layer to adjust uneven surfaces, a cement screed and a vapour control layer. Nevertheless, this type of roof is the most sensitive to dampening by condensing water vapour [2].

The difference in outdoor and indoor air temperatures, both in summer and winter, has a considerable influence on the roof design, especially on the design of a flat roof. In winter the surface of the roof covering cools to an average temperature of - 20° C and lower. In order to provide the attic space with proper ventilation, flat roof spaces should have ventilation openings (small gaps) that run uniformly and in two opposite sides to promote cross ventilation. The number and size of the openings should be selected adequately to allow the water vapour escape the attic and prevent dew point condensation [3].

The primary purpose of ventilation is to vent the moisture that passes through the ceiling from the attic to the void. The outdoor air is pushed by the wind into the gaps, where it heats, absorbing some of the water vapour, and leaves at the other side of the gaps carrying away the moisture. The air flow rate and thus the effectiveness of moisture removal depend on wind pressures, the distance travelled by the air in the gap and flow resistances. At strong winds acting perpendicular to the wall with intake vents, the air velocity in large gaps may exceed 1 m/s. On a windless day or with winds blowing parallel to the wall with openings, the wind speed falls to nearly zero. In the gaps and small-size channels, the air flow is low even with favourable wind rates [1].

2. Ventilated air gap

This section describes the steady thermal conditions for the partition with a gap and continuous air flow. The ventilated air gap is separated from the room at which temperature is t_i by an internal part of the partition with the heat transfer coefficient of U_i. The external part of the partition with the heat transfer coefficient U_e separates the gap area from the exterior air with temperature t_e. The air with temperature t_0 flows into the gap and changes its temperature while flowing through it. At a distance l_{kr} the air flow reaches the constant temperature value t_{sz}, dependent on the heat transfer

through the partition and independent of the initial air temperature. The problem involves determining air temperature t_x for any cross section of the gap and the amount of heat permeating through such a partition [5].

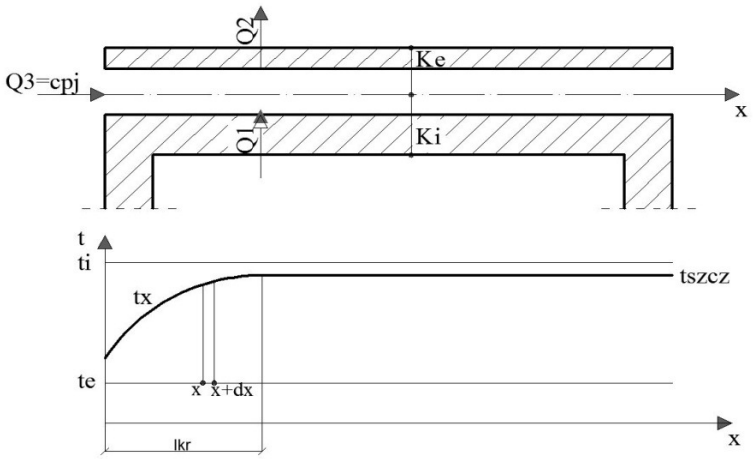

Fig.1. Heat transfer through the partition with a ventilated air gap

The heat flux flowing from the room to the air in the gap [4]:

$$Q_1 = k_i(t_i - t_x)dx \text{ [W]} \quad (1)$$

The heat flux passed from the air in the gap to the external air [4]:

$$Q_2 = k_e(t_x - t_e)dx \text{ [W]} \quad (2)$$

The heat flux taken for heating the air flowing through the gap [4]:

$$Q_3 = c_p\, j\, \mathrm{dt} \text{ [W]} \quad (3)$$

where:
t_x – air temperature in the gap at distance x from the inlet,
c_p – specific heat of the air at constant pressure,
j – air flow.

Air flow formula [4]:

$$j = 3600\, v\, \rho\, h \text{ [kg/mh]} \quad (4)$$

where:
v – air flow rate,
ρ – air density,
h - air gap height.

Heat fluxes are linked under the heat balance equation [4]:

$$Q_1 = Q_2 - Q_3 \text{ [W]} \quad (5)$$

From which the differential relationship was obtained [4]:

$$k_i(t_i - t_x)dx - k_e(t_x - t_e)dx = c_p\, j\, dt \quad (6)$$

After the separation of the variables and sides integration, the following equation was obtained [4]:

$$t_x = \frac{k_i t_i + k_e t_e}{k_i + k_e} + \left(t_0 - \frac{k_i t_i + k_e t_e}{k_i + k_e}\right) exp\left(-\frac{k_i + k_e}{c_p j} x\right) \quad (7)$$

The air temperature in the gap [4]:

$$t_{szcz} = \frac{k_i t_i + k_e t_e}{k_i + k_e} \text{ [°C]} \quad (8)$$

Critical length [4]:

$$l_{kr} = \frac{3 c_p j}{k_i + k_e} \text{ [m]} \quad (9)$$

Entering quantity t_{szcz} given by (8) to formula (7) and using [4]:

$$\frac{k_i + k_e}{c_p j} = A \text{ [m}^{-1}\text{]} \quad (10)$$

gives

$$t_x = t_{szcz} + (t_0 - t_{szcz})\, exp(-A_x) \text{ [°C]} \quad (11)$$

Formula for air flow rate in intake and exhaust channels [4]:

$$v_k = v_e \sqrt{\frac{K_i - K_e}{\sum \xi}} \text{ [m/s]} \quad (12)$$

Formula for the air flow rate in the gap[4]:

$$v = v_k \frac{F_k}{h} \text{ [m/s]} \quad (13)$$

where:
F_k – area of the channel in m² per 1 m air gap width perpendicular to the air flow direction,
h - air gap height.

3. Analysis of the calculation results

Data used in calculations are summarized in Tables 1- 3. Table 4 shows the results.

Case 1

Layer	d [m]	λ [W/mK]	d/λ [m² K/W]
Interior air			R_{si} = 0.10
Cement-lime plaster	0.015	1.05	R_1 = 0.014
Reinforced concrete ceiling	0.23	1.63	R_2 = 0.141
Polystyrene foam	0.20	0.041	R_3 = 4.878
Cement screed	0.03	1.05	R_4 = 0.029
Air layer	0.12		R_e = 0.085
			ΣR = 5.247
Air layer	0.12		R_i = 0.085
Timber lags	0.04	0.17	R_5 = 0.235
2 x roofing felt	0.01	0.17	R_6 = 0.059
Exterior air			R_7 = 0.04
			ΣR = 0.419

Table 1. Input data for calculations – flat roof construction with an open air layer without the snow cover

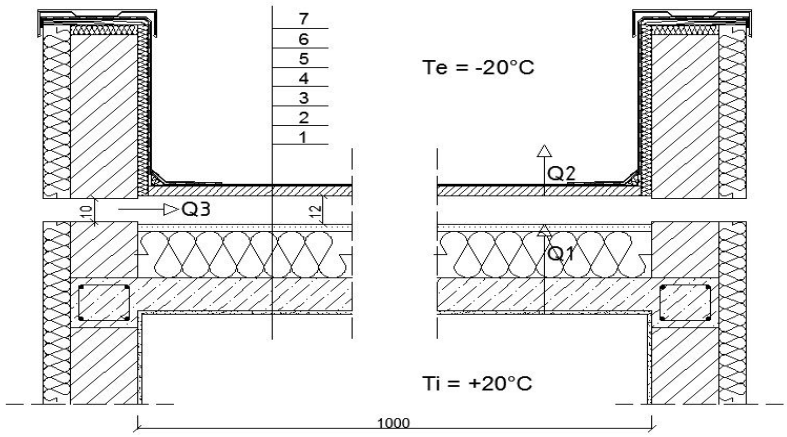

Fig.2. Case 1 – flat roof construction with an open air layer without the snow cover:1-cement-lime plaster, 1.5 cm thick, 2- reinforced concrete ceiling, 23 cm thick, 3- expanded polystyrene (EPS 100), 20 cm thick, 4- cement screed, 3 cm thick, 5- air layer, 12cm thick, 6-timber lagging, 4cm thick, 7- two layers of roofing felt, 1cm thick

Case 2

Layer	d [m]	λ [W/mK]	d/λ [m² K/W]
Interior air			R_{si} = 0.10
Cement-lime plaster	0.015	1.05	R_1 = 0.014
Reinforced concrete ceiling	0.23	1.63	R_2 = 0.141
Polystyrene foam	0.20	0.041	R_3 = 4.878
Cement screed	0.03	1.05	R_4 = 0.029
Air layer	0.12		R_e = 0.085
			ΣR = 5.247
Air layer	0.12		R_i = 0.085
Timer lagging	0.04	0.17	R_5 = 0.235
2 x roofing felt	0.01	0.17	R_6 = 0.059
Snow	0.05	0.11	R_7 = 0.454
Exterior air			R_8 = 0.04
			ΣR = 0.873

Table 2. Input data for calculations – flat roof construction with an open air layer and a 5 cm thick snow cover

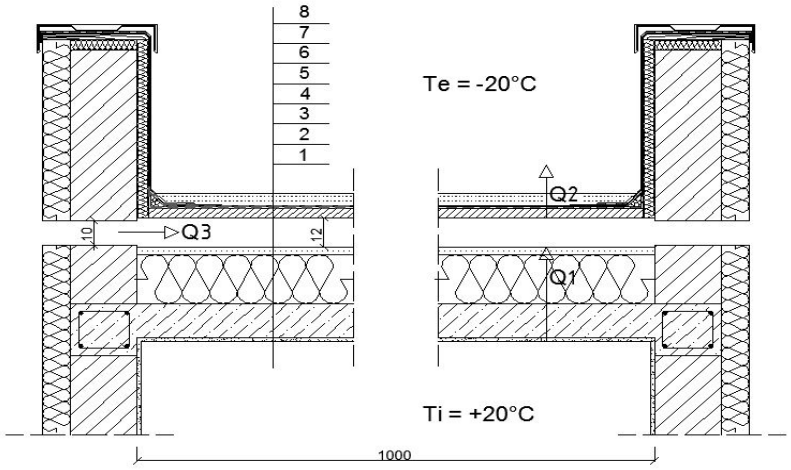

Fig.3. Case 2 – flat roof construction with an open air layer and a 5 cm thick snow cover: 1-cement-lime plaster, 1.5 cm thick, 2- reinforced concrete ceiling, 23 cm thick, 3- expanded polystyrene (EPS 100), 20 cm thick, 4- cement screed, 3

cm thick, 5- air layer, 12cm thick, 6-timber lagging, 4cm thick, 7- two layers of roofing felt, 1cm thick, 8- snow, 5 cm thick

Case 3

Layer	d [m]	λ [W/mK]	d/λ [m² K/W]
Interior air			R_{si} = 0.10
Cement-lime plaster	0.015	1.05	R_1 = 0.014
Reinforced concrete ceiling	0.23	1.63	R_2 = 0.141
Polystyrene foam	0.20	0.041	R_3 = 4.878
Cement screed	0.03	1.05	R_4 = 0.029
Air layer	0.12		R_e = 0.085
			ΣR = 5.247
Air layer	0.12		R_i = 0.085
Timer lagging	0.04	0.17	R_5 = 0.235
2 x roofing felt	0.01	0.17	R_6 = 0.059
Snow	0.10	0.11	R_7 = 0.909
Exterior air			R_8 = 0.04
			ΣR = 1.328

Table 3. Input data for calculations – flat roof construction with an open air layer and a 10 cm thick snow cover.

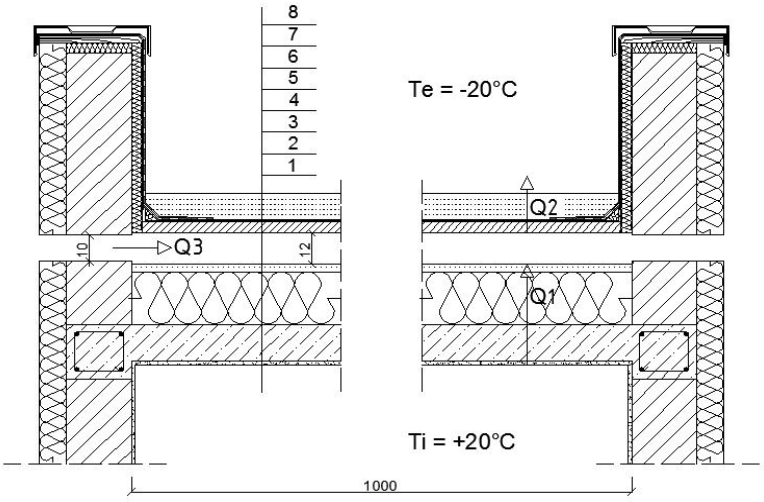

Fig.4. Case 2 – flat roof construction with an open air layer and a 10 cm thick snow cover: 1-cement-lime plaster, 1.5 cm thick, 2- reinforced concrete ceiling, 23 cm thick, 3- expanded polystyrene (EPS 100), 20 cm thick, 4- cement screed, 3 cm thick, 5- air layer, 12cm thick, 6-timber lagging, 4cm thick, 7- two layers of roofing felt, 1cm thick, 8- snow, 10 cm thick

x [m]	0	1	2	3	4	5	6	7	8	9	10
Case 1 [°C]	-20.00	-19.69	-19.41	-19.18	-18.97	-18.79	-18.63	-18.50	-18.38	-18.27	-18.19
Case 2 [°C]	-20.00	-19.67	-19.37	-19.08	-18.81	-18.56	-18.32	-18.10	-17.89	-17.69	-17.51
Case 3 [°C]	-20.00	-19.67	-19.35	-19.04	-18.76	-18.48	-18.22	-17.97	-17.72	-17.49	-17.27

Table 4. Calculation results for air temperature in the horizontal air gap.

Verification of the heat balance equation for Case 1:

$$Q_1 - Q_2 = Q_3$$

$$Q_1 = 0.190 \; x \; 10 \; x \; 1.0(20.000 - (-18.909)) = 73.927 \;\; [W]$$

$$Q_2 = 2.386\ x\ 10\ x\ 1.0(-18.909 - (-20.00)) = 26.031\ [W]$$
$$Q_3 = 0.28\ x\ 81.959\ x\ (-18.185 - (-20.00)) = 41.651\ [W]$$
$$73.927 - 26.031 = 47.896$$
$$Q_1 - Q_2 \neq Q_3$$

Verification of the heat balance equation for Case 2:

$$Q_1 - Q_2 = Q_3$$
$$Q_1 = 0.190\ x\ 10\ x\ 1.0(20.000 - (-18.635)) = 73.406\ [W]$$
$$Q_2 = 1.145\ x\ 10\ x\ 1.0(-18.635 - (-20.00)) = 15.629\ [W]$$
$$Q_3 = 0.28\ x\ 81.959\ x\ (-17.507 - (-20.00)) = 57.210\ [W]$$
$$73.406 - 15.629 = 57.777$$
$$Q_1 - Q_2 \approx Q_3$$

Verification of the heat balance equation for Case 3:

$$Q_1 - Q_2 = Q_3$$
$$Q_1 = 0.190\ x\ 10\ x\ 1.0(20.000 - (-18.543)) = 73.231\ [W]$$
$$Q_2 = 0.753\ x\ 10\ x\ 1.0(-18.543 - (-20.00)) = 10.971\ [W]$$
$$Q_3 = 0.28\ x\ 81.959\ x\ (-17.266 - (-20.00)) = 62.741\ [W]$$
$$73.231 - 10.971 = 62.260$$
$$Q_1 - Q_2 \approx Q_3$$

4. Conclusions

The calculation method presented in this paper for the air temperature in the ventilated air gap of the flat roof offers the simplest solution for ventilation openings distributed symmetrically and placed on the same level. More complicated cases were not taken into account in this method. In addition, the heat balance equation is not always satisfied. This method can be used only for the simplest cases. Otherwise, more factors should be accounted for to obtain more accurate calculation results.

References

[1] PŁOŃSKI W., POGORZELSKI J., *Fizyka budowli Zasady projektowania przegród budowlanych w zakresie cieplno-wilgotnościowym[Building Physics. Thermal-Moisture Design Principles for Partition Walls]*, Arkady, Warszawa 1979

[2] STANKIEWICZ H., *Zabezpieczenie budowli przed wilgocią, wodą gruntową i korozją [Securing building structures against moisture, groundwater and corrosion]*, Arkady, Warszawa 1959

[3] NECHAY J., *Budownictwo betonowe Tom X Budownictwo miejskie [Concrete Construction Vol. X Urban Construction]*, PAN, Komitet Inżynierii Lądowej, Arkady, Warszawa 1964

[4] POGORZELSKI J., *Fizyka cieplna budowli [Thermal Physics of Buildings]*, PWN, Warszawa 1976

[5] BOGOSŁAWSKI W., *Fizyka budowli [Building Physics]*, *Arkady, Warszawa 1975*

TRANSCOM 2015, 22-24 June 2015
University of Žilina, Žilina, Slovak Republic

Influence of the Air-Entrainment and the Prior Freezing and Thawing on the Sulphate Resistance of Portland and Blast-Furnace Cement Mortars

[*] Julia Marczewska, [*] Wojciech Piasta
[*] Kielce University of Technology, Faculty of Civil Engineering and Architecture, Al. Tysiąclecia Państwa Polskiego 7, 25-314 Kielce, Poland, {jmarczewska, wpiasta}@tu.kielce.pl

Abstract. This paper presents the results of sulphate expansion tests of air entrained (AE) and non-air entrained (nAE) Portland and blast furnace cement mortars subjected to prior freezing and thawing. Despite the significant strains experienced during freeze-thaw cycles, unlike the non-air entrained Portland cement mortars, the non-air entrained mortars made of blast furnace cement did not exhibit any significant expansion when exposed to Na_2SO_4. No expansion was found in the air-entrained mortars made of either of the cement types when immersed in Na_2SO_4 solution after the freeze-thaw cycles. The results of the SEM and XRD analyses showed that gypsum and ettringite were the sulphate attack products in all the mortars. The highest amounts of ettringite were found in air voids.

Keywords: Sulphate attack, freeze-thaw deterioration, air-entrainment, blast-furnace cement, expansion, ettringite, air void.

1. Introduction

A combination of interdependent factors occurring alternately or concurrently can cause concrete to deteriorate. Damage in concrete exposed to chemically aggressive environments falls into three basic types: dissolution of cementitious matrix, occurrence of phases with unbinding properties, and expansion.

The most deleterious and at the same time the most common causes of cement composite deterioration in our climate include freeze-thaw deterioration and corrosion due to sulphate attack. The typically used preventive measure against freeze-thaw deterioration is air-entrainment. Although multiple rules of air-entrainment optimization have been identified [1], the durability of AE concrete is evaluated only for freezing and thawing with no results reported for concrete behavior in other environments. However, air entrained concrete can also be subjected to deleterious effects of chemically aggressive exposure. As the air voids that are connected with capillary pores have a special structure, it is interesting how the sulphate attack products will precipitate in the microstructure of AE concrete. The distress of AE and nAE concrete by simultaneously occurring combined sulphate attack and cycles of freezing and thawing remains a completely unknown issue.

2. Experimental

2.1. Aim and Scope of Study

The aim of the study was to determine the effect of air-entrainment and short-term prior freeze-thaw attack on the sulphate resistance of mortars. Since data in the literature are scarce, the attention was paid to clarifying the sulphate attack process after an initial short-term frost action. After 28 days of curing in water, half of the specimens were immersed in the sodium sulphate solution and the other half were first subjected to 40 freeze-thaw cycles and then immersed in the sodium sulphate solution.

2.2. Materials

Tests were carried out using two mortars made from Portland cement CEM I 42.5R and blast furnace slag cement CEM III/A 32.5 N. Table 1 shows chemical and phase compositions of the clinker. The water-to-cement ratio was 0.55.

Chemical composition	**SiO_2**	**Al_2O_3**	**Fe_2O_3**	**CaO**	**$CaO_{(free)}$**	**MgO**	**SO_3**	**Cl-**	**Na_2O_{eq}**
	19.5	6.0	3.1	62.1	1.75	1.7	2.6	0.03	0.8
Phase composition	**C_3S**	**C_2S**	**C_3A**	**C_4AF**					
	54.0	17.0	11.5	10.1					

Tab. 1. The chemical and the phase compositions of Portland cement clinkers [%].

The half of the specimens was air-entrained to the same air content, using an air-entraining admixture (Tab. 2). After 28 days of curing, water absorption of AE mortars was higher than that of nAE mortars (Tab. 2). In compliance with the principle, AE mortars had lower compressive and flexural strengths.

Properties of mortars at 28 days	**CEM I**		**CEM III**	
	AE	**nAE**	**AE**	**nAE**
Air content in fresh mortar [%]	9.4	4.6	9.3	3.8
Compressive strength [MPa]	28.24	35.06	17.81	22.67
Flexural strength [MPa]	5.41	5.57	4.33	4.73
Absorption by weight [%]	9.13	8.95	9.14	9.08

Tab. 2. Physical properties of cement mortars cured for 28 days.

2.3. Methods

The air content in the fresh mortars was determined using the pressure method. All the tests on the hardened mortars were carried out on specimens with dimensions of 40×40×160 mm. Every four weeks, using a Graf-Kaufman extensometer, linear strain of hardened cement mortars immersed in 5% Na_2SO_4 solution and during cycles of freezing and thawing was determined [2].

Mortar microstructure was studied using XRD and SEM analyses. The study consisted of AE and nAE specimens made from Portland and blast furnace slag cements. Half of specimens was immersed in the sodium sulphate solution for 12 months. The other half was first subjected to 40 freeze-thaw cycles and then immersed in the Na_2SO_4 solution for the 12-month period.

Microstructure of mortars was studied using XRD and SEM analyses.

3. Test Results and Discussion

Non air entrained blast furnace slag cement mortars, earlier subjected to 40 freeze-thaw cycles, experienced a significant strain (10‰), which is indicative of microstructure damage. Later, after the specimens have been immersed in the sodium sulphate solution, the strain slightly increased by 2 ‰ for the first three months (Fig. 1).

The results suggest that sulphate ions react with aluminates containing hydrates in micro cracks from freeze-thaw deterioration and in large capillary pores to form ettringite, which affects insignificant expansion of 2‰. After “freely available” aluminates have reacted, further swell does not occur owing to the compact microstructure of the blast furnace slag cement paste [3], [4].

The nAE mortars made from Portland cement showed a slight strain (3.8‰) during the freeze-thaw cycles. The strain started to increase after about 7 months of storing the specimens in the sodium sulphate solution to reach 7.8‰ at 12 months. As the microstructure of this mortar was less

damaged than that of the mortar made from the blast furnace cement, no expansion occurred here immediately after the relocation.

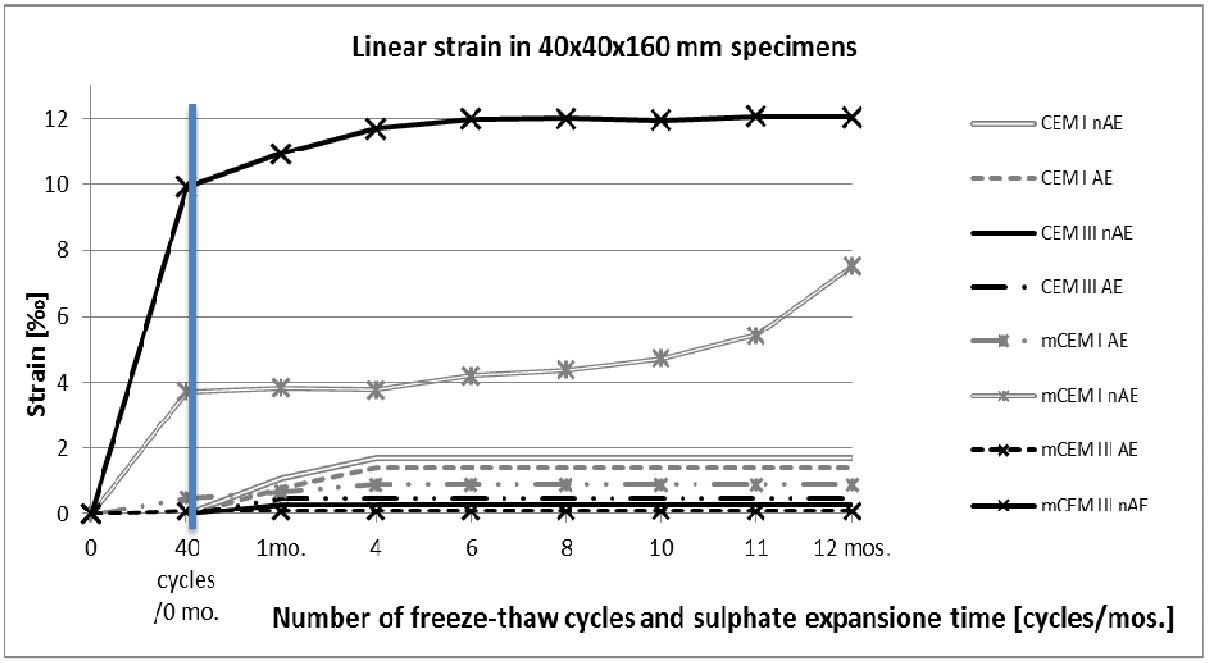

Fig. 1. Linear strain of AE and nAE mortar specimens made from CEM I and CEM III cements subjected to 40 freeze-thaw cycles and then immersed in the Na_2SO_4 solution for 12 months and immersed in the Na_2SO_4 solution alone for 12 months.

The AE specimens made from both types of cement, first frozen, thawed and then placed in the Na_2SO_4 solution, did not experience any strain. No strain was observed in the mortars both air entrained and non-air entrained, made from Portland cement and with blast furnace cement, stored exclusively in the Na_2SO_4 solution.

After 40 freeze-thaw cycles and 12-month storage in the sodium sulphate solution, the products of sulphate corrosion, i.e. ettringite and gypsum, were observed in the AE and nAE mortars made from Portland cement (Fig. 2.) and blast furnace cement (Fig. 3.). Quantitative comparison of gypsum and ettringite content is very difficult. The formation of the third product of sulphate attack, thaumasite, may be attributed to calcite present in this mortar.

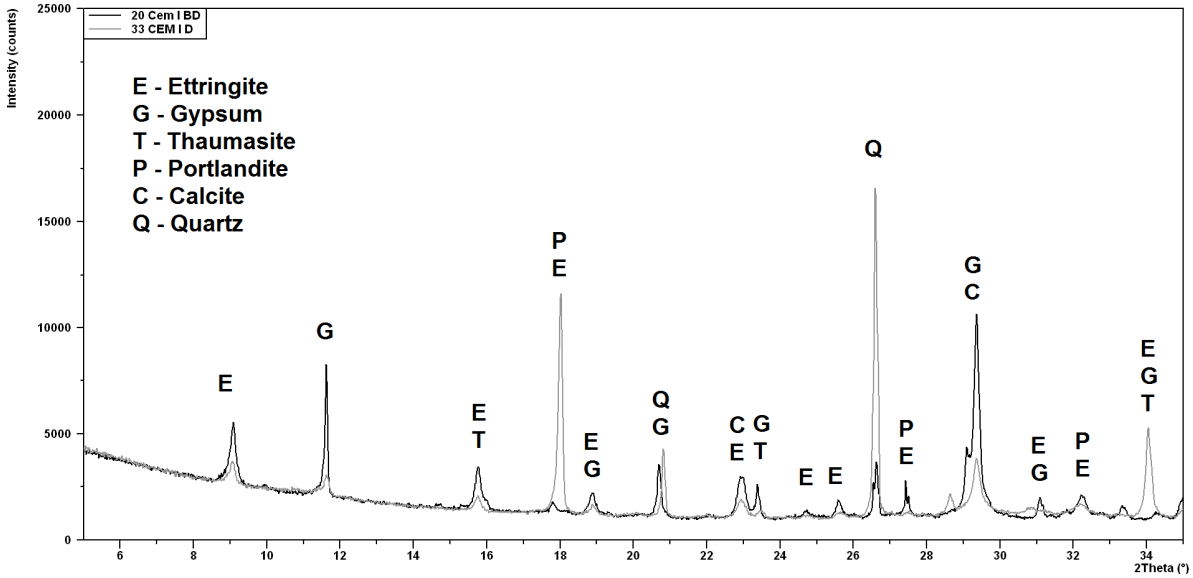

Fig. 2. The XRD analysis of nAE and AE Portland cement mortars exposed to 40 freeze-thaw cycles and 12 months of sodium sulphate attack.

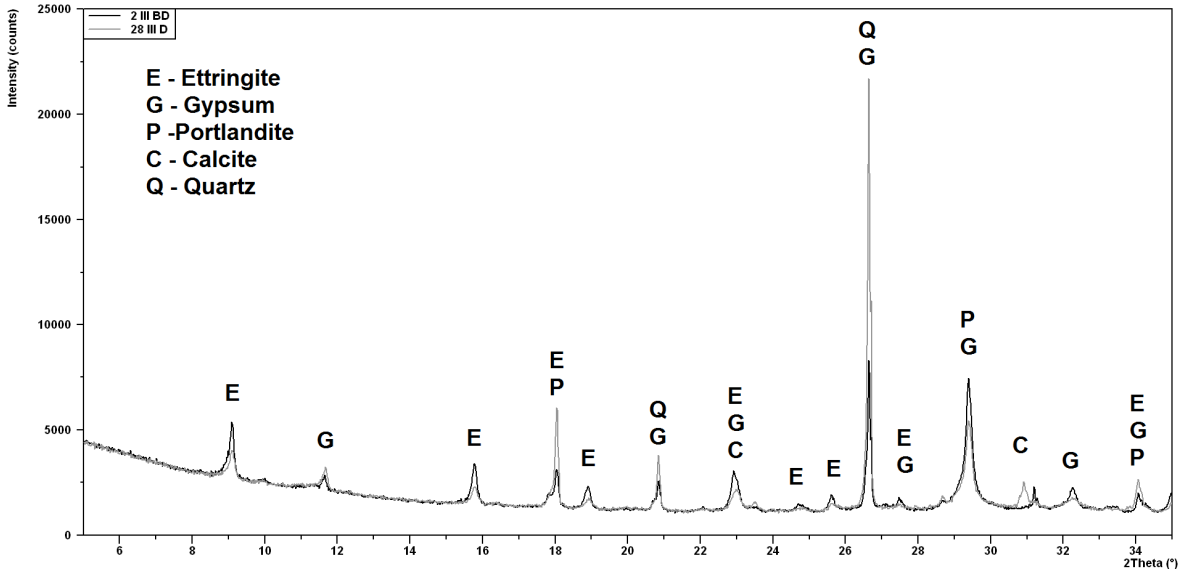

Fig. 3. The XRD analysis of nAE and AE blast furnace cement mortars exposed to 40 freeze-thaw cycles and 12 months of sodium sulphate attack.

In the nAE mortar made from Portland cement, where expansion reached approx. 8‰, gypsum and ettringite crystals are seen embedded in the compact structure of C-S-H (Fig. 4b). In the AE mortar, made from the same cement type and showing no expansion after 12 months, the air voids are partially filled with densely packed ettringite crystals (Fig. 4a). The SEM image shows that ettringite crystals appear in the pores of entrapped air in nAE blast furnace cement mortars (Fig. 5b), in which the strain that developed during freeze-thaw cycles increased slightly in the solution. Ettringite crystals were observed at the walls of air voids in AE mortar made from blast furnace cement CEM III (Fig. 5a). Far more ettringite was found in the air voids than in the microstructure of the paste at a distance from the mortar air voids. This may suggest that ettringite crystals forming in the air voids did not contribute substantially to the expansion of the mortar. Thus, expansion is associated with the formation of ettringite that becomes embedded in the compact microstructure of C-S-H. This agrees with the recently published expansion mechanism hypothesis.

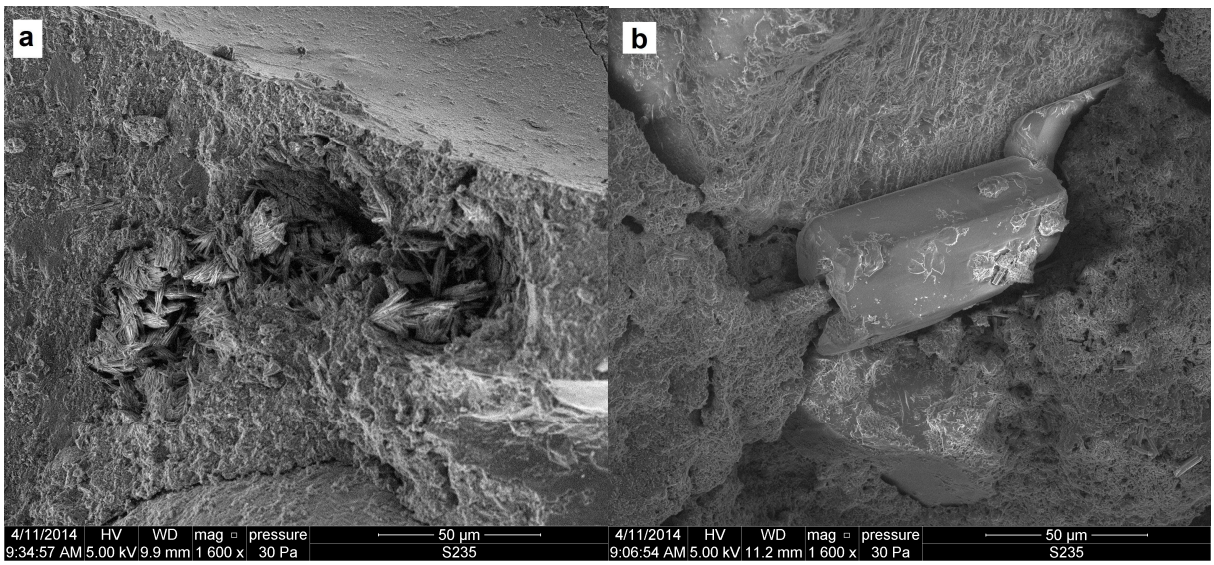

Fig. 4. Microstructure of the mortars with CEM I: a) air entrained, b) non-air entrained initially subjected to 40 freeze-thaw cycles and then immersed in 5% solution of Na_2SO_4 (SEM 1600x).

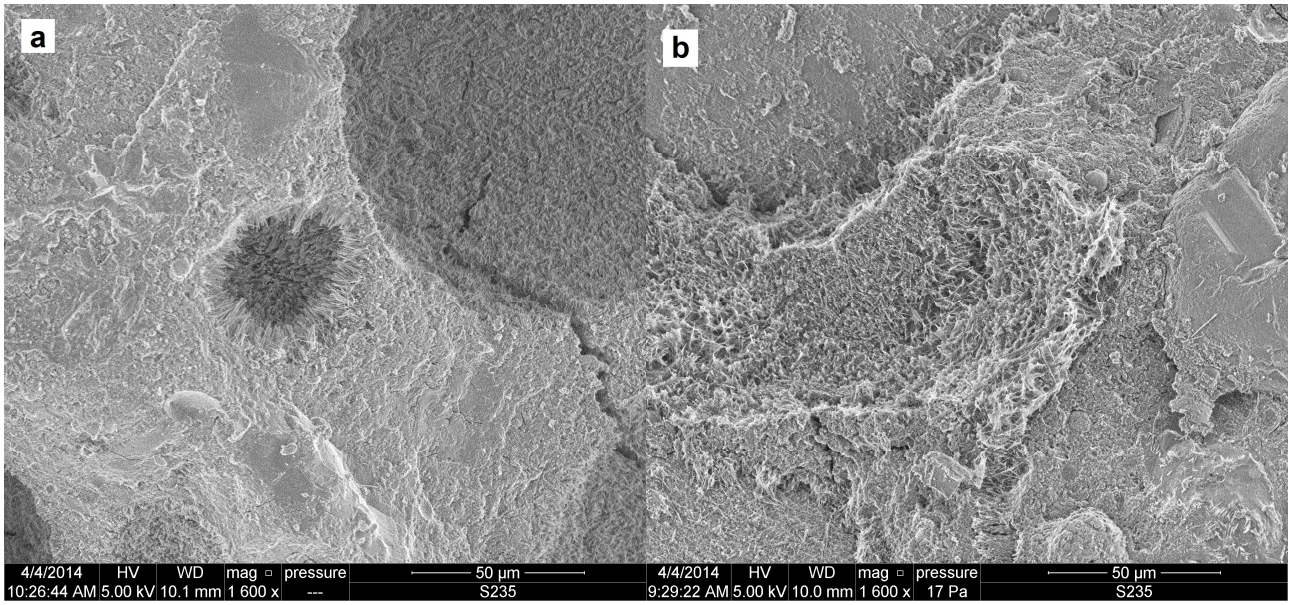

Fig. 5. Microstructure of the mortars with CEM III: a) air entrained, b) non-air entrained initially subjected to 40 freeze-thaw cycles and then immersed in 5% solution of Na_2SO_4 (SEM 1600x).

4. Conclusions

- Initial short-term freeze-thaw deterioration of non-air-entrained mortars made from Portland cement accelerated the expansion of those mortars in the sodium sulphate solution.
- Despite significant strain and damage experienced by non-air-entrained blast furnace cement mortars during freeze-thaw cycles, the initial freeze-thaw deterioration did not accelerate further sulphate expansion.
- The air-entrained mortar made from the blast furnace cement had the highest resistance to the combined action of freeze-thaw and sulphate attack.
- No expansion was detected in the air-entrained mortars despite the formation of the largest amounts of ettringite in the air voids. This confirms the hypothesis that the presence of ettringite in the compact C-S-H structure is necessary for the expansion to occur, as observed in the nAE Portland cement mortar.

References

[1] WAWRZEŃCZYK, J. *Air void structure in relation to the frost resistance of air-entrained concrete by with microspheres.* Cement, Wapno, Beton 5/2011, p. 278-287, 2011.

[2] PN-B-19707 *Cement - Special Cement - Composition, Requirements And Conformity Criteria.*

[3] KUNTHER, W., LOTHENBACH, B., SCRIVENER, K., *Influence of bicarbonate ions on the deterioration of mortar bars in sulfate solutions.* Cement and Concrete Research 46, p. 23–29, 2013.

[4] YU, C., SUN, W., SCRIVENER, K., *Mechanism of expansion of mortars immersed in sodium sulfate solutions.* Cement and Concrete Research 43, p. 105–111, 2013.

TRANSCOM 2015, 22-24 June 2015
University of Žilina, Žilina, Slovak Republic

The Impact of the Amount of Foamed Bitumen and Cement on the Standard Properties of Stabilized Soil

[*]Ewa Michta
[*]Kielce University of Technology, Faculty of Civil Engineering and Architecture, Department of Transportation Engineering, Al. Tysiąclecia Państwa Polskiego 7, 25-314 Kielce, Poland, e.michta@tu.kielce.pl

Abstract. The paper presents the results of research and analysis on the impact of the content of foamed bitumen and cement on the basic properties of soil stabilized. The research area includes the study: compressive strength after 7 and 28 days, frost resistance, indirect tensile strength in the air-dry conditions, indirect tensile strength in the after water soaking conditions, coefficient of resistance to the effects of water, elastic stiffness modules in the scheme of indirect tensile IT-CY at 25˚C. Studies have shown that the amount of foamed bitumen and cement has a significant impact on the basic properties of soil stabilized. The use of foamed bitumen and cement to stabilize soil allows for appropriate strength of soil stabilized to be obtain, simultaneously it causes reduce in the risk of formation of cracks and increase in resistance to the effects of water.

Keywords: cement, foamed bitumen, soil stabilization, road.

1. Introduction

Soli stabilization with binding materials is a method, which allow to use the uniform-grained or sensitive to changes in humidity soils for road construction. As a result of this process the physicochemical properties of the soil change, whereby it can be used to perform load-bearing and durable layers of road pavements [7]. An important element of this technology is the impact of the amount and type of used binding materials on the properties of soils stabilized.

The most frequently binding materials used for soil stabilization are mineral binders [8]. Both hydraulic binders: cement, fly ash, blast furnace slag, roads binder and air binder in the form of lime are applied.

The use of traditional mineral binders in soil stabilization and improvement revealed a number of disadvantageous phenomena, which are mainly related to a significant increase in the stiffness of stabilized courses. The cement hydration process, for example, causes shrinkage deformations. Those result in cracks in the stabilized courses, often propagating upward the pavement structure. That causes the formation of transverse reflection cracks, which reduce driving comfort and lead to premature pavement failure. To reduce those negative phenomena, bitumen binders started to be added to the stabilized soil layers. Those include liquid bitumen, bitumen emulsion and foamed bitumen. The binding materials alter the course characteristics, making it more flexible, which lowers the crack formation risk and increases the resistance to water action [10].

Foamed bitumen is a relatively novel material, which has been used in Poland only in the cold recycling of the courses of existing roads and for a rather short period of time. Foamed bitumen has not been used in soil stabilisation in Poland yet. The standards for soil stabilization with foamed bitumen have not been developed either in Poland or in Europe. The technology, however, has a great potential and should be researched further. The present paper provides experimental results and analysis of the effect foamed bitumen has on the properties of the stabilised soil.

The soils stabilized only with small quantities of foamed bitumen do not have sufficient compressive strength. An increase in the binder content produces an improvement in the load bearing capacity of the stabilised course, yet it pushes up the costs of the execution of works.

Therefore, soil stabilisation only with a bitumen binder is rarely performed, and mineral binders are added. Those operate as active fillers, i.e. binding materials which enhance the mix stiffness, and at the same time, complement the fine fractions of soils. The most commonly materials used for this purpose are cement and lime.

2. Methodology and Test Results

Test specimens were made of natural sand of ununiform-grained index less than 5, which meant that the ground was uniform-grained and thus it was classified as hardly compactable soil. In order to obtain compaction according to the standards, it is necessary to use stabilization for this kind of soli. Soil stabilizations were performed with portland cement CEM I 32.5 R and foamed bitumen obtained from the road bitumen 50/70. It were assumed three content of cement: 2%, 3%, 4% and three amounts of foamed bitumen: 2%, 3%, 4% for each content of cement.

The samples were subjected to laboratory testing, indicating the following properties:

- compressive strength after 7 and 28 days, in accordance with PN-S-96012,
- frost resistance, in accordance with PN-S-96012,
- indirect tensile strength in the air-dry conditions and in after water soaking conditions, in accordance with PN-EN 13286-42,
- coefficient of resistance to the effects of water, in accordance with „Cold Recycling Manual”,
- elastic stiffness modules in the scheme of indirect tensile IT-CY at 25 ° C, in accordance with PN-EN 12697-26.

Changes in the basic properties of stabilized soil depending on the amount and type of added binding materials are shown in Figures 1-7.

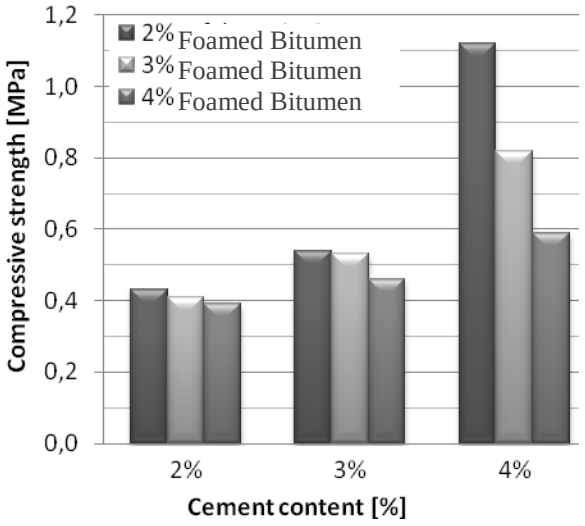

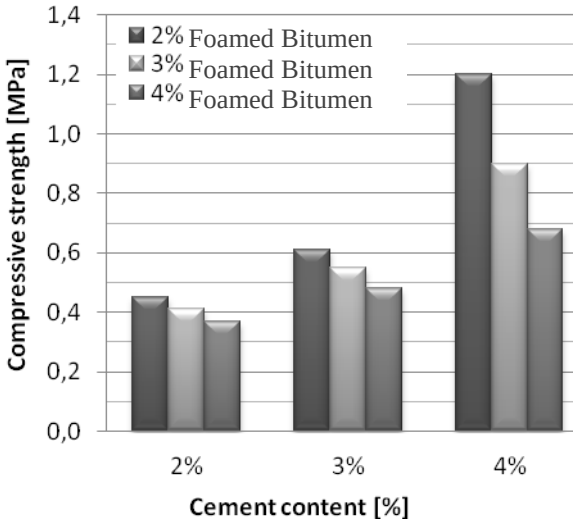

Fig. 1. Compressive strength after 7days.

Fig. 2. Compressive strength after 28 days.

The analysis of experimental results shows that with an increase in the cement content, the specimen compressive strength grows, both after 7- and 28-day curing. An increase in the foamed bitumen content in the mix, at the constant amount of cement, results in the decrease in the strength mentioned above. Additionally, it should be noted that the more cement is in the mix, the greater is the impact of foamed bitumen on the vales of the parameter of concern.

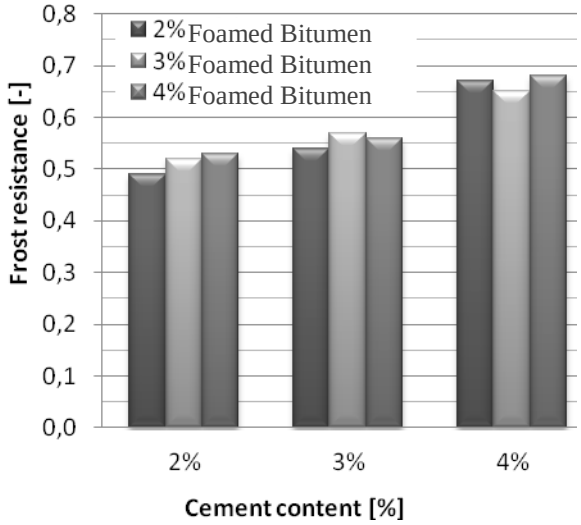

Fig. 3. Frost resistance.

The analysis of the test results shows that an increase in the cement content produces an increase in freeze-thaw resistance. In almost all cases, higher concentration of foamed bitumen in mixes resulted in the improvement in resistance to freeze-thaw cycles.

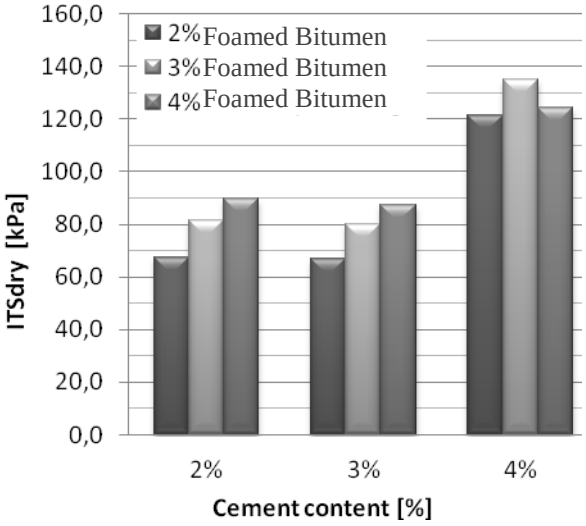

Fig. 4. Indirect tensile strength in the air-dry conditions (ITSdry).

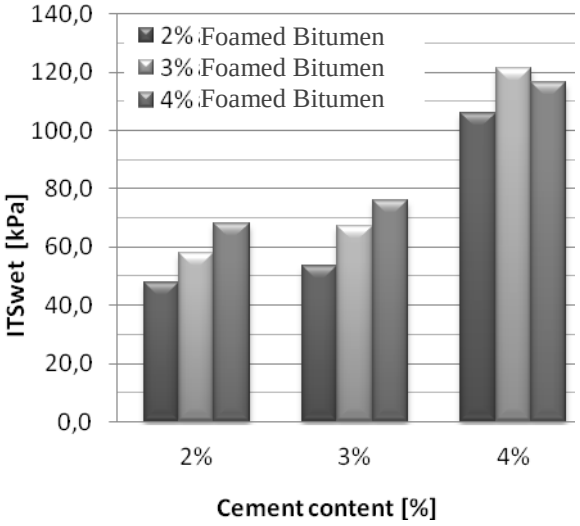

Fig. 5. Indirect tensile strength in the after water soaking conditions (ITSwet).

On the basis of the test results, presented in a graphic form in the figures above, it can be observed that for specimens both in dry-air conditions and after water soaking, the value of indirect tensile strength grows with an increase in the cement and foamed bitumen contents. Small differences in the parameter of concern are found in specimens that contain 2.0% and 3.0% of cement, and a greater impact is produced by the amount of foamed bitumen used. A major increase in ITS value is observed for the cement content of 4.0%.

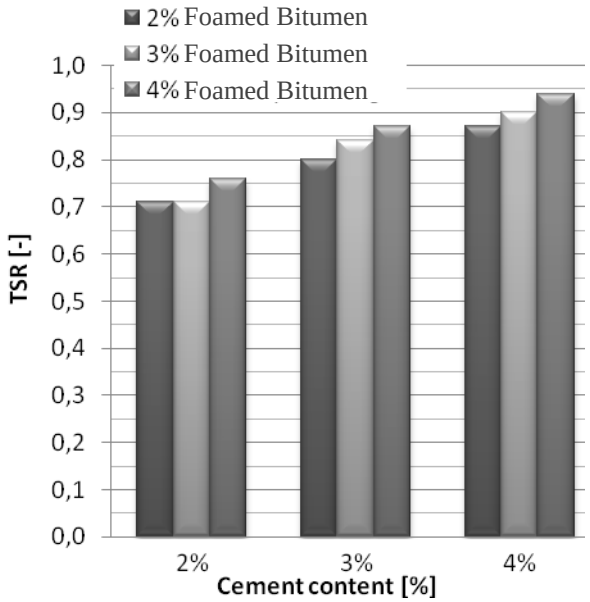

Fig. 6. Coefficient of resistance to the effects of water (TSR).

The experimental results indicate that an increase in the content of binding materials results in a rise in water resistance. Slightly higher differences in results are found when the cement content is changed, whereas foamed bitumen produces a lesser effect on TSR. For the lowest cement content, the coefficient of resistance to the effects of water was the same for both 2.0% and 3.0% content of foamed bitumen (TSR=0.71).

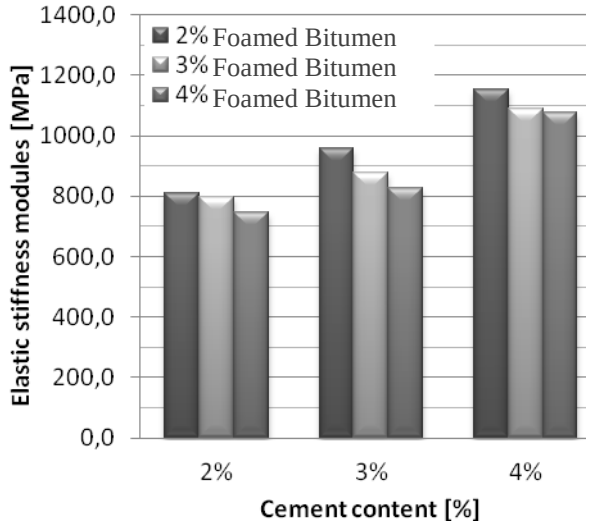

Fig. 7. Elastic stiffness modules in the scheme of indirect tensile IT-CY at 25 ° C.

Based on the obtained results it can be concluded that an increase in the cement content in the mixture causes an increase in the elastic stiffness. Simultaneously, this property reduces with an increase dosing of foamed bitumen, at the constant amount of cement.

3. Conclusion

Based on the analysis of the test results of stabilized soil with foamed bitumen and cement, the following conclusions can be drawn:

- the amount of foamed bitumen and cement has a significant impact on the basic properties of soil stabilized,
- an increase in the cement and foamed bitumen contents improves indirect tensile strength in the air-dry conditions and in after water soaking conditions,
- an increase in the foamed bitumen content, at the constant amount of cement results in a rise in resistance to the effects of water, what can improve water resistance of stabilized soil layers,
- the use of foamed bitumen reduces elastic stiffness modules of the sample, affecting the reduction in stiffness of layers of the stabilized soil with cement, simultaneously it lowers the shrinkage crack formation risk,
- the use of foamed bitumen to stabilize soil allows for uniform-grained soil to be used in road constructions,
- the use of foamed bitumen and cement to stabilize soil allows for appropriate strength of soil stabilized to be obtain, simultaneously it causes reduce in the risk of formation of cracks and increase in resistance to the effects of water.

References

[1] IWAŃSKI M.: *Podbudowa z asfaltem spienionym*. Drogownictwo, 2006, 3, s. 97-106

[2] IWAŃSKI M., BUCZYŃSKI P.: *Sposób głębokiego recyklingu nawierzchni drogowej w technologii asfaltu spienionego.* A1 396497; 2011, PL 214768 B1

[3] IWAŃSKI M., CHOMICZ-KOWALSKA A.: *Moisture and Frost resistance of the recycled base rehabilitation with foamed bitumen technology.* Archives of Civil Engineering., LVIII, 2, 2012, p. 185-198

[4] IWAŃSKI M., CHOMICZ-KOWALSKA A.: *The effects of using foamed bitumen and bitumen emulsion in the cold recycling technology.* 8th International Conference. Environmental Engineering. May 19-20, 2011, Vilnius, Lithuania, p. 1089-1096

[5] IWAŃSKI M., CHOMICZ-KOWALSKA A.: *Experimental study of water and frost resistance of foamed bitumen mixes in the cold recycling technology.* 0357. Proceedings USB 5th EUROSAPHALT AND EUROBITUME CONGRESS. 13-15 June 2012, Istanbul. Turkey, 8p

[6] IWAŃSKI M., CHOMICZ-KOWALSKA A.: *Laboratory Study on Mechanical Parameters of Foamed Bitumen Mixtures in the Cold Recycling Technology.* 11th International Conference on Modern Building Materials, Structure and Techniques, MBMST 2013, ELSEVIER, Procedia Engineering 57 (2013) p.433-442, htt://dx.doi.org/10.1016/j.proeng.2013.04.56

[7] IWAŃSKI M., MRUGAŁA J.: *Zastosowanie asfaltu spienionego do stabilizacji gruntu.* 56 Konferencja Naukowa Komitetu Inżynierii Lądowej i Wodnej PAN oraz Komitetu Nauki PZITB Kielce-Krynica 19-24 września 2010, ISBN 978-83-88906-58-9, 2010, s. 303-310

[8] KRASZEWSKI C.: *Kruszywa i grunty związane hydraulicznie w konstrukcjach drogowych.* Drogownictwo, nr 3, Warszawa 2009.

[9] MRUGAŁA J.: *Wpływ asfaltu spienionego na właściwości gruntu stabilizowanego.* Politechnika Śląska, Gliwice 2012, ISBN 978-83-7335-940-6, 2012,

[10]MRUGAŁA J.: *Soil stabilization with foamed bitumen.* Structure and Environment; 2011, 2/2011.

[11]PIŁAT J., RADZISZEWSKI R.: *Nawierzchnie Asfaltowe*. WKiŁ, Warszawa 2010.

[12]RAFALSKI L.: *Podbudowy Drogowe.* IBDiM, Warszawa 2007.

[13]WIRTGEN: *Cold Recycling Manual.* Wirtgen GmbH. Windhagen, Wydanie drugie, Niemcy 2004 r.

[14]WIRTGEN: *Cold Recycling Technology*. Wirtgen GmbH. Windhagen, Niemcy, 2004.

TRANSCOM 2015, 22-24 June 2015
University of Žilina, Žilina, Slovak Republic

Potential Thickness Reduction of Epoxy CIPP Liner Installed Without Preliner in Concrete Sewer Pipes

[*]Kamil Mogielski, [*]Emilia Kuliczkowska
[*]Kielce University of Technology, Faculty of Environmental Engineering, Geomatics and Power Engineering, Department of Water Supply and Sanitary Installations, Division of Water Supply and Sewage Systems, al. Tysiąclecia Państwa Polskiego 7, 25-314, Kielce, Poland, emkulicz@tu.kielce.pl, kamil.mogielski@gmail.com

Abstract. Samples preparation procedure made of concrete pipes and liners was presented together with test procedure of them. The tests were performed on universal testing machine. Samples were made of concrete DN 200 and 300 pipes while the liners were from 3,0 to 6,0 mm thick. Samples were prepared in two versions: with and without preliners to respectively avoid or provide adhesion between pipe and liner. The liners were introduced into the pipes using compressed air and cured with hot water. All pipes and liners used to make samples were brand new. Main aim of the research was to find out if there is any connection between adhesion between pipe and liner and load capacity growth after pipe rehabilitation due to the sticky properties of the resin used for liner soaking. Possible thickness reduction of the epoxy liners installed without preliner will be proven.

Keywords: CIPP liner, epoxy resin, sewer rehabilitation, load capacity tests.

1. Introduction

Underground sewers are getting more and more deteriorated. It is caused by their age, aggressiveness of wastewater, root ingress and many other factors [1]. Replacement of the sewers in an open trench is time consuming, expensive and troublesome. That's why almost 40 years ago there were introduced trenchless rehabilitation methods described in [2]. Most of these methods are to install a liner inside existing, deteriorated pipeline. Depending on the state of the existing pipeline the liner can seal it, enhance its stability or take the loads over it. The most popular CIPP (cured-in-place pipe) method is to put inside deteriorated pipeline a resin saturated fabric and to harden it using hot water, steam or UV radiation. Its big and still growing popularity results from the fact that this technology can be used for non-, semi- and fully structural rehabilitation of pipes conveying any kind of fluid, in a wide range of sizes and shapes.

From the very beginning of their use, CIPP liners were made of polyester resins. Such type of resin shrinks after curing for about 3% of its original size [8]. The most popular designing methods including:

- ASTM F 1216, Standard practice for rehabilitation of existing pipelines and conduits by the inversion and curing of a resin-impregnated tube, ASTM International Standard,
- Static calculations and dimensioning of the gravity sewer pipe renovation. Collective work developed by the Research Centre for Pipes Danish Technological Institute for Trenchless Team No-Dig,
- ATV-DVWK – M127P Part 2, Static calculations for technical rehabilitation of sewer lines by introducing liners or using installation methods,

take such shrinkage into account. The occurrence of it cause forming an annual gap between pipe and liner. The value of the coefficient depending on the width of annular gap decreases dramatically when annual gap increases. The wider annual gap is, the lower critical groundwater pressure can act on the liner. In practice it means that the liner with bigger annual gap exposed on the ground water pressure have to be thicker than the liner with smaller annual gap. If there is no annular gap, the

value of the coefficient is equal to 1. It means that the critical groundwater pressure in not reduced because of this liner imperfection.

2. Test Samples

The lack of annular gap is possible since epoxy resins are used in CIPP technology. Such resin do not shrink and have good sticky properietes. To check how it influence on the load capacity growth of the rehabilitated pipeline there were prepared test samples consisting of 30 centimeters long pieces of pipes and liners of the same length installed inside them. Figure 1 shows inversion drum during liner installation inside the pipes.

Fig. 1. Inversion drum during liner installation.

There were prepared two types of samples made of concrete pipes, all with liners with nominal thicknesses of 3.0, 4.5 and 6.0 mm. Some of the samples were prepared with preliner. Preliner is a thin polyethylene foil that is introduced into the host pipe before liner installation. In practice the preliner is used to avoid coming out the resin from cracked pipe. Using it is necessary when a polyester resin, which consist harmful styrene is used. In the case of epoxy resins the use of it is an option. During the tests the preliner was installed to compare load capacity growth of pipe with liner that adhered to it with load capacity growth of the pipe and liner working independently. There were also tested samples without liners (reference samples). Number of samples tested during the experiment is shown in Table 1. Tests described here are only part of wider research program the aim of which is to correct currently used liner designing methods [3, 4, 5].

Type of sample	Nominal diameter / liner thickness [mm]					
	200/0	200/3	200/4.5	200/6	300/0	300/4.5
Concrete pipe with liner and preliner	3	4	4	4	1	4
Concrete pipe with liner without preliner	1	2	1	2	1	2
TOTAL	29 samples					

Tab. 1. Number of samples

3. Test Procedure

The samples with and without liners were tested in accordance with the PN-EN 1916 standard [7]. The pipes were placed in the universal testing machine on the steel, V-shaped lower bearing element with spread angle of 170°. The load was applied from the top and distributed using a duralumin upper bearing element. Elastomeric belts were inserted between the specimen and both bearing elements. The scheme of test stand is shown in fig. 3.

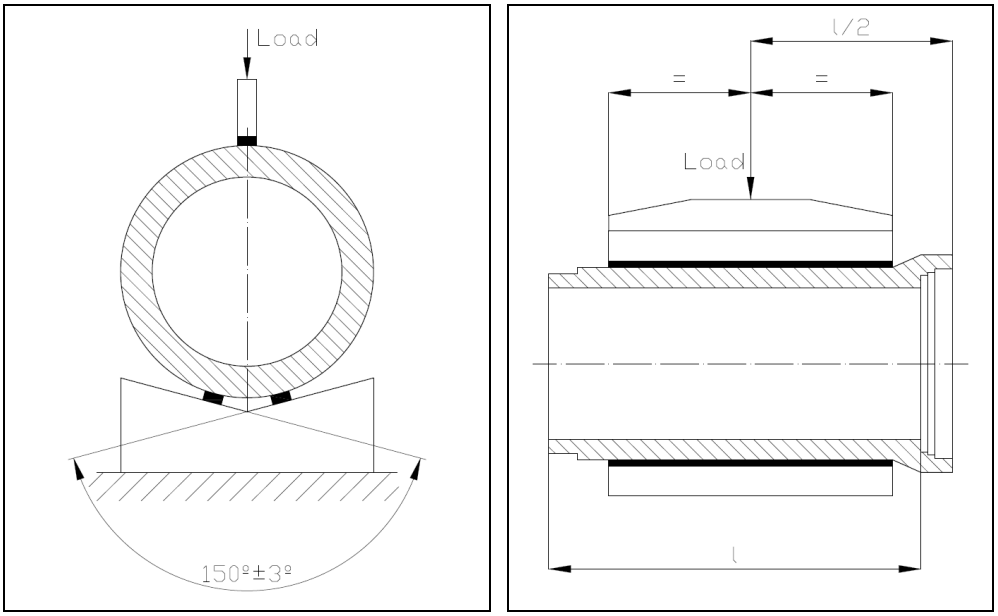

Fig. 2. Samples placing in the universal testing machine: front view (left side) and side view (right side) [7].

Actual thicknesses of the liners are different from their nominal thicknesses. It comes from the characteristics of the CIPP technology, in which the liner is formed in-situ, not in the factory. The thickness of the liners were measured to determine the correlation between the actual liner thickness and the load applied to the sample that makes it collapse. The measurements were performed to PN-EN 1228 standard [6] for each specimen at 12 sites distributed every 60° around the circumference on both sides. To this end, a digital caliper was used. The arithmetic mean from 12 measurements was taken to be the actual thickness of liner in each sample.

4. Results

Measured load capacities of the reference samples (without liners) weren't equal. Because of that to compare the results of all tests there were calculated relative load capacities of all samples with liners comparing to the load capacities of the samples made of the same pipe but without liner. The relative load capacity (F%) is the absolute load capacity of a given sample with liner divided by the absolute load capacity of reference sample.

To unify test results the regression models were created using SDR value (standard dimension ratio – the quotient of liner external diameter and its thickness). Because of that the total number of regression models was reduced to two. Additionally SDR was modified by raising it to the power of -1, hence it is possible to include in regression models tests results of reference samples. SDR in the case of the them is equal to $+\infty$ while SDR^{-1} is equal 0.0 and F% is equal to 100.0%. Before choosing type of regression there were established following assumptions:

- regression draws grow on full length – the bigger liner thickness the higher F% value,
- regression draws run through [0, 1] point which indicates test result of reference sample (liner thickness = 0.00 mm; F% = 100.0%),
- regression is not linear, because relations between liner thickness and its ring stiffness is not linear.

Additionally both regression models will be constructed on the same type of regression. Because of the above exponential regression was chosen. Equation (1) is a general formula of this kind of regression.

$$y_i = \alpha_0 e^{\alpha_1 x_i} \varepsilon_i \qquad (1)$$

Factor α_0 is equal 1.0 thus regression draws run through [0, 1] point. Factor ε_i is a residual while α_1 is constant value. Latter define mean change of F% as a reaction for the SDR^{-1} change. If SDR^{-1} grows by 0.001, F% grows by $\alpha_1 \cdot 0.1\%$.

Regression analysis gave two models showing F% value in the function of SDR^{-1}. For the samples with preliners the regression model is described by (2) while for the samples without preliner by (3). Parameters of them are set in Tab. 2. Regression draws for both models are shown in the Fig. 3 and 4.

$$F\% = e^{6{,}075\cdot\left(SDR^{-1}\right)} \tag{2}$$

$$F\% = e^{31{,}328\cdot\left(SDR^{-1}\right)} \tag{3}$$

model	p-value	χ^2	R^2
samples with liner and preliner	0,77675	0,505	0,858
samples with liner without preliner	0,05711	5,726	0,828

Tab. 2. Parameters of regression drawings shown in figs. 4 and 5.

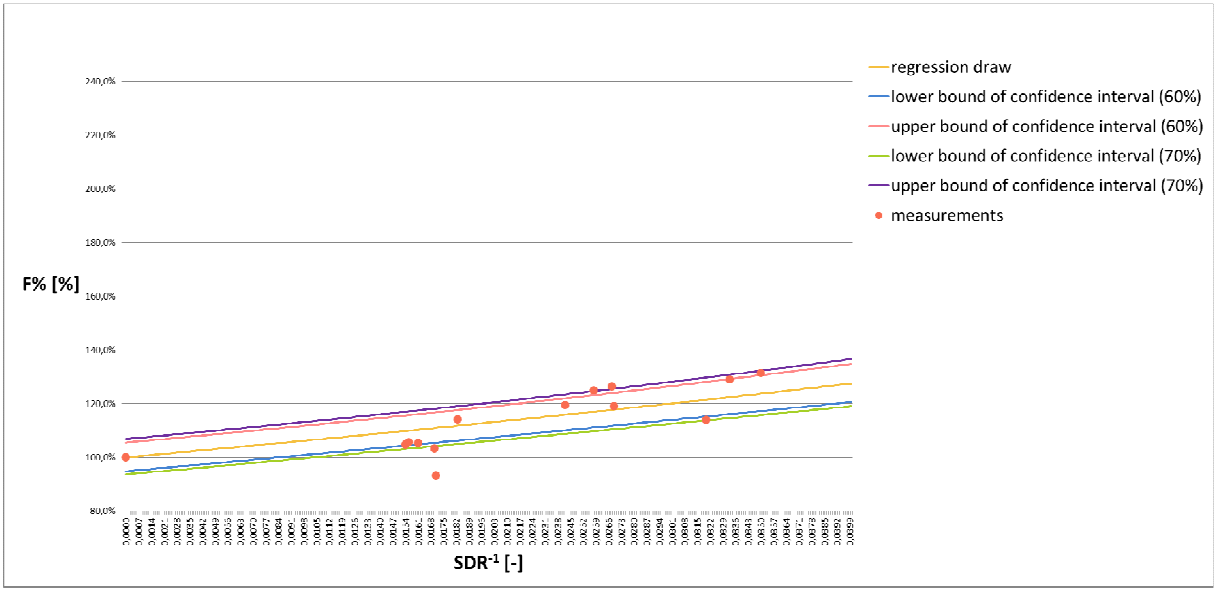

Fig. 3. Regression draw: model for the samples with liner and preliner.

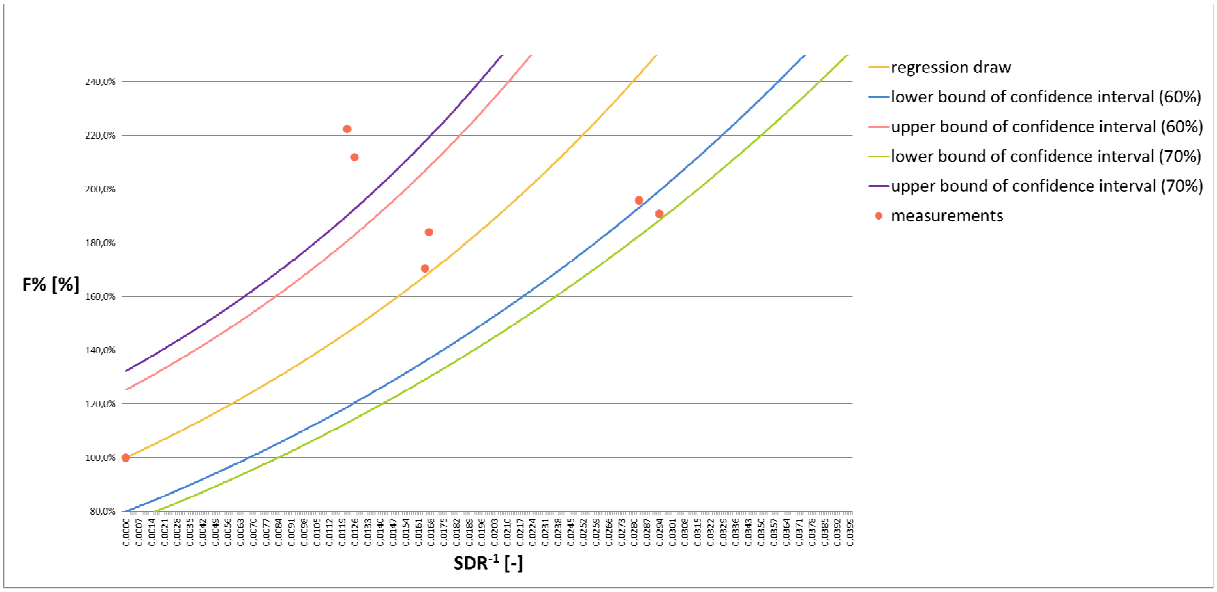

Fig. 4. Regression draw: model for the samples with liner without preliner.

Factors α_1 in the exponents indicates that the mean load capacity increase in the case of samples without preliners is 5.16 times higher than in the case of the same samples with preliners.

5. Conclusion

By making a number of load capacity tests of concrete samples rehabilitated with epoxy CIPP liners has been shown that it is possible to reduce thickness of the liner during planning its thickness in the case of installation it without preliner. Mean load capacity growth of the pipe rehabilitated with such liner is more than five times higher than of the pipe rehabilitated with the same liner with preliner. It gives a possibility of liner thickness reduction by more than 80% obtaining the same load capacity growth. Test results can be used in the future to make corrections of the currently used liner thickness designing methods.

Acknowledgement

The authors would like to thank the MC-Bauchemie and Unimark sp. z o.o. for the preparation of the samples examined in the study presented in the article and P.V. Prefabet Kluczbork S.A. for providing the pipes that were used to prepare the samples.

References

[1] KULICZKOWSKA E. *Kryteria planowania bezwykopowej odnowy nieprzełazowych przewodów kanalizacyjnych. Monografie, Studia, Rozprawy*. Kielce: wyd. Politechniki Świętokrzyskiej, 2008.

[2] KULICZKOWSKI, A. et al. *Technologie Bezwykopowe w Inżynierii Środowiska*. Warszawa: Wydawnictwo Seidel-Przywecki, 2010.

[3] KULICZKOWSKI A., MOGIELSKI K. *Results of tests of concrete, vitrified clay and PVC sewer pipes with CIPP liners*. In Proceedings: NASTT's No Dig Show Sacramento (USA), 2013.

[4] KULICZKOWSKI A., MOGIELSKI K., *The effect of glazing of vitrified clay pipes to load capacity growth of them after rehabilitation with CIPP liners*, In Proceedings: Underground Infrastructure of Urban Areas, Wroclaw (Poland), 2014.

[5] MOGIELSKI K., KULICZKOWSKI A., *A sewer pipes roughness influence to load capacity growth of them after renovation with CIPP liner*. In Proceedings: Transcom Zilina (Slovakia), 2013.

[6] PN-EN 1228 *Rury z termoutwardzalnych tworzyw sztucznych wzmocnionych włóknem szklanym (GRP). Oznaczanie początkowej właściwej sztywności obwodowej*. Warszawa: PKN, 1999.

[7] PN-EN 1916 *Rury i kształtki z betonu niezbrojonego, betonu zbrojonego włóknem stalowym i żelbetowe*. Warszawa: PKN, 2005.

[8] ŻUCHOWSKA D. *Polimery konstrukcyjne. Wprowadzenie do technologii i stosowania*. Wyd. II rozszerzone. Warszawa: WNT, 2000.

TRANSCOM 2015, 22-24 June 2015
University of Žilina, Žilina, Slovak Republic

Basic Properties of Asphalt Mixtures produced in Half Warm Mix Asphalt technology

[*]Justyna Mrugała, [*]Piotr Ramiączek, [*]Mateusz M. Iwański
[*]Kielce University of Technology, Faculty of Civil Engineering and Architecture, Department of Transportation Engineering, Al. Tysiąclecia Państwa Polskiego 7, 25-314 Kielce, Poland,
{mrugala, p.ramiaczek, matiwanski}@ tu.kielce.pl

Abstract. The paper presents an analysis of the basic properties of AC22W binding course asphalt concrete produced at 95°C. The basic properties of the mixture were assessed, including: V_m, ITSR, PRD_{AIR} and WTS_{AIR}. The designed asphalt concrete binding course mixes were based on limestone aggregates and comprised bitumen in amounts ranging from 4.2% to 5.1% in increments of 0.3%. The half-warm mix asphalt concrete was produced using foamed bitumen modified with synthetic F-T wax dosed in amounts ranging from 1.0% to 2.5% relative to the bitumen mass. This enabled to reduce the production and compaction temperatures by 60°C. The conducted study concluded that the processing temperatures of asphalt concrete mixes can be significantly lowered with good results by introducing the presented technique.

Keywords: Half Warm Mix Asphalt, foamed bitumen, paraffin wax, asphalt concrete.

1. Introduction

Hot mix asphalt (HMA) is currently the most widely used technique for producing mineral-bitumen mixes. The HMA requires that the components of the mixture (asphalt and aggregates) are heated to approx. 160°C to enable proper mixing and aggregate coating. The great disadvantage of this technology is its impact on the environment [2]. This fact was the reason behind the development of techniques for manufacturing and compacting asphalt mixtures at reduced temperatures. The first attempts in this field date back to 1956 and the works of prof. Ladis Csanyi at Iowa State University in the United States [1]. He successfully applied the innovative asphalt binder in the form of foamed bitumen. Since then, this technology has been used around the world, including the US, Australia and Europe, it has also been implemented in Poland [3, 4]. In German road construction practice, waxes have been used in the last twenty years to improve the workability of asphalt mixtures but not to lower the processing temperatures. It is only the last fifteen years that the reduction of energy intensity of bitumen mix production has been considered a priority. To achieve this goal, additives such as fatty acid amides and montana waxes have been used. At the same time the experiments were performed on modern foaming techniques. In this article, we show and evaluate a method for producing asphalt concrete mixes at temperatures below 100°C with the use of foamed bitumen and F-T waxes.

2. Materials

2.1. F-T wax modified bitumen

The F-T synthetic wax is used in asphalt mixes primarily to reduce their production temperatures by reducing bitumen viscosity. The viscosity of bitumen can be reduced, as the organic wax has the melting point lower than the asphalt mix lowered processing temperatures, which allows for increasing workability. As the temperatures drops to the service range, the crystallization in the F-T wax occurs causing the structure of the asphalt mix to stiffen, in turn

increasing its resistance to permanent deformation [5, 10]. In this case, waxes must be chosen very carefully in relation to the type of asphalt [11].

A 35/50 penetration grade bitumen modified with synthetic wax in amounts of 0.5% to 2.5%, was used in the laboratory tests described further. The basic tests of bitumen binders modified with F-T wax allowed for assessing the penetration index PI and temperature plasticity range TZP, which characterize the temperature susceptibility of the binder. The results of PI and TZP calculated values are presented in Fig. 1.

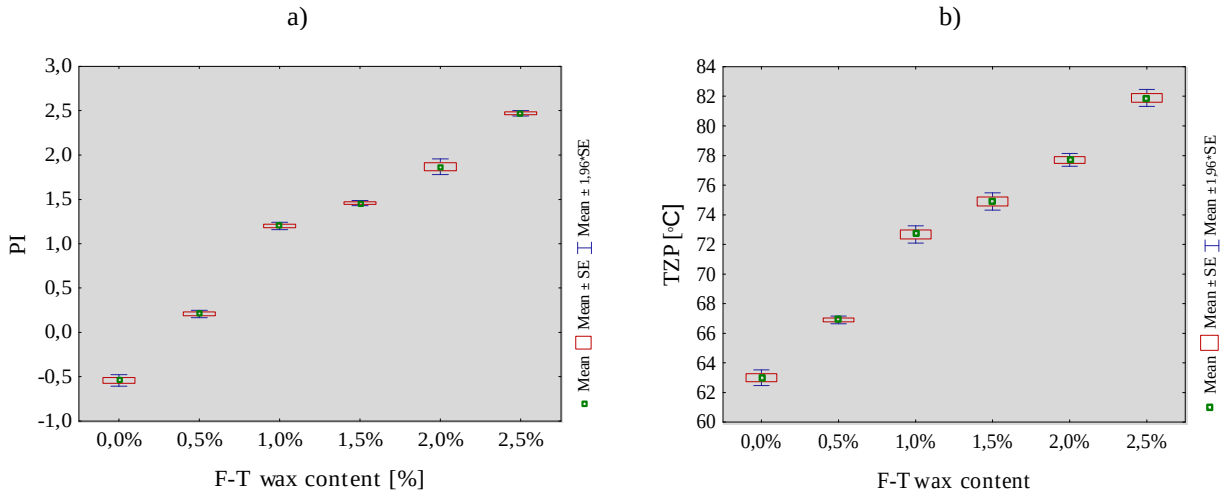

Fig. 1. Results of: a) penetration index and b) temperature plasticity range of F-T wax modified bitumen.

When analyzing the results of the penetration index it can be seen that increase in the amount of modifier increased the values of penetration index in the tested binders. The neat bitumen was characterized by -0.5 penetration index and after the application of synthetic wax additive in an amount of 0.5% the penetration index increased to a positive value of 0.2. The tested bitumens could be categorized as a rheological sol-gel type with penetration indices of -2 to +2. Only the binder with 2.5% F-T synthetic wax modification migrated from the sol-gel type to the gel state, with low temperature susceptibility and broad temperature viscoelastic range.

The obtained results shown that the increased F-T wax modification resulted in an increased temperature plasticity range and penetration index, improving the bitumen performance in a broad range of climatic conditions.

2.2. Properties of the foamed bitumen

The ability to produce bitumen foam that satisfies the stipulated requirements is a basic criterion for assessing the bitumen applicability for the foamed bitumen technology.

Therefore, the next step in the research was to evaluate the two basic parameters of foamed bitumen: expansion ratio (ER) and bitumen foam half-life ($\tau_{½}$). Expansion ratio is an indirect measure of viscosity of the bitumen foam and it determines how well the binder will be dispersed in a mineral mix. The half-life measures the stability of the bitumen foam and provides information on the rate of foam collapse during mixing with mineral material [6].

The laboratory production of foamed bitumen was conducted using Wirtgen WLB 10S laboratory foaming plant, which is shown in fig. 2.

Fig. 2. Wirtgen WLB 10S laboratory foaming plant [J. Mrugała].

To obtain the optimum foaming characteristics, water was dosed in accordance to the recommendations [7, 8] in amounts from 1.5% to 4.0% in relation to the mass of base bitumen, with a 0.5% steps. The measurements were taken four times for each amount of foaming water and F-T wax concentration. The bitumen before foaming was heated up 150°C.

The measurements of expansion ratio and half-life time allowed to establish optimum foaming water contents (tab. 1) of bitumen modified with varying amonts of synthetic F-T wax.

Binder type	Foaming water content [%]	Expansion ratio	Half-life time [s]
35/50	3.0	10.17	8.75
35/50 + 1.0% FT	3.0	11.65	10.84
35/50 + 1.5% FT wax	2.5	12.46	14.68
35/50 + 2.0% FT wax	2.5	14.38	15.41
35/50 + 2.5% FT wax	2.5	15.87	16.43

Tab. 1. Properties of foamed bitumen with optimum water content.

Figure 3 presents the established regression lines (with confidence intervals) for the relationships between the expansion ratio (ER) and bitumen foam half-life (τ½) in relation to the amount of F-T wax at the optimum foaming water content.

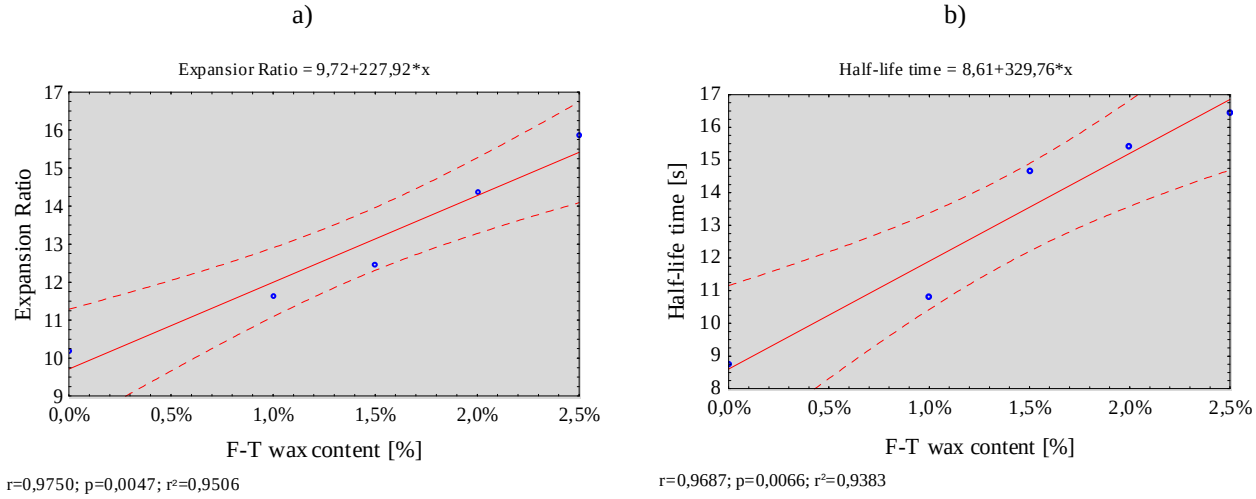

Fig. 3. Influence of F-T wax modification on the : a) expansion ratio and b) half-life.

From the drawing it can be seen that the tested parameters continuously rise with the increase in synthetic F-T wax content. It should be noted that the increase in ER and τ½ is beneficial because the expansion ratio translates to the increase of bitumen volume and the half-life states the time in which the foam loses half of its maximum volume, so that is possible to properly determine the conditions of mineral mix coating at lowered temperatures.

2.3. Mineral mix design

The mineral mix grading curves were established in accordance with technical requirements WT-2 z 2010 r. [12] and PN-EN 13108-1 [9].

In order to reduce the production costs of the asphalt concrete, local Devonian limestone aggregates were used. The framework composition of the mineral mix comprised 25% of the coarse aggregate 16/22, 22% coarse aggregate 8/16, 21% coarse aggregate 2/8, 26% fine aggregate 0/2 and 6% limestone filler.

Asphalt mixing and compaction was carried out in 95°C.

3. Results and discussion

The aim of the research was to assess the influence of the F-T wax modified foamed bitumen on the basic properties of asphalt concrete AC 22W.

The measured physical and mechanical properties of the asphalt mix comprised:

- air voids, V_m,
- resistance to moisture and frost damage, ITSR,
- resistance to permanent deformation, WTS_{AIR}, PRD_{AIR}.

Every test was conducted on six samples.

The graphical representation of results for air void contents and resistance to moisture and frost damage are presented in Fig 4.

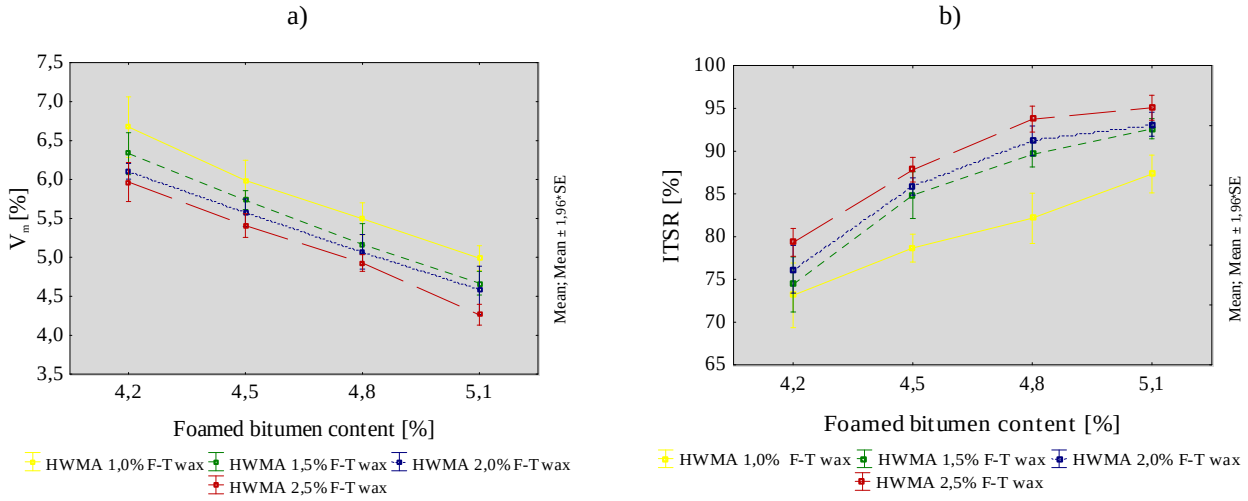

Fig. 4. Influence of F-T wax modification and bitumen content on the: a) V_m and b) ITSR.

The presented results show that the higher F-T wax and bitumen concentration caused a decrease in air void contents and an increase in the ITSR values. This can be explained by the fact that the increase in the amount of asphalt binder and F-T synthetic wax results in better workability of the asphalt, and therefore better compaction. In addition, an increase of both factors (foamed bitumen and synthetic wax F-T) resulted in a better coating of coarse aggregates.

The mix containing 5.1% of foamed bitumen modified with 2.5% synthetic F-T wax reached the smallest amount air void content, while the worst compaction was achieved in the mix with 4.2% of foamed bitumen modified with 1.0% synthetic F-T wax. Despite this varied performance, all produced mixes met the air void contents range of 4% to 7% required by the WT-2 z 2010.

As for the resistance to moisture and frost damage, not all of the asphalt concrete mixes met the requirements ITSR≥80%. This condition was not complied by the asphalt concrete with foamed bitumen content of 4.2%, regardless of the amount of synthetic wax. Additionally, the asphalt concrete with 4.5% content of foamed bitumen and 1.0% of synthetic wax did not reach the required ITSR value.

The next analyzed properties were the wheel tracking slope and proportional rut depth at 10000 cycles. The tests were carried out in a small wheel tracking apparatus, so the results are an average of two tests. The graphical representation of results for wheel tracking slope (WTS_{AIR}) and proportional rut depth (PRD_{AIR}) are presented in Fig 5.

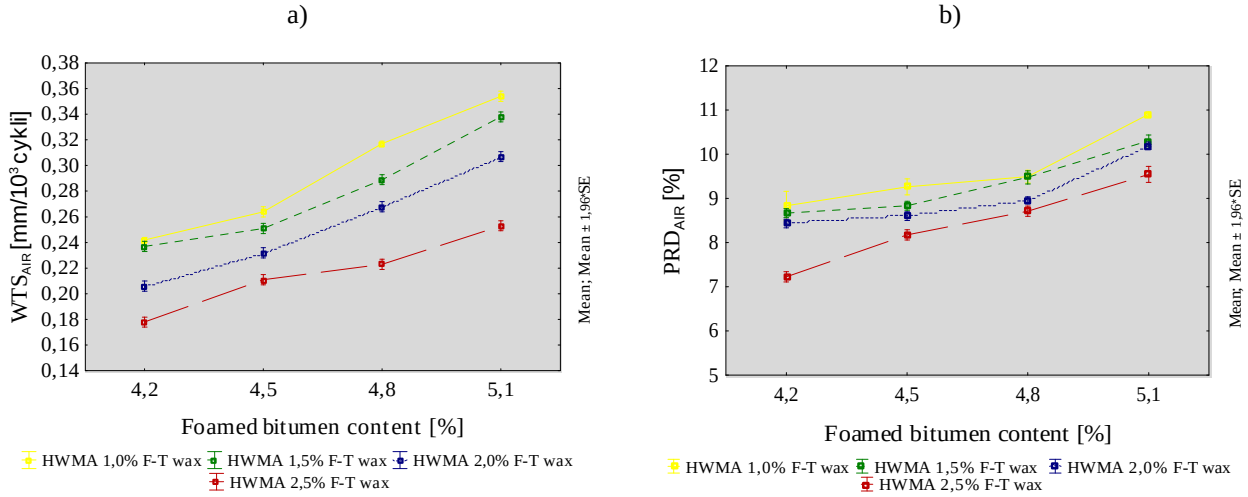

Fig. 5. Influence of F-T wax modification and bitumen content on the: a) WTS_{AIR} and b) PRD_{AIR}.

By studying the wheel tracking slope and proportional rut depth after 10000 cycles of the AC 22W asphalt concrete, it can be seen that the amount of foamed bitumen and synthetic F-T wax significantly affected the values of the studied parameters of asphalt concrete.

It was observed that with the increase of the synthetic F-T wax content the value of wheel tracking slope WTS_{AIR} and the proportional rut depth decreased. This result may be related to the characteristics of the F-T synthetic wax, as it beneficially affects the stiffness of asphalt at higher temperatures. What is more, the increase in the foamed bitumen content increased the values WTS_{AIR} and PRD_{AIR}, which translates into decreased resistance to permanent deformation. Asphalt concrete containing 5.1% of foamed bitumen with synthetic wax amounts of 1.0%, 1.5% and 2.0% and asphalt concrete with 4.8% bitumen content with the smallest amount of wax (1.0%) did not meet the requirements of WT-2 by 2010, because the maximum value of WTS_{AIR}=0.3 was exceeded.

The highest values of WTS_{AIR}=0.354 and PRD_{AIR}=10.91 were recorded for the asphalt concrete mix with 5,1% bitumen content and 1,0% of F-T synthetic wax. On the other hand, the best performing mix, with values of WTS_{AIR}=0.178 and PRD_{AIR}=7.23 was the one containing 4.2% of bitumen and 2.5% of synthetic wax.

4. Conclusions

The following conclusions were formulated based on the presented results of investigations regarding half-warm mix asphalt concrete for binding course:

- increase in bitumen content from 4.2% to 5.1% in the asphalt concrete produced HWMA technology reduced void content V_m;
- increase in F-T synthetic wax concentration from 1.0% to 2.5% in the foamed asphalt improved the resistance to moisture and frost damage of the asphalt concrete AC 22W;
- half-warm mix asphalt concrete produced with F-T synthetic wax at 2.5% concentration in the bitumen foam attained the highest measured resistance to permanent deformation;
- the use of half-warm asphalt mix technique brings a range of economic and environmental benefits.

References

[1] Csanyi, L. H., *Foamed Asphalt in Bituminous Paving Mixtures*, Bulletin No. 160, Vol. 10, Highway Research Board, Washington D.C., USA 1957.

[2] Iwański M., Mrugała J., *Moisture and frost resistance of asphalt concrete with foamed bitumen modified with synthetic wax*, 3rd International Conference on Transportation Infrastructure, Piza 2014.

[3] Iwański M., Chomicz-Kowalska, A., *Moisture and frost resistance of the recycled base rehabilitated with the foamed bitumen technology*, Archives of Civil Engineering, 58(2), 2012.

[4] Iwański M., Chomicz-Kowalska, A., *Laboratory Study on mechanical Parameters of Foamed Bitumen Mixtures in the Cold Recycling Technology*, Procedia Engineering 57, 2013.

[5] Iwański M., Chomicz-Kowalska A., Mrugała, J., *Application of the synthetic wax to improve the foamed bitumen parameters used in half-warm bituminous mixtures*, 9th International Conference "Environmental Engineering" Lithuania 2014.

[6] Jenkins K. J., Molenaar A.A. A., de Groot J. L. A., Van de Ven M. F. C., *Foamed Bitumen Treatment of Warmed Aggregates*, 2nd Euroasphalt and Eurobitume Congress Barcelona, Session 2, 2000.

[7] Jenkins, K. J., *Mix design considerations for cold and half-warm bituminous mixes with emphasis on foamed bitumen*, PhD dissertation University of Stellenbosch, South Africa 2000.

[8] Muthen K. M.: Foamed *asphalt mixes. Mix design procedure. Contract Report CR 98/077*, SABITA Ltd & CSIR Transportek (Council for Scientific and Industrial Research Transportek), Pretoria, South Africa, 1999.

[9] PN-EN 13108-1 *Mieszanki mineralno-asfaltowe. Wymagania. Część 1: Beton asfaltowy* [Bituminous mixtures - Material specifications - Part 1: Asphalt Concrete].

[10] Rubio M.C., Martínez G., Baena L., Moreno F., *Warm mix asphalt: an overview*, Journal of Cleaner Production 24, 2012.

[11] Silva, H.M.R.D., Oliveira, J.R.M., Peralta, J., Zoorob, S.E., *Optimization of warm mix asphalts using different blends of binders and synthetic paraffin wax contents*, Construction and Building Materials 24 (9), 2010.

[12] WT-2 *Wymagania Techniczne, Mieszanki mineralno-asfaltowe, Nawierzchnie asfaltowe na drogach krajowych* [Technical requirements. Asphalt pavements on national roadways], GDDKiA , Warszawa, 2010.

TRANSCOM 2015, 22-24 June 2015
University of Žilina, Žilina, Slovak Republic

Comparison and Analysis of Radial Compensation Calculation Methods

[*]Tomasz Musiał
[*] University of Technology, Faculty of Construction and Architecture, al. Tysiąclecia Państwa Polskiego 7, 25-314 Kielce, Poland, {Tomasz Musiał} tomekmusial2@o2.pl

Abstract. The paper discusses a comparison of methods used to calculate the dimensions of U-compensators, which are devices installed on heating networks to prevent pipe from damage. These devices allow extending pipe in such a way that the level of induced stress is less than allowable. The basic law that is used in calculations is Hooke's law for linear relation between deformation and stress level and if the deformation is known, we can calculate the stress level. There are a few methods to calculate stress inducted in U-compensators. In this paper two methods are presented: elastic center method and forces method, developed based on a different approach. Results obtained by this method are slightly different, as presented in the table.

Keywords: compensation heating networks, allowable stress, elastic centre method, forces method, thermal deformation

1. Introduction

The aim of the paper is to introduce the issue of damaging heating networks as a result of thermal deformation. This phenomenon is associated with thermal expansion of pipe. As a result of heating, pipes anchored between supports are under stress. When stress is higher than acceptable level, the pipe will be damaged. The value of stress generated in the pipe is proportional to the temperature difference during pipe assembly (which is equivalent to the ambient temperature) and the temperature during operation, which can increase to several hundred degrees Celsius. The resulting pipe thermal expansion and thereby the stress can be compensated by appropriate selection of network route with lots of changing direction. Changing directions make that there is a self-compensation of network, where there is such extension of pipe, which does not lead to an excess allowable stress level. In case there is no way to compensate network by self-compensation, special compensating devices called compensators should be used. If we analyse network failure, we can state that the pipes are often damaged, even if compensation devices were used. This fact means that the design methods, which are currently used, do not include all the factors that affect the stress level. Among these factors we can mention: outside air temperature changes, poor workmanship, corrosion and aging metal. Workmanship defects are related with defect pipe connections and poor quality of insulation. Another reason of failure is aging of the metal, which means declining material properties in the course of time. In the case of heating networks, most undesirable is the deterioration of mechanical properties of material. Another factor is corrosion of the metal, which leads to a decrease in the strength of the network due to oxidation of surface layers. The last failure factor is associated with external weather conditions, which are related to temperature variability of air, which leads to the requirement for changing heating medium temperature parameters. All these factors have a significant influence on the failure and should be considered in the model of heating network calculation.

2. Calculation of thermal stress in uncompensated straight heating pipe

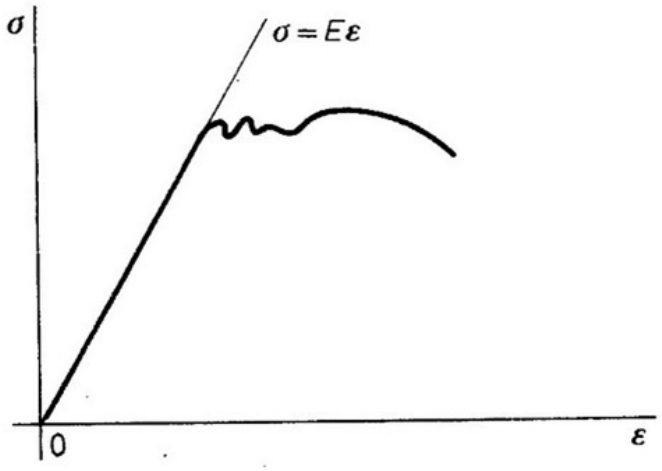

Fig. 1. Diagram showing Hooke's law

The basis for the calculation of thermal stresses in straight pipes mounted on fixed supports is Hooke's law. According to this law, the value of the resulting stress in the material is proportional to the deformation and is related with deformation by proportionality factor called Young's modulus according to formula 1. This ratio is constant for a particular type of material and its mechanical characteristics. Hooke's law can be used only in a small range of deformation to the Hooke's limit as illustrated in Figure 1, and not for all materials. Hooke's limit of deformation is the value beyond which the linear proportionality of stress from the deformation disappears.
Hooke's law:

$$\sigma = E\varepsilon \tag{1}$$

where:
σ - stress generated by thermal expansion, MPa
E - Young's modulus, MPa
ε - pipe deformation , m/m

3. Calculation of thermal stress in U-compensators using elastic centre method

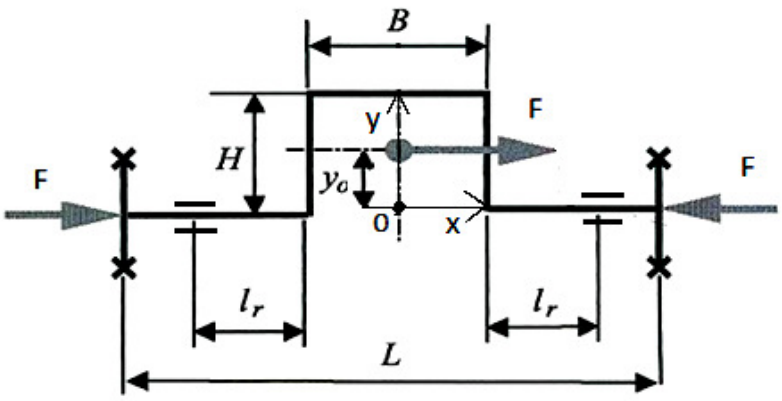

Fig. 2. Model of U-compensators calculated with the elastic centre method

In elastic centre method, U-compensator is subjected to axial force caused by thermal expansion, as presented in Figure 2. The axial forces induce bending moments, which have the greatest influence on stress level in heating pipes. Calculation of the U-compensator using the

elastic centre method consists of checking the condition of not exceeding the allowable stress. In this method, elastic centre is calculated, which is the static moments sum of particular network section related to its length in rectangular coordinate system. Elastic centre is a place in the coordinate system where bending moments are reset and only axial forces are acting. If the elastic centre is less than half of compensator height, the grater value of bending moment will occur on the compensator back, which means that there is higher level of stress.

Calculation of stress level depending on the location of elastic centre under or over half of height can be performed using equation 2 and 3:

$$\sigma_{lr} = \frac{1}{2} \frac{E\alpha\Delta TLD}{H^2\left(\frac{2}{3}H + B\right) - y_o{}^2\left(2H - 2l_r + B\right)} y_o \leq \sigma_{dop} \tag{2}$$

$$\sigma_B = \frac{1}{2} \frac{E\alpha\Delta TLD}{H^2\left(\frac{2}{3}H + B\right) - y_o{}^2\left(2H - 2l_r + B\right)} \left(H - y_o\right) \leq \sigma_{dop} \tag{3}$$

where:

σ_{lr} - stress generated on compensator arm, MPa

σ_B - stress generated on compensator back, MPa

σ_{dop} - allowable stress level, MPa

l_r - side arms of compensator, m

α - coefficient of thermal expansion, 1/K

y_o - location of elastic center in rectangular coordinate system, m

ΔT - difference of temperature before and after heating, K

D - diameter of pipe, m

4. Calculation of thermal stress in U-compensators using forces method

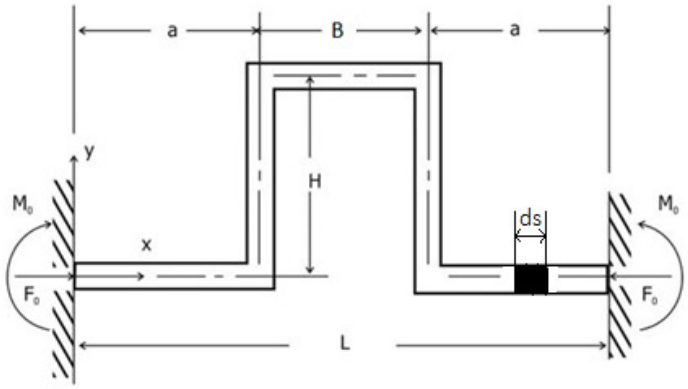

Fig. 3. Model of U-compensators calculated with forces method

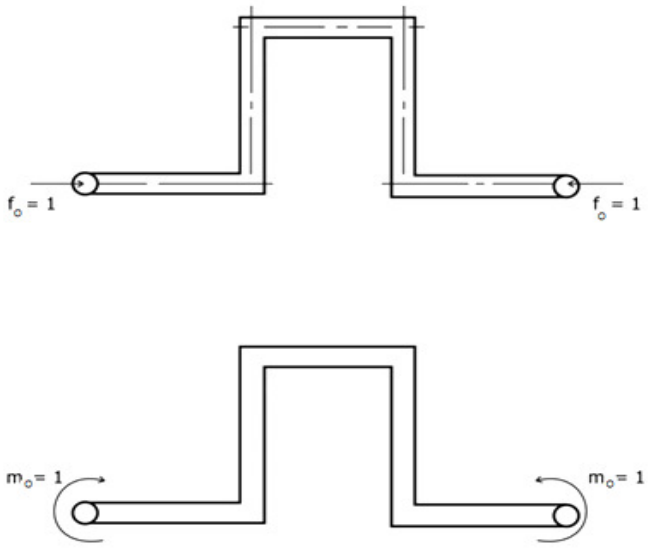

Fig. 4. Model of U-compensators with unit forces

The calculation of U- compensator can be performed using forces method. In that method we calculate axial forces and torque which are reaction on fixed supports as a result of the pipe expansion, and then stress induced by those forces. To find the real reaction on supports, we introduce unit axial forces and unit torque, and then calculate displacement and rotation of system, whose value is zero at the fixed supports. From the system of two equations for displacement and rotation we can find real reaction, which is presented in equation 4 and 5.

$$F_0 = (\alpha EJ\Delta TL)\left[\frac{3(2H+L)}{H^2(2HL+H^2+3BL-3B^2)+3\left(\frac{LJ}{A}\right)(2H+L)}\right] \tag{4}$$

$$M_0 = (\alpha EJ\Delta TL)\left[\frac{3(H+B)H}{H^2(2HL+H^2+3BL-3B^2)+3\left(\frac{LJ}{A}\right)(2H+L)}\right] \tag{5}$$

where:

M_0 - torque generated on fixed supports, Nm

F_0 - axial forces generated on fixed supports, Nm

J - pipe inertia moment, m^4

If we calculate reaction from equations 4 and 5, then we can determine bending moment and stress level from relationship 6 and 7, which should be less than allowable.

$$M_g = \begin{cases} M_0 \\ M_0 - F_0 H \\ M_0 \end{cases} \tag{6}$$

$$\sigma = \frac{F_O}{A} + \frac{M_g D}{2J} \leq \sigma_{dop} \tag{7}$$

where:

M_g - bending moment, Nm

σ - stress level, Pa

A - cross-sectional area, m^2

5. Summary

Diameter, m	Distance between fixed supports, m	Length of arm, m	Length of back, m	Stress calculated with elastic centre method for different distance between sliding supports lr, MPa						Stress calculated by forces method, MPa
				2lr B	σ	2lr B	σ	2lr B	σ	
0,05	60	1,4	0,7	4,7	134,3	39,3	171,8	60,0	177,3	192,7
0,1	80	2,3	1,1	9,1	137,0	52,2	169,6	80,0	175,9	194,4
0,2	120	4,0	2,0	18,0	140,3	78,0	168,7	120,0	175,6	196,5
0,3	120	4,9	2,4	26,4	144,1	77,6	165,8	120,0	173,5	198,2
0,4	160	6,5	3,2	35,2	139,4	103,4	161,1	160,0	168,8	193,4
0,6	200	8,9	4,4	52,4	148,7	128,9	167,0	200,0	175,1	201,7
Designation: **σ- stress level, MPa** **2lr B- distance between sliding supports, m**										

Tab.1. Comparison of stress calculation heating networks with different methods

Table 1 summarizes the comparison of the stress level calculated with different methods. For calculation in Table 1, we assume differences in temperature of 120^{o}C, distance between fixed supports is from recommendation for such networks, and length of the back is taken as half -length of the arm. In the elastic centre method, the stress was calculated for different distance between sliding supports. From Table 1 we can conclude that calculations give different results depending on the kind of method. For the elastic centre method, the level of stress is higher when distance between sliding supports is greater. Stress in the forces method is greater than that in elastic centre method because in the forces method we include to calculation elastic strain energy, which is ignored in the elastic centre method.

References

[1] KAMLER, W. *Ciepłownictwo*. Warszawa: PWN, 1979.

[2] ŁATKOWSKI, L. SZKAROWSKI, A., *Ciepłownictwo*. Warszawa: WNT, 2006.

[3] BARRON, R. F., BARRON, B. R. *Design for Thermal Stresses*. New Jersey: John Wiley & Sons, 2012.

[4] AMARAL, J. P., DA SILVA, V. *Development of calculation methodologies for the design of piping system*. Mechanical Engineering Department.

[5] HETNARSKI, R. B., REZA ESLAMI, M. *Thermal Stresses – Advanced Theory and Application*. Springer, 2009.

[6] WILLIAMS, A. *Structural Analysis: In Theory and Practice*. International Code Council, 2009.

[7] LIANG-CHUA, L.C., PENG TSEN-LOONG, A. *Pipe Stress Engineering*. Houston: Asme Press.

[8] ADWAIT, A., JOSHI R. T., CHERIAN GIRISH, R. *Piping Stress Analysis*. University of Mumbai, 2000.

TRANSCOM 2015, 22-24 June 2015
University of Žilina, Žilina, Slovak Republic

Evaluation of the THPP effect on compactability enhancement of SMA 8 S mix produced in WMA technology

[*] Karol Nowakowski
[*] Kielce University of Technology, Faculty of Civil and Environmental Engineering, Kielce, Poland, {k.nowakowski}@onet.eu

Abstract. The paper describes the effect of the THPP additive on the energy necessary to obtain standard compaction values in SMA mixes produced in the WMA technology. In the first stage of the study, a SMA mix intended for the wearing course was designed, with the PMB 45/80-55 binder, according tothe PN-EN 13208-5. The scope of the study included dosing THPP amounts in the range from 0.0 to 0.6% by mass of the binder, with an increment of 0.2%, and the evaluation of the effect of the additive on the mix density and air voids content in the mix compacted by varying the number of blows of the Marshall hammer. The results indicated that THPP allowedreducing the energy necessary to obtain standard parameters. In addition, the results suggest that at the THPP concentration ranging from 0.4 to 0.6%, both the compaction temperature and energycan be reduced.

Keywords: SMA mix, compaction energy, THPP, void space, density, modified bitumen.

1. Introduction

Striving to minimize production costs and maximize profits has led to accelerated development of chemical or organic additives allowing the producers of bituminous mixtures to achieve their goals. Energy-saving technologies fit into this trend by providing mixes that can be produced and placed at lower temperatures ranging from 110°C to 140°C [3-5] or by using less energy for compaction.[4] Warm Mix Asphalt (WMA) technology ensures obtaining standard values and joins worldwide attempts to reduce negative impacts on the environment [1].

Compaction is the parameter of the utmost importance with respect to durability of asphalt pavements. It is usually assessed by determining the content of air voids and density of the mix.[2] Proper parameters of the mix directly rely on its compactabilitywhich in turn depends on the aggregate type and bitumen used, as well as on the workability of the bituminous mixture. Lowering the surface tension present at the bitumen-aggregate interface can increase compactability of the mix. For this purpose chemical and organic agents are added. The use of fatty amines or other compoundsmay lead to the reduction in the amount of energy necessary for the production and placement of bituminous mixtures.

In order to reduce the energy necessary to obtain standard results, an additive has to be applied that will allow producing the SMA mix with improved workability and compactability levels.

2. Design of the SMA 8 S mix manufactured in WMA technology

To evaluate the influence of the surface-active agent THPP on the compaction energy, a SMA mix was designed. The grading of the mix, SMA 0/11 mm (Fig. 1) was developed based on the requirements in WT-2 2010 and PN-EN 13108-5. Bitumen PMB 45/80-55 was used as a binder, with THPP ranging from 0.0 % to 0.6 %. The concentration of the additive was increased with an increment of 0.2 %.

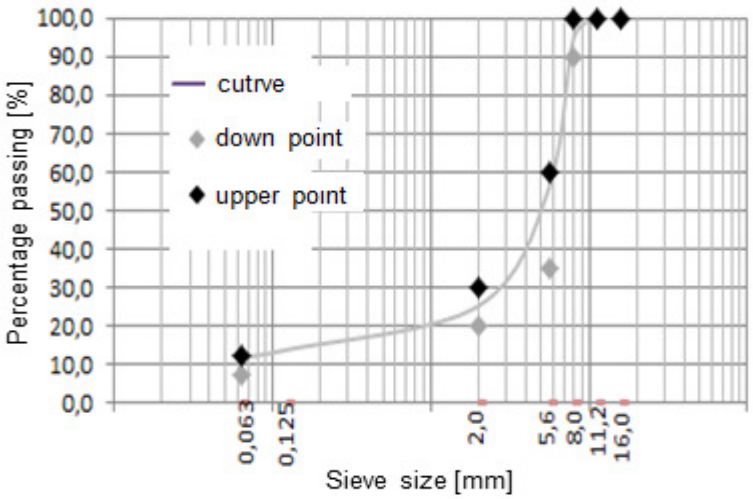

Fig. 1. Grain size distribution curve for the SMA 11 S mix

1. Preparation of samples and methodology of the study

In order to evaluate the effect of THPP on the energy necessary to obtain proper air voids content, the samples were prepared using the Marshall hammer. The tests were performed on the bituminous mixture with polymer-modified bitumen PMB 45/80-55. The concentration of the THPP additive was in the range from 0.2 to 0.6 % by mass of the bitumen used, with an increment of 0.2 %. The series of six samples were compacted at a temperature of 140°Cbyvarying the compaction energy. The compaction effort in the case of the SMA 8 S mix ranged from 700 J to 1000 J per side.

3. Effect of THPP and compaction energy on the density of the SMA mix

In order to evaluate the effects of THPP andcompaction energy on the density of the mix, the density of the prepared samples was determined in compliance with PN –EN 12697-6, method b. The results from the tests were used to assess the influence of the additive and compaction effort on the density of the SMA mix. Figure 2 presents the results obtained.

The results from the tests presented in Fig. 2 indicate that the density of the SMA mix increases with the increasing amount of THPP and increasing compaction effort. It was observed that the mix compacted with the energy of 700 J at the additive concentration ranging from 0.4% to 0.6% provides the densities that are close to the density of the reference mix compacted at 1000 J. The lowest density characterized by a mixture of samples produced without the addition. This dependence is due to a greater mix during compaction resistance resulting from a weaker workability.

To analyse the results, the evaluation of the significance level for the THPP and compaction energy effect on p-value was performed using Statistica software. The significance level for the compaction energy and the concentration of the additive was <0.0001. Based on the findings, a conclusion was drawn that both factors have a statistically significant influence on the results obtained from the study.

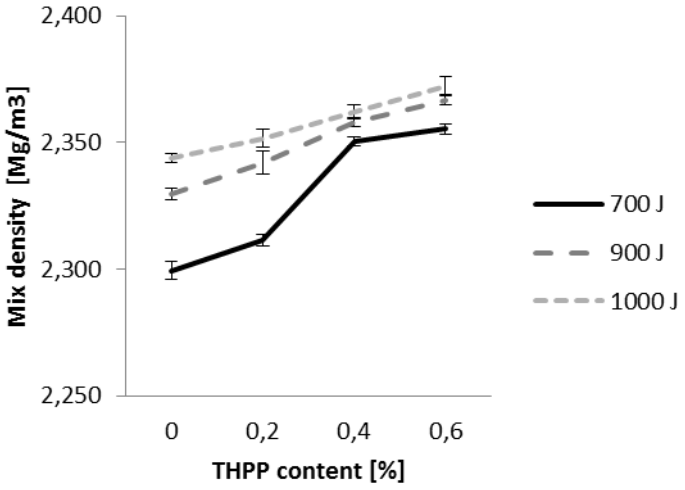

Fig. 2. Determination of the effect of compaction energy and THPP content on bulk density of mixture

4. Evaluation of the effect of THPP and compaction energy on the void space content in the SMA mix

The content of air voids in the mix is another parameter defining the influence of the compaction energy and THPP concentration on the compaction level of the SMA mix. The air voids content of the samples was calculated to PN-EN 12697-8 according to the formula

$$V_m = \frac{\rho_m - \rho_b}{\rho_m} \cdot 100\% . \qquad (1)$$

where:
V_m - void space content in the sample (v/v),
ρ_m - density of the bituminous mix (kg/m^3)
ρ_b - bulk density of the bituminous mix (kg/m^3).

Figure 3 summarises the air voids content (Vm) results. The results allowed defining the effect of the factors on the parameter under investigation. The analysis of the findings shows that the increase in the THPP concentration and compaction energy lead to the decrease in the air voids content in the samples. The lowest content of air voids was obtained for the samples compacted at the energy of 1000 J at 0.6 % THPP concentration, with an average value of 1.6%. The highest air voids content was observed in the samples compacted without the THPP additive. Regardless of the energy used for the compaction of the mix, absence of the THPP additive results in the reduction of the compactability of the mix and an increase in the air voids content, Vm.

The use of the additive at a concentration of 0.2 % slightly improves compactability, resulting in a small decrease in the value of the parameter. When the concentration of the additive is in the range from 0.4% to 0.6%, the value of the parameter being evaluated decreases to the level recorded for the mix compacted with the energy 30% higher with no additive used. The concentration at the level of 0.6% causes a 50 % reduction in the air voids content, Vm, in the mix compacted with an energy of 700 J. Research has shown blends produced without the additive has a higher void content than blending with the additive THPP. Lowering the void content of less than 2% can cause lack of resistance to permanent deformation.

To check the correctness of the performance, the significance level was estimated for the influence of THPP and compaction energy. The p-values obtained were < 0.0001. On this basis it can be concluded that the factors investigated have a significant influence on the parameter being studied.

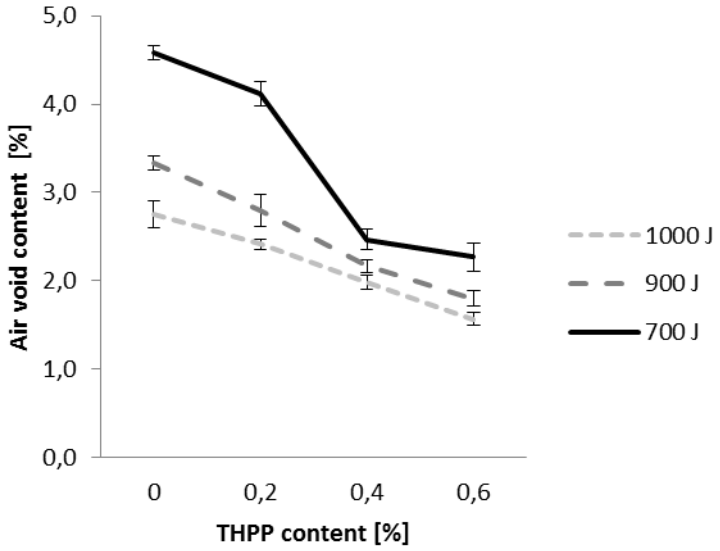

Fig. 3. Determination of void space content in the SMA mix

5. Conclusions

The results from the study of the effect of the THPP additive and SMA 8 S mix compaction energy, the following conclusions can be drawn:
- the THPP content has a significant influence on the density of the bituminous mixture,
- the use of the THPP additive in the concentration range from 0.4 to 0.6% allows obtaining density similar to that of the mix without THPP,
- the increase in the THPP amount added leads to the decrease in air voids content within the entire dosage range, irrespective of the energy applied during compaction,
-the use of the additive in the amounts ranging from 0.4 to 0.6% allows decreasing the compaction energy by about 30% at similar content of air voids.

References

[1] D'ANGELO J., HARM E., BARTOSZEK J., BAUMGARDNER G., CORRIGAN M., COWSERT J., HARMAN T., JAMSHIDI M., JONES W., NEWCOMB D., ROWELL B., SINES R., B. YEATON *Warm-Mix Asphalt: European Practice American Trade Initiatives* P.O. Box 8228 Alexandria February 2008

[2] GAWEŁ I., KALABIŃKA M., PIŁAT J. *AsfaltyDrogowe*WydawnictwoKomunikacjiiŁączności, Warszawa 2014

[3] IWAŃSKI M., MAZUREK G. *Zależnośćtemperaturyzgęszczaniabetonuasfaltowego w aspekciemodyfikatoraniskowiskozowego*. IV Międzynarodowa Konferencja Naukowo-Techniczna, Poznań 2009, październik 2009 s-94-102

[4] STEFAŃCZYK B., MIECZKOWSKI P. *Dodatki, katalizatory i emulgatory w mieszankach mineralno asfaltowych* Wydawnictwo Komunikacjii Łączności, Warszawa 2010

[5] Xiao F, Punith V.S., Amirkhanian S.N., *Effects of non-foaming WMA additives on asphalt bitumen sat high performance temperatures,* Fuel 2011

TRANSCOM 2015, 22-24 June 2015
University of Žilina, Žilina, Slovak Republic

The Modification of Calcium Silicate Products with Recycled Polymers

[*]Milena Nowek [*]Ryszard Dachowski
[*]Kielce University of Technology, Faculty of Civil Engineering and Architecture, Department of Building Engineering Technologies and Organization, al. 1000-lecia PP 7, 25-314 Kielce, Poland
milena.nowek@gmail.com, tobrd@tu.kielce.pl

Abstract. The paper presents the research results of calcium silicate products (called also sand-lime products or silicates) modified with polymers. Three types of plastics were considered, all are the products of recycling – in the form of regranulate or regrind. The main purpose of the research was to determine the impact of these additives on the functional properties of resulting products. The compressive strength, water absorption and bulk density of such materials were tested. The microstructure was also analyzed. Obtained results are presented in the form of graphs and the SEM micrographs.

Keywords: calcium silicate products, polymers, recycling, functional properties

1. Introduction

The sand-lime products are construction materials in the form of blocks and bricks. Traditional elements are manufactured only from natural components such as lime, sand and water. Thanks to the autoclaving process they obtain high compressive strength. Silicates are characterized also by relatively low water absorption, high bulk density and good acoustic properties. They are frost and fire resistant. All mentioned properties make silicates one of the most popular building materials.

During the last few years attempts to modify traditional sand-lime products have been made in order to influence certain characteristics of the final products. The use of basalt aggregate caused increase of the compressive strength of the products and drop in the water absorption. Similar effect on those properties was observed also with the use of barium sulfate and lithium silicate [1]. Foamed glass granulate was added to decrease bulk density of bricks and blocks and to improve their acoustic properties. [2,3]. Silicates products were also modified by polymers additives. Thanks to including the low density polystyrene regranulate (LDPE) it was possible to obtain silicates products with not only lower the bulk density but also the lower water absorption in comparison to traditional sand-lime products. LDPE is characterized by the low bulk density (not more than 900 kg/m^3) and low water absorbency (around 0.03%) [4,5]. The addition of the ABS regranulate contributes to a large reduction in water absorption but also reduces the compressive strength of sand-lime elements. The ABS is a material with high hardness and impact resistance which has good insulating properties and is characterized by a high softening temperature. The ABS found use in the production of machinery and equipment housing, interior elements of vehicles, various types of containers or elements of furniture [6,7].

Organic plastic materials are produced in the process of chemical synthesis, from raw materials such as crude oil, coal or natural gas. In the construction industry they are the youngest group of building products, a very large and extremely diversified in terms of the properties and possible application. Thousands of types of plastics are currently available in the world. Plastics are used in almost all areas of life and industry [8]. This paper presents the results of tests of sand-lime products with the addition of the high impact polystyrene regranulate (HIPS) and polypropylene

and polyethylene regrind (PP+PE). Those additives were supposed to help to achieve the higher compressive strength, lower water absorption and weight of silicate products.

2. The modification of sand-lime mass

Building lime, beside gypsum binders, is one of the oldest known binding materials used in construction. It was the basic binder until the discovery of cement. However, lime is now perceived as a valuable material not only in traditional techniques, but also in new development of the modern construction.

Among the properties and characteristics of the lime-based products, the health aspect is very important. Lime is a completely natural product and does not contain substances harmful to humans. Ecological purity of lime is an essential feature, because it affects a suitable microenvironment inside the buildings.

In the production of sand-lime elements quick lime is used. After mixing with quartz sand it is slaked by the addition of a small amount of water. Quick lime consists primarily of calcium oxide CaO and magnesium oxide MgO. It is manufactured through a firing treatment of limestone or dolomite. It occurs as a direct product of firing as quick lime in lumps, which produces an exothermic reaction with water.

The lime used in the manufacturing of silicates is made from pure limestone, which contains calcium carbonate $CaCO_3$ (calcite) as a basic ingredient [9]. Lime represents about 10% of the weight of the product. The sand used in the process has a grain size from 0 to 2 mm and constitutes around 90% of the silicate mass. Water is a complement of the mixture.

Nowadays, a number of admixtures and additives for modification of building materials can be mentioned. The most popular silicate mass modifiers are: energetic waste (fly ash), sand-lime mass thickeners, surface active agents that cause mass plasticizing, additives to accelerate and retard lime slaking, combinations of additives, active mineral additives, metallurgical waste and other waste materials.

The main (and sometimes the only) components of plastics are organic macromolecular substances, called polymers, and usually additional components affecting the processing and/or functional properties of polymers.

Polymers are macromolecular compounds created from identical, recurrent simple units called the mers.

The increasing use of polymers is a result of their characteristic properties. They seem to be interesting as additives for silicate products because of their low bulk density, relatively high strength and chemical resistance to many aggressive factors and water. Plastic materials used for construction and finishing of buildings have a significant impact on the health conditions of the rooms in which they were applied. Well polymerized and hardened macromolecular plastics should be chemically and biologically neutral materials [8].

The HIPS is a lightweight material with high stiffness, impact and crack resistant. The polystyrene HIPS contains caoutchouc bound physically or chemically. According to the share of the caoutchouc, physical and mechanical properties of the material are different. Products made of the polystyrene HIPS are used among others to make equipment cases, elements of lighting fixtures and in the food industry to manufacture of packaging.

Polypropylene has a very low water absorbency and permeability. It is characterized by a low density, high corrosion resistance and relatively high surface hardness. It is a thermoplastic material which is suitable for injection molding and extrusion and for the production of foils and fibers. The polypropylene products retain the shape to a temperature of 150^0C. Its properties depend largely on the molecular weight, the degree of polydispersity, the tacticity and crystallinity. Polyethylene minimally absorbs moisture. It has the low density compared to other materials and the high impact strength even at low temperatures. Its low weight and excellent insulation properties preferred polyethylene for use as a raw material in the manufacturing of the submarine cable under the

English Channel. During World War II polyethylene was used for the construction of the lightweight aircraft radars.. Today polyethylene is a popular material used in the production of many everyday items, household products and insulation materials or foils [7].

In order to perform tests modified silicate samples were made. The composition of each sample is presented in the following table.

Sample No.	Mass percent in the sample [%]	
	HIPS	PP+PE
1	-	-
2	10	-
3	20	-
4	30	-
5	-	10
6	-	20

Tab. 1. Mass percent of the additive in the sample.

Rectangular samples with dimensions of 40x40x160 mm were made. The sample number 1 is a traditional silicate whose composition comprises only lime, sand and water. The test specimens were prepared in laboratory conditions. Then they were subjected to autoclaving process at the temperature of 203°C and at the pressure of 1.6 MPa, during which a series of chemical reactions affecting the properties of final products took place.

3. Performed tests and obtained results

3.1. Bulk density

The bulk density of the material is related to its microstructure and it is a weight of a unit volume of dried material with pores. It is calculated using following formula:

$$\rho = \frac{m}{V} \text{ [kg/m}^3\text{]} \qquad (1)$$

where m represents the mass of dried material and V is the volume of the sample. Bulk density is a characteristic of a great practical importance. It allows defining approximately other characteristics of the material and its usefulness. The low value of bulk density is now often an advantage, since modern construction is lightweight. The low bulk density makes transport and assembly easier, reduces the load of the structure, but it may also impair the acoustic properties. The increase in bulk density is achieved by compacting the structure of the material through compression. The effect of used additives on the bulk density of modified calcium silicate elements is presented in Figure 1.

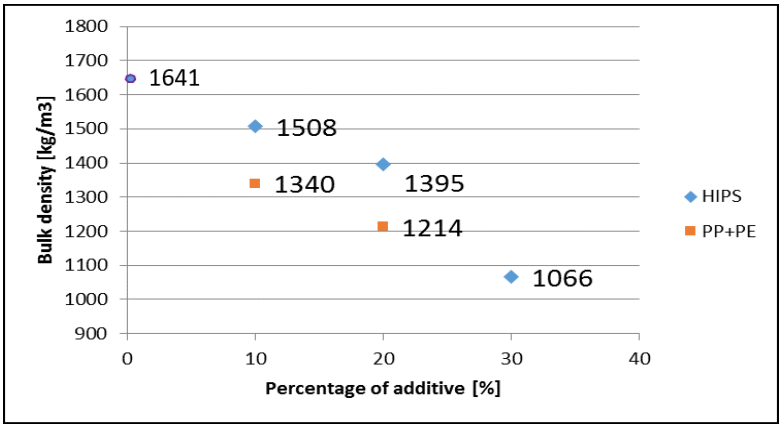

Fig. 1. Bulk density of modified silicate products.

3.2. Water absorption

Water absorption expresses relative amount of water that the material can absorb and retain. It is the maximum humidity that the material can achieve.

Water absorption is determined by the ratio of the mass of water absorbed by the sample under the conditions of room temperature +20 ±2°C and atmospheric pressure to the mass of the sample in a saturated state, according to the formula:

$$c_W = \frac{m_{so,s} - m_{dry,s}}{m_{dry,s}} \times 10^2 \ [\%] \qquad (2)$$

where $m_{so,s}$ means the mass of the sample after saturation and $m_{dry,s}$ is the mass of the sample after drying. The graph in Figure 2 shows the results of water absorption.

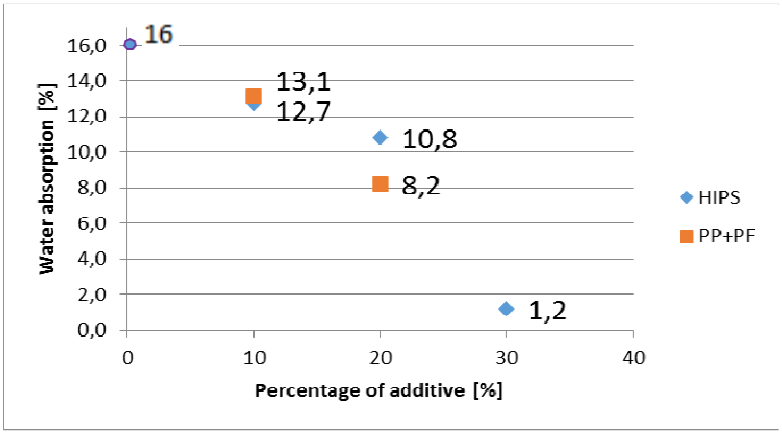

Fig. 2. Water absorption of modified silicate products.

3.3. Compressive strength

The compressive strength is the maximum compressive stress that the material can sustain. The compressive strength is the ratio of acting axially destructive compressive force to the surface size of the sample. The compressive strength test was performed using a press.

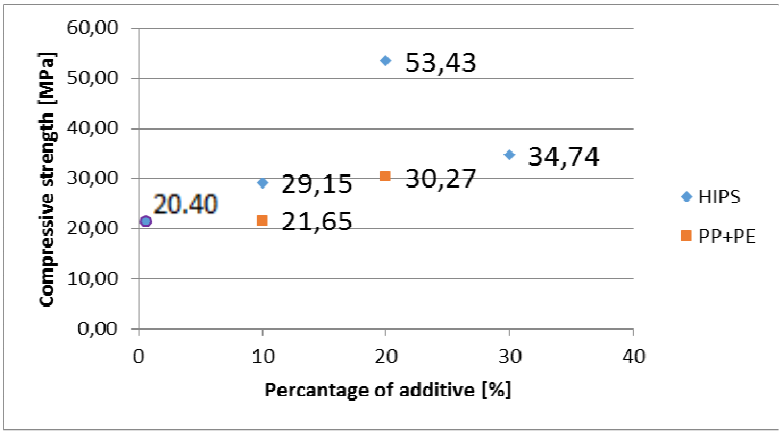

Fig. 3. Compressive strength of modified silicate products.

3.4. Microstructure

It was possible to interpret the structure of traditional silicate products thanks to the analysis performed by the use of the Scanning Electron Microscope. The interpretation revealed the existence of the C-S-H phase and the presence of the tobermorite. The C-S-H phase is a

configuration of hydrated calcium silicates with a different level of structural arrangement: CaO-SiO_2-H_2O, which emerges as a result of the reaction between the calcium silicates and water. The tobermorite is the most ideal form of the C-S-H phase. It is also a hydrated calcium silicate characterized by an arranged structure and specified inter-plane spaces [1,10]. Figure 4 and 5 present the structure of the particular phases in a traditional silicate product.

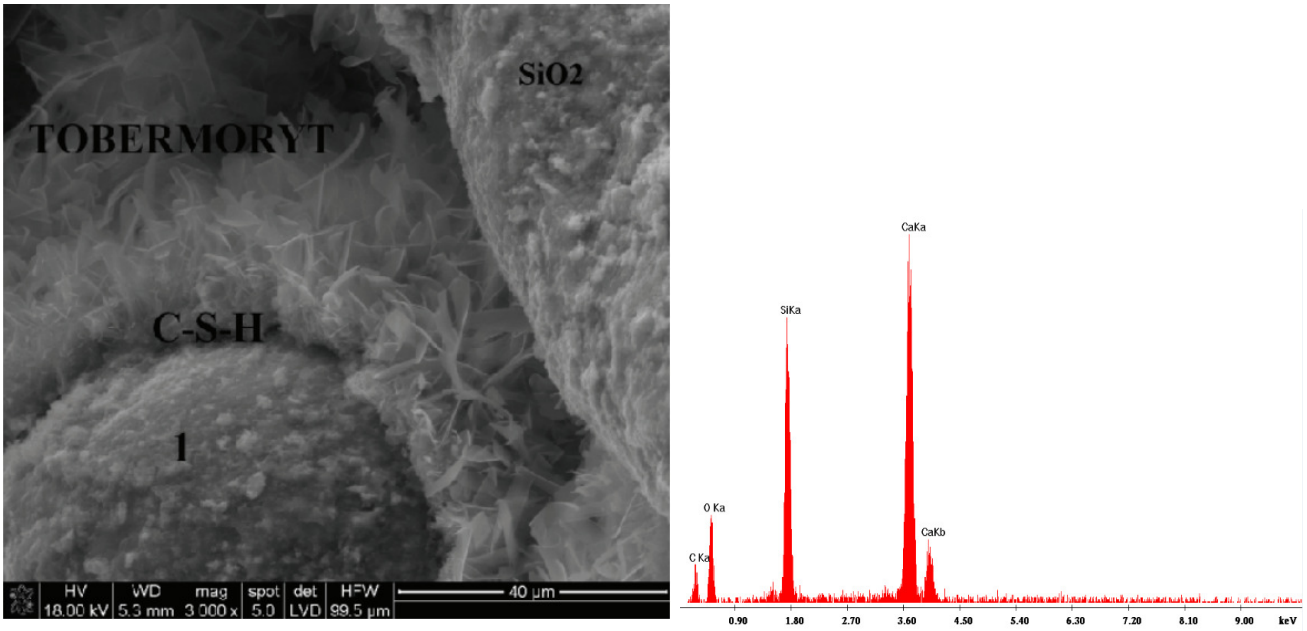

Fig. 4. Microstructure and elemental structure of traditional silicate products.

Figure 4 shows a sand grain surrounded by the C-S-H phase, which then transforms into a higher and more perfect form, i.e. tobermorite. The tobermorite phase in the traditional silicate product appears in the form of blades with flat endings. Figure 5 is a diphractogram presenting the elemental structure of traditional silicate product [1]. A small amount of carbon is due to a preparation of test samples on the Scanning Electron Microscope. The following pictures show the microstructure and elemental structure of the modified silicate products.

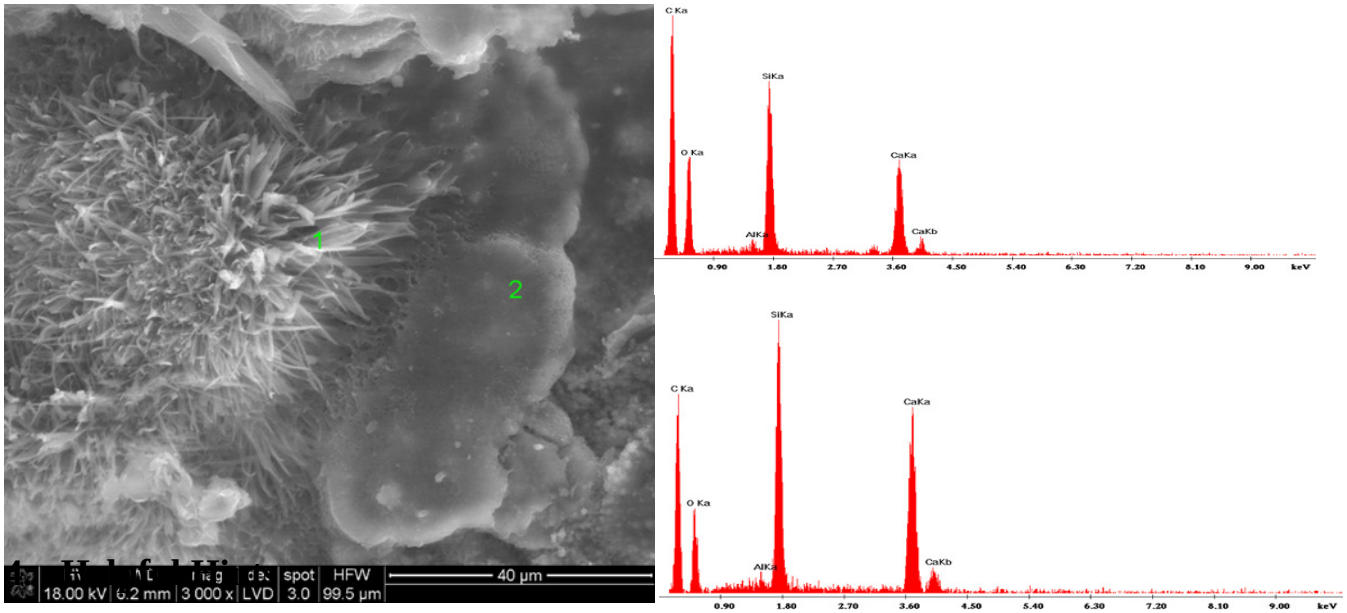

Fig. 5. Microstructure and elemental structure of the sample number 6.

The diffractogram above indicates, besides the elements that were found in a traditional silicate products, also a presence of carbon (from polymers) and aluminum (introduced with the sand). High compressive strength of silicate product containing PP+PE and HIPS is a result of a good contact between the polymer and sand-lime mass ingredients. In both the sample with HIPS and that with PP + PE, the presence of C-S-H phase and tobermorite was observed.

4. Conclusion

Performed tests prove that the use of plastic materials as additives in calcium silicate products can be beneficial. A very high increase in the compressive strength of modified materials was observed. Such modified products have also lower water absorption and mass in comparison to traditional ones. Moreover, only materials from recycling were used in the examination, which means that the resulting products are still environmentally friendly and the study on such modified silicates will be continued.

References

[1] DACHOWSKI R., STĘPIEŃ A., The impact of various additiveson the microsrtucture of silicate products, Procedia Engineering vol. 21, 2011, p.1173-1178

[2] JASIŃSKA I., DACHOWSKI R., Granulat szkła spienionego jako lekki dodatek masy silikatowej, Praca zbiorowa pod redakcją Joanny Bzówki pt. Badania doświadczalne i teoretyczne w budownictwie, monografia, Wydawnictwo Politechniki Śląskiej, Gliwice 2012

[3] DACHOWSKI R., JASIŃSKA I., Wpływ dodatku szkła spienionego na porowatość wyrobów silikatowych, Archiwum Instytutu Inżynierii Lądowej 2012

[4] JASIŃSKA I., NOWEK M., Wpływ modyfikacji wyrobów silikatowych dodatkiem w postaci LDPE na ich podstawowe właściwości użytkowe, Konferencja Młodzi dla Techniki, Wybrane problemy naukowo-badawcze budownictwa i inżynierii środowiska, Płock 2013, p. 153-158

[5] KOSZKUL J., Polipropylen i jego kompozyty, Wydawnictwo Politechniki Częstochowskiej, 1999

[6] NOWEK M., The impact of recycled polymers on the features of modified sand-lime product, Czasopismo Techniczne 1-B, Kraków 2014

[7] PIELICHOWSKI J., PUSZYŃSKI A., Chemia polimerów, Wyd. Naukowo-Techniczne Teza, Kraków 2004

[8] OSIECKA E., Materiały budowlane. Tworzywa sztuczne, Oficyna Wydawnicza Politechniki Warszawskiej, Warszawa 2005

[9] OSIECKA E., Wapno w budownictwie –tradycja i nowoczesność, Stowarzyszenie Przemysłu Wapienniczego, Kraków 2006

[10]KURDOWSKI W., Chemia cementu i betonu, Wydawnictwo Naukowe PWN, Warszawa 2010

TRANSCOM 2015, 22-24 June 2015
University of Žilina, Žilina, Slovak Republic

Effect of different values of soil shear strength parameters of the size of spread foundation

[*]Lucia Orininová, [*]Giang Nguyen
[*]University of Žilina, Faculty of Civil Engineering, Department of Geotechnics, Univerzitná 8215/1, 010 26 Žilina, Slovakia, {lucia.orininova, giang.nguyen}@fstav.uniza.sk

Abstract. Shear strength parameters have significant effect on size of spread foundation. When designing spread foundation, the parameters necessary to calculate the bearing capacity of foundation soil are angle of internal friction and cohesion. In this paper the effect of guiding standardized minimal, intermediate and maximal values of shear strength parameters introduced in the old Slovak Technical Standard STN 731001 as so as shear strength parameters vales obtained from geotechnical investigation report on the size of spread foundation is compared. The analysis of design of spread foundation, placed on homogeneous subsoil is also made and compared effect by various specific standard.

Keywords: spread foundation, shear strength parameters, internal angle of friction, cohesion, homogeneous subsoil

1. Introduction

Design of spread foundation can be made according to various design methods. The choice of used design methods effect bearing capacity of foundation soils and sizes of the foundation. Main factors, which influence on the size of foundation are angle of the internal friction and cohesion. The values angle of the internal friction can be found from laboratory tests, from which direct shear test (DST), or from standardized values introduced in the Slovak Technical Standard.

The design of spread foundation is usually realized according to different standard specifications. In this paper are compared 5 design approach in geotechnical practice in Slovakia. Namely, the Slovak Standard STN 73 1001 “Foundation of structures. Subsoil under shallow foundations” (in following text we will use the abbreviation “old STN” for it), next the Slovak Technical Standard STN 731001 “Geotechnical structures. Foundation” (abbreviation “new STN”) and last, Eurocode 7, where 3 Design Approaches (DAs) are included. [3]

2. Design spread foundation according to various standard specifications

Bearing resistance failure, which is a GEO ultimate limit state, is the relevant ultimate limit state to be considered for the design of the spread foundation in this example. When design for this ultimate limit state, the following inequality needs to be satisfied

$$V_d \leq R_d$$

where, V_d is the design vertical load and R_d is the design bearing resistance.[1]
The minimum footing size is checked for each Design Approach Eurocode 7 and STN 73 1001 and for drained conditions.

For drained conditions the value of the vertical bearing resistance is calculated using for Eurocode 7 Equation D.2 of Annex D: [2]

$$R_d = \left(c'.N_c.s_c.b_c.i_c + q'.N_q.s_q.d_q.i_q + 0{,}5.\gamma'.B.N_\gamma.s_\gamma.b_\gamma.i_\gamma\right)/\gamma_{R,v} \quad (1)$$

Design bearing capacity of the foundation soil for the drained conditional according to "new" STN 73 1001 calculated by the formula: [3]

$$R_d = \left(c'_d.N_c.s_c.d_c.i_c.j_c + q'.N_q.s_q.d_q.i_q.j_q + \gamma'.\frac{B}{2}.N_\gamma.s_\gamma.d_\gamma.i_\gamma.j_\gamma\right)/\gamma_{R,v} \quad (2)$$

And formula for calculated by "old" STN 73 1001 had been used until 01.04.2010:[5]

$$R_d = \left(c_d.N_c.s_c.d_c.i_c + \gamma_1.d.N_d.s_d.d_d.i_d + \gamma_2.b_{ef}/2.N_b.s_b.d_b.i_b\right) \quad (3)$$

where: R_d [kPa] is a design bearing capacity;
c_d' [kPa] is a design value of effective cohesion, $c_d' = c_k'/\gamma_c'$;
c_k' [kPa] is a characteristic value of effective cohesion;
γ_c' [-] is a partial factor for cohesion;
φ_d' [°] is a design value of angle of friction, $\varphi_d' = \varphi_k'/\gamma_\varphi'$, for STN and DA1 (C1) and DA2 in Eurocode 7, for DA1(C2) and DA3 $\varphi'_d = \tan^{-1}(\varphi'_k)/\gamma_\varphi'$ in Eurocode 7;
φ_k' [°] is a characteristic value of angle of friction;
γ_φ' [-] is a partial factor for an angle of friction;
q´ [kPa] is a design effective overloading above foundation base;
γ´ [kN.m^{-3}] is an effective unit weight of the soil under foundation base;
$\gamma_{R,v}$ [-] is a partial factor for the resistance (bearing capacity)
N_c, N_q, N_γ are bearing capacity factors, depending on design angle of internal friction φ_d
s_c, s_q, s_γ are foundation shape factors
d_c, d_q, d_γ are factors of foundation depth
i_c, i_q, i_γ are factor of load inclination
j_c, j_q, j_γ are factors of terrene slope

Significant differences are in partial factors. In Tab.1 are partial factors for various specific standard.

	γ_c'	γ_φ'	$\gamma_{R,v}'$
"new" STN	1,0	1,0	1,4
EN7, DA1(C1)	1,0	1,0	1,0
EN7, DA1(C2)	1,3	1,3	1,0
EN7, DA2	1,0	1,0	1,4
EN7, DA3	1,3	1,3	1,0
"old" STN	2,0	1,2	1,0

Tab. 1. Partial factor for various specific standard

3. Analysis of specific foundation

For analysis differences between various specific standard we will deal only with spread foundation square shape of foundation, vertical action, homogenous soil. The water level is one meter below the surface. At the Fig.1 is illustrated model example for the spread foundation design.

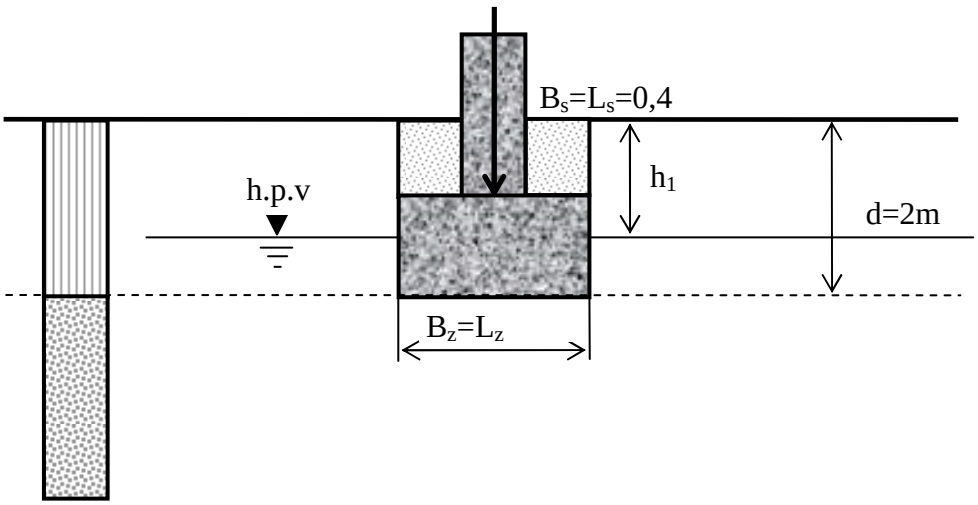

Soil properties: F4, γ_k= 18,5 kN.m^{-3}; $\gamma_{k,sat}$= 21,00 kN.m^{-3}
F6, γ_k= 21,00 kN.m^{-3}; $\gamma_{k,sat}$= 21,20kN.m^{-3}
The values of shear strength parameters from geotechnical investigation report:
φ_{F4}'=10 kPa, c_{F4}'=24°; φ_{F6}'=12 kPa, c_{F6}'=19°
Standardized values of shear strength parameters introduced in the STN 731001:
$\varphi_{F4}'_{,min}$=10 kPa, $c_{F4}'_{,min}$=22°; $\varphi_{F6}'_{,min}$=8 kPa, $c_{F6}'_{,min}$=17°
$\varphi_{F4}'_{,med}$=14 kPa, $c_{F4}'_{,med}$=24,5°; $\varphi_{F6}'_{,med}$=12 kPa, $c_{F6}'_{,med}$=19°
$\varphi_{F4}'_{,max}$=18 kPa, $c_{F4}'_{,max}$=27°; $\varphi_{F6}'_{,max}$=16 kPa, $c_{F6}'_{,max}$=21°

Fig. 1. Model example for the spread foundation design

In this paper, differences between various design procedures and differences between shear strength parameters were compared. Analysis was made based on values of angle of friction and cohesion, obtained from geotechnical investigation report on one side and minimum, maximum and medium standards values for given soil type on the other side. As we can see at fig. 1, design by various design procedures and shear strength parameters has significant effect on size of the foundation.

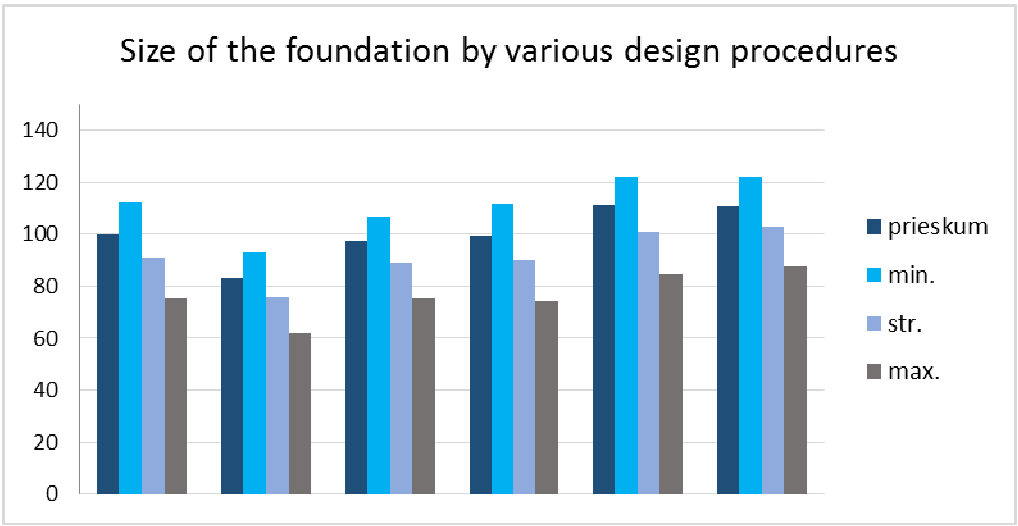

	STN 73 1001 „new“	STN EN 1997: (DA1)/C1	STN EN 1997: (DA1)/C2	STN EN 1997: (DA2)	STN EN 1997: (DA3)	STN 73 1001 „old“
report	2,09	1,74	2,04	2,08	2,32	2,31
min.	2,35	1,94	2,23	2,33	2,55	2,55
med.	1,9	1,58	1,86	1,88	2,11	2,15
max.	1,57	1,3	1,57	1,55	1,77	1,83

Fig. and Tab. 2 Differences of size of foundation by Slovak Technical Standard and Eurocode 7

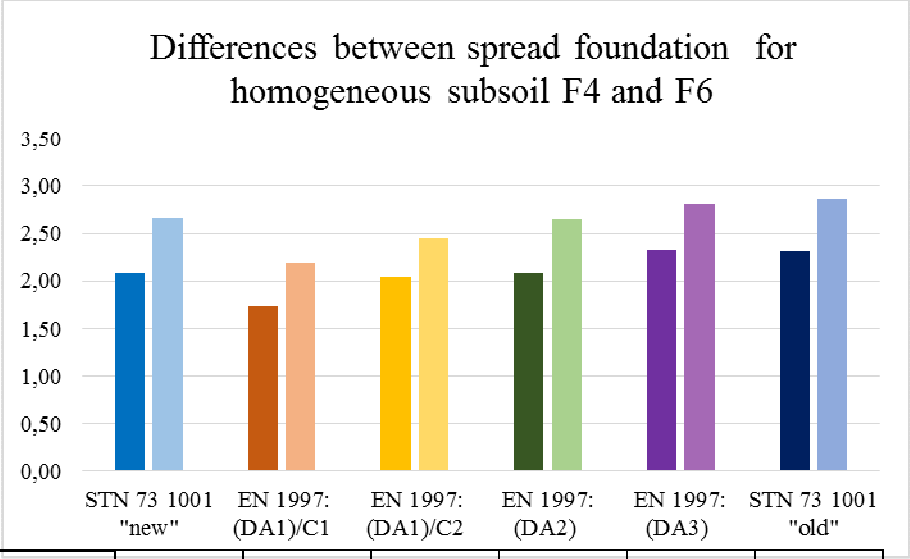

Size for F4	2,09	1,74	2,04	2,08	2,32	2,31
Size for F6	2,66	2,19	2,45	2,65	2,81	2,87
Differences [%]	21,43	20,55	16,73	21,51	17,44	19,51

Fig. and Tab. 3 Differences between subsoil F4 and F6

From the data in Tab.1 and Fig.2 we can see that differences in the size of foundation in the soil F4 designed using by various design procedures have reached the values from 2,09 m up to 2,31 m (different 9,5%) for values shear strength parameters from geotechnical investigation report and for standardized values of shear strength parameters introduces in the STN 73 100: for minimal values from 2,35 m up to 2,55 m (different 7,8%), for intermediate values from 1,9 m up to 2,15 m (different 11,6%) and for maximal values from 1,57 m up to 1,83 m (different 14,2%).

To compare the shear strength parameters, percentual difference between minimal and maximal values for „new“ STN is 33,2%, for EN 7, DA1 (C1) is 32,9%, for EN 7, DA1 (C2) is 29,6%, for EN 7, DA2 is 33,5%, for EN 7, DA3 is 30,6%, for „old“ STN is 28,2%.

From comparison of soils with better and worse properties we found out percentual difference for „new STN“ 21,43%, for EN 7,DA1 (C1) 20,55%, for EN 7,DA1 (C2) 16,73%, for EN 7, DA2 21,51%, for EN 7, DA3 17,44% and for „old“ STN 19,51%.

4. Conclusion

The fact, that shear strength parameters have significant effect on size of foundation. standardized values of shear strength parameters included in the STN 73 1001 have large range and we give significant differences size of foundation. Therefore is properly to made geotechnical investigation report to obtain as accurate shear strength parameters as possible, in order to not design an excessive spread foundation, what significantly impact on economic of the structure.

References

[1] TREVOR L. L. ORR.: Model solutions for Eurocode 7 Workshop Examples. Ireland, Trinity Colleg, Dublin University, 2005

[2] STN EN 1997-1: Geotechnical design. Part 1: General rules. (in Slocak language). Bratislava: Slovak Standards Institute, Slovak Republic, 2005

[3] STN 73 1001: Geotechnical structures. Foundation (in Slovak language). Bratislava: Slovak Standards Institute, Slovak Republic, 2010

[4] Frankovská, J., Suľovská, M., Turček, P.: Zakladanie stavieb. Podklady k navrhovaniu, plošné a hĺbkové základy. Vydavateľstvo STU, 2011

[5] STN 73 1001: Foundation of structures. Subsoil under shallow foundation (in Czech language). Prague: Institute for Standardizations and Measurements, Republic of Czechoslovakia, 1987

[6] NGUYEN, G.: Designing spread foundation by Slovak Technical Standard STN 73 1001 and Eurocode 7. Teoretical Foundation of Civil Engineering, XX. Polish - Russian – Slovak Seminar, Žilina 2011

TRANSCOM 2015, 22-24 June 2015
University of Žilina, Žilina, Slovak Republic

Synthesis of tobermorite on the $CaO-SiO_2-Al_2O_3-H_2O$ system under hydrothermal conditions

[*] Owsiak Z., [*] Sołtys A.
*Kielce University of Technology, Faculty of Civil Engineering and Architecture, Department of Building Engineering Technologies and Organization, al. Tysiąclecia Państwa Polskiego 7, 25-314 Kielce, Poland, owsiak@tu.kielce.pl

Abstract. Tobermorite has been successfully synthesized in the $CaO–SiO_2–Al_2O_3–H_2O$ system. This paper presents the results of the studies carried out in the model systems and concerning the tobermorite synthesis with an addition of halloysite. Quartz sand and quicklime were the main raw material constituents. The mixtures in the form of slurries underwent hydrothermal treatment with an addition of halloysite (5, 10, 30%) for 4 h. The resultant composites were analysed for their phase composition using XRD. The microstructure was examined using the SEM with the EDS analysis. Tobermorite was the principle reaction product. When 30% halloysite was added to the mixture containing CaO and SiO_2, the formation of katoite was found.

Keywords: tobermorite, halloysite,katoite

1. Introduction

Autoclaved aerated concrete (AAC) is an attractive, versatile building material used in Europe and other parts of the world [1]. Produced from available, cheap and carefully prepared raw materials, AAC is a product of hydrothermal treatment of quartz, Portland cement, gypsum, lime and aluminium powder. During autoclaving, silica reacts with calcium hydroxide to form a microcrystalline structure with a specific surface area smaller than that obtained through normal hardening [2]. The resultant material combines the characteristics of insulating and structural materials [1]. Tobermorite is the principal phase formed in autoclaved building composites, the one which provides the final products with appropriate mechanical properties. Understanding the mechanism of tobermorite formation in the autoclave process is very important for the production of AAC [3].

The tobermorite was synthesized with an addition of halloysite $Al_4[Si_4O_{10}](OH)_8 \cdot 4\ H_2O$. Halloysite is a 1:1 double layer monophyllosilicate clay mineral. Its layers are disjointedly shifted relative to each other in *a* and *b* directions, exhibiting chaotic assemblages. The misfit of the tetrahedral layer and the octahedral layer results in relaxation of strain, which leads to rolling and creates tubular morphology of halloysite. Water particles present in the interlayer spaces form a monomolecular layer and contribute to the weakening of hydrogen bonds [4,5,6,7].

The main objective of the tests was to determine the impact of various amounts of halloysite on the phase composition of autoclaved building composites in the $CaO-SiO_2-H_2O$ system. The tests of the phase composition and microstructure of the autoclaved materials were carried out using X-ray diffraction (XRD) and scanning electron microscopy (SEM).

2. Materials and methods

Raw materials used to obtain autoclaved composites included silica sand and quicklime. The silica sand chosen met the PN-EN 196-1 criteria. Grains with the size less than 0.5 mm were ground to reach the Blain fineness of 6560 cm^2/g. The quicklime was obtained by subjecting pure calcium

carbonate to the heat of 1000°C for 2 hours. Halloysite from the Dunino mine was used as an admixture, 5,10 and 30% by weight of the joint weight of CaO and SiO_2. Halloysite microstructure (SEM) and X-ray analysis (EDS) are shown in Fig.1

Tobermorite was synthesized at the CaO/SiO_2 molar ratio of 0.83. The ratio of water *w* to the amount of solid constituents *s* was 2 (W/S=2). The constituents were placed in plastic containers and homogenized for 5 minutes. Halloysite was added towards the end of mixing the main components. The slurries were then poured into PTFE moulds and moved into a laboratory autoclave and held at 180°C for 4 hours at a saturated steam atmosphere. The temperature in the autoclave was elevated with the rate of 1.5° C/min. The specimens were dried under vacuum to prevent them from being contaminated with CO_2.

An X-ray diffraction method (EMPYREAN manufactured by PANalytical) was used to analyse the phase composition of the composites. The microstructure was examined using a scanning microscope (Quanta 250 FEG) in the low vacuum mode. The steam atmosphere was 30Pa.

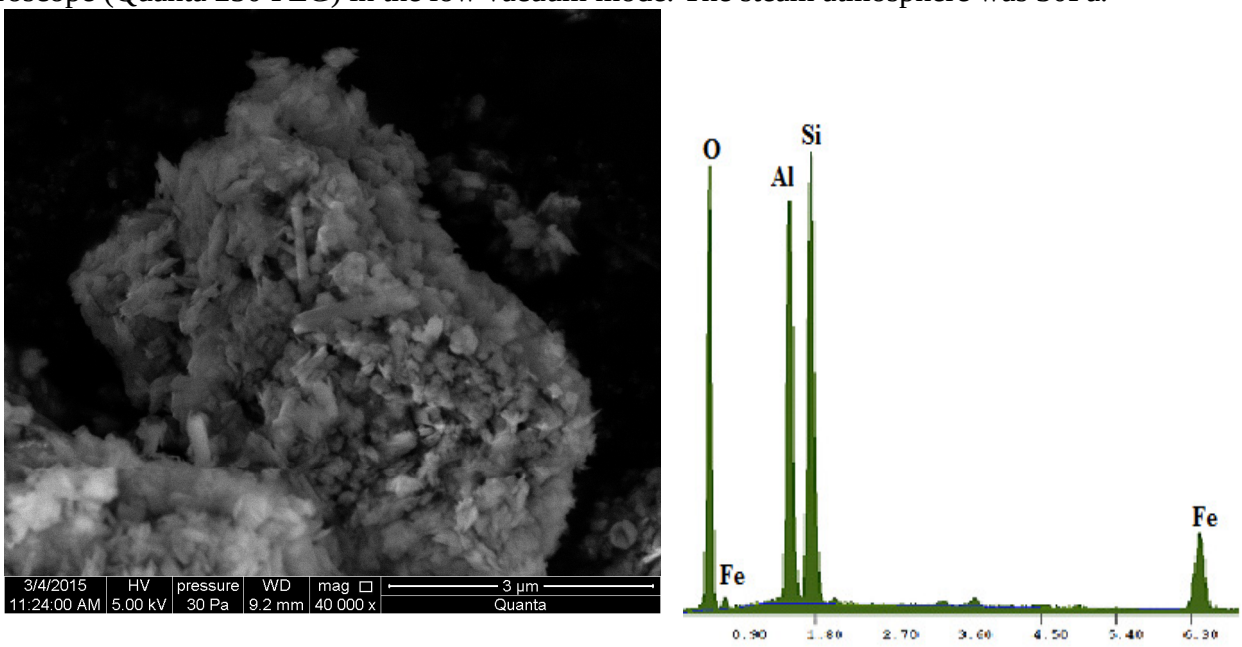

Fig.1. Microstructure (SEM) and microanalysis (EDS) of halloysite.

The microstructure in Fig.1 reveals that the mineral is made of dispersed nanotubes and nanolaths. An X-ray analysis of the microregion indicated silicon, aluminium and iron as its main constituents.

The designation of the mixtures with a varied amount of halloysite is shown in Table 1.

SPECIMEN	A1	A2	A3	A4
Halloysite content [%]	0	5,0	10,0	30,0

Tab.1. Designation of tobermorite specimens

3. Result and discussion

Figure 1 shows the phase composition of the synthesized samples with different halloysite contents, autoclaved at 180°C for 4 hours.

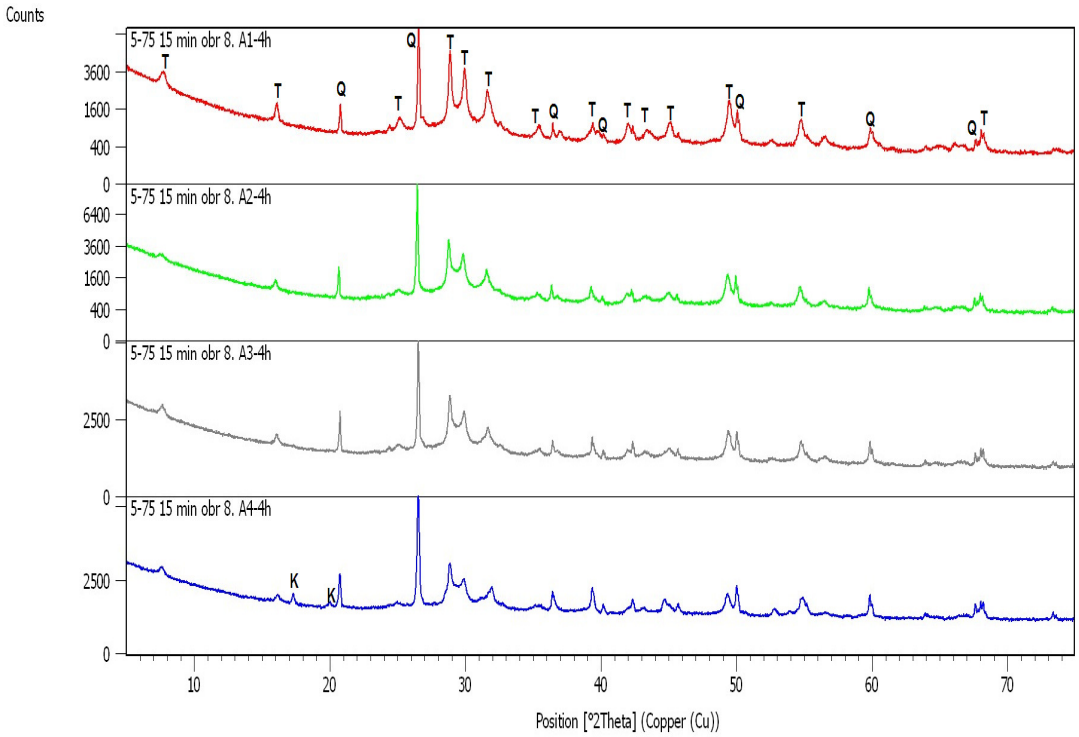

Fig.2. X-ray diffractogram of products obtained from a raw materials mix of CaO/SiO_2=0.83 and halloysite added at 0, 5, 10 and 30% (T-tobermorite, K-katoite, Q-quartz) autoclaved at 180°C for 4 hours

An analysis of XRD results for the samples without and with 5 or 10% halloysite addition indicates that the arrangement of peaks is similar regardless of the amount of the mineral added. Changes in the intensities of diffraction lines were observed, as associated with the introduction to the new product structure of additional amounts of silica and aluminium in the form of halloysite. No new phases occurred. An increased amount of residual SiO_2 was observed; silica is not used up completely and occurs in the unreacted form in the samples with an addition of the clay mineral. The intensity of the quartz line increases with an increase in the halloysite amount present in the autoclaved composite.

In the samples with 30% halloysite, besides toberomorite and unreacted quartz, a new katoite phase occurred.

Microscopic examinations confirmed the phase composition results from the XRD analysis. Figure 2 shows the photographs of the microstructure. Well-developed concentrations of tobermorite were observed in the samples without and with 10% halloysite. In the sample containing 30% halloysite, tobermorite is accompanied by hydrogarnets (Fig. 3c).

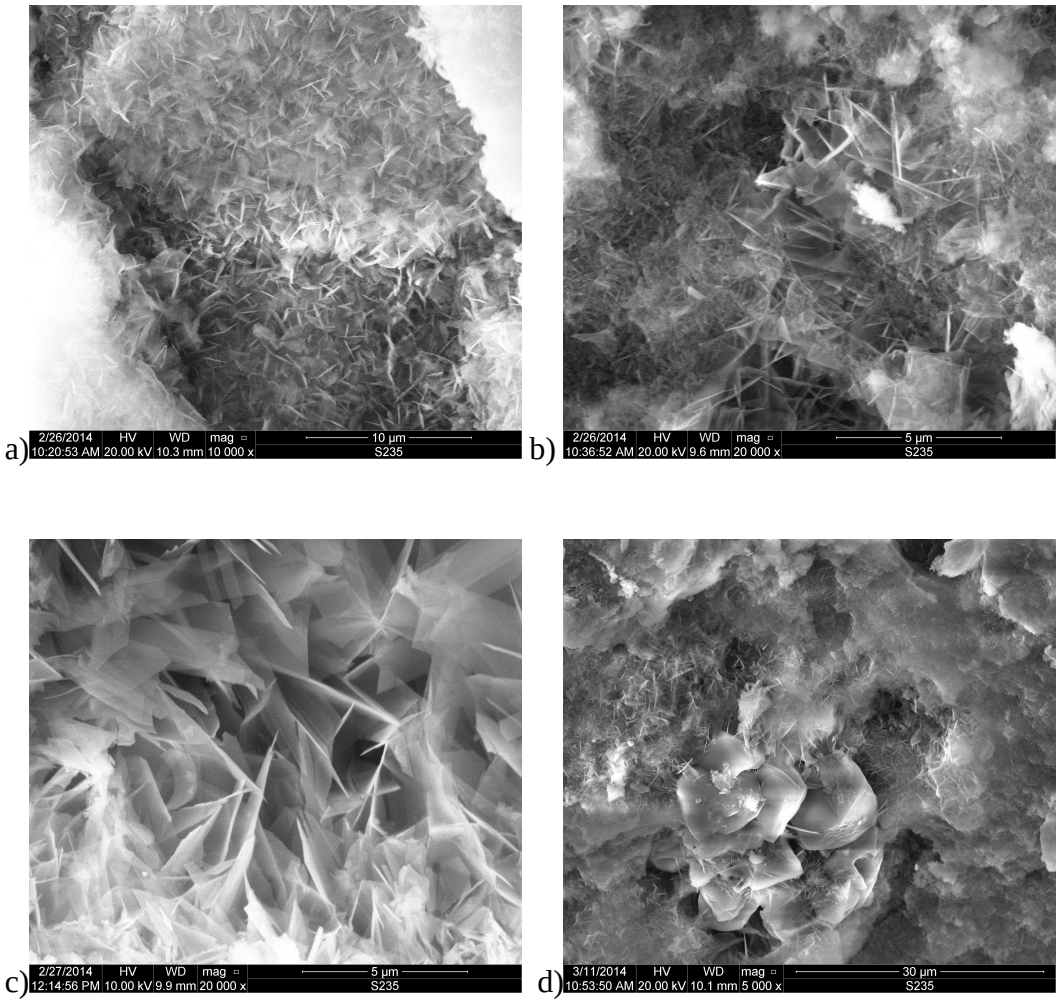

Fig.3. Morphology of products obtained from a raw materials mix of CaO/SiO_2=0.83 with an addition of a) 0% b) 5% c) 10% d) 30% halloysite autoclaved at 180°C for 4 hours

4. Conclusion

Tobermorite under hydrothermal conditions can be synthesized with an addition of a clay material such as halloysite. Regardless of its content in the reaction mixture, no unreacted halloysite was found, which may indicate that it was absorbed into tobermorite. The study shows that halloysite is active under hydrothermal conditions and may react before quartz does. An addition of 30% halloysite contributes to the formation of katoite.

References

[1] PICHÓR W. *Własciwości autoklawizowanego betonu komórkowego z dodatkiem mikrosfer glinokrzemianowych*, Cement Wapno Beton-1/2012, 32-37 (In polish)

[2] DZIEKAN E., LASKA J., MAŁOLEPSZY J., *Wpływ superplastyfikatorów polimerowych na właściwości autoklawizowanego betonu komórkowego*, 5. Międzynarodowa Konferencja dotycząca Autoklawizowanego Betonu Komórkowego Bydgoszcz, Polska 14-17 września 2011, 225-232 (In polish).

[3] MATSUI K., OGAWA A., KIKUMA J., TSUNASHIMA M., ISHIKAWA T., MATSUNO S., *Badanie wpływu domieszek gipsu i związku Al. Na powstawanie tobermorytu w autoklawizowanym betonie komórkowym za pomocą dyfraktometrii rentgenowskiej in situ*, 5. Międzynarodowa Konferencja dotycząca Autoklawizowanego Betonu Komórkowego Bydgoszcz, Polska 14-17 września 2011, 158-163 (In polish)

[4] HANDKE M. „ *Krystalochemia krzemianów*", Wydawnictwa AGH, Kraków 2008 (In polish).

[5] STOCH L. „*Minerały ilaste*", Wydawnictwa Geologiczne, Warszawa 1974 (In polish)

[6] SAND L.B., COMER J.J., *A study in morphology by electron diffraction*. Clays and Clay Minerals, 1955, 3, 26-30

[7] GUGGENHEIM S., ADAMS J.M., BAIN D.C, BERGAYA F., BRIGATTI M.F., DRITS F.A, FORMOSO M.L.L *Summary of recommendations of nomenclature committees relevant to clay mineralogy: report of the association internationale pour l'etude des argiles (aipea) nomenclature committee for 2006*. Clays and Clay minerals, 54, 761-772.

TRANSCOM 2015, 22-24 June 2015
University of Žilina, Žilina, Slovak Republic

Wood and Fruit Processing Waste as a Fully-fledged Component of Solid Fuels

[*]Joanna Pasternak, [*]Paweł Purgał
[*]Kielce University of Technology, Faculty of Budownictwo, al. Tysiąclecia P.P. 7, 25-314 Kielce, Poland

Abstract. The article aims to indicate possibilities of reducing the nationwide share of timber in biomass combustion as well as present opportunities to increase the amount of fruit processing waste, which, under appropriate physicochemical conditions, may constitute a valuable end-product or at least a component of ecological fuel.

Keywords: Biomass, biofuel, renewable energy, fruit processing byproducts.

1. Introduction

Share of biofuels in industrial and private energy production has been increasing after year 2000, thus supplementing traditional coal-burning structure. Power plant and thermal plant blocks dedicated to biomass combustion, where wood processing byproducts constituted the main solid fuel, appeared across the country. Fruit processing byproducts, which were considered a difficult to neutralize waste in the past, are now finding use as a renewable energy source.

2. Prospects for Renewable Energy Share in Poland Compared to European Union

European Union policy on energy and environment, approved at a meeting of the European Council in March 2007, establishes a prospective agenda leading to achieve 3 main goals of the energy policy in the European Union: economic competitiveness, security of supply and sustainable energy production. In order to implement those goals the EU pledged to fulfill before 2020 so-called **"20-20-20"** initiative comprising of 3 targets: **20%** reduction in EU greenhouse gas emissions, raising the share of EU energy consumption produced from renewable resources to **20%** and a **20%** improvement in the EU's energy efficiency.[5] The 15% target set for Poland regarding the share of energy coming from renewable sources in 2020 and general trend toward sustainable development implicate a necessity to broaden the horizons when it comes to acquiring material and technological solutions allowing for unwavering prospects for a solid biofuel economy.[4]

In continuation of the trend towards the reduction of carbon emissions an increase of the share of renewable energy to 30% and carbon dioxide emission reduction of 40% are expected by 2030.

Yearly technical potential of biofuels in Poland that are suitable for energy production has been estimated to be around 465.1PJ. It encompasses surplus biomass from agriculture - ca. 195PJ, forestry – ca. 158.6PJ, orchards – 57.6PJ and wood industry waste – 53.9PJ[5] [3]

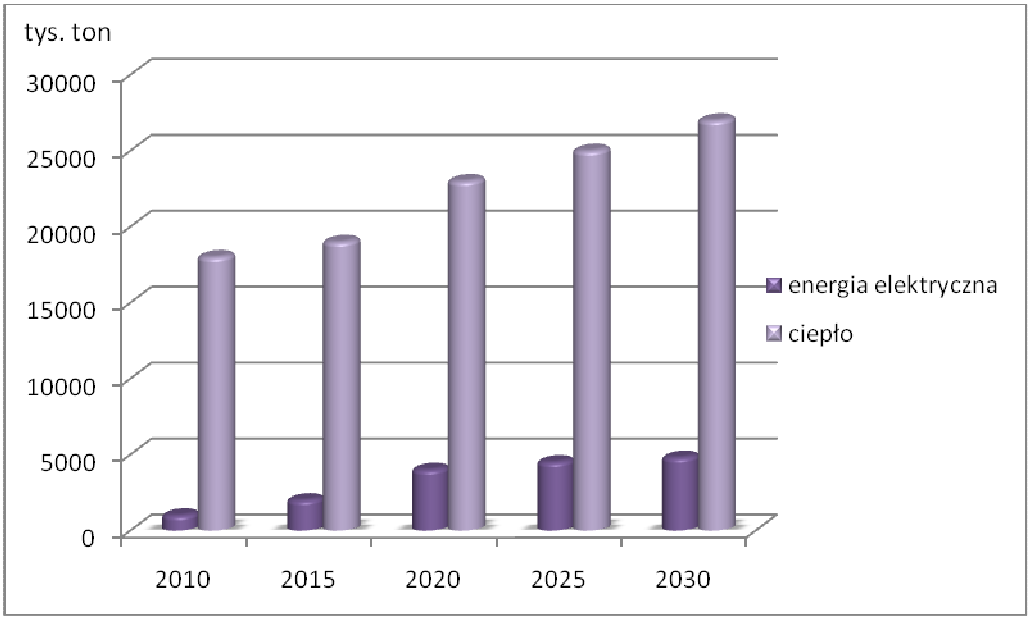

Fig. 1. Biomass demand according to Polish National Renewable Energy Action Plan 2010-2030 [2]

3. Biomass Supply for Power Stations and CHP Plants

Having years of professional experience in cooperation with power stations and CHP plants of Swietokrzyskie province when it comes to timber supply allowed me to assess the specificity of forest biomass. One of the most important physical parameters is humidity, which determines Lower Heating Value of solid biofuels. This is an important factor influencing the intensity of the combustion process.

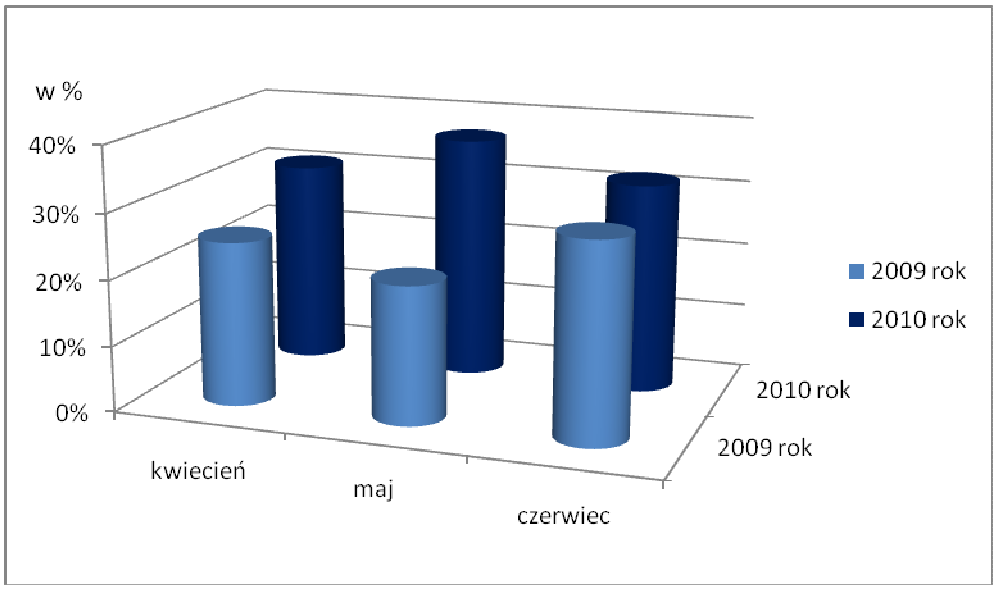

Fig. 2. Humidity differences between 3 selected months of 2009 and 2010

There are large discrepancies between humidity levels that were analyzed during the same 3 months of 2 consecutive years. Processing temperature in the lumber mill as well as storage temperature and the season during which the trees were cut down all substantially influence aforementioned humidity levels.

Measurements taken with moisture meters at power stations or CHP plants showed differences in the humidity levels between 30% and 50% among samples from the same shipment of biomass

from a single manufacturer. Some measurements exceeded 60%, especially in cases of wood sourced from timber roof truss processing.

Humidity is not the only significant parameter of biomass when used as a fuel. Wood supplied to power plants should not contain any fungi, mold or soil on its surface. Bark content should not exceed 10% of the furnace fuel input. Waste wood sourced from recycling or demolition, when used as a fuel, may not contain impregnates or metallic connectors.

The form of biomass is not without significance in regard to combustion process intensity: wood chips obtained from hammer mills are much thinner and their combustion time is shorter than wood chips produced using wood chippers with knives, dimensions of the latter allow for a longer energetic utilization process.

Lump wood, edgings, branches, roots or shavings constitute yet another form of waste wood. Shavings are a waste product, which in the form of pellets or briquettes is being successfully burned in furnaces of various constructions. Wide assortment of pellet and briquette dimensions allows easy adaptation to different furnace-matched feeding systems.

4. Biomass of Fruit Processing Origin

In the course of production of fruit preserves two types of leftover waste are created. The first type, storage waste, is a consequence of long-term storage of raw materials and intermediate or finished products. The second type comprises of byproducts created during the technological process of actual production. Marc and pomace, considered until recently to be a serious contamination hazard, are now a valuable, repurposed material in food, pharmaceutical and cosmetic industries. Lower quality pomace is used as a fodder additive. The drying process allows them to be used also in the energy industry. For example, 100kg of marc and pomace at 75% humidity after processing results in 28kg of dried material of 10% humidity.

An increasing number of processing plants introduces into their technological processes an additional cycle of waste pre-drying as an opportunity to increase their global income.[7] Processed marc and pomace turns into a fuel that can be used to generate energy used to heat factory halls and administration offices while surplus, dry biomass is suitable for sale.

Fig. 3. Bulk fruit pomace [6]

One of the less widespread biofuels are fruit pits. Fruit processing technologies allow obtaining this high-energy material for the purpose of electrical or thermal power production. As any other fuel source, it also has to fulfill certain humidity requirements to be considered appropriate for burning. The intensity of scraping process during a technological processing cycle decides the amount of pulp left over the seed surface and the amount of juice that accumulates in significant quantities in case of low efficiency pitting. It is therefore necessary to monitor the humidity level of the processed material. In case it is too high the seeds need to be dried. Not only cherry pits but also

plum, peach, apricot and other fruit pits may be considered a source of high-energy biofuel, which has already been under evaluation for years in numerous plants across the country.

Pomace type	Lower Heating Value [KJ/kg]
Chokeberry pomace	19641.3 ± 75.0
Apple pomace	15937.8 ± 62.3
Currant pomace	20863.0 ± 46.8
Coal	266103.0 ± 1195.2

Tab. 1.Lower Heating Value of chosen dried pomace types.[1]

Farming and orchard industries in Poland have the potential to grow fruit trees and shrubs from which it would be possible to obtain fully-valued biofuel.

Apple or pear pomace is a material which can be used in 100% to produce pellets without any additives.

Not all types of dried fruit pomace are appropriate for pelleting because of low content of bonding substances in their structure. In such case it is possible to combine them with wood shavings in order to obtain pellets or briquettes suitable for use as a biofuel.

However, in order to make the right decision regarding which mixture will become a fully valued fuel for the purpose of electrical and thermal energy, it is necessary to investigate their calorific value as an indicator of the amount of fuel input as well as combustion time and intensity.

It is also essential to determine the composition of exhaust gasses including amounts of: NO, NO_x, CO, CO_2, SO_2 and dust emissions.

5. Conclusion. Prospects for Further Development of Renewable Energy Sources in Poland in Light of the New Law

Polish Government stabilizes the legal state of nation's power industry and the Renewable Energy Sources Bill, dated 20th Feb 2015 and approved by the parliament estimates that between 200 and 300 thousand microplants utilizing renewable energy sources will appear before 2020. The bill initiated changes in the power sector thanks to an inclusion of a record guaranteeing fixed energy prices for energy coming from sub-10kW installations for 15 years after their commissioning. An auction system will take place of energy certificates and the Government will be a deciding party in regard to energy demand. Polish Council of Ministers outlined an action plan regarding Polish energy policy until 2030, which includes specifics concerning renewable energy share.[8]

References

[1] BORYCKA, B. *Walory ekologiczne spalania biomasy z odpadów owocowo-warzywnych*, Energetyka i Ekologia, 2009, pp. 848.

[2] GRZYBEK, A. *Biomasa w energetyce*, Instytut Technologiczno-Przyrodniczy, Oddział Warszawa, Poznań, 2011, pp. 3.

[3] WIŚNIEWSKI, G. *Praca Zbiorowa, Ekonomiczne i Prawne Aspekty Wykorzystania Odnawialnych Źródeł Energii w Polsce*, Warszawa, 2000, pp. 15.

[4] *Directive 2009/28/EC*, Annex I, pt. A.

[5] KURZAK, L. *Energia odnawialna w zrównoważonej polityce UE, Zeszyty Naukowe Politechniki Częstochowskiej*, Częstochowa, 2010, pp. 47-55.

[6] http://www.ppr.pl

[7] http://raport.no-ip.org

[8] http://energetyka.wnp.pl

TRANSCOM 2015, 22-24 June 2015
University of Žilina, Žilina, Slovak Republic

Reconstruction of the support zone in historical ceiling beams using glued joints method

[*] Elżbieta Piotrowicz
[*] Kielce University of Technology, Faculty of Civil Engineering and Architecture,
25-314 Kielce, al. Tysiąclecia Państwa Polskiego 7, Poland, elap@onet.pl

Abstract. The article discusses the issues concerning rehabilitation and strengthening of wooden beams in historical naked ceilings in their support area. The causes and effects of the damage in the wooden beams shear zones have been presented. Traditional methods of reinforcing beams along with the examples of their application have been shown. Moreover, modern methods of shear zone rehabilitation as proposed in the literature have been presented. What is more, the article also discusses the proposals of the research program with regard to technological solutions for reinforcing of historical ceiling beams in the shear zone, which will be carried out in the laboratories of the Kielce University of Technology.

Keywords: timber, strengthening of wooden beams , methods of rehabilitation.

1. Introduction

Nowadays, maintaining historical wooden structures is very important, because these structures have played a significant role in the historical development of construction and architecture and today they constitute Poland's indisputable cultural heritage. Wood, by its very nature is subject to destructive processes faster than other building materials, which requires taking appropriate actions with regard to conservatory and repair works. Extending the durability of wooden structural elements is possible as a result of appropriately early taken rehabilitation actions, which restore, where possible, the physical and mechanical properties of the material and the structural efficiency of components and systems. As far as wooden beam ceilings are concerned, one of the most commonly occurring defects is damage to beams support zone, most often caused by biological corrosion, development of which is accompanied by a lack of adequate protection from excessive moisture.

The Venice Charter for the Conservation and Restoration of Monuments and Sites, or the Venice Charter, adopted by The Second International Congress of Architects and Specialists of Historic Buildings in 1964 in Venice, constituting a set of rules with regard to treatment of historic objects allows such method of reinforcing the wooden elements, which does not affect the historical design solution, valuable historic architectural detail and unique design of significant artistic and aesthetic values. The methods of reinforcing wooden beams with the use of glued-in metal elements or synthetic tapes made of glass fibre and carbon fibre can be particularly useful in case of the necessity to preserve the historic carved and painting decoration design. In this way, it is possible to obtain the proper load-bearing capacity and reduce deflection for the expected utility function without the use of expensive transfers and restoration works. More detailed guidelines for the restoration of historic wooden structures were established in Mexico in 1999 by the International Wood Commitee / UNESCO. Although, the charter entitled Principles for the Preservation of Historic Timber Structures prefers the traditional methods of rehabilitation and reinforcement of historic wooden structures, it also allows for using modern materials and technologies, which had been examined and documented to a satisfactory extend. The works carried out in the Kielce University of Technology aim at developing modern technologies for reinforcing of historical ceiling beams.

2. Damages to the support zone of historical ceiling beams

Wood is an organic material, and in contrast to most construction materials, has a high susceptibility to the damaging effects of biological corrosion. The durability of wood, and thus the wooden beam ceilings varies widely and depends on a number of factors, both biotic and physical, which include the most commonly occurring destructive impact of fungi and insects - wood pest, as well as changes in the wood structure due to the natural processes of aging of the material. In beam ceilings, the support zone of wooden beams is the place where damage most often occurs, as these places are exposed to constant moisture, associated with direct contact with the support structures of external masonry walls in the buildings. On the basis of available studies it can be concluded that the main cause of destruction in ceiling beams support zones is biological corrosion, particularly the phenomena causing the complete decomposition of wood by fungi. Other factors often constitute the catalysts of the occurring destructive phenomena and in many cases occur in parallel, amplifying their effects.

Fig. 1. Damaged ceiling beam end. Wood decomposition due to fungi.

Fig. 1 presents damages to the support zone of a ceiling beam

3. Methods of rehabilitation and reinforcement of the support zone of ceiling beams

The degree of damage and degradation of the wooden ceiling beams support zones makes it necessary to undertake reinforcing and reconstruction works, which will allow to maintain the valuable ceiling structures and restore their full technical efficiency. The technological solutions will most often mean the reconstruction of the ceiling beams fragments in a way that ensures the structural safety of the entire wooden element. The adopted design solutions for reinforcing the support zone of the beams should not result in the loss of valuable carved designs or polychrome decoration and at the same time, they should create the possibility of reconstructing this design, ensuring obtaining such artistic and aesthetic effect that will be appropriate from the conservation point of view. Taking into consideration the scientific and research works carried out as well as the construction and conservation projects executed in historic buildings, one can make the following, general classification of applied methods of reinforcement and rehabilitation of the support zones of historical wooden ceiling beams:

- Traditional methods of reconstruction of the support zone of ceiling beams using various connection systems
- Reconstruction of the support zone using synthetic composites

Reconstruction of the support zone of ceiling beams using inserts and glued joints method

3.1. Traditional methods of reconstruction of the support zone of ceiling beams using various connection systems

Traditional methods of rehabilitation of wooden structures are mainly associated with the replacement of the entire damaged elements or their fragments on the basis of their earlier disqualification with regard to the further static operation and non-fulfillment of the basic requirements with regard to the structural and operational safety of the object. Traditional methods of reinforcement and rehabilitation of wooden structures include a replacement of the damaged elements with new ones, made of the same material, which will be - within the meaning of a conservatory procedure - a historical reconstruction, or supplementation of the structural elements. Such solution, with regard to the ceiling beam support zone is shown in the Fig. 2.

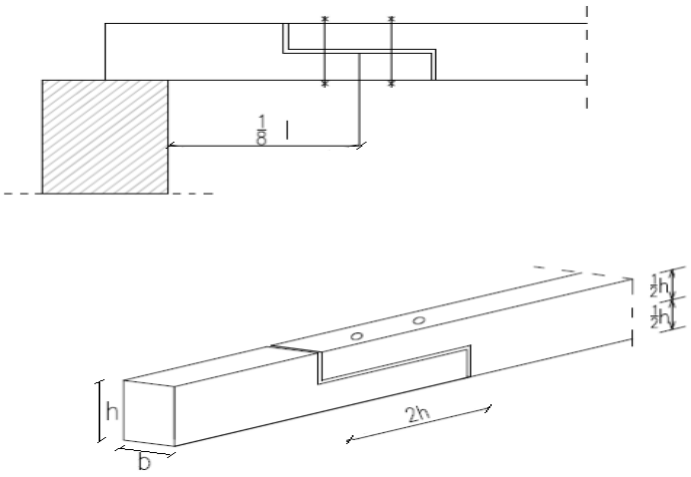

Fig. 2. Replacement of the damaged support fragment of a wooden beam in the distance of 1/8 l from the support in the a-a cross-section using a lap joint (drawing - E. Piotrowicz)

For greater value of the bending moment, which occurs in case of the section's distance from the support bigger than 0.125 l, it is necessary to use a half-lap joint, transferring the bending moment, thus the application of woodworking joints. It is preferable to use simple woodworking joints or sliding ones with wedges ensuring adequate pressure on the elements (Fig. 3)

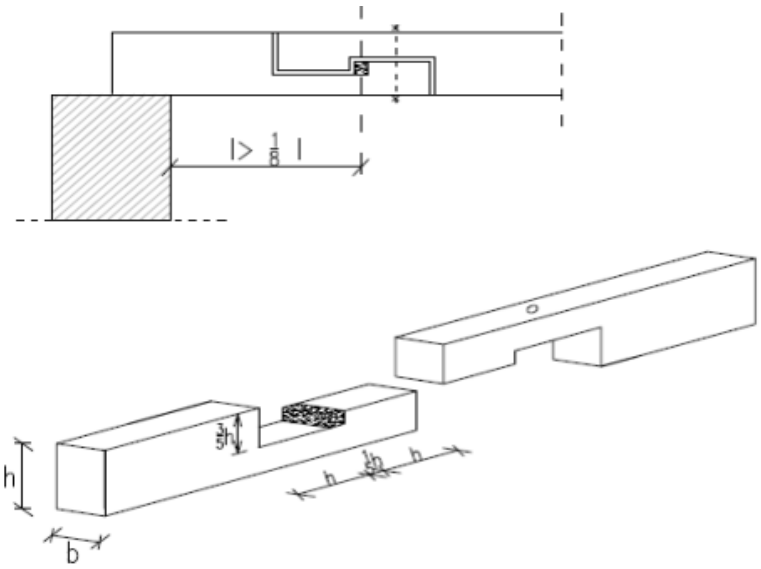

Fig. 3 Replacement of the damaged support fragment of a beam in the distance bigger than 1/8 l (a_1-$a_{1)}$ cross-section) using a lap joint with a wedge (drawing - E. Piotrowicz)

3.2. Reconstruction of the support zone using synthetic composites

The replacement of the damaged element of a wooden beam using the polymer composite inserts is shown in Fig. 4. The replaced fragment of the wooden element can be combined with the intact part of the beam using the inserts made of fiber polymer composites. Such connections may be additionally reinforced with tapes made of glass and carbon fibers.

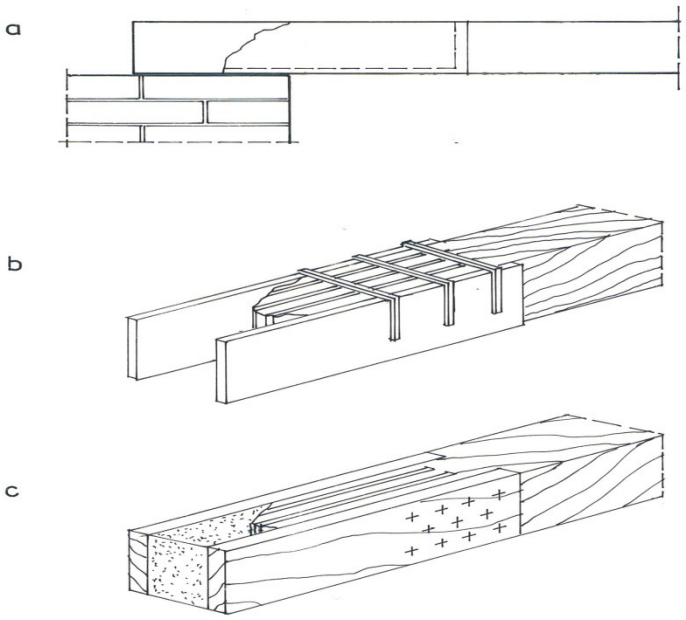

Fig. 4. Reconstruction of the support of the beam: a – view of the beam in the support location, b - method of completing using dismountable elements, c - method of completing using structural roof boards, (based on: A. Żaboklicki "Rehabilitacja i wzmacnianie zabytkowych konstrukcji drewnianych Pśk 2013)

3.3. Reconstruction of the support zone of ceiling beams using inserts and glued joints method

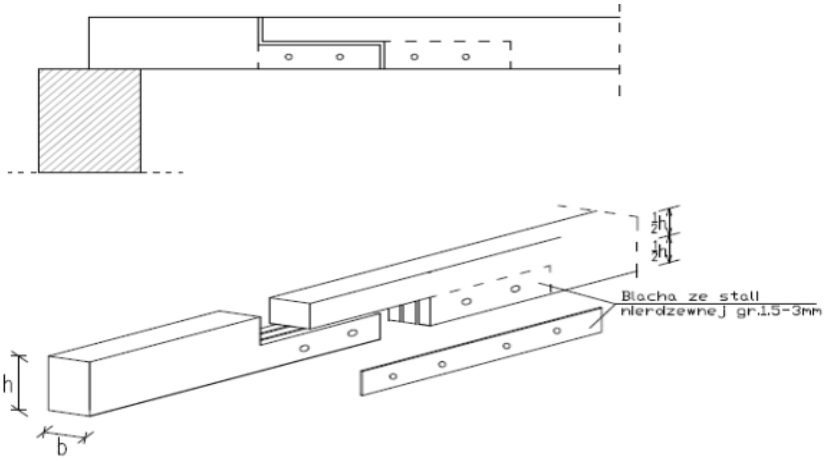

Fig. 5. Replacement of the damaged beam fragment using the inserts made of flat steel plate with a thickness of 1.5 to 3 mm and stud connectors (drawing - E. Piotrowicz)

The replacement of the damaged support element of a beam using metal elements has been shown in Fig. 5. In the connection's tension zone, we use inserts made of flat steel plate with a thickness of 1.5 to 3 m, inserted in previously made cuts. The inserts may be fixed through gluing-in and additionally reinforced by fixing pins with small diameters. In the beam's compression zone, stresses are transmitted through the pressure surfaces. In a similar way, a connection of the complemented support zones of wooden beams can be made with the use of glued-in inserts made of carbon tapes and reinforced with glass fiber.

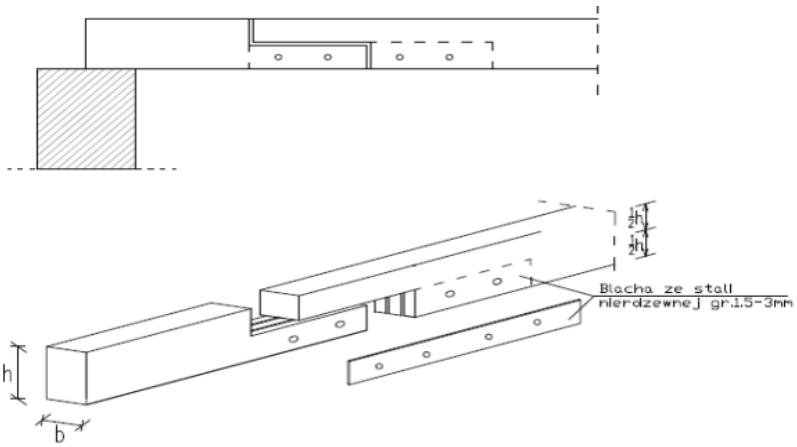

Fig. 6. Replacement of the damaged beam fragment using the inserts made of flat steel plate with a thickness of 1.5 to 3 mm and stud connectors (drawing - E. Piotrowicz)

4. Assumptions of the research program

The research program, aiming at providing solutions for reconstruction and reinforcement of the damaged support zone of ceiling beams covers the following issues:

- Solution for technology of execution of the completion of a beam end in two options: with glued-in metal insert and insert made of carbon tapes and glued-in austenic steel rods and composite materials rovings ;
- Determination of the location for the glued connection on the basis of the state of beams' cross-sectional stresses; execution of endurance tests with the measurement of the state of deformation of the glued connections of the reconstructed beam ends
- Statistical study of the test results will be the basis for the formulation of appropriate conclusions and a specific technology solutions for the glued connection in the reconstruction of the support zone of the ceiling beams.

5. Conclusions

The proposed studies, conducted on the test material, made of pine wood used in the nineteenth century's ceiling structures in the historic buildings allow to develop the optimal technological solutions for the reconstruction of the support zones of the wooden beams. The application of modern glued solutions for connecting the reconstructed beam ends will provide for a possibility of aesthetical completion of historical carved and painted decorations.

References

[1] BROL J.: Analiza doświadczalno teoretyczna wzmacniania konstrukcji drewnianych kompozytami polimerowo-węglowymi. Rozprawa doktorska, Gliwice, 2005

[2] Brol J.: Wzmacnianie stropów drewnianych taśmami z włókien węglowych. VII Konferencja Naukowa: Drewno i materiały drewnopochodne w konstrukcjach budowlanych. Szczecin-Międzyzdroje, 27-29 maja 2004, s. 301-308.

[3] DAVIS G., METTEM C.J.: The use of resin adhesives in repair of structural timber members. Structural Studies, Repairs and Maintenance of Historical Buildings, Computational Mechanics Publications, Southampton UK and Boston USA 1997

[4] JANOWSKI Z., KACZMARCZYK S., Zabytkowe stropy drewniane – konserwacja konstrukcji. Materiały V konferencji naukowo technicznej „Inżynieryjne problemy odnowy staromiejskich zespołów zabytkowych", Kraków maj 2000,

[5] JANKOWSKI L.J., JASIEŃKO J., NOWAK T.P.: Experimental assessment of CFRP reinforced wooden beams by 4-point bending tests and photoelastic coating technique. Materials and Structures, 2009, DOI 10.1617/s11527-009-9476-0

[6] NOWAK T.P.: Analiza pracy statycznej zginanych belek drewnianych wzmacnianych przy użyciu CFRP. Praca doktorska, Politechnika Wrocławska, Wrocław 2007:

[7] JASIEŃKO J.: Experimental investigation into the force distribution in glued steel bar and wood joints. Archives of Civil Engineering, XLVIII, 1, 2002

[8] JASIEŃKO J.: Połączenia klejowe i inżynierskie w naprawie, konserwacji i wzmacnianiu zabytkowych konstrukcji drewnianych. Dolnośląskie Wydawnictwo Edukacyjne, Wrocław 2003.

[9] JASIEŃKO J., NOWAK T., BEDNARZ Ł., - Wzmacnianie zginanych litych belek drewnianych prętami i blachami i blachami stalowymi oraz materiałami CFRP, Konf. Naukowa Drewno i materiały drewnopochodne w konstrukcjach budowlanych, Politechnika Szczecińska, Wydział Budownictwa i Architektury, Międzyzdroje 2004

[10] MŐNCK W. - Schaden an Holzkonstruktionen, Analyse und Berechnung, Verlag Bauwesen, Berlin 1999

[11] ŻABOKLICKI A., GĘBSKI M.: Continuity of wooden beams as a method of reinforcement and preservation of timber structures at monumental buildings. 5 th Int. Conference STREMAH'97, San Sebastian, Spain 23-25 June 1997, Computational Mechanics Publications, Southampton UK and Boston USA 1997 p. 541-546

[12] ŻABOKLICKI A., Wzmacnianie drewnianych stropów zabytkowych metodą inkluzji żywicznych. ''Inżynieria i Budownictwo'' 2/ 89, s. 78- 79, Warszawa 1989,

[13] ŻABOKLICKI A.: Diagnostyka i wzmacnianie konstrukcji drewnianych w zabytkowych obiektach architektury. III Konferencja Naukowo Techniczna Warsztat pracy rzeczoznawcy budowlanego, Kielce 24 -25 kwietnia 1997 r.

[14] ŻABOKLICKI A.- „Rehabilitacja i wzmacnianie zabytkowych konstrukcji drewnianych, Politechnika Świętokrzyska Kielce 2013

TRANSCOM 2015, 22-24 June 2015
University of Žilina, Žilina, Slovak Republic

A comparison of the dielectric constant of the asphalt concrete from different polarity of GPR signal

[*]Andrea Porubiaková
[*]University of Žilina, Faculty of Civil Engineering, Department of Highway Engineering, Univerzitná 8215/1, 01026 Žilina, Slovak Republic, andrea.porubiakova@fstav.uniza.sk

Abstract. This article deals with a comparison of the dielectric constant of the asphalt concrete from different polarity of GPR signal measured in the laboratory and in situ. Used GPR assembly contained air-coupled antenna with a central frequency of 2 GHz. The dielectric constant of the asphalt concrete was determined based on the travel time between the transmitted and received signal and the known thickness of layer. The different combinations of the polarity of the GPR signal were used to calculate the dielectric constant of the asphalt concrete. The experiments demonstrated that the used polarity of amplitudes can influence the value of calculated dielectric constant.

Keywords: GPR, dielectric constant, polarity, amplitude, frequency, asphalt, time

1. Introduction

Road users require safe, economic and comfortable drive. The actual state of the road network requires application of new equipment in road diagnosis. GPR (Ground Penetrating Radar) is one of these devices. It belongs among non-destructive methods and its wide range of applications gives a possibility for fast and continuous diagnosis of roads without negative influence on traffic flow.

1.1. Ground penetrating radar principle

GPR is a non-destructive and non-invasive method for investigation of roads. According [3] ground penetrating radar systems use discrete pulses of electromagnetic energy with a central frequency from 10 MHz up to 2,5 GHz to detect locations and dimensions of electrically distinctive layers and objects in materials. Pulse radar systems transmit short electromagnetic pulses into a medium and when the pulse reaches an electric interface in the medium, some of the energy will be reflected back while the rest will proceed forwards. The reflected energy is collected and displayed as a waveform showing amplitudes and time elapsed between transmission and reflection. The basic principle of GPR is shown in Figure 1.

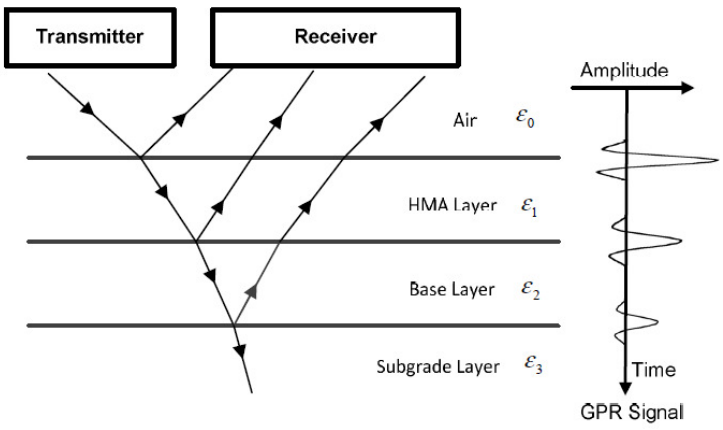

Fig. 1. Typical GPR reflections from a pavement system [2]

Velocity of GPR signal propagation through construction layers is influenced by the material through which it spreads. GPR signal changes its intensity at the interface between two materials due to the different dielectric constants of materials (table 1). Correct determination of the dielectric constants is important to set real thicknesses of pavement structure layers.

Material	Dielectric constant	Velocity [mm.ns^{-1}]
Air	1	299
Asphalt mixtures	4-10	90-160
Concrete	5-9	100-130
Aggregate	6-18	70-120
Water	81	33

Tab. 1. Range of dielectric constants [4]

Various GPR antennas are on the market that differ in a central frequency and consequently in depth range and accuracy. To distinguishing asphalt layers, the antenna with the central frequency of 1 GHz in minimum has to be used.

1.2. Basic theory

The dielectric constant is a important characteristic in the process of determination of asphalt layers thickness [1].

The dielectric constant can be determined from equation:

$$\varepsilon = \frac{D}{E} \tag{1}$$

where:
ε - dielectric of material
D - electric induction
E - intensity of electric field

The speed of the pulse through a layer depends on the dielectric constant:

$$v = \frac{299}{\sqrt{K^*}} \tag{2}$$

where:
K^* - dielectric constant

Based on the observed velocities of electromagnetic signal the layers thickness can be calculated. Correct identification of the speed is very important because it has a major impact on the accuracy of the method [1].

$$s = v \times \left(\frac{t}{2}\right) \tag{3}$$

where:
s - thickness [mm]
v - velocity of electromagnetic wave [mm.ns^{-1}]
t - one-way travel time of reflected signal [ns]

2. The experimental measurements

Experimental measurements were performed with the air-coupled antenna with a central frequency of 2 GHz, the control unit SIR 20 and the computer ToughBook Panasonic (Fig. 2). The antenna was hung on a support structure (Fig. 3A) and connected with the control unit by the cable. The antenna was moved over the studied surface and GPR signal was recorded. Using GSSI software, the dielectric constant of asphalt concrete slab positioned below the antenna path was calculated based on known thickness of asphalt concrete slab.

Fig. 2. Control unit SIR 20 and the computer

2.1. Measurements in the laboratory

In the laboratory, the experiment was performed using the air-coupled antenna that was moved over three different sections: floor, the steel plate, the asphalt concrete slab (see Figure 3). The antenna was hung above the surface at the distance of 490 mm. The steel plate was chosen as a perfect electromagnetic reflector.

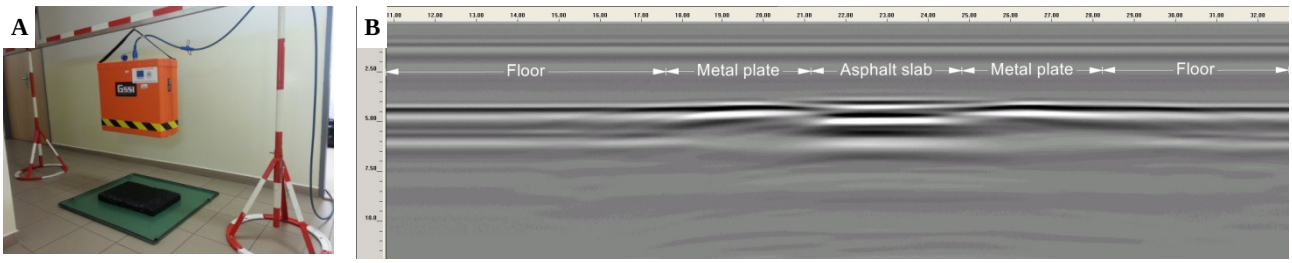

Fig. 3. A) Measurement in the laboratory, B) A example of GPR data output

2.2. Measurements in situ

Measurements were performed out of the laboratory using the same procedure that is described in the section 2.1, only the antenna was hung above the surface at the distance of 480 mm.

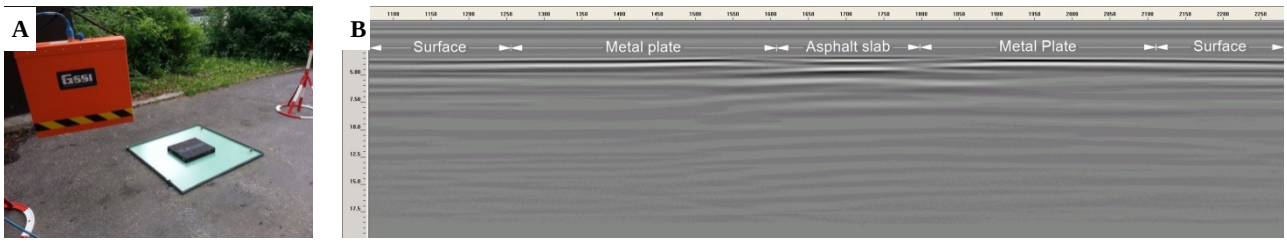

Fig. 4. A) Measurement in situ, B) A example of GPR data output

2.3. Data processing

The measured values were processed in the software RADAN that gives the possibility to carry out operations necessary to increase the readability of the record (gain, contrast). The GPR records were converted to an ASCII file and this one was imported into the GRAPHER software. The amplitudes of positive and negative reflections and time courses were subtracted from the radargram (Figure 5).

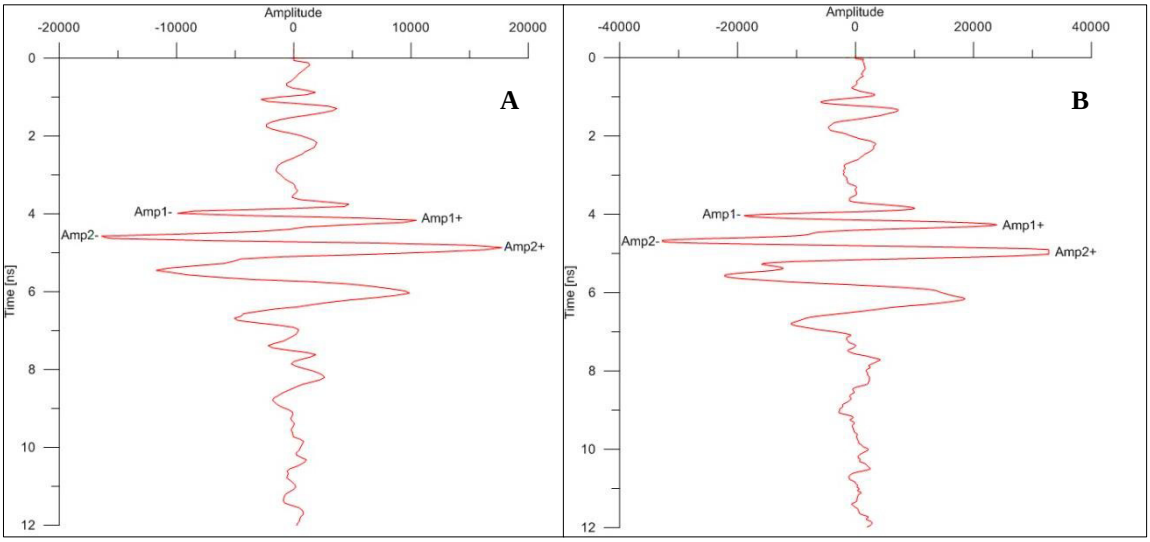

Fig. 5. A) Radargram asphalt mixture AC in the laboratory, B) Radargram asphalt mixture AC in situ

These readings were used to calculate the velocity of electromagnetic waves through the studied structure and the dielectric constant of the asphalt concrete slab. The different polarity amplitudes were chosen to compare the calculated dielectric constants.

3. Results of measurements

The Tables 2A and 3A show the values of the amplitudes and their respective time of passage through the studied structure. The time intervals of the same polarity amplitudes were used to calculate the passage time and signal velocity through the asphalt concrete slab. Then, the dielectric constants were calculated for both, laboratory and in situ measurements. It was calculated the value from laboratory tests for the negative amplitude was 4,797, for positive amplitude 6,904 and 5,802 for the mean value of negative and positive amplitudes. The dielectric constant for the measurements in situ were 5,597 (the negative amplitude), 6,670 (positive amplitude) and 6,122 (the mean value of negative and positive amplitude). Percentage difference in the dielectric constants between the laboratory and in situ tests was 14 % for negative polarity. It was only 3,4 % for the positive polarity and 5,3 % for the average polarity.

A. Measurements in the laboratory		
	Amplitude	**Time [ns]**
Amp1-	-9915	3,984
Amp1+	10459	4,16
Amp2-	-16405	4,57
Amp2+	17757	4,863

B. Calculated dielectric constants - in the laboratory				
Polarity	**Δt [ns]**	**s [mm]**	**v [mm.ns^{-1}]**	**K [-]**
Negative	0,586	40	136,519	4,797
Positive	0,703	40	113,127	6,904
Average neg. a pos.	0,6445	40	124,127	5,802

Tab. 2. A) Amplitude and time in the laboratory, B) Calculated dielectric constants from the laboratory measurements

A. Measurements in situ		
	Amplitude	**Time [ns]**
Amp1-	-18886	4,031
Amp1+	23968	4,266
Amp2-	-32760	4,664
Amp2+	32760	4,957

B. Calculated dielectric constants - in situ				
Polarity	**Δt [ns]**	**s [mm]**	**v [mm.ns^{-1}]**	**K [-]**
Negative	0,633	40	126,382	5,597
Positive	0,691	40	115,774	6,67
Average neg. a pos.	0,657	40	121,765	6,122

Tab. 3. A) Amplitude and time in situ, B) Calculated dielectric constants from the measurements in situ

4. Conclusion

Ground penetrating radar (GPR) is one of practical methods for non-destructive examination of the road structure. In this paper the procedure for determining the dielectric constant of the asphalt concrete in the laboratory and in situ was shown. It is important that the precise determination of the dielectric constant is critical to estimate the thickness of the layer in the construction of the road. The experiments demonstrated that the used polarity of amplitudes can influence the value of calculated dielectric constant.

Acknowledgement

The paper is a result of research supported by European Union and the state budget of Slovak Republic via the project “Výskumné centrum Žilinskej univerzity”, ITMS 26220220183.

References

[1] MATULA, R. 2013. Nedestruktivní diagnostika konstrukcí vozovek pozemních komunikací georadarem. Univerzita Pardubice Dopravní fakulta Jana Pernera. Pardubice, 2013. 142 s.

[2] Non-destructive survey of pavement layer thicknesses with Ground Penetrating Radar. Available at: <http://ieeexplore.ieee.org/stamp/stamp.jsp?arnumber=6718938>

[3] SAARENKETO, T. 2006. Electrical properties of road materials and subgrade soils and the use of ground penetrating radar in traffic infrastructure surveys, 2006. Oulu

[4] TP 3/2012 Využitie georadaru (GPR) pri návrhu rehabilitácie/rekonštrukcie vozoviek. Technické podmienky, MDPT SR, október 2012. Available at: <http://www.ssc.sk/files/documents/technicke-predpisy/tp2012/tp_03_2012.pdf>

TRANSCOM 2015, 22-24 June 2015
University of Žilina, Žilina, Slovak Republic

Moisture susceptibility prediction of asphalt concrete with warm mix asphalt water-bearing additive

[*]Agnieszka Róg
[*]Kielce University of Technology, Faculty of Civil Engineering and Architecture, Department of Transportation Engineering, Kielce, Poland, {arog}@tu.kielce.pl

Abstract. The reduction of temperatures in the process of manufacturing and paving asphalt mixtures, means a significant environmental contribution. Therefore the development of warm mix asphalt (WMA), allowing production at temperatures by as much as 55oC lower that the conventional ones, is justified. There are several WMA technologies that generally can be classified into three groups: foaming processes, addition of chemical additives and addition of organic additives. Irrespective of the type of WMA technology, the proper performance of resulting mixture must be secured. The primary objective of this study was to perform a laboratory testing to determine one of the most important asphalt mixture property - moisture sensitivity of an asphalt concrete produced in water-based WMA technology utilizing the synthetic zeolite.

Keywords: warm mix asphalt, road pavements, moisture susceptibility, synthetic zeolite

1. Introduction

Warm-mix asphalt (WMA) is a group of technologies that allow a reduction in the temperatures at which asphalt mixes are produced and placed. These technologies tend to reduce the viscosity of the binder and provide complete coating of aggregates at lower temperatures. WMA is produced at temperatures 20 to 55^{o}C lower than typical hot-mix asphalt (HMA). Fig. 1 shows a classification of various application temperatures for asphalt concrete, from cold mix to hot mix. [2]

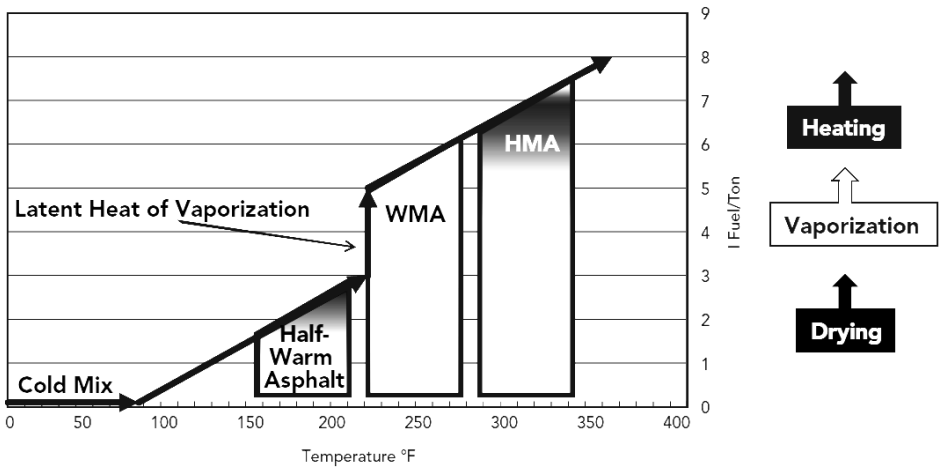

Fig. 1. Classification of asphalt mixtures by temperature range. [2]

WMA technologies classification enables to select the following three major types: those that utilize foaming process and those that use some form of organic or chemical additives. Foaming processes entail the addition of small amount of water, either injected into the hot binder via a foaming nozzle or by means of damp aggregate or hydrophilic material such as zeolite. These processes rely on the fact that when a given volume of water is dispersed in hot asphalt and turns to steam at atmospheric pressure, it results in an expansion of the binder phase and corresponding reduction in the mix viscosity. The amount of expansion depends on a number of factors, including the amount of water added and the temperature of the binder. [1, 2]

The usage of WMA technologies stands for certain benefits that can be divided as following:

- environmental aspects and sustainable development concerns or "green construction" – which means reduction in energy consumption and CO_2 emissions,
- improvement in field compaction – which means an extension of the paving season, possibility for longer haul distances and quicker turnover to traffic,
- welfare of workers – absence of harmful gases means better working conditions that is especially connected with mastic asphalt, produced at much higher temperatures than HMA. [1, 2]

The identification of these benefits, especially environmental ones, justifies the need to develop WMA as it meets worldwide nowadays requirements of environmental protection. But despite all the promising benefits, WMA technologies are not devoided of drawbacks, such as lack of data concerning their long-term performance, greater moisture susceptibility due to lower temperatures and problems with coating and bonding. That is why it is crucial to make sure that the overall performance of WMA is truly as good as HMA. On a life-cycle basis, if WMA does not perform as well, there will not be long term environmental benefits or energy savings.

There are several tests to evaluate moisture sensitivity of the asphalt mixes, that can be divided into two groups. The first one contains examination of selected fractions of loose aggregate coated with binder. The main objective is to visually assess the percentage of grains that remained coated with the asphalt after the procedure of submitting the samples to water saturation. The other group includes tests that are carried out on compacted specimens produced in the laboratory or cut from the existing pavement. Moisture susceptibility is evaluated by the decrease in mechanical parameters like stiffness or durability (resilient modulus or indirect tensile strength) of the conditioned specimens in comparison with unconditioned ones.

The purpose of this study was to perform a laboratory testing to investigate the influence of one of the water-based WMA technology that utilizes the synthetic zeolite on one of the most important asphalt mixture property - moisture sensitivity as the decrease in indirect tensile strength performed on the specimens compacted in the laboratory.

2. WMA with the Addition of the Zeolite

The following section provides general information about the zeolite and potential problem that might appear while using the WMA technology with this additive.

2.1. Specification of the Synthetic Zeolite

Zeolite is a sodium aluminum silicate, that can be natural or synthetic, in form of a very fine powder with large inter connected spaces and regular network of channels and chambers in its crystal structure. Thanks to this specific, diverse and loose internal "architecture", it can accommodate large cations, such as sodium and calcium. Zeolites framework also allow the presence of large cation groups, such as water molecules (approx. 25%) that can be reversibly removed without damaging their crystal structure in the temperature range of 85-180°C.

The presence and amount of this zeolitic water, as well as zeolite's ability to lose and absorb it, is the main property that determines the usefulness of this additive. When zeolite is added to the mix at the same time as the binder, as a result of their contact, this water turns into vapor, creating a microscopic foaming effect and volume expansion in the bitumen. The consequence of this phenomenon is the increase in workability and aggregate coating at lower temperatures.

2.2. Potential Moisture Susceptibility Problem

The process of releasing water from the zeolite structure is gradual. It means that after the compaction process performed at lower temperatures, moisture contained in the zeolite might not completely evaporate resulting in residual moisture trapped in the mixture. Depending on the amount of this trapped moisture, an adhesive failure can be the consequence at negative

temperatures and in the presence of water. It is commonly known, that water and frost have an adverse impact on such phenomena as cohesion of the mix and adhesion between the binder and the aggregate. Water activity enhances the stripping of the bitumen from the surface of aggregate grains, resulting in detachment, peeling, loosening and consequently deterioration of the mix. [6]

Even though the main objective of the zeolite is to create foaming effect, it seems to be vital to properly assess moisture susceptibility of the asphalt mixture with this additive, which is a measure of its durability at negative temperatures and in the presence of water. This parameter is crucial because of the connection with other vital mix properties. Computational analysis of the asphalt pavement construction have shown the significant effect of this parameter on fatigue life of the structure. [6]

3. Experimental Program and Procedures

For the purpose of testing, asphalt concrete AC on the binder course was designed in accordance with WT-2 2010. The following section includes the description of used materials and samples preparation as well as explanation of temperature ranges selection and test performance.

3.1. Materials

Local basic aggregate and asphalt 35/50 were used. The synthetic zeolite in a form of white powder with 100% passing the 0,063 mm sieve was chosen as WMA additive in amount of 0,2% from the total mix to enable the reduction in mixing and compaction temperatures. High homogeneity and uniform properties were the reasons for utilizing a synthetic form of zeolite in this study.

One of the design assumptions was the potential adhesion problem because of possible residual moisture presence described in the previous section. That is why one additional mixture was produced with anti-stripping agent - hydrated lime. The confirmed effectiveness [3-7] and formation of strong ionic bonds created by calcium cations from the hydrated lime and silicon atoms from the zeolite were the main reasons for the usage of this particular anti-stripping agent in amount of 1,0% from the total mix. When the zeolite, hydrated lime or both were added to the mix, the amount of filler was diminished by the respective percentage of used additives to maintain the designed mixture gradation.

In total, three types of mixtures were prepared, with the same aggregate gradation and binder content, but varied by the technological temperatures and the presence of additives:

- the comparative HMA (0% Z),
- WMA with the addition of the synthetic zeolite (0,2% Z),
- WMA with the addition of the synthetic zeolite and hydrated lime (0,2% Z + 1,0% HL).

3.2. Samples Preparation

The mixing and compaction temperatures were chosen regarding the chosen technologies as presented in the Tab. 1.

Temperature / Mixture type	Mixing temperature [^{o}C]	Compaction temperature [^{o}C]
HMA (0% Z)	165±5	125; 145
WMA (0,2% Z)	150±5	125; 145
WMA (0,2% Z + 1,0% HL)	150±5	125

Tab. 1. The range of temperatures used to produced designed mixtures.

The compaction temperature of 145^{o}C was chosen as the conventional one, used traditionally to compact HMA. Then it was lowered by 20^{o}C to perform compaction process of WMA with the zeolite. Additionally, each mixture was compacted at both temperatures in order to find out the influence of compaction temperature on the tested parameter. The exception was the mixture

containing the zeolite and hydrated lime. It was compacted only at lower temperature as the usage of both additives is justified only with reduction of temperature, otherwise it only increase costs.

The cylindrical specimens of designed mixtures were compacted with energy of 35 pestle blows and separated into two sets: dry and wet.

3.3. Testing Procedure

The evaluation of moisture susceptibility was based on the decrease in indirect tensile strength after conditioning process, simulating water and frost impact on the asphalt concrete, conducted in accordance with WT-2 2010 Appendix 1. That is why specimens from the dry set were stored on flat surface at ambient temperature, while wet ones were saturated with water, subjected to one freezing cycle and kept in high temperature conditions. All specimens from both wet and dry sets were then subjected to destructive force (P) and indirect tensile strength was evaluated (1).

$$ITS = \frac{2P}{\pi DL}. \quad (1)$$

A proportion of indirect tensile strength measured on conditioned specimens to unconditioned ones employed to evaluate indirect tensile strength ratio (ITSR) (2).

$$ITSR = \frac{ITSw}{ITSd} \cdot 100\%. \quad (2)$$

4. Test results

Indirect tensile strength results of the specimens from the dry set (ITS_d) and conditioned ones from the wet set (ITS_w) compacted at two temperatures with and without additives were presented in the Fig. 2.

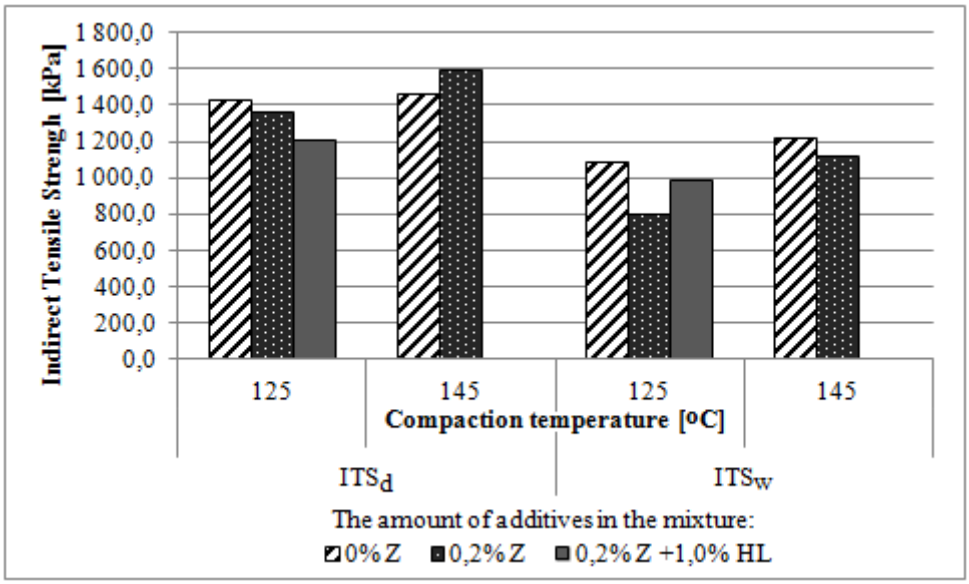

Fig. 2. Indirect tensile strength results.

From the indirect tensile strength test results, the following conclusions were made. First of all, visible downward trend was observed for the two mixtures compacted at both temperatures i.e. HMA and WMA with the zeolite: with the decrease of temperature, the testing parameter decreased. Such finding was irrespective of following factors: presence of additives in the mixture, production technology (HMA or WMA) and whether specimens were conditioned or not.

Another important observation was that the indirect tensile strength of the conditioned mixtures was the highest for the comparative HMA irrespective of compaction temperature. However, such

relationship did not occur in the case of mixtures that were not subjected to the conditioning process: the presence of the zeolite in the mixture compacted at higher temperature resulted in greater than HMA value of the indirect tensile strength.

Although the usage of hydrated lime in WMA resulted in reduction of indirect tensile strength in comparison to the HMA, no clear dependence can be indicated among mixtures compacted at 125^{o}C.

The ITSR results were presented in the Fig. 3 where minimum required value of 80% (according to [8]) was highlighted in grey.

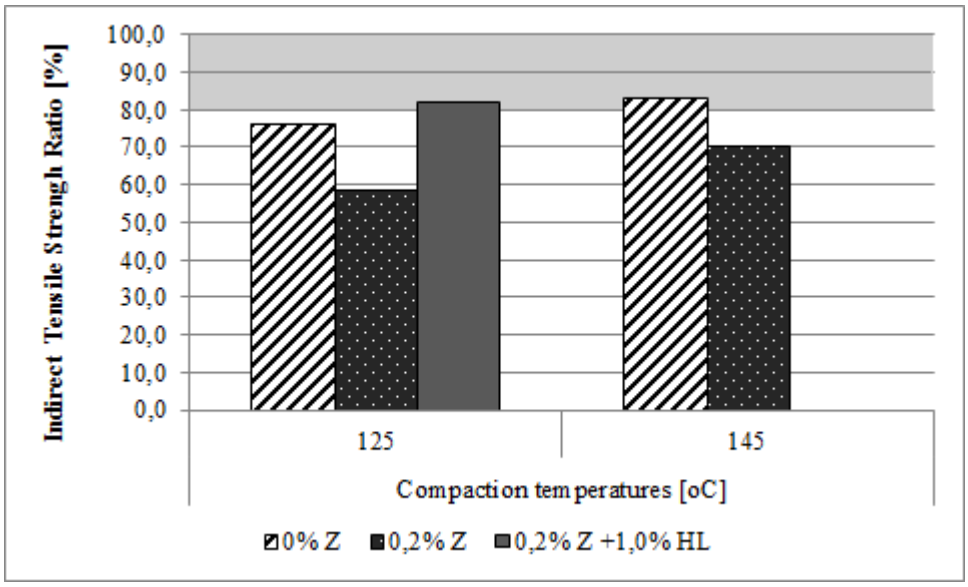

Fig. 3. Indirect tensile strength ratio results.

The analysis of presented results indicates that two of five examined mixtures met the requirements. The satisfactorily results were obtained by mixtures differed by compaction temperature and the presence of additives, i.e. HMA and WMA with both additives.Therefore, it can be concluded that the simultaneous use of synthetic zeolite in amount of 0,2% and hydrated lime in amount of 1,0%, allowed the mixing and compaction temperatures to be lowered by 15 and 20^{o}C respectively, ensuring the fulfillment of requirements.

It should be noted that the asphalt concrete with 1,0% of the hydrated lime turned out to achieve sufficiently high ITSR, despite medium values of indirect tensile strength obtained on both conditioned and unconditioned samples. This beneficial influence of hydrated lime stands for a clear evidence of effectiveness of this material as anti-stripping agent not only to traditional hot mixes, but also to mixtures produced in warm mix asphalt technology.

5. Conclusions

Based on the analysis of the tests results, the following conclusions can be drawn:

- moisture susceptibility of an asphalt concrete, characterized by the indirect tensile strength ratio, depends on the type of used technology that determines production and compaction temperatures and the presence of WMA additives (the synthetic zeolite) and anti-stripping agent (hydrated lime) in the mixture,
- the addition of 0,2% of synthetic zeolite and 1,0% of hydrated lime allows to reduce mixing and compaction temperatures by 15 and 20^{o}C respectively, without compromising the performance of resulting mixture with respect to moisture sensitivity,
- hydrated lime was found to be an effective anti-stripping agent to WMA, mitigating the potential for moisture damage caused by lowered temperatures.

References

[1] BAENA, L., MARTINEZ, G., MORENO, F., RUBIO, M. *Warm mix asphalt: an overview*, Journal of Cleaner Production, Elsevier Ltd., No. 24 (2014), 2011, p. 76-84

[2] BARTOSZEK, J., BAUMGARDNER, G., CORRIGAN, M., COWSERT, J., D'ANGELO, J., HARM, E., HARMAN, T., JAMSHIDI, M., JONES, H., NEWCOMB, D., PROWELL, B., SINES, R., YEATON, B. *Warm mix asphalt: European practice*, Federal Highway Administration, Washington DC, 2008, p. 72

[3] HURLEY, G. C., PROWELL, B. D. *Evaluation of Aspha-min zeolite for use in warm mix asphalt*, National Center for Asphalt Technology, NCAT Report 05-04 Auburn University 2005

[4] IWAŃSKI, M., MAZUREK, G. *Hydrated Lime Effect on Rutting Resistance of SMA Pavements*, Roads and Bridges, Vol. 12, No. 4, 2013, p. 361-383

[5] IWAŃSKI, M., MAZUREK, G. *Wpływ wapna hydratyzowanego na właściwości reologiczne lepiszcza odzyskanego z asfaltowej mieszanki mastyksowo-grysowej*, Cement-Wapno-Beton, 2014/6, p. 376-383

[6] JASKUŁA, P. *Analiza niszczącego oddziaływania wody i mrozu na mieszanki mineralno-asfaltowe*, PhD dissertation, Wydział Inżynierii Lądowej i Środowiska, doctoral supervisor: prof. dr hab. inż. Józef Judycki, Gdańsk 2004

[7] JASKUŁA, P., JUDYCKI, J. *Wapno hydratyzowane w mieszankach mineralno-asfaltowych: Asphacal wypełniacz mieszany*, Kraków 2007

[8] WT-2 Nawierzchnie asfaltowe 2010, Część 1: Mieszanki mineralno-asfaltowe

TRANSCOM 2015, 22-24 June 2015
University of Žilina, Žilina, Slovak Republic

Design Solution of the slab track system on steel bridges

[*]Kararína Serdelová, [*]Josef Vičan
[*]University of Žilina, Faculty of Civil Engineering, Department of Structures and Bridges, Univerzitná 8215/1 , 01026 Žilina, Slovakia, katarina.serdelova@fstav.uniza.sk
[*]University of Žilina, Faculty of Civil Engineering, Department of Structures and Bridges, Univerzitná 8215/1 , 01026 Žilina, Slovakia, josef.vican@fstav.uniza.sk

Abstract. Lately, despite the successes of the classic ballast, the slab track system (STS) is more promote. This structural solution is based on using more quality materials (concrete, asphalt). STS could be characterized as relatively maintenance-free structure of railway superstructure where the reinforced concrete slab accepts the load distribution function of the ballast.

This paper presents the development of different systems and structural solutions of STS, which were designed and implemented on bridge structures in recent years. The slab track systems are built mainly on concrete bridges where the rigid connection between the STS and the bridge deck is solved using the cross-shaped slab directly concreted on the bridge deck. Application of STS on steel bridges is rarer and therefore the design is not entirely clear. Therefore, the main purpose of this paper is to analyse the possibilities of utilization of STS on the steel bridges.

Keywords: ballastless track, railway steel bridges, sleeper, bridge deck, connector

1. Introduction

Currently the modernisation of Slovak railways is in progress in a large global scale. While classic ballast track was verified in the long term and was quite popular, the structural solutions using more quality materials (concrete, asphalt) are more and more preferred.

The need for solution using STS has a great significance in the recent years because of the more severe requirements on railway services from the viewpoint of transport speed. Using the classic ballast for high speed tracks could cause significant breakage of grains ballast resulting into failure of the track geometry. Mainly for these reasons, the utilization of the railway superstructure based on the ballast is apparently an inappropriate solution. Therefore, there is a need to replace this railway structural component by means of another suitable element based on the more quality materials (concrete, asphalt).

Improving the quality of the track geometry using the unconventional structure of railway superstructure – a slab trac – has importance not only for comfortable passenger transport, but especially for the operational safety and realiability and for reducing track maintenance costs. [1].

1.1. Advantages and Disadvantages of STS

Compared to the classic solution, the application of STS introduces the several advantages. The main reason for the application of STS, as it was mentioned above, is the gradual degeneration and deterioration of ballast caused by he repeated dynamic stressing. Gravel gradually loses its sharp edges and therefore the ballast deteriorates and reduces the permeability of the lower part of the ballast bed.

Advantages of STS:

- Maintenance-free structure of the railway superstructure;
- Reduction of the structural height (suitable for using the STS in tunnels and on bridges);
- A simple correction of track geometry up to 25 mm in the vertical direction and up to 5 mm in the transversal direction;
- Lesser vibration of railway subgrade including bridges and tunnels;
- High lateral stiffness [2], [3].

Disadvantages of STS:

- Higher investment costs compared to the classic ballast (from 30% to 50%);
- Higher requirement for sufficient stability of subgrade;
- Extensive and expensive repairs in the case of structural failure due to train accident;
- Higher noise emissions;
- Complicated transition between STS and classic ballast railway superstructure [3], [4].

1.2. Basic principles

Requirements for the STS [4] should be adapted to the particular speed ratio and load. The basic following requirements should be taken into account:

- The permanent placing of STS on the carrier slab without deformations, if possible;
- Ensured lateral stiffness of the track;
- Optimal noise and vibration;
- Minimum maintenance requirements.

STS is composed of a number of structural layers (Fig. 1), where the elastic modules are assumed to be increased upward, it means that $E_1 > E_2 > E_3 > E_4$ [4].

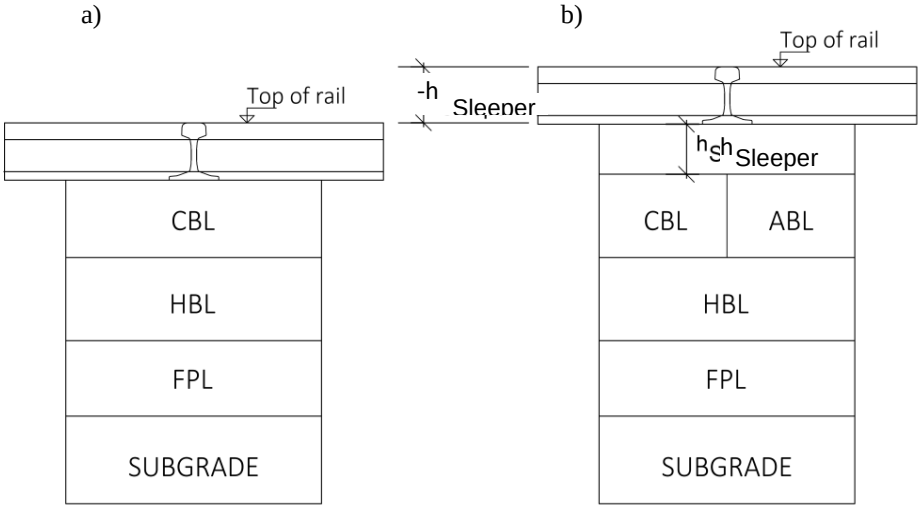

CBL- Concrete Bearing Layer
ABL- Asphalt Bearing Layer
HBL- Hydraulically Bonded Layer
FPL- Frost Protection Layer

Fig. 1 Construction profiles for slab tracks: a) structure without sleepers, b) with the sleeper [7]

All the types of STS can be divided into two main groups and several subgroups (Tab. 1).

Slab Track Systems					
Discrete Rail Support				Continuous Rail Support	
With Sleepers or Blocks encased in concrete	Sleepers on Top of Asphalt-Concrete Roadbed	Prefabricated Concrete Slabs	Monolithic Designs	Embedded Rail Structure	Continuously Supported Rail
Rheda, Rheda 2000, Züblin.	ATD, GETRACK	Shinkansen, Bögl, ÖBB- Porr	Lawn Track	Deck Track	Cocon Track, ERL

Tab. 1. Types of slab track systems [4]

2. The application of STS in Slovak Republic

In contrary to the utilization of STS abroad, the above described structural system of railway track is rather lagging behind in Slovakia. More recently, the Slovak Railways are paying attention to effort and financial resources to modernize corridor railway lines, where the slab tracks also operate. The system Rheda 2000® is mainly used in Slovakia.

Rheda 2000® (Fig. 2) is a flexible system that can be individually adapted to the specific requirements and the individual constraints of each project. The basic structural system consists of modified bi-block sleepers which are securely and reliably embedded into the monolithic concrete slab.

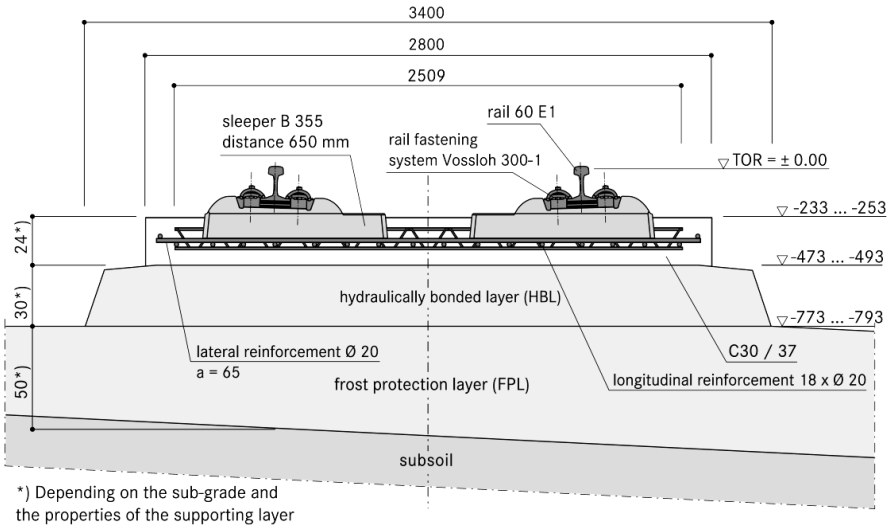

Fig. 2. STS Rheda 2000® on the frost protection layer (FPL) [6]

2.1. STS on bridges [1,5]

The application of the slab tracks on bridges can introduce problems when certain mechanical behaviour is not taken into account. A bridge provide a rigid foundation for slab track, but temperature changes and traffic loads cause bending, longitudinal movements and twist of the bridge structure over the supports. The bridge superstructure shall be able to carry those stressing and deformations.

Requirements for the design of STS are significantly different for bridges with spans up to 25 m long (short bridges) and for bridges with spans those lengths are more than 25 m (long bridges).

The following solutions are adopted for application of STS on the short bridges (Fig. 3):

• By reducing the clamping force in fasteners, the movements of the bridge structure are eliminated when the sleepers on top of the reinforced concrete slab are rigidly connected to the bridge deck or direct rail fastening systems are used.

• On the bridges up to 15 m long, a continuous rail-supports connected to the bridge deck provide adequate rigidity.

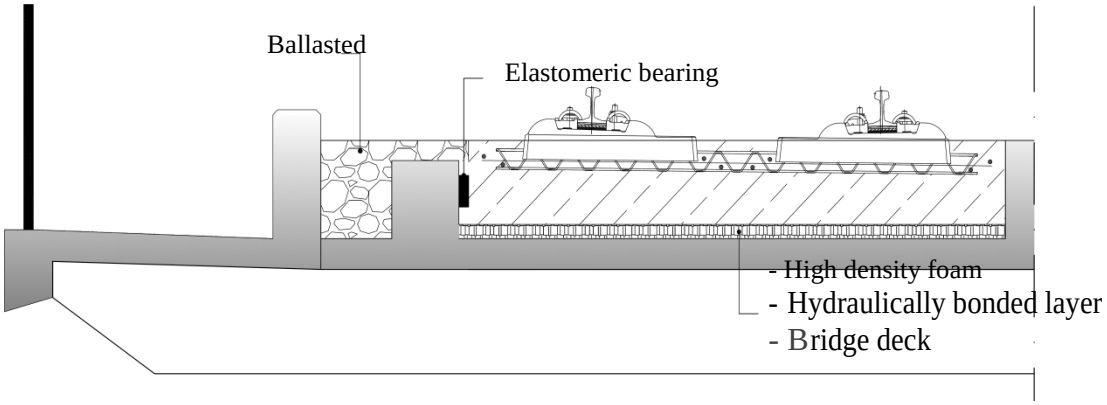

Fig. 3. The cross section for bridges ≤ 25 m

• For spans up to 25 m, sliding slabs allow the bridge structure moving freely underneath the slab track.

• By applying a track frame concrete or concrete-asphalt subbase, the track lies freely movable on top, due to the possible motions and torsion of the sleepers on top of the bridge structures (spans up to 10 m with frame-spans limited to 25 m).

In the case of long bridges (Fig. 4), the slab is fastened to the support structure. This connection is usually realized by cross-shaped base slab, which is directly concreted on the protective layer of bridge deck.

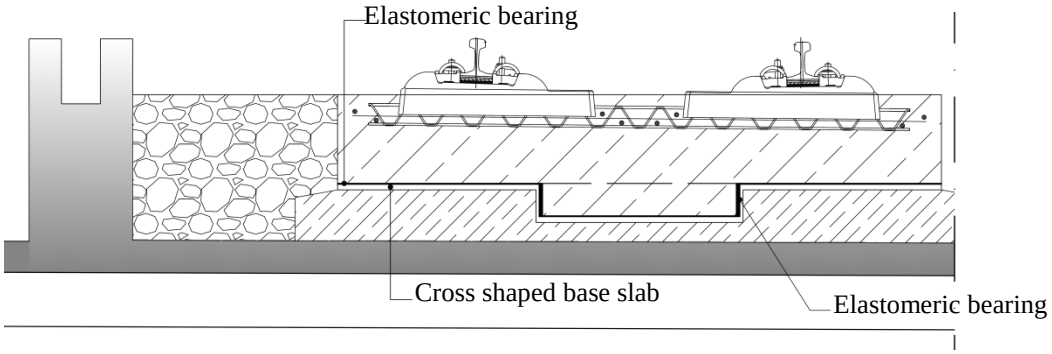

Fig. 4. The cross section for bridges > 25 m

3. Design of STS on steel bridges

In the case of application of the STS on large span steel bridges, (for small span bridges it is ineffective) the proposed solution is considered for truss bridges introducing the optimal structure for bridges with intermediate and long spans. As it is seen in Figs. 5 and 6, two alternatives are proposed for connection between STS and steel bridge deck.

3.1. Type 1

In the case of type 1, the design replicates (Fig. 5) the same solution used for STS on concrete bridges. The bridge deck is constructed as the composite steel-concrete slab. The STS is fixed with steel bridge deck by means of connectors. The thickness of the reinforced concrete bridge slab is

minimal of 200 mm. The reinforced concrete stoppers (800x800 mm) are installed on the slab in the longitudinal direction ensuring the transversal position of the STS on the composite bridge deck.

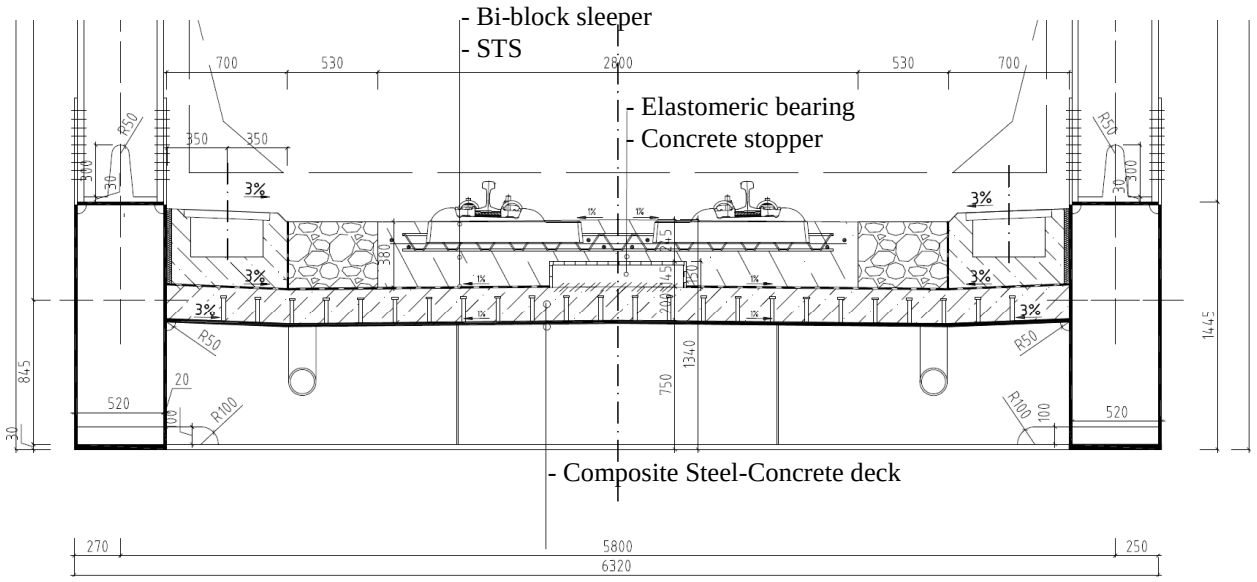

Fig. 5. Design solution Type 1

3.2. Type 2

The reinforced concrete stoppers of 150 mm high directly connected with the steel bridge deck are designed to ensure transversal and longitudinal position of STS on the bridge (Fig. 6). The STS is placed on the elastomeric bearings stuck on the concrete stoppers.

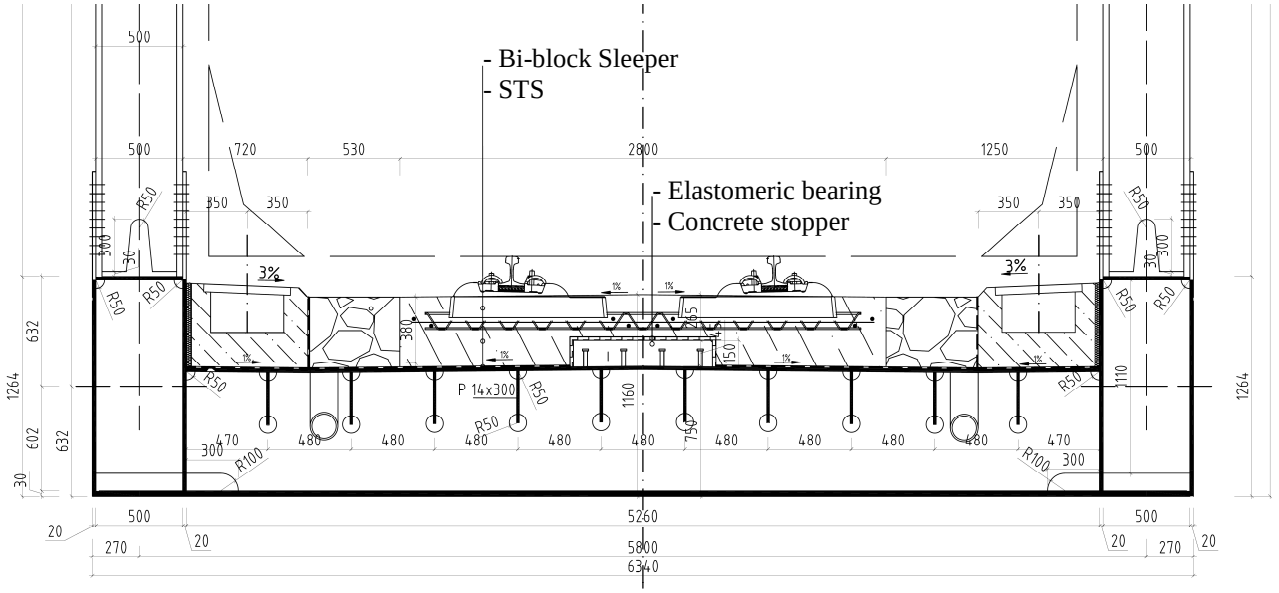

Fig. 6. Design solution Type 2

4. Conclusion

Application of the STS on steel bridges is less frequent and therefore the design solutions are not quite worked up and known. Therefore, the main objective of the paper was to analyse the possibilities and structural solutions of the connection of the STS with the steel bridge deck. The

research will continue by the parametric studies to verify the optimal type of connection and to prove actual possibilities of application of the STS for steel bridges.

Acknowledgement

This work was supported by the Slovak Research and Development Agency under contract APVV-0106-11. Moreover, the research presented here was supported by the European Regional Development Fund and the Slovak state budget for the project “Research Centre of University of Zilina”, ITMS 26220220183.

References

[1] ESVELD, C. – MARKINE, V. 2006. Slab Track design for Hight speed. [online]. Delft 2006. [30.11.2012]: http://www.esveld.com/Download/TUD/Bilbao_Esveld_Markine.pdf

[2] DARR, E. - FIEBIG, W. 1999. Feste Fahrbahn. Hamburg: Tetzlaff 1999. ISBN 3- 87814-700-7.

[3] ESVELD, C. 2001. Modern Railwaytrack, 2nd Edition. Delft: MRT Production 2001. ISBN 90-800324-3-3.

[4] Ifd. Nr. RO- 03/2002 Technische Mitteilung zum oberbautechnischen Regelwerk.

[5] ESFELD, C. 2003. Recent development of slab track in European Railway Review, Delft: University of Technology Delf, ISBN 1351-1599

[6] Rail.one GmbH Pfleiderer track systems. 2011. Rheda 2000® The ballastless track system. [online]. 2011. [11.4.2015] http://www.railone.com/fileadmin/daten/05-presse-medien/downloads/broschueren/en/Rheda2000_EN_2011_ebook.pdf

[7] MICHALS, G.2012. Slab Track Systems for Hight Speed Railways: Master Degree. Stockholm: School of Architecture of Technology Stockholm, 2012. 107 s.

TRANSCOM 2015, 22-24 June 2015
University of Žilina, Žilina, Slovak Republic

Mass concrete construction technologies for the prevention of the self-heating of concrete.

[*]Paweł Sikorski
[*] Kielce University of Technology, Faculty of Civil Engineering and Architecture, Department of Building Engineering Technologies and Organization, l. Tysiąclecia Państwa Polskiego 7, 25-314 Kielce, Poland, p.sikorski@vp.pl

Abstract. In line with the definition of mass concrete, this paper deals with elements with such dimensions that an increase in temperature of the hardening concrete significantly influences the formation of a monolithic concrete mass throughout the entire structure. Major problems and recommendations are presented in relation to mass concrete construction, methods of limiting hydration temperatures and reducing the path of heat released from the interior of the massive structures.

Keywords: mass concrete structures, heat of hydration, concrete mix design, concrete mix cooling.

1. Introduction

Self-heating of concrete is a well-known phenomenon in concrete structures. All concretes generate heat as a by-product of hydration of the cement. Full hydration of 1 kg of Portland cement causes the release of about 400 kJ of heat, most of which is generated during the first days after placement. In thin sections, the heat escapes as rapidly as it is generated. In a mass concrete placement, it is generated faster than it is dissipated, which is the major factor in temperature increase in the structure. Management of these temperatures is necessary to prevent damage in massive concrete elements. According to American Concrete Institute (ACI) mass concrete is defined as "any volume of concrete with dimensions large enough to require that measures be taken to cope with generation of heat from hydration of the cement and attendant volume change, to minimize cracking." [1].

Cooling of the surface layers of the structure at a relatively low coefficient of concrete thermal conductivity causes large temperature differentials between the concrete surface and its interior. Since the difficulty in heat of hydration removal increases with the dimensions of the block, the risk of thermal cracking grows with the massiveness of the structure. [2].

The degree of massiveness of concrete structures can be compared using the surface module m=F/V, where V is the volume of the element and F is the surface area of the element.

Structure type	Surface module: m=F/V	Self-heating of concrete
Non-massive	>15 m^{-1}	1-3°C
Medium-massive	2-15 m^{-1}	3-20°C
Massive	<2 m^{-1}	>20°C

Tab. 1. Classification of concrete structures [3], [5].

2. Massive structure construction technologies

Construction specificity of massive structures consists in taking into account the necessity of minimizing the temperatures that occur due to the self-heating process. Practical experience shows

that inside a massive structure 3 m thick, maximum self-hearing may reach 50-70°C. For this reason, the following rules have to be obeyed:

- The constituents of the concrete should be selected according to the lowest hydration heat.
- Heat release has to be slowed down.
- The energy path has to be shortened.

The curing of concrete in structures where the rules listed above have been followed contributes to the reduction of internal temperatures and related thermal stresses. [2].

2.1. Concrete mix composition

The concrete mix in massive structures has to be designed for the required concrete parameters with the amount of cement limited to the minimum, as this ingredient is responsible for the heat released in the interior during the hydration period. The ingredients of the mix should be selected very carefully with respect to quantity and quality. Recommended binders for use in mass concrete include those with large amounts of mineral admixtures and low hydration heat. The CEM III cement types, including CEM III/A 32.5 N-HSR/LH/NA or CEM III/B 32.5 N-NSR/LH/NA satisfy these recommendations. Due to the low heat of hydration, i.e., 270 J/g for CEM III/A and 210 J/g for CEM III/B, these cement types have been applied to the construction of the largest massive structures in Poland.

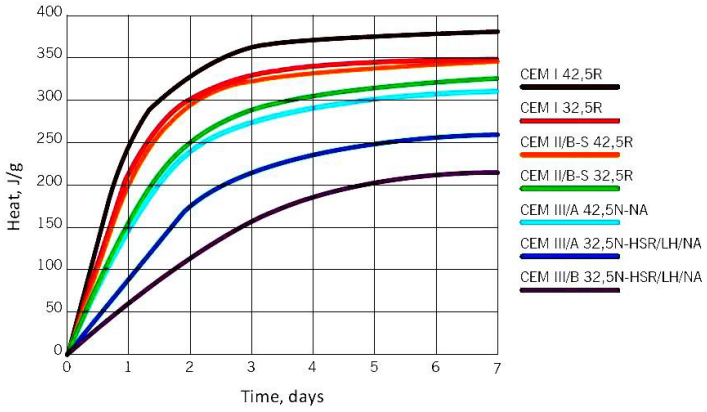

Fig. 1. Amount of heat released as a function of time for selected cement types [4].

The low heat of hydration allows a slow rise in temperature of an early age concrete and the distribution of the released heat over time. The use of these cement types limits the increases the temperature rise above critical values thus eliminating the need to apply costly cooling solutions. The amount of the cement used is an important factor. The increase of the maximum temperature (under adiabatic conditions) is about 12°C per 100 kg of cement in 1 m^3 of the concrete, when the binder content ranges from 300 to 600 kg/m^3, regardless of the cement type. In practice, the amount of the binder for mass concrete mixes per 1 m^3 should be around 300 kg. The water to cement ratio (w/c) should be less than 0.5 to reduce the shrinkage of concrete and ensure its proper water tightness and durability. Appropriate chemical admixtures have to be used to achieve this value. The admixtures allow reducing the amount of mixing water and improving mix workability. The workability of the concrete mix should be retained for up to 6 hours, depending on the adopted schedule, to obtain proper bonding between subsequent layers of the concrete.

Another important factor is the selection of aggregate. The maximum gravel grain size possible is recommended for use in mass concrete mixes. By reducing the amount of fine fractions, water demand can be limited thus improving water tightness and properties of the concrete. Coarse gravel contributes to the reduction of concrete shrinkage and requires less cement to bind its grains together. For these reasons, aggregates 63 mm in diameter or coarser should be used. Due to technological reasons, however, such as pumping the concrete and placing and compacting the mix between the reinforcement elements, the aggregate 31.5 mm maximum diameter is typically used. [4].

2.2. Pre-cooling of concrete materials

The reduction in the heat generation rate can be achieved by lowering the temperature of the concrete mix. This process helps reduce tensile stresses occurring in the elements of the structure because of restraint against volumetric change resulting from temperature drop in the phase of cooling to ambient temperature.
The concrete mix can be cooled by:

- reducing the temperature of its components,
- replacing the mixing water with ice,
- cooling the mix with an external agent, e.g., liquid nitrogen

Lowering the temperature of individual mix constituents

The aggregate comprises the largest single component of the mix, representing about 70% of the weight of concrete. Its temperature will have a great effect on the temperature of the concrete mix. The most common method for cooling the aggregate is using water at a temperature of about 2°C. This method allows aggregate to be chilled to about 5°C. The major disadvantage of this method is the moisture condition of the aggregate that has to be considered for batching the designed concrete mix. The silt resulting from using water to cool fine fractions or grains containing impurities may reduce the quality of the mix.
An alternate method for cooling all fractions of aggregate, without changing its moisture condition, employs ammonia or chilled air. This method can also be used to cool the cement. The gravel is dried, which allows accurate batching of other components thus obtaining the homogeneous concrete. The drop in the aggregate temperature achieved using this method is about 8-12°C relative to the ambient temperature.

Less effective method used to cool the concrete mix consists in adding cold mixing water with a temperature of 1-2°C in the amount of 1/3 required volume. The temperature is then reduced by 1-2°C relative to the ambient temperature. Due to the low effectiveness of this technique, it is only used as a complementary cooling method.

Generally, for every 10°C reduction in the initial temperature of aggregate, cement and water, the temperature of the mix will be changed as follows:

10°C temperature reduction	reduction in mix temperature	
- aggregate	7-8°C	
- cement	1-2°C	
- water	1-3°C	[3].

Cooling with ice

This method consists of replacing the mixing water or its portion with crushed ice, up to 40 mm in diameter. The ice is added directly to the concrete mixer during mixing. The constituents of the mix have to be mixed until the ice melts. Since the melting ice absorbs about 334 kJ/kg of heat, this method is quite effective and leads to 12-18°C reduction in mix temperature relative to the ambient temperature, causing no negative changes to consistency or air-entrainment of the mix. [3].

Cooling with liquid nitrogen

Liquid nitrogen at a temperature of -193°C is another option used to cool the concrete mix. The process takes place in the drum on a concrete mixing truck. The drum should rotate at the maximum speed and the nitrogen should be added in increments to protect the mechanical parts against damage. To reduce the temperature of 5.5 m^3 of the mix by about 5°C, it has to be mixed for about 8 minutes. This option can decrease the mix temperature by 10°C, but too long breaks between nitrogen dosages, fast rotation of the drum and the amount of time required to cool the mix have a negative effect on the mix quality, especially with respect to its air-entrainment. The attempts to

cool mixes in slow-running mixers have been reported to cause mechanical damage to the mixing blades.[3].

2.3. Post-cooling of concrete

Interior temperatures in thick mass concrete structures are controlled by steel cooling pipes embedded in the block together with the reinforcement. The limit thickness from which this method should be used is governed by a number of factors (cement type, dosage, initial temperature of the mix). For structural concretes made with Portland cement, the blocks built in summer should not be thicker than 0.6 m. Cooling pipes embedded in the massive structures found wide applications in hydro technical and civil engineering. In the years 1950-1960, pipe cooling was used in the construction of water dams in the USA and the USSR. The Krasnoyarsk hydroelectric station dam was built as a columnar block system. The columns 15.0 x 11.5 m and 3-9 m in height were made. In each element, a system of horizontal pipes 25.4 in diameter mm was installed with a vertical spacing ranging from 0.75 to 3.0 m, depending on the height of the column. Two stages comprised the cooling process. In the first stage, the cooling was started without stopping the concrete placement for the remaining section of the column, which prevented freshly placed concrete elements from overheating. After seven days following the concrete placement, the cooling was stopped. Stage two started when all the columns were ready to keep the vertical gaps (joints) between the columns open for grouting. A general rule of the controlled cooling of the dam blocks, conducted in stages, is illustrated in Fig. 2.

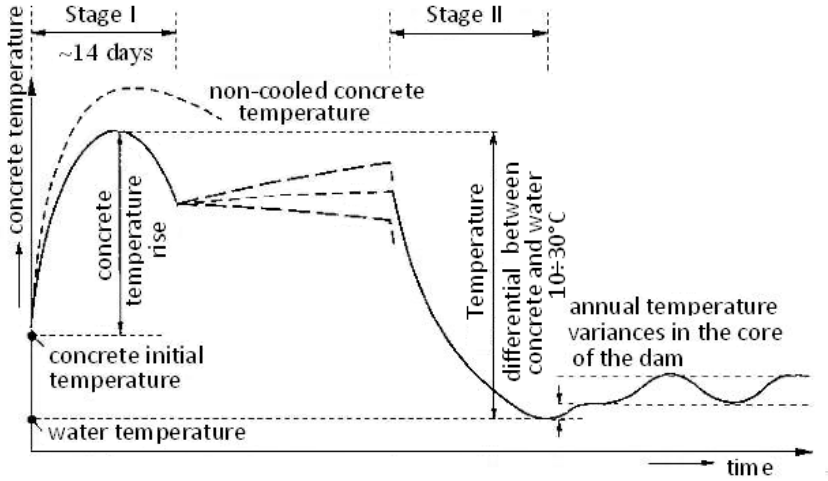

Fig. 2. The cooling of concrete inside large dams erected as columnar structures [3], [6].

In-field measurement results indicated that the internal pipe cooling system reduced the temperature of concrete by about 15°C with respect to the non-cooled concrete. The maximum internal temperature of the element did not exceed 40°C at the external temperature of 18-20°C. [3].

2.4. Concrete placement systems

Proper concrete placement technique is also important. The key issue is the division into blocks/sections, often referred to as the concrete placement system. There are six basic concrete placement systems:

- battens
- columns
- horizontal slip forms
- vertical slip forms
- strips
- blankets

Each of these systems is related to different shape and spatial configuration of individual blocks. [2].

3. Conclusions

Design and execution of massive concrete structures requires adopting entirely different rules than those used for conventional structures. Increasing the section of an element or the use of stronger cement in larger amounts may have a negative effect with respect to undesired stresses. Thermal stress in concrete may lead to fractures and cracking. Risk assessment is difficult, as in addition to a number of factors that influence the magnitude and type of early volumetric changes, no uniform standards have been developed. Recommendations relating to temperature reduction in hardening mass concrete are limited to the selection of suitable technology, i.e., the use of cements with low heat of hydration, the reduction of cement content in $1m^3$ of concrete, the use of proper aggregate and cooling of the concrete mix.

References

[1] JOHN GAJDA, MARTHA VNAGEEM. *Controlling Temperatures in Mass Concrete*. Concrete International, January 2002

[2] PIOTR WITAKOWSKI. *Technologia budowy konstrukcji masywnych z betonu*. Instytut Techniki Budowlanej. Warszawa.

[3] WŁODZIMIERZ KIERNOŻYCKI. *Betonowe konstrukcje masywne; Teoria, Wymiarowanie, Realizacja*. Polski Cement; Kraków 2003.

[4] SEBASTIAN KASZUBA, ARTUR GOLDA. *Zabudowa betonu w konstrukcjach masywnych*. Betotech Sp. z o.o.

[5] FLAGA K. *Naprężenia własne termiczne typu „makro" w elementach i konstrukcjach z betonu*. Zeszyt Naukowy Politechniki Krakowskiej, Monografia 106, Kraków, 1990.

[6] MAKEDONSKIJ G.M. i inni. *Razriezka massivnych plotin na bloki betonirovanija*. Energija, Moskva, 1969.

TRANSCOM 2015, 22-24 June 2015
University of Žilina, Žilina, Slovak Republic

The use of the Ground Penetrating Radar (GPR) for the assessment of the quality of the concrete cover execution in reinforced concrete members

[*]Łukasz Sławski
[*]Kielce University of Technology, Faculty of Civil Engineering and Architecture,
Kielce, Poland, lukaslaw@poczta.fm

Abstract. The paper presents the GPR results for the assessment of the concrete cover contour in the reinforced concrete members. The GPR scans were obtained using the RIS-K2 system with a high frequency (2GHz) dual-polarized antenna. Measurements were taken for different reinforced concrete members at prefabrication plants to check the reproducibility of the results. The ambient conditions were the same for all measurements. In all cases, the GPR was found to be a suitable system for determining the quality of the concrete cover execution. Other findings presented in the paper include the results from the analysis of the recorded signal amplitudes and the methods of data interpretation. The GPR survey was also the basis for determining possible causes of substandard performance of the rebar cover. The results from the investigations will allow monitoring and detecting potential technological errors and faulty workmanship.

Keywords: GPR, concrete cover, reinforced concrete structures

1. Introduction

Assessment of the concrete cover performance is one of the elements in the evaluation of the integrity of reinforced concrete members. The performance of the cover is considered a major factor in governing the rate of deterioration of reinforced concrete structures as it provides:

- safe transfer of bond forces;
- proper concrete compaction;
- protection against the corrosion of steel [1].

In engineering practice, the depth of the concrete cover is most often assessed using a detector or a cover meter, those instruments, however, do not account for the layer contour. One of the possible solutions is provided by the radar method. This high-resolution, mobile method is based on emitting electromagnetic waves of the frequency range from short to ultra short radio waves, and the recording the waves reflected from layers having different dielectric properties [2]. One of the devices based on this principle is georadar.

The aim of the paper was to find out whether it is possible to detect design errors or workmanship defects related to the concrete cover contour with the radar method.

2. Georadar principle of operation

Georadar generates an electromagnetic pulse, which is directly emitted into the target medium by the transmitting antenna. Part of the pulse energy is dispersed already at this stage, whereas the rest of it propagates inside the medium. The depth range of wave propagation depends primarily on the emitted frequency. The receiving antenna receives the reflected wave of the pulse and delivers it to the receiver. If the antennas are located close to each other, they need to be shielded so that the pulse and the reflected wave do not overlap. The test outcomes are given in the form of the so-called radargrams, i.e. recordings, in a graphic form, of all reflected signals recorded in profiling.

Radargrams contain many layers of information superimposed on each other, distortions, noise and disturbances, which must be analysed and processed [2].

3. Experimental

The tests were conducted using RIS-K2 GPR with 2 GHz TR200BP dual-polarized antenna. For concrete, the penetration range of this antenna is approx. 0.5m [3]. Concrete is a material of low conductivity, which provides excellent testing conditions when the radar method is selected because the medium can be treated as an insulator. Consequently, it is not necessary to make additional assumptions as it is the case with a lossy medium. Radar analysis in such a medium is much more complex [4].

The tests, run on many structural members, were performed at the prefabrication plant. The paper presents the cases in which inadequate contours of the concrete cover were detected. To properly identify the concrete cover, the following procedure was adopted:

1. Determining the velocity of the electromagnetic wave propagation. In accordance with [5], it was assumed to be 12cm/ns for concrete in the dry state.
2. Detecting two crossing bars with the GPR.
3. Near the crossing site, the structure is scanned along two perpendicular directions above both crossing bars.
4. Taking measurements of the concrete cover.

Two radargrams, on the basis of which the concrete cover is specified (scan A perpendicular to scan B) are presented below. The procedure described above was followed.

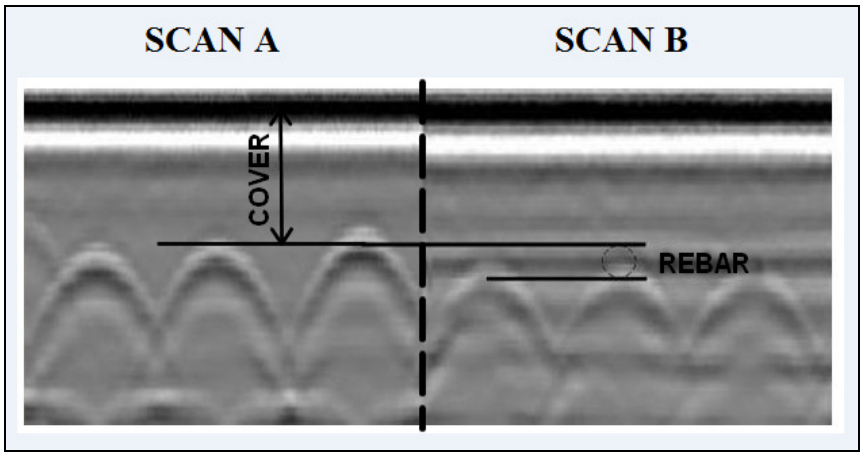

Fig. 1. Analysis of radaragrams aimed at the determination of the adequate depth of the concrete cover.

The procedure described above also makes it possible to estimate the diameter of the reinforcing bar, however, the accuracy of the method in this case is ± 6 mm[5]. At this level of accuracy, it is possible to find out whether the bar has a large or a small diameter. The accuracy with which the depth of the cover is assessed is the same.

Radargrams need appropriate filtering. That was performed with specialist GRED-3D software using the following filters:

- Background removing filter – it determines the so–called average trace of the profile.
- Amplifying filter – it amplifies the georadar signal over time.
- Smoothing filter – it determines a new value of the sample through the operations performed in the neighbouring samples in a single trace [6].

The filtering as described above produced the following results:

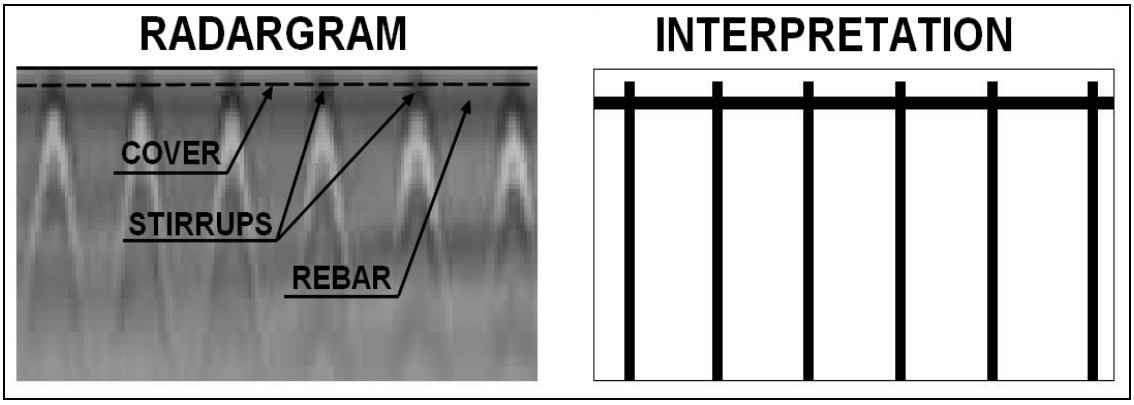

Fig. 2. Interpretation of the radargram showing the adequate contour of the concrete cover.

Fig. 2 presents the interpretation of the radargram for a reinforced concrete beam segment. The vertices of parabolas should be interpreted as stirrups in the radargram. Connecting those with a single line makes it possible to check the cover contour. In this case, the line is parallel to the upper edge of the member, thus it can be stated that the cover was fabricated properly.

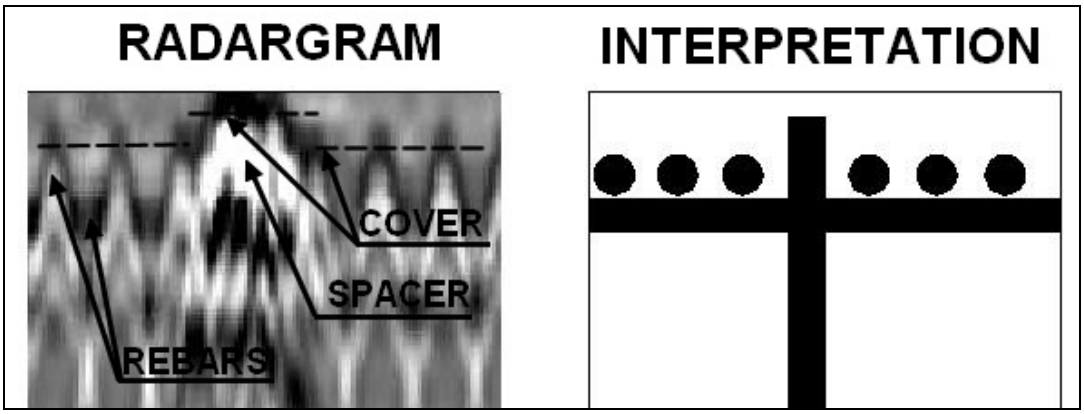

Fig. 3. Interpretation of the radargram showing a design error which affects the concrete cover contour

Fig. 3 presents the interpretation of the radargram for a reinforced concrete wall slab. The distance between rebar rows was maintained using a spacer. The geometry of the spacer, however, was inadequately defined. Consequently, the required concrete cover depth was not provided. When the element is in service, the concrete cover will fail at those sites due to the chemical aggression of the environment, as a result the bars will be exposed to corrosion. At each site, where the spacer was located in the radargram, the concrete cover contour was the same.

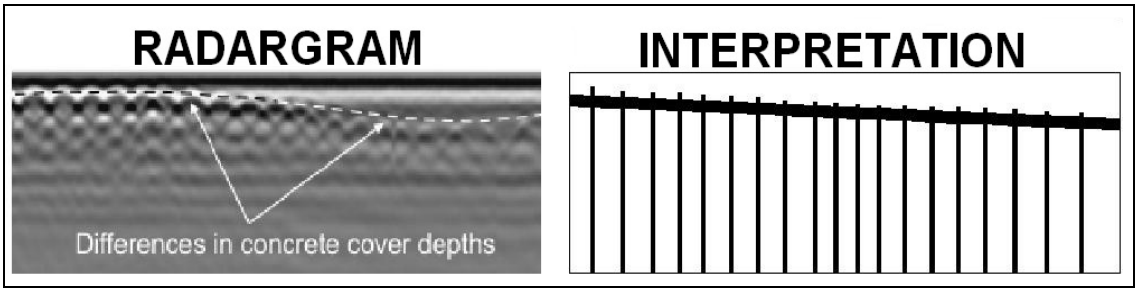

Fig. 4. Interpretation of the radargram showing workmanship defect which affects the concrete cover contour

Fig. 4 presents the interpretation of the radargram for a part of reinforced concrete column. It can be observed that the primary reinforcement was incorrectly shaped at the prefabrication plant, i.e. the reinforcing bar is not placed parallel to the member edge. That affects, to a large extent, the concrete cover contour and the column bearing capacity. A defect of this type can even result in the member failure, therefore, it is vital to detect it before the member is installed.

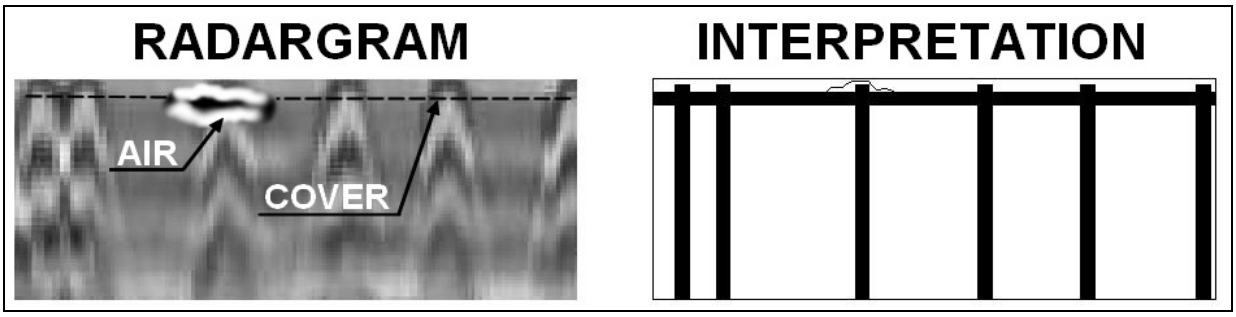

Fig. 5. Radargram showing the concrete cover which does not safely transfer bond forces.

Fig. 5 presents the interpretation of the radargram for a part of reinforced concrete beam. On the basis of the radargram, it is possible to locate the air void at the rebar-concrete interface. At this site, the failure of the bond between the materials is observed. As a result, the concrete cover does not carry out its function.

4. Conclusions

In georadar testing, it is important to filter the data. Much experience is required and huge workload must be done to perform the task. When properly conducted, however, that makes it possible to draw a number of conclusions that concern the quality of workmanship of a concrete member. The tests show that the concrete cover contour can also be monitored. The reasons why the concrete cover depth is inadequate can be found.

References

[1] STAROSOLSKI W., *Reinforced concrete structures in accordance with PN-B-03264:2002 and EUROCODE 2* (in Polish) PWN, Warszawa, 2007, vol. II, edition 11.

[2] KARCZEWSKI, J., ORTYL, Ł., PASTERNAK, M. *The outline of the Georadar Method* (in Polish). Kraków: Wydawnictwa AGH 2011.

[3] MALHORTA V. M., CARINO N. J., CRC Handbook on non-destructive testing of concrete, CRC Press, 1991.

[4] RÓŻAŃSKI L., *Electromagnetic field and waves* (in Polish), Wydawnictwo Politechniki Poznańskiej, Poznań, 2003.

[5] FORDE M. C., *Ground Penetrating Radar, Proc. , Introduction to Non-destructive Evaluation Technologies for Bridges Conference*, Transportation Research Board, 2004, p.20

[6] IZYDORCZYK J., KONOPACKI J., *Analog and digital filters* (in Polish), edited by the Jacek Skalmierski computer laboratory, Katowice, 2003.

TRANSCOM 2015, 22-24 June 2015
University of Žilina, Žilina, Slovak Republic

Timber beams reinforced with Fibre-Reinforced Plastic/Polymer under long-term load – research issues

[*] Ewa Stępień
[*] Kielce University of Technology, Faculty of Civil Engineering and Architecture,
25-314 Kielce, al. Tysiąclecia Państwa Polskiego 7, Poland, ewaste3@wp.pl

Abstract. This paper presents remarks concerning the study of fibrous composites reinforced timber beams subjected to long-term load. A great variety of formability features for both composite materials are considered and processes in the reinforced beams work connected with this variety are stated. Moreover, it highlights the benefits of researches over the long-lasting reinforced beams, as well as difficulties related to the need of performing appropriate conditions during the study.

Keywords: Timber, Fibre-Reinforced Plastic/ Polymer, long-term load, reinforcement of wood beams, creep.

1. Introduction

In many aspects, timber exceeds other construction materials. This is the oldest building material used by the man. The great value of wood is associated with its structure, which is an advantage not found in other materials. Because of the porous structure and the system of sub-microscopic capillaries, wood has a big durability with its own small specific gravity. Wood is an anisotropic and orthotropic material, its compressive strength, stretching and bending depend on the direction of the forces in relation to its fibres. It is the material, which is characterized by the low heat conductivity, and it is easy to process. On the other hand, due to its natural background, wood has also numerous disadvantages. Among others, a high hygroscopicity and, related to it, the phenomenon of shrinking, swelling and cracking. A significant problem is a change of mechanical properties, which appear with the increase of moisture, as well as the wood creep resulting from rheological properties even at the room temperature. This is one of the reasons of the lack of trust in wood as the construction material. Nevertheless, timber can be produced permanently. Numerous materials available on the market can be used to reinforce it and at the same time to improve the durability and stiffness of constructions made of wooden elements [1, 2].

Modern fibrous composites are more frequently used as a reinforcing material to wood constructions. Generally speaking, they are plastics reinforced with various types of fibres. The most common composites are as follow:

- CFRP – Carbon Fibre Reinforced Plastic
- GFRP – Glass Fibre Reinforced Plastic
- AFRP – Aramid Fibre Reinforced Plastic [3, 4].

Interest in fibres results, most of all, from the good strength parameters and small weight. Flexibility features of fibrous composites FRP are comparable with steel, and their durability is a few times higher. On the other hand, these materials possess also drawbacks, which include a lack of plastic reserves and a low module of resilience depending on the type of the fibres. Strengthening of the element with fibre-reinforced plastic is done with adhering carbon, glass or Aramid fibres tape or mats to the most load construction surfaces [5]. Examinations were also carried out on the beams, which were strengthened with the two carbon mats crossing in the middle of the bottom of the beam [6]. Other reinforcement methods are as follow: adhering tapes between each layer glued wooden slats, inserting tapes in beams cuts of solid wood. It is important to protect

the elements, which reveal the usage effects, and there is the necessity of increasing in load capacity and reduction of deflection, as well as strengthening of the damaged parts of beams.

2. Research issues appearing during work of timber beams strengthened with FRP under long-term load

The first scientific research with the use of carbon tapes to strengthen wood elements was carried out just in 1990s. Investigations on elements of bending, stretching and compression reinforced with carbon fibres have been conducted at university of technology in Śląsk, Szczecin, Wrocław and Poznań [7-10]. Results of many scientific researches have revealed significant increase in load capacity and stiffness of reinforced wooden elements, while beam deflection and the wood stress were highly reduced. Thanks to the research, as well as gained results, more and more often fibrous composites have been used to reinforce wood, already at the stage of production and in the renewal and refurbishment. There have been relatively few scientific researches connected with the behaviour of reinforced constructions under long-term load, or in different temperature – moisture conditions. As it can be concluded from the above information, examinations, which have been carried out so far, were related mostly to timber beams strengthened with Fibre Reinforced Plastics subjected to short-term load. It is worth analysing benefits of carried out examinations on wooden strengthen FRP subjected to long-term load, as well as pointing out problems resulting from the combination of these materials under such a load.

The analysis of the reinforced beams subjected to long-term load aims to have worked out the way of prevention from the effects of bending increase in time, taking into account their influence on usage and construction aesthetic [11]. It is crucial to observe the changes of beams bending during the examination, and to check after what time the stabilization of elements bending occurs. In the study of timber beams reinforced with FRP subjected to long-term load, differentiation of formability characteristics of both materials should be viewed. The effect of bonding various materials into one compatible completely depends on the similarity of their physical and mechanical parameters. To make combination of a composite material compatible with wood, it is important that their formability characteristics were comparable.

Those characteristics are as follow:

- creep factor φ,
- Poisson ratio μ,
- elasticity modulus E,
- shear modulus G,
- humidity deformability α_w,
- thermal expansion coefficient α_t.

Great differentiation of the above parameters for wood and fibre composites can lead to unfavourable distribution of internal forces in bonding construction under temporary load and their redistribution under long-term load. There can also appear additional tension connected with temperature – moisture deformations. A significant issue is also a fact that wood and fibre composites deformability parameters as the anisotropic materials are changeable depending on the fibres directions. For instance, mats resilience and carbon or glass tapes modules are bigger than modules of wood resilience along fibres about 6 – 25 times, while across fibres about 200 – 600 times. Taking that into account, the creep factor of composites and wood are then comparable along fibres, while across fibres they differ about 4 – 10 times [5]. The analysis of the reinforced FRP wood elements creep is a crucial point of investigation in the long-term load conditions. Carbon fibres are the most resistant to creep influence, while the Aramid fibres show moderate and glass fibres high susceptibility to creep. As a result of creep, durability of composite materials decreases,

and the drop depends on the type of the fibres and is at the level of 29-55%, 47-66% and 47-66% of the initial durability of the composites with fibres glass, Aramid and carbon, respectively [12].

Wood is a material of complex rheological properties. There is also a significant choice of an appropriate rheological model in order to describe behaviour of the reinforced element in plastic deformability conditions. In the work [11], a specific attention was drawn to the possibility of appearance of the local tension redistributions in the section, especially at the places of composite beams connections. A crucial issue here is also the stress relaxation and increasing global deformations. It should also be taken into account that, under the long-term load on bending elements, the stress rearrangement among the used adherents can occur. The influence of adhesive joint on the deformation of reinforced beams should be considered. Functions of the deformation increase in time (in creep rights) for adhesive joints, quantifying the size of deformation, presented in the literature, are based on the assumption of the uniform state of stress, what is an unacceptable simplification [13].

The studies of the FRP strengthened beams, subjected to the long-lasting load, are time consuming. In order to examine the phenomenon of creep, they should be carried out with the preservation of constant temperature - moisture conditions. In addition, here the problem occurs because it is difficult to get such conditions in required period to perform the research. From the research conducted by Jasieńko [14] it follows that the slight impact of moisture was revealed in irregularity of bending increase. Examining reinforced timber beams in the long-term load perspective, studied should be carried out at the same time for different reinforcement schemes or different FRP materials. That is difficult to fulfil, and doing research one after the other, for various strengthening methods and with the use of different mats or FRP tapes, then given results can not be comparable because of the differences in temperature and moisture conditions.

3. Conclusion

The use of fibre composites as the reinforcement of timber constructions is undoubtedly an efficient way for durability and stiffness improvement and for reduction of rheological growth deflection. Unquestioning the technical possibility of composites to strengthen building constructions, it is necessary to focus on the study, which take into account the specificity of the cooperation of wood with composites, especially under the long-term load, as well as in variable humidity conditions. The analysis of the basic rheological processes is a crucial point of work referring to multi-material working beams under the long-lasting load. Gaining positive effects in laboratory conditions, even in possibly constant temperature – moisture conditions, one should be very discerning during practical use of fibre-reinforced wood, as its behaviour is insufficiently known in the real operating conditions.

References

[1] KRZYSIK F., *Nauka o drewnie.* Państwowe Wydawnictwo Naukowe. Warszawa 1978.

[2] ŁAPKA M., *Rozprawa doktorska Wpływ efektu skali na mechanikę zniszczenia drewna konstrukcyjnego.* Politechnika Opolska 2013.

[3] JASIEŃKO J., PIETRASZEK P., NOWAK T., *Taśmy CFRP we wzmacnianiu elementów konstrukcyjnych drewna.* VI Konferencja naukowa: Drewno i materiały drewnopochodne w konstrukcjach budowlanych, Międzyzdroje 2004.

[4] BROL J.: *Wzmacnianie elementów drewnianych taśmami lub matami z włókien*. Zeszyty Naukowe Politechniki Śląskiej, seria: Budownictwo, Gliwice 2001.

[5] MIELCZAREK Z., ORŁOWICZ R., *Uwagi do stosowania kompozytów włóknistych w konstrukcjach drewnianych.* VI Konferencja naukowa: Drewno i materiały drewnopochodnew konstrukcjach budowlanych, Międzyzdroje 2004.

[6] MIELCZAREK Z., KURTZ K., *Problemy konstrukcyjne w budownictwie zabytkowym*. II Ogólnopolska Konferencja pt. Architektura ryglowa – wspólne dziedzictwo. Szczecin 1999.

[7] BROL J., *Analiza doświadczalno teoretyczna wzmacniania konstrukcji drewnianych kompozytami polimerowo-węglowymi*. Rozprawa doktorska, Gliwice, 2005.

[8] BROL J., *Skuteczność wzmacniania belek drewnianych taśmami CFRP*. VII Konferencja Naukowa: Drewno i materiały drewnopochodne w konstrukcjach budowlanych. Szczecin –Międzyzdroje, 12 – 13 maja 2006.

[9] BROL J., *Wzmacnianie stropów drewnianych taśmami z włókien węglowych*. VII Konferencja Naukowa: Drewno i materiały drewnopochodne w konstrukcjach budowlanych. Szczecin –Międzyzdroje, 27 – 29 maja 2004.

[10]NOWAK T., *Analiza pracy statycznej zginanych belek drewniany wzmacnianych przy użyciu CFRP*. Rozprawa doktorska . Wrocław 2007.

[11]JASIEŃKO J., *Połączenia klejowe i inżynierskie w naprawie, konserwacji i wzmacnianiu zabytkowych konstrukcji drewnianych.* Dolnośląskie Wydawnictwo Edukacyjne, Wrocław 2003.

[12]YAMAGUCHI T., KATO Y., NISHIMURA T., UOMOTO T., *Creep rupture of FRP rods made aramid, carbon and glass fibers.* Proceedings of the Third International Symposium on Non-Metallic (FRP) Reinforcement for concrete structures (FRPFCS-3). Japan Concrete Institute, Tokyo 1997.

[13]GODŹMIRSKI J., *Wytrzymałość doraźna konstrukcyjnych połączeń klejowych*. WNT, Warszawa 2002.

[14]JASIEŃKO J., *Połączenia klejowe w rehabilitacji i wzmacnianiu zginanych belek drewnianych*. Oficyna Wydawnicza Politechniki Wrocławskiej, Wrocław 2002.

TRANSCOM 2015, 22-24 June 2015
University of Žilina, Žilina, Slovak Republic

The Influence of Varied Aerobic Conditions on the Process of Dephosphatation of Wastewater and on the Composition of Filamentous Bacteria in the Active Sediment

[*]Renata Stoińska
[*]Kielce University of Technology, Faculty of Environmental, Geomatic and Energy Engineering, al. Tysiąclecia Państwa Polskiego 7, 25-314 Kielce, Poland , {rstoinska}@tu.kielce.pl

Abstract. The aim of the article was the analysis of the dephosphatation of wastewater in case of breakdown of the aeration system. The changes in the phosphorus reduction in wastewater was analyzed. Apart from this chemical indicator, the set of filamentous bacteria of the active sediment was also analyzed. Two measurement sequences of the wastewater sediments were conducted. Each measurement sequence represented different oxygenation conditions because the sediment was collected during a breakdown of the oxygenation system and 3 weeks after its repair. The analysis of results lead to a conclusion that in the examined active sediment in condition of lack of oxygenation, the percent of phosphorus reduction is lower than in the case of improvement of the aerobic conditions. The microscopic analysis of filamentous bacteria confirms the specific changeability according to the physical and chemical conditions in the wastewater treatment plant.

Keywords: phosphorus reduction, filamentous bacteria, breakdown of the oxygenation system

1. Introduction

Breakdowns of devices constituting the equipment of bioreactor of the wastewater treatment plants are a big problem for their users because of the disturbances of the biological treatment processes, which are sudden and hard to reverse. Such breakdown situations involve i.a. the damage of agitators or disconnection of the aeration system [1]. Such conditions, although they appear rarely in devices in technical scale, are very interesting from a scientific point of view. They allow to obtain information about the influence of given factors on the standard parameters of the wastewater treatment process and on organisms living in the wastewater sediment. This paper discusses the influence of wastewater sediment aeration system breakdown on phosphorus speciation in the wastewater sediment. Phosphorus is the basic element necessary for the functioning of every living organism. Unfortunately, its excess in the water environment may lead to eutrophication [2]. The problem of eutrophication, that is "over-enrichment" of water with biogenic compounds constitutes a threat to maintaining the ecological homeostasis. The excess development of phytoplankton in the landlocked water can be observed when the level of phosphorus concentration reaches over 0,03mg/dm^3. Because of the significant share of the municipal wastewater in the creation of eutrophication, advanced processes of biological wastewater treatment are applied. The biological treatment bases on the ability of some bacteria to increased collection of phosphorus in aerobic conditions and releasing phosphorus from cell in anaerobic conditions. Such application of alternating anaerobic and aerobic conditions allows some poli-P bacteria species (e.g, Acinetobacter, Pseudomonas) which gather phosphorus in their organisms to development and participate in biocenosis of the active sediment [3]. This element may be also accumulated by some filamentous bacteria which collect phosphorus in the form of polyphosphates. Filamentous bacteria play a positive and negative role in the wastewater sediment [4]. A positive role is creating a "skeleton" of flocks of wastewater sediment and oxidation of carbon, sulphur and iron compounds. Unfortunately, an excessive development of these

microorganisms causes the so called fibrous swelling of sediment which in turn has negative influence on sedimentations [5]. The domination of the filamentous bacteria in the active sediment may be an indicator of specific technological problems in wastewater treatment plants. Some species of filamentous bacteria develop in strictly determined conditions. Therefore the identification of the filamentous bacteria provides a lot of information about the parameters of sediment [6]: the share of dissolved oxygen, the ratio of food substrate to biomass of microorganisms, the content of sulphur, nitrogen, phosphorus compounds , pH value. Thus, besides the chemical indicator in form of analysis of phosphorus speciation, the set of filamentous bacteria of the active sediment was also analyzed.

2. Research methodology

The object of research was active sediment as well as raw and treated wastewater from mechanical-biological wastewater treatment plant. Two measurement sequences of the wastewater sediments were conducted. Each measurement sequence represented different oxygenation conditions because the sediment and wastewater were collected during a breakdown of the oxygenation system and 3 weeks after its repair. Samples were collected in April and May. The method of spectrophotometric analysis of phosphorus marking in raw and treated wastewater was applied in the experiment. The concentration of general phosphorus was marked by means of spectrophotometric method with the application of spectrophotometer UV-VIS Lambda 25. Measurements took place according to the procedure of analysis of general phosphorus, after oxidation of the sample with potassium (VI) monopersulphate [7].

The identification of filamentous bacteria was carried out by means of the method presented by Eikelboom [8]. The specimen were coloured with the application of method by Gramm and Neisser. The microscopic research, required in the microbiological diagnostics were carried out by means of a contract-phase microscope Delta Optical Evolution 100 connected with HDCE-X5 camera.

3. Results

The microscopic analysis of filamentous microorganisms of the active sediment showed that in the samples of the active sediment collected during the breakdown of the aeration system, the dominant species of the filametous bacteria were following: Beggiatoa, Type 1863, Type 021N (fig.1.). All three species are Neisser-negative bacteria. This means that they do not gather polyphosphates in their organisms. Additionally, the occurrence of these organisms is connected with a very low concentration of oxygen. The Beggiatoa species additionally gathers in their organisms globules of sulphur which is a sign of high content of hydrogen sulphide in the wastewater. Insufficient amount of oxygen, necessary for building sulphur compounds gathering in chambers, caused decomposition of sediment and secretion of gas hydrogen sulphide. The lack of Neisser-positive filamentous bacteria and occurrence of species of organisms characteristic for anaerobic conditions may prove that in these conditions phosphorus was not accumulated by microorganisms and was dispensed to the environment in the form of phosphates.

The microscopic analysis of the active sediment showed that in the samples of the active sediment collected 3 weeks after the aeration breakdown, the dominant species of the filamentous bacteria was Microthrix parvicella. This species has exceptionally high kinship with oxygen, what causes that the bacterium may use the oxygen metabolism with minimum amount of this gas in the environment. Therefore, in the case of repair of aeration breakdown, after the anaerobic conditions in the active sediment subside, it is the dominant species of the filamentous bacteria, because it is the fastest to colonise the environment [9]. This species also has an unusual ability. It can bind lipids not only in the aerobic but also in anaerobic conditions. In anaerobic conditions this

bacterium binds LCFA (Long Chain Fatty Acids) and stored them in cells in the form of lipids which may be used for growth right after restoring the minimal concentration of oxygen. Microthrix parvicella has then a potential similar to the poli-P bacteria. Although in contrast to them it does not bind short chain fatty acids (SCFA) and only LCFA, the alternate changes of oxygen conditions also allow this bacterium to compete despite the slower growth. This filamentous microorganism has the ability to assimilate and accumulate phosphorus in the form of polyphosphates in the aerobic conditions [10]. Polyphosphates are stored in the form of volutine granules which may be visible after dyeing the specimen by means of the Neisser's method (fig.2). The intensive growth of the Neisser-positive filamentous bacteria (accumulating polyphosphates) in the active sediment after the restoration of the aerobic conditions (after repair of the aeration system) may be the sign of an intensive consumption of phosphorus and possibility to obtain concentration lower than 1,0 mg P/dm^3 in the treated wastewater [11].

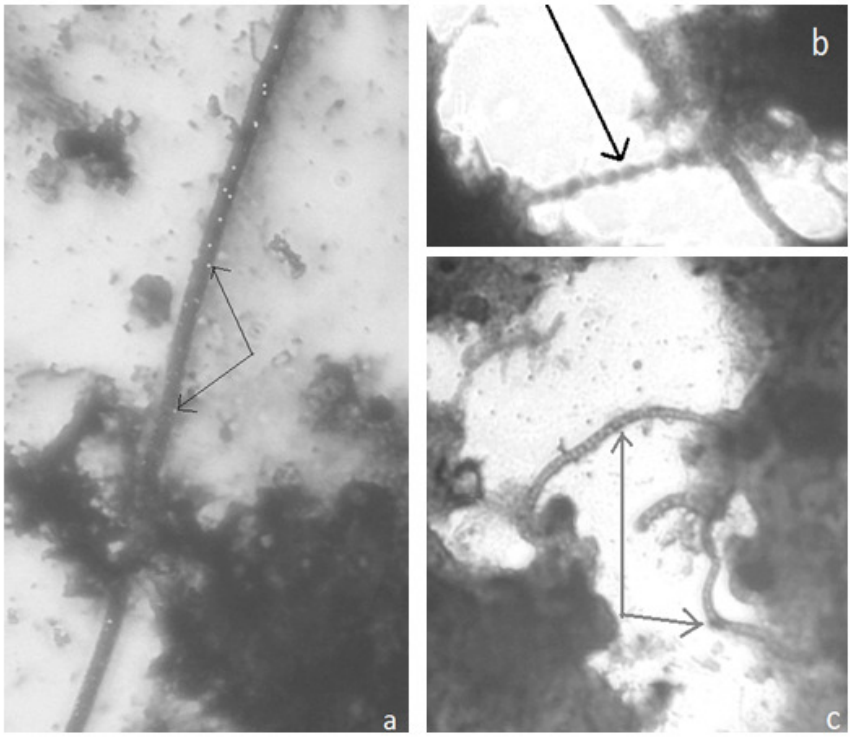

Fig. 1. Filamentous bacteria identified in the sediment during the aeration breakdown: a-Beggiatoa (marked sulphur globules), b-type 1863, c-Type 021N.

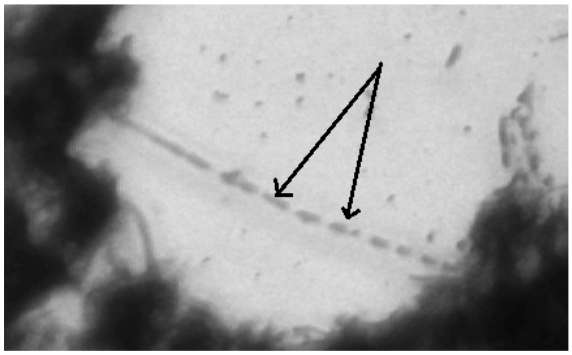

Fig. 2. The filamentous bacteria - Microthrix parvicella - identified in the sediment which was collected 3 weeks after repairing the breakdown (dark volutine granules are marked).

Analysis of the concentration of general phosphorus in the treated and raw wastewater which is a chemical indicator (fig. 3) confirmed the assumption based on the microbiological analysis, claiming that in anaerobic conditions a release of phosphates into the environment occurred because bacteria collect the products of anaerobic fermentation using the energy of high-energy decomposition of bond contained in the ATP particle. Therefore the phosphorus gathered in cells is released in the form of orthophosphates. This hypothesis is confirmed by the low percent of phosphorus reduction during the breakdown, which amounted at 63%. After the repair of aeration breakdown, the result if the chemical indicator also confirms the assumptions of the microscopic analysis of the sediment. After ceasing of the anaerobic conditions, a significant increase in the percent of phosphorus reduction occurs. The reduction of this element amounted at 89%. This indicates that the oxygen metabolism of microorganisms was restored, phosphates are intensively collected from the environment and then polyphosphates are increasingly assimilated in the cells of microorganisms.

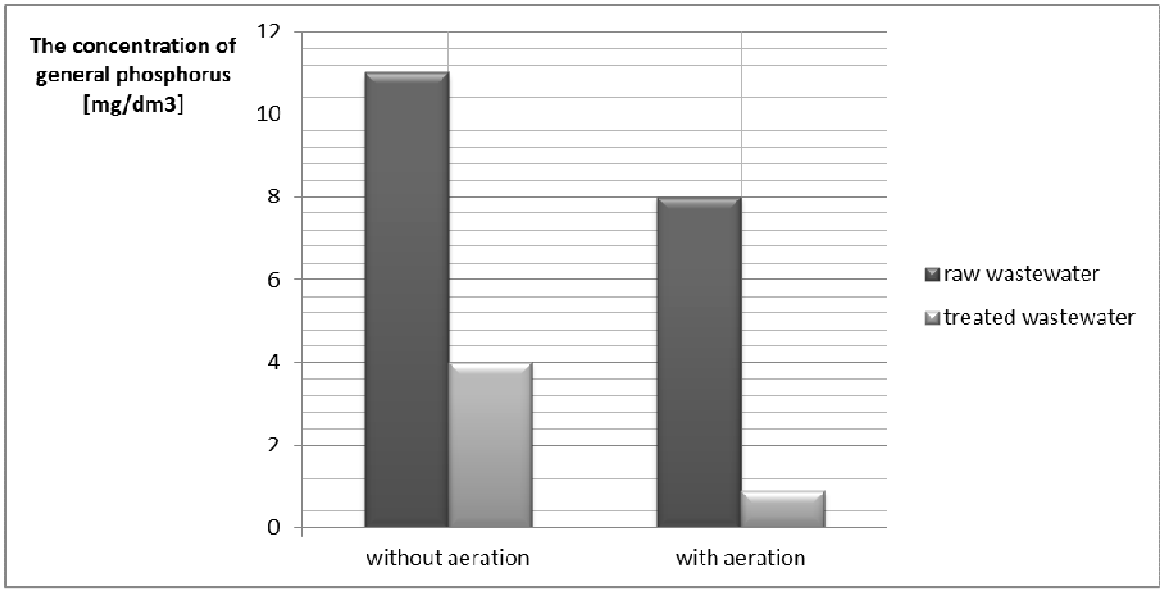

Fig. 3. Changes in the concentration of phosphorus according to diversification of aerobic conditions.

4. Conclusions

The paper presents the results of research concerning the species composition of the filamentous microorganisms in the active sediment as well as the percent of reduction of biogen, that is phosphorus.

The results of this research entitle to state the following conclusions:

- According to the changing aerobic conditions, the species composition of microorganisms of the active sediment also changes. This may directly influence the processes of dephosphatation of wastewater.
- According to the occurring technological conditions, the examined active sediment were characterised by a different species composition of filamentous bacteria. This may be a sign of a significant influence of physical factors on the microflora of the active sediment.

The knowledge about the influence of the chosen factors on the standard parameters of the wastewater treatment processes and on the organisms living in the wastewater sediment is significant for understanding the processes occurring there and their influence on the process of dephosphatation of wastewater.

Investigations were led using: spectrophotometer UV-VIS Lambda 25, contract-phase microscope Delta Optical Evolution 100 connected with HDCE-X5 camera. Equipments were founded by the MOLAB Project called ,,The development of laboratories of public universities in Świętokrzyskie Region''. Number of the Project in Kielce Univeristy of Technology: POIG 02.02.00-26-023/08-00.

References

[1] ŁAGÓD G., BABKO R., JAROMIN K., KUZMINA T. *Changes in structure of activated sludge Protozoa community at the different oxygen condition*, Proceedings of ECOpole 2012;6(1): 297-303.

[2] BEZAK-MAZUR E., STOIŃSKA R., *Analiza specjacyjna fosforu w różnych typach osadów ściekowych z wybranych oczyszczalni ścieków*, Proceedings of ECOpole 2014;8(1):127-133.

[3] BEZAK-MAZUR E., MAZUR A., STOIŃSKA R., *Phosphorus speciation in sewage sludge*, Environment Protection Engineering 2014, 40(3),161-175.

[4] LIWARSKA-BIZUKOJC E., BIZUKOJC M. *Nowa zautomatyzowana procedura oznaczania udziału bakterii nitkowatych w kłaczkach osadu czynnego*, Czasopismo Inżynierii Lądowej, Środowiska i Architektury 2013, 61:3-13.

[5] MIELCZAREK A.T., KRAGELUND C., ERIKSEN P.S., NIELSEN P.H. *Population dynamics of filamentous bacteria in Danis h wastewater treatment plant with nutrient removal* , Water Res., 2012, 46:3781 - 3795.

[6] SEVIOUR J.R., NIELSEN P.H. *Microbial Ecology of Activated Sludge* IWA Publishing, 2010: 162-166.

[7] The determination of phosphorus. Spectrophotometric method with ammonium molybdate, BS EN ISO 6878:2004.

[8] EIKELBOOM D.H., BUIJSENH.J.J. *Handbuch für die mikroskopische Schlammuntersuchung*, München: F. Hirthammer Verlag 1983.

[9] FIAŁKOWSKA E., FYDA J., PAJDAK-STÓS A., WIĄCKOWSKI K. *Osad czynny - biologia i analiza mikroskopowa*, Seidel Przywecki 2010.

[10] ROSSETTI S., TOMEI M.C., NIELSEN H., TANDOI V. *"Microthrix parvicella'', a filamentous bacterium causing bulking and foaming in activated sludge systems: a review of current knowledge*, FEMS Microbiology Reviews 2005, 29: 49–64.

[11] MACHNICKA A., GRÜBEL K., SUSCHKA J. *Improving of the biological removal and recovering of phosphorus from sewage by filamentous microorganisms*, Przemysł Chemiczny 2008,87(5): 509-511.

TRANSCOM 2015, 22-24 June 2015
University of Žilina, Žilina, Slovak Republic

The fire analysis of uninsulated steel frame

*Katarzyna Suckert
* Kielce University of Technology; Faculty of Civil Engineering and Architecture; Department of Mechanics, Metal Structures and Computer Methods, Poland, ksuckert@tu.kielce.pl

Abstract. The paper provides a fire analysis of steel uninsulated steel frame. The analysis was carried in accordance with the Eurocode. The fire impact on the structure was evaluated with respect to two criteria: bearing capacity and temperature. To carry out the numerical analysis, the Robot system was used.

Keywords: fire analysis, steel frame, critical temperature

1. Introduction

In the paper, the fire performance of a uninsulated steel frame was analyzed. During "normal" design process live and dead load are counted. Sometimes it is also need to include accidental actions as for example: seismic load, impact and fire load. Presently designers are required to ensure fire safety. It is usually done by using special fire resistant building materials and fire insulation. Fire analyses are rarely carry out, mainly for big buildings with important function. The paper shows/ The aim of the paper is to show that in case of steel structures fire analysis is essential due to properties of steel that worsen with increase of temperature.

2. Fire analysis

The analysis was carried out with using Robot system. The geometry of structure and profiles of bars are shown in the figure 1. The following loads were imposed: dead load, load of covering, wind load (1st zone) and fire load. The standard fire curve was assumed and members were designed as uninsulated.

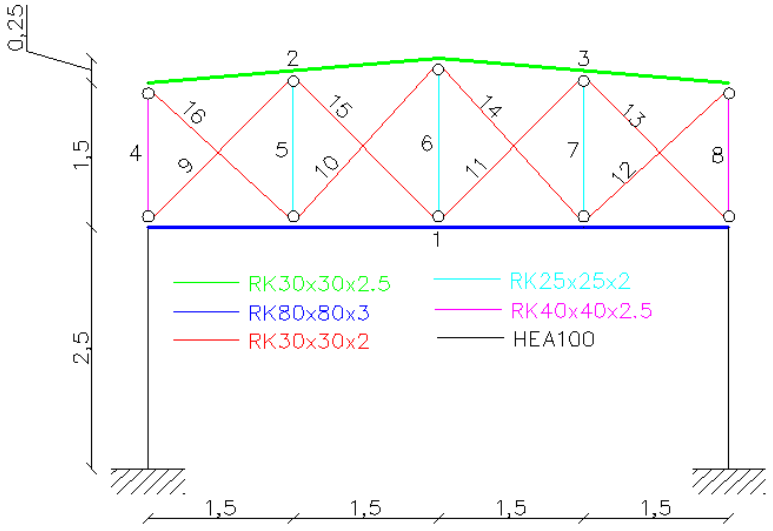

Fig. 1. The geometry of analyzed structures and profiles of bars.

2.1. Effort analysis

The results of fire analysis are shown in figures 2-7. Each graph presents how effort of bars changed during the fire. Dots at y-axis marks the effort of bars in "normal" design situation. For "normal" and accidental design situation appropriate combinations were used. The partial coefficient of safety are lower in accidental than in "normal" design situation, so in many cases (Fig.2-7) the effort under normal condition is higher than under fire.

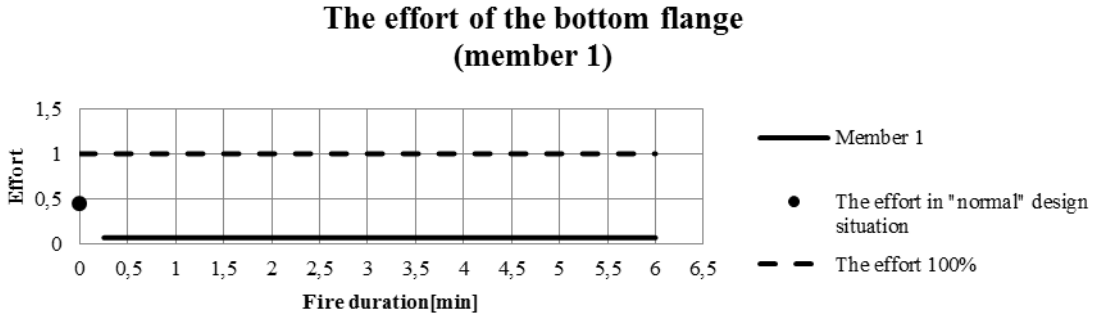

Fig. 2. The effort of the bottom flange.

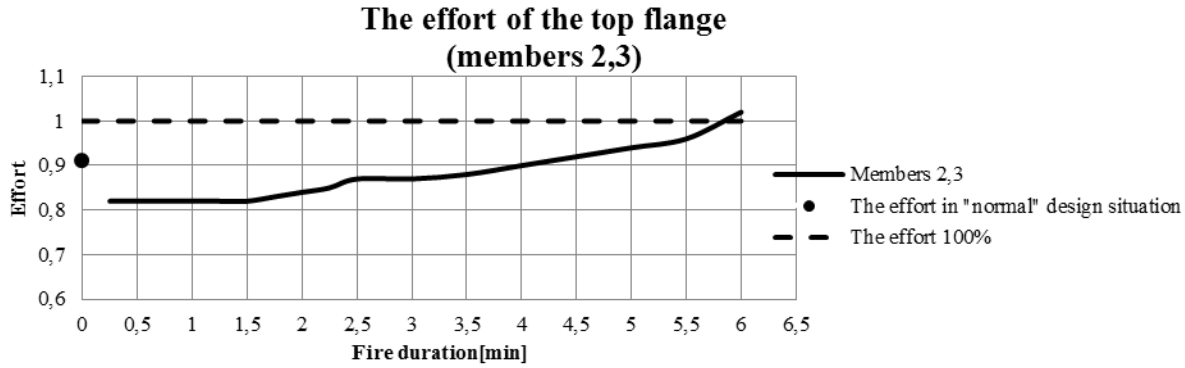

Fig. 3. The effort of the top flange.

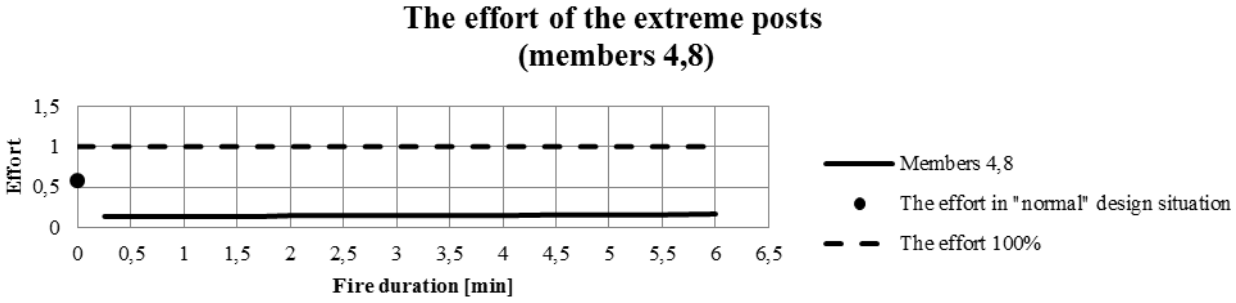

Fig. 4. The effort of the extreme posts.

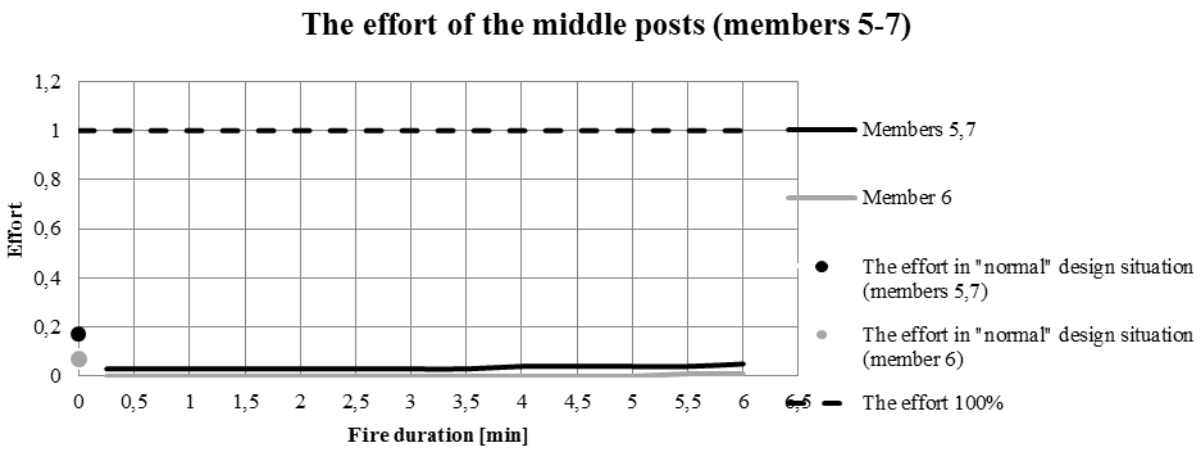

Fig. 5. The effort of the middle posts.

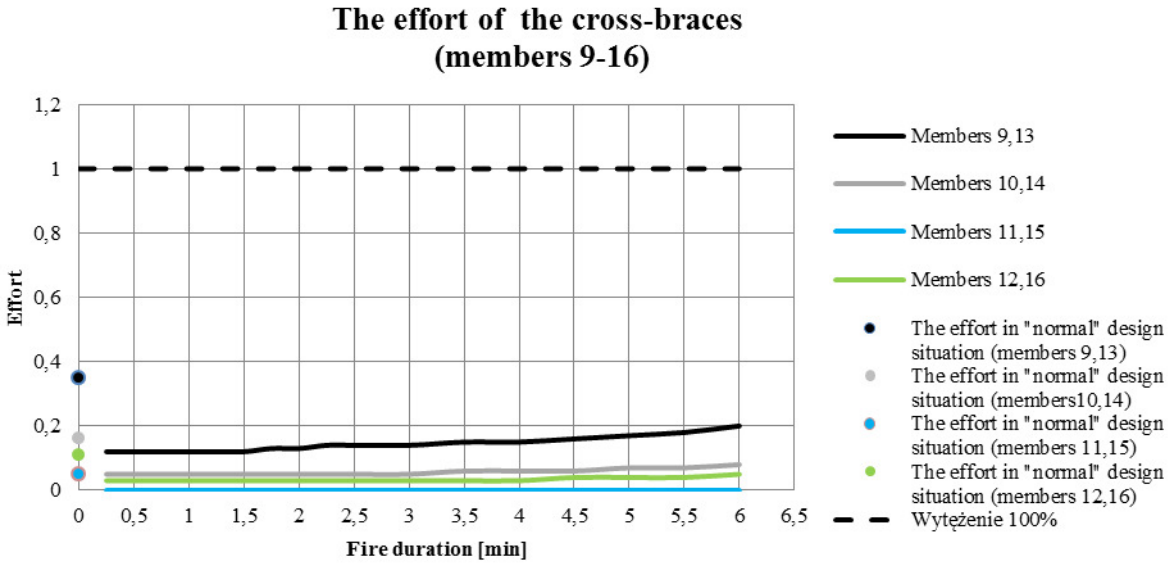

Fig. 6. The effort of the cross-braces.

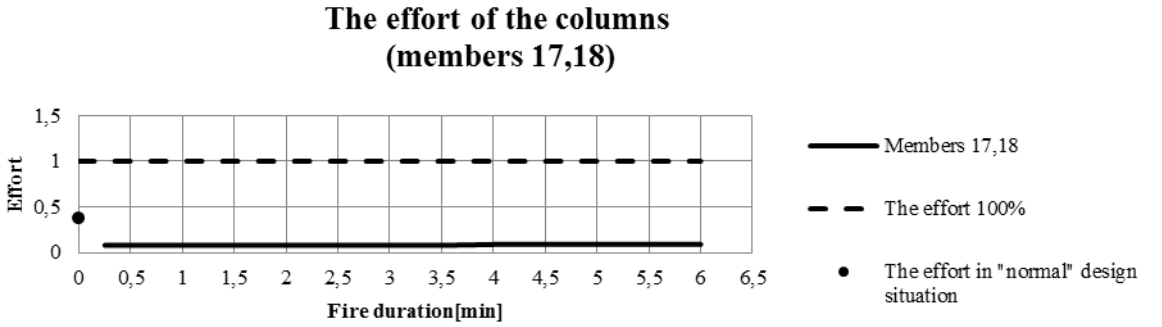

Fig. 7. The effort of the columns.

2.2. Temperature analysis

Changes of temperature of each bar are shown in figures 8-12. Dashed line shows critical temperature that shouldn't be exceeded.

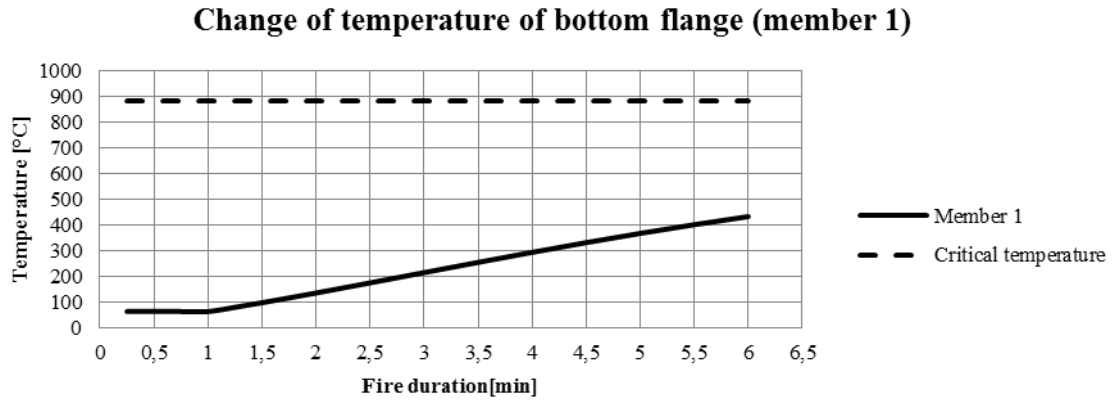

Fig. 8. The change of temperature of bottom flange.

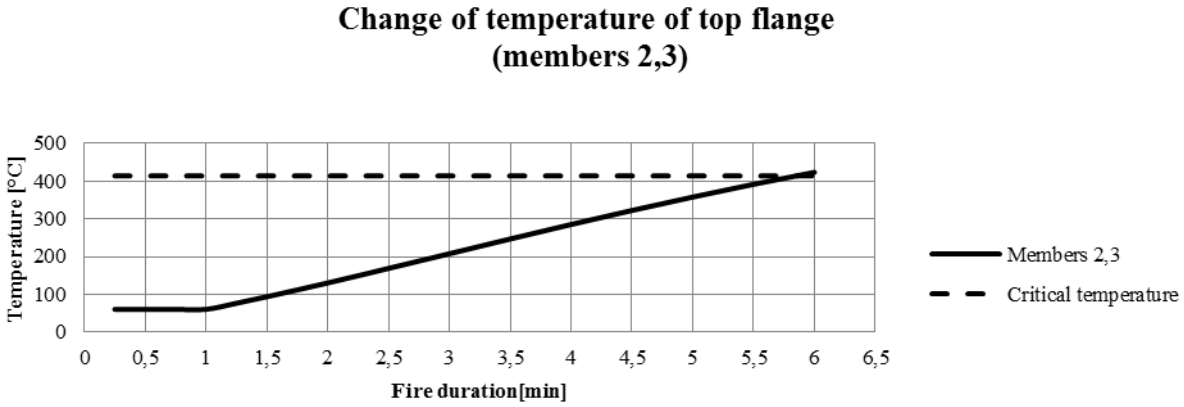

Fig. 9. The change of temperature of top flange.

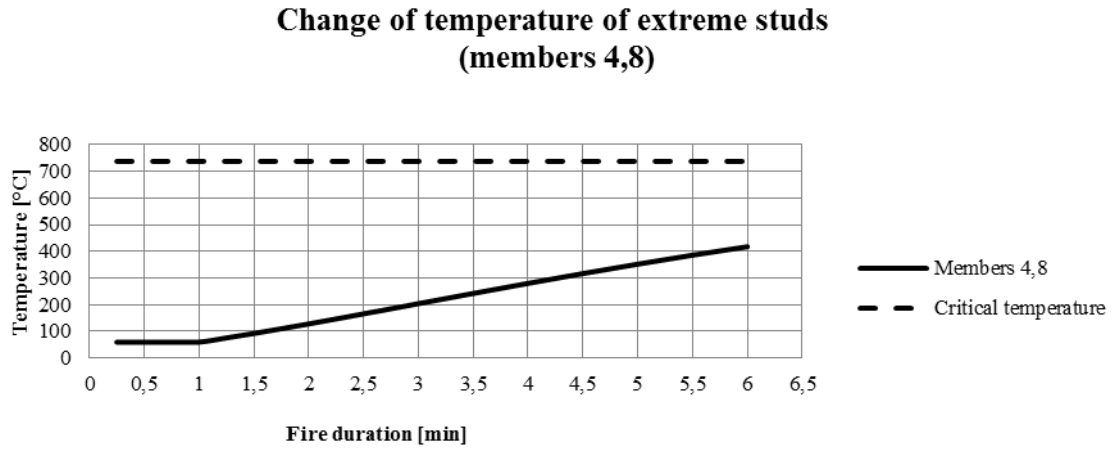

Fig. 10. The change of temperature of extreme posts.

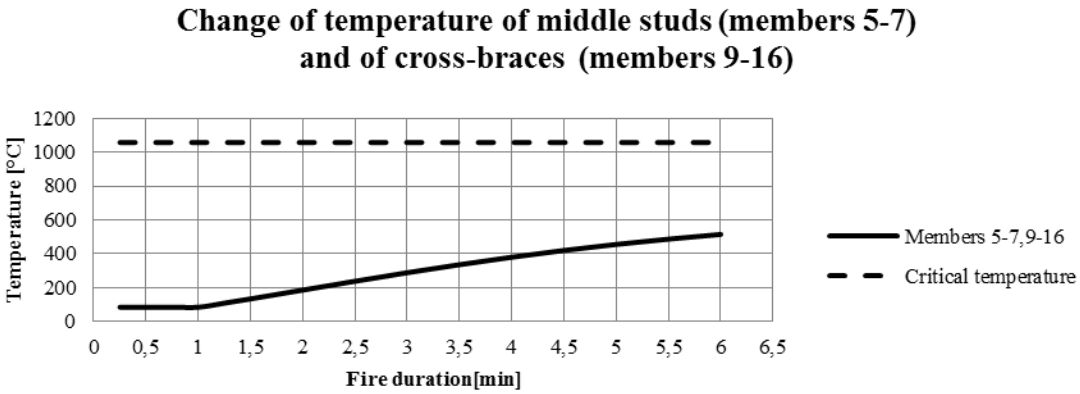

Fig. 11. The change of temperature of middle posts and of cross-braces.

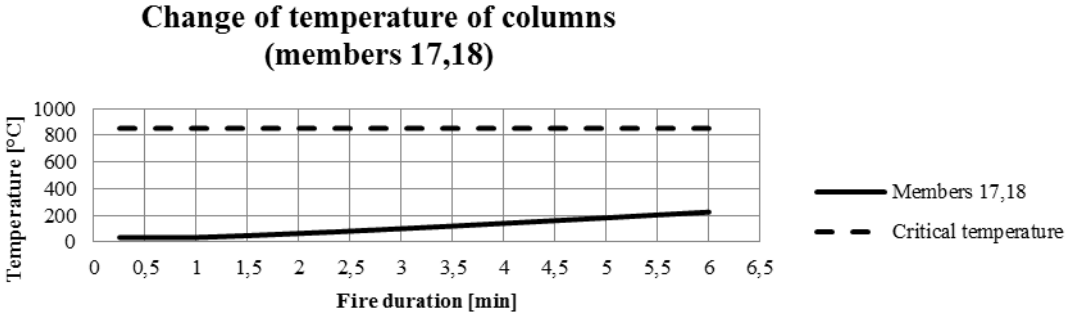

Fig. 12. The change of temperature of columns.

2.3. Material characteristics

The elevated temperature leads to weakness of steel, by decrease of yield strength and modulus of elasticity. According to Eurocode when temperature of fire gases reaches 200°C, the value of the modulus of elasticity start to decrease. Yield strength decreases when temperature of fire gases is higher than 400°C . The diagram below (Fig.13) presents change of modulus of elasticity for each member of analyzed structure.

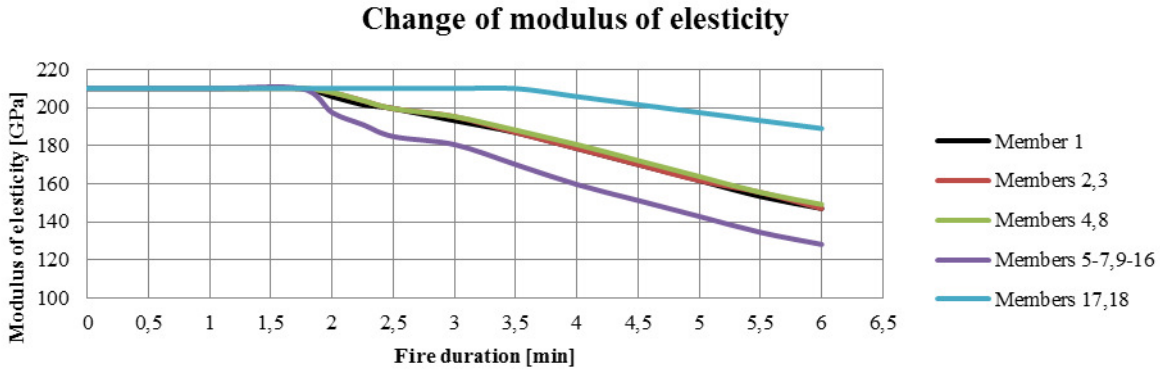

Fig. 13. The change of temperature of columns.

Change of yield strength isn't presented because only cross-braces and middle posts exceeded temperature of 400°C in the penultimate step, what doesn't influence significantly on the results.

3. Conclusions

Both effort and temperature analysis indicated that safety condition was exceeded after six minutes of fire duration. Then bars of top flange exceeded bearing capacity and critical temperature, whereas other bars held significant major of bearing capacity and reached lower temperature in comparison with critical temperatures for those bars. The bars of top flange had the biggest coefficient of utilisation of bearing capacity, what caused such low critical temperature (Fig.9). According to Eurocode critical temperature is inversely proportional to this coefficient.

The analyzed structure cannot work after plasticizing of top flange, so excess of bearing capacity and critical temperature in bars 2 and 3 causes that frame is not safe longer.

The most rapid changes of properties of steel occurs in bars 5-7 and 9-16 (Fig. 13). The less noticeable changes are observed in bars 17,18, what is connected with bigger cross-area than in other members. Both flanges and extreme posts act in similar way. Bar of bottom flange has a much bigger profile, but is heated from each side, whereas bars 2,3,4 and 8 are not.

In flanges, columns and extreme posts occurs both simultaneously tensile or compressing and bending. In the other bars only axial forces acts. In each type of bar the worsening of mechanical properties leads to decrease of bending, tensile and compressing strength. The effort shown in graphs 2-7 correspond to bearing capacity counted with accordance to Eurocode taking into account both bending and axial forces if it is needed. In case of compressed members also stability was checked. During analysis all forces acting at single member were counted. The most significant decrease in tensile strength occurred in cross-braces and middle posts (about 30-40%). This did not result in large increase of effort (Fig.5,6) because axial forces acting on these bars were very small.

Presented analysis unambiguously proves that fire analysis of steel structure is important issue that should be considered during design process to reach the best economy/safety ratio.

References

[1] BIEGUS A. , *The designing of steel structures by Eurocode 3. Fire safety of steel structures* (in Polish) Wrocław,2013

[2] SKOWROŃSKI W., *Theory of fire safety of steel structures* (in Polish) Warszawa,2011

[3] MAŚLAK M., *Fire durability of steel bar structures* (in Polish) Kraków, 2008

[4] MATHEJA M., *The plasticizing of steel structures under* fire (in Polish) Gliwice, 1999

SMARDZ P., *The determination of fire resistance of elements of structure by Eurocode* (in Polish) Fire protection

TRANSCOM 2015, 22-24 June 2015
University of Žilina, Žilina, Slovak Republic

Assessment of Track Superstructure Quality – Spot Method

[*]Michal Šmalo, [*]Libor Ižvolt
[*]University of Žilina, Faculty of Civil Engineering, Department of Railway Engineering and Track Management, Univerzitná 8215/1, 010 26 Žilina, Slovak Republic, michal.smalo@fstav.uniza.sk

Abstract. The quality of track alignment and track geometry is an essential precondition of safe and economical operation of railway track. The paper provides an analysis of diagnostics of relative track geometry parameters and evaluation of measurements deviations carried out by the spot method – gauge deviation (ΔRK) and cant (PK) for sections of the standard structure of railway superstructure, transition areas and sections with the slab track structure.

Keywords: Railway track, conventional railway superstructure, slab track, track geometry, diagnostics.

1. Introduction

There has been proven a standard structure of railway superstructure for many decades – from a structural point of view, the standard structure is referred to as a railway track whose track skeleton is stored in railway ballast. In the case of high line tonnage and axle load, increasing track speeds, it appears that such a structure has its operational and economical limits [1]. Standard structure of railway superstructure is characterized by "floating" placement of track skeleton, which causes the growth of dynamic forces during each passage of a train, which may be, and usually also are the cause of gradual degradation of track geometry. The elimination of irregularities in track geometry forces the operator in a period of time to remove deficiencies of track diagnosed by time and costly maintenance works. This phenomenon with increasing track speed grows, and thus increase the cost of maintaining and share of track possessions, which reduce the attractiveness of the track for a passenger. It is sufficient, however, if there is only replaced the weakest structural element of the standard railway superstructure in railway track, and the track ballast is another, more appropriate structural element, which shows no plastic behavior. The term slab track, as defined in [2], refers to such a structure of railway superstructure, in which a spread function of railway ballast is replaced by reinforced materials, and which is placed on a concrete or asphalt substructure (slab). Slab track structure consists of (top-down):

- track superstructure
  - rails and fastening of the rails to the rail support,
  - rail support (sleepers, single supporting points, pre-fabricated or monolithic slab),
  - concrete foundation layer (CFL) or asphalt foundation layer (AFL),
  - hydraulically bonded foundation layer (HBL);
- track substructure (if slab track construction is built on earthworks)
  - frost protective layer (FPL),
  - subsoil layers (consolidated or improved material of earthworks),
  - consolidated soil or bedrock.

2. Experimental section parameters

Experimental sections are situated on modernized double-track railway line Nove Mesto nad Vahom - Puchov and are located in areas of portals of the tunnel Turecky vrch. The track speed in both tracks is 160 km.h^{-1}, which ranks the railway line to the category of velocity zone No. 4

(RP4). Superstructure of each section is constructed as a construction with ballast bed and a slab track RHEDA 2000® (in tunnel, on bridges and on earthwork). The construction of the superstructure in the transition areas is constructed as improved ballast placed in concrete channel.

Monitoring of track geometry is aimed to determine condition of parts of the track structure and the track at all. This kind of monitoring is one of the basic diagnostics activities, in which is also monitored traffic and climatic load and the effect of maintenance on track skeleton.

The experimental track sections are labeled as [3]:

- section 1.1 (track No. 1, south portal of the tunnel Turecky vrch) and 2.1 (track No. 2, south portal; both sectors of length 175 m; km 102.360 000 – km 102.535 000):
  - km 102.360 000 – km 102.460 500 construction with ballast bed,
  - km 102.460 500 – km 102.480 500 construction with ballast bed in the concrete channel,
  - km 102.480 500 – km 102.535 000 slab track.
- section1.2 (track No. 1, north portal of the tunnel Turecky vrch) and 2.2 (track No. 2, north portal); both sectors of length 640 m; km 104.200 000 – km 104.840 000):
  - km 104.200 000 – km 104.720 500 slab track,
  - km 104.720 500 – km 102.480 500 construction with ballast bed in the concrete channel,
  - km 104.740 500 – km 104.840 000 construction with ballast bed.

3. Diagnostics methods and equipment

Diagnostic of track alignment design and track geometry realized by gauge-checkers ROBEL and GEISMAR. Each section No. 1.1 and No. 2.1 is for a comprehensive diagnostics represented by 288 fixation points and each section No. 1.2 and No. 2.2 is represented by 1 009 fixation points. Spot method is used to control deviations of gauge ΔRK (mm) and cant PK (mm) and monitoring is performed at each fastening point of the rail support [4].

4. Assessment of results of track alignment design and track geometry diagnostics by spot method

Assessment of results of track alignment design and track geometry by spot method is carried out according to valid technical standards and regulations [5]. Diagnostics of structure layout and track geometry of the track section:

- measurement before putting sections into operation (MSO) were made in period 10.07. – 11.7.2012, 2.10. – 3.10.2012,
- first operational measurement (PO1) 09.04. – 10.04.2013, 21.04 – 22.04.2013,
- second operational measurement (PO2) 08.10. – 09.10.2013, 21.10. – 22.10.2013,
- third operational measurement (PO3) 25.5.2014 and 28.5.2014,
- fourth operational measurement (PO4) 29.10.2014.

Measured parameters were evaluated according to limit input deviations for acceptance of works with use of new material (MSO) and according to operational deviations and limit operational deviations (PO1, PO2, PO3 and PO4) in *table 1*.

Results of measurement before putting sections into operation (MSO) has been compared to operational measurements (PO1, PO2, PO3 and PO4) and differences are shown in *table 2* [6]. Sections with the lowest quality shown by evaluation are section of track No. 1 in the area of southern portal and section of track No. 2 in the area of northern portal, where incidence of local errors is the highest. There is expected improvement of the quality of all sections after maintenance.

Progress of gauge deviation (ΔRK) and cant – differences between measurement before putting section into operation and operational measurements in each track and each section is shown in *fig. 1* to *fig. 8*.

Measured parameter	**Limit input deviations**		**Operational deviations**		**Limit operational deviations**		**Note**
***RK* (mm)**	-2	2	-3	5	-5	10	–
***ZR* (mm/m)**	2		3		4		–
***PK* (mm)**	-3	3	-6	6	-8	8	–
Measured parameter	**Limit value**		**Operational value**		**Limit operational value**		**Note**
***ZK* (1:*n*) (mm / base)**	1:250 (7,2; 4,0)		1:250 (7,2; 4,0)		1:167 (10,8; 5,99)		on measuring base 1.8 m
	1:832 (7,2; 1,20)		not evaluated		1:250 (24,0; 4,0)		on measuring base 6.0 m
	not evaluated		not evaluated		1:333 (36,0; 3,0)		on measuring base 12.0 m
Measured parameter	**Limit input relative deviations**		**Relative operational deviations**		**Limit operational relative deviations**		**Note**
***VL, VP* (mm)**	-3	3	-6	6	-8	8	–
***SL, SP* (mm)**	-3	3	-6	6	-8	8	–

Tab. 1. The deviations of the relative geometric parameters of the track for RP4 [5]

Track / section	**Differences of measurement ΔRK (mm)**								**Differences of measurement PK (mm)**							
	PO1–MSO		**PO2–MSO**		**PO3–MSO**		**PO4–MSO**		**PO1–MSO**		**PO2–MSO**		**PO3–MSO**		**PO4–MSO**	
	max.	min.	max.	min.	max.	min.	max.	min.	max.	min.	max.	min.	max.	min.	max.	min.
Track No. 1 / Section No. 1	1,2	-1,0	0,7	-1,0	2,1	-0,9	1,1	-1,0	0,6	-4,2	-1,1	-4,6	0,8	-3,1	-0,6	-4,7
Track No. 1 / Section No. 2	1,4	-1,0	0,7	-1,5	0,6	-1,8	0,9	-1,7	1,8	-2,0	1,1	-3,8	3,3	-4,4	1,4	-4,1
Track No. 2 / Section No. 1	0,8	-2,7	0,5	-2,5	0,5	-2,8	0,4	-1,5	1,6	-2,2	1,9	-3,2	1,7	-2,8	1,3	-3,4
Track No. 2 / Section No. 2	1,3	-1,3	2,0	-3,1	1,0	-3,6	1,2	-2,9	2,0	-4,5	2,2	-4,4	2,3	-4,9	1,2	-2,9

Tab. 2. Differences of measurement of ΔRK and PK – operational measurement (PO1, PO2, PO3, PO4) and measurement before putting sections into operation (MSO).

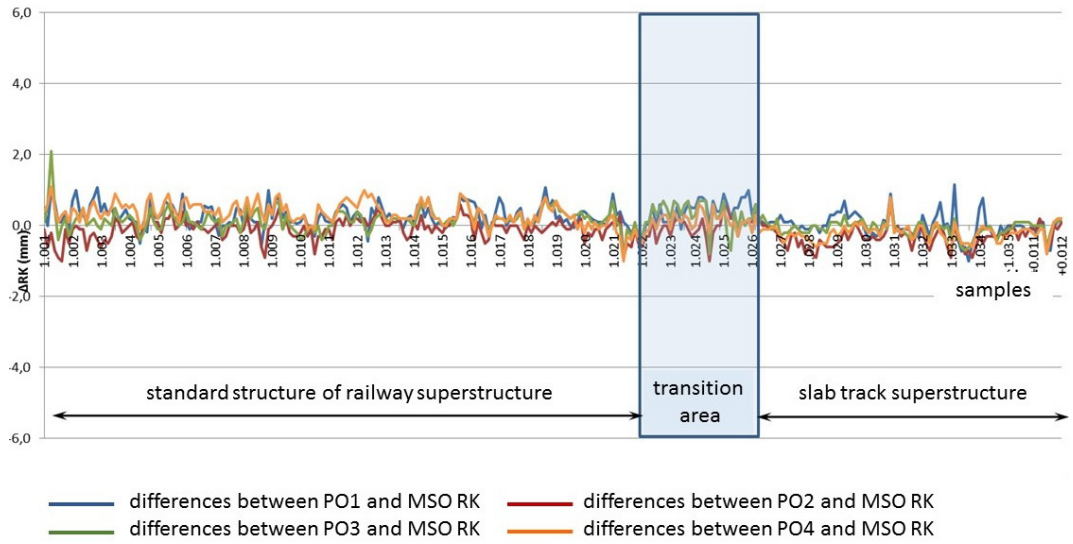

Fig. 1. Gauge deviation (ΔRK) – differences between measurement before putting section into operation and operational measurements - track No. 1, section No. 1 (southern portal); km 102.360 500 - km 102.535 000

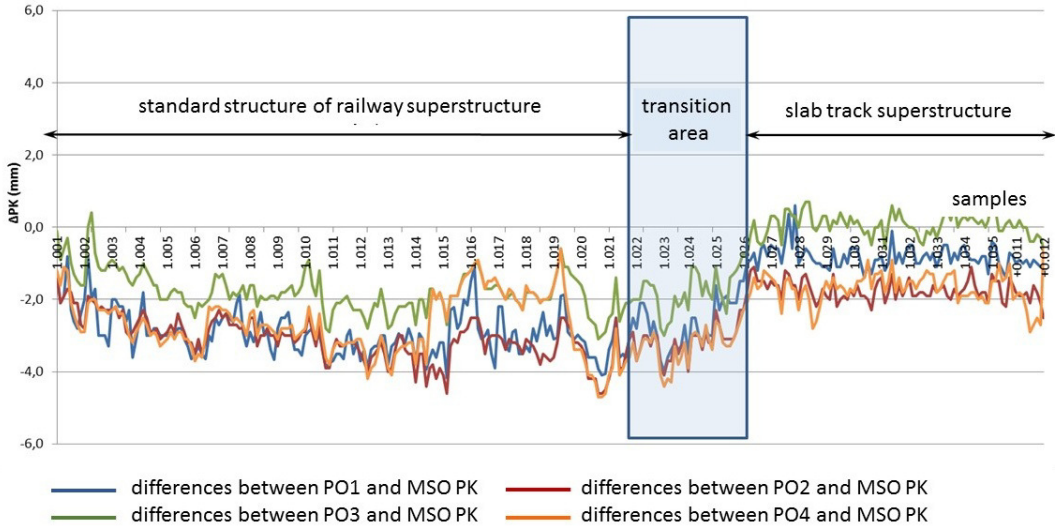

Fig. 2. Cant (PK) – differences between measurement before putting section into operation and operational measurements - track No. 1, section No. 1 (southern portal); km 102.360 500 - km 102.535 000

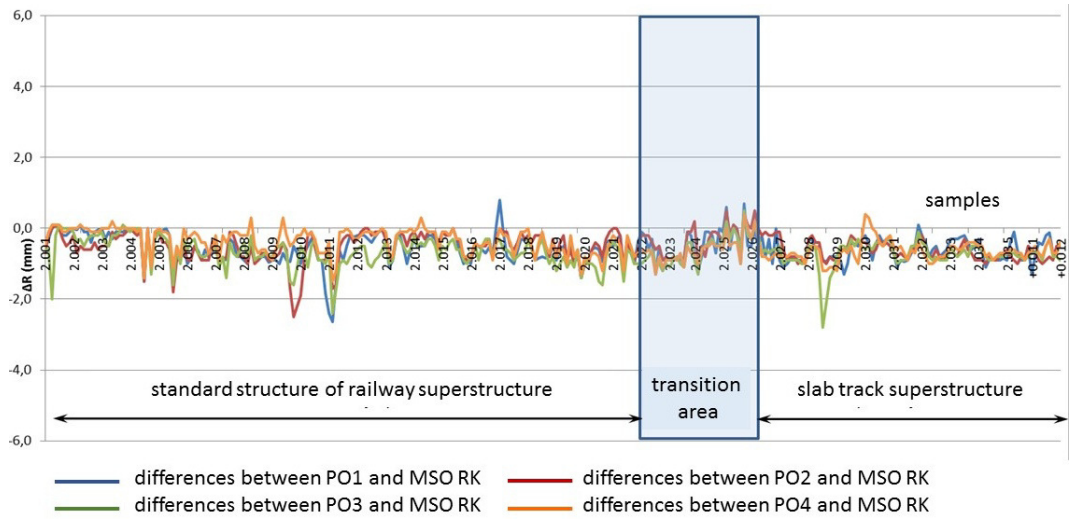

Fig. 3. Gauge deviation (ΔRK) – differences between measurement before putting section into operation and operational measurements - track No. 2, section No. 1 (southern portal); km 102.360 500 - km 102.535 000

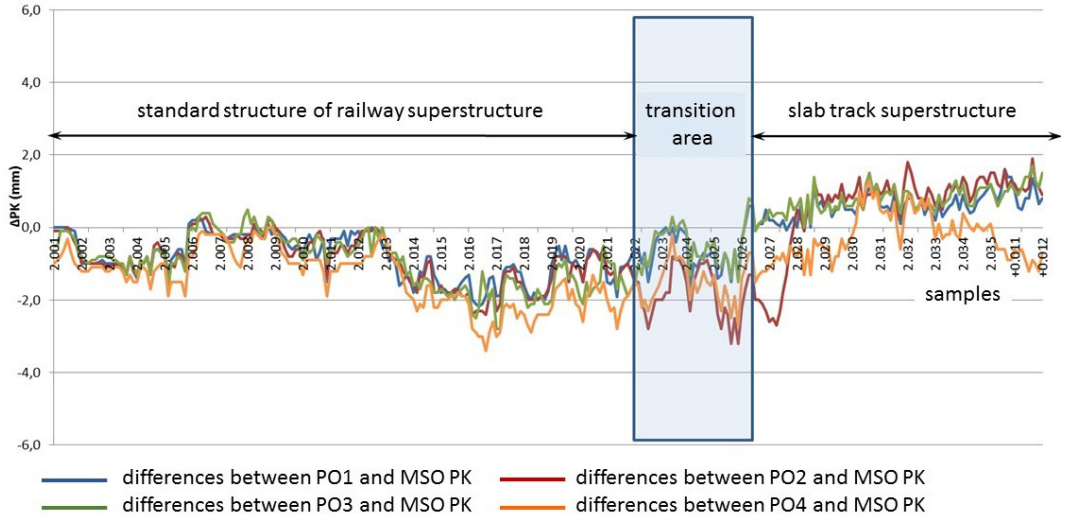

Fig. 4. Cant (PK) – differences between measurement before putting section into operation and operational measurements - track No. 2, section No. 1 (southern portal); km 102.360 500 - km 102.535 000

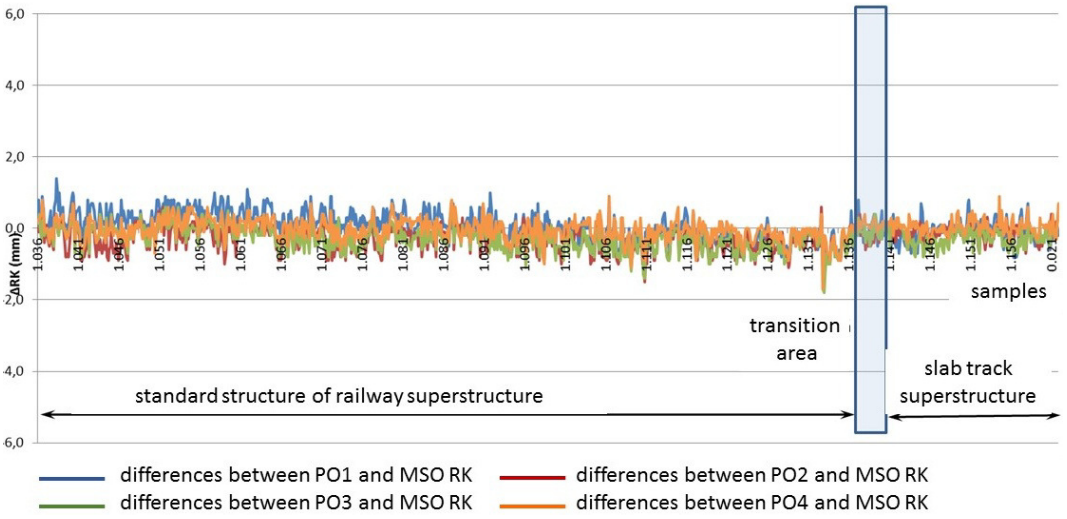

Fig. 5. Gauge deviation (ΔRK) – differences between measurement before putting section into operation and operational measurements - track No. 1, section No. 2 (northern portal); km 104.200 000 - km 104.842 000

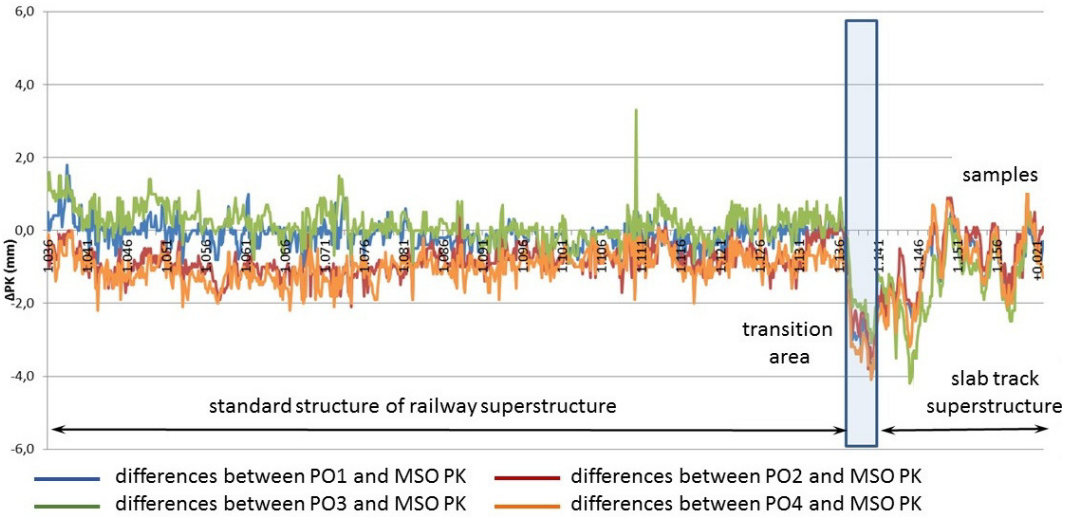

Fig. 6. Cant (PK) – differences between measurement before putting section into operation and operational measurements - track No. 1, section No. 2 (northern portal); km 104.200 000 - km 104.842 000

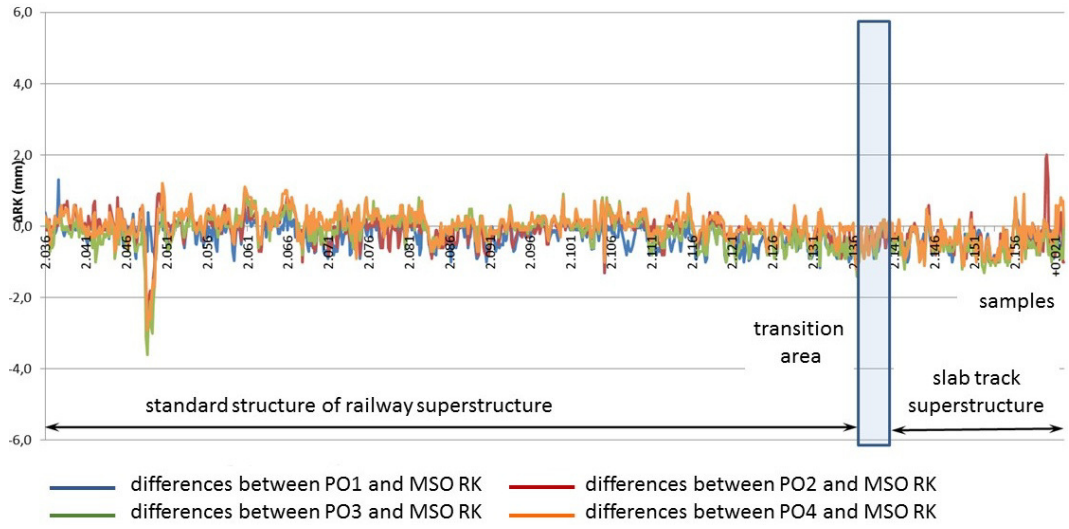

Fig. 7. Gauge deviation (ΔRK) – differences between measurement before putting section into operation and operational measurements - track No. 2, section No. 2 (northern portal); km 104.200 000 - km 104.842 000

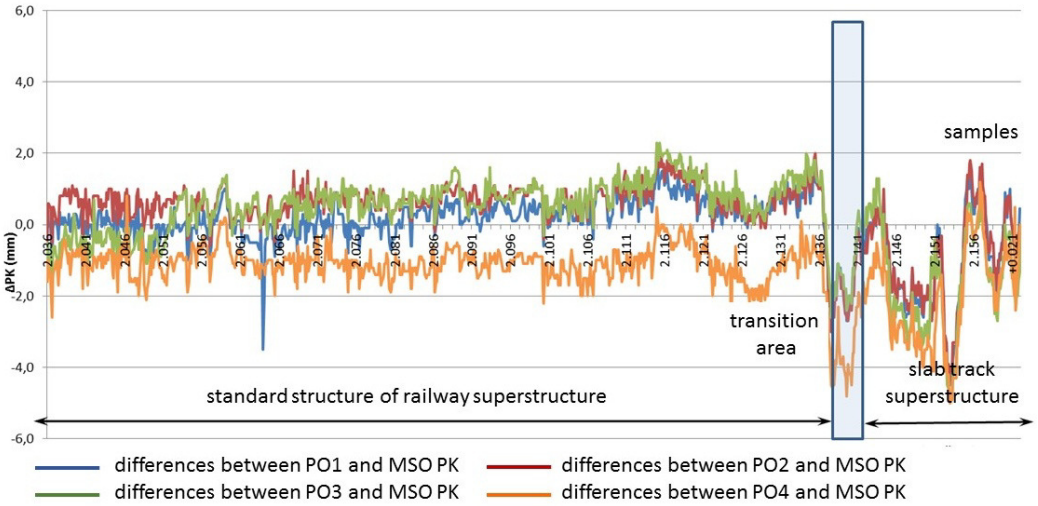

Fig. 8. Cant (PK) – differences between measurement before putting section into operation and operational measurements - track No. 2, section No. 2 (northern portal); km 104.200 000 - km 104.842 000

5. Conclusions

An essential precondition for the competitiveness of rail transport is the reliable operation of the railway lines, considering the technological understanding, it means a safer and more stable movement of vehicles along the track – rail. The development and validation of a number of technical solutions of slab track in the longer term can ensure the quality of the track geometry parameters, reduce maintenance costs, extend the service life of structure and increase the competitiveness and attractiveness of railway lines. On the basis of experimental measurements made so far, it is possible to expect that further development of the monitoring of track alignment design and track geometry in experimental section confirms the relevance of the applications of slab track to the tracks, which are standard, not only on the tracks for higher or high speeds.

Acknowledgement

There are partial results of the grant VEGA 1/0597/14"Analysis of methods used to measure the unconventional railway track construction from the point of view of accuracy and reliability" in the paper.

This paper was created with the support of the project "Supporting of quality education and research in the field of transport as the engine of the economy" (ITMS: 26110230076), supported by the Education Operational Program funded by the ERDF.

References

[1] IŽVOLT, L. – ŠMALO, M.: *Historical Development and Applications of Unconventional Structure of Railway Superstructure of the Railway Infrastructure of the Slovak Republic*, In: Civil and Environmental Engineering. Volume 10, Issue 2 (2014). EDIS, University of Žilina, 2014. ISSN 1336-5835, Žilina.

[2] ZSR SR 103-8 (S) *General requirements for the design, construction, repair, maintenance and acceptance of construction repair and maintenance works on the slab track construction* (in Slovak), GR ZSR, 2012

[3] ŠESTÁKOVÁ, J.: *Quality of Slab Track Construction – Track Alignment Design and Track Geometry*, In: Civil and Environmental Engineering. Vol. 11, Issue 1. EDIS, University of Žilina, 2014. ISSN 1336-5835, Žilina, 2015.

[4] IŽVOLTOVÁ, J. – ŠESTÁKOVÁ, J.: *Analysis of the Impact of Traffic Load on the Slab Track Construction* (in Slovak). Geodézia a kartografia v dopravě. XII. Mezinárodní konference, Olomouc, 04.09. – 05.09.2014. Praha: Český svaz geodetů a kartografů, 2014, ISBN 978-80-12-02553-5.

[5] STN 73 6360 *Track Alignment Design and Track Geometry of Normal-gauge Tracks*, SÚTN Bratislava, 1999 and *Amendment 1*, SÚTN Bratislava, 2002.

[6] IZVOLT, L. et al.: *Monitoring of Sections of Non-conventional Constructions of the Railway Superstructure and the Transition Areas - 5th and 6th Stage. ZSR Modernization of Railway Track Nove Mesto nad Vahom - Puchov, km 100.500 to 159.100, part 24-32-01 Nove Mesto - Trencianske Bohuslavice* (in Slovak), Zilina: KZSTH: SvF: University of Zilina, 03/2014

TRANSCOM 2015, 22-24 June 2015
University of Žilina, Žilina, Slovak Republic

Geosynthetic reinforced soil bridge abutments on the bridge across the stream Pavlovski potok in Slovenia

[***]Jure Šuler, [**]Matevž Kralj, [**]Samo Peter Medved, [*]Stanislav Lenart,
[*]Slovenian National Building and Civil Engineering Institute (ZAG), Dimičeva ulica 12, 1000 Ljubljana, Slovenia, {stanislav.lenart}@zag.si
[**]Lineal d. o. o., Jezdarska ulica 3, 2000 Maribor, Slovenia, {matevz.kralj, samo.medved}@lineal.si
[***]University of Ljubljana, Faculty of Civil and Geodetic Engineering, Department of Civil Engineering, 2nd cycle master study - Structural Engineering, Jamova 2, 1000 Ljubljana, {js9849}@student.uni-lj.si

Abstract. The bridge across the stream Pavlovski potok is a part of investment into Modernization of railway line Pragersko – Hodoš, the biggest investment in infrastructure in Slovenia at the moment. Its design was accompanied with very short deadlines and difficult foundation conditions with deep layer of soft foundation soil. Therefore reinforced concrete abutments of nearby railway bridge were founded on deep pile foundations. Short deadlines and limited budget have forced authors of this paper to find alternative solution. Deep pile foundations were substituted by shallow foundations made of compacted fill material reinforced with geosynthetics. From laboratory test results, which were obtained within the research project »Raziskovalni vavčer«, basic characteristics of building materials for geosynthetic reinforced soil bridge abutments as well as deformation properties of typical reinforced soil were obtained. Those data were used for later design of the abutments. The procedure for retaining structure construction without using temporary support system was used for construction of bridge abutments from reinforced soil. Partial pre-stressing and increased stiffness of reinforced soil were obtained in that way. Monitoring system to enable further optimization of this kind of structures was established on the bridge that was completed by the end of 2014.

Keywords: Reinforced soil, geosynthetics, GRS bridge abutments, deformation, compacted fill

1. Introduction

A conventional short span (up to 50 m) type bridges are normally constructed whether as frame structures or as a single girders supported by a pair of abutments via fixed, hinged or moveable shoes. In order to provide smooth transition from and towards the superstructure, bridge approach slabs are usually constructed on the top of unreinforced embankments. In the traditional type bridge abutment (reinforced concrete cantilever structure) large internal moment and shear forces are mobilized due to the soil pressure on its back. Pile foundation often becomes necessary to prevent any kind of movements and settlements, but a bump behind a bridge may still be formed due to uneven settlements of abutment and approach embankment. Construction and maintanance of those types of structures are also generally costly. Due to many drawbacks of conventional construction type other technologies have been successfuly used for construction of approach embankments in the last few decades, especially geosynthetic reinforced soil technology, enabling construction of much steeper embankment slopes. Bridge abutments can also be constructed.

Shortly after Vidal firstly presented the Terre Arme patent in the world of geotechnical engineering [1], the reinforced soil retaining structures had been constructed also in Slovenia ([2], [3], [4], [5]), mainly to support highway road embankments. Technology has been mainly used for building noise barriers in the last decade in Slovenia. With further research and development of modern polymer geosynthetics, geogrids (reinforcement for cohesionless soils) and geotextiles (reinforcement for cohesive soils), reinforced soil technology also improved in a way of being able to limit deformation in geosynthetics to very small values ([6], [7], [8]).

Research projects of Slovenian companies („Raziskovalni vavčer") in 2013 and 2014, was co-funded by the Slovenian Ministry of Education, Science, Culture and Sport in cooperation and co-fundation of European Union. Within the available funds of the research project some preliminary research and necessary laboratory tests have been performed by Slovenian National Building and Civil Engineering Institute (ZAG) on initiative of Lineal, d. o. o. in order to obtain all required data for design of reinforced soil bridge abutments [9].

First idea to design reinforced soil bridge abutments in Slovenia was already presented when designing a bridge over stream Lipnica [10], but the project was not realized. However, at the end of 2014, the design of new bridge over the stream Pavlovski potok, accompanied with very short deadlines and deep layer of soft foundation soil, offered a chance to use theory and laboratory tests results in practice. Bridge was finished in December 2014.

2. General information of the bridge across Pavlovski potok in Žerovinci

The bridge across the stream Pavlovski potok in Žerovinci is a part of investment into Modernisation of railway line Pragersko – Hodoš, the biggest investment in infrastructure in Slovenia at the moment. In order to maintain roads and local traffic infrastructure the municipality of Ormož have made an investment into construction of the bridge on the public way 802501 across Pavlovski potok. In a case of high water levels an existing bridge was constantly flooded due to its box shaped culvert insufficient throughput capacity.

Due to solution provided by designer, an existing bridge was demolished and replaced by reinforced concrete slab, supported by a pair of geosynthetic reinforced soil bridge abutments. Range between the facings of the abutments is 5,50 m wide. Since the crossing of the stream and the road is not perpendicular (crossing under 114°), parallelogram-shaped slab was chosen for the design of reinforced concrete superstructure. Cross-section of the bridge is shown in Fig. 1.

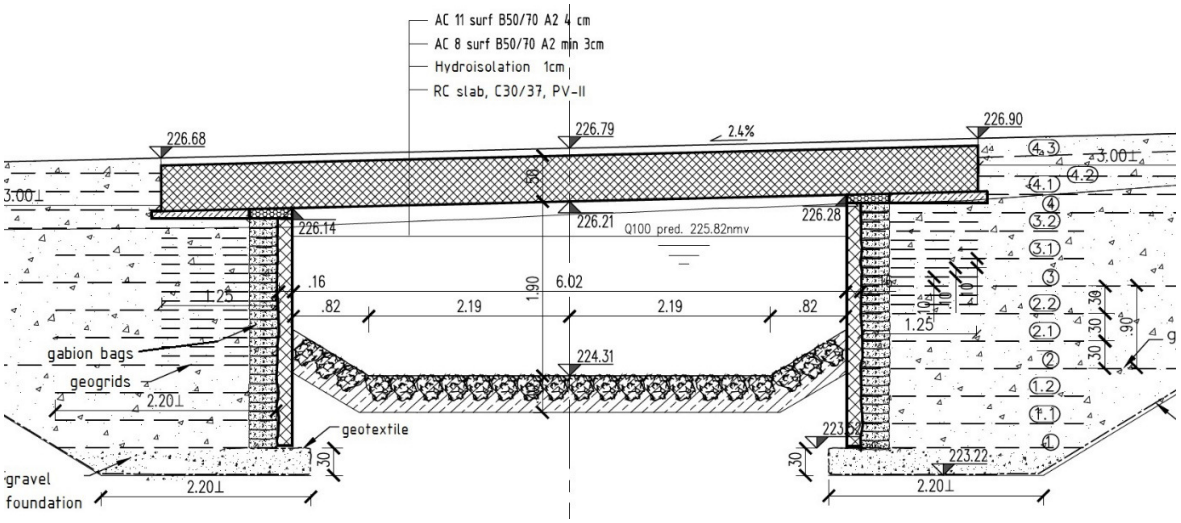

Fig. 1: Cross-section of new designed bridge supported by reinforced soil abutments

Any preliminary geological-geotechnical investigation of the ground has not been made for the exact location of the bridge in particular. Instead, all available data and results, evaluated from investigation of another bridge, positioned 50 m upstream and supported by deep foundations using piles, have been taken into consideration. Standard penetration test results have also been evaluated for the same structure [11]. Tab. 1 summarizes geological-geotechnical data for upstream bridge.

Bridge design and construction, presented in this paper, comprises reinforced concrete simple supported slab, supported by geosynthetic reinforced soil bridge abutments as shown in Fig. 2. Construction type used represents an effective way of reducing construction time and costs, eliminating the need of using heavy machinery as well as alleviating the bump behind the bridge, formed due to differential settlements [10].

Depth [m]	Description	Soil properties
0.0 – 0.5	sandy gravel	c'= 0 kPa, φ'=36°
0.5 – 3.0	sandy clay with inclusions of gravel and sand	c'= 17,5 kPa, φ'=23,9°
3.0 – 5.0	clayey and silty sand	c'= 1,6 kPa, φ'=25,7°
5.0 – 8.0	silty sand	c'= 1,6 kPa, φ'=25,7°
8.0 – 11.0	decayed stratified mart	c'= 5 kPa, φ'=25°
11.0 – 17.0	sandy mart	c'= 0 kPa, φ'=39°
17.0 – 23.3	sandy-silty clay	c'= 17,5 kPa, φ'=23,9°
23.3 – 26.3	sandy mart - solid	
Water level depth: 2.7 m		

Tab. 1: Geological – geotechnical data available, evaluated from investigation of 50 m upstream bridge

3. Preliminary laboratory testing

Within the available funds of the research project (Raziskovalni vavčer) some preliminary research and necessary laboratory tests have been performed by Slovenian National Building and Civil Engineering Institute (ZAG) in order to obtain all required data for design of reinforced soil bridge abutments.

In the first phase of testing, basic characteristics of building materials (granularity, compaction of backfill material, geosynthetic tensile strength) and their interaction (soil-geosynthetic interface strength) were obtained.

In second phase results from large scale laboratory test have been evaluated to obtain deformation properties of typical reinforced soil. Formwork outer shell was first positioned as a support for further construction of the prismatic shaped composite specimen (910 mm x 910 mm x 2130 mm) of well compacted granular backfill and intermediate layers of geosynthetic reinforcement. After construction, formwork was removed from the surface of internally stable specimen. Vertical load has then been continuously applied on the top of the specimen in order to evaluate its stress-strain relation (Fig. 2 and Fig. 3). Laboratory test results can be properly applied to in-situ conditions.

Fig. 2: Geosynthetic reinforced soil laboratory specimen during loading test

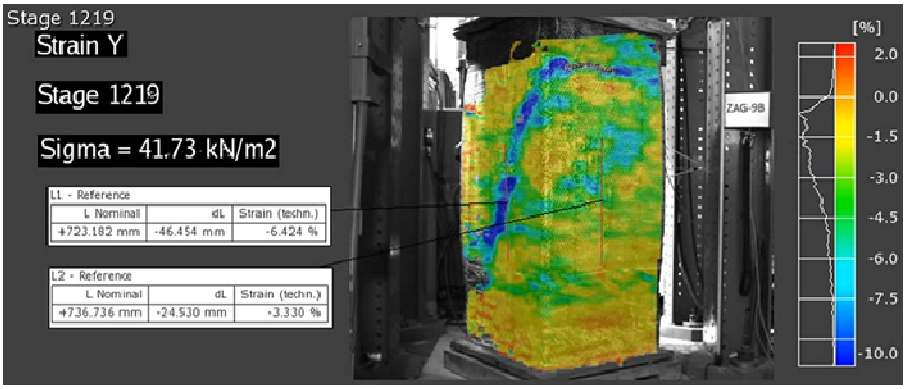

Fig. 3: Optically measured (GOM Aramis) vertical deformation of the collapsing GRS specimen

Other important properties (stiffness in a case of very small deformation, maximum shear resistance, initial load curve and stiffness after unloading and reloading) have also been taken into consideration due to their significant influence on a behavior of composite material when used for construction of bridge abutments.

4. Implementation

Firstly, foundations of the abutments were constructed using well compacted gravel material, wrapped in geosynthetic to prevent moisture infiltration, followed by construction of geosynthetic reinforced soil mass of bridge abutments. Individual layers of geosynthetics (Miragrid GX 80/80, nominal tensile strength - 80 kN/m, elongation at nominal strength - 10%) have been installed at vertical distances of 30 cm, with intermediate layers at critical positions (under the bridge seat), where vertical distance of 10 cm have been used.

Bearing direction of geosynthetic layers was always positioned perpendicular to the facing structure in order to provide adequate behavior of the abutment. The procedure for retaining structure construction without using temporary support system was used for construction of bridge abutments from reinforced soil [6, 8]. Partial pre-stressing and increased stiffness of reinforced soil were obtained in that way. Firstly, geosynthetics are wrapped around the gabion bags (Fig. 4), then the backfill material is built-in and being compacted until required density is achieved.

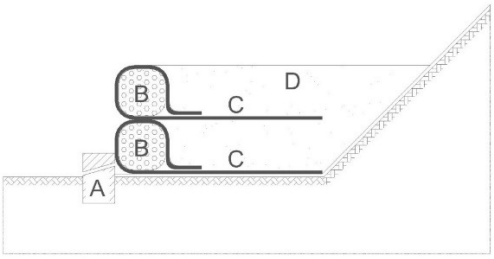

Fig. 4: Procedure for retaining structure construction without using temporary support system (B – gabion bags, C – geosynthetic layers, D – backfill material) [6, 8]

Both GRS bridge abutments have been constructed in less than 10 days due to simple construction processes. Since the bridge was crossing the water, reinforced concrete facing of 15 cm in depth was chosen to be constructed in order to prevent scouring of GRS mass. Horizontal layers of geosynthetic reinforcement were rigidly connected to the vertical reinforcement in the facing structure by using additional stripes (anchors). Concrete facing structures were constructed using appropriate formworks and cast in place concrete. Superstructure was placed directly on top of the bridge abutments via thin layer of concrete embedment (bearing width). In order to provide scour protection, rip-rap structure (rocks in concrete) has also been constructed as a channel for the stream, extending for another 5 m from each side of the abutments. One of the construction phases of the GRS bridge abutments is shown in Fig. 5.

Fig. 5: Construction of the GRS bridge abutments

5. Observations, cognitions and field monitoring

In order to provide further research of the abutments, some of the installed geosynthetic layers were equipped with strain gauges. Strain values in the geosynthetic layers could be directly obtained at construction site and have already been properly recorded and monitored before and during installation as well as during construction of the abutments. Monitoring will also take place in the future, considering the impact of different types of loads on the behavior of GRS abutments.

Until the end of construction approximately 1/3 (1.5 cm) of the final expected settlement has already been measured. In a case of pile foundation the rest of the settlement would probably be formed as differential settlements behind the bridge, but on the contrary this is not expected in a case, presented in this paper. In order to monitor any potential formation of uneven settlements in the future, horizontal inclinometers were installed in both abutments.

A lot of useful information and data have been obtained during construction of the first bridge, supported by GRS abutments in Slovenia, as listed below.

5.1. Foundations

Considering geological structure of the ground on the construction site, in case of conventional type bridge abutments deep pile foundations of diameter 100 cm and length of 24 m would be necessary as in the case of nearby bridge, positioned 50 m in upstream direction. Geosynthetic reinforced soil technology has significantly reduced construction costs and time.

5.2. Concrete works

Piles, pile girders, reinforced concrete abutments, wing walls and approach slabs become unnecessary in a case of using GRS technology, which significantly reduces the required quantity of concrete. Research for the bridge across the stream Pavlovski potok has been made and the results obtained show that in a case of reinforced concrete abutments almost 120 m^3 of additional concrete would be used in comparison to geosynthetic reinforced soil abutments.

Less concrete quantity also results in less formwork quantity. But despite that only one side formwork is required to construct facing structure of the GRS abutment, implementation is far more complex since strong foundation to support formwork is not available.

In order to provide the same thickness of facing structure (15 cm) across the whole height of the abutment, gabion bags must be placed in completely vertical direction with no or very little deviation. Due to relatively thin reinforced concrete facing structure additional problems may apply when vibrating cast in place concrete if the facing of gabion bags is poorly constructed. As alternative also self-compacted concrete could be used as in case, presented in this paper.

5.3. Static design

Since superstructure is constructed as a single slab, directly supported by a pair of GRS abutments, internal moment line is much lower in comparison with frame structures. Consequently more reinforcement is needed in the lower zone and less in the upper zone. Also larger span length is required in order to provide sufficient bearing width for the superstructure.

5.4. Construction time

Construction time of the GRS abutments is significantly reduced due to simple construction processes and techniques in comparison to reinforced concrete abutments. GRS bridge abutments could be constructed within few days or weeks without being influenced by outside weather conditions. Considering the Slovenian legislation, concrete bridge superstructures have to be constructed in conventional way using formworks, reinforcement placing and cast in place concrete. Using precast concrete superstructures is not allowed in Slovenia, otherwise construction time would be even shorter. In a case of high water levels pumping from the construction pit is required.

6. Conclusion

First bridge with geosynthetic reinforced soil abutments in Slovenia has been constructed across the stream Pavlovski potok in Žerovinci at the end of 2014. Its design was accompanied with very short deadlines and deep layer of soft foundation soil, where deep pile foundations would become necessary in case of conventional construction type of the abutment, using reinforced concrete. Knowledge and experiences gained from design and construction of the project, presented in this paper, show many significant advantages of the geosynthetic reinforced soil bridge abutments in comparison to conventional reinforced concrete cantilever structures. However, also some potential hazards need to be taken into consideration in order to ensure proper design and construction of geosynthetic reinforced soil bridge abutments.

Acknowledgements

Authors of this paper would like to give special thanks to Slovenian Ministry of Education, Science, Culture and Sport, which enabled the research and development of the presented technology by co-funding research projects of Slovenian companies (“Raziskovalni vavčer”) in 2013 and 2014. Special thanks also go to construction company Pomgrad, d. d., which constructed the bridge with expertise and constructive approach.

References

[1] VIDAL, H. *Reinforced Earth*, Annales de I'Institut Technique du Batiment et des Travaux Publics, Paris (1972).

[1] BATTELINO, D. *10 years of reinforced soil retaining structures in Slovenia*. Gradb. Vestn., 39, št. 9/10/11, str. 261-270 (1990). (*Source is in Slovenian language)*

[2] BATTELINO, D., VILHAR, M., ŽMAVC, J. *Reinforcing soils*. Ljubljana: Faculty of architecture, civil and geodetic engineering: Republic community for roads, professional service: Slovenija ceste tehnika: KOTO - KOTRADE; Brestanica: Novoles - Sigmat; Mengeš: Tekstil - Filc, 31 str. 1981. (*Source is in Slovenian language)*

[3] MAJES, B., LOGAR, J., BATTELINO, D. *Reinforcement of soft soils under road embankments.* Acta geotech., št. 98/101, str. 1-17 (1989).

[4] PROKOP, B., BATTELINO, D. *Model test of reinforced soil*, Razprave prvega posvetovanja slovenskih geotehnikov, Bled 93 (1993). (*Source is in Slovenian language)*

[5] TATSUOKA, F., TATEYAMA, M., UCHIMURA, T., AND KOSEKI, J. *Geosynthetic-reinforced soil retaining walls as important permanent structures*, Mercer Lecture, Geosynthetic International, Vol.4, No.2, 81-136 (1997).

[6] LENART, S., KOSEKI, J., MIYASHITA, Y., SATO, T. *Large-scale triaxial tests of dense gravel material at low confining pressures*, Soil and foundation, Vol. 54, Issue 1, str. 45-55 (2014).

[7] LENART, S. *Procedure for retaining structure construction without using temporary support system*, patent SI 24321A (2014). (*Source is in Slovenian language)*

[8] LENART, S. *Final report of development of reinforced soil bridge abutments*, P 320/13-710-8, Oddelek za geotehniko in prometnice, Zavod za gradbeništvo Slovenije, 30 str. (2014). (*Source is in Slovenian language)*

[9] LENART, S., TATSUOKA, F., MEDVED, S.P., KRALJ, M. *Bridging objects with reinforced soil bridge abutments*., 11. slovenski kongres o cestah in prometu, DRC, Družba za raziskave v cestni in prometni stroki Slovenije (2012). (*Source is in Slovenian language)*

[10]ŠTERN, K. *Report of soil investigation and geotechnical project*, PGD, Geoinženiring, 9/31 (GMM 6683-10/10) (2010). (*Source is in Slovenian language)*

TRANSCOM 2015, 22-24 June 2015
University of Žilina, Žilina, Slovak Republic

Influence of Creep on the Results of Crack Width for Loaded Reinforced Concrete Beams

[*]Justyna Tworzewska
[*]Kielce University of Technology, Faculty of Civil Engineering and Architecture, Department of Strength of Materials and Concrete Structures, al. Tysiąclecia Państwa Polskiego 7, 25-314 Kielce, Poland, j.tworzewska@tu.kielce.pl

Abstract. The paper presents the influence of creep on the measurement results of the crack width and deflection. Creep occurs in concrete even at very low stress. When measuring the width of cracks with traditional method - Brinell microscope, increase of force must be stopped. It was shown that 7-10 minutes influence of constant load is enough to reveal the effect of creep. An example of analysis was performed on two reinforced concrete beams with symbols R2M-1 and R2M-2. The analysis was possible due to use of modern testing equipment – the 3D optical scanner. The device allowed to measuring the crack width and deflection at the beginning and end of each load increment downtime. It has been shown that in those studies creep resulted in an increase of 8.2% in the average perpendicular crack width, whereas the average deflection increase was 4.4%.

Keywords: reinforced concrete, crack, creep, beam, system ARAMIS.

1. Introduction

Formation of cracks in concrete elements is a natural phenomenon, as they result from the low tensile strength of concrete. Understanding the development process of cracks is a very important feature because of its impact on the durability. The greater the width of the cracks, the easier penetration of the external environment into the element takes place. Thus, the corrosion of the reinforcement proceeds faster. The main problem with durability is environmental impact on construction [1]. Use of the Brinell microscope is a traditional method of measurement of the crack width perpendicular to the axis of the element. This method brings together a number of limitations in the performance of measurements during laboratory research. In laboratory studies of reinforced concrete beams, to measure the crack width the increase of force must be stopped and kept at a constant level. Consequently, creep affects the results of the crack width at a given level of force, and this influence cannot be eliminated. The development of technology makes possible to overcome those barriers by equipping laboratories with modern equipment. One such device is a 3D optical scanner with the Aramis system that allows measurements on a continuous basis. Possibility of using the scanner for testing concrete elements was presented in the works [2,3,6]. The aim of this paper was to present an analysis of the effect of creep on crack width and deflection using the results obtained from the scanner.

2. The 3D optical scanner with ARAMIS system

The 3D optical scanner type ARAMIS allows the measurement of deformations and displacements in three directions, which are performed in a non-contact way [3,4]. The principle of operation of the 3D optical scanner is based on Stereophotogrammetry. The scanner consists of a set: the tripod equipped with two cameras, and a central unit computer with software that allows calculation of the deformation of the test surface. Figure 1 shows the test stand for reinforced concrete beam with scanner tripod prepared for measuring.

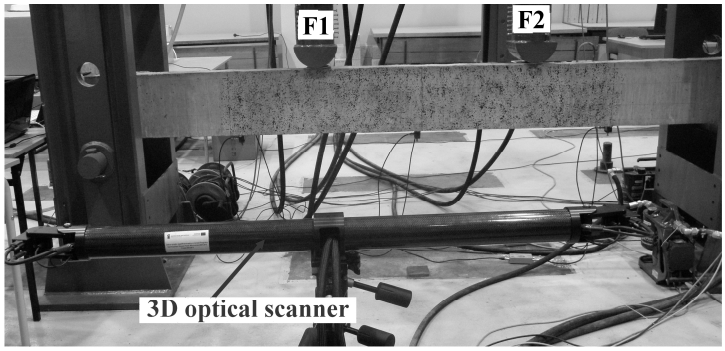

Fig. 1 Test stand.

Calibrated device allows for obtaining the measurements on the test surface, elaboration of data with ARAMIS software and creating reports with results. Deformation calculated by the program can be presented as strain map (Figure 2).

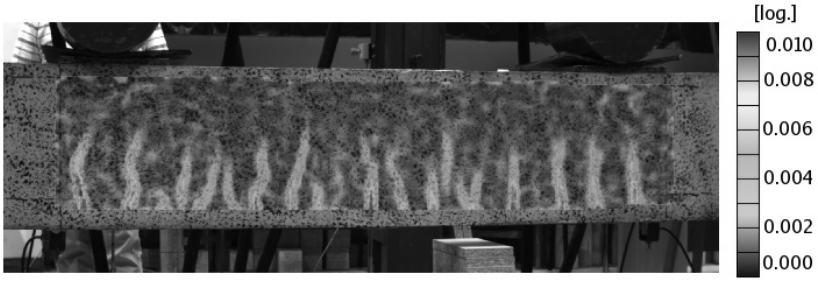

Fig. 2 Deformation map obtained with the use of the 3D optical scanner

Due to the fragile nature of the work of concrete visible accumulations of deformation in Figure 2 correspond to the cracks of reinforced concrete beam. The width of cracks is calculated as the change in length of the segment comprising a single accumulation of strain. Measurements of the perpendicular crack width are carried out at the height of center of gravity of the reinforcement in the tension zone.

3. Research elements

The paper presents the results for the two beams with symbols R2M-1 and R2M-2. The beams with dimensions 120x300x3300mm were made of concrete class C40/50 and steel BS500. The construction of the reinforcement for tested beams, with a ratio of longitudinal reinforcement of 2% is shown in Figure 3.

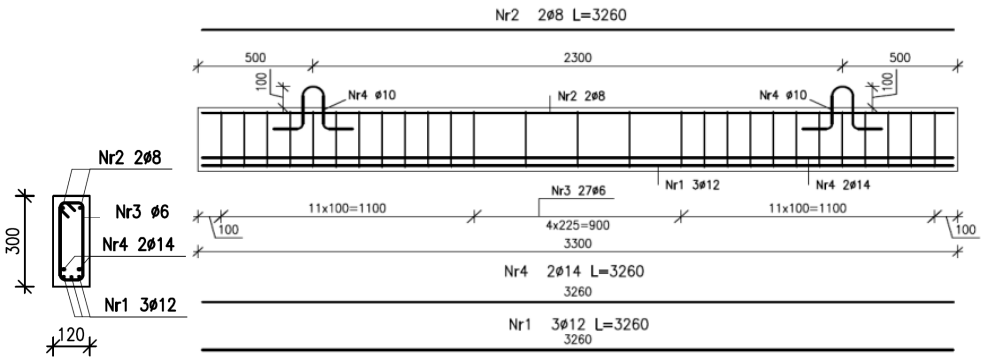

Fig. 3 Reinforcement scheme

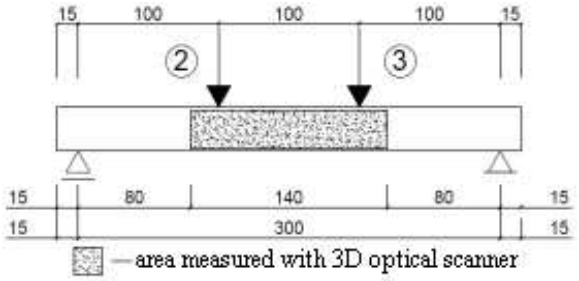

Fig. 4 Static scheme of beam with the selected measurement area

The beams were loaded with two concentrated forces, as shown in Fig. 4. Such method of load allows for getting the constant moment value in the middle section of the beam - pure bending. The analysis of cracks formation and development was carried out in this area of the beam with the use of the 3D optical scanner. The load has been programmed as increasing with downtimes. Force-time graph is shown in Figure 5. During the downtimes lasting about 7-10 minutes, the crack width was measured at the beginning and at the end of it, with the use of scanner. During the increment of load lasting about 30 seconds, images were taken every 1 second.

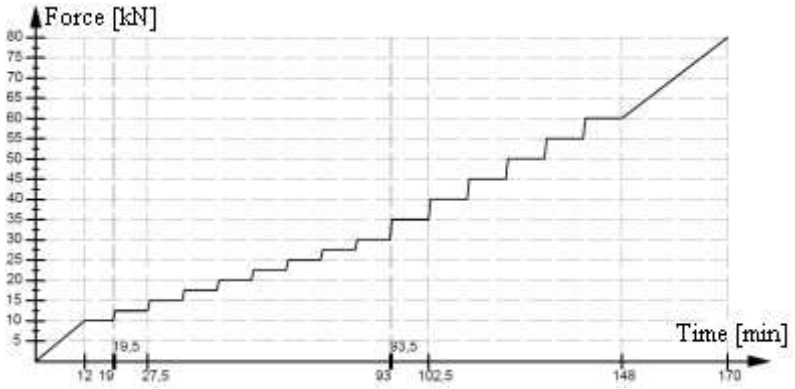

Fig. 5 Force-time graph for the tested beams

4. Analysis of the effect of creep on crack width

The creep is progressive increment of deformation in time occurring under the influence of constant load applied to the element. Creep occurs in concrete at very low stress values [5], so the analysis was performed in a wide range of loads.

Image was taken at the beginning and at the end of the downtime at each level of the force downtime. It helped to confirm the occurrence of creep, which is visible in the growth of the crack width, despite of the constant load. The results of measurements are shown in Figure 6 and Table 1. The graph shows the average width of cracks determined for both tested beams. Horizontal dashed line shows the value of the width of the crack – 0.05 mm, adopted as the minimum value. The results are shown for the force up to 60kN, because there was the last downtime in force increment as shown in Figure 5.

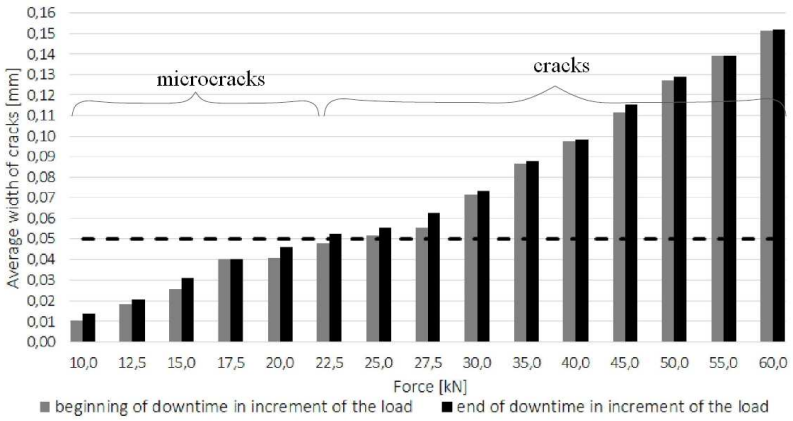

Fig. 6 The average cracks width for both beams at the beginning and at the end of the load increment downtime

Table 1 shows the mean value of the cracks width at the specified load level, measured at the beginning and at the end of load increment downtime, and the increase in the width of cracks because of creep. Figure 6 and Table 1 show that during the 7-10 minutes downtime the crack width tends to increase significantly. The average increase in the average width of the cracks in the process of loading achieved 0.003 mm, which amounts to 8.2%.

Force [kN]	Average cracks width [mm]		The increase in the crack width [mm]
	beginning of downtime in increment of the load	end of downtime in increment of the load	
10,0	0,010	0,014	0,004
12,5	0,019	0,021	0,002
15,0	0,026	0,031	0,005
17,5	0,040	0,040	0,000
20,0	0,040	0,046	0,006
22,5	0,048	0,052	0,004
25,0	0,051	0,055	0,004
27,5	0,055	0,063	0,008
30,0	0,071	0,073	0,002
35,0	0,086	0,088	0,002
40,0	0,097	0,098	0,001
45,0	0,112	0,115	0,003
50,0	0,127	0,129	0,002
55,0	0,139	0,139	0,000
60,0	0,151	0,152	0,001

Tab. 1 The results of the variation of the average cracks width for the downtime in load increment

In order to confirm the occurrence of creep, graph of deflection for beam R2M-2 in the middle of the span was drawn. The phenomenon of cracks and deflection are closely related. The larger the crack width, the greater the deflection and vice versa. In places of downtime in load increment deflection increases, as illustrated in Figure 7. The increase in deflection translates into an increase in the average crack width. Table 2 shows the increment of deflection for selected values of strength. The average increase at different stages of loading reached 4.4%.

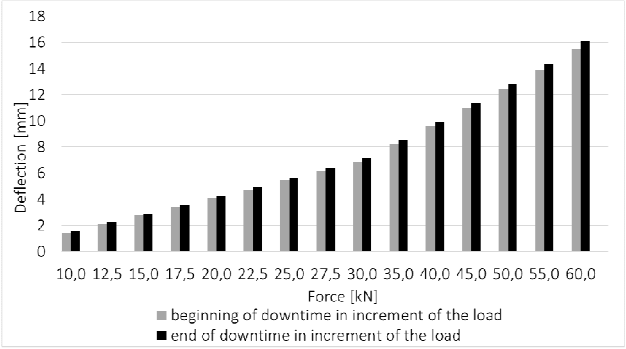

Fig. 7 The increase in deflection for the downtime in load increment - R2M-2 beam

Force [kN]	Deflection in the middle of the span of the beam [mm]		The increase of deflection [mm]	The increase of deflection [%]
	beginning of downtime in the load	end of downtime in the load		
10	1,44	1,51	0,07	4,9
12,5	2,07	2,25	0,18	8,7
15	2,75	2,93	0,18	6,5
17,5	3,41	3,59	0,18	5,3
20	4,06	4,23	0,17	4,2
22,5	4,73	4,95	0,22	4,7
25	5,44	5,67	0,23	4,2
27,5	6,14	6,35	0,21	3,4
30	6,83	7,13	0,30	4,4
35	8,23	8,53	0,30	3,6
40	9,59	9,94	0,35	3,6
45	11,01	11,34	0,33	3,0
50	12,42	12,81	0,39	3,1
55	13,89	14,37	0,48	3,5
60	15,52	16,06	0,54	3,5

Tab. 2 The results of deflection in the mid span of the beam for downtime in load increment

5. Conclusions

The use of the 3D optical scanner made possible to estimate the influence of creep on the results of studies related to the analysis of the development of cracks in reinforced concrete beams. The influence of creep caused:

- for deflections - an average increase of 4.4%,
- for perpendicular cracks width - the increase in the average cracks width of 8.2%.

It can be concluded that creep affects the crack width of reinforced concrete beams, which was confirmed by the results of the increase in deflection during breaks in the load.

The presented results were obtained from study of two beams. Cracking process is a highly random phenomenon in reinforced concrete elements; therefore, the more extensive study needs to be carried out. For a more detailed analysis, to assess the impact of creep on crack width in the process of loading, more samples should be examined.

References

[1] AJDUKIEWICZ A. *Beton a środowisko – zasady projektowania konstrukcji betonowych z uwagi na trwałość i wpływ na środowisko*. Materiały konferencyjne AWARIE BUDOWLANE 2011, tom 1 s.23-38.

[2] AJDUKIEWICZ C., GAJEWSKI M., MOSSAKOWSKI P. *Zastosowanie systemu optycznej korelacji obrazu „Aramis" do identyfikacji rys w elementach betonowych*, Logistyka, 6/ 2010, s. 27-34.

[3] GOLEWSKI G. L. *Wykorzystanie systemu Aramis do analizy propagacji rys pierwotnych w betonach z dodatkiem popiołów lotnych*. Przegląd Budowlany 11/2010 str. 30-35.

[4] GOSZCZYŃSKA B., TRĄMPCZYŃSKI W., BACHARZ K., BACHARZ M., TWORZEWSKA J., TWORZEWSKI P. *Doświadczalna analiza odkształceń przestrzennych belek żelbetowych z zastosowaniem skanera optycznego 3D*. Inżynieria i Budownictwo 3/2014 str. 156-159.

[5] NEVILLE A.M. *Właściwości betonu*. Polski Cement, Kraków 2000.

[6] TWORZEWSKI P., TWORZEWSKA J., GODOWSKA M., BACHARZ K. *An application of a 3D optical scanner to reinforced concrete elements analysis.* Transcom 2013, Section 7 Civil Engineering, s.333-336.

TRANSCOM 2015, 22-24 June 2015
University of Žilina, Žilina, Slovak Republic

Errors during Manufacturing of Reinforced Concrete Beams at the Example of Concrete Cover Deviations

[*]Paweł Tworzewski
[*]Kielce University of Technology, Faculty of Civil Engineering and Architecture, Department of Strength of Materials and Concrete Structures, al. Tysiąclecia Państwa Polskiego 7, 25-314 Kielce, Poland, ptworzewski@tu.kielce.pl

Abstract. This paper presents an attempt to assess the impact of the workmanship quality at the thickness of concrete cover in reinforced concrete beams. The analysis is based on the inventory of reinforcing bars performed for 43 tested beams. The elements were made in the precast factory and all errors were made at the stage of manufacturing of those elements. Concrete cover deviations were analyzed in specific locations in the beam cross-section. The presence of values, which exceed the permissible deviations, was found based on the distribution of the values. The deviations appeared mainly in the lower part of concrete cover thickness in reinforced concrete beams.

Keywords: beam, concrete, reinforcement, durability, concrete cover, manufacturing errors

1. Introduction

The problem of durability for buildings is closely linked with the quality of workmanship, which unfortunately is not always satisfactory at every stage of their realization. Swiss concluded in their study [3] that 80% of construction failures resulted from mistakes made by people. Those include, for example, the errors that appeared during the design phase, which mainly are connected with the use of incorrect models and errors occurring during manufacturing of elements of construction. Incorrect execution arises mainly due to insufficient quality control. Research of Building Research Institute [4] underlines that the most frequently reinforced concrete structures are damaged due to lack of reinforcing bars, incorrect spacing between bars and deformed bars. Such errors significantly decrease the durability of reinforced concrete structures, especially when they cause concrete cover deviations.

The concrete cover provides the best protection against corrosion of reinforcement on condition that it is properly executed. In addition to the appropriate properties of concrete [5], particularly important is the thickness of concrete cover. Too small thickness is associated with more rapid diffusion of damaging compound and accelerates the corrosion of reinforcement. It is assumed that during the lifetime of the construction reinforcement should not corrode, because that may cause reduction in area of cross-section of bars and lower the capacity of the structure [6, 7].

Improper distribution the longitudinal reinforcement bars also affects the distribution of stiffness in the element, causing deformations. In reinforced concrete beams, it can lead to warping of element [2].

In the present study, the attempt to assess the quality of workmanship of reinforced concrete beams, based on the thickness of the concrete cover, was carried out. The analysis is based on the elements studied in the framework of the realized Research Project.

2. Description of studies

The subject of the study were 43 single and double span reinforced concrete beams with the distance between supports axis respectively 3.00 m and 6.00 m with cross sections of 0.12×0.30 m.

Reinforcement scheme in each beam was different. The elements were made in precast factory. In order to verify the correctness of rebar deployment an inventory was carried out. Elements were hammered in the mid-span of beam, and then the position of the reinforcement was determined. Examples of inventory results are shown in Figure 1. Deviations in the position of the reinforcing bars were not planned. These errors were made at the stage of manufacturing of elements in the precast factory.

The results of the real position of the reinforcing bars were used to determine the concrete cover thickness in selected areas, which were shown in Figure 2, where:

- c_d - concrete cover at the bottom of the cross-section of the beam in the tension zone,
- c_{d1}^L, c_{d1}^P - concrete cover on the left and right hand side of the cross-section of the beam in the tension zone for the first row of reinforcing bars,
- c_{d2}^L, c_{d2}^P - concrete cover on the left and right hand side of the cross-section of the beam in the tension zone for the second row of reinforcing bars,
- c_g - concrete cover on the top of the cross-section of the beam in the compression zone,
- c_g^L, c_g^P - concrete cover on the left and right-hand side of the cross-section of the beam in the compression zone.

Concrete cover deviation Δc_i was calculated using the results of the real thickness of the concrete cover and the thickness defined in the project.

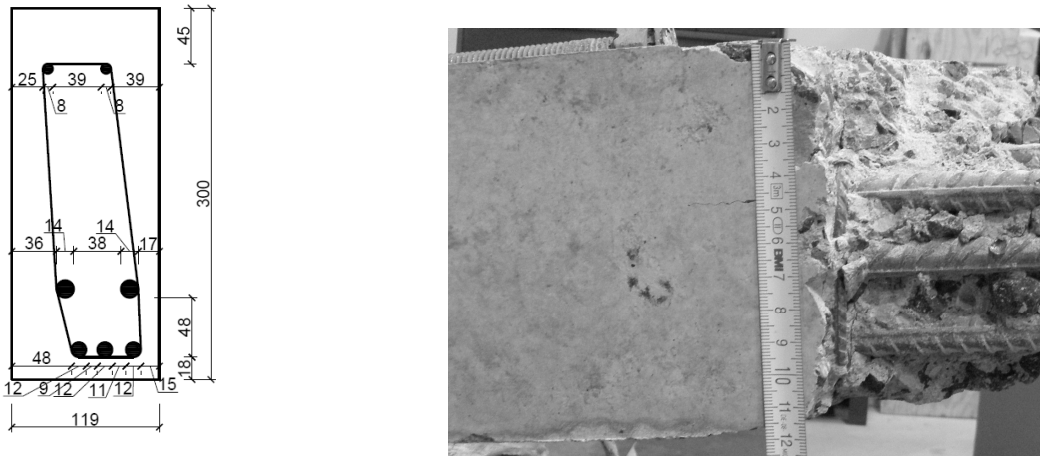

Fig. 1. Example of reinforcement scheme after stocktaking.

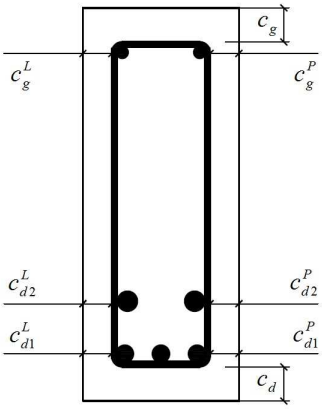

Fig. 2. Scheme of determining the real thickness of the concrete cover.

3. Results

The following values were calculated in order to determine the quality of workmanship of the elements in terms of the proper protection of reinforcement against corrosion using result of Δc_i concrete cover deviations:

- $\overline{\Delta c}$ - mean value of the concrete cover deviation,
- $\Delta c_{\max}$ - maximum value of the concrete cover deviation,
- $\Delta c_{\min}$ - minimum value of the concrete cover deviation,
- s - the standard deviation of the concrete cover deviation,
- ν - variance.

Deviations, which were negative and reduce the thickness of the concrete cover received the "-" sign, while increasing or positive the "+" sign. Obtained values were summarized in Table 1. Histogram and box plot were prepared in order to analyze the distribution of concrete cover deviations (Figure 3). The calculated deviation values were in the range from -12 mm to 22 mm. The largest number of values concentrated within the range from 0 to 5 mm. The results asymmetry was noticeable. The greater part of the deviations was within the range from -5 mm to 0 mm.

$\overline{\Delta c}$ [mm]	$\Delta c_{\max}$ [mm]	$\Delta c_{\min}$ [mm]	s [mm]	ν [%]
2,16	22,00	-12,00	6,41	41,04

Tab. 1. Parameters calculated to assess the workmanship quality of the concrete cover in beams.

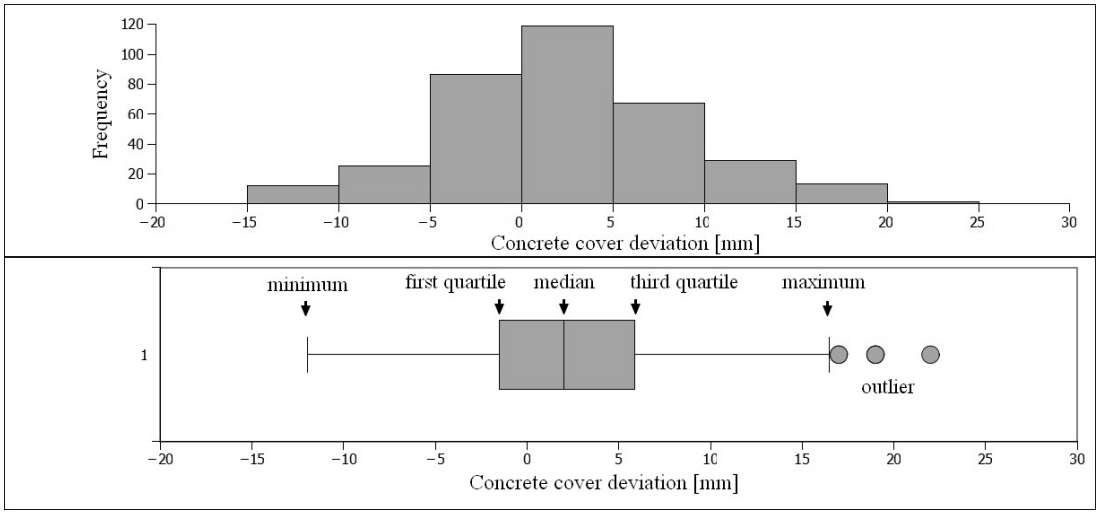

Fig. 3. Distribution of the concrete cover deviations.

According to the guidelines of EN 13670 [1] for the elements with dimensions similar to the tested beams and tolerance class 2, negative deviation should not exceed 13 mm and -10 mm while positive. Unfortunately, in the case of calculated values of deviations, part of the results exceeded the limits. These were mainly negative deviations. Graph in figure 4 was prepared in order to analyze how deviations changed depending on the position in the cross-section. The deviation Δc^P was the sum of the deviations for the right-hand side of the cross-section, which included deviations Δc_{d1}^P, Δc_{d2}^P and Δc_g^P. A similar situation took place for the deviation Δc^L. Box plot in Figure 4 marked Δc, included all calculated deviations. Most disturbing results were obtained for the concrete cover deviations on the right and left-hand side of the cross-section of the beam in the

tension zone: Δc_{d1}^{P}, Δc_{d2}^{P} and Δc_{d1}^{L}, Δc_{d2}^{L}. The distribution of results for these deviations was the largest and included a large range of negative values, which were reducing the thickness of the concrete cover.

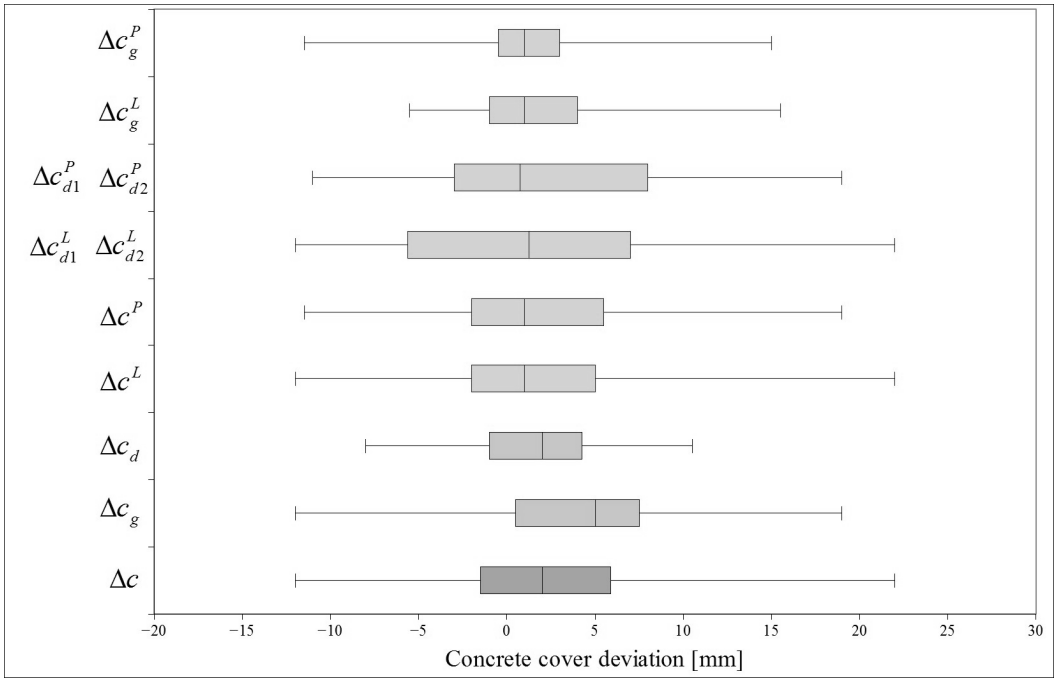

Fig. 4. Box plots of concrete cover deviations in selected areas

4. Conclusion

Based on the results it can be concluded that a large part of the reinforced concrete beams was not manufactured properly. This resulted from exceeding the permissible deviations of concrete cover, and the high value of the coefficient of variation. Significant exceeding the positive deviations indeed increase the thickness of the cover, but for the bottom and the top cover, it can result in reducing load capacity of the cross section of the beam. The greatest distribution of the values was observed in the case of the side concrete cover, protecting tension reinforcement. Occurrence of large negative deviations for this cover is particularly undesired. Insufficient protection of tension reinforcement is associated with the accelerated corrosion. The decrease in the cross-sectional area of the bars may result in failure of the structure.

Acknowledgement

Work was done under the Project NR 04 0007 10.

References

[1] EN 13670**:** Execution of concrete structures

[2] Goszczyńska B., Trąmpczyński W., Tworzewski P.: Analiza wpływu rozmieszczenia prętów zbrojeniowych na deformacje i obraz zarysowania belki żelbetowej, Budownictwo i Architektura, 2014, nr 13(3), s. 87-94,

[3] Matousek M., *Massnahmen gegen Fehler im Bauprozess*. ETH Zürich -Birkhuser Verlag, Basel etc. January 1982,

[4] Pawłowski W., Przewłocki S., Procedury pomiarowe dla potrzeb diagnostyki obiektów budowlanych, Zeszyty Naukowe Politechniki Łódzkiej, nr 715, Budownictwo, z. 45, 1994, s. 69-84,

[5] Raczkiewicz W., Grzmil W., Ocena betonu jako otuliny stali zbrojeniowej, Przegląd Budowlany, nr 5, 2014, s. 56-58,

[6] Ściślewski Z., Ochrona Konstrukcji Żelbetowych, Arkady, Warszawa 1999,

[7] Zybura A., Metody zapewniania trwałości budowli na przykładzie budownictwa betonowego, 54 konferencja naukowa Komitetu Inżynierii Lądowej i Wodnej PAN oraz Komitetu Nauki PZITB, tom IV, 2008, s. 235-252.

TRANSCOM 2015, 22-24 June 2015
University of Žilina, Žilina, Slovak Republic

Simulation of Motion of Vehicle Quarter Model Along the Road Unevenness

*Veronika Valašková, *Jozef Melcer,
*University of Žilina, Department of Structural Mechanics, Univerzitná 8215/1, 010 26 Žilina, Slovak Republic, {veronika.valaskova, jozef.melcer}@fstav.uniza.sk

Abstract. Vehicle excitation by passing along road unevenness represents the actual problem which is being solved at many departments at this time. Road unevenness represents the surface of transport structures subjected to dynamic effects of moving vehicles. Number of effects influences the values of vehicle tire forces. Unevenness located on the road represents one of the most important attribute that affects the magnitude of tire forces. Number of data can be obtained by experimental measurement or by numerical simulation. This article shows the results of numerical simulations in the form of vehicle response and tire forces with respect to unevenness located on the road.

Keywords: numerical simulation, dynamic load, pavement, quarter model of vehicle, computing model, road unevenness

1. Introduction

The roads and the transport structures are subjected to direct dynamic effects of moving load. Unevenness on the surface of the pavement is the main source of kinematic excitation of vehicle. It significantly effects the size of the tire forces between the pavement and vehicle. This is the reason to deal with it. The dimension of road unevenness is the higher order then pavement deflection or tire unevenness. So it is fully reasonable to take into account the unevenness located on the road only as a source of kinematical excitation of vehicle. The real load acting on the roads is variable in time and in frequency composition. This should be known for the solution of many engineering tasks as lifetime, design, reliability, structure development, micro tremor, etc. The successful resolution to the problem usually consists of theoretical and experimental solution. One of the most important part of the process of numerical simulation is to create a proper computing model. The equations of motion describing the computing model of the system are solved in time domain and consequently can be analyzed in frequency domain. For this case the quarter model of TATRA 815 lorry was chosen (Fig.1).

2. Numerical model of vehicle

Important step for proper simulation is to choose the computing model of vehicle. Model has to be represented with appropriate mathematical formulation. Quarter model is usually preferred and used for 1D analysis as a combination of mass, spring and damping elements (Fig.1). This discrete model of the vehicle with finite degrees of freedom makes solution easier from the mathematical point of view. The equations of motion are written in the form of ordinary differential equations.

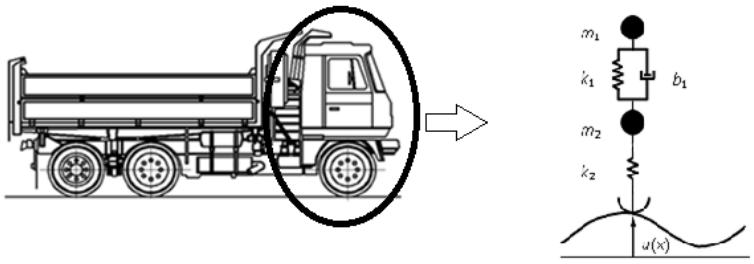

Fig. 1. Quarter model of lorry T 815

The main characteristic of the quarter model is defined by three diagonal matrices. They are the mass $\{m\}$, stiffness $\{k_i\}$ and damping $\{b_i\}$ matrices which contain experimentally measured values [1]. The mass-less degree of freedom corresponds to the vertical movements of the point in contact with the surface of the roadway. Vibration of the mass objects of the quarter model are described in two functions of time: $r_i(t)$, i=1,2. The mass-less degree of freedom is coupled by the tire force $F(t)$ acting at the contact point located on the road. The equations of motions and the expressions for the tire forces have following form:

$$\ddot{r}_1(t) = \{-k_1[r_1(t) - r_2(t)] - b_1[\dot{r}_1(t) - \dot{r}_2(t)]\}/m_1 \quad (1)$$

$$\ddot{r}_2(t) = \{+k_1[r_1(t) - r_2(t)] - k_2[r_2(t) - u(t)] + b_1[\dot{r}_1(t) - \dot{r}_2(t)]\}/m_2 \quad (2)$$

$$F(t) = -G + k_2 . [r_2(t) - u(t)]. \quad (3)$$

The numerical parameters of the model are as follows:
Constants of stiffness of the coupling members: k_1 = 143 716.5 N/m, k_2 = 1275 300.0 N/m.
Constants of damping: b_1 = 9 614.0 kg · s^{-1}.
Mass model parameters: m_1 = 2 930.0 kg, m_2 = 455.0 kg.

Numerical simulation is based on mathematical Runge Kutta 4 order method. Runge Kutta 4 order method has been used since computers calculation started as one of the possible way to find solution on systems of differential equations. This method is very adaptable and useful for engineering solution. This method is based on the Taylor series function, but indirectly that we did not determine the value of derivatives of functions - these are approximate calculation functions in appropriately selected strategic points. Their general scheme is of the form:

$$y_{i+1} = y_i + \frac{1}{6}(k_1 + 2k_2 + 2k_3 + k_4)h \quad (4)$$

$$k_1 = f(t_i, y_i), \quad (5)$$

$$k_2 = f\left(t_i + \frac{1}{2}h,\ y_i + \frac{1}{2}k_1 h\right), \quad (6)$$

$$k_3 = f\left(t_i + \frac{1}{2}h,\ y_i + \frac{1}{2}k_2 h\right), \quad (7)$$

$$k_4 = f(t_i + h, y_i + k_3 h). \quad (8)$$

As a result, the time is discredited and the solution is given in a form of the functional values that are defined for each geometrical point in every time step. It is very important to choose the right value of the time step.

3. Numerical model of road surface unevenness

Road unevenness represents surface of transport structures subjected to dynamical load of moving vehicles. The dimension of road unevenness is the higher order then pavement deflection or tire unevenness. The rigid pavement with random road profile is assumed for the purpose of numerical solution. The random unevenness in the road $u(x)$ is assumed as stationary ergodic function with zero mean value and normal distribution. The properties of the road random profile are described by Power Special Density (PSD) function in following form:

$$S_u(\Omega) = S_u(\Omega_0)\left(\frac{\Omega}{\Omega_0}\right)^{-k}, \quad (9)$$

where Ω in [rad/m] denotes the wave number, Ω_0= 1 rad/m is the reference wave number and the waviness k =2. Depending to the international directive ISO 8608 [2], typical road profiles can be grouped into classes from A to E. Each class has your own reference values $S_u(\Omega_0)$. Then a random road profile of single track can be approximated in following form:

$$u_{(x)} = \sum_i^N \sqrt{2S(\Omega_i)\Delta\Omega}\cos(\Omega_i x + \varphi_i) \quad (10)$$

where φ_i is the uniformly distributed phase angle and x is the length coordinate. The random road profile u on the base of known power spectral density for the values $S_u(\Omega_0) = 4\cdot10^{-6}$ [m^2/(rad/m)] [2]. Extreme values of unevenness are following:
u_{MAX}= 0.0183769 mm, u_{MIN}= -0.02148554 mm, $\Delta u = u_{MAX} - u_{MIN}$ = 0.03986244 mm.

The load profile was generated with a time step 0.0001 m with adjustable length 0.01 m = 1 cm. Total length of road profile of unevenness was L =102.4 m, Fig.2.

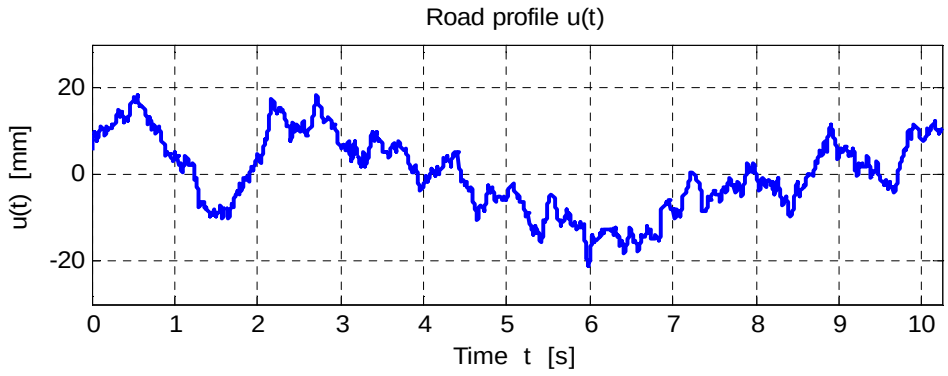

Fig. 2. Random road profile $S_u(\Omega_0) = 4\cdot10^{-6}$ [m^2/(rad/m)]

4. Results of numerical solution

The numerical simulation of vehicle motion along random road profile was performed. The model of vehicle moves at the constant speed V = 36 km/h,(10 m/s) along the random road profile. The response of vehicle was calculated at each time step. The kinematic excitation is caused by the movement of vehicle along the road unevenness. The response of vehicle is the time function of vertical deflection $r_1(t)$ of upper mass (m_1) Fig.3, the time function of vertical deflection $r_2(t)$ of lower mass (m_2) Fig.4, and the time function of the tire force $F(t)$ Fig.5.The conclusion exemplifies the main results and the fundamental ideas presented in the paper.

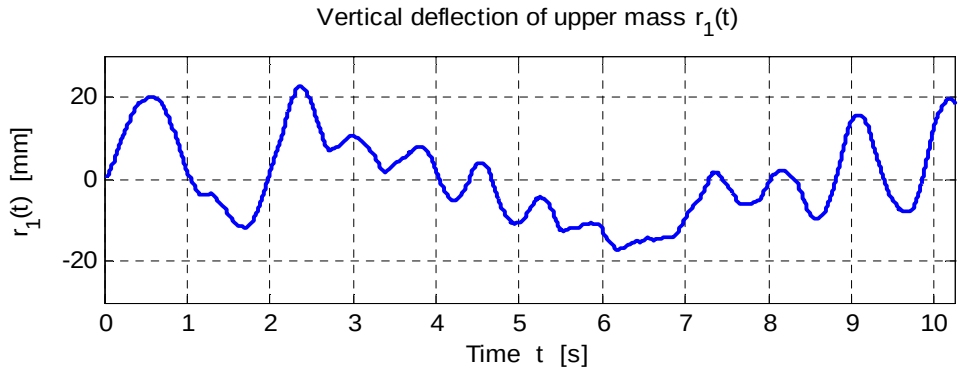

Fig. 3. Time history of upper mass deflection, constant speed V = 36 km/h

The time function of vertical deflection of upper mass of vehicle is shown in Fig.3. The maximum deflection is: r_{1MAX}= 22.781 mm. The minimum deflection: r_{1MIN}= -17.034 mm. The amplitude fluctuation of upper mass is: $\Delta r_1 = r_{1MAX} - r_{1MIN}$ = 39.815 mm.

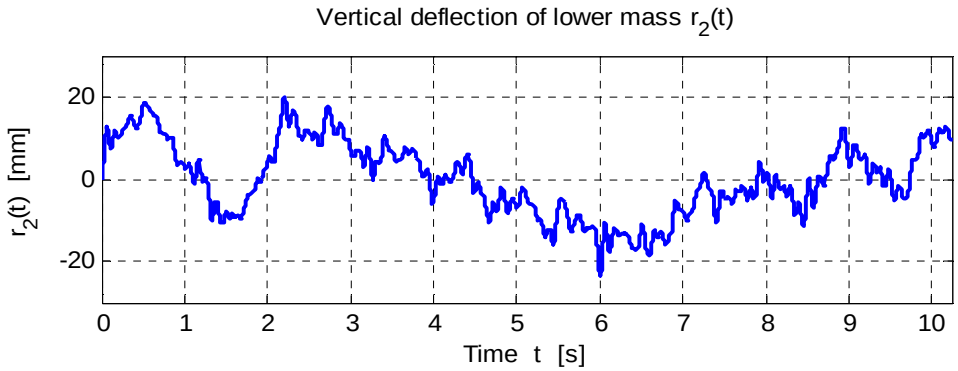

Fig. 4. Time history of lower mass deflection, constant speed V = 36 km/h

The time function of vertical deflection of lower mass of vehicle is shown in Fig.4. The maximum deflection is: r_{2MAX}=19.785 mm. The minimum deflection: r_{2MIN}=-23.507 mm. The amplitude fluctuation of lower mass is: $\Delta r_2 = r_{2MAX} - r_{2MIN}$ = 43.292 mm.

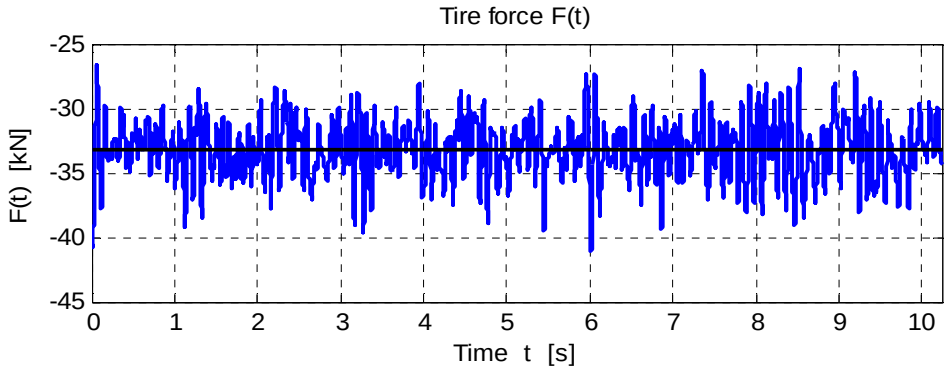

Fig. 5. Time history of tire force, in constant speed V = 36 km/h

Extreme values of tire forces are following (Fig.5): F_{MAX} =-41.128 kN, F_{MIN} =-26.712 kN, $\Delta F = |F_{MAX}| - |F_{MIN}|$ = 14.416 kN.

5. Conclusions

There are many methods which can be used for numerical solution of equations of motion. Our personal experience is that all methods for numerical solution of differential equations give good applicable results when they are used correctly and expertly [5]. We have very good experience by the use of Runge Kutta 4 order numerical method. The results of simulation also reveal that the moving load effect on pavements with unevenness can be regarded as the source of kinematical excitation of vehicle. The plans for next steps of research are to compare the results of numerical simulations with experimental measurements.

Acknowledgement

This contribution is the result of the research supported by GA MŠVVaŠ SR VEGA, grant No. 1/0259/12.

References

[1] MARTINICKÁ I., Výpočet vlastných frekvencií a tvarov vlastného kmitania výpočtových modelov vozidiel. In: Pozemné komunikácie a dráhy, roč. 6, č. 1-2, 2010, s. 41-50.

[2] STN ISO 8608 Mechanické kmitanie, profily povrchu cesty. Zaznamenávanie nameraných údajov, SÚTN, Bratislava, 2000.

[3] ČAČKO J. A KOL., Meranie, vyhodnocovanie a simulácia prevádzkových náhodných procesov. VEDA, Bratislava, 1984.

[4] MELCER J. – LAJČÁKOVÁ G., Aplikácie programového systému MATLAB pri riešení úloh dynamiky stavebných konštrukcií. EDIS, ŽU Žilina, 2011.

[5] MELCER J., Dynamické výpočty mostov na pozemných komunikáciách. EDIS ŽU Žilina, 1997.

TRANSCOM 2015, 22-24 June 2015
University of Žilina, Žilina, Slovak Republic

Deconvolution of DSC Signal in Order to Obtain the Real Thermal Effects

[*]Łukasz Walaszczyk, Tomasz Kozłowski, Katarzyna Kurpias-Warianek
[*]Kielce University of Technology, Faculty of Environmental Engineering, Geomatics and Power Engineering, Al. 1000-lecia P.P.7., 25-314 Kielce, Poland, {lukaszw, tomkoz, kkurpias}@tu.kielce.pl

Abstract. The paper presents the DSC signal deconvolution method in order to obtain the real thermal effects in clay minerals. The DSC peaks obtained during heating the cohesive soils are blurred and broadened. DSC signal is a convolution of the real functions of the thermal effects and apparatus function. In order to consequent use the recorded DSC signal, for example to determine the pore distribution in a moist cohesive soil, we need to extract the real thermal effects. Therefore, the deconvolution of DSC signal has to be performed. For this purpose the UNFLOOP program has been used. The program repeatedly performs a hypothetical thermal pulse distribution and then calculates the DSC signal. The distribution of the thermal effects, for which the calculated signal is the closest to the observed DSC is considered as real. In the paper, the program was applied to samples of two source clays: STx-1b from Texas and SWy-2 from Wyoming.

Keywords: Deconvolution, real thermal effects, Differential Scanning Calorimetry, bentonites, montmorillonite.

1. Introduction

Due to the wide range of applications, the porous materials are becoming more popular in many science and technology fields. Currently, they are used in engineering issues, such as construction, aviation, catalysis [1, 2], separation [1] and electronics [3]. The structure of porous materials has a significant impact on the real processes of adsorption and filtration. Therefore, the knowledge of the mechanisms governing the filtration in the soil is required for the proper modeling of this phenomena in relation to the many problems of civil engineering, water engineering and environmental engineering [4, 5]. Many specific research studies show that the distribution of the pores have the greatest impact on the characteristics of liquid transport in soils [6].

Cohesive soils are very specific porous material. Every year the usage of cohesive soils in construction industry increases. Existing methods used for determining pore space were limited to the study of dry soil. However, in practice the soil in its natural state are wet. It is known that the structure of the pore space may change for example as a result of swelling due to water saturation. Therefore, it is very important to be able to test wet soils. Using thermoporometry equation allows to specify the pore space of wet cohesive soils [7]. For this aim, it is necessary to know the real thermal effects at a specific temperature. They can be obtained using Differential Scanning Calorimetry DSC.

Differential Scanning Calorimetry method assumes a continuous variation in the temperature of the chamber in which the test sample and the reference sample are. The device records the difference in a heat flow between the test sample and the reference sample. An important disadvantage of this measure is that all thermal events occurring within the sample are recorded with a time-phased shift. A single thermal pulse is presented as the peak of a certain width. The peaks of adjacent pulses overlap. In thermoporometry this phenomena is particularly unfavorable, because this method assumes a close functional relationship between the pore size and the phase transition temperature of the water enclosed. Because the received data are partially superimposed, it causes some misstatement in pore size distribution curve. Scientists who deal with thermoporometry are aware of this problem, but there is a widespread belief that it is the

imperfection of the method, which simply must be reconciled. Attempts using software such as FitPeak presented in [8], are rare. Unfortunately, the FitPeak program works well only if imposed peaks are clearly prominent peaks. Usually this does not happen on the thermograms obtained by DSC for the clay-water samples.

2. Material and Method

2.1. Sample Specification

The tests were performed for natural bentonite STx-1b (Texas, USA) and SWy-2 (Wyoming, USA). These soils are considered clay models [9]. The clays were obtained from the Source Clay Repository of the Clay Mineral Society, Chantilly, Virginia, USA. Selected properties of the tested bentonite are presented in Tab. 1.

PROPERTIES	Bentonite STx-1b	Bentonite SWy-2	TESTING METHOD
Water content after sorption at RH=0,50, %	16,90	9,47	water sorption test
Water content after sorption at RH=0,95, %	28,76	22,68	water sorption test
External specific surface area S', m^2/g	98,87	55,42	water sorption test
Total specific surface area S, m^2/g	593,24	332,53	water sorption test
Dust fraction, %	85,5	54,50	laser diffraction
Clay fraction, %	14,5	45,50	laser diffraction
water content w, %	64,86	34,1	dryer-weight method
Mass of water, mg	4,06	2,53	dryer-weight method
Sample mass, mg	10,32	9,95	

Tab. 1. Selected properties of the tested bentonite.

Phases were identified based on PDF base 4+. Bentonite from Texas contains more than 92% of a montmorillonite fraction, whereas Wyoming bentonite often considered for exemplary contains only 69% of a montmorillonite.

Phase analysis - STX-1b (bentonite from Texas):
- montmorillonite $(Na,Ca)_{0,3}(Al,Mg)_2Si_4O_{10}(OH)_2*xH_2O$ about 44%
- bentonite (Na-Al-Si-O-OH-H_2O) about 29%
- montmorillonite-15A $Ca_{0,2}(Al,Mg)_2Si_4O_{10}(OH)_24H_2O$ about 16%
- Silicon Oxide SiO_2 about 8%
- montmorillonite (clay) $CaMg_2AlSi_4(OH)_2H_2O$ about 3%

Phase analysis - SWY-2 (bentonite from Wyoming):
- montmorillonite-22A $Na_{0.3}(Al,Mg)_2\ Si_4O_{10}(OH)_2*H_2O$ about 39%,
- quartz, syn SiO_2 about 28%,
- bentonite Na-Al-Si-O-OH-H_2O about 15%,
- montmorillonite $(Al(OH)_2)_{0.33}Al_2(Si_{3.67}O_{10})*8H_2O$ about 15%,
- quartz, low SiO_2 about 15%.

2.2. Methodology

In order to obtain the real thermal effects associated with the changes occurring in samples Differential Scanning Calorimetry has to be used. The thermograms obtained by DSC for the clay-water samples are characterized by previously mentioned error. All thermal events occurring within the sample are recorded with a time-phased shift. Thus, Kozlowski [10, 11, 12] attempted to solve the problem, and DSC signal processing techniques called "stochastic deconvolution". Differential Scanning Calorimetry work is based on the continuous change of the sample temperature in a predetermined time range. Temperature changes in the differential system apply to both: the vessel with the sample and reference vessel called a link. The observed thermal effects in the material cause delay or overtake the sample temperature with respect to the link temperature. Thermal power graph *g(T)* which is revealed in the form of a peak is shown in Fig. 4. Peak area *F*

under the curve *g(T)* with respect to time is equal to the observed heat of phase change (constant scanning speed has to be considered):

$$\Delta H = \int_{Tp}^{T_k} h(T)dT \tag{1}$$

where *h(t)* is the power function *g(t)* corrected with respect to the quasi-liner baseline (Fig. 1), which is a smooth transition from the occurrence of phase transformation until complete conversion (*h(T) = 0* if there are no phase transitions) and T_p and T_k are the estimated temperatures of the beginning and end of the peak.

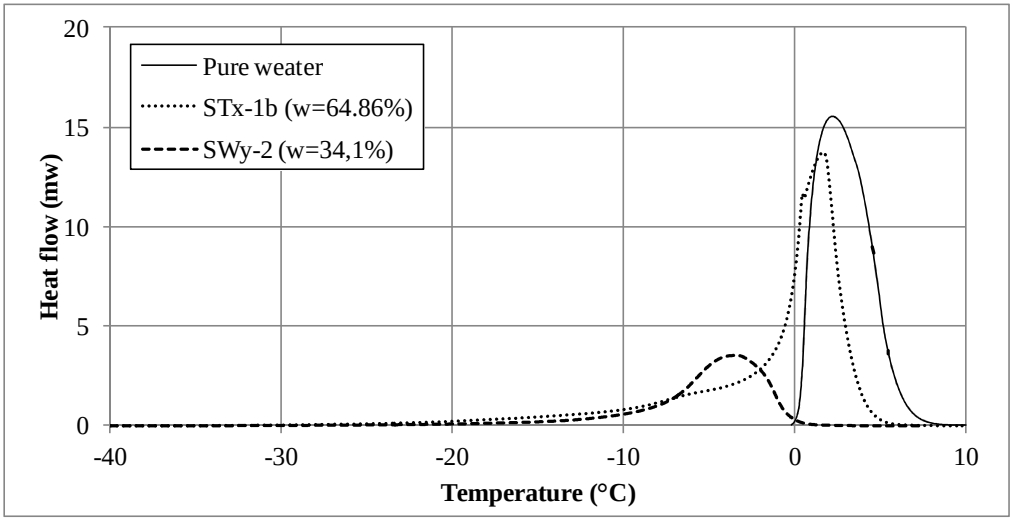

Fig. 1. DSC peaks corrected with respect to the quasi-liner baseline.

The temperature of the beginning of phase change is represented as the temperature of the beginning of the peak T_p. Due to the thermal inertia of the system, "thermal pulse" associated with the phase transition at some temperature T_0 appears as a blurred peak in the observed thermogram *g(T*). Therefore, in the case when multiple phase transformation occurs at a similar temperature or there is a so-called continuous phase transition, direct DSC analysis of the data does not allow identification of both the temperature and the enthalpy changes in each phase transition, due to overlap of the individual peaks. The research obtained only the beginning of the phase transitions temperature and the sum of the heat of all phase transitions. Regardless of the construction of the calorimeter, DSC thermogram does not correspond exactly to the real function of the thermal power absorbed by the sample at a specific temperature.

Blur of a peak will be analyzed on the example of one endothermic "thermal pulse" related to a phase transition of the crystalline material. It can be assumed that the dissociation of the crystal lattice of the solid takes place almost instantaneously at a specific temperature T_0 called the melting point.

Thermal pulse of the value *Q* can be written as a function of temperature *q(T)*:

$$q(T) = Q \cdot \delta (T - T_0) \tag{2}$$

and taking into consideration Dirac delta:

$$\int_{-\infty}^{\infty} \delta (x - x_1)dx = 1 \tag{3}$$

we get:

$$\int_{-\infty}^{\infty} q(T)dT = Q \tag{4}$$

During the calorimeter test a peak function *h(T)* is recorded instead of "the real function of the thermal pulse" *q(T*). It results from the thermal inertia of the measurement system (Fig. 2).

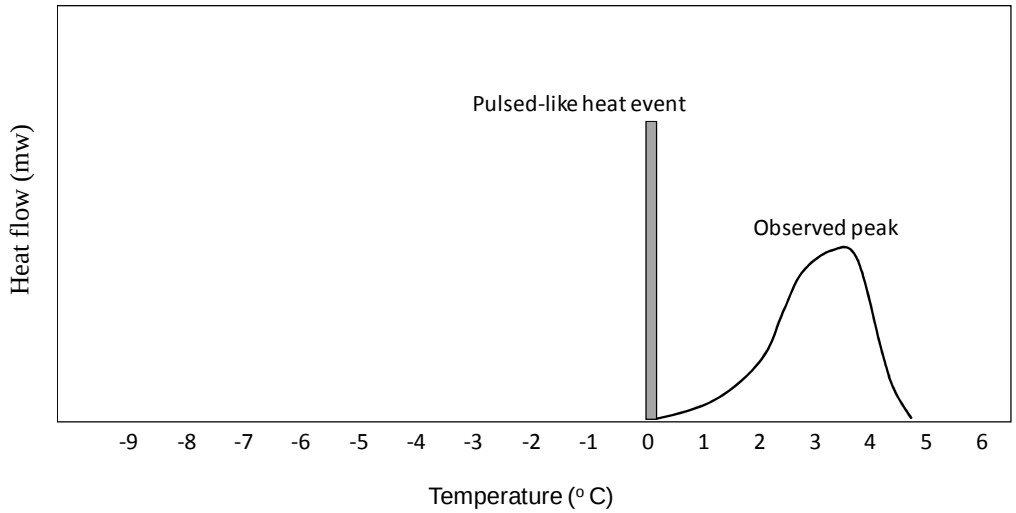

Fig. 2. The calorimeter response *h(T)* into the single thermal pulse *q(t)* [10]

For the function registered by the device there exists a relationship analogous to (4):

$$\int_{-\infty}^{\infty} h(T)dT = Q \tag{5}$$

However, in practice, the integration is carried out within the range indicated by the start and the end a peak according to (1). The function *h(T)* determines the peak of which the initial temperature is equal to T_0 and the width is determined by means of a scanning speed increasing function. The greater number of thermal pulses gives a peak being a superposition of corresponding number of constituent peaks, which is presented in Fig. 3.

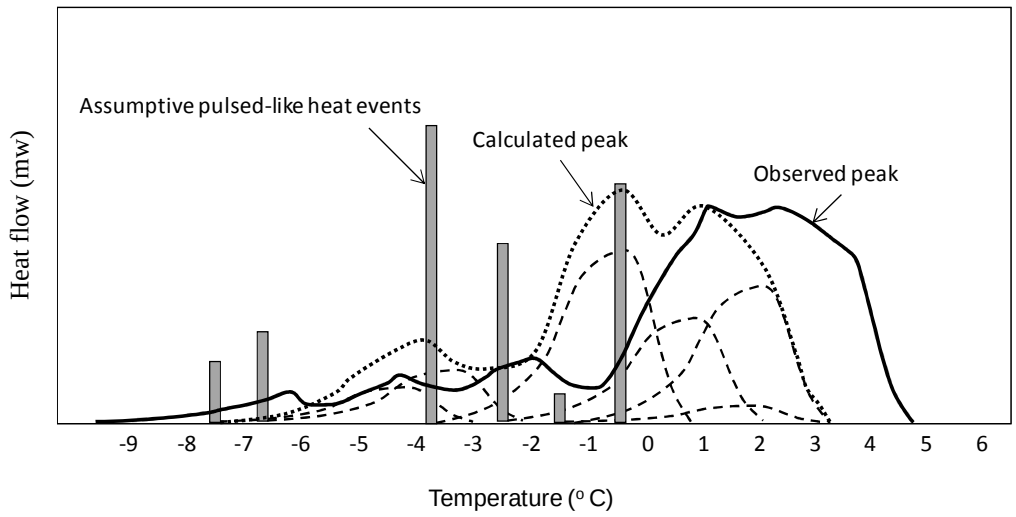

Fig. 3. Response of calorimeter to several pulse like heat events as a superposition [10].

Using the normalization of the function *h(T)* with respect to the pulse value *Q* and the transition temperature T_0 gives so-called an apparatus function *f(T)*:

$$f(T - T_0) = \frac{h(T - T_0)}{Q} \tag{6}$$

The apparatus function determines the distribution of the unit thermal pulse on the observed thermogram. It depends on the scanning speed and must be determined experimentally, as it is closely associated with a particular copy of the calorimeter.

In the case of multiple thermal pulses at different temperatures *T'*, the observed peak function *h(T)* can be presented in the form of a so-called of the real effects *q(T)* and the apparatus *f(T)*:

$$h(T) = \int_{-\infty}^{\infty} f(T - T')q(T')dT' = q(T) * f(T) \qquad (7)$$

The right side of (7) is called the convolution product [13].

2.3. Deconvolution Procedure

In order to make the DSC signal deconvolution the following steps were performed:

1. Before the research equipment TA Instruments Q200 calibration was performed.
2. A sample of the soil was placed in a calorimetric hermetic vessel Tzero^{TM} and smeared uniformly over the bottom and was weighed.
3. The test was proceeded in two cycles. First the samples were cooled with the scanning rate 2.5 K·min^{-1} to −90°C and then warmed with the scanning rate 5 K·min^{-1} to +20°C. Due to the effect of supercooling, the use of data from the cooling process was impossible.
4. After the experiment, the vessel was weighed again to control any unexpected loss of hermeticity. Next, pinholes were punched in the sample covers and the total water content was determined by drying to a constant mass at 110°C.
5. The apparatus function was obtained from melting peak of a sample of pure water at the scanning rate 5K·min^{-1}.
6. The DSC signal correction was performed by Kozlowski's JETHRO program.
7. In the last step Kozlowski's UNFLOOP program was used to make deconvolution of DSC signal with the apparatus function. The program has repeatedly made assumptive distribution of thermal pulses and then calculates the DSC signal. The distribution of the thermal effects, for which the calculated signal is the closest to the observed DSC is considered real.

3. Results

The presented method was applied to determine the real thermal effects of bentonite samples STX-1b from Texas and bentonite SWY-2 of Wyoming. Fig. 4 and 5. The results are presented in Fig. 4 and 5.

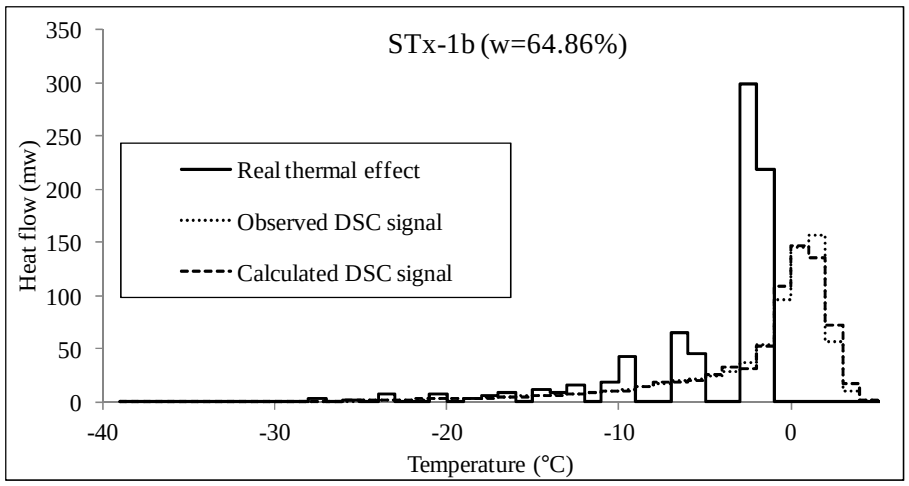

Fig. 4. Real thermal effects for the sample of bentonite STX-1b with water content w=64.86% discretized into intervals at 1 °C

It is clearly seen that the fit of the calculated DSC signal is very good. The obtained real thermal effects are shifted toward lower temperatures and do not correspond to the observed DSC signal directly.

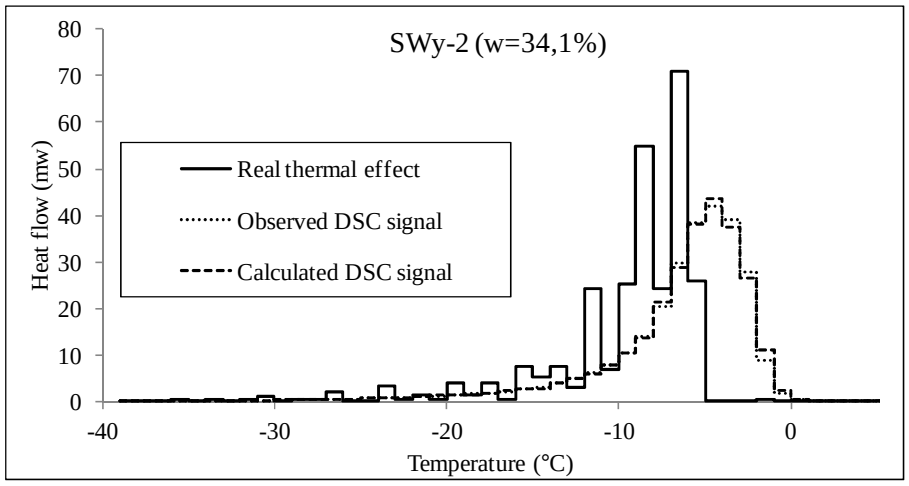

Fig. 5. Real thermal effects for the sample of bentonite SWy-2 (w=34.1%) discretized into intervals at 1 °C

4. Conclusions

The application of the stochastic deconvolution method to the analysis of the DSC signal enables the determination of the distribution of the pulse-like heat events *q(T)* absorbed by the frozen soil sample during the warming DSC run. It is based on searching for a distribution of "heat events" in relation to the temperature, which convoluted with the apparatus function *a(T)* gives a minimal deviation from the observed heat flux function *h(T).* Such an algorithm ensures stability, because, in some way, a testing procedure is involved in it.

The deconvolution of the DSC signal is necessary in order to use the DSC signal in calculations of the pore size distribution by use of thermoporometry [7]. The method enables to obtain the real thermal event independently of the time-phased shift and the resultant smearing.

References

[1] CIESLA, U., SCHUTH, F. *Ordered mesoporous materials.* Microporous Mesoporous Mater 27, 1999, 131-149.

[2] TAGUCHI, A., SCHUTH, F. *Ordered mesoporous materials in catalysis*. Microporous Mesoporous Mater 77, 2005, 1-45.

[3] PARKHUTIK, V. *Porous silicon-mechanisms of growth and applications.* Solid-State Electron 43, 1999,

[4] ROMERO, E., GENS, A., LLORET, A. *Water permeability, water retention and microstructure of unsaturated compacted boom clay*. Engineering Geology 54, 1999, 117-127.

[5] USYAROV, O.G. *Experimental study of small-scale spatial variation in filtration coefficient using tracer method.* Colloid Journal 65, 2003, 100-104.

[6] TULLER, M., OR, D. *Hydraulic functions for swelling soils: pore scale considerations*. Journal of Hydrology 272, 2003, 50-71.

[7] MAJDA, D., MAKOWSKI, W., MAŃKO, M., MLEKODAJ, K., MICHALIK-ZYM, A., NAPRUSZEWSKA, B.D., ZIMOWSKA, M., SERWICKA, E.M. *Porosity characterization of SBA-15 silicas with thermoporosimetry of water and n-alkanes – The effect of the probe liquid nature.* Microporous and Mesoporous Materials 201, 2015, 141-150.

[8] FASHANDI, H., KARIMI, M. *Characterization of porosity of polystyrene fibers electrospun at humid atmosphere.* Thermochimica Acta 547, 2012, 38-46.

[9] BERGAYA, F., LAGALY, G. *Surface modification of clay minerals.* Applied Clay Science 19, 2001, 1-30.

[10] KOZŁOWSKI, T. *Skład fazowy wody w gruntach spoistych poniżej 0 °C*. Monografie, PŚk, Kielce 1997.

[11] KOZLOWSKI, T. *A comprehensive method of determining the soil unfrozen water curves. 1. Application of the term of convolution*. Cold Regions Science and Technology 36, 2003, 71-79.

[12] KOZLOWSKI, T. A comprehensive method of determining the soil unfrozen water curves. 2. Stages of the phase change process in frozen soil–water system. Cold Regions Science and Technology 36, 2003, 81-92.

[13] HÖHNE, G.W.H., HEMMINGER, W.F., FLAMMERSHEIM, H.-J. Differential Scanning Calorimetry. Springer-Verlag, Berlin Heidelberg New York 2003.

TRANSCOM 2015, 22-24 June 2015
University of Žilina, Žilina, Slovak Republic

Assessment of technical condition of wooden structures

*Agnieszka Wdowiak
*Kielce University of Technology, Faculty of Civil Engineering and Architecture, Department of Communication Engineering, al. Tysiąclecia Państwa Polskiego 7, 25-314 Kielce, Poland, awdowiak@tu.kielce.pl

Abstract. The paper presents the definition of wood, its macroscopic and microscopic structure and factors that affect the mechanical properties of this material including, among others, wood moisture content and structural defects. In the paper, wooden buildings made of light wood-frame technology, good operating practices that need to be followed, and also regular and proper maintenance of such structures were characterized. Principles of examination and visual inspection of wooden members and structures were analyzed in a very detailed and accurate manner. On the basis of inventory compiled and the examination of the condition of wooden members and structures, the type and scope of rehabilitation is determined, the stability and strength report, and also mycological report are produced. Then the methods of the structural upgrading of the existing structure to increase its load bearing capacity are devised.

Keywords: wood, moisture, wooden buildings, technical condition assessment, structural upgrading of wooden members and structures.

1. Introduction

Wood is an organic material, the properties of which are immensely varied depending on the biological species. Wood is anisotropic, i.e. it shows different properties in different directions, and non-uniform due to many defects. Wood macroscopic features, the size of which is greater more than 0.1 mm, include the following: annual growth rings, latewood and early wood zones, heartwood, wide medullary rays, large vessels, resin leaks and knots. On the basis of macroscopic features, it is possible to distinguish the type of structure, identify the specific wood species, and determine its properties. These features are most commonly observed on three basic wood sections: tangential, radial and transverse (Fig. 1). Wood microscopic structure can be studied by examining the material under an optical microscope. Most cells are arranged in parallel to the longitudinal axis of the trunk. Some cells have a shape of very elongated spindles.

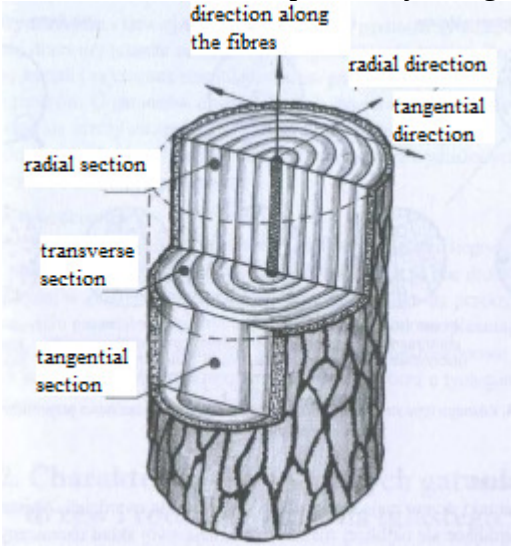

Fig. 1. A cut-through of a tree trunk - wood sections and anatomical directions according to [2].

The factors that most significantly affect wood mechanical properties include the following: wood anatomical direction, moisture content, and the distribution of structural defects (knots, cross grain, cracks, resin pockets, bark pockets and cankers, larval galleries). Wood moisture content, which is the most important parameter of this material, affects its weight, dimensions, volume, strength, and resistance to fungal or insect attack. As a hygroscopic material, wood is capable of exchanging water vapour with the surrounding air. Surface sorption mechanism is dominant in the process. Wood moisture content changes until the pressure of the water vapour inside the material and that of the water vapour in the surrounding air reach equilibrium. Changes in the moisture content within the hygroscopic range alter wood dimensions and volume. That is a two-way process resulting in wood shrinking or swelling. In wood, shrinkage involves reduction in size and volume due to vapour release. Swelling increases wood linear dimensions and volume as a result of water vapour absorption, which leads to a higher moisture content. Changes in wood dimensions, together with the material anisotropy and non-uniformity produce a number of adverse effects, including shape deformation of wooden elements (warping) and disruption of the material structure (cracking).

2. Assessment of the technical condition

Wooden buildings were erected in different time periods, some of them date back to the end of the 19th century. They constitute a part of the built environment in villages, small towns, and the outskirts of larger cities. Those are usually one-storey or two-storey structures, three-storey buildings are rarely found. Most are slab-on-grade structures. Most residential timber buildings were erected in the Podkarpacie region (Fig. 2). In other parts of the country, those are temporary or farmstead buildings, summer homes, or garden structures.

Fig. 2. Villa Koliba - Museum of the Zakopane Style designed by Stanislav Witkiewicz [11].

Wood and wood-based materials have a limited service life, they are highly susceptible to biological corrosion and show low moisture resistance. As a result, they need good operating practices, and also regular, proper maintenance. It is necessary to carry out annual condition surveys and those based on five-year cycle so that the beginning of destructive process could be easily identified and damages removed. When evaluating technical condition, a number of factors should be taken into account. Those include the age of the building, number of storeys, shape, dimensions, structure, the condition of walls, ceilings, roof, roof covering and deck, and also foundation and type of soil. Attention should be paid to changes in the shape and position (bending, deflection, displacement, torsion, section loss, change of direction, changes in metal elements). On the basis of the results of inspection and condition surveys, it is possible to evaluate if the building suitable for further use. The causes of damages must be identified and repair options examined. The analysis of the structural integrity of the building has to be made taking into account the assumed service load and expected events. Structural upgrading should be considered.

2.1. Examination and visual inspection of wooden members and structures

The evaluation of the technical condition of a wooden building is based on the examination and visual inspection of wooden members and structures. The latter make it possible to assess the quality of the workmanship, selection and quality of the building materials used, the structure

performance in service and its expected lifespan. The stability of the structure and that of the walls are major factors that affect the condition of the wooden building. They depend on the foundation, its stiffness and that of the basement storey.

When examining wooden members and structures, it is necessary to find out the deterioration level, including the attack by fungi and insects. The presence of insects is indicated by exit holes produced by adult insects, visible on the surface of wooden elements, and also traces of sawdust. Fungal attack on wooden elements can be evaluated on the basis of a specific musty smell, damp walls, stains and efflorescence on the plaster, coming off and spalling of plaster. Other signs of decay include a dull sound produced when wood is struck with a hammer, wood softening shown when it is prodded with a sharp tool, wood cracking, deflection of ceilings, warped floorboards, and the presence of mycelium. When examining and inspecting wooden houses, it is also necessary to locate the sites where growth of surface mould is found. Typically, these include corners of exterior and partition walls, the corners of the exterior walls and ceilings, and sides and tops of openings.

For monitoring wood decay and classifying wooden elements, a graduated metal drilling needle, which is inserted into wood, proves to an effective tool. More accurate instruments, namely ultrasonic testers, pulse-resistivity testers and resistographs are used for monitoring constructed features of special importance like heritage buildings or sports facilities. Resistograph is capable of detecting approx. 50% more wood defects than a human conducting a visual inspection and equipped with mechanical tools (Fig. 3). An annual (spring) preventative survey of the building makes it possible to identify the initial stage of biological corrosion. As regards newly designed, repaired or upgraded timber buildings, it is vital that those structures allow for periodic surveys and application or reapplication of wood protective agents.

Fig. 3. Evaluation of wood condition with resistograph [12].

In buildings with masonry walls, deformations and cracks are to be sought on the exterior. Inside the building, the examination starts from the basement, and proceeds upwards into the attic. Damp wooden elements, especially those located in the basement and the attic, should be subjected to thorough visual inspection. Covered wooden elements have to be uncovered and carefully examined. All the sites without access to daylight, poorly ventilated, located close to water and sewage systems, sanitary fixtures or central heating should be carefully inspected.

The ceiling structure and beam system can be identified by, among others, anchors on the building facades as those define the position of the beams. Other helpful features include ceiling plaster appearance with a distinctive pattern of scratches or smudges, which indicates the positioning of the beams, and also the arrangement of windows, height of window heads, etc. Having taken into account all the factors above, it is possible to select the sites that need to be uncovered. They are most often located close to the walls that support the ceiling. Then, it is possible to evaluate how beams are supported and the level of deterioration on the support, where biological corrosion may develop. The arrangement and dimensions of the bearing elements of the ceiling can most often be reconstructed uncovering 2-3 sites. It is also necessary to observe whether the reconstructed system supports the beams properly. At all storeys, ceiling and floor beams, intermediate ceiling, eaves soffit, door and window frames, and walls have to be examined. In the

roof structure evaluation, the condition of the timber wall plate, damages to the members and joints, too large gaps in joints, deflection in rafters, battens or purlins need to be examined. The condition of wood joinery is checked by examining the tightness, the correct setting in the frames, and the precise execution of dock shelters. When assessing the condition of the foundations, it is necessary to excavate the test pits to find out about the foundation structure and depth, and the presence of the moisture barrier. Deeper excavation should be run to determine the foundation subbase. Wall geometry also affects the stability of the foundation.

Surveys and visual inspections are followed by compiling inventory documentation, which is accompanied by photographic evidence.

2.2. Statistical analysis of wooden structures

Statistical analysis can help when taking decisions on changes in the functional system, the selection of appropriate methods for repairs of walls, ceiling and roof in wooden structures. On the basis of the inventory and condition assessment, the type and scope of rehabilitation is determined, the stability and strength report and also mycological report are made. Rehabilitation works include the repairs and upgrading of the building members and structure. The upgrading of wooden structures may involve a replacement of the existing structure, or increasing its bearing capacity. The addition of new members, made from modern materials and following new design solutions, should result in the reconstruction of the existing items or structural system. The new members entirely bear the loads, while the existing system does no longer perform the structural function, yet it may be preserved for its architectural or historic values. The upgrading intended to increase the load bearing capacity may not alter the static scheme (increase in member cross-sections, strengthening the structure of the material, incorporation of elements made of other materials), or may make changes in the static scheme by redistributing internal forces. As regards beam structures, fixed on supports or redesigned beams split on supports for continuous beams, the static scheme is changed although no additional bearing members are incorporated. The addition of bearing elements is widely used. The simplest way to upgrade bending members such as ceiling beams, binding joists or girders is to use additional supports in the bays. That will unload the existing supports, but will also make it necessary to construct additional foundation and will be disadvantageous for the building use. To reduce the span of the bending element, at the supports, struts from the bottom or diagonal hangers from the top are used if the column exceeds the beam being reinforced. It is also possible to run cantilever beams from the support head to increase the support plane, and to reduce the span of the member being strengthened. In timber structures, strength properties depend on the wood type and biological species, and also on the level of in-service deterioration. For a given wood type and class (depending, among others on the number of knots and cross grain), it is possible to establish admissible standard values and to determine how much the original properties deteriorated. In the examination, it is necessary to determine wood damage caused by fungi and insects and also cracks, which indicate that the limit state has been exceeded. In wooden buildings, cracks are measured with a feeler gauge or a thin, flexible gauge with the measuring plate thickness of 0.2 mm. Cracks are categorised as shallow when their depth does not exceed 1/10 of the section width *b* or height *h*. Larger than those are classified as deep cracks. For symmetrical weakening, in accordance with [10], the minimum cross-sectional dimension should not be less than 30 mm, nor should it constitute less than half of the thickness (the element width or height), while for non symmetrical weakening, the latter value cannot be lower than 0.6 of the thickness. The standard mentioned above, however, does not specify the permitted crack width r_b. In accordance with Plessner [5], the sum of the crack widths $\sum r_b$ on one side of the element should not exceed b/20 for shallow cracks, and b/10 for deep cracks. These cracks only slightly decrease the element strength, but they have to be accounted for in strength analysis of wooden structures. In solid wood and glued laminated timber, shrinkage cracks or dryouts are found

on the section external side. Shrinkage causes the formation of, among others, transverse tensile stress, which exceeds the wood capacity, and cracks compensate for stress that develops in the material. Crack location in the section is extremely important when the element is subjected to a vertical load. Vertical cracks do not affect the section modulus W or moment of inertia I, whereas horizontal or diagonal cracks reduce the load limit. Glued laminated timber does not have any cracks, because it is manufactured at low humidity. In the components assembled on the site, small cracks in glued laminated timber generally do not reduce the static stability of the element, unless they exceed the admissible depth limits. Polish literature on the subject does not specify the strength of the element depending on the crack size, consequently when evaluating the timber condition, it is necessary to use German guidelines. In Table 1, the coefficients reducing the cross-sectional area of the element A, moment of inertia I, and the section modulus W are defined depending on the total width of the cracks.

The sum of the crack widths	Coefficient α reducing the cross-sectional area	Coefficient β reducing moment of inertia I and modulus W
$\sum r_b \le b/10$	0.95	0.91
$\sum r_b \le b/20$	0.98	0.96
$A_g = \alpha \cdot A \qquad W_{xg} = \beta \cdot W_x$ $I_{xg} = \beta \cdot I_x$		

Table 1. Coefficients α and β in accordance with [5].

Condition of wood depends mainly on the ambient moisture conditions in which the structures is located. Consequently, it is necessary to examine the structure quality in a damp environment, analyzing, for the sake of calculations, the dimensions of sound sections of elements. It is usually not possible to uncover the whole structure, so fragmentary data from individual uncovered sites can provide only approximate evaluation of the structure performance. Then, indirect information, like deflections observations, needs to be relied on. For structures that require immediate visual inspection and examination, deflection is determined on the basis of height-to-span ratio h:l of the element, or on the maximum deflection-to-span ratio u:l of the element, which are described in Table 2.

Type of structure	Height-to-span ratio h:l of the element	Maximum deflection-to-span ratio u:l of the element
Ceiling beams with solid section	1/20	1/80
Beams made of square-sawn timbers and logs: - Spliced with longitudinal blocks - Jointed with lateral pads and nails	 1/15 1/15	 1/120 1/100
Full girders, nailed	1/10	1/100
Truss jointed with: - split rings - notches, nails	 1/5 - 1/6 1/5 - 1/6	 1/150 1/120
Single-section columns	-	1/80*
Columns with complex section	-	1/80*

***** The ratio of buckling magnitude to the column buckling length

T**able 2**. Deflection limit for wooden structures that need immediate inspection and examination in accordance with [8].

3. Conclusions

1. Wood strength decreases with an increase in the moisture content within the hygroscopic range, and in the capillary range, the moisture effect is negligible. From the air-dry state to fibre saturation (15% ÷ 30%), wood compressive strength is reduced by approx. 50%, and its bending strength by about 40% according to W. Michniewicz, L. Rudziński.
2. In deformation, wood behaves like elastic-plastic material, which means a linear relationship holds between stress and deformation and flow processes occur, which result in plastic deformation. Timber resilience varies for different anatomical directions (parallel to the fibres, tangential, radial) and depends on the duration and the size of the load. Wood moisture content lowers the modulus of elasticity and increases susceptibility to creep. The latter determines strain increment over time under constant load. As a result, creep deformation of solid wood depends on the load magnitude and duration, wood species and the moisture content according to H. Neuhaus.
3. According to Kerntopf - Ślusarczyk B., in the examination and inspection of wooden structure buildings, the factors that reduce the service life of wooden elements should be accounted for [4]: plinth course which is too low above the ground level – the recommended height is 40 cm, wall base which does not extend outside the plane of the outer wall, the use of styrofoam instead of mineral wool, discontinuities in the vapour barrier, too small eaves – the recommended width is 50 cm, too small distance between the ground and the bottom surface of the basement ceiling.
4. For the classification of wooden elements with respect to the material deterioration, a graduated metal drilling needle is an effective tool. More accurate instruments, namely ultrasonic testers, pulse-resistivity testers and resistographs are used for monitoring constructed features of special importance like heritage buildings or sports facilities. Resistograph is capable of detecting approx. 50% more wood defects than a human conducting a visual inspection and equipped with mechanical tools.
5. Mechanical drilling is used to assess a decrease in strength of wood attacked by fungi or insects. That makes it possible to evaluate the decay penetration and specify the sound part of the element section. The actual section, determined in this way, provides basis for statistical calculations [6]. Endoscope (borescope) with the tip inserted into the bore-hole can be employed to evaluate wood quality. Images taken at different borehole depths can be recorded and archived. The phenomenon of propagation of acoustic waves, induced mechanically or ultrasonically, to evaluate wood quality, strength and modulus of elasticity is also used [9]. On the basis of the experimental results obtained by Słubnikow, wood strength loss can be determined from a decrease in weight by volume. Samples are collected from sound and damaged parts, and then weight by volume is determined. Depending on the percentage reduction in weight in damaged wood in relation to sound wood, timber strength is found [6].

References

[1] RUDZIŃSKI L., *Wood structures, repairs, strengthening, examples of calculations* (in Polish). Kielce University of Technology, Kielce, 2010.

[2] KOZAKIEWICZ P., *Wood physics - theory and problems. Selected issues* (in Polish). SGGW ed. III edition, revised, Warsaw 2006.

[3] MICHNIEWICZ W., *Wood structures* (in Polish). Warsaw, Arkady 1958.

[4] KERNTOPF-ŚLUSARCZYK B., *Wood houses - a review of the technologies* (in Polish). Murator 1997, No. 1, pp. 54-65.

[5] PLESSNER H., *Examples of damages to wooden structures* (in Polish). Materiały Budowlane 2000, No. 5, pp. 30-31.

[6] PLESSNER H., *Some problems in calculating damaged roof structures* (in Polish). Przegląd Budowlany 1984, No. 11, pp.530-533.

[7] NEUHAUS H., *Wood construction* (in Polish). Rzeszow, Polskie Wyd. Tech., 2004.

[8] MASLOWSKI E., SPIŻEWSKA D., *Upgrading of building structures* (in Polish). Warsaw, Arkady 2000.

[9] JASIEŃKO J., *Engineering and adhesive connections in the repair, maintenance and upgrading of historic wooden structures* (in Polish). Wroclaw, Dolnośląskie Wydawnictwo Edukacyjne, 2003.

[10] PN-B-03150: 2000 Timber structures. Static calculations and design (in Polish).

[11] *http://www.podroze.pl/polska/malopolskie/zakopane/zakopane-wille-atrakcje-noclegi-pensjonat-tatry/981/*

[12] *http://projektus.blogspot.com/2014/01/pomiary-stanu-drewna-rezystografem.html*

TRANSCOM 2015, 22-24 June 2015
University of Žilina, Žilina, Slovak Republic

Usage of the non-destructive method to assess the compressive strength based on example of the road section made of cement concrete

[*]Paweł Wolka
[*]Kielce University of Technology, Faculty of Civil Engineering and Architecture, Department of Transportation Engineering, al. Tysiąclecia Państwa Polskiego 7, 25-314 Kielce, Poland, {pawel.polwlk}@gmail.com

Abstract. The article presents theusage of the non-destructive sclerometric method to assess compressive strength of the road section made of cement concrete. To diagnose a 200 m long two lane road section made of cement concrete the N type Schmidt hammer was used . The brief characteristic of the method is presented before the analysis of results. The operation of the Schmidt hammer, the equipment used and the required conditions were presented as well. The analysis of the results is shown in graphs of the average compressive strength. The average hardness of concrete in the road structure was 46 MPa. It follows that the sclerometric method can be used as a way to diagnose the points of reduced compressive strength for cement concrete roads. And precisely done analysis with the use of the Schmidt hammer can help with estimating compressive strength parameters.

Keywords: Schmidt hammer, sclerometric analysis, diagnostics, pavement, cement concrete.

1. Introduction

For a few years so far diagnostics has become a significant issue in the maintenance concrete pavements. In the case of concrete roads it is used to determine their bearing capacity and compressive strength and to define the class of concrete. A basic technique to assess strength of concrete is to sample the element and to test it which means damage to its structure that commonly leads to necessity of obtaining consent of the holder and to secure the area where the sample was taken from. Because of this reason, the non-destructive methods have been used more frequently. The non-destructive methods, when the proper rigor of results interpretation is maintained, also constitute the basis for assessing the element given and both agility and ease of execution prove their big potential.

The following text presents a possibility of using the results defining compressive strength by Schmidt hammer method. The analyzed road section made of concrete was 200m long in total.

2. Methodology

To diagnose the road section, the sclerometric analysis with the N type Schmidt hammer was used (a medium hammer with the impact energy of 2.21 Nm and the mandrel diameter of 1.5 cm). The measurement method consist of determining compressive strength of concrete in structures through assessing the surface hardness. The relationships between local surface resistance of concrete to the action of point load and its strength [2]. The hammer specifies surface strength of the analyzed material described by so called bounce number L, which characterizes the quantity of mandrel bounce connected to impact mass and spring mechanism from the surface analyzed after its previous blow with the specific force [1]. Note that the method is used to estimate compressive strength and cannot be used as an alternative for traditional destructive methods. It can also be used as the detector of lower resistance places.

In the most modern DIGI type instruments the results are recorded using a recording instrument which after setting the suitable program automatically records the measurement and directly converts on compressive strength.

Figure 1 presents the hammer and the measuring equipment, i.e., a recorder, wires, grinding stone and accessories.

Fig.1. Schmidt hammer type DIGI

Technical guidelines and measurement canons are determined in the standard [6] and in the no. 210 ITB instruction [4] along with the manufacturers. Valuable information is also included in the out-dated standard [5].

During the measurement the proper attention must be paid to the place of measurement as it is specified in standard [5]. The surface analyzed should be smooth, with no visible damage, layers or signs of corroded concrete. When the points of measurement does not meet the requirements it is advised to clean it using the abrasive stone or the grinder. The points of measurements [6] should be minimum 25 mm apart.

In the case of hammers for digital measurements, after setting necessary input data i.e. impact direction, number of measurements in a sequence, R-L equation of dependence, criterion of elimination of the bounce number not considered in calculations, concrete strength may be read directly from the display screen or recorded in memory of device and transferred on the computer disk [3].

3. Results

The analysis was conducted for the section of road made of cement concrete 200 m long, for two road ruts each 3m wide. The measurement considered both left and right wheel-rut and the axis of the road. The measurements were made in research points located every 25m, in 3 series for each measurement location and the number of 12 impacts. The distances between individual sequences was 10 cm.

The gained results were analyzed to achieve the average compressive strength of particular measurement places. Figures 2 and 3 the summarize compressive strength of particular cross sections of the road lanes.

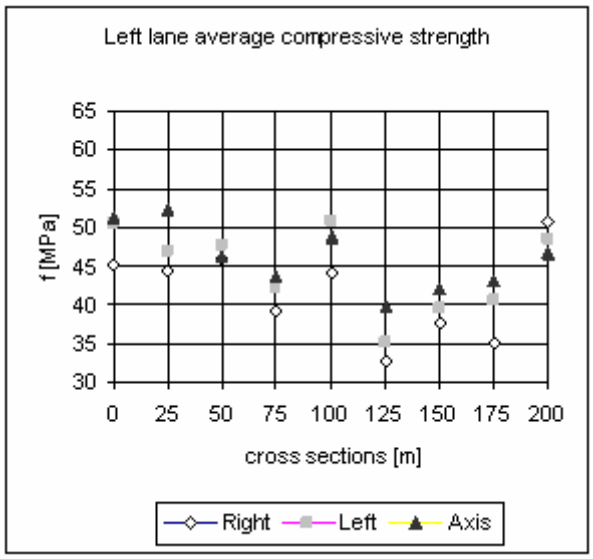

Fig.2. Left lane`s average compressive strength

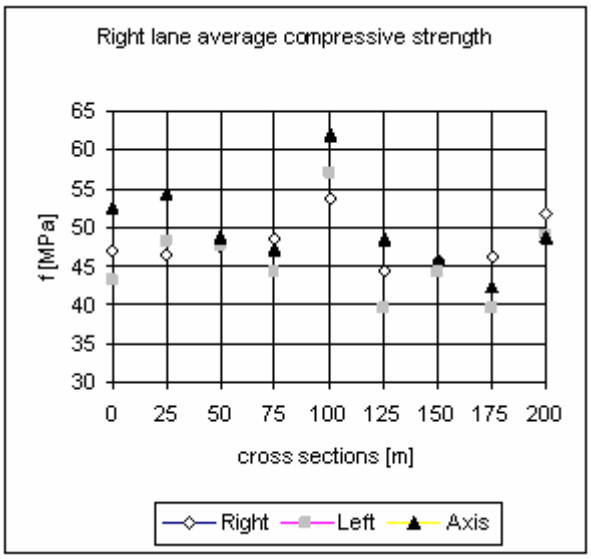

Fig.3. Right lane`s average compressive strength

Taking under consideration both the first and the second graph the discrepancy depending on the measurement point was asserted. The highest strength was recorded for the right rut axis (62 MPa), whereas the lowest strength was recorded for the right wheel-rut of the left lane (33 MPa). The closest values were registered for the 50th meter. In analysis of the sections of measurement places, strengths on the right and left ruts are similar and do not vary more than 1 MPa. Between the measurement points 0 m and 75 m the values remain the equal level as well for the right and left lane of the road. From 125 m to 175 m the values decreased for both lanes. For both lanes the fluctuation in strength was discovered on the 100th meter of the road. It can be observed that in vast majority, the lowest parameters were recorded in the right wheel-rut and the best ones in the lane axis. It is caused by the traffic and the road cross slope.

Figure 4 presents an average compressive strength distinguishing the analyzed intersection for particular road lanes.

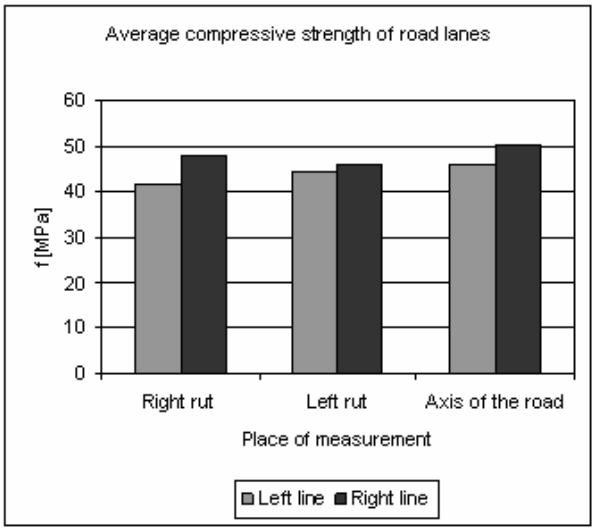

Fig.4. Average compressive strength of road lanes

Analyzing data presented in graph 4 higher average values of compressive strength for the right rut were recorded at each point of the sections. The highest values occur in the axis where the traffic is sporadic. The lowest value was found for the right wheel-rut of the left rut (42 MPa), the highest for the road axis of the right rut (50 MPa). An average compressive strength determined for the whole road equals 46 MPa, based on the average class of concrete specified as C30/37.

4. Conclusion

In the case of the analyzed road section the average compressive strength was 46 MPa. The results proved the discrepancies of the compressive strength parameter both in the example of the lines and the measuring points in the road lane vertical section. The probable cause differences in strength was the structure by type of traffic.

Thoroughly done analysis with the usage of the Schmidt hammer can help with estimating compressive strength parameters but cannot be used as an alternative for traditional non-destructive methods of analysis.

The sclerometric method can be used as a way to diagnose the points of reduced compressive strength for cement concrete roads.

References

[1] NAGRODZKA-GODYCKA, K. Badanie właściwości betonu i żelbetu w warunkach laboratoryjnych, Wydawnictwo Naukowo-Techniczne, Warszawa 1999;

[2] SZYDŁO, A. Nawierzchnie drogowe z betonu cementowego. Teoria, wymiarowanie, realizacja, Wydawnictwo Polski Cement, Kraków 2004;

[3] DOMAŃSKA, D. Wykorzystanie pomiarów sklerometrycznych do określenia parametrów wytrzymałościowych obudów szybowych, Górnictwo i Geoinżynieria, Rok 33, Zeszyt 3/1, 2009;

[4] BRUNARSKI, L., RUNKIEWICZ, L. Instrukcja stosowania młotków Schmidta do nieniszczącej kontroli jakości betonu w konstrukcji, Instrukcja ITB nr 210, ITB, Warszawa 1977;

[5] PN-B-06262:1974, Nieniszczące badania konstrukcji z betonu. Metoda sklerometryczna badania wytrzymałości betonu na ściskanie za pomocą młotka Schmidta typu N;

[6] PN-EN 12504-2:2013, Badania betonu w konstrukcjach - Część 2: Badanie nieniszczące - Oznaczanie liczby odbicia.

TRANSCOM 2015, 22-24 June 2015
University of Žilina, Žilina, Slovak Republic

Influence of the volume of cement paste on the compressive strength of high-performance concretes

[*]Bartłomiej Zarzycki
[*]Kielce University of Technology, Faculty of Civil Engineering and Architecture, Department of Technology and Organization of Construction, al. Tysiąclecia Państwa Polskiego 7, 25-314 Kielce, Republic of Poland, bzarzycki@tu.kielce.pl

Abstract. The article presents the results of the author's research concerning the influence of the volume of cement paste in the concrete mixture on the compressive strength of hardened concrete. A higher influence of the volume of cement paste on the concrete compressive strength has been found in case of high-performance concretes, while in the case of conventional concretes such an influence is considerably lower.

Keywords: Compressive strength, cement paste volume, high-performance concrete, self-compacting concrete.

1. Introduction

The need for erecting more and more complicated building structures made of concrete requires using concrete mixtures of adequate parameters. The main parameter describing concrete in respect to its usability in particular applications is its compressive strength, which is commonly determined by water/cement ratio (or water/binding agent ratio in case of binding agents composed of several components) [1, 2, 3]. It has been repeatedly proved that concrete compressive strength is inversely proportional to the size of w/c ratio and it has been assumed that high-performance concretes (of compressive strength over 60 MPa) must be characterized by the w/c ratio < 0.38, which enables obtaining concrete of increased durability, apart from high strength [1, 2].

Traditional calculations of concrete mix composition, made by means of three equations, covering coarse aggregate grains with mortar or filling cavities of coarse aggregate with mortar, do not allow for the volume of cement paste as the factor influencing concrete properties, including its compressive strength [2, 3].

An analysis of composition of several dozen high-performance concrete mixtures made based on literature makes it possible to state that there are considerable differences between the volumes of cement paste in these concretes. Among high-performance concretes, one can distinguish three types: massive (with the lowest volume of paste), typical high-performance concretes and high-performance self-compacting concretes (with the highest volume of paste) [4]. Volumes of paste are characteristic of particular types of concretes – in the case of the above-mentioned concretes, the volume change ranges from 220 to 450 dm^3 in a cubic meter of a concrete mixture. As can be seen, the difference between the extreme values is even over 200 dm^3 of paste. Those are the most-commonly used values, occurring in dozens of concrete mixture compositions that have been analyzed.

2. Methods and materials

The tests covered six types of concrete – three high-performance concretes and three standard ones. All concretes were made of blast furnace cement CEM III/A 42,5 N-LH/HSR/NA, river sand 0/2 mm and coarse basalt aggregate of grain-size of 2/8 and 8/16 mm. The choice of cement was determined by its usefulness for making different types of concrete mixtures. The cement used in

tests has the lowered heat of hydration, which permits preparation of concretes for monolithic and massive structures and, at the same time, it is suitable for self-compacting and high-performance concretes. This cement is also characterized by high strengths in a subsequent curing period and its light color offers a wide variety of applications in concrete architecture. Concrete compositions are presented in Tab. 1. In order to keep constant proportions between the volume of paste, mortar and coarse aggregate for particular types of mixtures, permanent values of sand point for particular volumes of paste have been adopted i.e. 28%, 34% and 40% for the paste volumes of 220, 320 and 420 dm^3, respectively.

	w/c = 0.30			**w/c = 0.60**		
V_z	**220**	**320**	**420**	**220**	**320**	**420**
W	103.8	151	198.3	141.1	205.2	269.4
C	346.2	503.5	660.8	235.2	342	448.9
P	631.8	663.8	661.1	631.8	663.8	661.1
K_{2-8}	812.4	644.3	495.8	812.4	644.3	495.8
K_{8-16}	812.4	644.3	495.8	812.4	644.3	495.8
PP	28	34	40	28	34	40
SP	3.46	1.98	3.17	-	-	-

Tab. 1. Compositions of concrete mixtures used in tests.

V_z – volume of paste in a concrete mixture [dm^3/m^3],
W – amount of water [kg/m^3],
C – amount of cement CEM III/A 42,5 N-LH/HSR/NA [kg/m^3],
P – amount of sand fraction 0/2 [kg/m3],
K_{2-8} – amount of basalt aggregate fraction 2/8 mm [kg/m^3],
K_{8-16} – amount of basalt aggregate fraction 8/16 mm [kg/m^3],
PP – sand point [%],
SP – amount of water-reducing admixture [dm^3/m^3].

The compositions of concrete mixtures that were used in tests include, in respect of paste volumes, the full range of concretes commonly used in construction. Therefore, the below-presented strength test results can be useful in designing high-performance concrete mixtures. Knowledge of relation of compressive strength to w/c ratio and the volume of paste may facilitate designing economical concrete mixtures with the limited use of cement.

The concrete mixture designed as high-performance self-compacting concrete (w/c = 0.3, V_z = 420 dm^3/m^3) underwent additional technical tests, based on of which it is determined whether it meets the conditions of self-compacting: slump-flow test, L-Box test and V-Funnel [5]. Test results and their interpretations are presented in Table 2.

	slump-flow test	**Slump-flow time T_{500}**	**V-funnel**	**L-box**
Technical test result	670 mm	1.8 s	5.7 s	PL = 0.80
Result interpretation	slump-flow class SF2	viscosity class VS1	viscosity class VF1	flow capacity class PL1 (2 bars)
Short characteristics of test	diameter of free slump-flow	time of mix slump-flow up to 500 mm in diameter	time of outflow from V-funnel	flow capacity between obstacles without segregation

Tab. 2. Results of technical tests of self-compacting mixture.

Technical tests, made on the concrete mixture designed as high-performance self-compacting concrete, showed that the produced mixture meets the self-compacting requirements with the simultaneous absence of segregation of its components.

Each of the concretes was represented by 5 cubic specimens of an edge of 10 cm. The specimens were demoulded after 24 hours from the placing of mixtures in moulds, and immersed in the containers with water. The specimen maturing conditions remained stable (constant, completed immersion in water, constant temperature), after 24 days of maturing the specimens were dried at 80°C for 72 hours, then cooled for 6 hours in air-dry conditions. The strength tests were conducted by means of Tecnotest Modena press of maximum compression force of 3000 kN.

3. Test results and their analysis

In Table 3, the results of concrete compressive strength tests are presented. They clearly show that the diversity of results among concretes of w/c ratio = 0.6 is small, however with a rising tendency when the volume of paste increases, contrary to concretes of w/c ratio = 0.3. In these cases, the change in the volume of paste considerably affects the results of compressive strength, which is inversely proportional to the volume of paste. In the case of concretes of w/c ratio = 0.6 an increase in the volume of paste results in a slight increase in compressive strength.

	w/c = 0.3			**w/c = 0.6**		
Volume of paste [dm^3/m^3]	220	320	420	220	320	420
Compressive strength [MPa]	113.3	103.6	95.9	37.2	38.1	40.9

Tab. 3. Compressive strength test results.

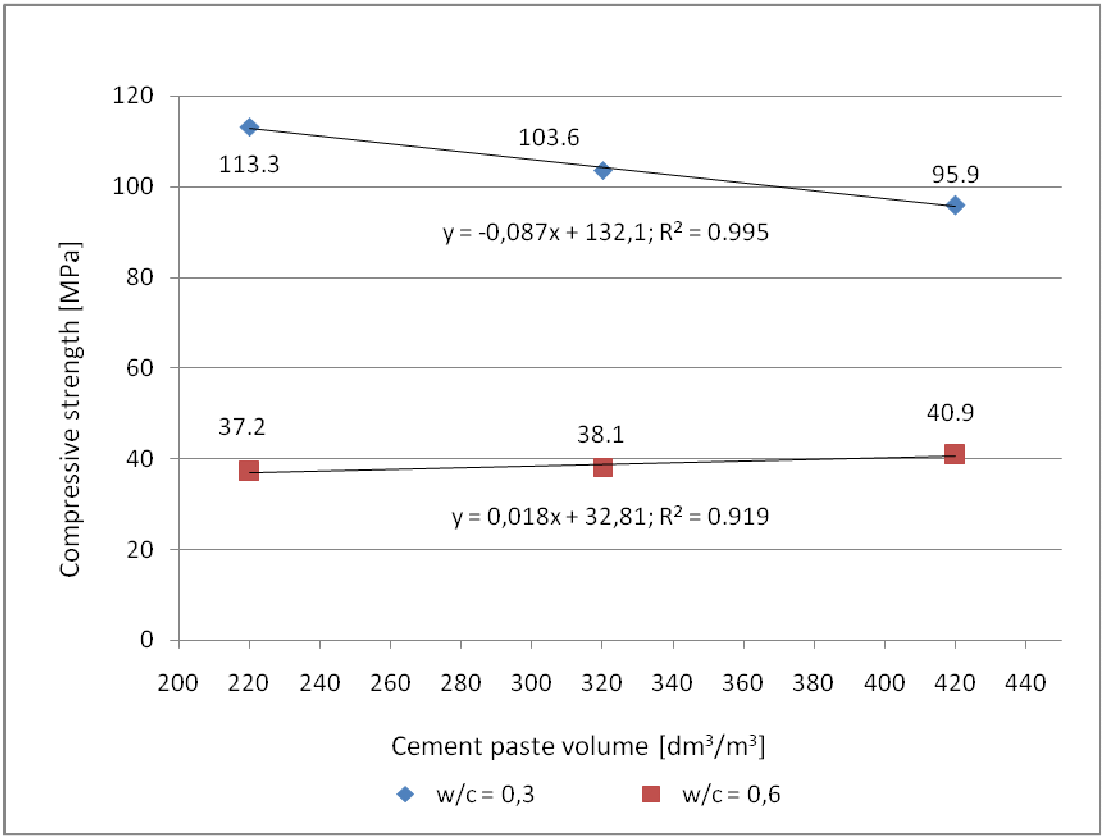

Fig. 1. Relationship between compressive strength and cement paste volume.

In both cases, in the tested range of paste volume, a linear relationship was found, confirmed by the analysis of regression with a high value of coefficient of determination R^2. Thus, the obtained results can be described in detail by means of linear regression equations.

As expected, concretes of the w/c ratio = 0.6 reached the lowest compressive strengths. The difference between particular results, depending on the volume of cement paste is small and is up to 10% for concretes with the extreme paste volumes where the difference in the volume of paste between these concretes is 200 dm^3/m^3, i.e. nearly 100%.

A distinct difference in the strength results can be observed in concretes of w/c ratio = 0,3. The concrete with the volume of paste V_z = 220 dm^3/m^3 obtained the highest result while the high-performance self-compacting concrete with the volume of paste V_z = 420 dm^3/m^3 obtained the lowest result.

Figure 1 shows the trend lines and equations that describe them together with the coefficient of determination. Figures 2 and 3 show standardized strengths for concretes of w/c ratios of 0.3 or 0.6, respectively. In both cases, the result obtained for concretes with the volume of paste 220 dm^3/m^3 was adopted as the base value.

The presented results should also be interpreted in an economical aspect – the concrete with the highest compressive strength contains a relatively small amount of cement – the most expensive component of the mixture – but also meeting requirements set in respect of any class of exposure.

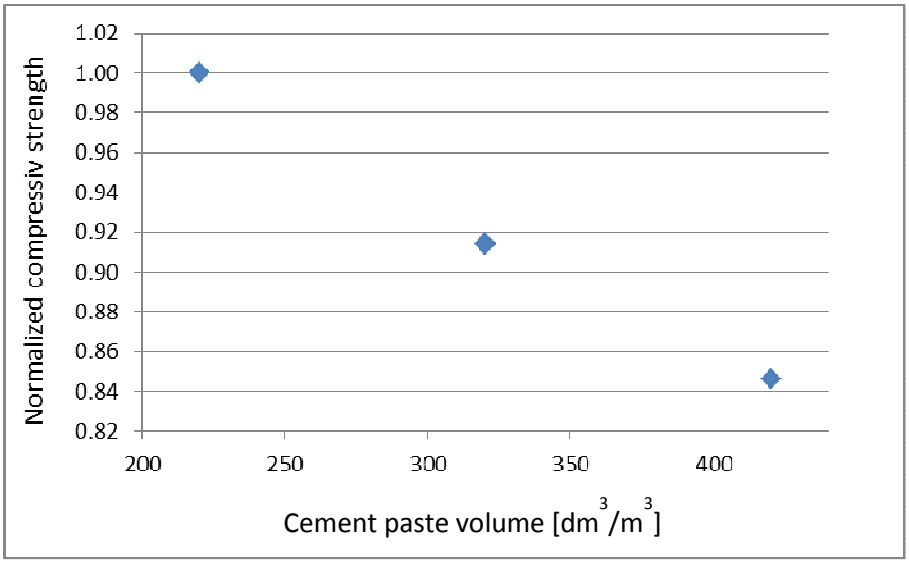

Fig. 2. Relationship between normalized compressive strength and concrete paste volume of w/c ratio = 0.3

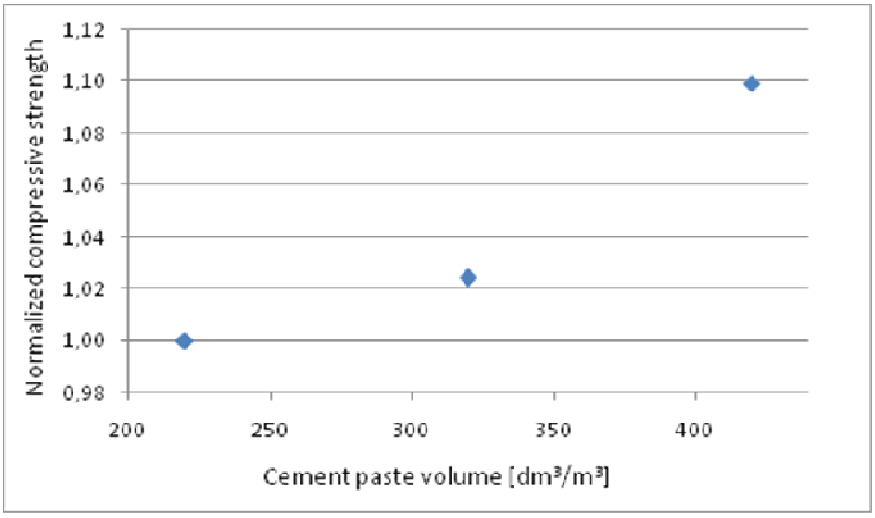

Fig. 3. Relationship between normalized compressive strength and concrete paste volume of w/c ratio = 0.6

4. Conclusion and summary

The above-presented test results make it possible to formulate some conclusions concerning the influence of the paste volume on compressive strength:

1. Concrete compressive strength shows a linear relationship to the volume of paste. Concretes with w/c ratio = 0.6 show a slight correlation between compressive strength results and the volume of paste, contrary to concretes with w/c ratio = 0.3, where this correlation is significant.
2. In the case of high-performance concretes with w/c ratio = 0.3, compressive strength is inversely proportional to the volume of paste while in case of concretes with w/c ratio = 0.6, compressive strength slightly increases in relation to the increase in the volume of paste.
3. In the analyzed range of paste volumes between 220 and 420 dm^3/m^3 relative compressive strength of high-performance concretes changes by 15%, therefore one can assume that an increase in paste volume by 40 dm^3/m^3 causes a relative decrease in strength by 3%.
4. In the case of standard concretes with water-cement ratio equal to 0.6, relative compressive strength changes by 9% in the analyzed range of paste volumes, therefore we can assume that an increase in paste volume by 40 dm^3/m^3 causes an increase in compressive strength by 1.8%.
5. W/c ratio in comparison to the volume of paste occurring in a concrete mixture is a definitely stronger factor of influence on concrete compressive strength.

References

[1] NEVILLE, A. M., *Właściwości betonu*, Polski Cement, Kraków 2000.

[2] ŚLWIŃSKI, J., *Beton zwykły – projektowanie i podstawowe właściwości*, Polski Cement, Kraków 1999.

[3] ZIELIŃSKI, K., *Podstawy Technologii betonu*, Wydawnictwo Politechniki Poznańskiej, Poznań 2012.

[4] KOSTRZANOWSKA, A., *Kształtowanie samozagęszczalności betonów wysokowartościowych*, doctoral dissertation, Gliwice 2011.

[5] SZWABOWSKI, J., GOŁASZEWSKI, J., *Technologia betonu samozagęszczalnego*, Polski Cement, Kraków 2010.

TRANSCOM 2015, 22-24 June 2015
University of Žilina, Žilina, Slovak Republic

Relationship between the roughness and texture of the concrete road pavement

*Wojciech Żebrowski, Łukasz Wójcik
*Kielce University of Technology, Faculty of Civil Engineering and Architecture, Department of Transportation Engineering, al. Tysiąclecia Państwa Polskiego 7, 25-314 Kielce, Poland, {w_zebrowski}@wp.pl, {lukasz.wojcik}@interia.pl

Abstract. The paper presents the method for friction coefficient evaluation using the British pendulum tester and the texture depth evaluation using the sand patch method. The tests aimed to determine the performance parameters of the two-lane single carriageway road in service. The investigated road segment was 400 m long and made of cement concrete. The results from the field measurements, the representative friction coefficient and the mean texture depth, were compared and discussed.

Keywords: coefficient of friction, roughness, texture, diagnostics, cement concrete, British pendulum tester, sand patch test

1. Introduction

During a long service life, a road is periodically diagnosed to evaluate its condition and the variations in the surface characteristics that occur over time. Roughness is one of the basic road surface performance parameters, as it determines proper grip and traction of tyres [4]. Observations of the concrete pavement surfaces indicated that during the service life, the roughness and roughness-related macrotexture are subject to changes. Texture is understood [3] as a surface microprofile, that is, its irregularities.

The studies [2] of the road pavements showed that with microtexture, the adhesion between the wheel and pavement is limited. For this reason, a proper macrotexture needs to be developed at the construction stage.

The paper presents the results from the roughness tests conducted to [6] using the British pendulum and those for the mean texture depth determined according to the volumetric method with the use of a sand patch [5]. The road section under investigation was 400 m long and produced from cement concrete.

2. Methodology

Roughness was determined in the British pendulum test. The British pendulumtester is used in the point measurement of friction characteristics. Its main element, the pendulum is fitted with a rubber slider mounted on the end of its arm to simulate a skid of a wheel on the pavement surface at a speed of 50-60 km/h [4]. The pendulum is released from the horizontal position at an initial angle of inclination and moves in the direction of the vehicle movement. Under the force of gravity, it strikes the investigated surface, which is cleaned and wetted with water, as is the rubber slider. The final inclination of the pendulum defines the friction coefficient [1]. At one contact point, five measurements are made and recorded. The calculated mean from these five readings of each measurement point along the given section yields the representative roughness value for the surface [1, 2, 4, 6].

The measurement results are the basis for computing the representative friction coefficient which is a difference between the friction coefficient mean value and the standard deviation.

Table 1 and table 2 shows required values of the mean friction coefficient.

Class roughness by SOSN	The values of the mean friction coefficient	Assessment of the pavement
A	above 0.48	good
B	0.35 ÷ 0.48	satisfactory
C	0.29 ÷ 0.34	disappointing
D	0.28 or less	bad

Tab.1. The values of the mean friction coefficient included in [8]

Class of road	Element of surfaces	The values of the mean friction coefficient at a speed of 60 km/h
A	Essential traffic lanes, additional traffic lanes, emergency traffic lanes	0,46
	Traffic lanes on and off	0,48
S, GP, G	Traffic lanes, additional traffic lanes, hard shoulders	0,39

Tab.2. The values of the mean friction coefficient according to element of surfaces [7]

Figure 1 shows the British pendulum tester during the test.

Fig. 1. The British Pendulum Tester

In order to determine the depth of the texture, the volumetric patch method was used. The method consists of spreading a known volume of granular material on the clean and dry surface of the pavement and measuring the area covered. The average macrotexture depth is calculated as a difference between the level of grooves and peaks in the surface. The material spread uniformly over the area fills the spaces between the grains up to their peaks. This technique is a repeatable, contact point measurement performed manually [1, 2, 4, 5].

The mean texture depth (MTD) is calculated from formula (1): [5]

$$MTD = 4V / \pi D^2 \tag{1}$$

where:

MTD – the mean texture depth expressed in millimetres (mm);

V – the volume of the granular material expressed in cubic millimetres (mm^3);

D – the average diameter of the circular area covered with the granular material, expressed in millimetres (mm).

Figure 2 shows the volumetric patch method conducted with sand.

Fig. 2. Measurement of texture - the sand patch test

3. Results

The tests were performed on the cement concrete road section 400 m in length for two traffic lanes, 2.5 m wide each. The measurement points for the right and left rut were located every 50 m. Three series of tests were conducted for each measurement point to assess the surface roughness in the British pendulum test. Four series of tests were conducted to assess the mean texture depth.

The results from the tests were analyzed. Roughness measurements for the left traffic lane are summarized in Fig. 3 and those for the right traffic lane are shown in Fig. 4.

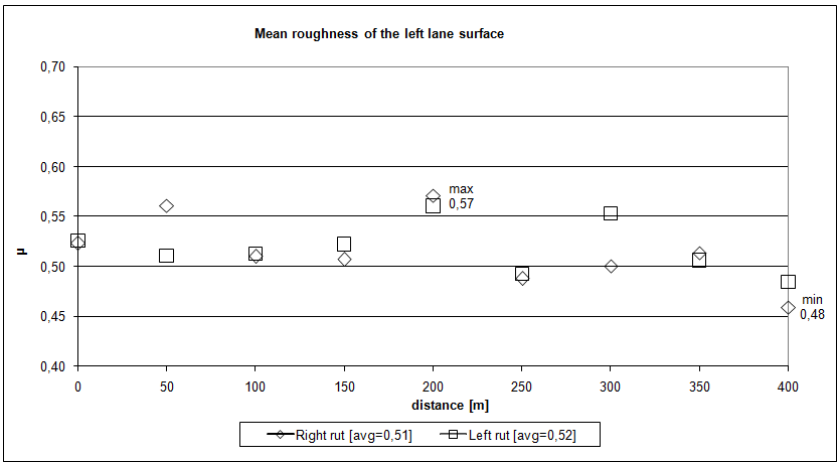

Fig.3. Mean roughness of the left lane surface

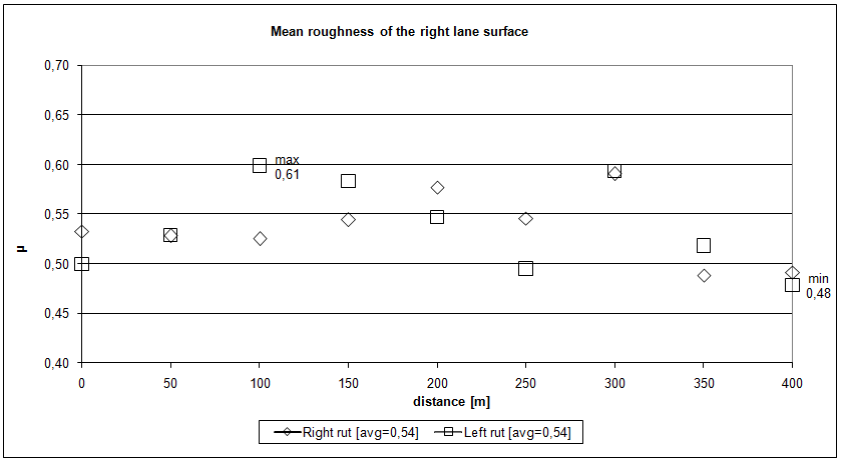

Fig.4. Mean roughness of the right lane surface

The values of the mean friction coefficient satisfy the requirements contained in SOSN [8] for the grip class A and those in [7] for centre lanes. The minimum value of the representative friction coefficient, 0.48, was recorded for the left lane, with the maximum value, 0.61, recorded for the right lane. The difference between the extreme values calculated for the right and left ruts in both lanes does not exceed 0.11.

Figure 5 shows the mean depths of the left lane surface texture, and Fig. 6 presents the mean texture depth results for the right lane.

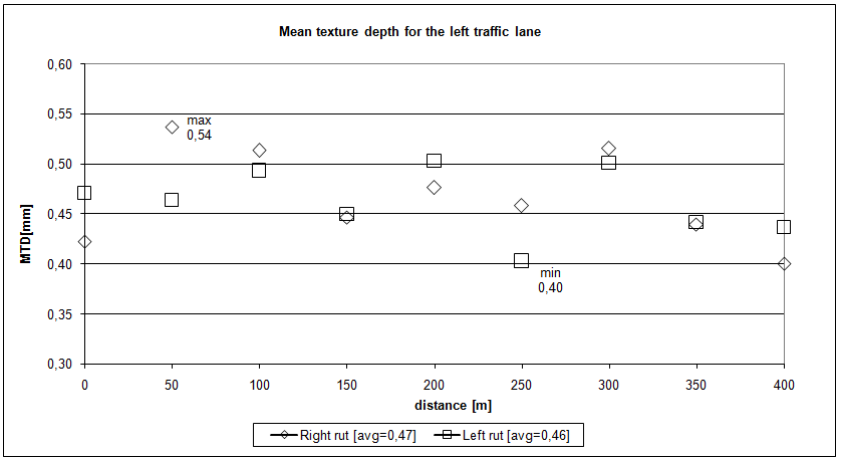

Fig.5. Mean texture depth for the left traffic lane

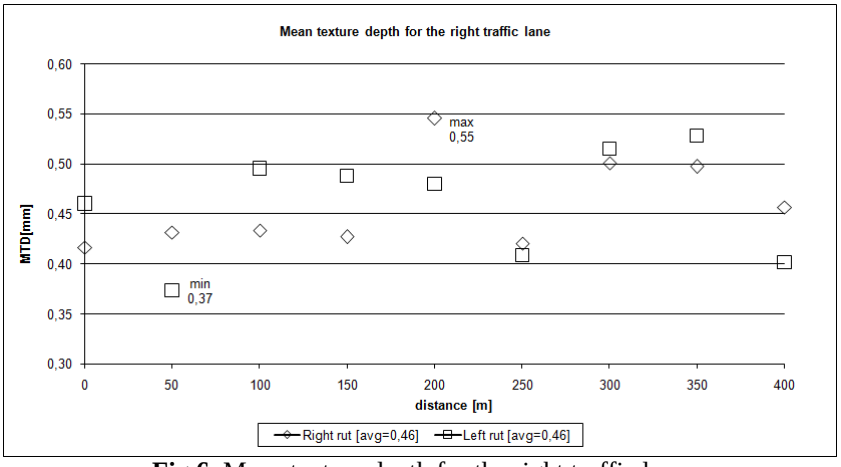

Fig.6. Mean texture depth for the right traffic lane

Table 3 shows ratio correlation between roughness and mean depth texture (MTD).

Ratio correlation	Roughness/MTD			
	Left traffic lane		Right traffic lane	
	Right rut	Left rut	Right rut	Left rut
R^2	0,539	0,795	0,330	0,607

Tab.3. The ratio correlation (R^2) between roughness and MTD.

Comparison of the mean texture depths (MTDs) on the road being investigated shows that the discrepancies between the results are not significant, which indicates good quality of the pavement. For the right carriageway lane the least value recorded was 0.37 mm along the 50m section, with the greatest value of 0.55mm along the 200m section. The values recorded for the left lane are the following: minimum – 0.40mm along the 250m section, maximum 0.54mm along the 50m section. The difference between the extreme values on the right lane for the ruts was 0.18mm, while for the left lane it did not exceed 0.14mm.

4. Conclusion

- For the road section under investigation, the representative friction coefficient values satisfy the requirements set forth in SOSN [8] and the Regulation [7].
- High friction coefficient value is associated with the high depth of the texture.
- The roughness tests conducted with the British pendulum tester or the texture depth tests with the sand patch can be used for assessment of the quality and parameters of pavements.
- Providing proper macrostructure, determinant for the adhesion of a wheel to the pavement, is a key issue during the test section or actual road pavement construction phase.
- The ratio correlation R^2 between roughness and mean depth texture is low, therefore the investigation cannot be used interchangeably.

References

[1] D. Godlewski, Nawierzchnie drogowe, Oficyna Wydawnicza Politechniki Warszawskiej, Warszawa 2011;

[2] A. Szydło, Nawierzchnie drogowe z betonu cementowego. Teoria, wymiarowanie, realizacja, Wydawnictwo Polski Cement, Kraków 2004;

[3] S. Rolla, Nowoczesne nawierzchnie Betonowe, Wadawnictwa Komunikacji i Łączności, Warszawa 1983;

[4] M. Kalabińska, J. Piłat, P. Radziszewski, Technologia materiałów i nawierzchni drogowych, Oficyna Wydawnicza Politechniki Warszawskiej, Warszawa 2008;

[5] PN-EN 13036-1:2010, Cechy powierzchniowe nawierzchni drogowych i lotniskowych. Metody badań. Część 1: Pomiar głębokości makrotekstury metodą objętościową;

[6] PN-EN 13036-4:2011, Drogi samochodowe i lotniskowe. Metody badań. Część 4: Metoda pomiaru oporów poślizgu /poślizgnięcia na powierzchni: Próba wahadła;

[7] Rozporządzenie Ministra Transportu i Gospodarki Morskiej z dnia 2 marca 1999 r. w sprawie warunków technicznych, jakim powinny odpowiadać drogi publiczne i ich usytuowanie. Dziennik Ustaw Nr 43 poz. 430;

[8] System Oceny Stanu Nawierzchni „SOSN", Wytyczne stosowania. GDDP, Warszawa 2002

TRANSCOM 2015, 22-24 June 2015
University of Žilina, Žilina, Slovak Republic

Application of infrared camera in civil engineering

[*]Kinga Ziętala
[*]Kielce University of Technology, Faculty of Civil Engineering and Architecture
Al. 1000-lecia P.P. 7, 25-314 Kielce, Poland,
{kzietala}@tu.kielce.pl

Abstract. The paper presents the use of infrared camera to measure the surface temperature in civil engineering, illustrated with examples of infrared camera application to assess the state of the thermal insulation of building partitions, locate thermal bridges, workmanship of installation but also to observe the phenomenon of heat transfer in minichannels, air handling units and heat exchangers. Some issues related to temperature measurements, especially thermography using infrared radiation, are discussed. It describes the operation of the infrared camera with an indication of the factors affecting the accuracy of measurements. On the basis of the measurements a few applications of the infrared camera in the modern civil engineering are discussed.

Keywords: Infrared thermography, visualizations, thermal camera, infrared radiation.

1. Introduction

In the past, infrared thermography (i.e., non-contact temperature measurement) was used in military operating systems during the First World War. In later years, the main areas of application of IR cameras have become areas such as military technology, medicine, firefighting, industry and construction (it is quite widespread due to the thermal performance analysis) and complex scientific measurements. Infrared technology used to be an expensive testing method, nevertheless, today even small firms may buy simple IR equipment [1, 2].

In recent times, energy conservation has become an important aspect of construction. All over the world, the purpose of modern building is to design the most energy-efficient buildings. Countries of the European Union will have to increase the number of nearly zero-energy buildings, that is, buildings that have a very high energy performance [3]. Consequently, the search for new materials and methods that will isolate the structure from the environment in the best possible way and will allow avoiding energy losses by thermal bridges in the building is being observed. Infrared thermography (IRT) is used to evaluate energy efficiency of the building [4]. Poorly insulated space can be localized in a fast and simple way by using advanced infrared cameras. The result of inadequate insulation or improper performance of an object is heat loss, very well visible on thermograms [5].

Currently, thermal imagers are also studying the issues of heat transfer, which can be used in developing construction. Minichannels can serve as an example, as they can be used as small-sized heat exchangers to be installed where there is a need to save space, e.g. in suspended air handling units.

Heat exchangers are devices for heat transfer between fluids at different temperatures. Heat exchangers appear in various technical fields, and are often called according to their intended use, e.g., heaters, coolers, recuperators, radiators, etc. [6]. In addition to these heat exchangers, minichannels, which can be studied using IR cameras, have attracted significant interest among scientists around the world in recent times [7-11].

2. Infrared thermography - characteristics of measurement method

Infrared thermography is one of the most universal technologies that use detection of infrared radiation. The radiation can be calculated according to the Stefan –Boltzmann law:

$$\frac{q}{A} = s\sigma T^4 \quad (1)$$

where q- is the rate of energy emission (W), A - is the area of the emitting surface (m^2), T - is the absolute temperature (K) , σ - is Stefan–Boltzmann's constant ($\sigma = 5.67x10^{-8}W/(m^2K^4)$), ε - is the emissivity of the emitting surface [12].

Infrared light was discovered by an English astronomer, Sir William Herschel (1738-1822) around 1800. Thermal radiation is emitted by objects with a temperature higher than absolute zero (-273 °C/0 K). Infrared radiation is electromagnetic radiation and has a thermal nature. The electromagnetic spectrum is associated with electromagnetic radiation, and it is divided wavelength band differentiated by generating and detection of radiation. The difference between these bands is different wavelength, as illustrated in figure 1. Spectrum of infrared radiation was used in the study of infrared cameras. The infrared radiation region is between visible light and microwaves within the wavelength spectrum of 0.7 – 100 µm. The infrared spectrum can be divided into several spectral regions, which are contractually defined as: near-infrared (NIR, 0.78 – 1 µm), short wavelength IR (SWIR, 1 – 3 µm), mid-wavelength IR (MWIR, 3 – 6 µm), long-wavelength IR (LWIR, 6 – 15 µm) and far-infrared (FIR, 15 – 1000 µm) [13-14].

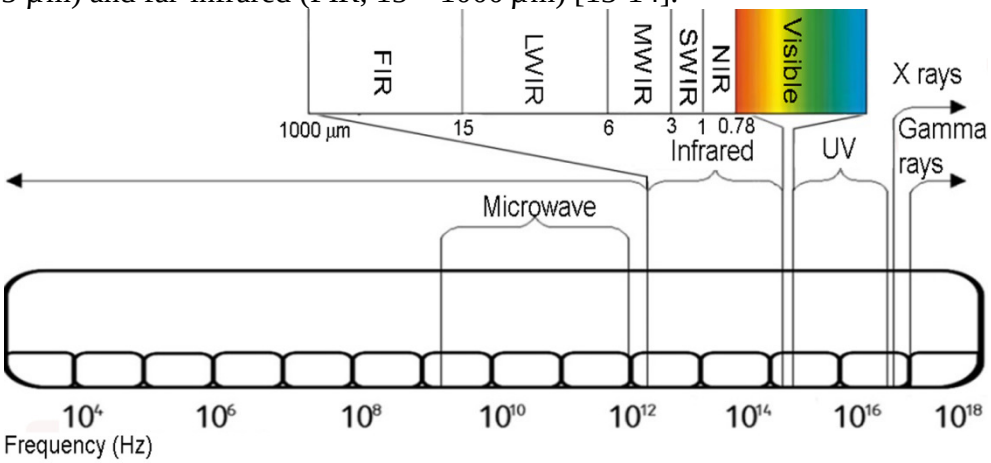

Fig. 1. The division of electromagnetic radiation as a function of wavelength [7].

In thermal radiation, a blackbody is an object that absorbs all incident radiations and radiates a continuous spectrum. The blackbody is defined according to Planck's law:

$$L_\lambda = \frac{c_1}{\lambda^5 [\exp\left(\frac{c_2}{\lambda T}\right) - 1]} \quad (2)$$

where λ - is the wavelength of the radiation (µm), L_λ - is the power radiated by the blackbody per unit surface and per unit solid angle for a particular wavelength ($W/(m^2\mu m^1 sr^1)$), T - is the temperature in absolute scale (K), c_1, c_2 - are the first and second radiation constants respectively [12].

In the case of real objects, in addition to the absorption of thermal radiation there is also emissivity and reflection. In the study of infrared thermography, the emissivity of the object is an important parameter as it determines the ratio of radiation emitted from an object (real body) to the radiation emitted from a blackbody at the same temperature. The emissivity is in the range from 0 to 1 and determines the ability of the test object to emit its own energy. When the emissivity has a value close to unity, the measurement is more accurate. Emissivity of roughened and metallic surfaces is difficult to determine. Devices with known emissivity are used to study such surfaces. When the emissivity of the test surface is not known, two solutions are possible. The first solution is to stick the foil to the surface of an object with known emissivity. The second option is to paint

the object with a thin layer of paint or oil with known parameters. A good knowledge of this coefficient reduces measurement errors, and allows obtaining reliable test results [15, 1].

3. Thermal camera - characteristics and design

An infrared camera is a device that is used for non-contact measurements and non-destructive thermal studies (NDTT). Infrared camera sensor converts the radiation to a physical quantity (images). The images are then transformed electrically into temperature parameters of the test surface. Infrared cameras show the temperature distribution over the entire surface of the test object on a thermogram [16, 17].

Infrared camera is characterized by a number of parameters. The most important of these is the subjective video quality perceived by the human. There are two standards that present detailed measurement procedures of the minimum resolvable temperature differences (MRTD) and the minimum detectable temperature difference (MDTD) of infrared cameras for NDTT applications. IR camera images are interpreted by people, which can affect the image quality and the temperature distribution of the test surface [16].

The literature reports different criteria for the classification of infrared cameras (IR). One of the options is to divide IR cameras into two main groups: thermal imaging cameras for monitoring and thermal imaging cameras for measuring. IR cameras for monitoring are most often used in the military applications to make observations in the dark or in difficult weather conditions. Infrared cameras are used for measurements in civil applications in industry, science, and laboratory tests for contactless temperature measurement, as well as to measure the relative or absolute temperature.

Research carried out using IR cameras is two-dimensional, i.e., the resulting image allows the user to preview the object. After the measurement, the IR camera image is recorded on a computer screen in the form of a drawing in JPG (*Flir*) or BMP (*VIGO*) and assigned to the corresponding thermogram [18].

A thermogram (an image illustrating the temperature) is a type of image showing the surface of objects. The infrared camera image is formed by sending and reflecting through the tested object the infrared radiation invisible to humans. This technique allows determining a surface temperature distribution in a short time. Lighting us not necessary to record temperatures using this technique. Research IR cameras can also be used at night because every object sending infrared radiation is visible on the thermogram [19]. Figure 2 shows the design of an IR camera.

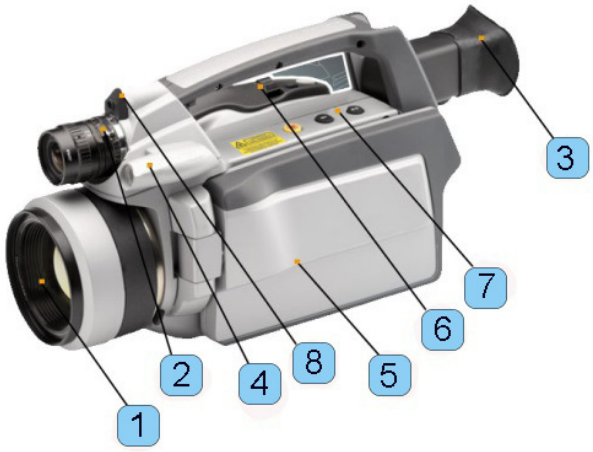

Fig. 2. Design of an infrared camera: 1-lens, 2-digital camera, 3-tilting eyepiece, 4-lamp, 5-LCD monitor, 6-handle, 7-software buttons, 8-laser pointer.

Infrared thermography provides visual image records that are qualitative (image) and quantitative (temperature) information for deeper knowledge of thermal conditions and thermodynamic processes in the research object. The infrared camera allows measuring static

conditions and monitoring dynamic processes in a laboratory. To accurately analyze and interpret thermograms recorded, a good knowledge of the properties of the object, the material, the effect of climatic conditions is required, along with the knowledge of measurement techniques. The sources of interference occurring in practice are an important issue when testing infrared cameras.

These include: the impact of sunlight on the test object, a hot heating element (i.e. radiator), lamp light incident on the test surface, air flow, or the effect of moisture on the test object [18, 20]

Two infrared cameras were used in the study: *Flir type SC640* and *VIGO System S.A* type *VIGOcam v50*. Technical specifications of both IR cameras are shown in Table 1.

Type of IR camera	**Flir type SC640**	**VIGO System S.A type VIGOcam v50**
Detector	Focal Plane Array (FPA), uncooled microbolometer 640 x 480 pixels	FPA (Focal Plane Array) microbolometer 384 x 288 pixels
Spectral range	7.5 to 13 µm	8 - 14 µm
Field of view	24°x18°	22°x16°
Min focus distance	0.3 m	0.5 m
Spatial resolution (IFOV)	0.65 mrad	0.71 mrad
Thermal sensitivity	60 mK at 30°C	≤0.08°C for 30°C
Image frequency	30 Hz non-interlaced	30/60 Hz
Focus	automatic or manual	manual
Zoom	electronic, 1 - 8 x continuous	digital x2, x4
Temperature range	-40 °C to +1,500 °C, in 3 ranges; up to + 2000°C, optional	-10 to 100 °C, 0 to 350 °C or individually specified up to 1500 °C
Accuracy	±2 °C, ±2 % of reading	±2 °C, ±2 % of range, whichever is higher
Operating temperature range	-20 °C to 40 °C	-20 °C to 40 °C
Storage temperature range	-40 °C to +70 °C	30 °C to 70 °C

Tab. 1. Technical specification [18, 21].

4. Examples of the measurements

In the construction industry buildings consume significant amount of energy - in the winter for heating purposes, and in the summer – for air cooling. Reducing heat losses can lead to considerable reductions in the amount of energy consumed. Infrared thermography can be a useful tool.

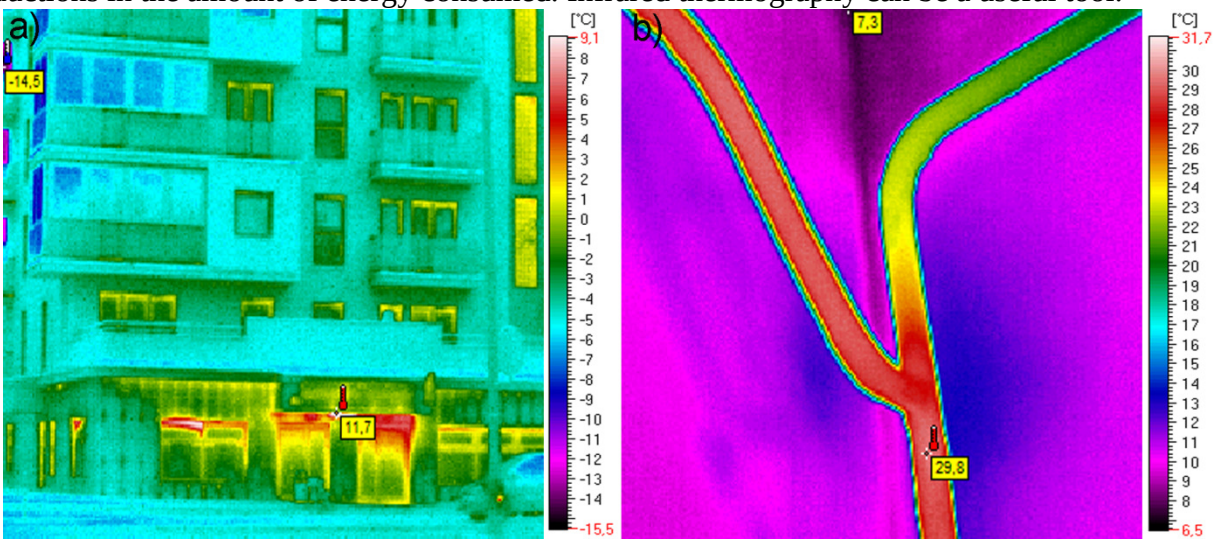

Fig. 3. Examples of thermal images: a) the façade of a multi-storey building, b) central heating pipes.

The figures show the author's own thermograms made using two IR cameras: VIGO (Fig. 3 and
Fig. 4) and Flir (Fig. 5). Figure 3a presents the façade thermogram of a multi-storey building with thermal bridges located at the corners of the doors and windows (areas of elevated temperature shown in red). Particularly large heat losses are shown on the ground floor of the building, which may indicate that the mounting of doors and windows was incorrect.

An infrared camera can be used to verify the correctness of the completed installation. Sometimes the defects made during the installation are difficult to identify. Infrared cameras make it possible to locate them. Figure 3b shows the execution of the central heating pipes. As can be seen, this system is badly balanced because one a pipe has lower and the second higher temperature. Consequently, heat distribution to the individual radiators is incorrectly balanced. The temperature difference between the two pipes from the main distribution pipes is about 8 °C.

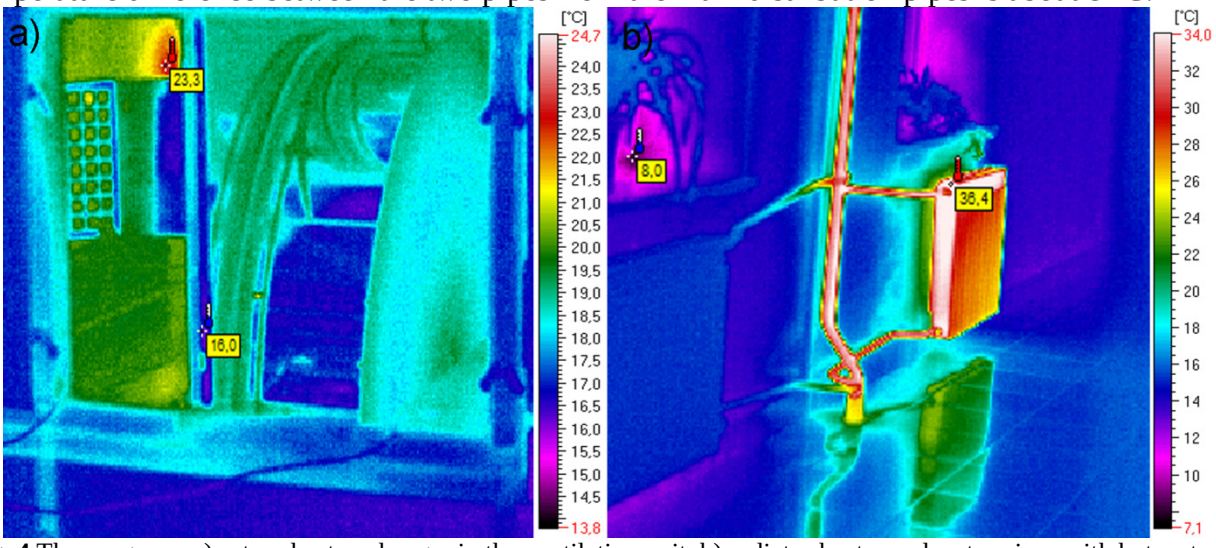

Fig. 4 Thermograms a) rotary heat exchanger in the ventilation unit, b) radiator heater and water pipes with hot water (inflow) and slightly colder water (outflow).

Figure 5a shows a thermogram of the heating foil surface (of the rectangular minichannel) obtained by infrared thermography. The thermogram presents the heating surface temperature distribution along the distance from the minichannel inlet.

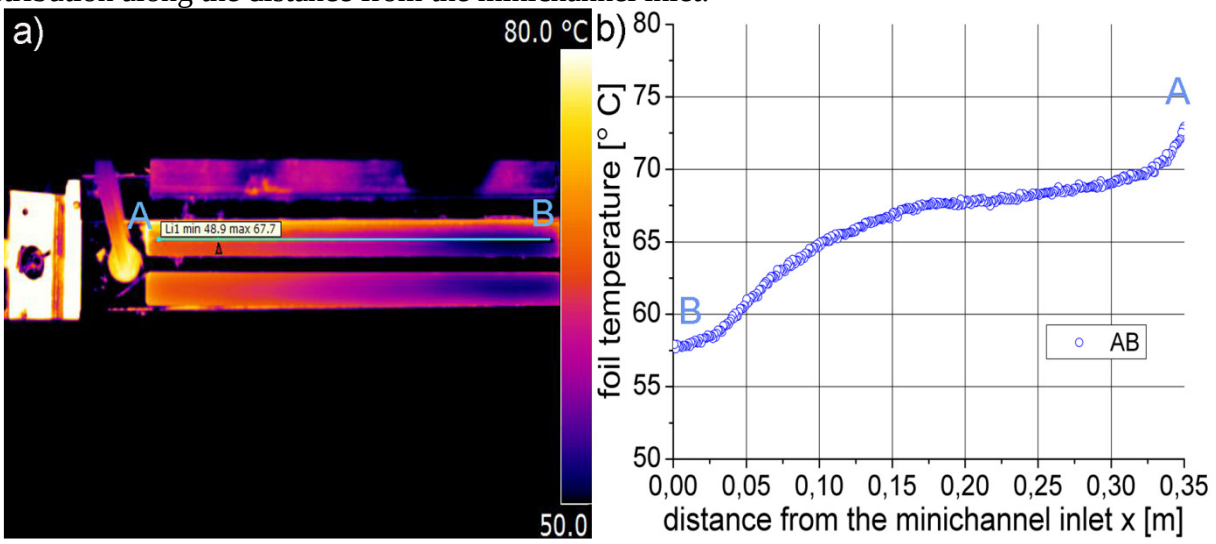

Fig. 5 a) A thermogram of the heating foil surface obtained by infrared thermography, b) heating foil temperature vs. the distance along the length of the minichannel.

Figure 5b shows a graph of temperature distribution relative to the distance between points B - A. The temperature increases with the distance from the minichannel inlet. Temperature distribution along these points is in the range of approximately 58 °C to 74 °C.

5. Conclusions

Infrared thermography measurements are becoming more common in various areas of construction and in areas that are closely connected to it. Such areas are, for example, ventilation, air conditioning and heat transfer. Availability of test systems IR is associated with lower hardware prices. This enables their wide application in many fields such as construction for analyzing heat loss in buildings, measuring components of heating systems, and ventilation systems. Owing to such a wide range of thermovision applications, this method will undoubtedly become more widespread.

References

[1] KARWAT, T. Termowizja - zasady ogólne, środowisko pomiarowe, budowa kamer, przykłady zastosowania, Izolacje 5, 2008, 33-36 (in Polish).
[2] MINKINA, W. A., RUTKOWSKI, P., WILD, W. A. *Podstawy pomiarów termowizyjnych, Pomiary, automatyka kontrola 1*, 2000, 7-14 (in Polish).
[3] ŻMIJEWSKI, K. *Nearly zeroenergy buildings.* Materiały budowlane, 1 (2013), No. 485 (in Polish).
[4] MOLIN, A., ROHDIN, P., MOSHFEGH, B. *Investigation of energy performance of newly built low-energy buildings in Sweden*. Energy & Buildings, October 2011, 43, 10, 2822-2831.
[5] OCAÑA, S. M., GUERREROA, I. C., REQUENA, I. G. *Thermographic survey of two rural buildings in Spain.* Energy and Buildings, June 2004, 36, 6, 515-520.
[6] WIŚNIEWSKI, S., WIŚNIEWSKI, T. S. *Wymiana ciepła*, WNT, Warszawa 2012 (in Polish).
[7] ZIĘTALA, K., PIASECKA, M. *Bezkontaktowe metody pomiaru temperatury powierzchni stosowane w badaniach wymiany ciepła w minikanałach*, Logistyka 6, 2014, 11784-11793 (in Polish).
[8] PIASECKA, M., MACIEJEWSKA, B., ZIĘTALA, K. *Research on flow boiling in minichannels with enhanced heating walls using liquid crystal thermography and infrared thermograph*, 9th International Conference on Boiling and Condensation Heat Transfer April 26-30, 2015 – Boulder, Colorado, in press.
[9] MEHTA, B., KHANDEKAR, S. *Infra-red thermography of laminar heat transfer during early thermal development inside a square mini-channel*, Experimental Thermal and Fluid Science 42, 2012, 219–229.
[10] PIASECKA, M., MACIEJEWSKA, B. *Enhanced heating surface application in a minichannel flow and the use of the FEM and Trefftz functions for the solution of inverse heat transfer problem*, Experimental Thermal and Fluid Science 44, 2013, 23–33.
[11] PIASECKA, M. *Heat transfer mechanism, pressure drop and flow patterns during FC-72 flow boiling in horizontal and vertical minichannels with enhanced walls,* International Journal of Heat and Mass Transfer 66, 2013, 472–488.
[12] BAGAVATHIAPPAN, S., LAHIRI, B., B., SARAVANAN, T., PHILIP, J., JAYAKUMAR, T. *Infrared thermography for condition monitoring – A review.* Infrared Physics & Technology 60, 2013, 35–55
[13] GADE, R., MOESLUND, T. B., *Thermal cameras and applications: a survey*, Machine Vision and Applications 25, 2014, 245–262.
[14] ROGALSKI, A., CHRZANOWSKI, K. *Infrared devices and techniques*, OPTO-ELECTRONICS REVIEW 10(2), 2002, 111–136.
[15] PIASECKA, M., PASTUSZKO, R. *Wyznaczanie pól temperatury przy zastosowaniu termografii ciekłokrystalicznej oraz kamery termowizyjnej w badaniach wymiany ciepła w minikanałach*, PAK 6, 2005, 23-26 (in Polish).
[16] CHRZANOWSKI, K., PARK, S. N., *Evaluation of thermal cameras for non-destructive thermal testing applications*, Infrared Physics & Technology 42, 2001, 101-105.
[17] PIOTROWSKI, J., BUCHCZIK, J., ILLEWICZ, W. *Pomiary. Czujniki i metody pomiarowe wybranych wielkości fizycznych i składu chemicznego*, WNT, Warszawa 2009 (in Polish).
[18] *User's manual ThermaCam B640, P640, SC640*, Publ. No 155850 Rev.a 201-ENGLISH (EN), 2007.
[19] PICHNIARCZYK, P., ZDUNIEWICZ, T. *Wykorzystanie w budownictwie metody termowizji w podczerwieni*, Izolacje 7/8, 2010 (in Polish).
[20] PEŠEK, M., PECH, O. The determination of field usability of method measuring temperature fields in the air using an infrared camera, EPJ Web of Conferences 67, 02091, 2014.
[21] VIGO System S.A: *VIGOcam v50.*

TRANSCOM 2015

Proceedings, Section 7

Published by University of Žilina
First Editions
Printed by EDIS - Žilina University publisher
Printed in 500 copies

ISBN 978-80-554-1049-4
ISSN of Transcom Proceedings CD-Rom version: 1339-9799
ISSN of Transcom Proceedings online version: 1339-9829
(http://www.transcom-conference.com/transcom-archive)


9 788055 410494